

AD-A256 711



PL-TR-92-2210

ENVIRONMENTAL RESEARCH PAPERS, NO. 1106

2

PROCEEDINGS OF THE 14TH ANNUAL
PL/DARPA SEISMIC RESEARCH SYMPOSIUM,
16-18 SEPTEMBER 1992

DTIC
ELECTE
SEP 14 1992
S A D

Editors:

James F. Lewkowicz

Jeanne M. McPhetres

17 August 1992

92-25065



APPROVED FOR PUBLIC RELEASE; DISTRIBUTION UNLIMITED



PHILLIPS LABORATORY
Directorate of Geophysics
AIR FORCE MATERIEL COMMAND
HANSCOM AIR FORCE BASE, MA 01731-5000

92 9 11 015

"This technical report has been reviewed and is approved for publication."

Katharine Kadinsky-Cade
KATHARINE KADINSKY-CADE
Acting Branch Chief
Solid Earth Geophysics Branch
Earth Sciences Division

Donald H. Eckhardt
DONALD H. ECKHARDT
Director
Earth Sciences Division

This report has been reviewed by the ESD Public Affairs Office (PA) and is releasable to the National Technical Information Service (NTIS).

Qualified requestors may obtain additional copies from the Defense Technical Information Center. All others should apply to the National Technical Information Service.

If your address has changed, or if you wish to be removed from the mailing list, or if the addressee is no longer employed by your organization, please notify PL/IMA, Hanscom AFB, MA 01731-5000. This will assist us in maintaining a current mailing list.

Do not return copies of this report unless contractual obligations or notices on a specific document requires that it be returned.

| REPORT DOCUMENTATION PAGE | | | Form Approved OMB No. 0704-0188 | |
|----------------------------------------------------------------------------------------------------------------------------------------------------------------------------------------------------------------------------------------------------------------------------------------------------------------------------------------------------------------------------------------------------------------------------------------------------------------------------------------------------------------------------------------------------------------------------------------------------------------------------------------------------------------------------------------------------------------------------------------------------------------------------------------------------------------------------------------------------------------------------------------------------------------------------------------------------------------------------------------------------------------------------------------------------------------------------------------------------------------------------------------------------------------------|----------------------------------------------------------|----------------------------------------------------------------------------|------------------------------------|--|
| Public reporting burden for this collection of information is estimated to average 1 hour per response, including the time for reviewing instructions, searching existing data sources, gathering and maintaining the data needed, and completing and reviewing the collection of information. Send comments regarding this burden estimate or any other aspect of this collection of information, including suggestions for reducing this burden, to Washington Headquarters Services, Directorate for Information Operations and Reports, 1215 Jefferson Davis Highway, Suite 1204, Arlington, VA 22202-4302, and to the Office of Management and Budget, Paperwork Reduction Project (0704-0188), Washington, DC 20503. | | | | |
| 1. AGENCY USE ONLY (Leave blank) | 2. REPORT DATE 17 August 1992 | 3. REPORT TYPE AND DATES COVERED Scientific, Final | | |
| 4. TITLE AND SUBTITLE Proceedings of the 14th Annual PL/DARPA Seismic Research Symposium, 16-18 September 1992 | | 5. FUNDING NUMBERS PE 61102F PR 2309 TA G2 WU 10 | | |
| 6. AUTHOR(S) Editors: James F. Lewkowicz Jeanne M. McPhetres | | | | |
| 7. PERFORMING ORGANIZATION NAME(S) AND ADDRESS(ES) Phillips Laboratory (GPEH) Hanscom AFB, MA 01731-5000 | | 8. PERFORMING ORGANIZATION REPORT NUMBER PL-TR-92-2210 ERP, No. 1106 | | |
| 9. SPONSORING/MONITORING AGENCY NAME(S) AND ADDRESS(ES) DARPA/NMRO 3701 North Fairfax Drive Arlington, VA 22203-1714 | | 10. SPONSORING/MONITORING AGENCY REPORT NUMBER | | |
| 11. SUPPLEMENTARY NOTES This research was supported by DARPA under PE 62714E. | | | | |
| 12a. DISTRIBUTION/AVAILABILITY STATEMENT Approved for Public Release; distribution unlimited | | 12b. DISTRIBUTION CODE | | |
| 13. ABSTRACT (Maximum 200 words) These Proceedings contain papers presented at the Fourteenth Annual PL/DARPA Seismic Research Symposium held 16-18 September 1992, in Tucson, Arizona. PL's Solid Earth Geophysics Branch (GPEH) manages its own Air Force funded basic research program in verification seismology and is the Technical Agent for part of the DARPA Nuclear Monitoring Research Office's (NMRO) research program in the same field. Representatives from the new Air Force Office of Scientific Research (AFOSR) program in this field attended the Symposium and are expected to collaborate closely with GPEH in the future. Also present were representatives of the Air Force Technical Applications Center (AFTAC), user of this technology. Other interested participating Government agencies include the Department of Energy, the National Science Foundation and the U.S. Geological Survey. The scientific objectives of the research programs are to improve the Air Force's capability to seismically detect, locate, identify, and estimate the yield of underground nuclear explosions. The purpose of this Symposium, organized | | | | |
| 14. SUBJECT TERMS underground nuclear explosions, discrimination, intelligent processing of seismic signals, regional seismic waves and sources, yield estimation | | 15. NUMBER OF PAGES 486 | | |
| | | 16. PRICE CODE | | |
| 17. SECURITY CLASSIFICATION OF REPORT UNCLASSIFIED | 18. SECURITY CLASSIFICATION OF THIS PAGE UNCLASSIFIED | 19. SECURITY CLASSIFICATION OF ABSTRACT UNCLASSIFIED | 20. LIMITATION OF ABSTRACT UL | |

annually by GPEH and assisted this year by the University of Arizona, Tucson, is to provide the sponsoring agencies an opportunity to review research, particularly contractor research, accomplished during the preceding year and outline areas of investigation for the coming year. For the researchers, it provides a forum for the exchange of scientific information to help achieve program goals, and an opportunity to meet with AFOSR, GPEH and NMRO staff to discuss results and future plans. In addition, the Symposium and the technical presentations serve as an important avenue for technology transition to AFTAC and other Government agencies. The papers include studies of the identification and characterization of seismic explosion sources (discrimination), intelligent processing of regional seismic signals, the acquisition and processing of seismic data from the Former Soviet Union, regional seismic wave propagation from both an empirical and theoretical viewpoint, and yield estimation.

TABLE OF CONTENTS

| | <u>PAGE</u> |
|---------------------------------------------------------------------------------------------------------------------------------------------------------------------------|-------------|
| Baek, J.; Gray, H.L.; McCartor, G.D.; Woodward, W.A.; and Fisk, M.D. <i>A Generalized Likelihood Ratio Test in Outlier Detection or Script Matching</i> | 1 |
| Barker, Jeffrey S. <i>Analysis of Regional Bodywave Phases from Earthquakes in West China</i> | 8 |
| Barker, Terrance G. and McLaughlin, Keith L. <i>Numerical Models of Quarry Blast Sources</i> | 15 |
| Baumgardt, Douglas R. <i>Regional Seismic Event Discriminants: What Works, What Doesn't, and Why</i> | 22 |
| Bennett, Theron J.; Scheimer, James F.; Campanella, Antoinette K.; and Murphy, John R. <i>Seismic Discrimination of Rockbursts in Mines</i> | 29 |
| Benz, H.M.; Unger, J.D.; and Leith, W.S. <i>Deep Seismic Sounding in Northern Eurasia: Interpretation of the Murmansk-Kizil Ultra-Long-Range Profile</i> | 36 |
| Boitnott, G.N. <i>Non-linear Attenuation in the Near Source Region: Characterization of Hysteresis in the Deformation of Rock Joints</i> | 48 |
| Cansi, Y.; Plantet, J.L.; and Massot, J.P. <i>Epicentral Azimuth Determination by Mini Array Processing</i> | 55 |
| Chapman, Martin C.; Bollinger, G.A.; and Sibol, M.S. <i>Source Function Deconvolution of Delay-Fired Explosions and Earthquakes at Regional Distances</i> | 63 |
| Chun, Kin-Yip; Zhu, Tianfei; and Shih, Xiao Rung <i>Regional Wave Attenuation in Eurasia</i> | 69 |
| Clouser, Robert H. and Langston, Charles A. <i>Effects of an Irregular Free Surface and Moho on Regional Wave Propagation</i> | 76 |
| Comer, Robert P.; Marcus, David J.; and White, James V. <i>Global Seismic Evidence Combination</i> | 79 |

| Availability Codes | |
|--------------------|----------------------|
| Dist | Avail and/or Special |
| A-1 | |

| | <u>PAGE</u> |
|----------------------------------------------------------------------------------------------------------------------------------------------------------------------------------------------------------------------------------------|-------------|
| Cormier, Vernon F. <i>Generalized Ray/Born Synthesis of Complete Regional Seismograms in Three-Dimensional Crustal Models.....</i> | 86 |
| Davis, J.P. and Henson, I.H. <i>An X-Windows Graphics Tool to Compute Synthetic Seismograms for 2-D Models Using Gaussian Beams.....</i> | 92 |
| Davis, Paul M.; Gao, Shanxing; Liu, Hong; and Slack, Philip D. <i>Seismic Array Study of the Baikal Rift Zone, Siberia.....</i> | 99 |
| Day, Steven M.; Minster, J. Bernard; and Yu, Lois <i>Numerical Simulation of Nonlinear Attenuation Using an Endochronic Formulation.....</i> | 111 |
| Der, Zoltan A.; Hirano, Michael R.; Baumgardt, Douglas R.; and Shumway, Robert H. <i>Applications of Array Spectral Factorization Methods to Regional Seismic Discrimination and Three-Component Processing.....</i> | 118 |
| Fielding, Eric J.; Isacks, Bryan L.; and Barazangi, Muawia <i>A Network-Accessible Geological and Geophysical Database for Eurasia.....</i> | 125 |
| Fisk, Mark D.; Gray, Henry L.; and McCartor, Gary D. <i>Multivariate Seismic Calibration for the Novaya Zemlya Test Site.....</i> | 132 |
| Grant, Lori and Coyne, John <i>Ground-Truth Data for Seismic Discrimination Research.....</i> | 139 |
| Gupta, I.N. and Davis, J.P. <i>High-Precision Relative Event Location with Cross-Spectral Analysis and Related Studies.....</i> | 146 |
| Gurrola, Harold; Minster, Bernard; and Owens, Tom <i>Depths of Upper Mantle Discontinuities Beneath Broad Band Seismic Stations by Velocity Spectrum Stacks of Receiver Functions.....</i> | 153 |
| Harjes, H.-P.; Gestermann, N.; Jost, M.L.; Schweitzer, J.; and Wüster, J. <i>Site Effects, Regional Wave Path and Source Characteristics at GERESS.....</i> | 160 |
| Harkrider, D.G. <i>Single Station Time Domain Time Estimates of Semipalatinsk Moments.....</i> | 167 |

| | <u>PAGE</u> |
|-----------------------------------------------------------------------------------------------------------------------------------------------------------------------------------------------------|-------------|
| Helmberger, D.; Zhao, L.; and Dreger, D. <i>Source Estimation from Regional Seismograms.....</i> | 173 |
| Henson, Ivan and Cessaro, Robert <i>Source Multiplicity Examined with Minimum Entropy Deconvolution.....</i> | 180 |
| Herrmann, R.B.; Al-Eqabi, G.; and Hutchensen, K. <i>High Frequency Wave Propagation.....</i> | 187 |
| Husebye, E.S.; Ruud, B.O.; and Hestholm, S. <i>Eurasian Seismic Surveillance: 2D FD Seismic Synthetics and Event Discrimination.....</i> | 193 |
| Jih, Rong-Song and Lynnes, Christopher S. <i>Re-examination of Regional Lg Q Variation in Iranian Plateau.....</i> | 200 |
| Jih, R.-S.; Wagner, R.A.; and Shumway, R.H. <i>Path-Corrected Body-Wave Magnitudes and Yield Estimates of Soviet Nuclear Explosions.....</i> | 207 |
| Johnson, Lane R. and McEvilly, T.V. <i>Wave Propagation Near Explosive Sources.....</i> | 214 |
| Kafka, Alan L. and Jacobson-Carroll, Matthew R. <i>Variation of Amplitudes and Waveforms of Seismic Phases Recorded by a Small-Aperture Array Surrounding Weston Observatory.....</i> | 219 |
| Katz, Simon and Aki, Keitti <i>High Resolution Algorithms for Adaptive Beam-Forming and Adaptive Polarization Analysis.....</i> | 226 |
| Kennett, B.L.N. <i>The Distance Dependence of Regional Discriminants.....</i> | 233 |
| Kennett, B.L.N. <i>Phase Identification and Location for Regional and Teleseismic Events.....</i> | 239 |
| Kim, Won-Young; Richards, Paul G.; and Shi, Jinghua <i>Studies of RMS Lg Data.....</i> | 245 |
| Koch, Karl and Stump, Brian W. <i>Far-Regional Seismogram Analysis for the Western United States and the Role of Short-Period Mantle S Waves.....</i> | 252 |

| | <u>PAGE</u> |
|---------------------------------------------------------------------------------------------------------------------------------------------------------------------------------------------------------------------------------------------------|--------------------|
| Kværna , Tormod; Mykkeltveit , Svein; Ringdal , Frode; and Fyen , Jan <i>Concepts for Processing of Data from a Network of Regional Arrays</i> | 260 |
| Lacoss , R.T.; Curtis , S.R.; and Cunningham , R.K. <i>Seismic Phase and Event Recognition Using Algorithms that Learn from Examples</i> | 267 |
| Lay , Thorne; Xie , Xiao-bi; and Zhang , Tianrun <i>Lg Propagation in Eurasia</i> | 274 |
| Magnier , S.A.; Minster , J.B.; and Orcutt , J.A. <i>Finite Difference Modeling of Scattering by a Minimal Grid Technique</i> | 282 |
| Mangino , Stephen and Ebel , John <i>The Receiver Structure Beneath the Chinese Digital Seismograph Network (CDSN) Stations: Preliminary Results</i> | 289 |
| Matzko , R. <i>Geology of the Chinese Nuclear Test Site Near Lop Nor, Xinjiang Province, China</i> | 297 |
| Murphy , J.R.; Barker , B.W.; Jenab , J.N.; and Marshall , M.E. <i>Yield Estimation Research</i> | 304 |
| Pan , Y.; Mitchell , B.J.; Xie , J.; and Ni , J. <i>Lg Coda Q Across Northern Eurasia</i> | 311 |
| Patnaik , Gagan B.; Sereno , Thomas J.; Mortell , Mari J.; and Jenkins , Richard D. <i>A Regional Seismic Data Set, and Results on Automated Interpretation of Seismic Data Using Neural Networks</i> | 318 |
| Patton , Howard J. and Walter , William R. <i>Regional Moment: Magnitude Relations for Earthquakes and Explosions</i> | 325 |
| Priestley , Keith F. and Cipar , John <i>From Rift to Rift: The Yamal Peninsula-Lake Baikal Deep Seismic Sounding Profile</i> | 330 |
| Pulli , Jay J. and Dysart , Paul S. <i>Neural Network Processing of Seismic Signal Parameters for Small Event Identification</i> | 337 |

| | <u>PAGE</u> |
|---------------------------------------------------------------------------------------------------------------------------------------------------------------------------------------------------------------------------|-------------|
| Richards, Paul G.; Kim, Won-Young; and Ekström, Göran <i>Initial Visit to the Borovoye Geophysical Observatory, North Kazakhstan.....</i> | 344 |
| Saikia, C.K.; Helmberger, D.V.; and Burdick, L.J. <i>Regional Wave Propagation and High-Frequency/Low-Frequency Energy Level Discriminant.....</i> | 351 |
| Schwartz, Susan Y. and Mandel, Ron <i>Characterization of Regional Phase Propagation in Eurasia Using Data from Historic Nuclear Explosions in the U.S.S.R.....</i> | 361 |
| Schwartz, Susan Y.; Lay, Thorne; and Beckers, Joseph <i>Analysis of the Effects of Eurasian Crustal and Upper Mantle Structure on Regional Phases Using Broadband Seismic Data.....</i> | 369 |
| Shearer, Peter; Masters, Guy; and Orcutt, John <i>Limits on Aspherical Structure in the Outer Core.....</i> | 375 |
| Shumway, Robert H. <i>Multivariate Calibration and Yield Estimation.....</i> | 381 |
| Stagat, R.; Wortman, W.; Terry, D.; Moore, S.; Froli, M.; McLaughlin, K.; Peyton, S.; and Ahrens, T. <i>CORRTEX Analysis System.....</i> | 387 |
| Stump, Brian W. and Yang, Xiaoning <i>Equivalent Seismic Source Functions for Chemical and Nuclear Explosions.....</i> | 394 |
| Suteau-Henson, A.; Ryaboy, V.Z.; Rivière-Barbier, F.; Israelsson, H.; and Carter, J.A. <i>Analysis of IMS Locations of Mine Blasts and RMS LG Magnitudes in Scandinavia.....</i> | 401 |
| Swanger, H. J.; Sereno, T. J.; Williams, D. J.; and Ryall, F. <i>Eurasian Bulletin Produced by the Intelligent Monitoring System from Four Arrays and Six IRIS/IDA Stations.....</i> | 408 |
| Sykes, Lynn R. and Lyubomirskiy, Paul <i>Analysis of Small Seismic Events Near Azgir, Kazakhstan: Implications for Identifying Chemical and Decoupled Nuclear Explosions in a Major Salt Dome Province.....</i> | 415 |

| | <u>PAGE</u> |
|----------------------------------------------------------------------------------------------------------------------------------------------------------------------------------------|--------------------|
| Taylor, D.W.A. and Leonard, S.K. <i>Generalized Beamforming for Automatic Association.....</i> | 422 |
| Thurber, Clifford H. and Quin, Howard R. <i>Location and Waveform Modeling of Shagan River Nuclear Explosions from Satellite Images and Regional Seismograms.....</i> | 429 |
| Toksöz, M. Nafi; Coates, R.T.; and Charrette E.E., and Rodi, W.L. <i>Research on Monitoring at Regional Distances: Scattering from Small-Scale Heterogeneities</i> | 436 |
| Toksöz, M. Nafi and Mandal, Batakrishna <i>Research in Regional Seismology: The Effects of Anisotropy and Heterogeneity.....</i> | 443 |
| Vogfjörd, Kristín S. and Langston, C.A. <i>Short-Period Regional Phases from Fennoscandian Arrays.....</i> | 450 |
| Wallace, Terry C. <i>Regional Distance Recordings of Large Mining Explosions: Distance Dependent Discrimination.....</i> | 457 |
| Woods, Bradley B.; Kedar, Sharon; and Helmberger, Donald V. <i>$M_L : M_0$ as a Regional Seismic Discriminant.....</i> | 463 |
| Wu, Francis T. and Levshin, Anatoli <i>Tomography of China using Surface Waves from CDSN.....</i> | 470 |

A GENERALIZED LIKELIHOOD RATIO TEST IN OUTLIER DETECTION OR SCRIPT MATCHING

J. Baek, H. L. Gray, G. D. McCartor,
and W. A. Woodward
Southern Methodist University
Dallas, TX

M. D. Fisk
Mission Research Corporation
Santa Barbara, CA

CONTRACT NO: F29601-91-K-DB25

OBJECTIVE

A generalized likelihood ratio test is developed to detect an outlier associated with monitoring nuclear proliferation. While the classical outlier detection methods consider continuous variables only, our approach allows both continuous and discrete variables or a mixture of continuous and discrete variables to be used. In addition, our method is free of the normality assumption, which is the key assumption in most of the classical methods. The proposed test is constructed by applying the bootstrap (Efron 1979, 1982) to a generalized likelihood ratio. We investigate the performance of the test by studying the power both with simulations and real data.

RESEARCH ACCOMPLISHED

Suppose for a given event, the variables $V = (Z', X')$, with $Z = (Z_1, \dots, Z_r)'$ and $X = (X_1, \dots, X_p)'$, are used to characterize the occurrence of the event, where Z_1, \dots, Z_r are discrete and X_1, \dots, X_p are continuous. The Z_i and X_i will be referred to as "script" variables or "features." Suppose further that a training sample $\{V_i = (Z_i', X_i')\}_{i=1}^n$ is available from past events and a new observation, V_{n+1} , is obtained which must be classified as to whether or not it belongs to the same population as the training sample. This problem is referred to as outlier detection or script matching.

More specifically, let the j th discrete variable Z_j have k_j categories, $j = 1, \dots, r$. Then the vector of discrete variables Z may be expressed as a multinomial random variable $Y = (Y_1, \dots, Y_k)'$, where $Y_m = 0$ or 1 , $m = 1, \dots, k$, $\sum_{m=1}^k Y_m = 1$, and $k = \prod_{j=1}^r k_j$. Thus, each distinct pattern of Z defines a multinomial cell uniquely. Then, following Olkin and Tate (1961), it is assumed, for specificity, that X has a multivariate normal distribution with mean μ_m given Z corresponding to cell m of Y , i.e., when $Y_m = 1$ ($m = 1, \dots, k$), and common covariance matrix Σ in all cells. Furthermore, it is assumed that the probability of obtaining an observation in cell m is p_m ($0 \leq p_m \leq 1$, $\sum_{m=1}^k p_m = 1$). Hence we consider the training sample $\{V_i\}_{i=1}^n$ to be from the joint probability density function $f(\cdot; p_1, U_1, \Sigma)$, where

$$f(V; p_1, U_1, \Sigma) = f_1(Y; p_1) f_2(X; U_1, \Sigma | Y)$$

with

$$f_1(\mathbf{Y}; \mathbf{p}_1) = \prod_{m=1}^k p_{1m}^{Y_m}, \quad (1)$$

$$f_2(\mathbf{X}; \mathbf{U}_1, \Sigma | Y_m = 1, Y_j = 0, j = 1, \dots, m-1, m+1, \dots, k) \\ = (2\pi)^{-p/2} |\Sigma|^{-1/2} \exp\{-(1/2)(\mathbf{X} - \mu_{1m})' \Sigma^{-1} (\mathbf{X} - \mu_{1m})\}, \quad (2)$$

$\mathbf{p}_1 = (p_{11}, \dots, p_{1,k-1})'$, $p_{1k} = 1 - \sum_{j=1}^{k-1} p_{1j}$, $0 \leq p_{1m} \leq 1$, $m = 1, \dots, k$, and $\mathbf{U}_1 = (\mu_{11}, \dots, \mu_{1k})$. Similarly let the new individual \mathbf{V}_{n+1} have the joint probability density $f(\cdot; \mathbf{p}_2, \mathbf{U}_2, \Sigma)$, where

$$f(\mathbf{V}; \mathbf{p}_2, \mathbf{U}_2, \Sigma) = f_1(\mathbf{Y}; \mathbf{p}_2) f_2(\mathbf{X}; \mathbf{U}_2, \Sigma | \mathbf{Y}),$$

f_1 and f_2 are similarly defined as in (1) and (2) with $\mathbf{p}_2 = (p_{21}, \dots, p_{2,k-1})'$ and $\mathbf{U}_2 = (\mu_{21}, \dots, \mu_{2k})$ in place of $\mathbf{p}_1, \mathbf{U}_1$, respectively.

Now we employ a hypothesis-testing approach to classify \mathbf{V}_{n+1} . That is, the classification of \mathbf{V}_{n+1} is accomplished by testing the hypothesis $H_0 : \mathbf{p}_1 = \mathbf{p}_2, \mathbf{U}_1 = \mathbf{U}_2$ versus $H_1 : \mathbf{p}_1 \neq \mathbf{p}_2$ or $\mathbf{U}_1 \neq \mathbf{U}_2$. We use the generalized likelihood ratio method to construct a test. Let $\Omega_0 = \{\theta = (\mathbf{p}_1, \mathbf{p}_2, \mathbf{U}_1, \mathbf{U}_2, \Sigma) | p_{1j} = p_{2j} \in [0, 1], j = 1, \dots, k-1, \mu_{1m} = \mu_{2m} \in R^p, m = 1, \dots, k, \Sigma : \text{positive definite}\}$, and let $\Omega = \{\theta = (\mathbf{p}_1, \mathbf{p}_2, \mathbf{U}_1, \mathbf{U}_2, \Sigma) | p_{ij} \in [0, 1], \mu_{im} \in R^p, i = 1, 2, j = 1, \dots, k-1, m = 1, \dots, k, \Sigma : \text{positive definite}\}$. Furthermore, let n_m denote the number of members of the training sample whose discrete variables fall in cell m . Then, the likelihood of the training sample $\{\mathbf{V}_i\}_{i=1}^n$ is given by

$$L(\theta; \mathbf{V}_1, \dots, \mathbf{V}_n) \\ = \{(2\pi)^p |\Sigma|\}^{-n/2} \left(\prod_{m=1}^k p_{1m}^{n_m} \right) \exp\left\{ - (1/2) \sum_{i=1}^n (\mathbf{X}_i - \mu_i)' \Sigma^{-1} (\mathbf{X}_i - \mu_i) \right\},$$

where μ_i takes the value μ_{1m} if \mathbf{Y}_i falls in the m th cell, $m = 1, \dots, k$. Consider now that \mathbf{V}_{n+1} is to be classified, and suppose that the discrete components place it into cell m . Then

$$L(\theta; \mathbf{V}_1, \dots, \mathbf{V}_{n+1}) = L(\theta; \mathbf{V}_1, \dots, \mathbf{V}_n) (2\pi)^{-p/2} p_{2m} |\Sigma|^{-1/2} \\ \cdot \exp\left\{ - (1/2) (\mathbf{X}_{n+1} - \mu_{2m})' \Sigma^{-1} (\mathbf{X}_{n+1} - \mu_{2m}) \right\}.$$

The generalized likelihood ratio is therefore defined by

$$\lambda_1 = \frac{\sup_{\theta \in \Omega_0} L(\theta; \mathbf{V}_1, \dots, \mathbf{V}_{n+1})}{\sup_{\theta \in \Omega} L(\theta; \mathbf{V}_1, \dots, \mathbf{V}_{n+1})} \quad (3)$$

$$= \frac{L(\hat{\theta}_0; \mathbf{V}_1, \dots, \mathbf{V}_{n+1})}{L(\hat{\theta}; \mathbf{V}_1, \dots, \mathbf{V}_{n+1})}, \quad (4)$$

where $\hat{\theta}$ is the Maximum Likelihood Estimate (MLE) of θ , and $\hat{\theta}_0$ is the MLE of θ under the restriction that H_0 is true. It intuitively follows that small values of λ_1 provide evidence against H_0 , and thus the generalized likelihood ratio test is

to reject H_0 if $\lambda_1 \leq \lambda_1(\alpha)$, where $\lambda_1(\alpha)$ is chosen to provide a size α test.

For the continuous variable case ($\mathbf{V} = \mathbf{X}'$), Caroni and Prescott (1992) showed that the hypothesis-testing approach with the likelihood ratio statistic can be used successfully for outlier detection. That is, the likelihood ratio statistic for testing $H_0^* : \mathbf{X}_i \sim N(\boldsymbol{\mu}_1, \boldsymbol{\Sigma})$, $i = 1, \dots, n+1$, against $H_1^* : \mathbf{X}_i \sim N(\boldsymbol{\mu}_1, \boldsymbol{\Sigma})$, $i = 1, \dots, n$, and $\mathbf{X}_{n+1} \sim N(\boldsymbol{\mu}_2, \boldsymbol{\Sigma})$, leads to Wilks's statistic (Wilks 1963), $W = |\mathbf{A}_n|/|\mathbf{A}_{n+1}|$, where $\mathbf{A}_n = \sum_{i=1}^n (\mathbf{X}_i - \bar{\mathbf{X}}_n)(\mathbf{X}_i - \bar{\mathbf{X}}_n)'$ and $\mathbf{A}_{n+1} = \sum_{i=1}^{n+1} (\mathbf{X}_i - \bar{\mathbf{X}}_{n+1})(\mathbf{X}_i - \bar{\mathbf{X}}_{n+1})'$, which is commonly used for multivariate outlier detection. It is also easily shown that W is essentially Hotelling's T^2 statistic (Anderson 1984), where $T^2 = n/(n+1)(\mathbf{X}_{n+1} - \bar{\mathbf{X}}_n)' \mathbf{S}_n^{-1} (\mathbf{X}_{n+1} - \bar{\mathbf{X}}_n)$ with $\mathbf{S}_n = \mathbf{A}_n/(n-1)$. This test statistic is generally used for testing the equality of two normal population means when the covariance matrices are assumed equal but unknown. In our case, however, one population has a sample $\{\mathbf{X}_i\}_{i=1}^n$ while the other has only one observation, $\{\mathbf{X}_{n+1}\}$. Thus the outlier detection or script matching problem when based on location is a special case of testing the equality of two population means in the continuous variable case.

We have assumed that the covariance of the new observation \mathbf{V}_{n+1} is the same as that of the population of the training sample. In many situations in practice, however, it may be more realistic that they are different from each other. If they are not equal, we can not obtain $\hat{\boldsymbol{\theta}}$, the MLE of $\boldsymbol{\theta}$ in the denominator of (3) since it is not reasonable to estimate the covariance of \mathbf{V}_{n+1} with the only one observation. Thus we need to modify the likelihood ratio λ_1 to make it applicable to our problem. Let λ_2 be a modified version of λ_1 defined by

$$\lambda_2 = \frac{\sup_{\{\boldsymbol{\theta} \in \Omega_0\}} L(\boldsymbol{\theta}; \mathbf{V}_1, \dots, \mathbf{V}_{n+1})}{\sup_{\{\boldsymbol{\theta} \in \Omega_0\}} L(\boldsymbol{\theta}; \mathbf{V}_1, \dots, \mathbf{V}_n) f(\mathbf{V}_{n+1}; \hat{\boldsymbol{\theta}}_n)} \quad (5)$$

$$= \frac{L(\hat{\boldsymbol{\theta}}_0; \mathbf{V}_1, \dots, \mathbf{V}_{n+1})}{L(\hat{\boldsymbol{\theta}}_n; \mathbf{V}_1, \dots, \mathbf{V}_{n+1})}, \quad (6)$$

where $\hat{\boldsymbol{\theta}}_n$ is the $\boldsymbol{\theta} \in \Omega_0$ which attains $\sup L(\boldsymbol{\theta}; \mathbf{V}_1, \dots, \mathbf{V}_n)$. It is noted that $\hat{\boldsymbol{\theta}}_n$ is the MLE of $\boldsymbol{\theta}$ from the training sample under the null hypothesis H_0 while $\hat{\boldsymbol{\theta}}_0$ is the estimator defined in (4). From (5) it is clear that large values of λ_2 provide evidence against H_0 , and thus \mathbf{V}_{n+1} can be classified by rejecting H_0 if $\lambda_2 \geq \lambda_2(1 - \alpha)$, where $\lambda_2(1 - \alpha)$ is the $(1 - \alpha)$ th percentile of the distribution of λ_2 under H_0 . Thus we can use either λ_1 or λ_2 depending on the assumption about the equality of the covariances.

The distribution of the test statistic λ_1 and λ_2 under H_0 is intractable due to the nature of the observations whose elements are discrete and continuous variables. For example, since the regularity conditions do not hold for $-2 \log \lambda_1$ to have its usual asymptotic chi-square null distribution, it is not easy to determine the critical value $\lambda_1(\alpha)$. This difficulty is, however, overcome using the bootstrap method (Efron 1979, 1982).

The likelihood ratio statistic for the test of the null hypothesis H_0 versus the alternative H_1 can be bootstrapped as follows. Given the training sample $\{\mathbf{V}_i\}_{i=1}^n$ and \mathbf{V}_{n+1} , a bootstrap sample $\{\mathbf{V}_i^*\}_{i=1}^{n+1}$ is generated randomly from $f(\mathbf{V}; \hat{\boldsymbol{\theta}}_0)$, where $\hat{\boldsymbol{\theta}}_0$ is the MLE of $\boldsymbol{\theta}$ under the null hypothesis from the original

sample $\{\mathbf{V}_i\}_{i=1}^{n+1}$. The value of λ_1 , to be denoted λ_1^* , is computed for the bootstrap sample using (4). This process is repeated independently B times, and the replicated values of λ_1^* , $\{\lambda_{1j}^*\}_{j=1}^B$ evaluated from the successive bootstrap samples, can be used to assess the true null distribution of λ_1 . In particular, the α th empirical quantile of $\{\lambda_{1j}^*\}_{j=1}^B$, denoted by $\lambda_1^*(\alpha)$, approximates the true α th quantile $\lambda_1(\alpha)$. That is, $\lambda_1(\alpha) \approx \lambda_1^*(\alpha)$. Thus we use $\lambda_1^*(\alpha)$ as a critical value for the test of size α . Therefore, we reject H_0 if $\lambda_1 \leq \lambda_1^*(\alpha)$, where $\lambda_1^*(\alpha)$ is obtained as discussed above.

McLachlan (1987) showed the relationship between $\lambda_1^*(\alpha)$ and the bootstrap replication size B for the specified test size α . If the bootstrap and true null distribution of λ_1 were the same, the original and subsequent bootstrap values of λ_1 can be treated as the realizations of a random sample of size $B + 1$, and the probability that a specified member is smaller than j of the others is $j/(B + 1)$. That is, $\alpha = j/(B + 1)$. For example, for $\alpha = 0.05$, we need $B = 199$ with $j = 10$. Therefore $\lambda_1^*(\alpha)$ is the 10th smallest value of $\{\lambda_{1j}^*\}_{j=1}^{200}$ for $B = 199$ and $\alpha = 0.05$.

Now we investigate the performance of the test by examining the power with simulations. We consider a simple situation in which we have a discrete variable from a Bernoulli(p) distribution, and an independent continuous variable distributed $N(\mu, \sigma^2)$. Let $\{\mathbf{V}_i = (Y_i, X_i)\}_{i=1}^n$ be a training sample, where $Y_i \sim \text{Bernoulli}(p_1)$ and $X_i \sim N(\mu_1, \sigma^2)$, $i = 1, \dots, n$. Let $\mathbf{V}_{n+1} = (Y_{n+1}, X_{n+1})$ be a new observation where $Y_{n+1} \sim \text{Bernoulli}(p_2)$ and $X_{n+1} \sim N(\mu_2, \sigma^2)$. Then the goal is to test $H_0 : p_1 = p_2, \mu_1 = \mu_2$ versus $H_1 : p_1 \neq p_2$ or $\mu_1 \neq \mu_2$.

First, we examine how well the bootstrap estimate of the critical value, $\lambda_1^*(\alpha)$ approximates the true critical value, $\lambda_1(\alpha)$, by comparing the power with the power associated with the bootstrap likelihood ratio test λ_i , $i = 1, 2$. We consider $p_1 = p_2$ and $\mu_2 = \mu_1 + \Delta\sigma$, where $\Delta \in \{0, 1, 2, 3\}$. We set $n = 100$, $p_1 = p_2 = 0.5$, $\mu_1 = 0$ and $\sigma = 1$ in the simulation. For the likelihood ratio λ_1 , the power of the test is defined by $P(\lambda_1 \leq \lambda_1(\alpha) | \Delta)$. Though the true critical value $\lambda_1(\alpha)$ is unknown, since we know the parameters we can get a very close estimate of $\lambda_1(\alpha)$ using a Monte Carlo procedure and estimate the power. The procedure is described as follows:

For given n , Δ and very large positive integers K, M ,

Do $i = 1, K$

Generate a random sample $\{\mathbf{V}_{i1}, \dots, \mathbf{V}_{i,n+1}\}$ under H_0 .

Calculate λ_{1i} using (4) with $\{\mathbf{V}_{ij}\}_{j=1}^{n+1}$.

Continue

$\lambda_1(\alpha) \approx \alpha$ th quantile of $\{\lambda_{1i}\}_{i=1}^K$.

Do $i = 1, M$

Generate a random sample $\{\mathbf{V}_{i1}, \dots, \mathbf{V}_{in}\}$ under H_0 .

Generate $\mathbf{V}_{i,n+1}$ randomly under (H_1, Δ) .

Calculate λ_{1i} using (4) with $\{\mathbf{V}_{ij}\}_{j=1}^{n+1}$.

Continue

$P(\lambda_1 \leq \lambda_1(\alpha) | \Delta) \approx \sum_{i=1}^M I(\lambda_{1i} \leq \lambda_1(\alpha)) / M$, where $I(\cdot)$ is the indicator function.

Now the power of the bootstrap likelihood ratio test is estimated as follows:
For given n , Δ and very large positive integers B , M ,

Do $i = 1, M$

Generate a random sample $\{V_{i1}, \dots, V_{in}\}$ under H_0 .

Generate $V_{i,n+1}$ randomly under (H_1, Δ) .

Calculate $\hat{\theta}_{0i}$ and $\hat{\theta}_i$ in (4) with $\{V_{ij}\}_{j=1}^{n+1}$.

Calculate λ_{1i} using (4).

Do $j = 1, B$

Generate bootstrap sample $\{V_{ij1}^*, \dots, V_{ij,n+1}^*\}$ using $\hat{\theta}_{0i}$.

Calculate λ_{1ij}^* using (4) with $\{V_{ijk}^*\}_{k=1}^{n+1}$.

Continue

$\lambda_{1i}^*(\alpha) \approx \alpha$ th quantile of $\{\lambda_{1ij}^*\}_{j=1}^B$.

Continue

$P(\lambda_1 \leq \lambda_1^*(\alpha) | \Delta) \approx \sum_{i=1}^M I(\lambda_{1i} \leq \lambda_{1i}^*(\alpha)) / M$, where $I(\cdot)$ is the indicator function.

$P(\lambda_2 \leq \lambda_2^*(\alpha) | \Delta)$ can be obtained similarly using (6) in the above procedure. Table 1 shows $P(\lambda_1 \leq \lambda_1(\alpha) | \Delta)$, $P(\lambda_1 \leq \lambda_1^*(\alpha) | \Delta)$ and $P(\lambda_2 \leq \lambda_2^*(\alpha) | \Delta)$ for $M = 1000, 10000$ with $K = 100000$, $B = 199$, and $\alpha = 0.05$. As M increases, both powers of the bootstrap likelihood ratio test λ_1 and λ_2 converges to the power of λ_1 . In this case we see that the bootstrap likelihood ratio tests λ_1 and λ_2 , are essentially equivalent. Note also that the estimate of Type I error, $P(\lambda_i \leq \lambda_i^*(\alpha) | \Delta = 0)$, is very close to its true value $\alpha = 0.05$, $i = 1, 2$, for $M = 10000$.

Now set $p_2 = p_1 + 0.2\Delta_1$ and $\mu_2 = \mu_1 + \Delta_2\sigma$, where $\Delta_1 \in \{0, 1, 2\}$ and $\Delta_2 \in \{0, 0.25i, i = 1, 2, \dots, 12\}$. For $p_1 = 0.5$, $\mu_1 = 0$ and $\sigma = 1$, $P(\lambda_1 \leq \lambda_1^*(\alpha) | \Delta_1, \Delta_2)$ are calculated and plotted in Figure 1 with $n = 100$, $B = 199$, $M = 1000$, and $\alpha = 0.05$. As μ_2 gets far away from μ_1 , the power of the bootstrap likelihood ratio test increases. On the other hand, the test is not sensitive to departures of p_2 from p_1 . Corresponding power curves were obtained for λ_2 and their behavior was similar to that shown in Figure 1.

Table 1. Simulated power of the test of size $\alpha = 0.05$ for $n = 100$ using 199 bootstrap replications ($p_1 = p_2 = 0.5$, $\mu_1 = 0$, $\sigma = 1$)

| | $\Delta = 0$ | $\Delta = 1$ | $\Delta = 2$ | $\Delta = 3$ |
|--------------------------------------------------|--------------|--------------|--------------|--------------|
| $M = 1000$ | | | | |
| $P(\lambda_1 \leq \lambda_1(\alpha) \Delta)$ | 0.054 | 0.162 | 0.495 | 0.832 |
| $P(\lambda_1 \leq \lambda_1^*(\alpha) \Delta)$ | 0.056 | 0.157 | 0.491 | 0.826 |
| $P(\lambda_2 \leq \lambda_2^*(\alpha) \Delta)$ | 0.057 | 0.158 | 0.488 | 0.826 |
| $M = 10000$ | | | | |
| $P(\lambda_1 \leq \lambda_1(\alpha) \Delta)$ | 0.0497 | 0.1624 | 0.4986 | 0.8451 |
| $P(\lambda_1 \leq \lambda_1^*(\alpha) \Delta)$ | 0.0494 | 0.1619 | 0.4940 | 0.8373 |
| $P(\lambda_2 \leq \lambda_2^*(\alpha) \Delta)$ | 0.0495 | 0.1607 | 0.4967 | 0.8359 |

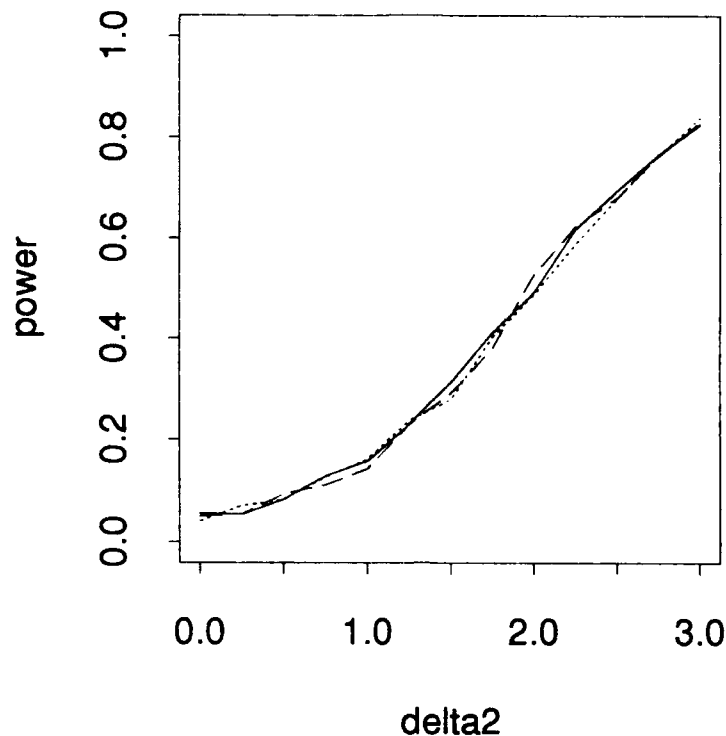


Fig. 1. Power curves of the bootstrap likelihood ratio test λ_1 . solid line: $\Delta_1 = 0$, dotted line: $\Delta_1 = 1$, and broken line: $\Delta_1 = 2$. Delta2 denotes Δ_2 .

CONCLUSIONS AND RECOMMENDATIONS

This research implies that for the outlier detection in the mixed variables (discrete and continuous) case, the bootstrap likelihood ratio method may be a useful tool. Moreover, although we have assumed normality for clarity, the methodology considered here can be applied to any mixture of continuous and discrete variables for which the likelihood ratio is defined. We can always construct the bootstrap likelihood ratio test as far as the MLEs exist in either (3) or (5) even if the continuous distribution is not normal.

It is planned to apply the bootstrap likelihood ratio test to the real data at MRC or the DARPA Center for Seismic Studies to assess the effectiveness of the test. The results of that study will be available in a forthcoming SMU/MRC report. It should be noted that the power of the test depends on the training sample size n and the bootstrap replication size B . Small sample size of multi-dimensional data may force the test less powerful, and large value for B costs much of the computing time though it increases the accuracy. Thus the sensitivity of the test against n and B may be studied further.

REFERENCES

- Anderson, T. W. (1984), *An Introduction to Multivariate Statistical Analysis*, John Wiley & Sons, New York.
- Caroni, C. and Prescott, P. (1992), "Sequential Application of Wilks's Multivariate Outlier Test," *Appl. Statist.*, 41 (2), 355-364.
- Efron, B. (1979), "Bootstrap Methods: Another Look at the Jackknife," *Ann. Statist.*, 7, 1-26.
- Efron, B. (1982), *The Jackknife, the Bootstrap and Other Resampling Plans*, SIAM, Philadelphia.
- McLachlan, G. J. (1987), "On Bootstrapping the Likelihood Ratio Test Statistic for the Number of Components in a Normal Mixture," *Appl. Statist.*, 36 (3), 318-324.
- Olkin, I. and Tate, R. F. (1961), "Multivariate Correlation Models with Mixed Discrete and Continuous Variables," *Ann. Math. Statist.*, 22, 92-96.
- Wilks, S. S. (1963), "Multivariate Statistical Outliers," *Sankhya*, 25, 407-426.

ANALYSIS OF REGIONAL BODYWAVE PHASES FROM EARTHQUAKES IN WESTERN CHINA

Jeffrey S. Barker
State University of New York, Binghamton

CONTRACT NO: F19628-90-K-0042

OBJECTIVE:

The purpose of this study is to improve our understanding of the regional crustal waveguide phases encompassed by P_n and P_g (often termed P_{nl}), by modeling regional waveforms in eastern Asia. Saikia and Burdick (1991) showed that deterministic modeling of short-period P_{nl} can provide a good fit to waveforms at ranges of 200 to 420 km from NTS explosions. Zhao and Helmberger (1991) have demonstrated similar success in modeling broad-band P_{nl} from the Saguenay earthquake recorded at HRV, while Burdick et al. (1992) modeled regional earthquake recordings at the IRIS station, Garm.

If we want to understand the development and propagation of P_{nl} , we must have observations at a number of ranges from the source. Unfortunately, while high-quality, broad-band seismometers are now available in China and the Commonwealth of Independent States (CIS), the station spacing is quite sparse. At the review meeting last year, we presented the results of modeling a profile of earthquakes recorded at the Chinese Digital Seismic Station, WMQ (Barker, 1991; Wu and Barker, 1992). This is not the reciprocal problem to wave propagation from a single source to a number of stations because the earthquakes have different depths, magnitudes and mechanisms. However, by simultaneously modeling waveforms from each of these earthquakes, we gain an understanding not only of the propagation of specific crustal phases near WMQ, but also of the kinds of variation observed for different source depths and mechanisms.

Last year we presented results for a profile of earthquakes southwest of WMQ (Figure 1). These events occurred within the crust in the Tien Shan region, and propagated along the structural trend of the Tien Shan and the Tarim Basin. A plane-layered velocity structure and frequency-wavenumber integration synthetics proved quite adequate in modeling most of the P_{nl} waveform. For these earthquakes, the P_{nl} waveforms are not dominated by crustal multiples (e.g., $P_M P$), but by S waves that depart upward, then reflect and convert to P waves at the free surface (e.g., sP_n). Since the interference of different phases that depart the source either upward or downward is very sensitive to source depth, modeling P_{nl} can serve as an excellent discriminant.

RESEARCH ACCOMPLISHED:

Since the conclusions presented last year are radiation-pattern dependent, this year we present similar results, but using profiles of earthquakes along two different azimuths from WMQ. The first profile is SSE of WMQ, including earthquakes in the vicinity of the Lop Nor Test Site (Figure 1; Table 1). The propagation paths cross the eastern margin of the Tien Shan, the Tarim Basin and, at the largest distances, the Altyn Tagh and Qaidam Basin. Vertical component broad-band seismograms recorded at WMQ were obtained from CSS and are plotted on the left side of Figure 2. In order to facilitate comparison, the seismograms have been integrated to displacement and band-pass filtered (0.5 - 2.0 Hz) to a band that approximates the WWSSN short-period instrument response. The same filters are applied to the synthetics.

Superimposed on the seismograms of Figure 1 are travel-time curves for a source at a depth of 20 km in the velocity structure listed in Table 2. This structure model is modified from models of surface wave dispersion in the Tarim Basin and seismic refraction in the Qaidam Basin (SSB, 1986), removing thin low- and high-velocity layers and adjusting crustal thickness and velocities so that the travel-time curves are in agreement with the observed arrival times. As noted in Table 2, there is substantial uncertainty in the depths of the earthquakes listed in the PDE, but those that

are well determined fall in the 21-32 km depth range. The travel-time curves are plotted assuming that most of the earthquakes occurred near 20 km depth. If the average depth of the sources is actually deeper, to maintain the time separation between P_n and P_g , the crustal thickness of the model would have to be increased. In our model, crustal thickness is 48 km, which is consistent with estimates based on gravity data (Hu et al., 1989; Shi et al., 1989). For this study, we also assume a plane-layered velocity structure, which would certainly be invalid if we were to consider propagation from earthquakes farther south on the Tibetan Plateau. Surface-wave tomography (Wu and Levshin, "Tomography Of China Using Surface Waves At CDSN", these proceedings) suggests that crustal thickness varies only slightly in the region from the Qaidam Basin to WMQ. However, the wave propagation along our profile may be slightly up-dip, so crustal thickness should be considered a lower bound, while P_n velocity (8.0 km/s) is an upper estimate.

Synthetic seismograms were computed using a frequency-wavenumber integration technique (Barker, 1984), and are plotted on the right side of Figure 2. Anelastic attenuation is assumed (Table 2) to move the poles off the real- k axis. No wavenumber filtering is imposed, so the synthetics include S waves and surface waves in addition to the P wavetrain. The source parameters assumed are listed in Table 3. These include Harvard CMT mechanisms (PDE) when available; otherwise an average thrust mechanism is assumed. For the narrow band considered for these profiles, the source corner frequency has little effect, so the synthetics are simply bandpassed from the ground displacement impulse response computed to 4 Hz. Source depth is assumed to be 20 km. At the meeting, we will present the results of modeling the broad-band seismograms at different source depths, but space limitations prevent that presentation here.

Profiles of the observed and synthetic seismograms are plotted at the top of Figure 2, with a reduction velocity of 8.0 km/s. At this scale only P_n , P_g and S_g (or L_g) are identifiable, and the synthetics provide a reasonable agreement in character to the observed waveforms. On the lower part of the figure are the same profiles, but limited in time to show the P_{nl} portion of the waveforms. Also plotted are the travel-time curves P , P_n , $P_M P$, and the surface reflections of P_n and $P_M P$. This is not to suggest a one-to-one correspondence of arrivals, but simply to suggest which phases are predicted to arrive between P_n and P_g . At the closest sources, P and S are the largest amplitude arrivals. The Moho critical distance is about 110 km, so $P_M P$ becomes a significant arrival shortly beyond this range. At the largest ranges (700 km and beyond), the P_{nl} wavetrain consists of a series of low-amplitude arrivals. In the synthetics, P_g begins with the direct P wave travelling nearly horizontally through the crust. At the largest ranges, the observed P_g is more emergent, undoubtedly due to scattering and lateral heterogeneity in the crust.

Another profile of earthquakes is located to the NNE of WMQ, through the western tip of Mongolia and into Siberia (Figure 1; Table 1). In this region, very little has been published on the crustal structure. The surface-wave tomography of Wu and Levshin once again suggests that crustal structure varies slowly along this profile. Therefore, we have developed a crustal velocity structure based on fitting travel-time curves to observed seismograms. Once again, vertical-component broad-band seismograms were obtained from CSS and, for purposes of the initial modeling, have been band-pass filtered (0.5 - 2.0 Hz). The seismograms recorded at WMQ from the NNE profile of earthquakes is shown on the left side of Figure 3, along with travel-time curves computed for a source at 20 km depth in the velocity structure in Table 2. For this depth, the crustal thickness is 59 km, and would be even greater for a deeper source. The linear moveout of P_g (Figure 3) suggests a very low velocity gradient in the crust. P_n goes from 8.15 km/s at 400-600 km range to 8.26 km/s at greater ranges, constraining the mantle gradient. If we identify several observed secondary arrivals with $P_M P$, the velocity at the base of the crust is 7.4 km/s.

Synthetic seismograms were once again computed for a source at 20 km by the frequency-wavenumber integration technique, band-pass filtered (0.5 - 2.0 Hz) for the source parameters listed in Table 3. In this case, the mechanisms are predominantly strike slip, with increasing normal component to the northeast. The synthetic profiles are plotted on the right side of Figure 3. Once

again, the timing and character of P_n , P_g and S_g are quite adequately modeled, and surface reflected phases provide arrivals between P_n and P_g . Modeling of the broadband data for details of the arrivals that interfere to generate P_{nl} will be presented at the meeting.

CONCLUSIONS AND RECOMMENDATIONS:

For the earthquake profiles SSE and NNE of WMQ, bandpassed P_{nl} waveforms are adequately modeled using frequency-wavenumber integration synthetics with plane-layered velocity structure models. For the SSE profile, previous studies provide starting models for crustal velocity and thickness, however for the NNE profile, no such studies have been found. At the review meeting, we will present the results of modeling broad-band P_{nl} waveforms for various source depths. Following our experience with the profile SW of WMQ, the interference of upgoing and downgoing crustal phases can serve as a valuable indicator of source depth.

REFERENCES:

- Barker, J.S. (1984). A seismological analysis of the 1980 Mammoth Lakes, California, earthquakes, *PhD Thesis*, Pennsylvania State Univ.
- Barker, J.S. (1991). Analysis of regional bodywave phases from earthquakes and explosions in eastern Asia, Papers Presented at 13th annual PL/DARPA Seismic Research Symposium, Keystone, CO, 64-70. PL-TR-91-2208, ADA241325
- Burdick, L.J., C.K. Saikia, J.P. McLaren, L.S. Zhao and D.V. Helmberger (1992). Specialized studies in yield estimation, *Final Report*, PL-TR-92-2070, Phillips Laboratory.
- Hu F., Hu J., Bai M., Chen S., Zhou D. and Liu J. (1989). Seismotectonics of Xinjiang Uygur Autonomous Region, in *Lithospheric Dynamics Atlas of China*, Ma Xingyuan, chief editor, China Cartographic Publishing House, Beijing, 57.
- Saikia, C.K. and L.J. Burdick (1991). Fine structure of P_{nl} waves from explosions, *J. Geophys. Res.*, 96, 14,383-14,401.
- Shi Z., Liu Z. and Yin X. (1989). Crustal Thickness by Gravity Inversion, in *Lithospheric Dynamics Atlas of China*, Ma Xingyuan, chief editor, China Cartographic Publishing House, Beijing, 12.
- State Seismological Bureau (1986). *Results of Geophysical Exploration of the Crust and Upper Mantle in China*, Beijing.
- Wu, F.T. and J.S. Barker (1992). Studies of regional body and surface waves in eastern Asia - Data analysis and modeling, *Scientific Report No. 1*, PL-TR-92-2171, Phillips Laboratory.
- Zhao, L.S. and D.V. Helmberger (1991). Broadband modeling along a regional shield path, Harvard recording of the Saguenay earthquake, *Geophys. J. Int.*, 105, 301-312.

Table 1 - Earthquakes Recorded at WMQ

| Date | Time (GMT) | Lat. (°N) | Lon (°E) | R (km) | Az (°) | Depth (km) | m _b |
|--------------------|---------------|--------------|-------------|-----------|-----------|---------------|----------------|
| SSE Profile | | | | | | | |
| 10/6/87 (87279) | 1306:20.3 | 43.44 | 88.55 | 82.0 | 302 | 32 | 4.8 |
| 9/29/88 (88273) | 0700:3.1 | 41.75 | 88.47 | 238.9 | 345 | 33* | 4.7 |
| 11/15/88 (88320) | 1656:46.2 | 42.02 | 89.30 | 239.4 | 327 | 33* | 5.0 |
| 12/22/87 (87317) | 0016:39.04 | 41.36 | 87.69 | 316.9 | 330 | 21 | 5.9 |
| 2/25/87 (87056) | 1957:52.0 | 38.10 | 91.18 | 699.9 | 336 | 26 | 5.7 |
| 12/6/87 (87340) | 1620:44.9 | 37.39 | 94.52 | 917.8 | 323 | 33* | 4.7 |
| NNE Profile | | | | | | | |
| 10/6/87 (87279) | 1306:20.3 | 43.44 | 88.55 | 82.0 | 302 | 32 | 4.8 |
| 9/18/87 (87261) | 2159:15.0 | 47.02 | 89.66 | 387.6 | 204 | 33* | 5.3 |
| 4/1/88 (88092) | 0127:16.0 | 47.53 | 89.64 | 439.4 | 201 | 10 | 4.6 |
| 7/23/88 (88205) | 0738:9.7 | 48.71 | 90.56 | 586.4 | 203 | 19 | 5.5 |
| 6/30/88 (88182) | 1525:15.5 | 50.23 | 91.14 | 759.4 | 202 | 33* | 5.0 |
| 9/16/87 (87259) | 1759:30.6 | 52.09 | 95.70 | 1095.5 | 216 | 33* | 4.8 |

* Depth uncertain. 33 km is the PDE default.

Table 2 - Velocity Structure Models

| V _P (km/s) | V _S (km/s) | Density (g/cm ³) | Thickness (km) | Q _P | Q _S |
|--------------------------------------|--------------------------|---------------------------------|-------------------|----------------|----------------|
| SSE Profile (near Lop Nor) | | | | | |
| 4.80 | 2.77 | 2.58 | 12.0 | 300 | 150 |
| 6.25 | 3.78 | 2.79 | 26.0 | 1000 | 500 |
| 6.80 | 3.93 | 2.85 | 10.0 | 1000 | 500 |
| 8.00 | 4.62 | 3.34 | 10.0 | 1200 | 600 |
| 8.10 | 4.68 | 3.36 | h.s. | 1200 | 600 |
| NNE Profile (Altai Mountains) | | | | | |
| 4.80 | 2.77 | 2.58 | 5.0 | 300 | 150 |
| 6.00 | 3.46 | 2.79 | 45.0 | 800 | 400 |
| 6.90 | 4.00 | 2.85 | 3.0 | 1000 | 500 |
| 7.40 | 4.27 | 3.00 | 6.0 | 1000 | 500 |
| 8.15 | 4.70 | 3.20 | 10.0 | 1200 | 600 |
| 8.26 | 4.77 | 3.30 | h.s. | 1200 | 600 |

Table 3 - Source Parameters for the Synthetics

| Date | R (km) | Az (°) | Strike (°) | Dip (°) | Rake (°) | M ₀ (x10 ²³ dyne-cm) |
|--------------------|-----------|-----------|------------------|-----------------|-----------------|-----------------------------------------------|
| SSE Profile | | | | | | |
| 87279 | 82 | 302 | 270 ^b | 60 ^b | 70 ^b | 1.8 ^b |
| Syn2 | 160 | 330 | 270 ^b | 60 ^b | 70 ^b | 1.8 ^b |
| 88273, 88320 | 240 | 330 | 270 ^b | 60 ^b | 70 ^b | 1.8 ^b |
| 87356 | 317 | 330 | 316 ^a | 53 ^a | 54 ^a | 2.1 ^a |
| Syn5 | 500 | 330 | 270 ^b | 60 ^b | 70 ^b | 1.8 ^b |
| 87056 | 700 | 336 | 267 ^a | 60 ^a | 68 ^a | 5.8 ^a |
| 87340 | 918 | 323 | 270 ^b | 60 ^b | 70 ^b | 1.8 ^b |

| Table 3 - (continued) | | | | | | |
|-----------------------|-----------|-----------|------------------|-----------------|------------------|--------------------------------------|
| Date | R (km) | Az (°) | Strike (°) | Dip (°) | Rake (°) | M_0 ($\times 10^{23}$ dyne-cm) |
| NNE Profile | | | | | | |
| 87279 | 82 | 302 | 120 ^b | 90 ^b | 180 ^b | 1.8 ^b |
| Syn2 | 200 | 200 | 120 ^b | 90 ^b | 180 ^b | 1.8 ^b |
| 87261, 88091 | 400 | 200 | 154 ^a | 90 ^a | 180 ^a | 1.3 ^a |
| 88205 | 586 | 203 | 331 ^a | 66 ^a | 170 ^a | 9.0 ^a |
| 88182 | 759 | 201 | 152 ^a | 50 ^a | -50 ^a | 3.5 ^a |
| Syn6 | 950 | 200 | 70 ^b | 70 ^b | -40 ^b | 1.8 ^b |
| 87259 | 1095 | 216 | 70 ^b | 70 ^b | -40 ^b | 1.8 ^b |

^a Mechanisms are Harvard CMT solutions published in the PDE.

^b No mechanism published. These values are assumed.

Earthquake Profiles Recorded at WMQ

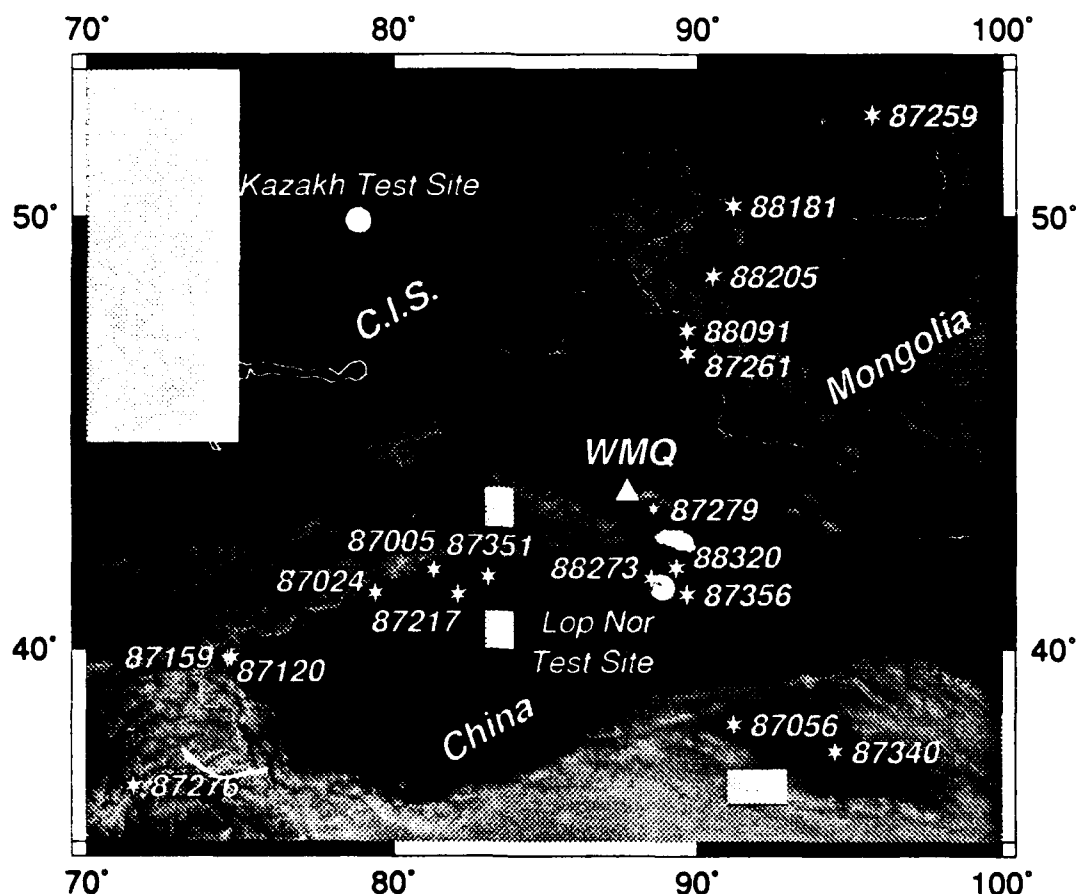
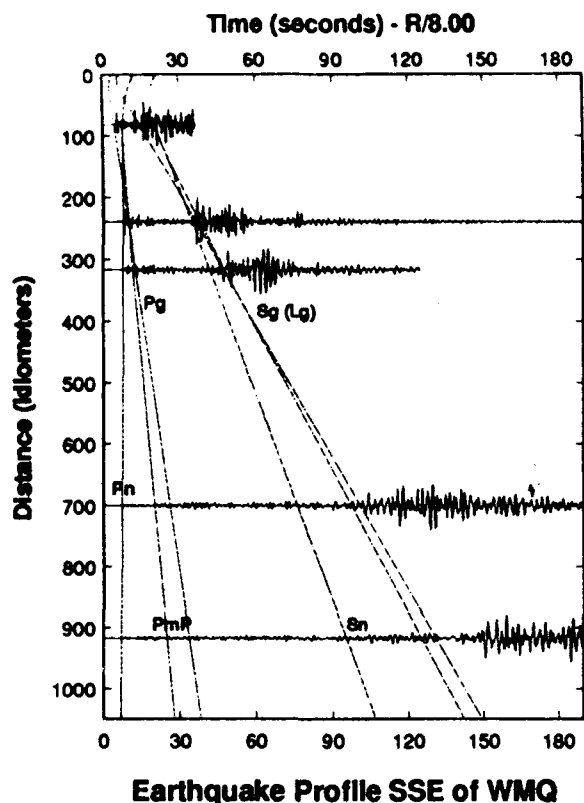
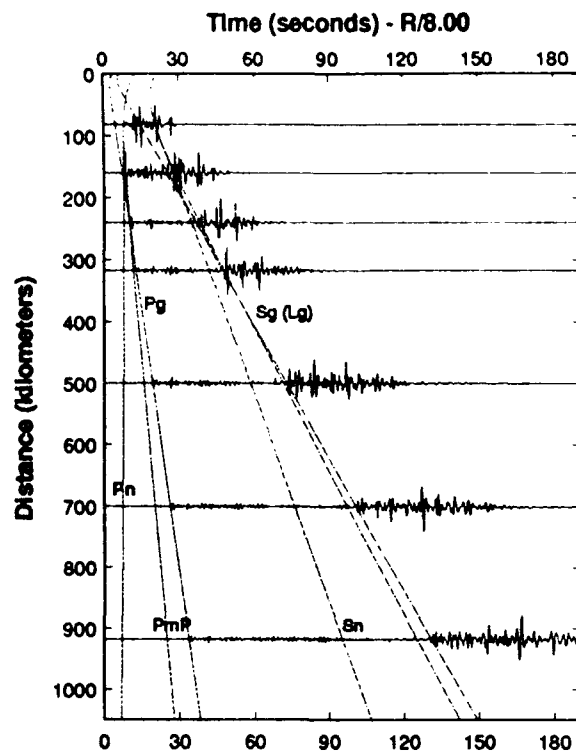


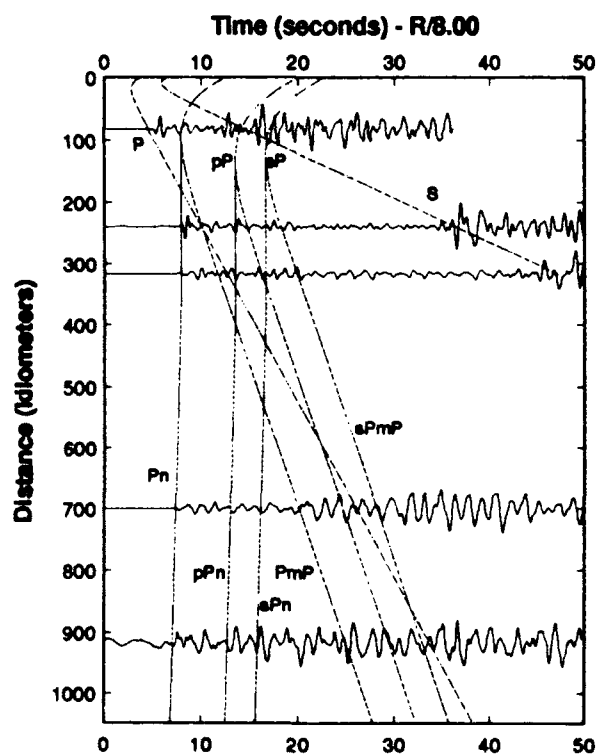
Fig. 1 Shaded topographic map of northwestern border region of China showing the locations of earthquakes (stars) recorded at CDSN station WMQ (triangle). Earthquakes SSE and NNE of WMQ are modeled in this study (see Table 1). Also shown are the locations of the Kazakh Test Site and the Lop Nor Test Site (circles). Topography (courtesy of Eric Fielding at Cornell) is plotted with lighter shades indicating higher elevations. Gray squares indicate missing elevation data. The small gray oval SE of WMQ is the Turfan Basin, which is below Sea Level. The light region to the south is the edge of the Tibetan Plateau.



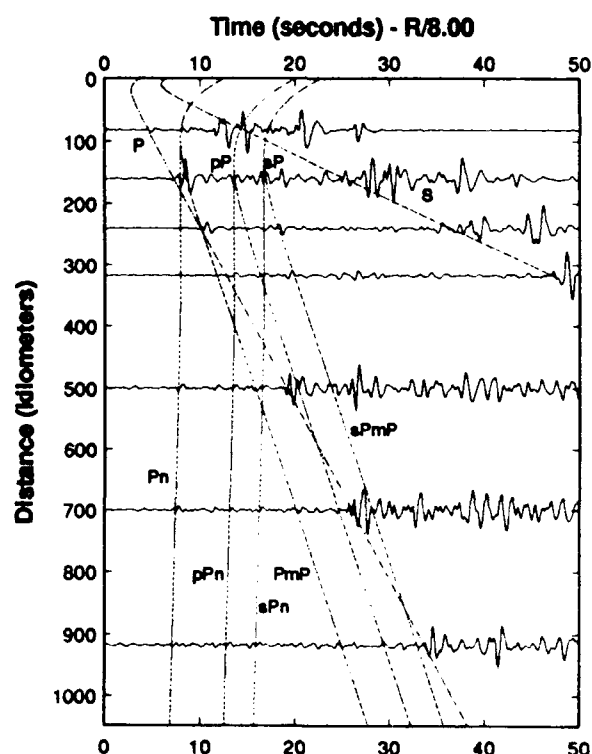
Earthquake Profile SSE of WMQ



F-K Synthetic Profile (20 km Depth)



Earthquake Profile SSE of WMQ



F-K Synthetic Profile (20 km Depth)

Fig. 2 Profiles of observed (left) and frequency-wavenumber integration synthetic (right) vertical-component displacement waveforms for earthquakes from the SSE recorded at CDSN station WMQ. The full waveforms are shown in the top profiles, while the P_n portions of the same waveforms are shown in the bottom profiles. Also shown are travel-time curves for important P- and S-wave phases computed for a source at 20 km depth in the velocity structure model in Table 3.

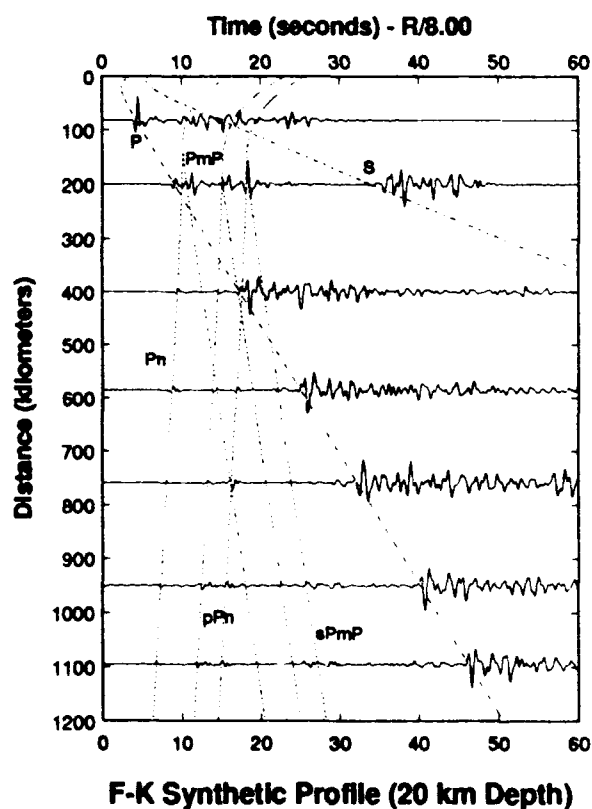
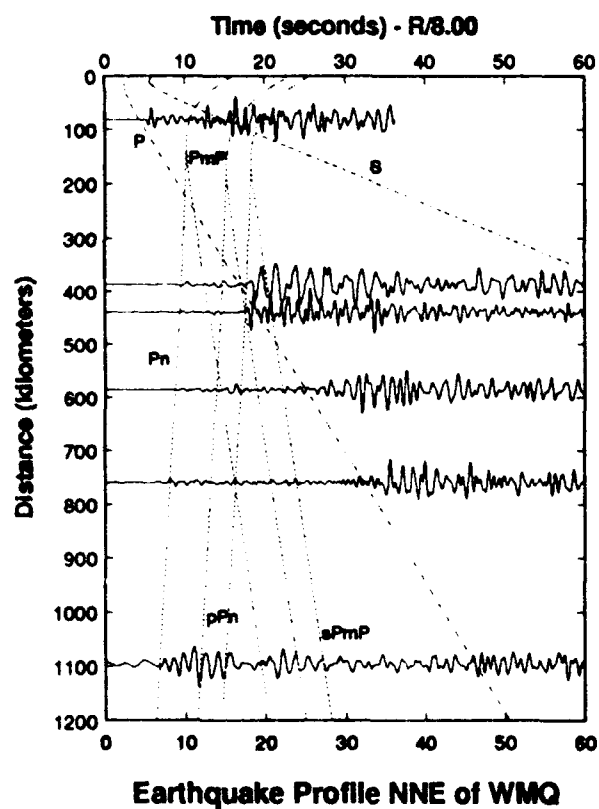
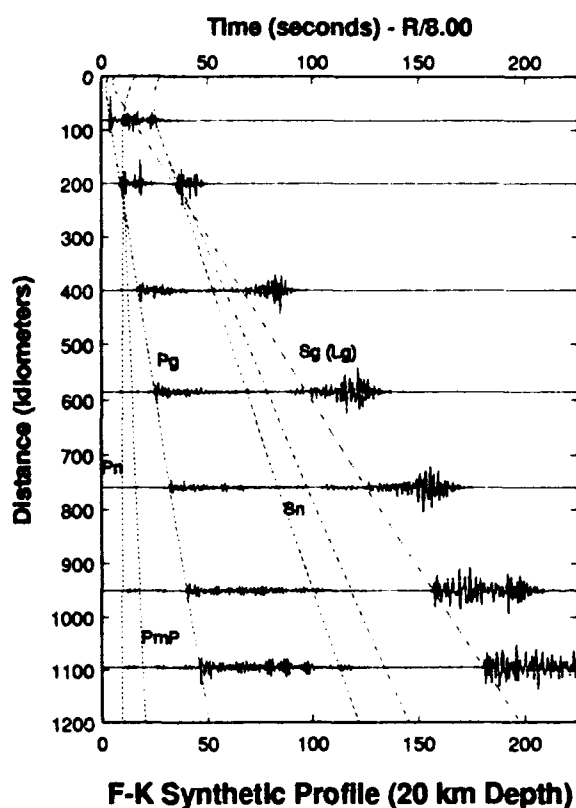
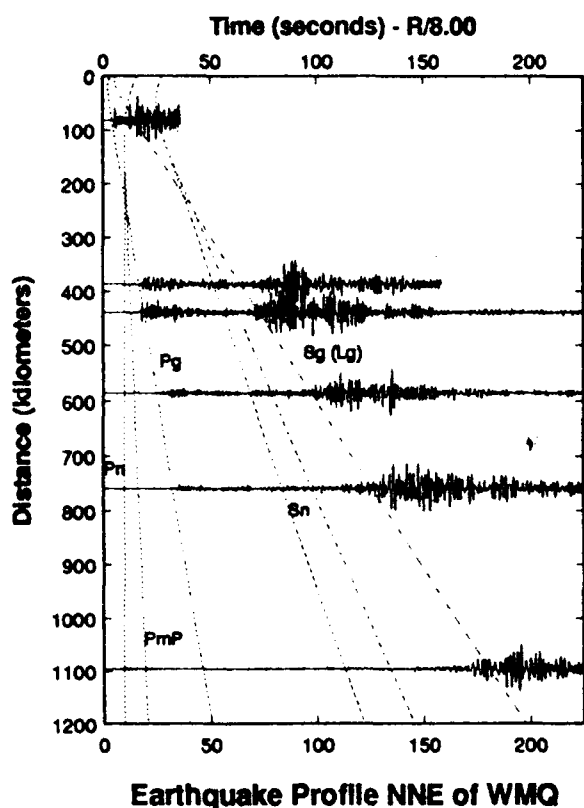


Fig. 3 Profiles of observed (left) and synthetic (right) vertical-component displacement waveforms for earthquakes from the NNE recorded at WMQ. The full waveforms are shown in the top profiles, while the P_{Δ} portions of the same waveforms are shown in the bottom profiles. The travel-time curves are computed for a source at 20 km depth in the velocity structure model listed in Table 3.

NUMERICAL MODELS OF QUARRY BLAST SOURCES

Terrance G. Barker and Keith L. McLaughlin

barker@scubed.scubed.com and scatter@scubed.scubed.com

S-Cubed, Division of Maxwell Laboratories, Inc.
P.O. Box 1620, La Jolla, CA 92038
Contract No. F29601-91-C-DB27

1. OBJECTIVES

It has been suggested that evading detection of nuclear weapons testing may be accomplished by detonating the weapons in conjunction with large quarry blasts. The objective of this project is to compare the regional seismic radiation from QB sources and small, shallow, overburied nuclear explosions to determine whether it may be possible to discriminate between the two sources. Our approach is to use simple seismic models, derived from realistic numerical simulations and from field tests, as sources in synthetic seismogram calculations. We can then examine synthetic seismograms and sonograms for discrimination features. In this paper, we concentrate on the differences in regional seismic signals due to differences in source excitation, duration and size of the QB and nuclear bomb sources. We model the quarry blast as a series of shots distributed on a grid using a variety of temporal and spatial shot patterns. Each shot is a charge which creates a spalling of the material above, which is modeled as an explosion plus a tension crack.

2. RESEARCH ACCOMPLISHED

2.1 Blasting Practices

For this paper, we consider the scenario that an evader wishes to hide a one kiloton tamped explosion under a simultaneous chemical quarry blast of comparable yield. It is unlikely that this scenario would be used to hide a shot with a seismic source larger than 1 kT tamped.

The spatial scale of the QB can be estimated from the total explosive yield and from standard blasting practices. Most quarrying is done by removing material from the face of a bench using multiple rows of charges parallel to the bench. The largest bench height in practice is about 30 m (Langefors and Kihlstrom, 1963). The burden Q (distance from the face of the bench to the charge) is, as a rule, one-half the bench height, (Langefors and Kihlstrom, 1963, Dupont, 1942), or about 15 m. The standard spacing between holes in a row as well as the spacing between rows is 1.25 times the burden. This geometry is shown schematically in Figure 1. The standard charge size (per hole) is $0.6Q^3$, or 2025 Kg, or about two metric tons. So, if the total charge is one kiloton, the total number of holes is 500. In the calculations described here, we used 20 rows with 25 charges per row, as shown in Figure 2.

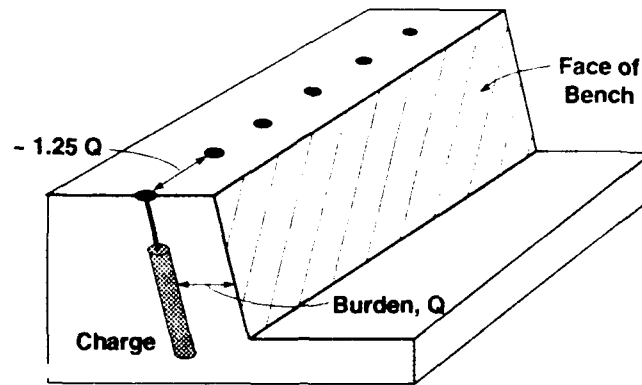


Figure 1

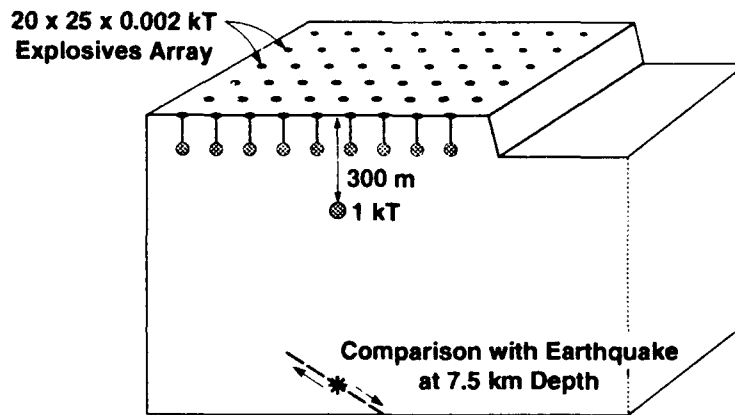


Figure 2

The charges are detonated in firing patterns that vary with the requirements and constraints of the quarry. The most typical pattern is to fire the shots within a row simultaneously or at very short intervals, and detonate the rows at even intervals beginning with the row nearest the face. The intervals between rows are a few tenths of a second. The objective of progressive firing within a row is to encourage gas driven fracture between holes to make the rock separate more readily along a line between the holes. The rows are fired at intervals so that the rocks thrown from a particular row do not interfere with the detachment of the subsequent row.

Chapman, *et al.* (1991) examined the drilling practices of quarries in eastern Kentucky. The charge pattern for an excavation with a total yield of 0.115 kT is shown in Figure 3. In this case, there were 56 charges arranged in 4 rows of 14. The charge size per hole was 1.87 metric tons. The spacing is about 12 m between shots within a row and about 8 m between rows. This pattern is similar to other charge patterns shown in their report. Since there is a practical upper limit of about two metric tons per hole (determined by the maximum practical bench height, as discussed above), a larger yield can be achieved only by increasing the number of holes. If the example in Figure 3 were to be scaled up to 1 kT, the number of holes would be increased to around 500. The detonation times are also indicated in Figure 3. Each row is initiated at the center and the duration of firing in each row is 165 msec. The interval between rows is about 250 msec.

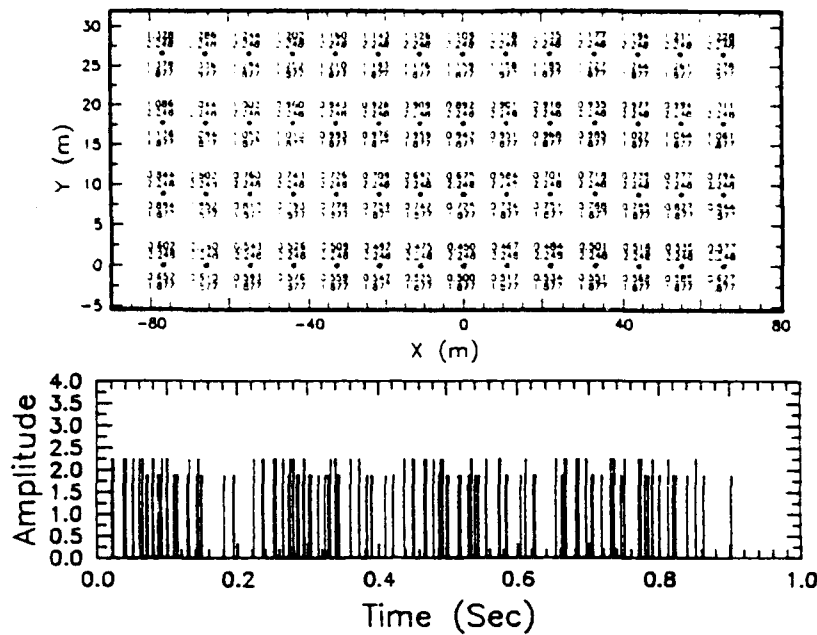


Figure 3. Example of a 0.1 kT QB shot layout from Chapman (1991). (Top) shot layout, 1000 lbs. of explosive and ms delay times. (Bottom) shot size versus time.

2.2 Model of Quarry Blast Source

Material is removed from the face by a spall process in which the compressional wave from the explosives reflects from the face as a tension wave which causes the material to detach and become airborne. The spall process initiated by nuclear explosions has been modeled well by a tension crack (Day, *et al.*, 1983, Barker and Day, 1990, McLaughlin, *et al.*, 1990), and we use it here. At each shot hole, the model consists of an initial charge modeled as a Mueller-Murphy explosion source plus a tension crack at the same depth. Stump and Reinke (1988) showed that the Mueller-Murphy source represents the explosive part of the signals from QBs well. We place the tension crack at the depth of the charge since firing patterns are designed to crack along a line through the charges (Langefors and Kihlstrom, 1963).

Photographic observations of material thrown in the air by the explosions by Langefors and Kihlstrom (1963) show that typical velocities at which the material leaves the ground is in the range from 2 to 10 m/sec. These are also typical values for vertical ground velocities above nuclear explosions. Barker and Day (1990) used a tension crack model to describe numerical simulations of nuclear events. The parameters of the model, vertical velocity, spall mass and momentum were consistent with observations. The parameters, scaled to 2 tons, are consistent with a block of material 20m on a side, ejected from a depth of 25 m at a velocity of 3.5 m/sec. These are reasonable values for the quarry blast charge described above, and are what we used in the calculations for this report. A review of blasting literature reveals that individual shots are generally conducted with scaled burdens of between 50 and 100 m/kt^{1/3}.

We compute the signal from the total QB by linearly superposing the signals from individual holes. Several observations made during mine operations (Stump and Reinke, 1988, Reamer, *et al.* 1992, and Reamer and Hinzen, 1991) show that this approximation is valid. These authors also show that a point source representation of the cylindrical charges typically used in QBs is valid.

2.3 Analysis of Synthetic Seismograms and Sonograms

We have computed synthetic seismograms at a range of 1000 km using an earth model typical of the crust in central Asia. A fullwave integration procedure was used to calculate the Green's functions for the explosive and tension crack sources. A Green's function was calculated for every row of explosives to ensure that phase interference between rows was accurately computed. The calculations were done for the band from 0 to 2.5 Hz. To investigate the bomb-under-quarry scenario, we have also computed seismograms from a tamped 1kT explosion buried at 300m. Earthquake seismograms for a dislocation at 7.5 km are also computed for reference.

Figure 4 shows the signals filtered passing the frequency band from 2.0 to 2.5 Hz. The unfiltered records are so dominated by the Rayleigh wave that it is the only visible phase. The filtered signals are from the QB simulation (20×25 shots at 0.002 kT), the tamped 1kT explosion, the sum of the QB and the tamped explosion, and from a single hole in the QB. For the QB simulation, the time interval between rows was 200 msec, starting with the row nearest the receiver. All charges within the rows were fired simultaneously. The explosion-plus-QB and explosion-only records in Figure 4 are dominated by the Pg signal arriving at about 160 sec. In the QB-alone seismogram, however, the Lg phase, arriving between 275 and 375 seconds, is somewhat bigger than Pg. Note that the signal from a single hole has a somewhat different character than the full QB, exhibiting the effects of phase interference between rows. The Lg enhancement relative to Pg is due to the effectiveness of the tension crack source in generating Lg. This was found to be the case in McLaughlin, *et al.* (1990), also. The Pg from the 1kT bomb swamps the QB signal in Figure 4. A much smaller bomb with a yield of 0.05 kT is shown with the QB in Figure 5. Here, the Lg from the QB is visible.

A sonogram for the QB is shown in Figure 6. The sonograms have gain ranging which normalizes each band-passed signal to the maximum at each frequency. Larger amplitudes appear darker on the figure. At low frequencies, the Rayleigh wave dominates. The Rayleigh wave is the dispersed signal arriving near 330 seconds at the lowest frequency. At higher frequencies (above 1 Hz), the Pg and Lg phases are apparent. Again, we can see the enhancement of Lg from the QB source.

We show spectra of the signals in Figure 7. The low frequencies (below 1 Hz) are dominated by the Rayleigh wave. Of interest is the scallops in the spectrum from the QB. The period of the scallops is duration of the source, or the time required for the firing of the charges to propagate across the grid. We have confirmed this by computing spectra from different size grids. We also note that the spectrum from the quarry blast falls off at higher frequencies much faster than for the bomb. This is due to the band-limited nature of the spall model (Barker and Day, 1990), whose duration is determined by the dwell time of the material in the air.

3. CONCLUSIONS AND RECOMMENDATIONS

We have computed synthetic seismograms from models of a multiple-shot QB. The charge size, distribution, spall momentum and detonation intervals used in these calculations were chosen to be representative of actual mining practices. Our calculations show that

- 1) Detection of a nuclear explosive in a simultaneous quarry blast will require broadband recording,

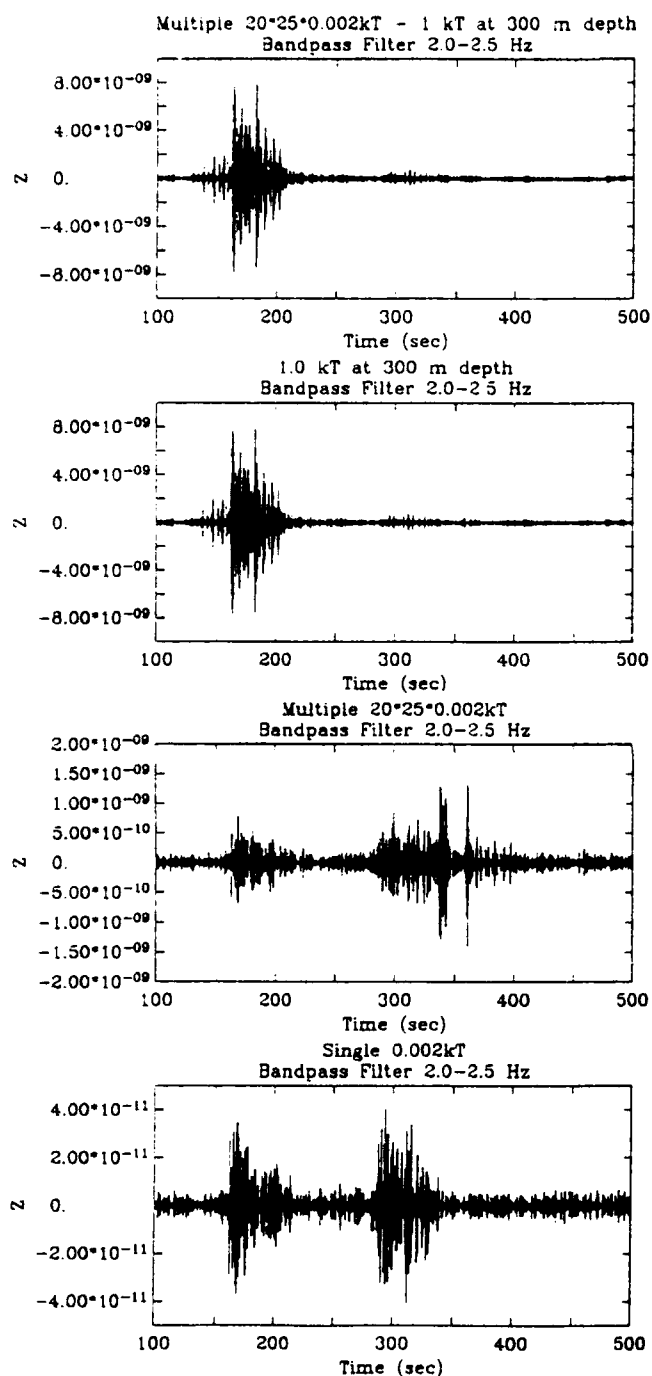


Figure 4. From top to bottom; sum of QB and 1 kT nuclear, 1 kT nuclear alone, QB alone, and single shot from QB.

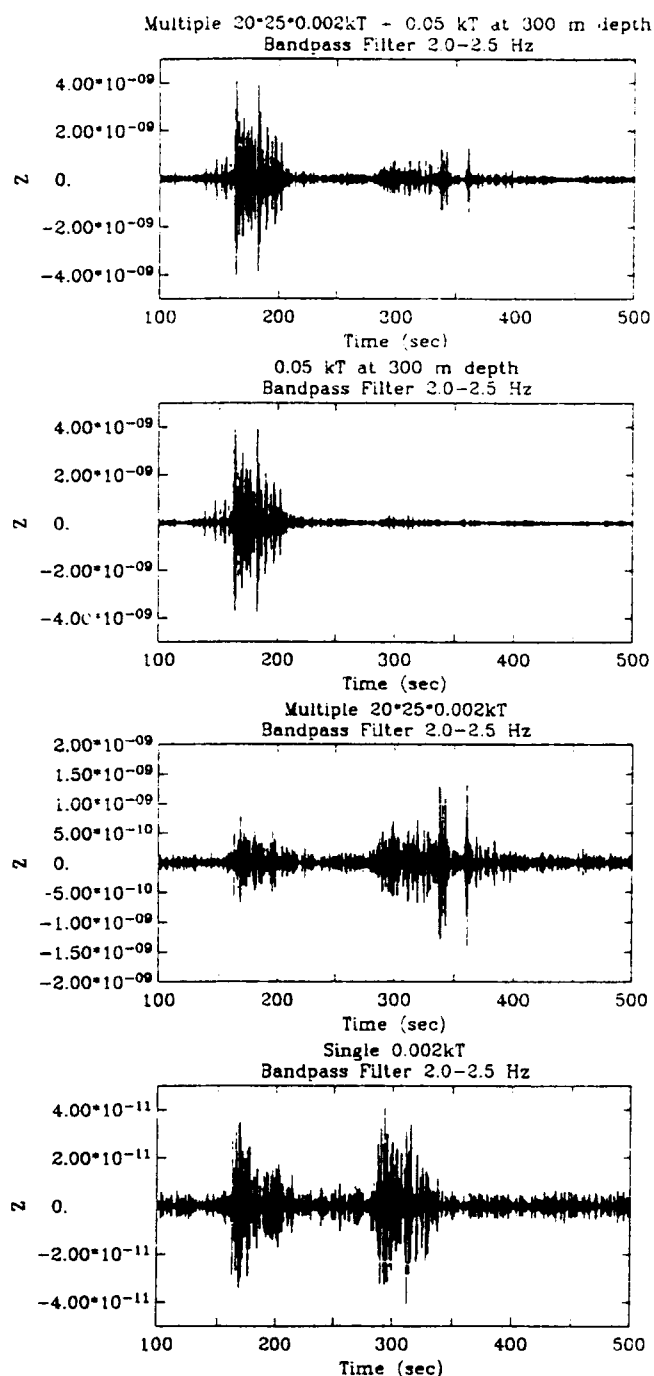


Figure 5. From top to bottom; sum of QB and 0.05 kT nuclear, 0.05 kT nuclear alone, QB alone, and single shot from QB.

1.0 kT Multiple Quarry Shot (20*25*0.002kT)

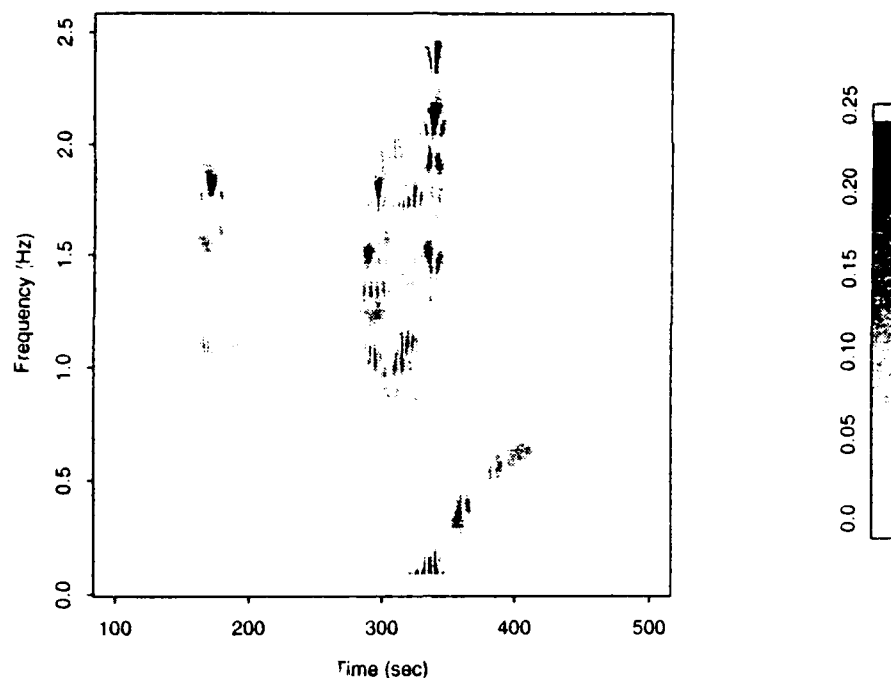


Figure 6. Sonogram of 1.0 kT (20 × 25 × 0.002 kT) QB. Note scalloping at 0.25 Hz intervals, and the large Lg/Pg ratio above 2 Hz.

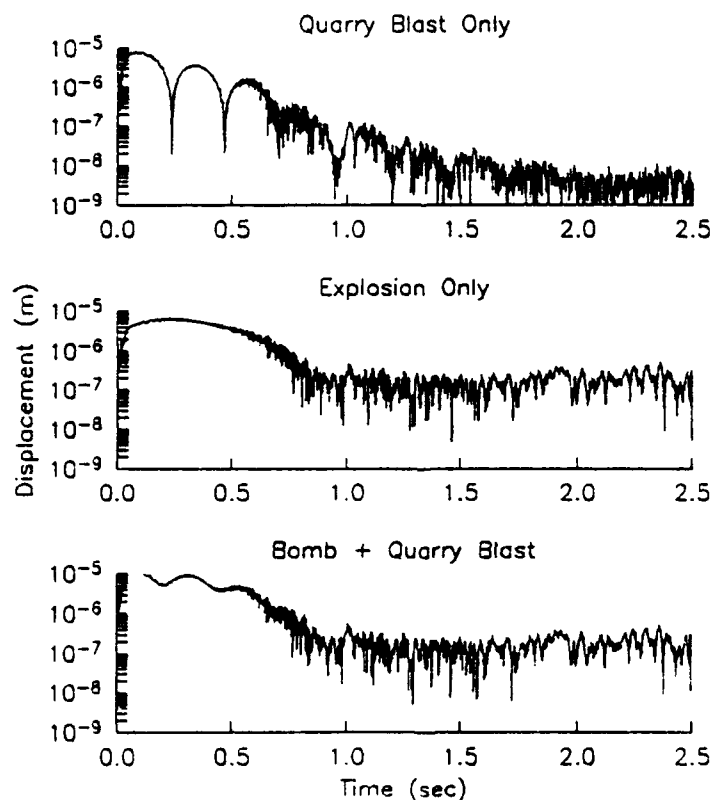


Figure 7. Spectra of the QB (top), 1 kT nuclear (middle) and sum of the two sources (bottom). Discrimination will require a broadband signal.

- 2) the quarry blast source generates higher values of the ratio L_g/P_g at higher frequencies than the buried explosion,
- 3) the quarry blast source is a narrow band signal compared to the overburied explosion, and
- 4) the quarry blast source has scallops in the spectrum due to the finite size of the source.

Work continues in several areas:

- 1) Cooperative data collection of near-source data to validate source models,
- 2) modeling of near-source data using simple source models, and
- 3) simulation of evasion scenarios using realistic quarry blast and explosion source functions.

4. REFERENCES

- Barker, T.G. and S.M. Day (1990), "A Simple Physical Model for Spall from Nuclear Explosions Based Upon Two-Dimensional Nonlinear Numerical Simulations", S-Cubed Scientific Report to DARPA, SSS-TR-11550.
- Chapman, M.C., G.A. Bollinger, and M.S. Sibol (1991), "Spectral Studies of the Elastic Wave Radiation From Appalachian Earthquakes and Explosions—Explosion Source Spectra Modeling Using Blaster's Logs", Phillips Laboratory, PL-TR-91-2231, ADA243956
- Day, S.M., N. Rimer and J.T. Cherry (1983), "Surface Waves from Underground Explosions with Spall: Analysis of Elastic and Nonlinear Models". Bull., Seism. Soc. Am., 73, 247-264.
- Reamer, S.K. and K.-G. Hinzen (1991), "Seismic Study of the Dynamic Response of Rock to Cylindrical Charges Fired in a Half and a Quarter-Space Geometry", in Proc. of the 17th Conference on Explosives and Blasting Research.
- Reamer, S.K. Hinzen, K.-G. and B.W. Stump (1992), "Near-Source Characterization of the Seismic Wavefield Radiated from QBs", preprint.
- Langefors, U. and B. Kihlstrom (1963), "The Modern Techniques of Rock Blasting", John Wiley and Sons.
- Dupont (1942), "Blasters' Handbook", E.I. du Pont de Nemours & Co.

REGIONAL SEISMIC EVENT DISCRIMINANTS: WHAT WORKS, WHAT DOESN'T, AND WHY

Douglas R. Baumgardt
ENSCO, Inc., 5400 Port Royal Rd.
Springfield, Virginia 22151
Contract No. F29601-92-C-0009

OBJECTIVE

In this study, the effectiveness of several regional waveform discriminants and processing methods are being evaluated, using the large database of regional waveforms generated by the Intelligent Monitoring System (IMS), currently operating continuously in Norway on signals detected by the four regional arrays NORESS, ARCESS, FINESA, and GERESS. Waveform features are to be measured with the Intelligent Seismic Event Identification System (ISEIS), which has been developed as an automatic and interactive backend system to identify events formed by the IMS (Baumgardt et al, 1992). There are specifically three overall objectives in this study:

- (1) Process through ISEIS the large database of waveforms in the IMS database, extract and store in a database numerous regional waveform features which may be useful discriminants, and test the discriminatory performance of the current rules in ISEIS on events of known identity.
- (2) Use multivariate and statistical analysis techniques to identify those waveform features which are most discriminatory.
- (3) Revise the rules in the ISEIS expert system to utilize the best discriminant features which optimizes event identification performance.

RESEARCH ACCOMPLISHED

The Intelligent Seismic Event Identification System (ISEIS) has been installed at the Center for Seismic Studies (CSS) where it is being used to process and analyze discriminants for seismic events formed the Intelligent Monitoring System (IMS). The ISEIS processing approach is described in detail by Baumgardt et al (1991). In brief, the processing steps include: (1) *incoherent beam* computation in nine primary filter bands, ranging from 0.5-2.5 Hz (for possible *Rg* phases analysis) to 8-16 Hz; (2) *stapick* selection for key phases and amplitude computation (maximum and average) within the *stapick* windows; (3) amplitude-ratio computation (same frequency) for selected phases; (4) array-stacked spectral density computation in the *stapick* windows; (5) spectral ratio computation for all phases; (6) cepstrum calculation for ripple-fire detection and depth estimation; (7) storage of all key features to an Oracle database; (8) rule-based processing, using rules coded in the NASA expert systems shell, CLIPS, to identify events on the basis of individual discriminants extracted from the database; and (9) overall event identification using a voting scheme. A number of new capabilities have been added to ISEIS, beyond those discussed by Baumgardt et al (1991), in order to facilitate the processing of data at the CSS.

The processing at the CSS consists of two passes on each event in the IMS database, automated initial processing (autoISEIS) and interactive review. In the automated mode, event parameters (origins) determined by the IMS and analyst review in the Analyst Review Station (ARS), are passed to autoISEIS along with the associated phase identifications. The computation of the incoherent beams is keyed off the first arrival *P* times and then autoISEIS makes its time- and frequency-domain measurements on predefined group velocity windows beginning at the times determined by IMS for each of the key phases. It is assumed that IMS/ARS identifications of the regional phases *Pn*, *Pg*, *Sn*, *Lg*, and *Rg* are correct and the event has been accurately located based on these phases. If any of these phases are missing, autoISEIS predicts the phase arrival times, using the IMS location, and selects *stapicks* based on the predicted times. All subsequent

processing (amplitude ratios, spectral analysis, ripple-fire detection, rule processing) are done automatically utilizing these *stapicks*.

However, the IMS/ARS phase identifications are often incorrect or incomplete. Thus, ISEIS provides interactive displays where the IMS/ARS phase picks and resultant incoherent beam phase picks can be examined. Figure 1a shows an example of an earthquake recorded at NORESS for which the first arrival compressional phase was labeled P_x . This phase is obviously P_n but was not so identified for some reason by the IMS/ARS analyst. ISEIS measures incoherent beams, keying off the first P_x phase, as shown in Figure 1b, producing the incoherent beams shown in Figure 1c. ISEIS provides an interface which allows the *stapicks* to be interactively determined, as was done in Figure 1c, where the darkened regions indicate the *stapick* windows. In this example, the P_n phase has been identified and a P_g phase, not detected by IMS, can be clearly observed in the incoherent beams and is so labeled. After repicking the phases, the rest of the processing steps can be redone automatically. Correct phase identification and event location is vital in order for subsequent event identification to be successful.

Figure 2 shows an example of a new top-level event identification display bulletin interface which has been included in ISEIS, in addition to the spreadsheet displays discussed by Baumgardt et al (1991). This display shows the event parameters, the true event identification, if available, or that determined by the analyst, a codified display of the results of the ISEIS combined discrimination (ICOMP), and the individual discriminants which are active. This display allows a quick overview of the results of the automated and subsequent interactive processing and allows a comparison to be made of the ISEIS event identifications to those provided by ground truth. This interface provides a number of other subfunctions, accessible through the menus, for selecting events, reading in new events, setting the event identification, and entering comments in the database.

ISEIS is now being applied to events in the IMS database, beginning in January of 1992. This database consists of the most complete set of waveform data for all three arrays, NORESS, ARCESS, FINESA, and GERESS. Each event is being processed automatically and all events are subsequently reviewed interactively with the results stored in the database for subsequent analysis.

CONCLUSIONS AND RECOMMENDATIONS

A preliminary study of regional waveform discriminants was done using ISEIS-extracted features and a number of multivariate statistical and visualization techniques. This study, reported by Baumgardt (1992), is continuing with the larger IMS database. Figure 3 shows the locations of the events which were studied. The events at NORESS include mine explosions (BLA, TITA), reported to NORSAR by the mine operators, earthquakes reported in the Bergen bulletins, and presumed marine blasts identified by Baumgardt and Young (1990). The ARCESS events include mine explosions reported by in the Helsinki bulletins, nuclear explosions at Novaya Zemlya, presumed earthquakes reported in the Helsinki bulletins, and a lone event which has been identified by Baumgardt (1991) as an explosion on board a Soviet nuclear submarine which sank off the northern coast of Norway in 1989. Figures 4a and 4b show plots of P_n/L_g ratios at NORESS and P_n/S_n ratios at ARCESS (L_g is not observed for many of the events at ARCESS). So far, the analysis indicates that the best separation between explosion and earthquake groups is provided by P_n/S_n and P_n/L_g ratios measured at high frequencies, 8 to 10 Hz for NORESS and 6 to 8 Hz for ARCESS. This result is consistent with a number of other studies in other regions (e.g., Bennett et al, 1989) which have shown that earthquakes have stronger shear excitation than explosions. Because of the similarity of paths and distances for the earthquake and explosion groups, these differences must be a reflection of source differences between earthquakes and explosions. Comparisons of P_n/S_n and P_n/L_g ratios for Norwegian mine explosions recorded at NORESS and Kola mine explosions recorded at ARCESS were found to not be significantly different.

We also found for NORESS a significant separation of earthquakes and explosions using an "inferred" R_g -to- L_g ratio in a low-frequency filter band (0.5-2.5 Hz), where the inferred R_g was measured in the L_g coda at the predicted group-velocity time for R_g . Explosions seem to

generate stronger *Lg* coda energy at the time of *Rg* even though a distinct *Rg* phase is not strongly apparent.

Figure 5 shows a summary, in the form of a boxplot, of spectral ratio measurements for the *Lg* waves recorded at NORESS. Although a number of earlier studies suggested this discriminant separates nuclear explosions and earthquakes in western U.S. (Bennett and Murphy, 1988), our studies have so far shown complete overlap between mine blasts and earthquakes recorded at NORESS. However, as shown in Figure 5, spectral ratios of underwater blasts appear to be considerably higher than those of either mine blasts or earthquakes. We are continuing to study spectral ratios on the expanded database.

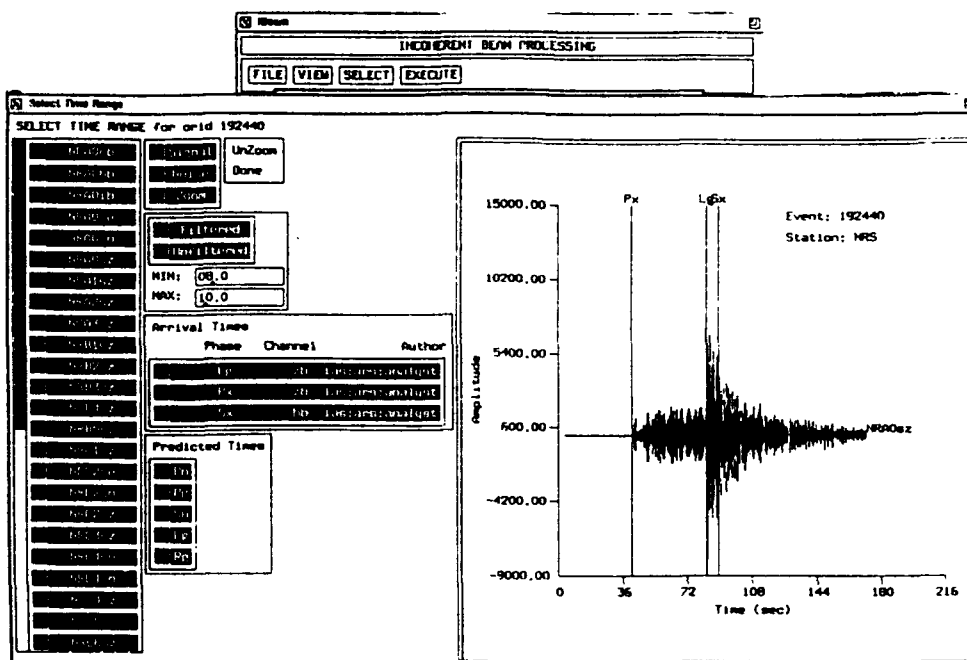
The clustering technique of *minimal spanning tree* (MST) was tested on two classes of *Pn/Sn* and *Pn/Lg* ratio measurements for 13 earthquakes and 13 explosions recorded at NORESS in order to reveal how well separated these events are on the basis of multivariate feature measurements of these ratios in different frequency bands. Most of the events were separated, although some events intermediate between the classes were evident.

Finally, we have also explored a number of novel visualization schemes for enabling the visual clustering of multivariate data. One example is *star plots*, shown for the NORESS-recorded mine explosions and earthquakes in Figure 6. Each star point in Figure 6 is determined by a value of a *Pn/Lg* ratio in some frequency band. Clearly, earthquakes have larger stars than explosions, which reflects the fact that their ratios are larger, consistent with Figure 4a. Other techniques we have explored include Chernov faces and multivariate planing for displaying minimal spanning tree clustering. These techniques provide useful insights into the behavior of various multivariate type discriminants and how well they perform in the classification of seismic events.

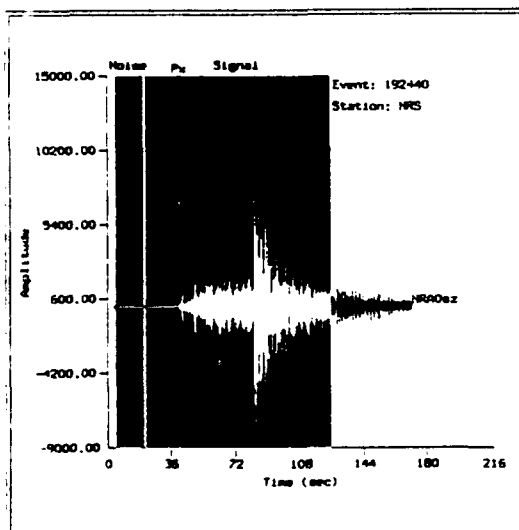
For future work, we make the following recommendations: (1) The phase identification capabilities of the IMS need to be improved to make automatic event identification possible. Currently, IMS often does not identify all the phases needed for complete event characterization and sometimes, phases are erroneously identified with the final event locations also being inaccurate. Accurate phase identifications and event locations are extremely important for reliable event identification. (2) Although regional *P/S* type ratios have proven to be good discriminants, we have observed a surprisingly large variation in these ratios for mine blasts, as seen in Figures 4a and 4b. These variations may be due to differences in blasting practice and/or associated tectonic release associated with the blasts. The cause of these variations needs to be further investigated.

REFERENCES

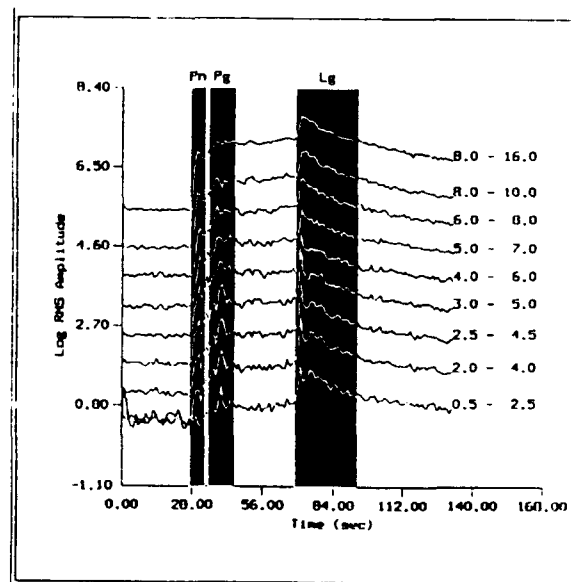
- Baumgardt, D.R. (1992). Investigation of seismic discriminants in Eurasia, Final Report, SBIR Phase I, SAS-TR-92-81, ENSCO, Inc., Springfield, VA.
- Baumgardt, D.R. (1991b). Possible seismic signals from a nuclear submarine accident in the Norwegian Sea, abstract in *EOS*, **72**, 343.
- Baumgardt, D.R. and G. B. Young (1990). Regional seismic waveform discriminants and case-based event identification using regional arrays, *Bull. Seism. Soc. Am.*, **80**, 1874-1892.
- Baumgardt, D.R., S. Carter, M. Maxson, J. Carney, K. Ziegler, and N. Matson (1991a). Design and development of the intelligent event identification system, *PL-TR-91- 2298(I)*, Final Report, Volumes I, II, and III, ENSCO, Inc., Springfield, VA. ADA248381
- Bennett, T.J. and J.R. Murphy (1986). Analysis of seismic discrimination capabilities using regional data from western United States events, *Bull. Seism. Soc. Am.*, **76**, 1069-1086.
- Bennett, T.J., B.W. Barker, K.L. McLaughlin, and J.R. Murphy (1989). Regional discrimination of quarry blasts, earthquakes and underground nuclear explosions, Final Report, *GL-TR-89-0114*, S-Cubed, La Jolla, CA. ADA223148



(a)



(b)



(c)

FIGURE 1: Displays of analyst phase picks and ISEIS stapick time selections. (a) Original phase from IMS/ARS; (b) Selected time windows for signal and noise incoherent beams; (c) Incoherent beam plots showing corrected phase identifications and stapick windows.

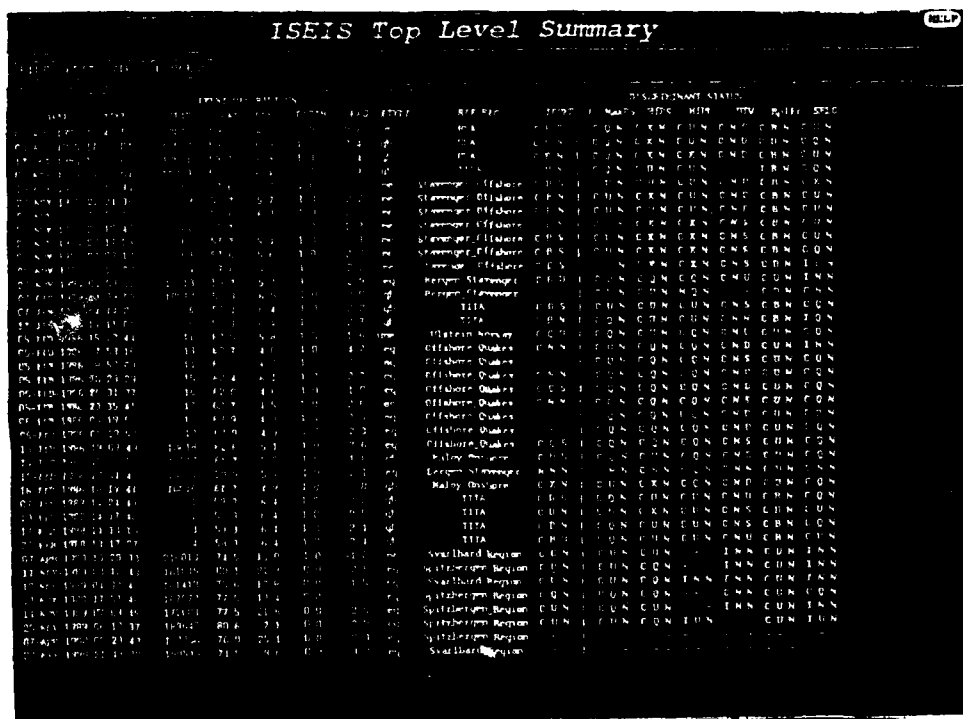


FIGURE 2: Example of ISEIS event identification summary bulletin interface.

Principle Study Regions

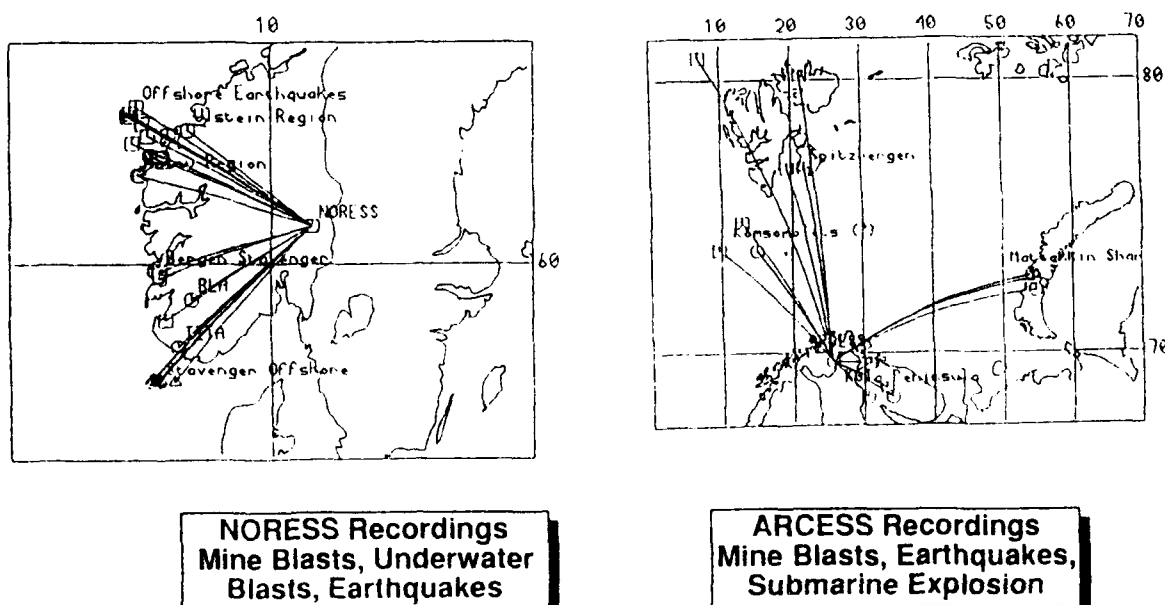
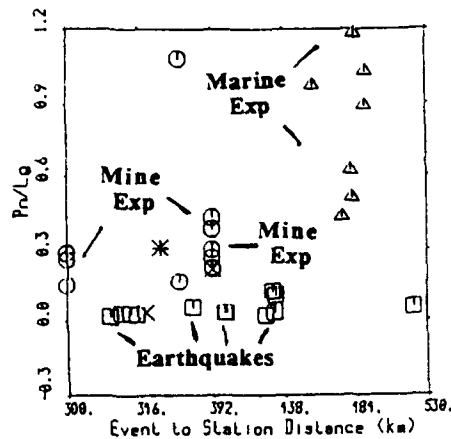


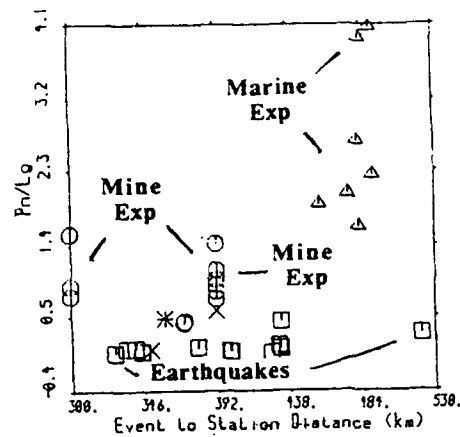
FIGURE 3: Maps showing locations of events analyzed at NORESS and ARCESS in the preliminary discriminant study.

**Pn / Lg Amplitude Ratio Discriminants
NORESS Incoherent Beam Maximums
300 to 530 Km**

- : Earthquake
- : Quarry Blast
- △ : Marine Explosion
- X : Unknown



Incoherent Beam Filter
4 - 6 Hz

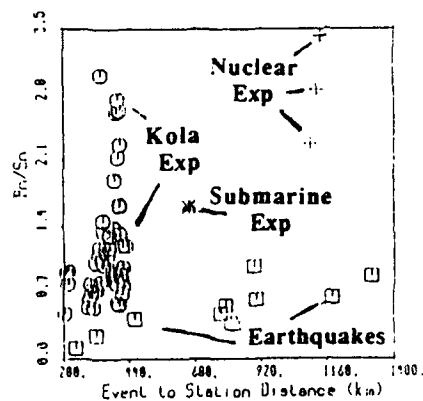


Incoherent Beam Filter
8 - 10 Hz

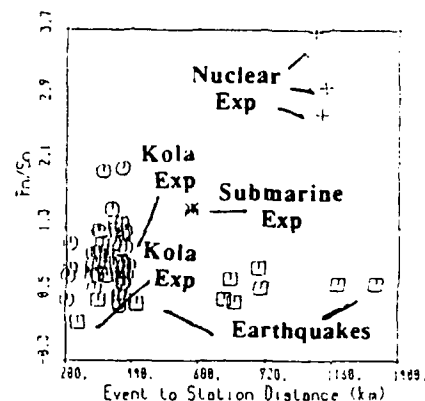
(a)

**Pn / Sn Amplitude Ratio Discriminants
ARCESS Incoherent Beam Maximums
Comparison With Presumed Underwater Explosion**

- : Earthquake
- : Quarry Blast
- △ : Marine Explosion
- + : Other Explosion



Incoherent Beam Filter
6 - 8 Hz



Incoherent Beam Filter
8 - 10 Hz

(b)

FIGURE 4: (a) Pn/Lg amplitude ratios for mine explosions, marine explosions, and earthquakes at NORESS; (b) Pn/Sn amplitude ratios for mine explosions, earthquakes, nuclear explosions, and a submarine explosion at ARCESS.

Boxplot Comparison of Spectral Ratios For Explosions, Earthquakes, and Underwater Explosions NORESS Recordings

2.5-4.5 Hz/5.0-7.0 Spectral Ratios: Max Log RMS; NORESS Recordings

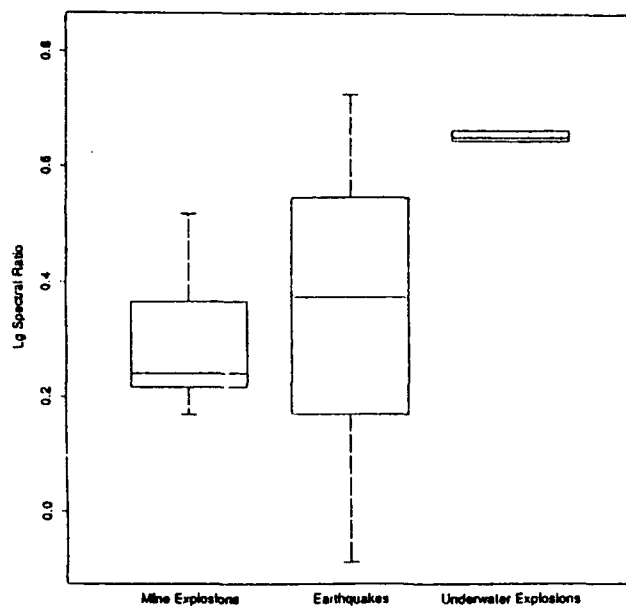


FIGURE 5: Comparison of boxplots for Lg spectral ratio measurements for mine explosions, earthquakes, and marine explosions.

Multivariate Visualizations Star Diagrams

Star Representation of Pn/Lg Ratios, NORESS Recordings, Western Norway Events

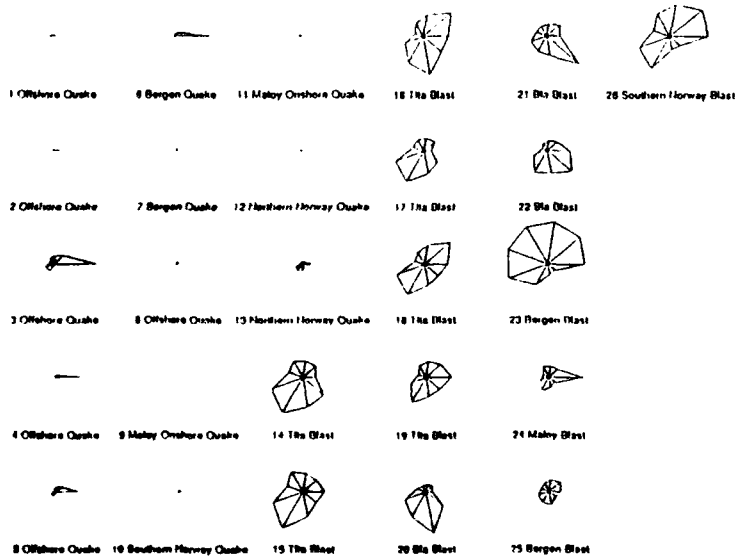


FIGURE 6: Star plot visualization for Pn/Lg ratio measurements for blasts and earthquakes recorded at NORESS. Events 1-13 are earthquakes and 14-26 are explosions.

Seismic Discrimination of Rockbursts in Mines

T. J. Bennett, J. F. Scheimer, A. K. Campanella and J. R. Murphy

S-CUBED

11800 Sunrise Valley Dr., Suite 1212

Reston, Virginia 22091

Contract No. F19628-91-C-0186

Objective

S-CUBED is currently conducting a research project aimed at characterization of rockbursts and other stress-release events in mines for use in their seismic identification. Of the four types of seismic sources pertinent to the problem of event identification (viz underground nuclear explosions, natural earthquakes, chemical blasts and rockbursts) the greatest attention over the years has been directed at discriminating nuclear explosions from earthquakes. However, interest in lowering the discrimination threshold has indicated in recent years that consideration should be given to the frequent mine and construction blasts which occur routinely in many parts of the world. The fourth event type, rockbursts, have received the least attention in this discrimination context even though they occur in hard-rock mining areas throughout the world at depths comparable to nuclear explosion emplacements. We believe that a complete understanding of the seismic signals produced by these latter events will improve capabilities to distinguish normal stress-release activity in mining areas from anomalous events including possible clandestine nuclear tests, which might be concealed in a deliberately triggered, large rockburst.

Research Accomplishments

Much of the publicity and research related to rockbursts and other stress-release events associated with rock excavation have focused on South African gold mines. However, similar types of events have been reported in many parts of the world including central Europe, Great Britain, Scandinavia, China, India, Australia, Zambia, the United States and Canada. Furthermore, it seems likely that the potential for comparable stress-release events exists in other regions. To improve our capability to identify these induced seismic events, we have reviewed reports on the occurrence and mechanisms of such events and have begun collecting and analyzing seismic waveform data for these events from each of the various source areas. By analyzing events from different source regions, we

hope to discern inherent characteristics which will enable distinction of these events from other source types. We are also seeking to obtain data from different events in common source regions to enable determination of the variability between events of similar source type and to identify differences between distinct source types.

Although there is extensive published literature regarding the phenomenology of rockbursts and engineering techniques for their mitigation, relatively few studies deal with theoretical models of rockbursts and associated seismic source mechanisms. According to the rock mechanics model developed by Cook (1983), stress-release events occur when the removal of material from an excavation (either deep underground or near the surface) sufficiently modifies the local stress field that the strength of the local rock or the coefficient of static friction on an existing fracture is exceeded, thereby releasing the accumulated strain energy. The occurrence of such events is therefore dependent on several factors including magnitudes and orientations of local stresses at the depth of the excavation, volume of the excavation, and the rate at which material is being removed. In this environment the changes in local stress due to the mining trigger latent seismic events which are then driven by differences in tectonic stresses in the vicinity of the excavation. Alternatively, the seismic events may be explained as the release of the potential energy produced by the removal of rock in the excavation. McGarr *et al.* (1975, 1990) investigated the seismic source mechanism of mine tremors from South African gold mines recorded at near-regional stations. Although these studies suggested that the body-wave spectra from mining-induced events could in large measure be explained by double-couple rupture models similar to earthquakes, in some cases the mechanisms were more complex requiring a multiple rupture model or elements of explosive or implosive sources along with shear (cf. McGarr *et al.*, 1990; Gibowicz *et al.*, 1990). The data we are acquiring from stress-release events in the different regions will be used to help resolve these model complexities and to identify causes of variation.

In some parts of the world the magnitudes of rockbursts have exceeded 5.0 m_b ; however, in most areas these stress-release events are seldom much larger than 3.0 m_b . For the larger events it should be possible to include teleseismic and far-regional stations as part of the monitoring effort, but the smaller events will require regional or even near-regional monitoring. Our initial studies have focused on two regions where both large and small stress-release events have occurred: South Africa and Central Europe. Although South Africa is generally regarded as a stable continental platform region, the region is not seismically quiet. This is illustrated in Figure 1 which shows the locations of events in southern Africa south of 20°S latitude for the ISC/NEIS database covering the

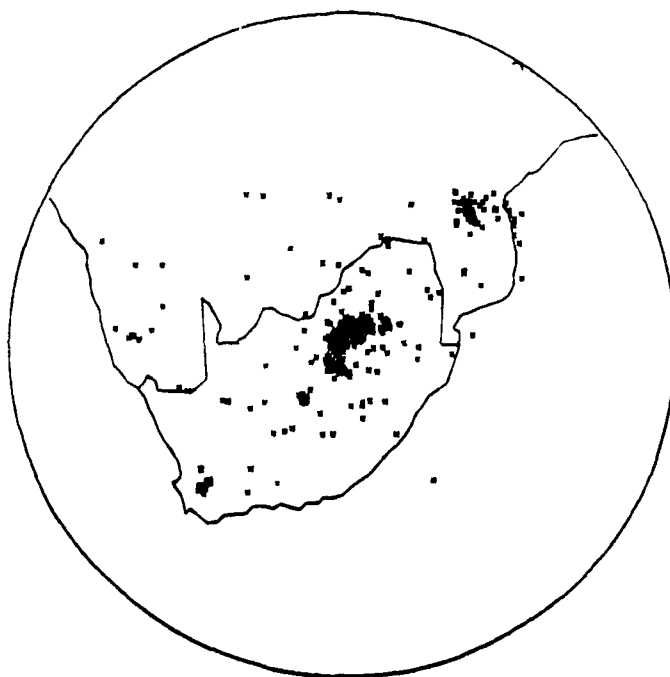


Figure 1. South African seismicity south of 20°S.

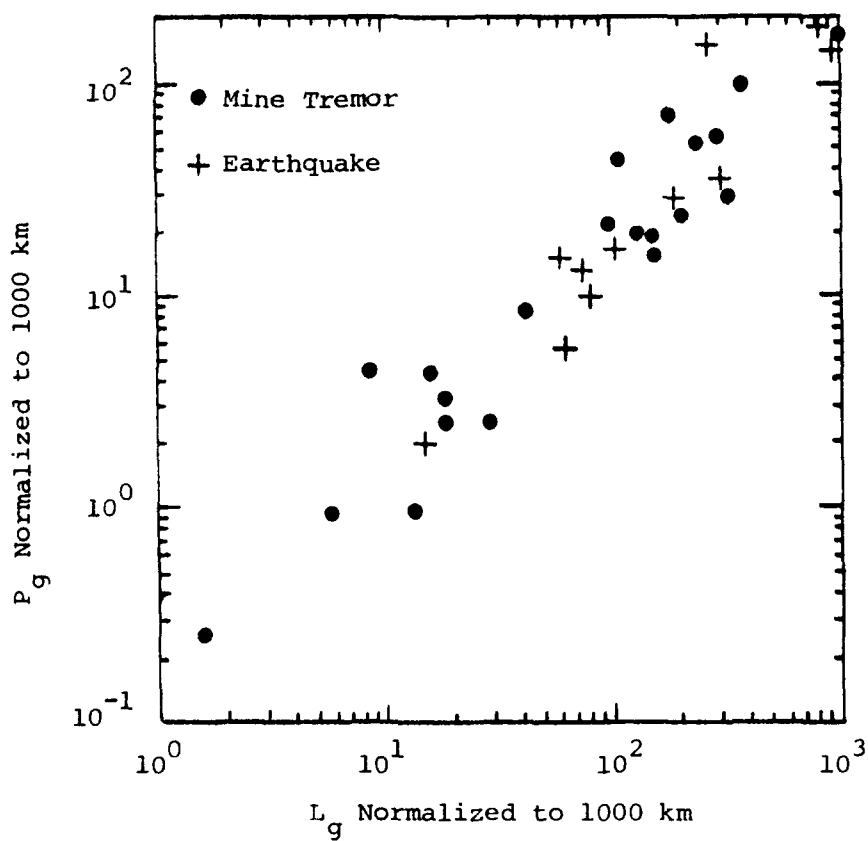


Figure 2. P_g versus L_g amplitudes for South African events observed at SLR.

time period from 1966 through the beginning of 1985. The most prominent feature of the seismic activity is the heavy concentration of events located near the center of the projection in the vicinity of $27^{\circ}\text{S}, 27^{\circ}\text{E}$. This activity consists mainly of mine-related events in the deep, gold-mining area of the Witwatersrand Basin near Johannesburg. The majority of these events appear to be caused by stress release in the surrounding rock associated with closure or partial closure of mine openings - i.e. rockbursts. Some seismic events in the cluster may also be attributable to mineblasts related to continuing development, although such blasts would be expected to have relatively small seismic magnitudes. Outside the main gold-mining area, a relatively low level of natural earthquake activity is scattered throughout much of the remainder of the country; and some blasting associated with strip-mining and construction activity is also known to be present. Thus, South Africa includes three of the four types of events of concern in seismic monitoring (viz rockbursts, mineblasts and earthquakes) and provides an appropriate environment for investigating the characteristics of seismic signals from such sources.

During the time period from 1971-1979, the South African regional seismic network reported 764 mine tremors with local magnitudes ranging from 3.8 to 5.4 M_L . For the time period 1980-1991, the NEIS catalog includes 515 events in the vicinity of the South African gold mining area. Fourteen of these more recent events had body-wave magnitudes equal to or greater than 5.0 m_b , the largest having a magnitude of 5.5 m_b . We are currently in the process of retrieving IRIS, SRO and DWWSSN waveform data from all available seismic stations for several of these larger rockbursts. In addition, we have been analyzing waveform data recorded at the regional station SLR from a selected sample of smaller events including 28 mine tremor events and 11 earthquakes from the surrounding region. The distances to the mining events from SLR are between 50 and 300 km, depending on the specific mine; and distances to the regional earthquakes are between 170 and 1040 km. We have been evaluating a variety of standard regional discriminant measurements applied to these data. Figure 2 shows a comparison of the relative amplitudes in the compressional (P_g) and shear (L_g) wave windows from the vertical component records. After applying a correction for possible attenuation differences, the results suggest that the mine tremor events and the regional earthquakes have similar L_g relative to P_g excitation. However, additional analyses are needed of the scatter in the observations and of the influence of possible regional attenuation variations. We have also looked at the P-wave signals from several of these events in greater detail. Consistency in the signals between events from common source areas suggests that prominent aspects of the signal are controlled by propagation, but we have also identified some differences which may be related to source complexity and variation between events. We are continuing to analyze these

regional data and the data currently being collected for the larger stress-release events from the South African source region.

In central Europe mining districts in Germany, Poland and Czechoslovakia have experienced frequent and, in some cases, large rockburst events. Figure 3 shows the seismicity in the region as determined from the ISC catalog for the period 1987 through 1990. The two prominent clusters in the outlined area to the east correspond to the Lubin and Belchatow mining districts near the border between Poland and Czechoslovakia. The area outlined to the west shows a somewhat more diffuse pattern of seismicity; however, within this pattern are included several clusters known to be associated with stress-release events in mines in the Ruhr district. In addition, some smaller events in the region may be associated with blasting in mines; and some epicenters have been identified as earthquakes. Based on ISC catalog data for the past decade, the eastern mining district experiences about 90 events per year with magnitudes up to near 5 M_L . The western mining district reports about 40 events per year with magnitudes generally smaller, normally around 3 M_L or less. In addition, the largest earthquake in recent history ($m_b = 5.4$) occurred in the region between the two outlined mining districts on March 13, 1992. Thus, like South Africa, Central Europe includes rockbursts, earthquakes and mine blasts within a relatively limited geographical region which should provide useful data for analyzing the effects of source differences on seismic signals.

We are in the process of retrieving IRIS/GDSN waveform data from all the available stations for the largest events and from regional stations for a large sample of smaller events. In addition, the GSETT-2 database includes several events from the central European mining areas; and we are analyzing the amplitude and spectral characteristics of those regional waveforms. Figure 4 shows the waveform data from GRFO for seven typical events from the Lubin and Belchatow mining districts. Within a given mining district there is a strong consistency in the overall character of the signals between events; however, there are some differences in the relative amplitudes of phases and their frequency content which may represent source variation. Differences in signal character between the two districts (e.g. weak P_g from the more distant area) is probably indicative of propagation differences. In any case, these events from the mining districts, which at this point we assume to be related to stress release, produce regional waveforms with strong L_g signals relative to P . This behavior is similar to that reported previously for earthquakes in many parts of the world.

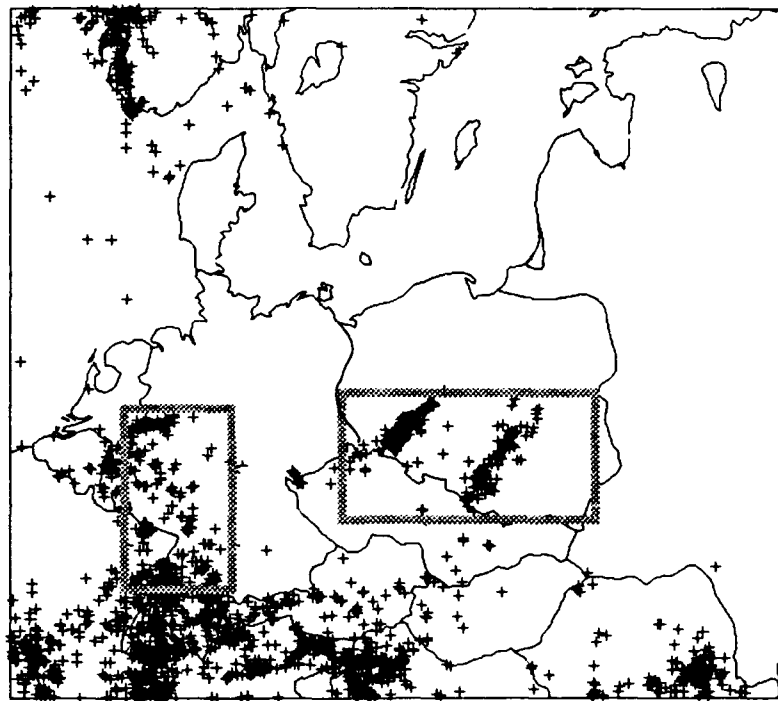


Figure 3. Four years of European seismicity from the ISC catalog with outlined regions enclosing the Ruhr region on the west and the Polish and Czech mining districts on the east.

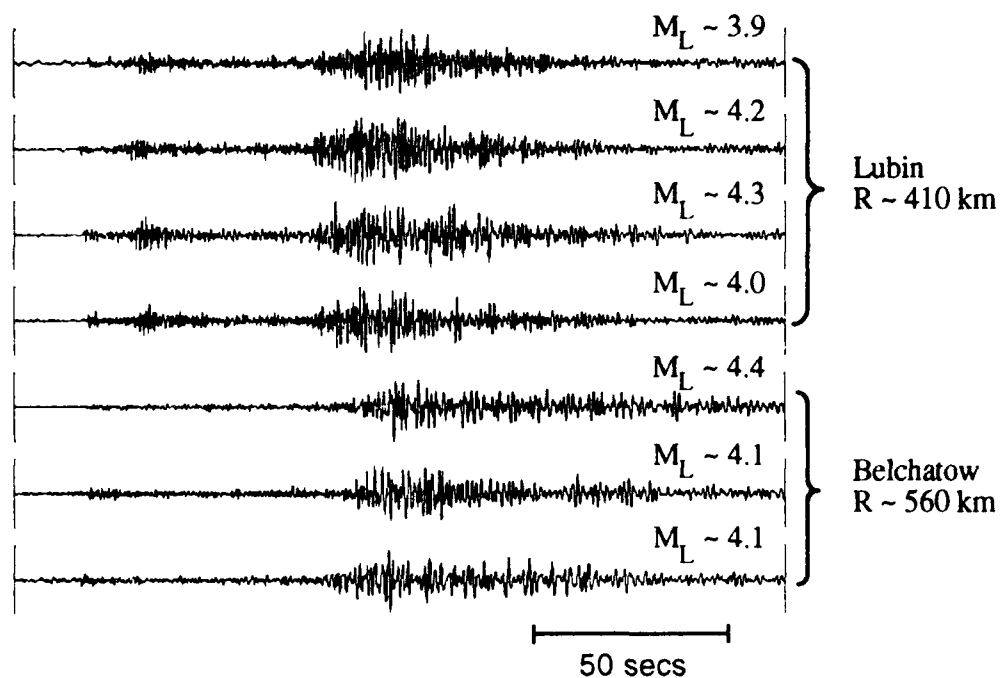


Figure 4. GRFO signals from apparent stress-release events in the Polish/Czech mining districts.

Conclusions

Our preliminary results indicate that mining-induced events show some variations between regions but frequently produce some signal features similar to those of natural earthquakes. In particular, L_g/P ratios are normally greater than 1.0. The South African rockbursts show evidence of relatively strong low-frequency surface waves. In both regions, the P waves show indications of variations between nearby events and for events from different mining districts. We are continuing to collect and analyze the data from these and other worldwide rockburst regions.

References

- Cook, N. G. W. (1983), "Origin of Rockbursts," in Rockbursts: Prediction and Control, The Institution of Mining and Metallurgy, London, 1983.
- Gibowicz, S. J., H. P. Harjes and M. Schafer (1990), "Source Parameters of Seismic Events at Heinrich Robert Mine, Ruhr Basin, FRG: Evidence for Nondouble-Couple Events," *Bull. Seism. Soc. Am.*, 80, pp. 88-109.
- McGarr, A., S. M. Spottiswoode and N. C. Gay (1975), "Relationship of Mine Tremors to Induced Stresses and to Rock Properties in the Focal Region," *Bull. Seism. Soc. Am.*, 65, pp. 981-993.
- McGarr, A., J. Bicknell, J. Churcher, and S. Spottiswoode, "Comparison of Ground Motion from Tremors and Explosions in Deep Gold Mines," *J. Geophys. Res.*, 95, pp. 21777-21792.

**DEEP SEISMIC SOUNDING IN NORTHERN EURASIA:
INTERPRETATION OF THE MURMANSK-KIZIL ULTRA-LONG-RANGE PROFILE**

H.M. Benz, J.D. Unger, and W.S. Leith
U.S. Geological Survey
Menlo Park, California and Reston, Virginia
Contract No. GLHO-6064

Objective

For nearly 40 years the former Soviet Union has carried out a program of seismic studies in northern Eurasia, known as "Deep Seismic Sounding" or DSS (Piwinskii, 1979; Zverev and Kosminskaya, 1980; Egorkin and Pavlenkova, 1981; Egorkin and Chernyshov, 1983; Scheimer and Borg, 1985). To date, DSS profiling has completed nearly 150,000 km of profiles covering all major geological provinces of northern Eurasia. The program is unique in the routine use of nuclear explosions to record profiles to lengths in excess 2000-3000 km. About half of the 115 Peaceful Nuclear Explosions (PNE) detonated since 1966 have been associated with the DSS program. Under the 1990 US-USSR Agreement on Basic Scientific Research, the USGS obtained the three-component digital seismic data for the Murmansk-Kizil ultra-long-range DSS profile.

The Murmansk-Kizil profile, started in 1984 and completed in 1987, extends more than 4000 km from the Kola peninsula to the Altay-Sayan region. The profile crosses tectonic provinces of the Baltic Shield, the eastern European Platform, the Ural Mountains fold belt, the West Siberian Basin, and the Altay-Sayan Foldbelt. The profile was recorded using 42 chemical explosions and 3 PNE's with an average station spacing of 16.4 km. The chemical explosions were recorded to maximum offsets of 600 km, while the PNE's were recorded to distances of roughly 3200 km. We have begun plotting and processing the record sections for both the chemical and nuclear explosions. Forward travel-time and amplitude modeling are being used to determine the crust and upper mantle velocity and attenuation structure beneath northern Eurasia.

DSS profiling: 1960-90

Beginning in 1939-40 with a series of small-scale seismic experiments in the vicinity of Moscow, DSS profiling has broadened into a national multi-institutional exploration effort that has covered all major geological provinces of northern Eurasia (Ryaboy, 1989). The acquisition of DSS data has been supervised by two principal organizations: MinGeo (reorganized into the Geological Committee of Russia in 1991), which oversees most land and some offshore operations, and the Academy of Sciences, which conducts offshore profiling and some DSS land

recording. Within MinGeo, DSS profiling is conducted by several geophysical expeditions and scientific research organizations. For long-range DSS profiling using nuclear explosions, Neftegeofizika (the largest Soviet organization for oil and gas exploration) formed the Special Geophysical Expedition (SGE) to collect and interpret DSS data. In 1991, the SGE was renamed Center for Regional Geophysical and Geoecological Research (GEON) and broadened its services to include commercial offerings of geophysical data for exploitation of certain areas of northern Eurasia. Prior to about 1989, foreign contacts were limited, but recent developments in the Commonwealth of Independent States (CIS) have led to USGS-MinGeo scientific agreements and the availability of digital DSS data for analysis by United States scientists.

Depending on the region of interest and the types of sources used, DSS profiles range from 200 to nearly 4000 km in length. Early findings of DSS investigations indicated that variations in crustal structure correlated with the age provinces and tectonic setting, which prompted the systematic recording of long-range DSS profiles across much of northern Eurasia. In 1963 and 1964, the first detailed DSS study of the Earth's crust and upper mantle was conducted in central Asia, providing details to depths of approximately 100 km (Ryaboy, 1966a,b). Subsequently, recording of long-range profiles using chemical explosions became wide-spread in northern Eurasia, western Europe, Scandinavia, Australia and India (Finlayson et al., 1974; Fuchs, 1979; Muller and Ansorge, 1986, Kaila and Krishna, 1992).

Starting in the early 1970's, the DSS program routinely used nuclear explosions in the recording of ultra-long-range profiles (Figure 1). About half of the 115 "Peaceful Nuclear Explosions (PNE's)" detonated since 1966 have been associated with the DSS program (Nordyke, 1973; 1975). Most PNE's were used for other purposes, excavation, cavity construction, hydrocarbon stimulation; consequently, many DSS profiles were "piggy-back" experiments on the principle application of the PNE. Figure 1 shows the locations of the known long-range DSS profiles recorded using PNE's and additional profiles recorded by Neftegeofizika using conventional sources. These profiles represent roughly 30% of the total number of profiles acquired. Interpretation of some of these and other DSS profiles can be found in Zverev and Kosminskaya (1980), Egorkin and Pavlenkova (1981), Egorkin et al. (1987), and Ryaboy (1989). Table 1 provides a guide to the DSS line numbers, dates recorded, and associated PNE's.

DSS studies have suggested the presence of significant lateral and vertical velocity and attenuation structure to depths of at least 200-300 km beneath the Earth's surface. Despite recent economical and political difficulties in the CIS, the DSS program is continuing to develop and improve. There are plans to acquire new long-range profiles in Siberia and in the European

region of the CIS, as part of the Europrobe transect.

A variety of analog seismic recording systems have been used by Soviet geophysicists for collecting DSS data. Early seismographs utilized oscillographs to make permanent photographic records of the seismic waves or arrivals. From 1950 to 1970, approximately 50,000 km of profiles were recorded in this manner, resulting in approximately 200 land and offshore DSS profiles (Vol'vovskiy, 1973). In about 1970, the photographic instruments were replaced by modern analog systems that record on magnetic tape. The specific systems used are the Tayga, Cherepakha, and Zemlya seismographs.

The Zemlya and Cherepakha seismic systems record directly onto magnetic tape recorders and can run for up to 24 days on batteries. Consequently, these systems have been used in both profiling and aftershock experiments. Unfortunately, the Zemlya system has considerable phase distortion and cannot be used in detailed waveform modeling. An improved Tayga recording system is radio-triggered and records an FM signal on magnetic tape. The Tayga recording system is generally considered to be the better of the seismographs, but records for only 45 minutes.

During the recording of a typical ultra-long-range profile (>1500 km), portable seismic stations are located about 10-km-apart. They are located 1-to-5 km apart for shorter profiles. GEON has recently experimented with dense arrays (~100 m spacing) for mapping karst in the subsurface of the Moscow metropolitan region. Profiles with a 0.5-1.0 km station spacing have also been recorded in the aftershock region of the M7.2 1988 Armenia earthquake. Over the past twenty years, GEON has recorded DSS profiles using three-component seismometers with 1-2 Hz resonance frequencies.

Unlike DSS profiles, which are still recorded with analog systems, institutions in North America converted to large numbers of digital recorders (>300) in the late 1980's. Comparatively, North American seismic profiles are relatively short (200 to 600-km-long) and generally lacking three-component recordings. The emphasis has primarily been on high-resolution imaging of the crust (Mooney and Braile, 1989). Consequently, DSS profiles represent the most comprehensive source of seismic data on continental lithospheric and asthenospheric P and S-wave velocity structure.

The Murmansk-Kizil Ultra-Long-Range Profile

The Murmansk-Kizil DSS profile (line 32, Figure 2) was started in 1984 and completed in 1987. The profile extends more than 4000 km across five major tectonic provinces, all of which differ from one another both in terms of their tectonic history

and crustal structure. These provinces are: the Baltic Shield, the eastern European Platform (Moscow basin), the Ural Mountains fold belt, the West Siberian Basin, and the Altay-Sayan Foldbelt. Importantly, this single profile samples the lithosphere in an ancient continental craton, a platform region that has been stable throughout the Phanerozoic, an eroded Hercynian mountain belt, a broad extensional basin with thinned crust and very thick sediments, and an active Alpine fold belt.

Figure 3 shows the vertical component partial P-wave record sections for shotpoints 123 and 321, the northernmost and southernmost PNE's on the Murmansk-Kizil profile. The record sections shows that the Pg phase is observed as a first arrival to offsets of roughly 200 km, while Pn is clearly observed as a first arrival from 200 to 1600-1800 km. An increase in apparent velocity of Pn, for offsets greater than 900 km, suggests a strong increase in velocity with depth in the subcrustal lithosphere. The amplitude of the Pn phase decays markedly beyond 1600 km, suggesting that the phase is bottoming into the top of the mantle LVZ. Beyond 1600 km, the most prominently observed phases is the wide-angle reflection off the 410-km-discontinuity.

Shown in Figure 4 is a preliminary one-dimensional velocity model for shotpoint 321, based on iterative travel time and reflectivity synthetic seismogram modeling. The most prominent feature of the velocity model is a pronounced upper mantle LVZ that extends from 150 km to 235 km. The LVZ is constrained by the termination of the Pn phase beyond 1600 km and an observed reflection off the bottom of the LVZ (1400 km and 11 sec reduced time). Our model of a simple LVZ differs from the complex series of high and low velocity layer that characterize the model of Egorkin (per. comm.). A more complex LVZ was not warranted in our preliminary modeling. The most interesting upper mantle feature is a distinct velocity increase at a depth of 500 km. This feature is observed as a high apparent velocity and relatively high amplitude phase (Figure 3) that is observed from 2200 km (3 sec) to 2600 km (-10 sec). Also shown for comparison with our preliminary velocity model is the IASPEI91 velocity model. Figure 5 is a comparison between the observed seismic data and reflectivity synthetic seismograms for shotpoint 321. The amplitudes and travel times are reasonably well matched by our model. Additional work is required to improve the fit, especially the relative amplitudes observed for distances greater than 2000 km. This can primarily be achieved by modifications to velocity gradients and introducing depth-dependent attenuation. Final modeling results for the PNE data will be presented.

References

- Egorkin, A.V., and N.I. Pavlenkova, Studies of mantle structure of USSR territory on long-range seismic profiles, *Physics of the Earth and Planet. Int.*, 25, 12-26, 1981.
- Egorkin, A.V., and N.M. Chernyshov, Peculiarities of mantle waves from long-range profiles, *J. Geophys.*, 54, 30-34, 1983.
- Egorkin, A.V., S.K. Zukanov, N.I. Pavlenkova, and N.M. Chernyshev, Results of lithospheric studies from long-range profiles in Siberia, in *Seismic Studies of the Continental Lithosphere*, edited by S. Asano and W.D. Mooney, *Tectonophysics*, 140, 29-47, 1987.
- Finlayson, D.M., J.P. Cull, and B.J. Drummond, Upper mantle structure from the trans-Australia seismic survey and other seismic refraction data, *J. Geol. Soc. Austral.*, 447-458, 1974.
- Fuchs, K., Structure, physical properties and lateral heterogeneities of the subcrustal lithosphere from long-range deep seismic sounding observations on continents, *Tectonophysics*, 1-15, 1979.
- Kaila, K.L. and V.G. Krishna, Deep seismic sounding studies in India and major discoveries, in *Seismology in India-An Overview*, edited by S. Ramaseshan and H.K. Gupta, Indian Academy of Science, *Current Science*, 117-154, 1992.
- Mooney, W.D. and L.W. Braile, The seismic structure of the continental crust and upper mantle of North America, in *The Geology of North America-An overview*, edited by A.W. Bally and A.R. Palmer, Geological Society of America, *The Geology of North America*, 39-52, 1989.
- Muller, S. and J. Ansorge, Long-range seismic refraction profiles in Europe, in *Reflection Seismology: A Global Perspective*, edited by M. Barazangi and L. Brown, *Geodynamic Series*, 13, 167-182, 1986.
- Nordyke, M.D., A review of Soviet data on the peaceful uses of nuclear explosives, *UCRL-5414*, Lawrence Livermore National Laboratory, 1973.
- Nordyke, M.D., A review of Soviet data on the peaceful uses of nuclear explosions, *Ann. Nucl. Energy*, 2, 657-673, 1975.
- Piwinskii, A.J., Deep structure of the Earth's crust and upper mantle in the USSR according to geophysical and

seismological data, UCID-18099, Lawrence Livermore National Laboratory, 69 pp., 1979.

Ryaboy, V.Z., Kinematic and dynamic characteristics of deep waves associated with granites in the Earth's crust and upper mantle, *Bulletin of the USSR Academy of Sciences, Earth Physics*, 3, 177-184, 1966a.

Ryaboy, V.Z., Structure of the Earth's crust and upper part of the mantle along the Kopet-Dag-Aral Sea profile, *Soviet Geology*, 5, 159-162, 1966b.

Ryaboy, V.Z., *Upper Mantle Structure Studies by Explosion Seismology in the USSR*, Delphic Press, 1989.

Scheimer, J. F., and I. Y. Borg, Deep seismic sounding with nuclear explosives in the Soviet Union, *Science*, 226, 787-792, 1985.

Vol'vovskiy, I.S., *Seismicheskie issledovaniya zemnoi kory v SSSR*, Nedra, Moscow, 207 pp., 1973.

Zverev, S.M., and I.P. Kosminskaya (Editors), *Seismic models of the main geostructures of the USSR territory*, Nauka, Moscow, 184 pp., 1980.

Figures

Figure 1. Long-range DSS profiles recorded by GEON through 1990. Circles indicate the locations of the PNE's that were used as sources for the DSS profiles. The locations of the broad-band seismic stations of the Joint Seismic Program (JSP) are shown as triangles, including both existing and proposed station locations.

Figure 2. Location of the Murmansk-Kizil Ultra-Long-Range DSS profile (Line 32) started by GEON in 1984 and finished in 1987. The profile was recorded using 3 PNE's and 42 chemical explosions. Circles indicate the locations of the PNE's and triangles represent the JSP stations, but both existing and proposed station locations.

Figure 3. P-wave record sections for shotpoints 123 and 321, the northernmost and southernmost PNE on the Murmansk-Kizil DSS profile. Plotted trace normalized are every other seismogram in the direction of longest offset. Record sections are plotted with a reducing velocity of 8.2 km s^{-1} .

Figure 4. Preliminary one-dimensional velocity model for shotpoint 321. The velocity is compared to IASPEI91 and generalized one-dimensional velocity model based on iterative travel time model by geophysicists at GEON (Egorkin, per. comm.).

Figure 5. Comparison of the P-wave record section for shotpoint 321 and the reflectivity synthetic seismograms for our preliminary velocity model (Figure 4). Record sections are plotted with a reducing velocity of 8.2 km s^{-1} .

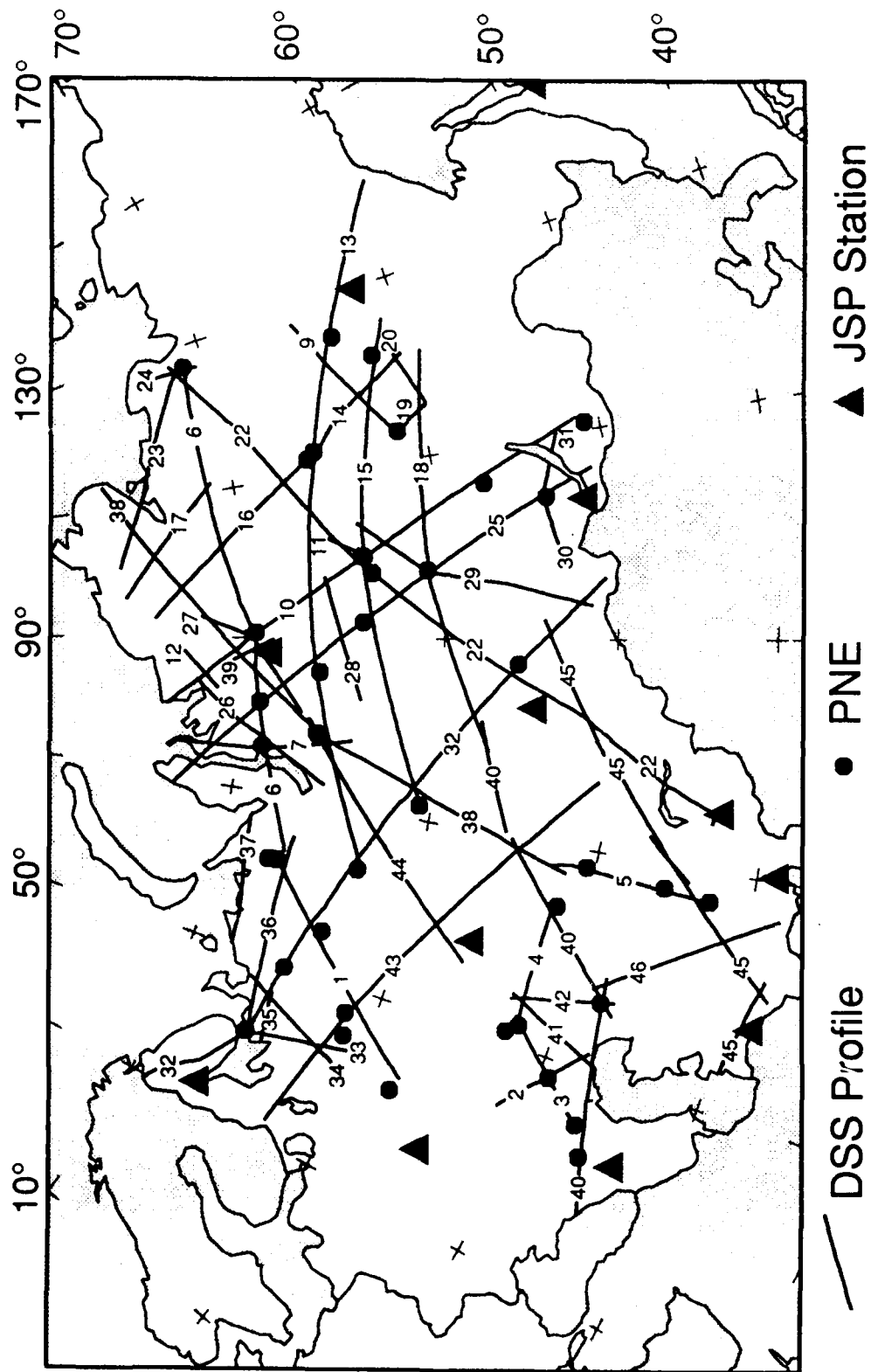
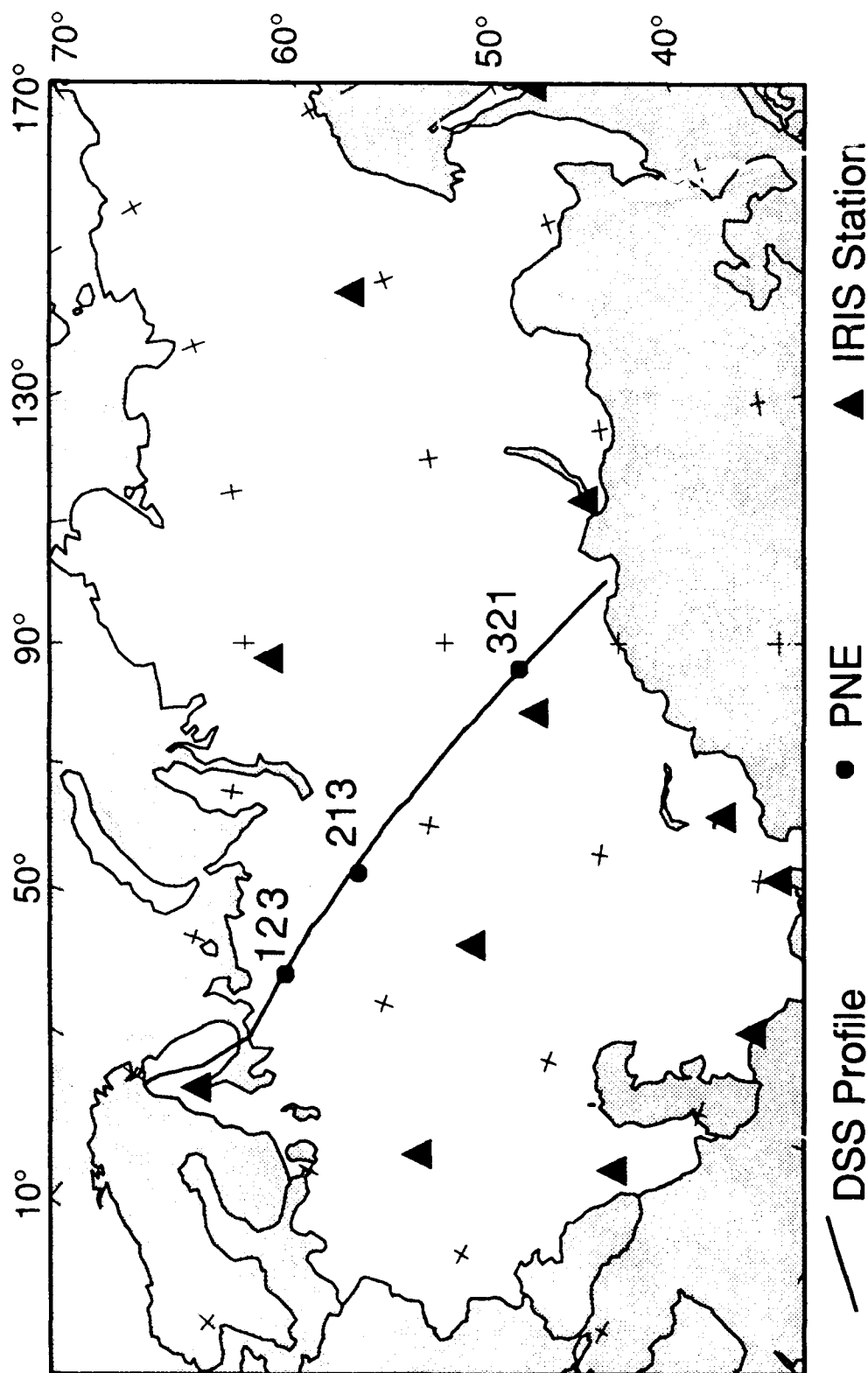
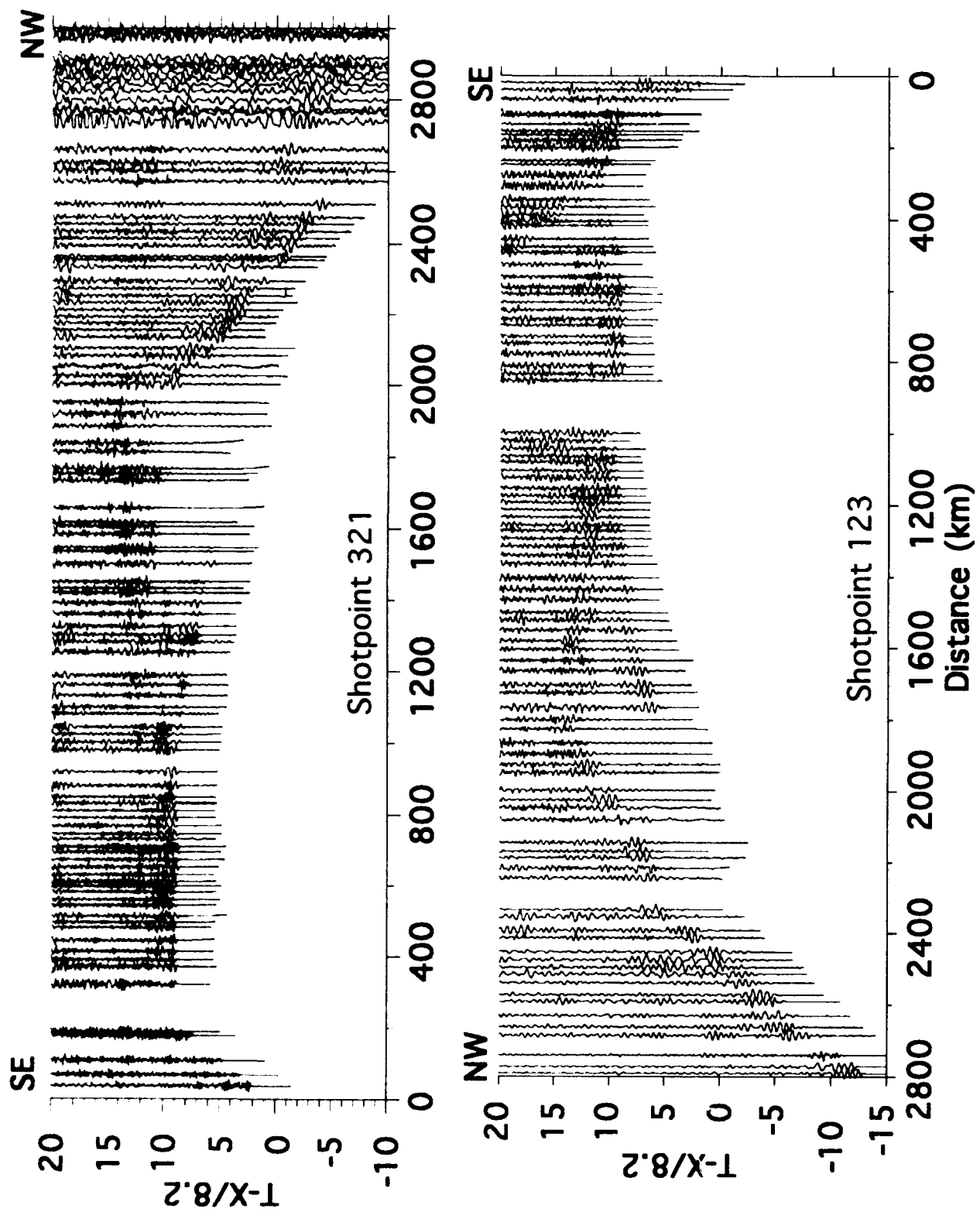
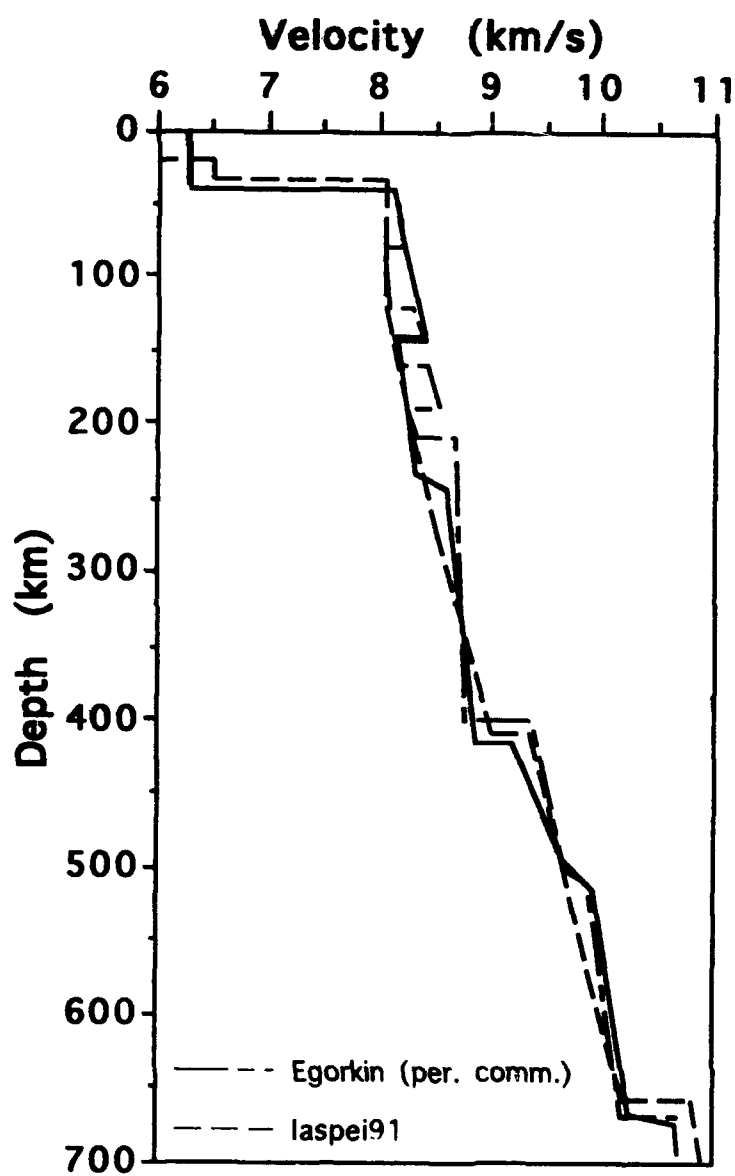


Figure 1

Murmansk-Kizil DSS Profile







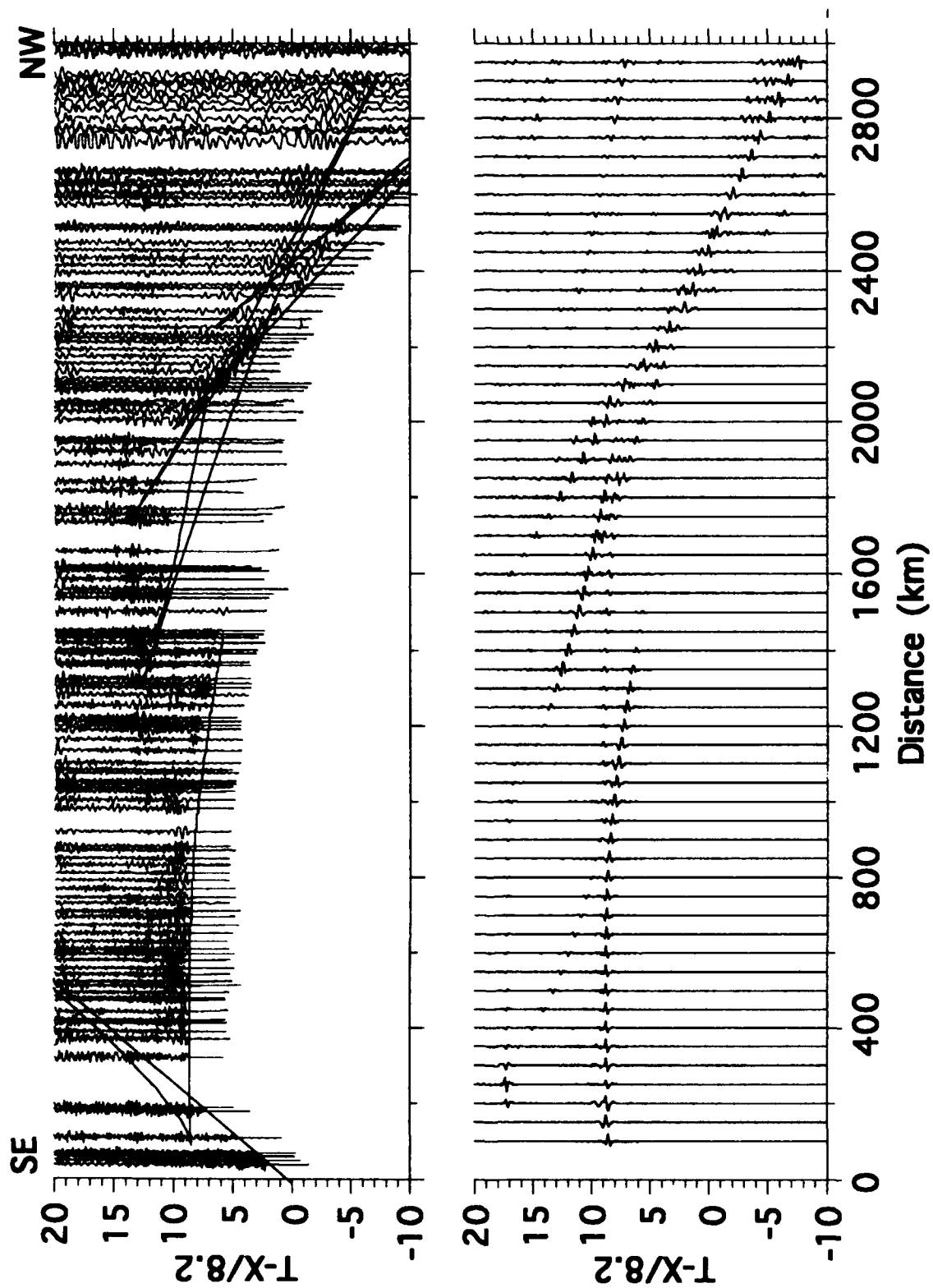


Figure 5

Non-linear Attenuation in the Near Source Region: Characterization of Hysteresis in the Deformation of Rock Joints

G. N. BOITNOTT

New England Research, Inc., White River Junction, Vt.

Contract number F29601-91-C-DB26

OBJECTIVE

The importance of joints in the attenuation of high amplitude - high frequency seismic waves originates from two principal causes. First, the mechanical properties of rock joints contrasts greatly in comparison to the mechanical properties of intact rock, with the excessive compliance of the joint causing partial reflection of an incident wave [*Schoenberg, 1980; Kitzunezaki, 1983; Pyrak-Nolte et al., 1990*]. The reflection (or scattering) causes apparent attenuation. Second, rock joints act as zones of weakness to shear motion, with some of the shear motion being taken up by frictional sliding at the points of contact across the joint. In addition, normal deformation of joints has long been known to exhibit noticeable hysteresis which has been attributed to frictional sliding at oblique contacts [i.e. *Scholz and Hickman 1983*]. The mechanics of frictional dissipation at the contact points has been discussed for the case of rocks containing micro-cracks [*Stewart et al., 1983*] and will be developed quantitatively in this study for the case of rock joints and jointed media.

The work for this study is evolving along three lines. First low frequency normal load hysteresis loop experiments are underway to empirically quantify the shape of hysteresis loops as a function of normal load, loop amplitude, and joint roughness. In addition to the hysteresis loop experiments, ultrasonic wave transmission across the joint is being measured to characterize the small strain dynamic stiffness of the joint. Second, a constitutive model [*Boitnott et al., 1992*] is being extended to predict the mechanical properties of joints subject to shear oscillations. The model predicts the hysteresis loops expected as a function of normal load, shear oscillation amplitude, and joint roughness. The constitutive model will be experimentally tested with shear hysteresis loop experiments. Third, a model is being developed which allows for coupling of the dynamic scattering and frictional energy loss. This model will then be used in conjunction with the experimental results to assess the conditions under which pre-existing rock joints are important in the attenuation of high amplitude elastic waves.

RESEARCH ACCOMPLISHED

Normal Load Hysteresis Loop Experiments

Although the mechanisms are qualitatively understood [*Scholz and Hickman, 1983; Boitnott and Scholz, 1990*], there is little experimental data to quantify, even empirically, the energy loss per cycle for the normal load hysteresis loops on single joints. As part of this study, a series of experiments are being conducted on artificial joints to try to empirically quantify the energy loss per cycle as a function of joint roughness, normal load, and cycle amplitude. The experiments are being conducted using a hydraulically servo-controlled uniaxial apparatus. Hysteresis loop and ultrasonic wave propagation tests are performed on the same samples, allowing direct comparison of the results of the two types of measurements.

To date, experiments have been done on glass and granite samples. Two samples of Schott BaK1 optical quality glass containing artificial joints have been tested. The artificial joints were prepared by hand lapping surface ground surfaces with 120 and 60 grit silicon carbide powder. While these jointed samples exhibit hysteresis for load cycles from 0 to 10 MPa, hysteresis loop experiments at mean loads of 4 MPa and greater and stress perturbations of 2.5 MPa and less show surprisingly little hysteresis (see figure 1). This indicates that the hysteresis observed in the overall loading curves for these nominally flat and smooth joints results from either large deformations or mechanisms active only at low stress. In contrast, experiments on a laboratory induced tension fracture in Sierra White granite show considerable hysteresis, with the loops being highly dependent on mean normal load and loop amplitude (see figure 1). The different response between the lapped surfaces and the tension fracture indicate that the presence of long wavelength topography on the joint surfaces is important factor in causing frictional attenuation.

The goal of this phase of the study will be to develop an empirical description of hysteresis loop shape as a function of normal load, cycle amplitude, and joint roughness. Preliminary results suggest that the stiffness versus load relationship will be fairly easy to characterize and may provide the basis for models requiring realistic rheologies for arbitrary loading histories.

Dynamic vs. Quasi-static Stiffness

Models to incorporate fractures in wave propagation models have primarily been based on treating an individual joint as a displacement discontinuity [*Schoenberg, 1980; Pyrak-Nolte et al., 1990*]. When an elastic wave encounters a displacement discontinuity, part of the energy is reflected and part transmitted. The transmission coefficient is a function of the stiffness of the displacement discontinuity (the joint stiffness) and the frequency of the elastic wave. For example, the transmission coefficient for a wave with normal incidence is given by

$$T = \frac{2K/Z}{-i\omega + 2K/Z} \quad (1)$$

where K is the joint stiffness, ω is the frequency of the incident wave, and Z is the acoustic impedance of the host material. The validity of such a model has been tested by *Pyrak-Nolte et al.* [1990] who found that the functional form of equation (1) did a

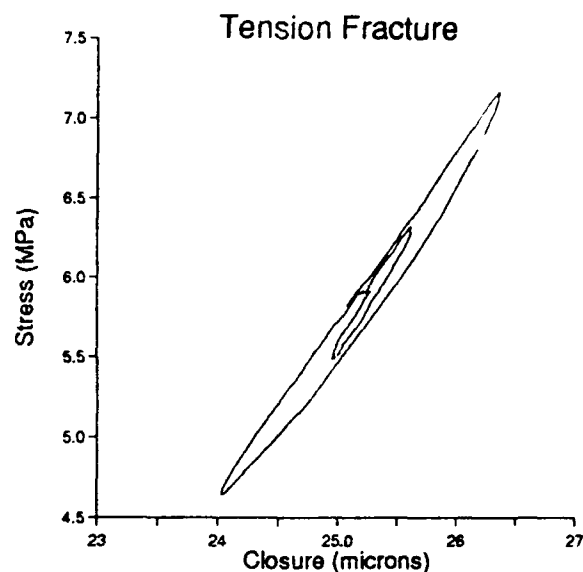
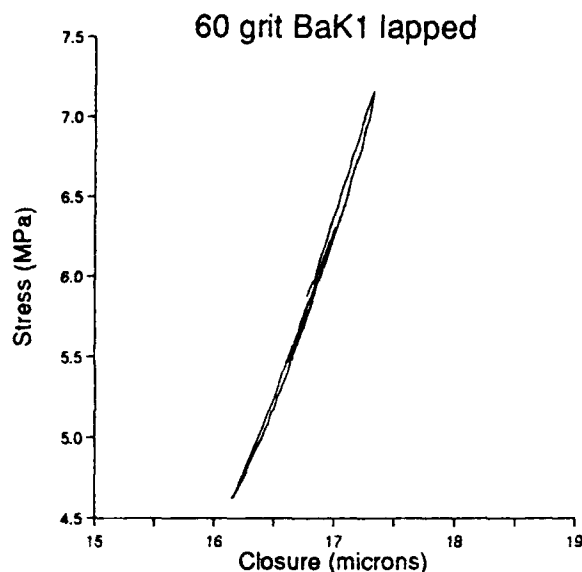


Fig. 1 Examples of normal closure hysteresis loops for a 60 grit lapped glass joint and a tension fracture in Sierra White granite. Both series of loops were conducted at a nominal load of 6 MPa. The lapped glass joint exhibits little hysteresis while the tension fracture exhibits considerable hysteresis. No correction for intrinsic rock deformation has been applied to the Sierra White granite data.

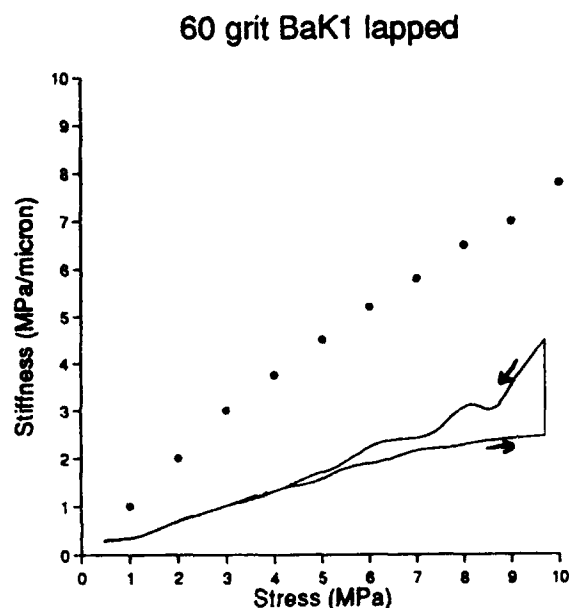
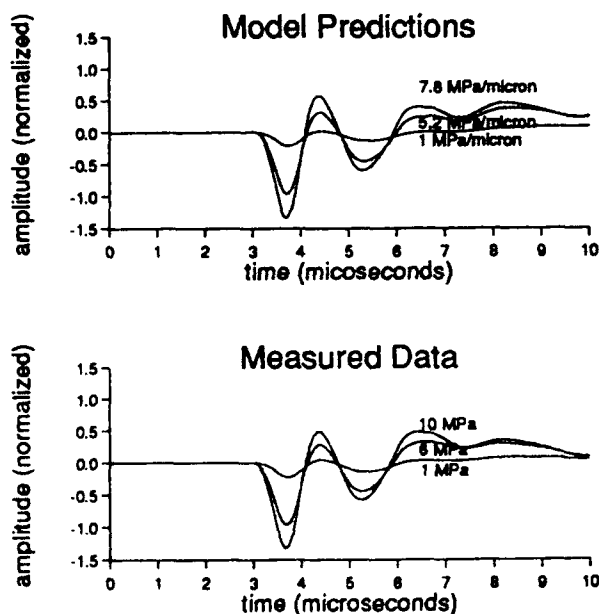


Fig. 2 (a) Comparison of measured compressional waveforms transmitted through the 60 grit lapped joint in glass subject to normal loads of 1, 6, and 10 MPa with theoretically derived waveforms. Waveform matching is used to measure the dynamic stiffness of the joint as a function of normal load.

(b) Comparison of ultrasonically derived compressional stiffnesses (circles) with quasi-statically measured stiffness (solid line) for the 60 grit lapped joint in glass. The ultrasonically derived stiffnesses are systematically higher than the quasi-statically measured values, however more work is needed to interpret and constrain this conclusion.

good job of quantitatively describing the spectrum of the transmitted energy for ultrasonic frequencies in the band 200 kHz to 1.0 MHz. However, the stiffnesses needed to model the observations were considerably higher than quasi-static normal load stiffnesses measured on the same sample. As postulated by [Pyrak-Nolte and Nolte, 1992], this difference (by as much as a factor of 10) may be explained by the apparent frequency dependent stiffness caused by spatial variations in fracture stiffness at the scale of the wavelength of the elastic wave. It may also be explained by the observation that joint stiffness exhibits strong hysteresis (loading path dependence). The stiffness to small normal stress oscillations has been shown to be considerably higher than the quasi-static loading stiffness [Scholz and Hickman, 1983; Boitnott and Scholz, 1990], possibly consistent in magnitude with the discrepancy found by Pyrak-Nolte *et al.*, [1990]. This argument for the discrepancy between dynamic and quasi-static stiffnesses is similar to that proposed by Walsh [1965] to explain the difference between static and dynamic moduli of a wide variety of rocks.

For this part of the study, we plan to systematically examine the dynamic stiffness measured at ultrasonic frequencies in order to test the relationship between dynamic and quasi-static joint stiffness. A waveform inversion technique has been developed to constrain the dynamic stiffness from the measured transmitted waveform. Example waveform matching and stiffness measurements for the 60 grit glass sample are shown in figure 2. Tests will be conducted to attempt to distinguish between the various explanations for the difference between static and dynamic stiffness.

Constitutive Model for Shear Oscillation

A number of constitutive models have been developed and experimentally tested which predict the macroscopic mechanical properties of the joint from the material properties of the solid and the surface topography (or equivalently the aperture distribution) [Greenwood and Williamson, 1966; Swan, 1983; Brown and Scholz, 1985, 1986; Hannan, 1988]. The models all belong to a class of model referred to as non-interacting contact models, where the macroscopic force resisting an applied deformation is determined by a simple linear summation of the forces contributed from each contact.

The contact model has recently been applied to shear loads by Boitnott *et al.* [1992], and it is this model which we have extended to the case of an oscillatory shear load. Example computations for the case of oscillatory shear loads are shown in figure 3. Note that the stiffness versus displacement relationship predicted by the model is fairly easy to parameterize, having a great deal of symmetry and scaling easily with cycle amplitude. It is these characteristics, which are also expected for the normal load hysteresis loops as well, which we will try to exploit in developing a rheological description for moderate strains. For this phase of the study, the primary goal is to experimentally test the validity of the micromechanical model and to derive a constitutive model for shear hysteresis loops.

Coupling of Scattering and Frictional Attenuation

Through use of the micromechanical model and/or empirically derived rheology, we can develop a model which predicts, for a single joint, both the intrinsic attenuation

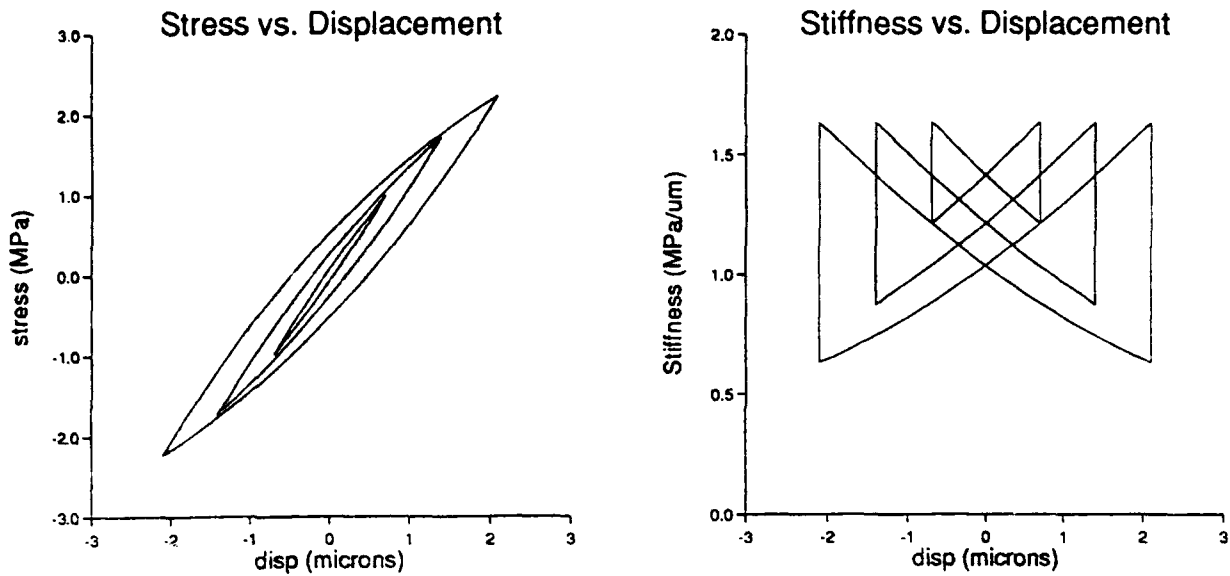


Fig 3. Examples of shear hysteresis loops predicted by the micro-mechanical model for a single joint. Stress - displacement and Stiffness - displacement records for three loops with varying amplitudes are shown. Each loop is for the same joint with a composite topography having a standard deviation of 43 microns and number of degrees of freedom of 19.

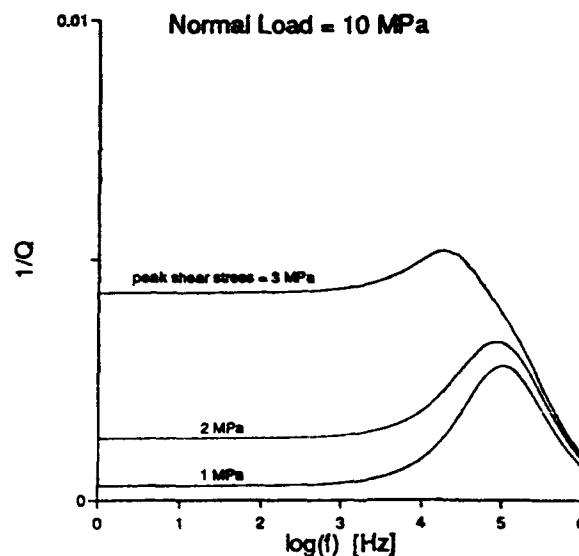


Fig 4. The values of apparent $1/Q$ from calculations based on the micromechanical model assuming a shear wave with peak stresses of 1, 2, and 3 MPa normally incident to a series of joints with a fracture spacing of $1\text{ msup}-1$. Topography parameters are the same as used in figure 3. At low frequencies ($f < 1$ kHz) the dominant mechanism is frictional loss while for high frequencies reflection (scattering) is most important. Increase in the wave amplitude does not effect the relative energy loss to scattering but can strongly effect the energy loss to friction by an amount dependent on normal load and surface roughness.

due to friction as well as the energy lost to elastic reflection. As an example of the approach we will take, we can use the micromechanical shear model to predict the joint stiffness from the joint surface topography. The joint stiffness can be used to predict the transmission and reflection coefficients (i.e. equation 1) and thus gives us an estimate of the energy lost to elastic reflection. The transmission coefficient also provides an estimate of the stress build-up at the joint which can then be fed back into the micromechanical model to predict the energy loss per cycle to friction. Using this procedure we have computed the energy loss ratios for friction and elastic reflection where we normalize by the energy per unit area in one cycle of the incident wave. The preliminary model results show that the dominant attenuation mechanism for a typical joint in the upper kilometer of the crust depends strongly on joint aperture distribution, normal load, frequency and amplitude of the elastic wave. For laboratory scale joints, low frequency ($<100\text{Hz}$) - high amplitude waves are attenuated primarily by frictional loss, with the inherent properties of the attenuation being highly non-linear and amplitude dependent. High frequency ($>10\text{kHz}$) - low amplitude waves are attenuated primarily by elastic scattering, which has the properties of being strongly frequency dependent but independent of wave amplitude. For field scale joints, the frequency cutoff between these two mechanisms can be expected to be lower and the magnitude of the attenuation higher.

The energy loss ratios can be combined to compute an apparent attenuation coefficient, $Q^{-1} = (E_r + E_f)/2\pi E$, where E_r is the energy lost per cycle to reflection, E_f is the energy lost to friction per cycle, and E is the peak elastic strain energy during the cycle. Computations of Q^{-1} are shown in Fig. 4 assuming a fracture density of 1m^{-1} . We find that when the frictional mechanism dominates, Q^{-1} is frequency independent but is strongly influenced by joint roughness, normal load, and wave amplitude. The elastic reflection contribution to Q^{-1} is strongly frequency dependent and somewhat dependent on joint roughness and normal load, but there is little dependence on wave amplitude.

CONCLUSIONS and RECOMMENDATIONS

Hysteresis loop experiments on joints comprised of lapped glass surfaces show very little hysteresis for moderate strain loops at mean pressures above a few MPa. In contrast, a tension fracture in Sierra White granite exhibits considerable hysteresis which is strongly dependent on the mean load and loop amplitude. For the lapped glass joints, dynamic stiffness measured at ultrasonic frequencies is consistently higher than quasi-statically measured joint stiffness. The difference, however, is considerably less than that observed by [Pyrak-Nolte *et al.*, 1992] on natural fractures. More tests are needed to distinguish between different explanations for this discrepancy. The preliminary results confirm the idea that pre-existing rock joints will play an important role in attenuation of moderate amplitude seismic waves. The planned experimental program will hopefully help constrain the conditions under which joints are the dominant cause of attenuation.

REFERENCES

- Boitnott, G. N., N. Yoshioka, R. Biegel, C. Scholz, and W. Wang, Micromechanics of rock friction: 2, quantitative modeling of initial friction with contact theory, *J. Geophys. Res.*, 97 8965-8978, 1992.
- Boitnott, G. N., and C. H. Scholz, Direct measurement of the effective pressure law: Deformation of joints subject to pore and confining pressures, *J. Geophys. Res.*, 95 19279-19298, 1990.
- Brown, S. R., and C. H. Scholz, Closure of random elastic surfaces in contact, *J. Geophys. Res.*, 90, 5531-5545, 1985.
- Brown, S. R., and C. H. Scholz, Closure of rock joints, *J. Geophys. Res.*, 91, 4939-4948, 1986.
- Greenwood, J. A., and J. Williamson, Contact of nominally flat surfaces, *Proc. R. Soc. London Ser. A*, 295, 300+, 1966.
- Hannan, S. S., An experimental study of fracture closure in elastically and non-elastically deformable rocks, Ph.D. thesis, Dep. of Geol., Univ. of Toronto, Toronto, Ont. 1988.
- Kitzunezaki, C., Behavior of plane elastic waves across a plane crack, *J. Mining Coll. Akita Univ., Ser. A*, 6, 173-187, 1983.
- Pyrak-Nolte, L. J., L. Myer, and N. Cook, Transmission of seismic waves across single natural fractures, *J. Geophys. Res.*, 95, 8617-8638, 1990.
- Pyrak-Nolte, L. J., and D. D. Nolte, Frequency dependence of fracture stiffness, *Geophys. Res. Lett.*, 19, 325-328, 1992.
- Schoenberg, M., Elastic wave behavior across linear slip interfaces, *J. Acoust. Soc. Am.*, 68, 1516-1521, 1980.
- Scholz, C. H., and S. H. Hickman, Hysteresis in the closure of a nominally flat crack, *J. Geophys. Res.*, 88, 6501-6504, 1983.
- Stewart, R. R., M. N. Toksoz, and A. Timur, Strain dependent attenuation: observations and a proposed mechanism, *J. Geophys. Res.*, 88, 546-554, 1983.
- Swan, G., Determination of stiffness and other joint properties from roughness measurements, *Rock Mech. Rock Eng.*, 16, 19-38, 1983.
- Walsh, J. B., The effect of cracks on the uniaxial elastic compression of rocks, *J. Geophys. Res.*, 70, 399+, 1965.

EPICENTRAL AZIMUTH DETERMINATION BY MINIARRAY PROCESSING

Y.Cansi, J.L. Plantet and J.P. Massot

Radiomana

27, rue Claude Bernard

75005, Paris, France

n° 90-0356

OBJECTIVE:

During the 80's, substantial efforts have been carried out to use local mini-arrays for automatic event detection (e.g.: MIKKELTVEIT et al., 1983). Beside these studies, some researches have also been undertaken to evaluate their capabilities of automatic azimuth and slowness determination, for location purpose.

For similar objectives, the *French Laboratoire de Détection et de Géophysique* (LDG) has installed in 1990 a small temporary local network in the Center of France, provisory composed of 5 vertical component short period seismometers with an aperture of 1.2 km x 2 km. (In the next future 10 stations should be set up). 98 teleseismic events have been recorded by the network during 6 months of operation. We present here the main results concerning the automatic determination of azimuth and slowness for each event of this dataset. Two different methods of data processing are tested and compared for that purpose.

RESEARCH ACCOMPLISHED:

1) *The methods:*

- The first method, so-called "*frequency-wavenumber (f-k) method*", has often been used by seismologists (e.g.: CAPON, 1969, GUPTA et al., 1990). At the opposite of the original use of this method which computes the k-spectrum using filtered signals in a narrow band, we have followed the algorithm proposed by NAWAB et al., (1985), which uses the zero-delay spectrum to obtain a k-spectrum containing information integrated over the whole frequency range. Then the azimuth is evaluated by searching the maximum value of the radial energy of the k-spectrum.

- The second method is just a "*correlation method*". In a first step, the cross-correlation function of stations taken two by two leads to the determination of arrival-time differences, with an accuracy of one sampling interval (i.e.: 0.02 s in our case). In a second step, the cross-spectrum phase allows to compute the residual arrival-time difference, less than 0.02 s. This residual arrival-time difference is determined by the slope of the phase as a frequency function in the characteristic frequency band of the signals.

Then, assuming a plane wave as a propagation model, these arrival-time differences are used to compute both azimuth and slowness of the wave.

2) The results:

We have processed the whole dataset of 98 teleseismic events. Figure 1 shows the results given by the "*f-k method*". It represents a plot of the differences between theoretical and computed azimuths versus distance.

Besides 12 events (given by numbers), the standard deviation of the residuals is 15 degrees, in the 1000-8500 km range. For larger distances, the incident wave being very close to the vertical axis leads to a poor azimuthal determination, as expected.

A similar study has been made with the correlation method. Figure 2 shows the results for the determination of azimuth using, first, arrival-time differences obtained from the cross-correlation functions (bottom plot), and secondly, those computed by both cross-correlation functions and cross-spectrum phases. It clearly shows the gain obtained by the use of the cross-spectrum, specially in the 1000-8500 km range. This is again demonstrated by testing the consistency of the arrival-time differences set which must verify the triangular Chasles relation: $\Delta t_{ij} = \Delta t_{ik} + \Delta t_{kj}$ for all i,j,k. The RMS value of the residuals of the Chasles relation is 0.013 s when we only use arrival-time differences determined by cross-correlation, and 0.002 s in the second case.

Another advantage can be attributed to the "*correlation method*". At the opposite of "*f-k method*" which assumes a plane wave model, we can use a more refined model defined by a plane wave and a set of time delays affecting the arrival-times. Using the global dataset, we can statistically compute each station anomaly as the

mean value of the residuals. This leads to time delays ranging from -0.008 s to 0.005 s producing time differences greater than half a sampling interval for some couples of stations.

Figure 3 shows the residual azimuths as a function of the true azimuths obtained from USGS, where the computed azimuth takes into account the station anomalies. It clearly shows a cosine dependance which might be explained by a deeping structure of the crust layers below the network. Final results taking into account this cosine dependance are presented in figure 4: within the range of 1000-8500 km, the standard deviation becomes less than 10 degrees with only two aberrant points.

CONCLUSION AND RECOMMENDATIONS:

We have used a set of 98 telesismic events recorded by a temporary 5 stations mini-array set up in the Center of France to test two methods for automatic measurement of P-wave azimuth.

The first method, or "*f-k method*", gives as expected consistant results in most of the cases (azimuth determination with an error of 15 degrees and 12 aberrant evaluations).

A second method, the "*correlation method*", derived from the doublets method (POUPINET et al., 1982, PLANTET et al., 1985), uses a step-by-step algorithm, computing first, on set time differences, then uses the cross-spectrum as a vernier to refine these differencies. It also allows to introduce station anomalies to correct the propagation model before the azimuth computation. Azimuth is then determined with an error of less than 10 degrees in the 1000-8500 km range with only two aberrant determinations. Consequently, better results are obtained with this method.

Further studies will investigate the regional domain for which the higher frequency content will give a better accuracy in the arrival-time differences.

We suggest such a correlation method to be tested with seismic data recorded in other mini-arrays.

REFERENCES

- CAPON J., "High-resolution frequency-wavenumber spectrum analysis". Proc. IEEE, Vol 57, no. 8, pp. 1408-1418, 1969.
- GUPTA I.N., C.S. LYNNE, T.W. MCELFFRESH and R.A. WAGNER, "F-k analysis of NORESS array and single station data to identify sources of near-receiver and near-source scattering", BSSA, Vol. 80B, pp. 2227-2241, 1990.
- MYKKELTVEIT S., K. ASTEBOL, D.J. DOORNBOS and E.S. HUSEBYE, "Seismic array configuration optimization", BSSA, Vol. 73, pp. 173-186, 1983.
- NAWAB S.H., F.U. DOULA, and R.T. LACOSS, "Direction determination of wide-band signals", IEEE Transactions on acoustics, speech and signal processing, Vol. ASSP-33, No 4, October 1985.
- PLANTET J.L. and Y. CANSI, "Accurate epicenters location with a large network, example of the 1984/1985 Remiremont sequence", in "Seismic hazard in Mediterranean regions", Kluwer Academic Publishers, 1985.
- POUPINET, G., F. GLANGEAUD and P. COTE, "P-time delay measurement", Proc. IEEE ICASSP82, Paris, 3-5 Mai, pp. 1516-1519, 1982.

Figure 1: Differences between true azimuth (USGS) and computed one using "*f-k* method" plotted versus distance. In the 1000-8500 km distance range, the standard deviation is 15 degrees without taking into account the 12 aberrant events (numbers).

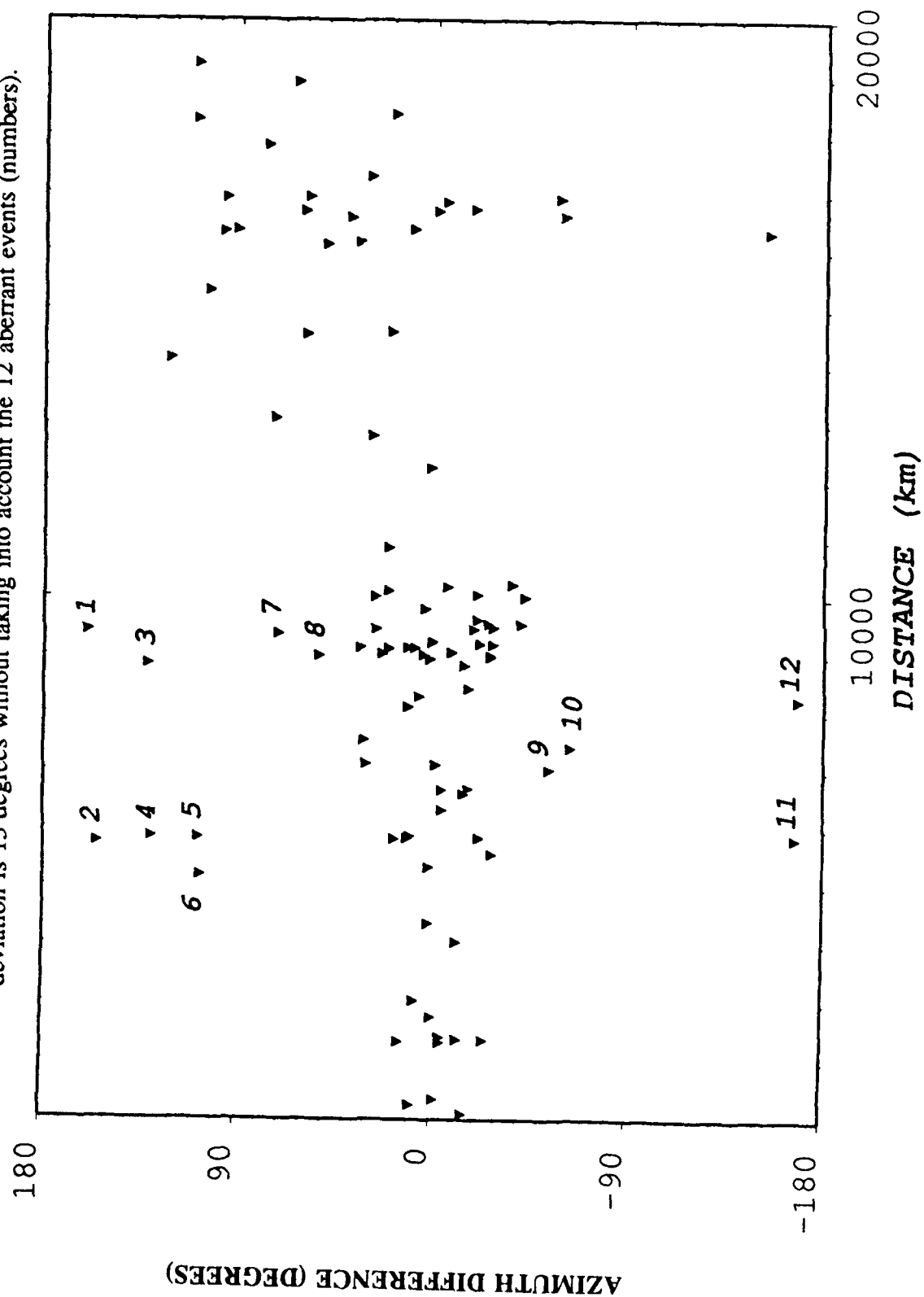


Figure 2: Differences between true azimuth (USGS) and computed one using "*correlation method*" plotted versus distance. For the bottom plot the arrival-time differences are computed from the cross-correlation functions only (step 1); for the top plot both cross-correlations and cross-spectra are used (step 2).

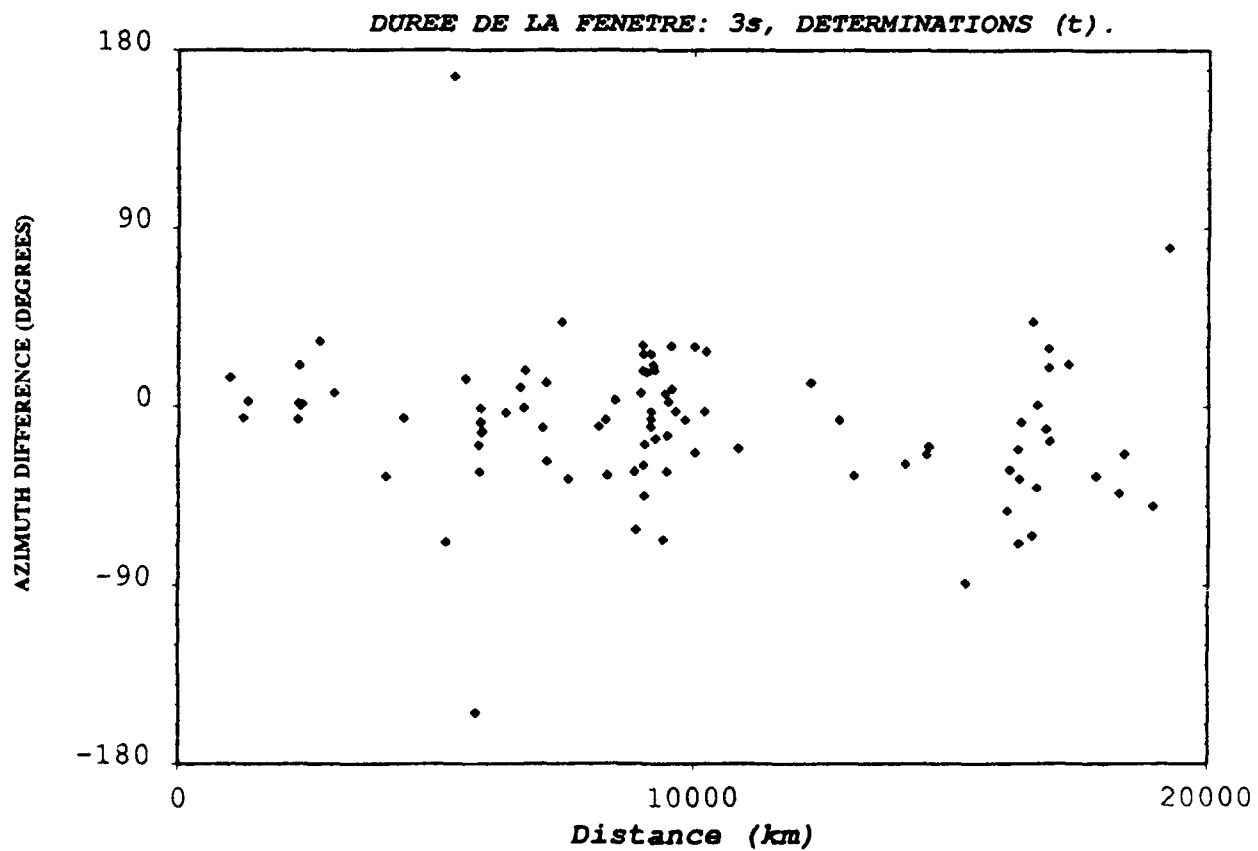
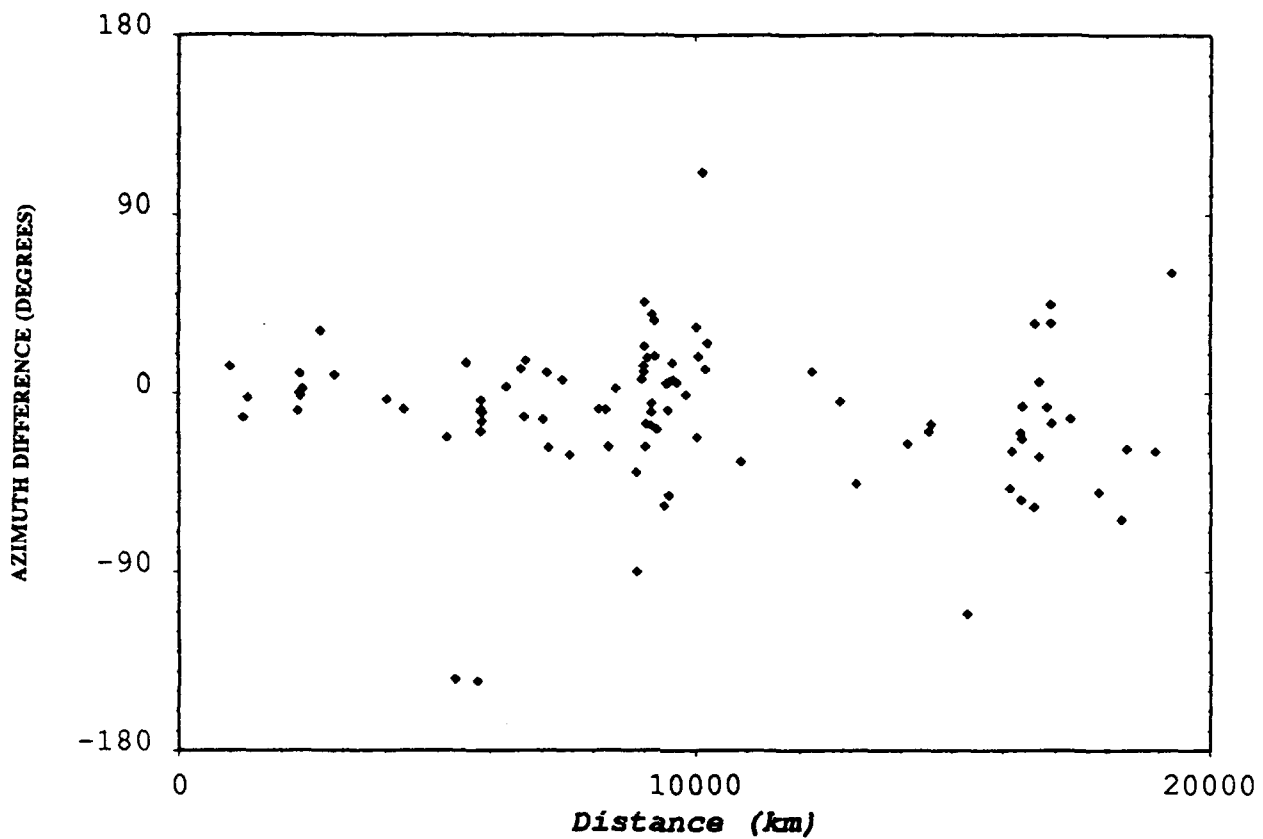


Figure 3: Differences between true azimuth (USGS) and computed one using "correlation method" plotted versus true azimuth. The cosine dependance obtained by least-square inversion does not take into account the black symbols.

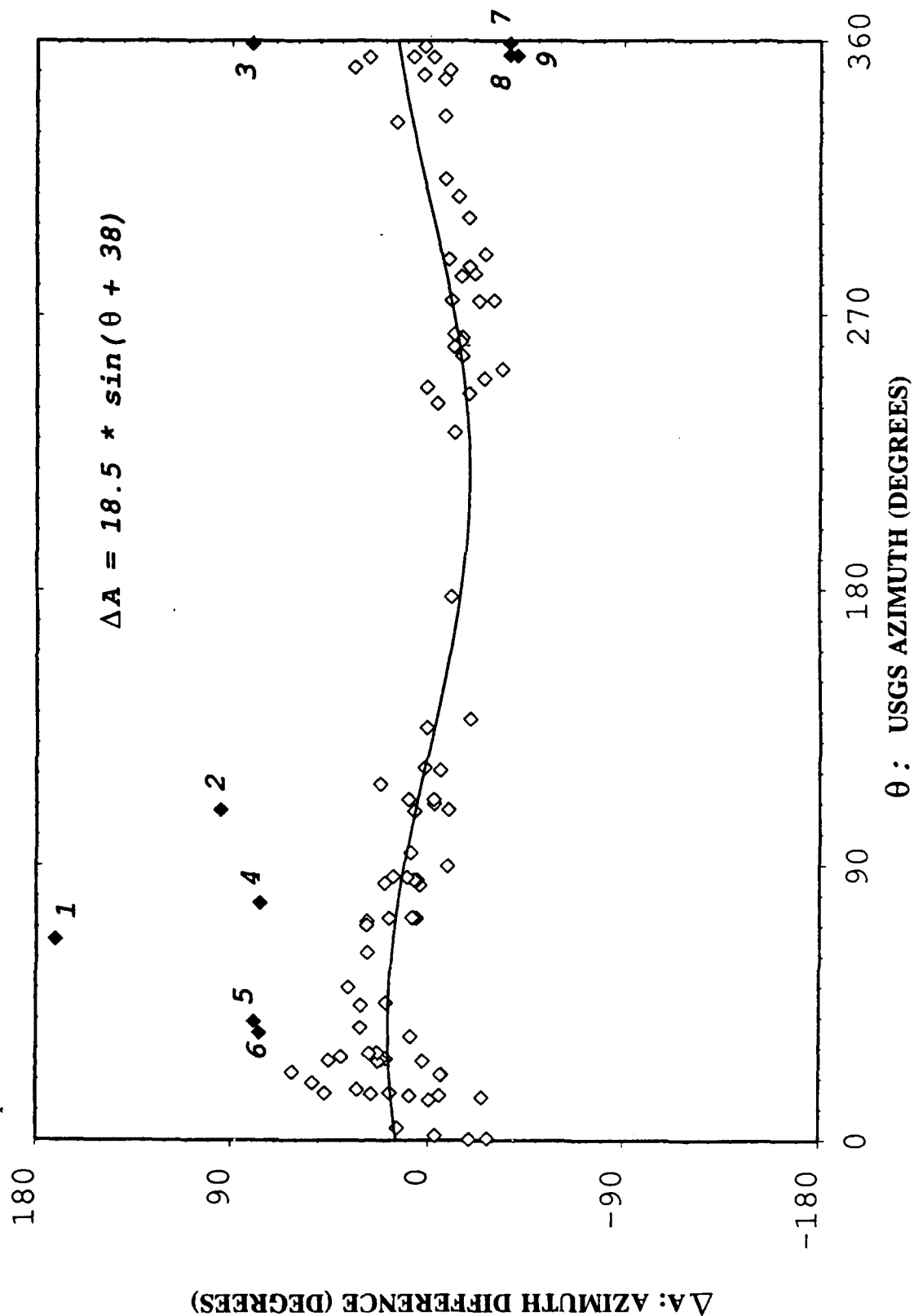
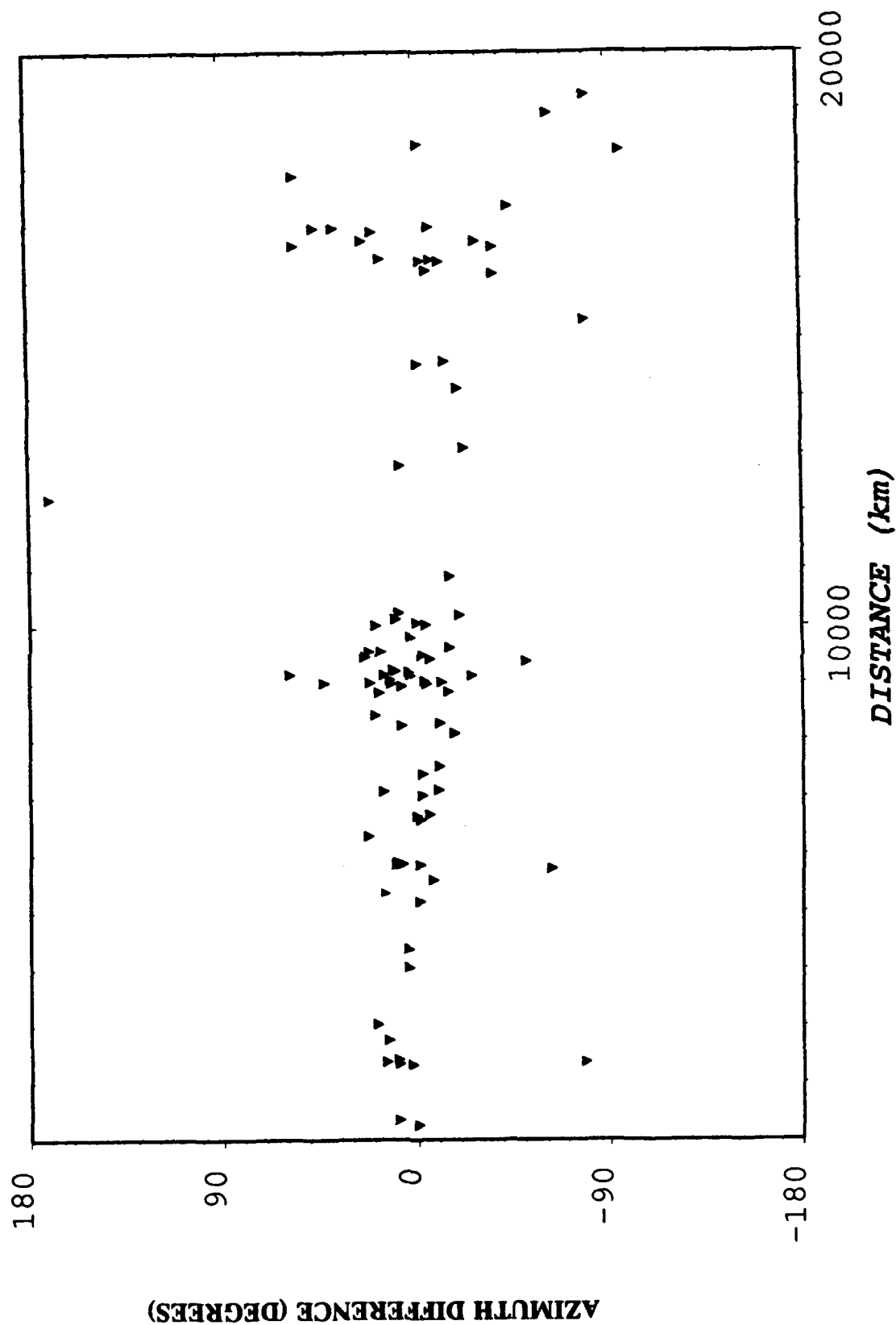


Figure 4: A plot versus distance of the differences between true azimuth (USGS) and computed one using "correlation method" including station anomalies and azimuth correction deduced from figure 3. The standard deviation is decreasing to 9 degrees in the 1000-8500 km range with only two aberrant evaluations.



SOURCE FUNCTION DECONVOLUTION OF DELAY-FIRED EXPLOSIONS AND EARTHQUAKES AT REGIONAL DISTANCES

Martin C. Chapman, G. A. Bollinger, and M. S. Sibol
Department of Geological Sciences
Virginia Tech, Blacksburg, VA 24061-0420

Contract no.: F19628-90-K-0052

OBJECTIVE

The objective of this past year's work has been to compare the spectral characteristics of known delay-fired industrial explosions with those of natural earthquakes recorded at regional distances and to test the utility of a simple deconvolution scheme to recover the source time function of the explosions.

RESEARCH ACCOMPLISHED

Previous work under this contract is described in Chapman et al. (1991). In that previous work, shot pattern and delay time information was obtained from the blasters and was used to successfully model the low frequency amplitude spectra of delay-fired mining explosions. This past year's work has focused on testing a deconvolution scheme to recover the source time function of the explosions. We also compare the results of deconvolutions of the explosion signals with those of some regional earthquakes.

Source Deconvolution

We use the technique of low-time cepstral gating to recover the source time function of the explosion signals (Ulrych, 1971; Tribolet, 1979). We assume that the recorded seismic signal is a convolution of the source time series with a random sequence representing the impulse response of the transmission path. Under these assumptions, the source in the cepstral domain is confined to low times (small quefrency values). Hence, the effects of the transmission path can be reduced by suppressing late time values of the complex cepstrum. A difficulty arises in computing the complex cepstrum, because a continuous phase function must be defined. This generally requires that the principle values of the phase spectrum be "unwrapped". Various approaches to the problem are discussed by Tribolet (1977). However, if the source time function is "minimum phase" the continuous phase function can be defined uniquely as the Hilbert transform of the logarithm of the amplitude spectrum.

Let $x(t)$ be the recorded time series and $X(\omega)$ represent its Fourier transform. Then, in polar form,

$$X(\omega) = |X(\omega)| \exp\{i\Theta(\omega)\}$$

where $\Theta(\omega)$ is the phase spectrum. The Fourier transform of the complex cepstrum is given by

$$S(\omega) = \ln \{X(\omega)\} = \ln|X(\omega)| + i\Theta(\omega)$$

where $\Theta(\omega)$ is a continuous function of frequency. The complex cepstrum, $s(t)$, is obtained via the inverse Fourier transform. In general, the function $\Theta(\omega)$ is obtained by unwrapping the principle values of $\arg\{X(\omega)\}$. However, if $x(t)$ is minimum phase, the continuous phase is defined uniquely by

$$\Theta(\omega) = H\{\ln|X(\omega)|\}$$

where H indicates the Hilbert transform. Low time cepstral gating is accomplished by

$$s'(t) = a(t) s(t) \quad \begin{array}{l} a(t) = 0, \quad t < 0 \\ a(t) = 1, \quad 0 \leq t \leq T \\ a(t) = 0, \quad t > T \end{array}$$

In the above, T represents the width of the cepstral gate. The deconvolved time series is recovered by computing the direct Fourier transform of $s'(t)$, followed by exponentiation and inverse Fourier transformation.

An example of the process, using synthetic data, is shown in Figure 1. The source function is represented by 4 acceleration pulses, equally spaced in time, with equal amplitudes. This source series is convolved with a random sequence, to simulate a recorded seismic signal, then deconvolved using the minimum phase assumption. In this example, the minimum phase deconvolution preserves the time intervals and amplitudes of the original source time series. This will not be the case in general, as shown in Figure 2. The minimum phase deconvolution preserves the proper time intervals between source pulses only if the pulses are equally spaced in time. When that is the case, the process will give a useful result when the pulse amplitudes are nearly equal or else distributed such that the energy is concentrated early in the source time series. Many, if not most, large mining explosion designs incorporate shot patterns and explosion delay intervals which result in near constant time intervals between the firing of rows of explosions. These row delays strongly impact the low frequency spectra recorded at larger distances, and may be resolved using the process described above.

Study Events

Figure 3 shows the epicentral locations of the events studied. A detailed blasting log was available for Explosion 1, permitting us to model the source time function, as described by Chapman et al. (1991). The three small earthquakes (magnitudes 3.3 to 4.0) were examined for comparison with results obtained from the explosions.

Figure 4 shows the vertical component time series recorded from Explosion 1. Figure 5 shows the results of the minimum phase deconvolution for each network station, as well as the network average deconvolution. In this and in all later examples, the time series analyzed consisted of 20 second duration windows, beginning with the onset of the Lg phase. The recorded data were instrument corrected to ground acceleration, and band-passed with 6-pole Butterworth filters with corner frequencies at 0.3 and 15 Hz. The duration of the cepstral gate was 1.0 second. Also shown in Figure 5 is the firing time sequence for Explosion 1, as derived from the blasting

log. The explosion consisted of 4 rows of charges, with a 50 msec delay between individual charges in the upper and lower parts of each charge hole. The firing times of the rows were separated by 0.2 sec.

A model acceleration source time series was constructed for Explosion 1 and is plotted for comparison with the network average deconvolution in Figure 6. The model time series incorporates a Brune source pulse with corner frequency 10 Hz, and anelastic attenuation represented by $\exp(-\omega t^*)$, where $t^*=0.04$. As shown in Figure 5, this explosion design involving 4 rows of explosives with a constant row delay of 0.2 sec is clearly resolved in the deconvolved seismic data.

Figure 7 shows the recorded time series from Earthquake 1 and the associated deconvolutions. Figure 8 shows the deconvolutions for Earthquakes 2 and 3. Identical processing was performed on all events, as described above. Note that the earthquake deconvolutions indicate single short duration source time functions.

Figure 9 compares the deconvolutions derived from all events shown in Figure 3. Information on the charge patterns and delay times used in Explosions 2 through 4 was not available. However, by analogy with the results obtained from Explosion 1, and in contrast to the results from the earthquakes, the deconvolutions for the other explosions appear to exhibit evidence for source multiplicity.

CONCLUSIONS AND RECOMMENDATIONS

Deconvolution of the Lg phase by low-time cepstral gating effectively reveals source multiplicity in some large mining explosions recorded at near regional distances. The accuracy of the deconvolution procedure used here depends upon the nature of the phase characteristics of the source function. Minimum phase source series appear to be accurately preserved. Further work needs to be done to extend this result to source functions with mixed phase characteristics.

REFERENCES

- Chapman, M. C., G. A. Bollinger, and M. S. Sibol (1991), Spectral studies of the elastic wave radiation from Appalachian earthquakes and explosions - explosion source spectra modeling using blastor's logs, Report PL-TR-91-2231, Phillips Laboratory, Hanscom Air Force Base, MA. ADA243956
- Tribolet, J. M. (1977), A new phase unwrapping algorithm, IEEE Trans. ASSP, 25, no. 2, pp. 170-177.
- Tribolet, J. M. (1979), Seismic Applications of Homomorphic Signal Processing, Prentice Hall, Englewood Cliffs, NJ, 195 p.
- Ulrych, T. J. (1971), Application of homomorphic deconvolution to seismology, Geophysics, 36, no. 4, pp. 650-660.

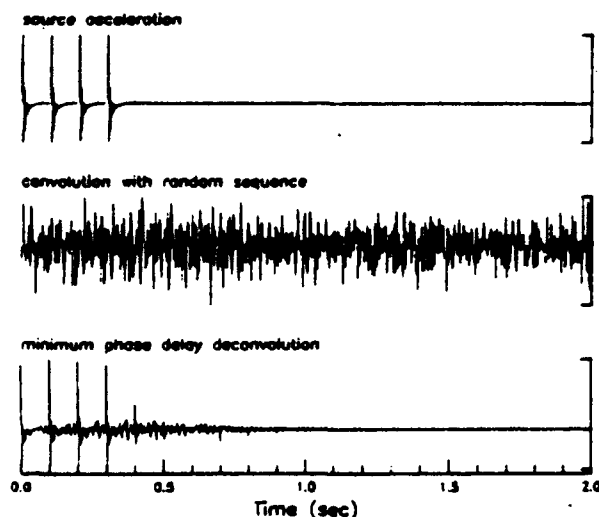


Figure 1. Example deconvolution: (top) Synthetic source time series. (middle) Simulated seismic trace obtained by convolution with random sequence. (bottom) Result of minimum phase deconvolution.

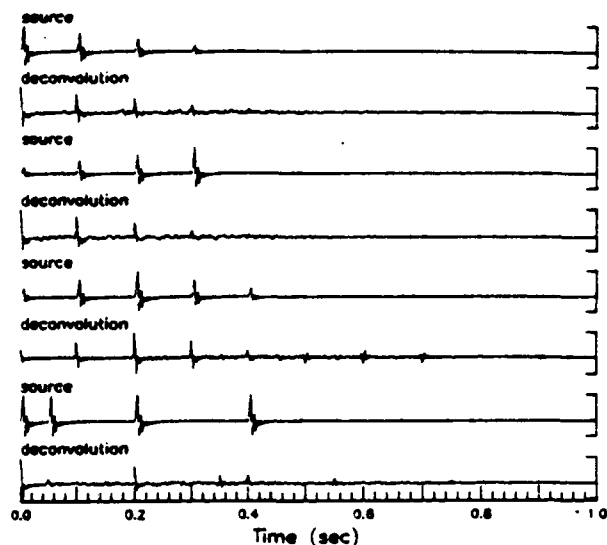


Figure 2. Four examples of minimum phase deconvolutions, with different source time series.

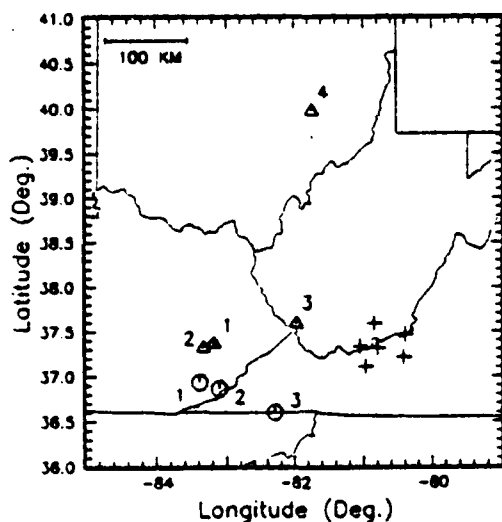


Figure 3. Map showing the locations of four explosions (triangles), three earthquakes (circles), and network stations (crosses) used in the study.

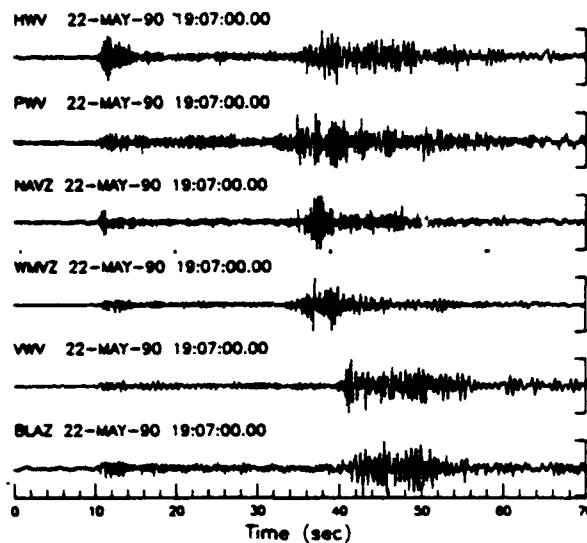


Figure 4. Time series for Explosion 1.

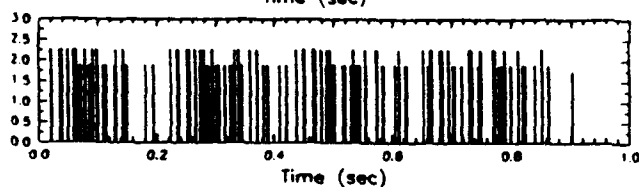
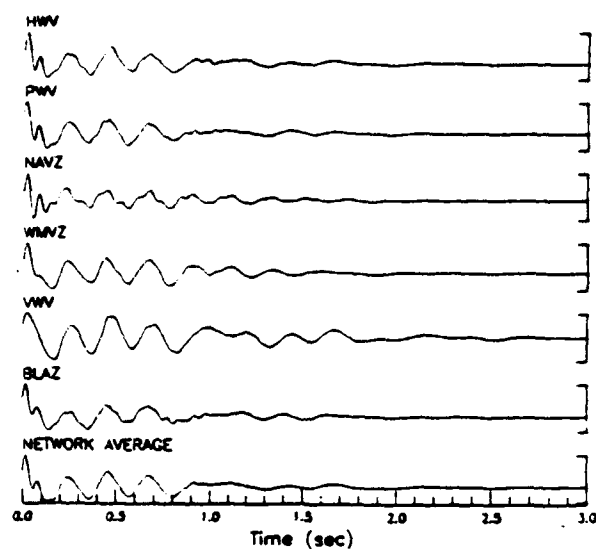


Figure 5. (Top) Deconvolved acceleration source time series for Explosion 1. (Bottom) Firing sequence for Explosion 1.

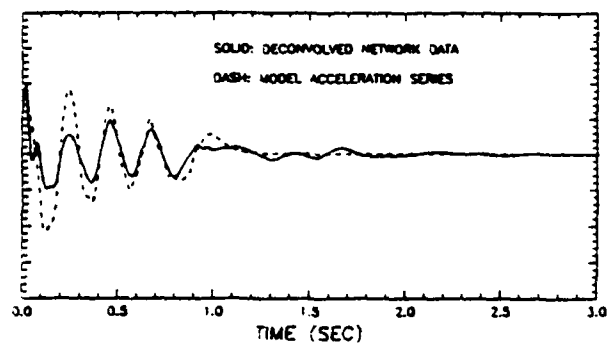


Figure 6. Comparison of network average deconvolution with model source acceleration time series (Explosion 1).

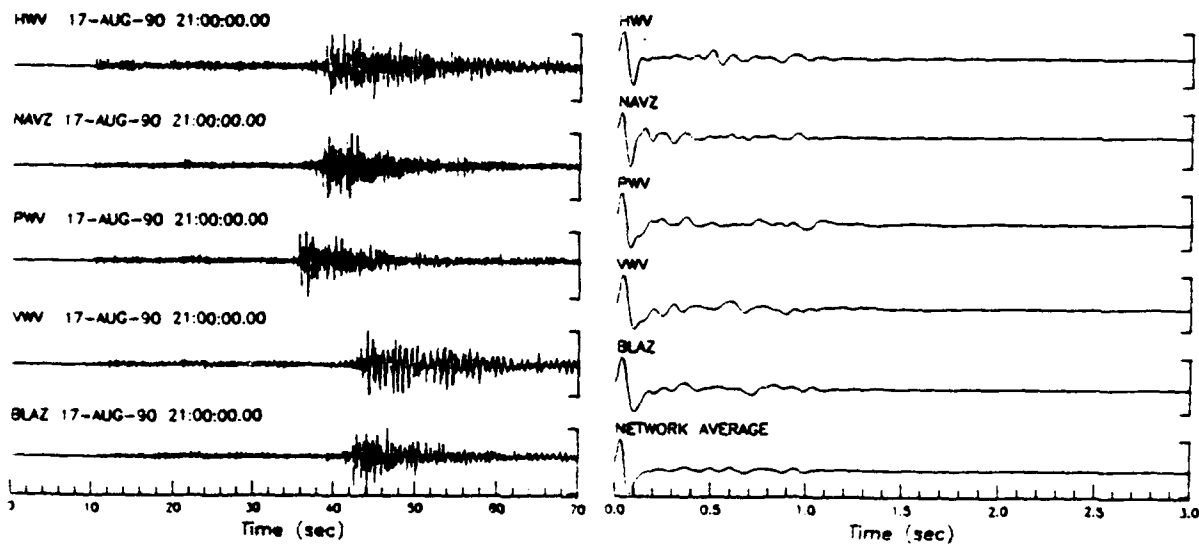


Figure 7. (Left) Recorded time series from Earthquake 1. (Right) Deconvolved acceleration series.

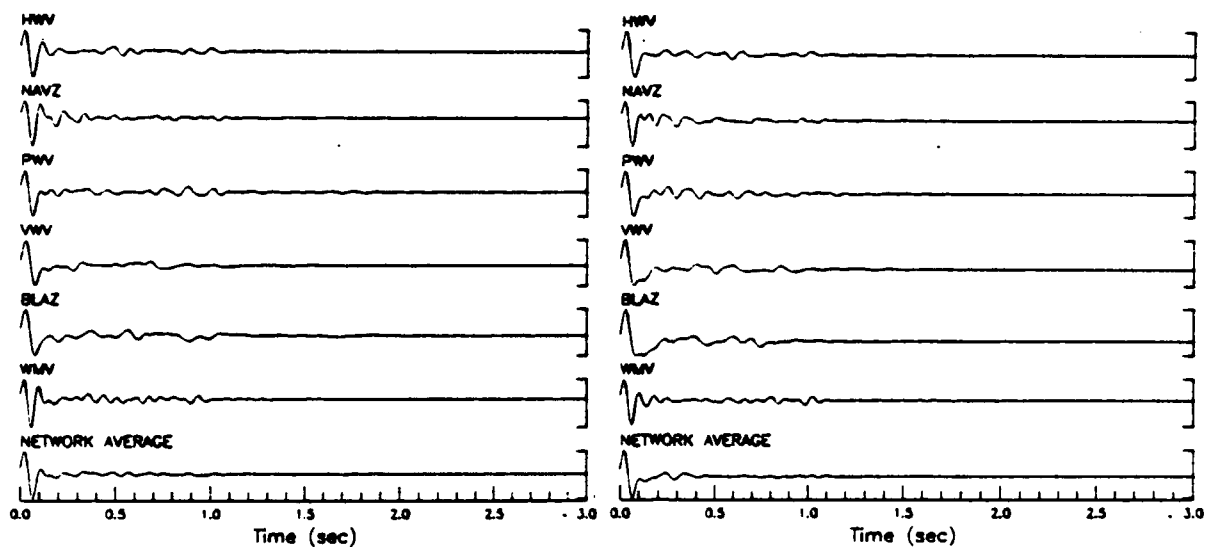


Figure 8. Deconvolved acceleration time series from Earthquake 2 (Left) and Earthquake 3 (Right).

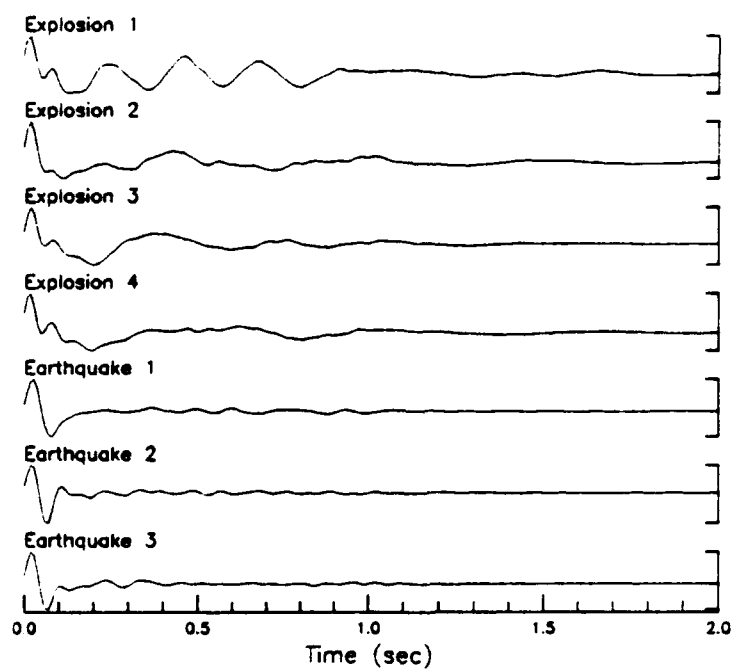


Figure 9. Network average deconvolved acceleration series for all events in Figure 3.

REGIONAL WAVE ATTENUATION IN EURASIA

Kin-Yip Chun, Tianfei Zhu and Xiao Rung Shih
Geophysics Division, Department of Physics
University of Toronto, Toronto, Ontario M5S 1A7

Contract Number: F29601-91-C-DB24

OBJECTIVE

The program objective is to obtain frequency-dependent P_n and L_g attenuation measurements in Eurasia, which are accurate enough to result in a significant improvement in seismic monitoring of nuclear test in Eurasia. Measurement reliability and areal coverage density are two key considerations surrounding the project. Central to our strategy is the generalization of our previously developed methodologies for isolating frequency-dependent, non-propagating contaminants (geological site effects, instrument response error, etc.) from seismic wave propagation effects (geometrical spreading and attenuation).

RESEARCH ACCOMPLISHED

Our research under DARPA funding has focused on developing methods to study regional phase attenuations under Eurasia. With increasing high quality broadband digital data recorded at the IRIS/IDA stations, we are able to test and apply the methodologies we have developed for regional phase studies at close ranges in Eastern Canada to those recorded at regional and far-regional distances in Eurasia. We here report a generalized version of the reversed two-station method (RTSN, Chun et al., 1987), the source pair/receiver pair (SPRP) method, resulting from our recent studies. We have successfully applied it to the L_g attenuation study in the time domain. We have found that the frequency-dependent attenuation of L_g waves in the low frequency range (0.1-1 Hz) is more stable and consistent than those above 1 Hz derived from previous studies.

Time-domain method for measuring L_g attenuation

We denote by $A_{i,j}$ the time-domain L_g amplitude due to i^{th} source and recorded at the j^{th} station. Inserting instrument amplification I_j , site amplification S_j and source radiation pattern R_i , we parameterize $A_{i,j}$ as

$$A_{i,j} = A_i R_i I_j S_j d_{i,j}^{-1/3} (\sin \Delta_{i,j})^{-1/2} e^{\gamma d_{i,j}}, \quad (1)$$

where A_i is the source excitation, $d_{i,j}$ the epicentral distance in kilometers between the i^{th} source and j^{th} station, and Δ the same epicentral distance in degrees. The geometrical spreading coefficient used here follows Nuttli (1973). γ is the coefficient of anelastic attenuation, and is related to the quality factor $Q(f)$ as

$$\gamma(f) = \frac{\pi f}{UQ(f)}, \quad (2)$$

where U is the group velocity.

In RTSN (Chun et al., 1987; Zhu et al. 1991), the pairs of sources and stations are along a great-circle path as shown by the solid line in Figure 1. It can be readily shown that

$$\left[\frac{A_{2,1}}{A_{1,1}} \frac{A_{1,2}}{A_{2,2}} \right] \left[\frac{d_{2,1}}{d_{1,1}} \frac{d_{1,2}}{d_{2,2}} \right]^{1/3} \left[\frac{\sin \Delta_{2,1}}{\sin \Delta_{1,1}} \frac{\sin \Delta_{1,2}}{\sin \Delta_{2,2}} \right]^{1/2} = e^{-\gamma(D_1 + D_2)}, \quad (3)$$

where $D_1 = d_{2,1} - d_{1,1}$ and $D_2 = d_{1,2} - d_{2,2}$. Note that all source excitation and radiation pattern terms are canceled when the product of the amplitude ratios is taken.

We now assume that the source radiation pattern is azimuthally independent for the

regional phases (e.g., Sereno, 1990; Bennett et al., 1990). For L_g phases, the assumption is justified by the fact that the observed L_g phase is actually the superposition of wave propagation in many modes, which tends to smooth out the azimuthal character of the source radiation. Under this assumption, the sources and receivers are no longer required to be co-linear, and the geometrical restriction is relaxed as shown by the dashed line in Figure 1. We call this generalized version the source pair/receiver pair (SPRP) method.

Application to L_g attenuation study in time domain

In the regional phase study in the time domain and in the frequency domain following, we used 22 earthquakes from the CDSN and USSR databases managed by the Center of Seismic Studies (CSS) (Table 1 and Figure 2). Data were recorded by the broadband instruments at a 20 points/s sampling rate. These events were mostly from crustal depths (Table 1), and thus generated good L_g phase at epicentral distances ranging from a few hundreds to more than 5000 kilometers.

The maximum amplitudes of the L_g phases in a series of specific narrow frequency bands are used in time domain analysis. The $A_{i,j}$ in Equation 1 is the maximum zero-to-peak (trough) L_g amplitudes in the group velocity window 3.6 to 2.9 km/s. The band width is half of the center frequency, e.g., if the center frequency is 0.5 Hz the filter bandwidth is 0.375 - 0.625 Hz. We found that the best result of time domain analysis is in the frequencies from 1 to 0.1 Hz. Figure 3 illustrates the distribution of the $\text{Log}Y$, a term proportional to γ , versus ΔD , the sum of the epicentral differences of SPRP, at central frequencies 1, 0.5, 0.25, 0.167, 0.125 and 0.1 Hz. In general, variation of $\text{Log}Y$ with ΔD in each frequency band is quite linear to at least 4000 kilometers with reasonably small scattering. Based on its value obtained from each narrow-band evaluation, the results of linear regression shows γ is proportional to $f^{0.51}$ with Q_0 , the constant of the proportionality, equal to 564 when the group velocity is taken to be 3.5 km/s (Figure 4).

γ , Q , and their frequency dependence thus derived provide information about L_g attenuation in a much lower frequency range than those from the previous regional phase studies in Eurasia. The coefficient 0.51 is in the range of the values 0.4 (Given et al., 1990) and 0.6 (Mitchell, personal communication, 1992) determined in the higher frequency range in the region. The Q_0 value is intermediate between 206 for the Great Basin (Chavez and Priestley, 1987) and 1,100 for the Canadian Shield (Chun et al., 1987). The result is also intermediate in the range of Q_0 , from 452 to 818, at some IRIS/CDSN stations obtained from the time-domain analysis of L_g phases in regional distances (Bennett et al., 1990). Based on frequency dependence coefficient 0.51, Q at 0.5 Hz is 396, compared to the value of 398 at the same frequency, which we obtained from ten events in the region in the previous study (Chun and Zhu, 1992).

Application to L_g attenuation study in frequency domain

Determination of anelastic attenuation of L_g was attempted in the frequency domain, using the same earthquakes. The length of the L_g window is again the group velocity window from 2.9 to 3.6 km/s. To compare with the L_g result in time-domain analysis, we used exactly the same paths for the frequency-domain analysis. The coefficient of geometrical spreading (d^n) used in the calculation is -0.5, a commonly-accepted value (e.g., Sereno et al., 1988).

In the lower frequency range, we found the similar frequency dependence from 0.155 to 0.5 Hz (Figure 5), corresponding to the range in which the best time domain results are observed (Figure 3). The Q_0 thus derived is 239, much lower than the time-domain Q_0 . A major cause of this discrepancy may lie in the lateral inhomogeneity of the crust, which gives rise to secondary phases in the group velocity window (Bennett et al., 1990; Given, 1991), and also makes the application of a fixed group velocity window improper. The effect of inhomogeneity may result in large scattering in the frequency-domain analysis while causing much less harm to the time-domain maxima. Therefore, the time-domain procedure is superior in analyzing regional characteristics of the L_g attenuation.

P_n at regional and far-regional distances

In the range of epicentral distances from a few hundreds to more than 5,000 kilometers from the events to the IRIS/CDSN stations, observed P_n phases may belong to distinctly different groups. Based on their epicentral distances, P_n phases are observed at the ranges from 300 to 2,000 km and from 2,200 to 3,000 km, with an apparent velocity of approximately 8.0 km/s for the first group and 8.4 km/s for the second group, respectively (Figure 6). While the first group is the normal P_n waves propagating immediately below the Moho, the second group has the characteristics of the high velocity P_n observed beneath Tibet (8.42 km/s) and the Indian Shield (8.4 km/s) (Ni and Barazangi, 1983). The existence of the high velocity P_n from China to the Siberia Platform may indicate a possible efficient wave guide at greater depth than the Moho in the region (Figure 7). The P_n attenuation studies in the region using data from sparsely located IRIS/CDSN stations must deal with these two groups of P_n separately.

CONCLUSIONS AND RECOMMENDATIONS

The research accomplished above has shown:

1. The SPRP method is more flexible than RTSM, and hence allows attenuation measurements to be made using sparse recordings from a seismic network with only a brief recording history. Results in both time and frequency domains indicate that isolating the path effect by taking spectral ratios following a much relaxed geometry is justified.
2. The application of this method to the attenuation study of L_g phases in time domain gave quite consistent results in the frequency range from 0.1 to 1 Hz. For the region and distance range concerned, it is superior than the frequency-domain analysis.
3. In the region, L_g phase propagation is quite efficient up to 5000 km. P_n propagations, which were observed as two distinct groups with different velocities, may take different paths at regional and far-regional epicentral distances.

References

- Bennett, T. J., J. F. Scheimer, A. K. Campanella, and J. R. Murphy (1990). Regional discrimination research and methodology implementation : Analyses of CDSN and Soviet IRIS data, *S-Cubed Report SSS-TR-90-11757*, Technical Report on Contract No. f19628-89-C-0043.
- Chun, K.-Y., G. F. West, R. J. Kokoski, and C. Samson (1987). A novel technique for measure L_g attenuation - results from Eastern Canada between 1 to 10 Hz, *Bull. Seism. Soc. Am.*, **77**, 398-419.
- Chavez, D. E., and K. F. Priestley (1987). Apparent Q of P_g and L_g in the Great Basin, paper presented at the 9th Annual DARPA/AFGL Seismic Research Symposium, June 1987. GL-TR-90-0300, ADA229025
- Chun, K.-Y., and T. Zhu (1992). regional wave attenuation in Eurasia, *Semi-Annual Tech. Rep.*.
- Given, H. K., N. T. Tarasov, V. Zhuravlev, F. L. Vernon, J. Berger, and I. L. Nersesov (1990). High-frequency seismic observations in eastern Kazakhstan, USSR, with emphasis on chemical explosion experiments, *J. Geophys. Res.*, **95**, 295-307.
- Given, H. (1991). Heterogeneous propagation and blockage of L_g in the Caspian Sea-Caucasus Mountain area of the USSR, paper presented at the 13th Annual PL/DARPA Seismic Research Symposium, October 1991. PL-TR-91-2208, ADA241325
- Ni, J., and M. Barazangi (1983). Velocities and propagation characteristics of P_n , P_g , S_n and L_g seismic waves beneath the Indian Shield, Himalayan Arc, Tibetan Plateau and surrounding regions: High upper mantle velocities and efficient S_n propagation beneath Tibet, *Geophys. J. R. Astron. Soc.* **72**, 665-689.
- Nuttli, O. W. (1973). Seismic wave attenuation and magnitude relations for eastern North America, *J. Geophys. Res.*, **78**, 876-885.
- Sereno, T. J. (1990). Frequency-dependent attenuation in eastern Kazakhstan and implications for seismic detection thresholds in the Soviet Union, *Bull. Seism. Soc. Am.*, **80**,

2089-2105.

Zhu, T., K.-Y. Chun, and G. F. West (1991). Geometrical spreading and Q of P_n waves: an investigative study in eastern Canada, *Bull. Seism. Soc. Am.*, **81**, 882-896.

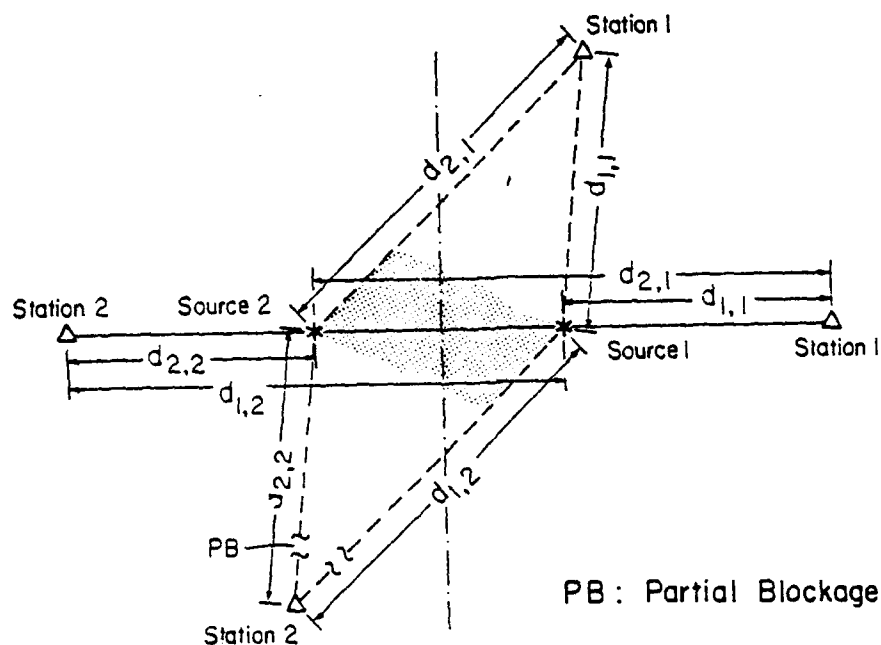


Figure 1. Schematic drawing illustrating the source pair/receiver pair (SPRP) method. Solid horizontal line shows an ideal great-circle alignment; dashed lines show the 'generalized' configuration which is actually used in the study.

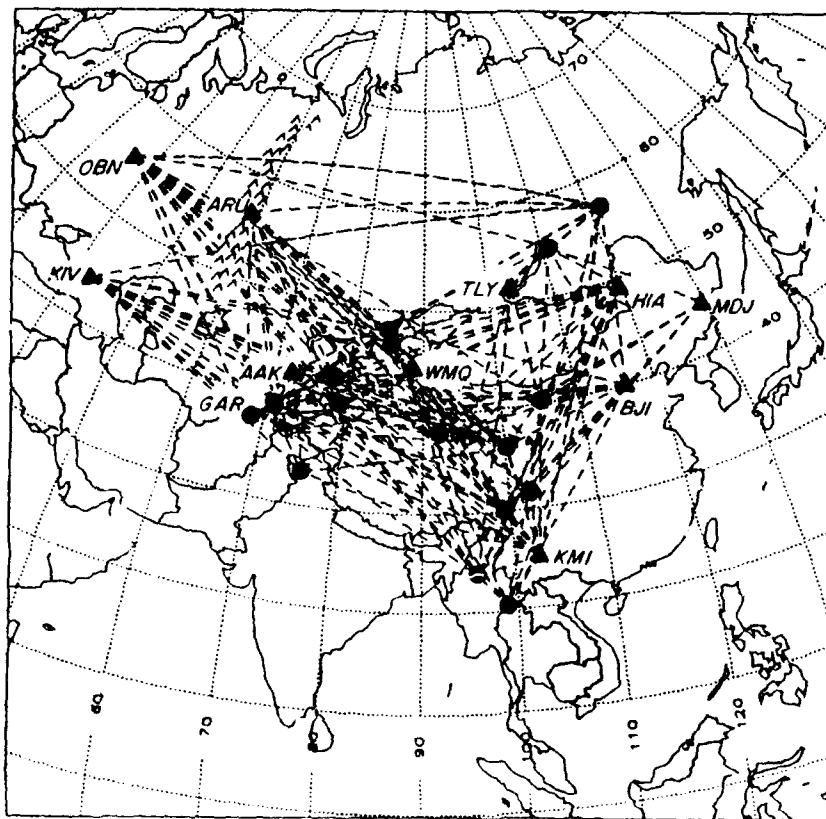


Figure 2. Great-circle paths linking the locations of the 22 selected earthquakes (Table 1) and the IRIS/CDSN stations.

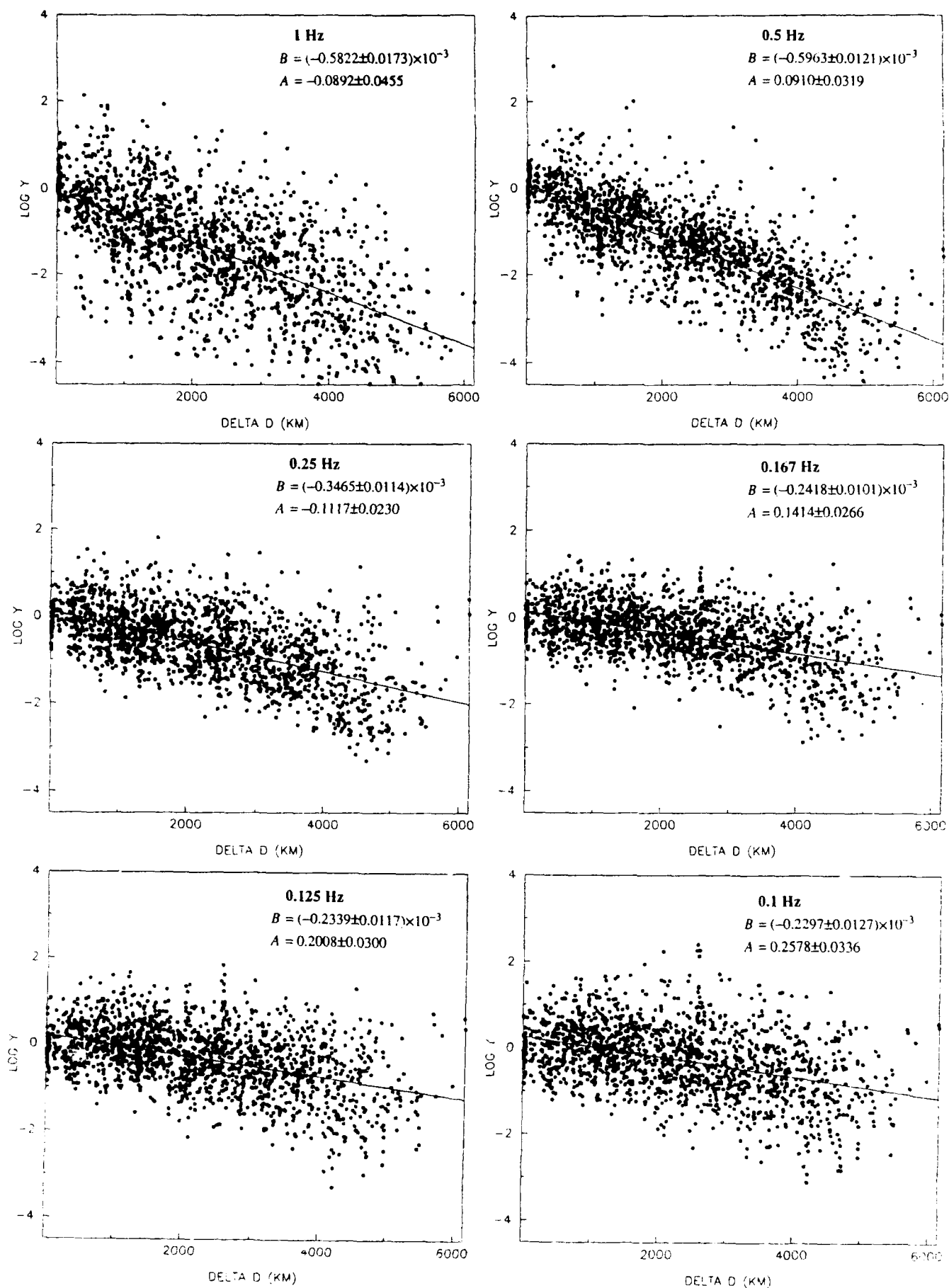


Figure 3. Plots of $\log y$ versus ΔD , where $\log y = \Delta D \gamma \log e$ and $\Delta D = D_1 + D_2$, at 1, 0.5, 0.25, 0.167, 0.125 and 0.1 Hz. B is the slope ($\gamma \log e$) and A is the intercept, which should be close to 0.

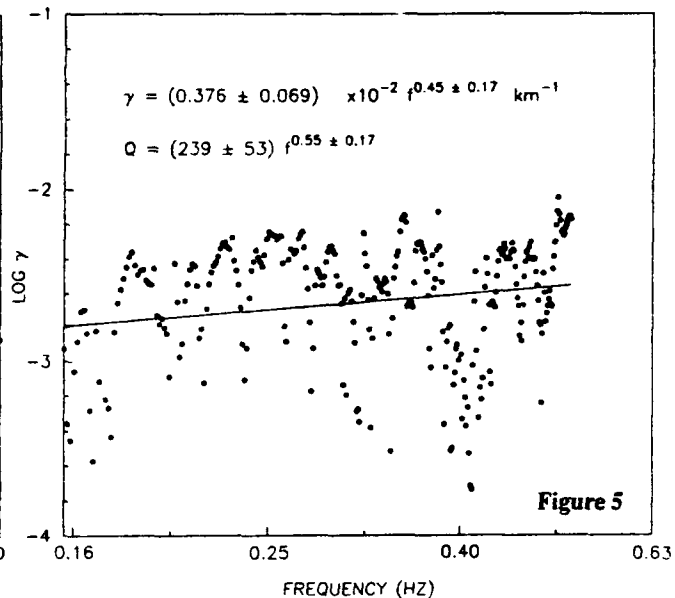
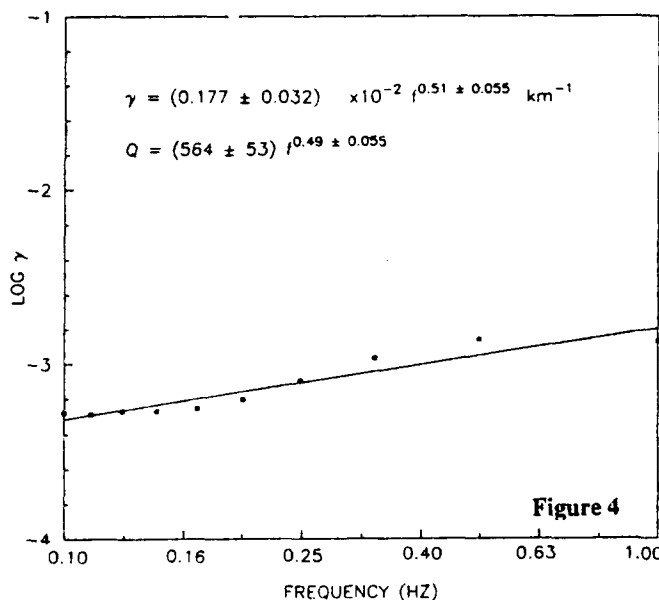


Figure 4. Plot of $\log \gamma$ versus frequency in log scale for L_g wave analysis in time domain. γ is obtained from the result in each narrow frequency band.

Figure 5. Plot of $\log \gamma$ versus frequency in log scale for L_g wave analysis in frequency domain.

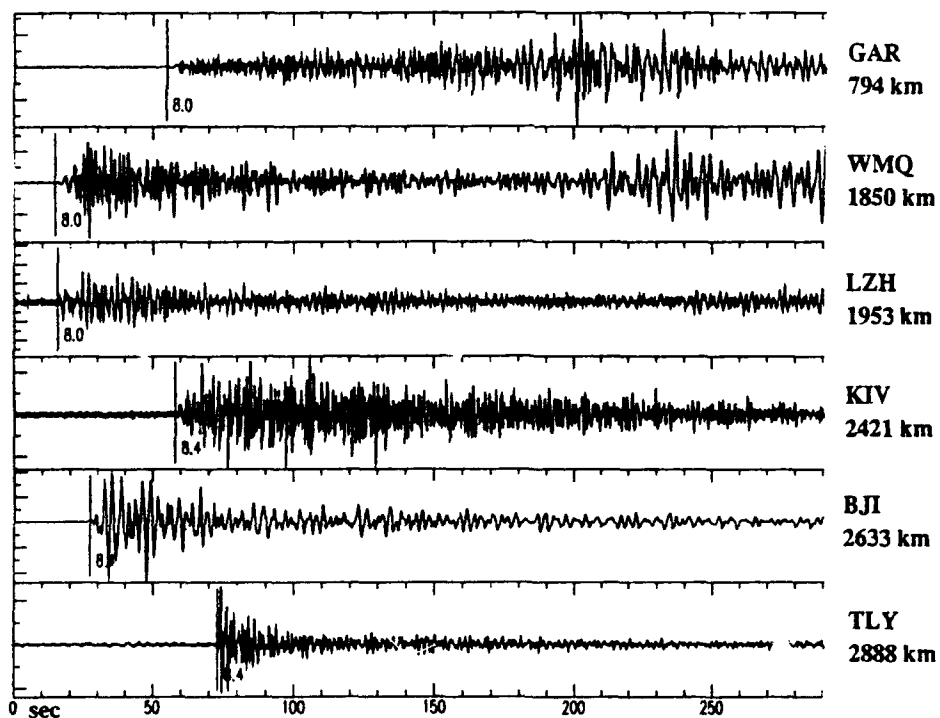


Figure 6. Examples of P_n phases with apparent velocities of 8.0 and 8.4 km/s observed at IRIS/CDSN stations. These shown here are the vertical component seismograms, and are filtered by a 0.25-4 Hz bandpass filter. Station name and epicentral distance are on the right side of each trace.

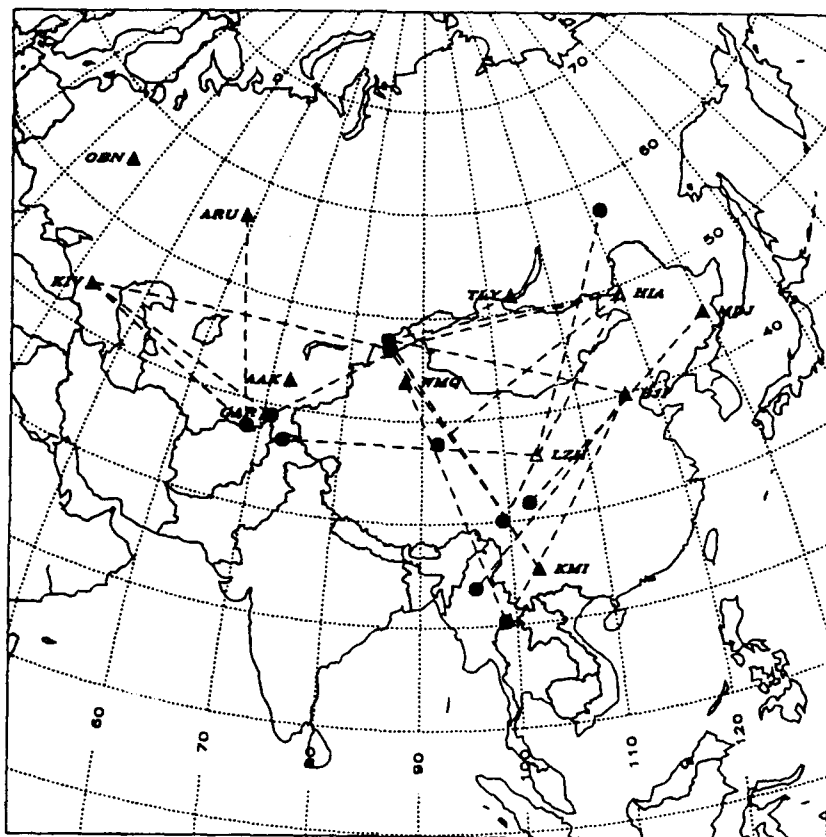


Figure 7. Great-circle paths linking the station (triangle) and event (circle) showing the observed ray paths of P_n phases with an apparent velocity of 8.4 km/s.

TABLE 1

| Event No. | Date | Origin Time (Hr:Min:Sec) | Latitude (N) | Longitude (E) | Depth (km) | Magnitude (mb) |
|-----------|-------------|--------------------------|--------------|---------------|------------|----------------|
| 1 | 15 Apr 1989 | 20:34:09 | 29.99 | 99.20 | 13 | 6.2 |
| 2 | 20 Apr 1989 | 22:59:54 | 57.17 | 121.98 | 26 | 6.1 |
| 3 | 03 May 1989 | 05:53:01 | 30.09 | 99.48 | 14 | 6.1 |
| 4 | 03 May 1989 | 15:41:31 | 30.05 | 99.50 | 8 | 5.8 |
| 5 | 17 May 1989 | 05:04:36 | 57.09 | 122.02 | 31 | 5.6 |
| 6 | 22 Sep 1989 | 02:25:51 | 31.58 | 102.43 | 15 | 6.1 |
| 7 | 30 Sep 1989 | 18:19:23 | 23.24 | 98.85 | 13 | 5.3 |
| 8 | 14 Jan 1990 | 03:03:19 | 37.82 | 91.97 | 12 | 6.1 |
| 9 | 05 Mar 1990 | 20:47:01 | 36.91 | 73.02 | 12 | 5.8 |
| 10 | 26 Apr 1990 | 09:37:45 | 36.24 | 100.25 | 10 | 6.3 |
| 11 | 15 May 1990 | 22:29:59 | 36.11 | 100.12 | 14 | 5.5 |
| 12 | 14 Jun 1990 | 12:47:29 | 47.87 | 85.07 | 58 | 6.1 |
| 13 | 12 Nov 1990 | 12:28:52 | 42.96 | 78.07 | 19 | 5.9 |
| 14 | 25 Dec 1990 | 03:56:46 | 33.33 | 75.71 | 51 | 5.3 |
| 15 | 05 Jan 1991 | 14:57:12 | 23.61 | 95.90 | 20 | 6.2 |
| 16 | 25 Feb 1991 | 14:30:28 | 40.39 | 78.96 | 21 | 5.5 |
| 17 | 18 Apr 1991 | 09:18:31 | 37.45 | 68.33 | 21 | 5.5 |
| 18 | 26 Apr 1991 | 22:24:04 | 38.96 | 71.05 | 33 | 5.4 |
| 19 | 19 Aug 1991 | 06:05:51 | 46.94 | 85.30 | 30 | 5.5 |
| 20 | 02 Sep 1991 | 11:05:50 | 37.44 | 95.40 | 10 | 5.5 |
| 21 | 12 Sep 1991 | 00:33:31 | 54.91 | 111.11 | 25 | 5.1 |
| 22 | 14 Sep 1991 | 13:16:40 | 40.17 | 105.05 | 25 | 5.1 |

Effects of an Irregular Free Surface and Moho on Regional Wave Propagation

Robert H. Clouser and Charles A. Langston
Department of Geosciences
Pennsylvania State University
University Park, PA 16802

Contract No. F29601-91-K-DB12

Objectives

Lg waves are used extensively in the analysis of earthquakes and explosions, mainly because Lg is often the largest phase on regional seismograms. Its primary uses are as a stable estimator of nuclear explosion yield (Nuttli, 1986; Nuttli, 1988), and in conjunction with other regional phases in earthquake/explosion discrimination (Pomeroy *et al.*, 1982). Regional seismic phases are also employed to study earth structure and the seismic source. For these reasons, it is imperative that all factors affecting regional wave propagation be understood.

This research focuses on the scattering effects of irregular interfaces on regional SH-wave propagation. Objectives include the computation of synthetic seismograms in models with an irregular Moho and free surface. Conventional seismic techniques can then be applied to measure coda, and frequency content and amplitude changes with distance of regional phases. The immediate problem considers only an irregular free surface, but an irregular Moho will also be included to investigate effects on Sn and SmS. This report explains the scattering theory employed, then presents some preliminary results.

Research Accomplished

The scattering theory employed is largely derived in Varadan *et al.* (1987), and stems from the T-matrix, or extinction theorem, method of Waterman (1969, 1975). The problem geometry is shown in Figure 1. An SH-wave line source is embedded in a layer-over-halfspace earth model with sinusoidally undulating free surface. The irregularities are required to be periodic, and the choice of sinusoidal irregularities yields a closed form solution and thus speeds up the computations. The theoretical approach is based on the integral form of Huygen's principle, with the SH-wave fields in the layer and halfspace expanded into a set of plane waves. The unknown coefficients in this expansion are found by solving a pair of matrix equations. Once these are known, the response at a free surface receiver is obtained by numerical integration (over horizontal wavenumber) of the plane wave expansion basis functions and these coefficients. This integral is expressed in Equation (1):

$$w_a(x;k) = \frac{1}{4\pi i} \int_{-\frac{\pi}{L}}^{\frac{\pi}{L}} d\alpha \sum_{n=-N}^N \left\{ \frac{B_n(\alpha)}{\beta_n(\alpha)} \exp[i(\alpha + 2\pi n/L)x] \right\}, \quad (1)$$

where

$$\beta_n(\alpha) = \sqrt{k^2 - (\alpha + 2\pi n/L)^2}.$$

In (1), $w_s(x;k)$ is the free surface SH displacement for a receiver at x , k is the wavenumber in the layer ($=\omega/\beta$), and $(\alpha+2\pi n/L)$ is the horizontal wavenumber (k_x). Because of the periodicity of the interfaces, we need only consider $|\alpha| \leq \pi/L$. The coefficients $B_n(\alpha)$ are found from solution of a pair of matrix equations (see Varadan *et al.*, 1987) for each α . The (infinite) sum in (1) must be truncated at some $n=N$ sufficient to ensure convergence of the $B_n(\alpha)$. Poles of the integrand exist when $\beta_n(\alpha)=0$.

Figure 2 shows an example of the integrand in (1) (including the $1/4\pi i$) for a flat free surface and one with $L=43$ km, $b=0.75$ km (representing Basin and Range topography). Receiver distance (x) is 500 km, the frequency is 0.53 Hz, and source depth 15 km in a 30-km-thick crust. Poles of the integrand lie near $\pm\pi/L$. Note that the major features in the integrand are not due to boundary roughness (at least at this frequency), since they are common to both plots. The behavior is complex, depending on the behavior of $B_n(\alpha)$ and $\beta_n(\alpha)$.

At this point in the project, we have written programs to ensure that the coefficients $B_n(\alpha)$ converge to within a specified tolerance (0.1%) for each α and k as N increases. Once N is determined for each α and k , these will be used in an adaptive numerical integration scheme (Romberg integration) to compute the synthetic seismogram spectrum. To move the troublesome integrand poles off the real α axis, slight damping will be included in the computations through a complex velocity.

Conclusions

Judging from current work, this problem is (relatively) not computationally difficult. The difference between the flat and irregular boundary case is only an extra matrix calculation for the latter. Other possible directions for this research include incorporating a point source, an irregular Moho, and tackling the corresponding P-SV problem.

References

- Nuttli, O. W. (1986). Yield estimates of Nevada test site explosions obtained from seismic Lg waves, *J. Geophys. Res.* **91**, 2137.
- Nuttli, O. W. (1988). Lg magnitudes and yield estimates for underground Novaya Zemlya nuclear explosions, *Bull. Seism. Soc. Am.* **78**, 873.
- Pomeroy, P. W., W. J. Best, and T. V. McEvelly (1982). Test ban treaty verification with regional data -- a review, *Bull. Seism. Soc. Am.* **72**, S89.
- Varadan, V. K., A. Lakhtakia, V. V. Varadan, and C. A. Langston (1987). Radiation characteristics of elastodynamic line sources buried in layered media with periodic interfaces. I. SH-wave analysis, *Bull. Seismol. Soc. Am.* **77**, 2181-2191.
- Waterman, P. C. (1969). New formulation of acoustic scattering, *J. Acoust. Soc. Am.* **45**, 1417-1429.
- Waterman, P. C. (1975). Scattering by periodic surfaces, *J. Acoust. Soc. Am.* **57**, 791-802.

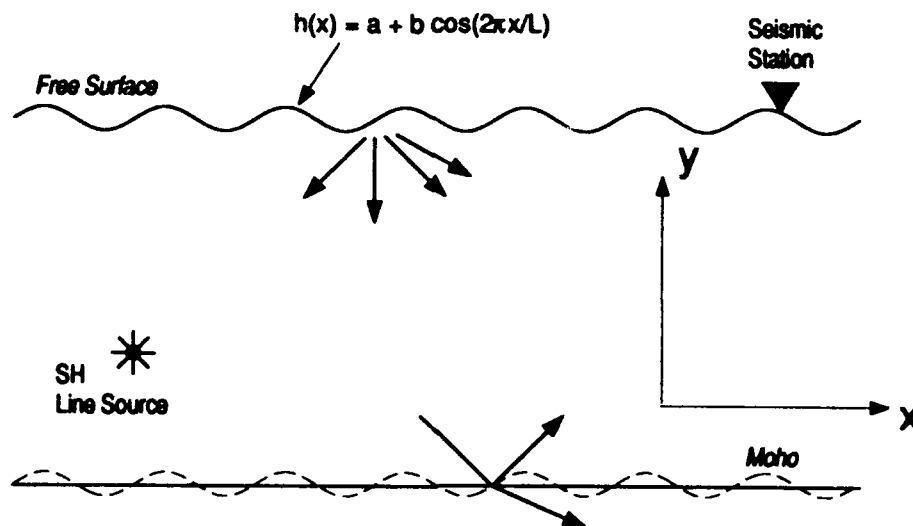


Figure 1. Geometry for the scattering problem. The free surface is sinusoidal with period L and relief $2b$. A sinusoidal Moho can also be considered, with little extra computational expense.

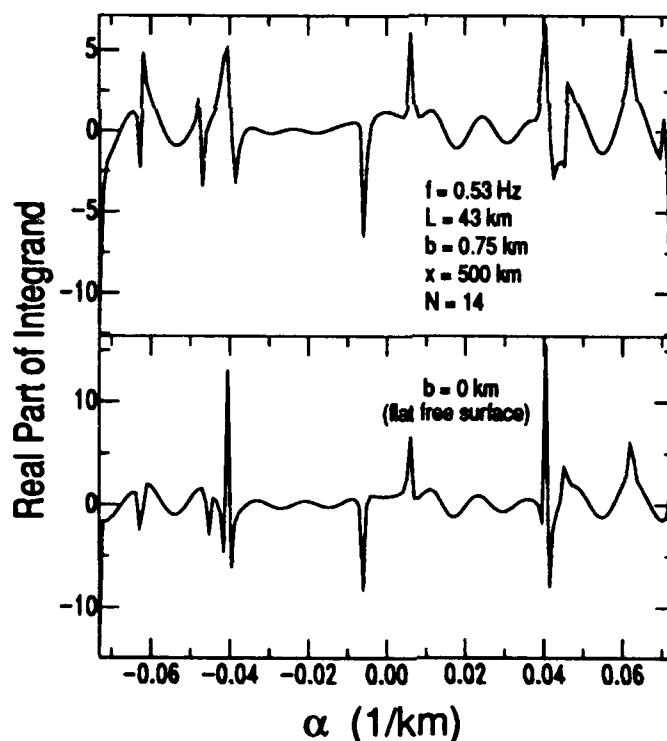


Figure 2. Plot of the real part of the integrand in Equation 1 for a free surface with $b = 0.75$ km (top) and $b = 0$ km (bottom). The abscissa runs from $-\pi/L$ to $+\pi/L$. For these parameters, integrand poles lie near the endpoints of the plot. Other features are related to the behavior of the $B_n(\alpha)$ and $\beta_n(\alpha)$.

Global Seismic Evidence Combination

Robert P. Comer, David J. Marcus, and James V. White

TASC
55 Walkers Brook Drive
Reading, MA 01867

Contract No. F29601-91-C-DB05

Objective

Our project consists of research and exploratory development on a new approach to seismic monitoring that we call *global evidence combination*. The goal is to develop and demonstrate ways to improve the sensitivity of seismograph networks to small earthquakes and explosions. We do this by combining the information available from an entire network without applying detection thresholds to the data from individual stations. This should result in a network sensitivity that is better than the sensitivity of the individual stations. Our initial effort has focused on the use of information in the amplitudes of single-channel seismograms.

Research Accomplished

Background — In the traditional approach to seismic monitoring, seismic phases are detected at individual stations or array beams. The detected phases are then associated with event locations and times. An event will go undetected unless it produces signals above the detection threshold at several individual stations, because signals that are below the threshold play no further role and several stations are usually needed to form an event location.

In contrast, we start with a particular monitoring location and time and ask the question: Are the seismograms observed by the network consistent with an event whose hypocenter matches this location and time? Global evidence combination combines signal processing and probability theory to answer this question.

Aside from voting detectors [1], we are only aware of two other attempts to combine information from a seismograph network for event detection. Beroza and Jordan [2] described an approach for detecting slow earthquakes which generate very long period free oscillations. Ringdal and Kvaerna's "generalized beamforming" [3] involves monitoring a grid of points over time using a network of regional arrays (NORESS, ARCESS, and FINESA). Generalized beamforming resembles global evidence combination at the kinematic level, but differs greatly in its underlying philosophy and detailed processing. We discuss this point in a later section.

Overview — This section introduces global evidence combination (for greater detail, see [4]). We begin by selecting a set of locations, distributed throughout a region (or the entire world). We refer to these locations as *monitoring points*, or *m-points*. For each m-point and time, we consider two mutually-exclusive possibilities: either a seismic event occurred or it didn't. For each of these two possibilities, we build a stochastic model for the seismic data recorded by the network. Then

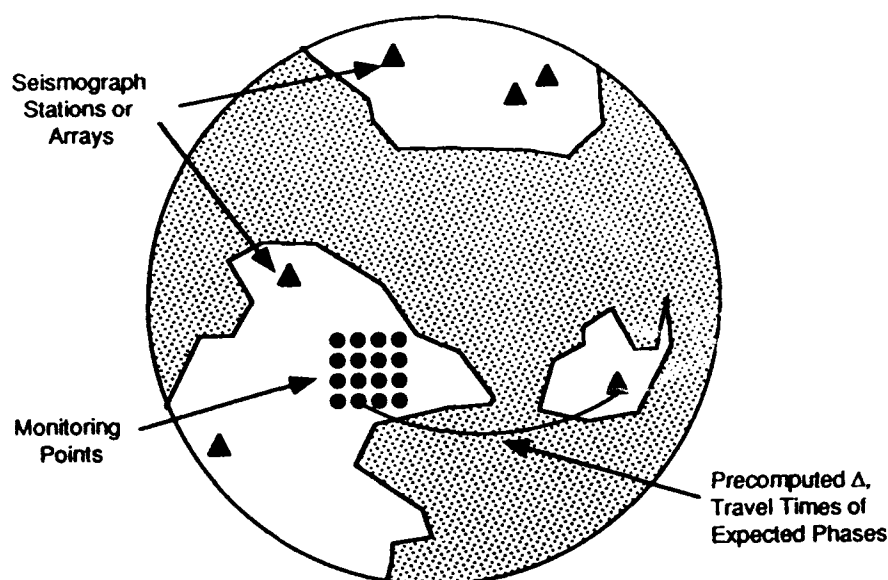


Figure 1: Global Network with Regional Grid of Monitoring Points

we use the "relative fit" of each model to the actual data, the *likelihood* of the model, to compute the probability that an event occurred at the m-point and time. In practice, we build individual models for each station in the network, compute the likelihoods for each station, then use the rules of probability theory to combine these likelihoods.

Because they are processed independently, the points to be monitored can be distributed arbitrarily. As an example, Figure 1 shows a schematic view of the globe with a grid of m-points in a selected region.

Much of the effort goes into building the stochastic models. The data to be modeled can consist of waveforms from any type of sensor system (e.g., vertical-only, three-component, or array). The waveforms can be continuous or they can consist of segments selected with traditional single-station detectors. Derived signal parameters (signal-to-noise estimates, azimuth estimates, etc.) can also be used. Any mixture of these types of data can be included as long as appropriate stochastic models are developed.

An important feature of our approach is that the models are compared only to one another, not to any kind of absolute truth. The models don't have to fit the data closely in an absolute sense to yield accurate results. For example, a pair of models, one for background quiescence and the other for a seismic event, will be successful as long as the latter model reflects the features of the signal better than does the background model. This means that global evidence combination is robust with respect to approximations in the models. We can select the complexity and detail of the models to trade off performance, computational effort, and robustness with respect to unusual signals.

To date, we have worked primarily with a class of models for single-channel (short-period vertical-component) seismograms that we call *baseline amplitude* models. They model the fact that a seismogram increases in amplitude at the time of a phase arrival. The baseline amplitude models realistically model the spectral content of the background noise, but simplistically model the arriving phase as an increase in amplitude without a change in spectral content. The following

section discusses the representation of these models.

In current work, we are extending the baseline amplitude models to three-component waveforms. These three-component models will reflect the polarization of phase arrivals. The polarization can be predicted based on the azimuth and distance from a given station to a given m-point. (The construction of such models is different from the widely-addressed problem (e.g., [5], [6]) of *estimating* the polarization characteristics of signal arrivals recorded by three-component instruments; we cannot make direct use of work on that problem.)

Baseline Amplitude Models — We need a *background-noise* model for the case in which there is no event at the m-point and a *phase-arrival* model for the case in which there is an event.

Consider the background-noise model first. This model depends on the station and channel, but not on the phase type. The noise is stationary on the time scale of interest, although the model may need to change occasionally to reflect various slow (e.g., diurnal) temporal fluctuations. The background-noise model should reflect the level and the correlation structure of the background noise on the sz channel (or, equivalently, the power spectral density of the noise).

All of our stochastic models are from the class of linear state-space models [7]. For each channel to be processed, we estimate the state-space model parameters using a signal-free segment near the beginning of the seismogram. The class of state-space models, while parameterized differently, is essentially the same as the class of ARMA models (e.g., [8]). This class provides a rich, full framework which has been sufficient to accurately model every seismic noise process we have so far encountered, and is also convenient computationally.

The phase-arrival model is really a model for a phase superposed on the background noise. While there is plenty of data available from which to construct an accurate model for the background noise, modeling the signal is more problematic. One clear characteristic is that the amplitude will increase when a signal arrives. Therefore, as a baseline, we model the signal as having the *same correlation structure as the noise*; i.e. our phase-arrival model is the same as the background-noise model except that its amplitude is greater. This approach has the advantages of being simple and robust. We have demonstrated that it works well, even at low signal-to-noise ratios, using both theoretical analyses and real data.

We have considered two alternatives for moving beyond this baseline. Both require considerably more effort both to construct a model and to ensure that it reflects important features that will really help to discriminate signals from noise. One alternative is to proceed empirically, by constructing and pooling models for the phase of interest as observed from high signal-to-noise events in the appropriate distance range from the station. The other alternative is more theoretical: assume a seismic source spectrum typical of a small event, then convolve this spectrum first with a theoretical transfer function for the propagation path, including an average t^* to model anelastic attenuation, and finally with the instrument response. In both cases, the signal model is then combined with the background-noise model. We want to explore these alternatives in future research.

Evidence Combination — Having constructed background-noise and phase arrival models for all the stations in a network, it is straightforward to combine evidence from the network to compute the probability of an event at an m-point and time. For each station and selected phase, use an earth model or travel-time table to predict the arrival time at the station, and select a short waveform segment corresponding to the predicted phase arrival. We have been using a 10-s segment duration for the direct P phase at teleseismic distances.

Each of our two models corresponds to a gaussian probability density for the selected waveform segment. Substituting the actual values of the waveform into the density formula gives the likelihood of the model. As explained in [4], our state-space representation of the model leads to a highly

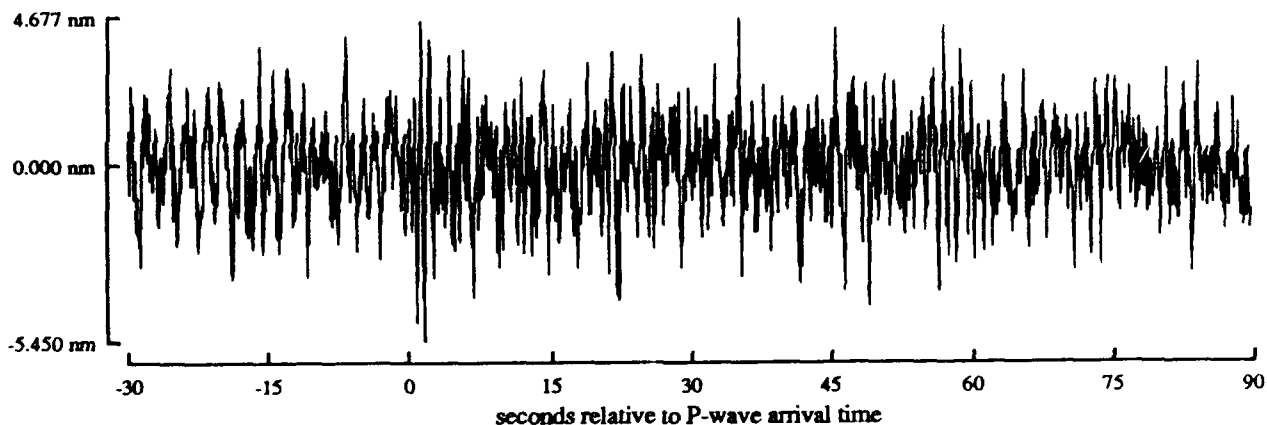


Figure 2: Seismogram from ARA0 with Added Noise

efficient approach to computing this likelihood. The *likelihood ratio* is the likelihood of the phase arrival model divided by the likelihood of the background noise model. Let r be the product of the likelihood ratios from the various stations and phases. Let Q be the prior probability of an event and P be the posterior probability. Then Bayes's rule gives

$$P = \frac{rQ}{(1 - Q) + rQ}.$$

The prior probability of an event at an m -point is chosen to be consistent with historical seismicity in the region containing the m -point. The multiplication of the likelihood ratios is appropriate because the stations in the network have independent noise processes due to their wide spatial separation.

Small-Scale Experiments — We first demonstrated the baseline amplitude models using short segments of vertical-component seismograms segments from a 4-station network [4]. Figures 2 and 3 describe one of our 4-station monitoring experiments. We started with four two-minute short-period vertical-component seismograms known to contain P arrivals from an Alaskan earthquake with $m_b = 4.6$. These data were obtained from the GSETT database at the Center for Seismic Studies.

In one experiment, we added noise to each seismogram to reduce the signal-to-noise ratio. We used our state-space modeling tools [7], to construct a highly accurate noise model and realization corresponding to each seismogram. Figure 2 shows the seismogram from ARA0 with noise added. This technique of adding noise is quite powerful, enabling us to exert greater experimental control than is possible with raw data alone. We then constructed somewhat simpler stochastic models for the background noise on each seismogram, for use as our baseline amplitude models. (The baseline amplitude models need not be highly accurate. On the other hand, we want to make the additive noise as realistic as possible.)

We monitored an m -point placed at the known origin of the earthquake every 5 seconds for a period of 105 seconds, and computed the probabilities as previously described. The results are shown in Fig. 3. On the basis of each station's evidence, the probability of an event is well below $1/2$ at the origin time, but the event is clearly detected when the evidence from all four stations is combined. The experiment demonstrates the promise of multi-station evidence combination to improve network sensitivities.

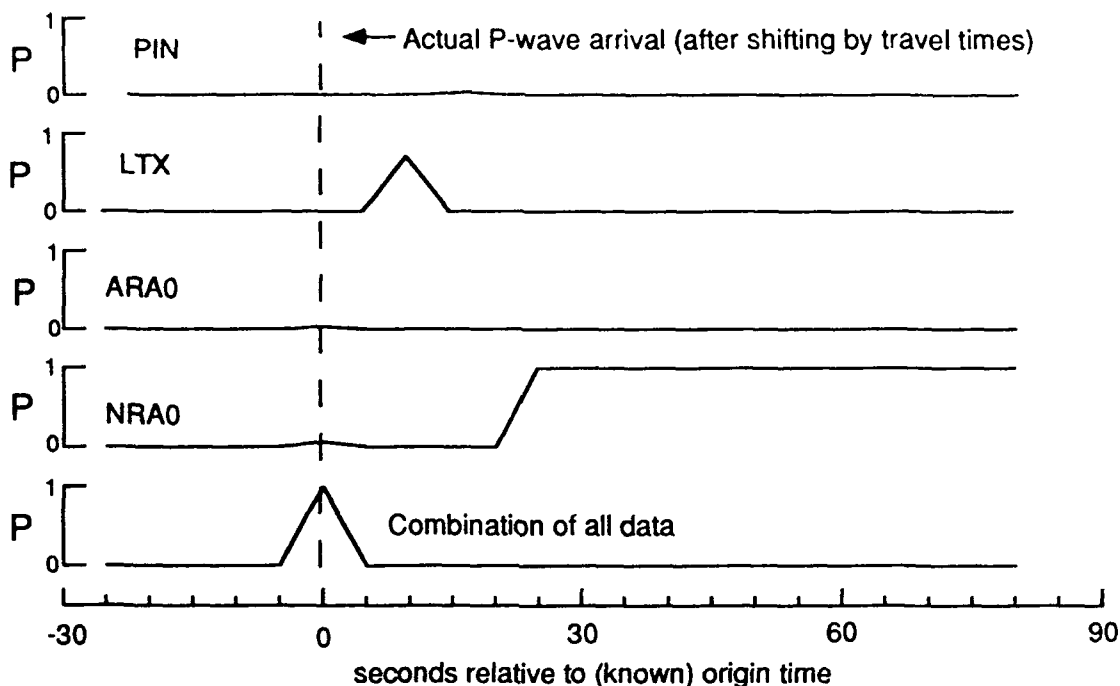


Figure 3: Posterior Probability of Seismic Event Using Degraded Signals

Moderate-Scale Experiments — We are currently conducting larger-scale monitoring experiments, with a network of about a dozen stations and 30 to 60 minutes of continuous waveform data for time periods rich with seismic activity. These experiments enable us to explore the spatial and temporal resolution of global evidence combination by working with grids of multiple m-points and widely-spaced seismic sources. The data sets supporting these experiments correspond to the GSETT period (22 April through 2 June, 1991). They include USA and USSR stations participating in the GSETT, for which we obtained continuous waveforms obtained from the USA National Data Center (NDC) in San Diego and the USSR database at the Center.

Theoretical Performance Analysis — We have conducted an error analysis for the detection of events via global evidence combination using the baseline amplitude models. Among other standard measures, we computed the probability of false alarm and the probability of detection as functions of the modeled and true mean-square signal-to-noise ratio (SNR). Here we have space only for a few highlights.

As an example, Fig. 4 shows the probability of detection as a function of the mean-square SNR for the case in which the modeled SNR matches the true SNR. These are based on a detection threshold of 0.5 (which minimizes the probability of error), a prior event probability of 10^{-9} , and 400 degrees of freedom (appropriate to roughly 6 to 8 stations). We also computed the corresponding false-alarm probabilities. They indicate, for example, that for $\text{SNR} = 0.7$, corresponding to a detection probability of 0.9, that the probability of false alarm is about 3×10^{-11} .

Comparison to Generalized Beamforming — It is instructive to contrast global evidence combination with the "generalized beamforming" techniques introduced by Ringdal and Kvaerna [3]. They present two specific techniques for seismic monitoring using a network of arrays: (1) regional phase association and (2) continuous monitoring of upper event magnitude limits (detection

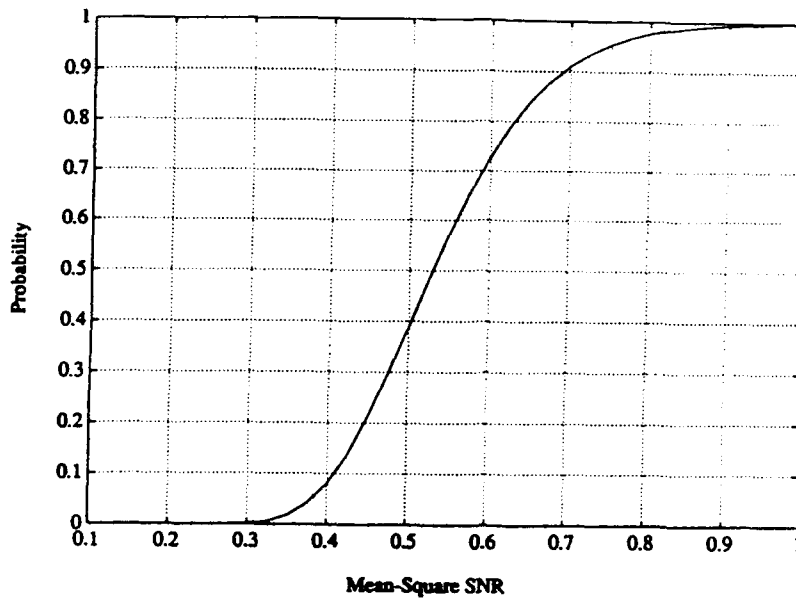


Figure 4: Probability of detection as a function of SNR, where modeled SNR equals true SNR

threshold monitoring). Generalized beamforming [3] consists of choosing a grid of “beam points” (analogous to our m-points), computing a beam for each of the beam points from each array, and shifting the beam outputs to account for the travel times from each array to each beam point.

Global evidence combination shares some of the kinematic features of generalized beamforming. Both use a network of stations to detect seismic events at pre-specified locations and perform a time shift to account for predicted travel times. However, at a deeper level, in terms of what one computes with the time-shifted beams or signals, our technique differs fundamentally from both regional phase association and continuous threshold monitoring.

Regional phase association uses a simple voting scheme. Each array responds with a “yes” or “no” to the question of whether or not a seismic event occurred at the specified beam point and time. It does this by first running a threshold detector. If the threshold detector indicates that there is a signal, then various parameters such as phase velocity and azimuth are checked for consistency with an event at the beam point. If at least two arrays agree that there is an event, then a detection is declared. This regional phase association is clearly different from our approach since it (1) applies detection thresholds to a detection statistic computed at the individual station level and (2) combines the binary array outputs in an ad hoc manner. In contrast, we do not apply thresholds at the station level. Instead (1) we compute a likelihood ratio, using models for the background noise and signal and (2) we use the fundamental principles of probability theory in consistently combining the likelihoods from multiple stations.

Global evidence combination also differs substantially from continuous threshold monitoring. For each beam point and time, continuous threshold monitoring attempts to calculate a magnitude such that there is a probability of 0.9 that at least one of the arrays would detect an event of that magnitude. In contrast, our technique rigorously combines evidence from multiple stations in a network and calculates the probability that there was an event at each monitoring point and time.

Conclusions and Recommendations

Our initial work indicates that we can easily detect known events of moderate size using teleseismic P phases. Moreover, we have achieved greater sensitivity by combining evidence from multiple stations. We have a preliminary indication that the use of evidence from multiple stations improves rejection of unwanted local events. And we have theoretical evidence that our baseline amplitude models perform effectively even when the actual signal-to-noise ratio departs significantly from the modeled signal-to-noise ratio.

In our continuing work we are using the baseline amplitude model with larger networks, longer monitoring intervals, and additional phase types. The goal is a system that can continuously monitor a network of stations.

A major part of our work is developing stochastic models. We are currently developing stochastic models appropriate to three-component sensors. These will incorporate information on the polarization of the arriving signal, which we can predict from the phase type and the distance and azimuth from the station to the m-point.

In the future, we envision research to develop models that use spectral information in the signal (as opposed to our current models, which only use spectral information in the background noise). We also want to develop models to utilize data from seismic arrays.

References

- [1] Wirth, W.H., R.R. Blandford, and R.H. Shumway, Automatic seismic array and network detection, *Bull. Seism. Soc. Am.*, **66**, 1375-1360, 1981.
- [2] Beroza, C.G. and T.H. Jordan, Searching for slow and silent earthquakes using free oscillations, *J. Geophys. Res.*, **95**, 2485-2510, 1990.
- [3] Ringdal, F. and T. Kvaerna, A multichannel processing approach to real time network detection, phase association, and threshold monitoring, *Bull. Seism. Soc. Am.*, **79**, 1927-1940, 1989.
- [4] Comer, R.P., D.J. Marcus, and J.V. White, Global Seismic Evidence Combination — Semianual Technical Report No. 1, TR-6408-1, TASC, 31 March 1992.
- [5] Jurkevics, A., Polarization analysis of three-component array data, *Bull. Seism. Soc. Am.*, **78**, 1725-1743, 1988.
- [6] Suteau-Henson, A., Three-component analysis of regional phases at NORESS and ARCESS: polarization and phase identification, *Bull. Seism. Soc. Am.*, **81**, 2419-2440, 1991.
- [7] White, J.V., Stochastic state-space models from empirical data, *Proceedings ICASSP 83*, Vol. 1, IEEE International Conf. Acoustics, Speech and Signal Processing, 243-246, April 1983.
- [8] Box, G.P., and G.M. Jenkins, *Time Series Analysis — Forecasting and Control*, Revised Edition, Holden-Day, 1976.

GENERALIZED RAY/BORN SYNTHESIS OF COMPLETE REGIONAL SEISMOGRAMS IN THREE-DIMENSIONAL CRUSTAL MODELS

Vernon F. Cormier
Department of Geology and Geophysics, Box U-45
University of Connecticut
Storrs, CT 06269-2045

Contract No. F19628-90-K-0043

OBJECTIVE

This paper summarizes a portion of a two year project titled "Crustal and Upper Mantle Gradients in the Vicinity of the Kazakh Test Sites and their Effects on Regional Discriminants." The objectives of this project are to investigate the effects of crustal structure, including the effects of velocity gradients, on the amplitude, frequency content, and decay with distance of regional seismic phases.

RESEARCH ACCOMPLISHED

Under our current contract, we have modeled Lg wavetrains by dynamic raytracing (DRT) in three-dimensionally varying crustal waveguides. Lg is synthesized as a sum of multiply critically reflected S waves in the (Figure 1). Topography of the Moho is correlated with given or known surface topography under the assumption of Airy isostasy. The starting assumptions are essentially the same as those used by Kennett (1986) in identifying gross effects of crustal thickness on Lg by plotting the bounce points of critically reflected S waves in the crust. Here, however, waveforms are calculated and the effects of geometric spreading are included. Lg blockage due to sedimentary basins (e.g., Baumgardt, 1990; 1991) are also included.

Results obtained under our current GL contract suggest that is worthwhile to use ray theory not only to predict Lg transmission qualitatively but also to model complete Lg waveforms (Figures 2). In this work, Lg wavetrains have been modeled by dynamic raytracing (Červený, 1985) in three-dimensionally varying crustal waveguides. Unless major sedimentary basin structure is ignored or inaccurately given, good correlation with predicted and observed Lg waveforms is observed. Results obtained in experiments with hypothetical mountain ranges found Lg transmission to be only weakly dependent on the angle of the path with respect to the strike of the mountain range or basin, and strongly dependent on the slopes of the Moho or basin boundary. Transmission across wider transition zones in crustal thickness is more efficient because a shallower Moho dip reduces Lg leakage into the mantle. An upper bound on SV to SH conversion due to Moho topography was found for the case of sources and receivers within the mountain belt. The amount of SH energy, however,

was too small to account for the equalization of Lg energy on all components of motion commonly observed from explosion sources.

Initially we assumed a homogeneous crust bounded by a rough surface and Moho. More recently, we have included the effects of random heterogeneities within a crustal waveguide of variable thickness by adding dynamically traced rays to point scatterers (Figure 3). A standard Born approximation (e.g., Wu and Aki, 1985) is used to calculate the radiation pattern of the point scatterers. The assumption of first order scattering within the crustal waveguide acts to fill up coda between multiple reflected S waves (Figure 3).

Complete regional seismograms (excluding fundamental mode surface waves) can readily be synthesized by summing ray theoretical arrivals. Except in the case of a homogeneous crust overlying a uniform mantle, parameterization of the propagation medium by discontinuous layers makes it cumbersome to catalogue and sort ray codes (the description of multiply reflected and converted rays). A remedy to this difficulty is to parameterize the medium without discontinuities, representing the Moho and other important reflectors and three-dimensional scatterers by regions of strong gradient. Reflections and conversions at strong gradient zones can be estimated by a generalized Born approximation, which gives a low frequency correction to ray theory in regions of high gradient. In this approach, Sn/Lg interactions at a laterally varying Moho are automatically included. Inclusion of the generalized Born correction (Coates and Chapman, 1991) for scattering by high gradient zones fills up the Lg coda between multiple SmS arrivals and is useful for mapping the region of scattering that contributes to the late Lg coda.

Examination of intermediate output of dynamic ray tracing in continuous models of the crust and upper mantle suggests that scatterers located within the Moho transition play a dominant role in forming complex Lg coda. Since ray theoretical Green's functions of Lg rays touch a caustic surface coincident with the Moho transition, the scattering effects of any heterogeneity located there are strongly magnified.

CONCLUSIONS AND RECOMMENDATIONS

Ray/beam modeling of Lg as a sum of multiply, critically reflected S waves demonstrates that basin structure and Moho topography can have a profound influence on the efficiency of Lg propagation. Comparison of observed with synthetic waveforms suggests that the essential ingredients needed to accurately model Lg codas may simply consist of (1) a deterministic description of sedimentary basins (2) a deterministic description of Moho topography, and (3) a statistical description of finer scale heterogeneity within the crust. The regions of the crust in which it is most important for the statistical component of the model to be accurate are within the upper and lower several kilometers of the crust.

REFERENCES

- Coates, R.T., and C.H. Chapman, Generalized Born scattering of elastic waves in 3-D media, *Geophys. J. Int.*, 107, 321-363, 1991.
- Baumgardt, D.R., High frequency array studies of long range Lg propagation and the causes of Lg blockage and attenuation in the Eurasian continental craton, Final Report, PL-TR-91-2059(II), Phillips Laboratory, Hanscom AFB, MA, 1991. ADA236984
- Červený, V., The application of ray tracing to the propagation of shear waves in complex media, in *Seismic Exploration*, pp. 1-124, Treitel and Helbig, Vol. on Seismic Shear Waves, G. Dohr, ed., Geophysical Press, 1985.
- Kennett, B.L.N., Lg waves and structural boundaries, *Bull. Seism. Soc. Am.*, 76, 1133-1141, 1986.
- Wu, R.-S., and K. Aki, Scattering characteristics of elastic waves by elastic heterogeneity, *Geophysics*, 50, 582-595, 1985.

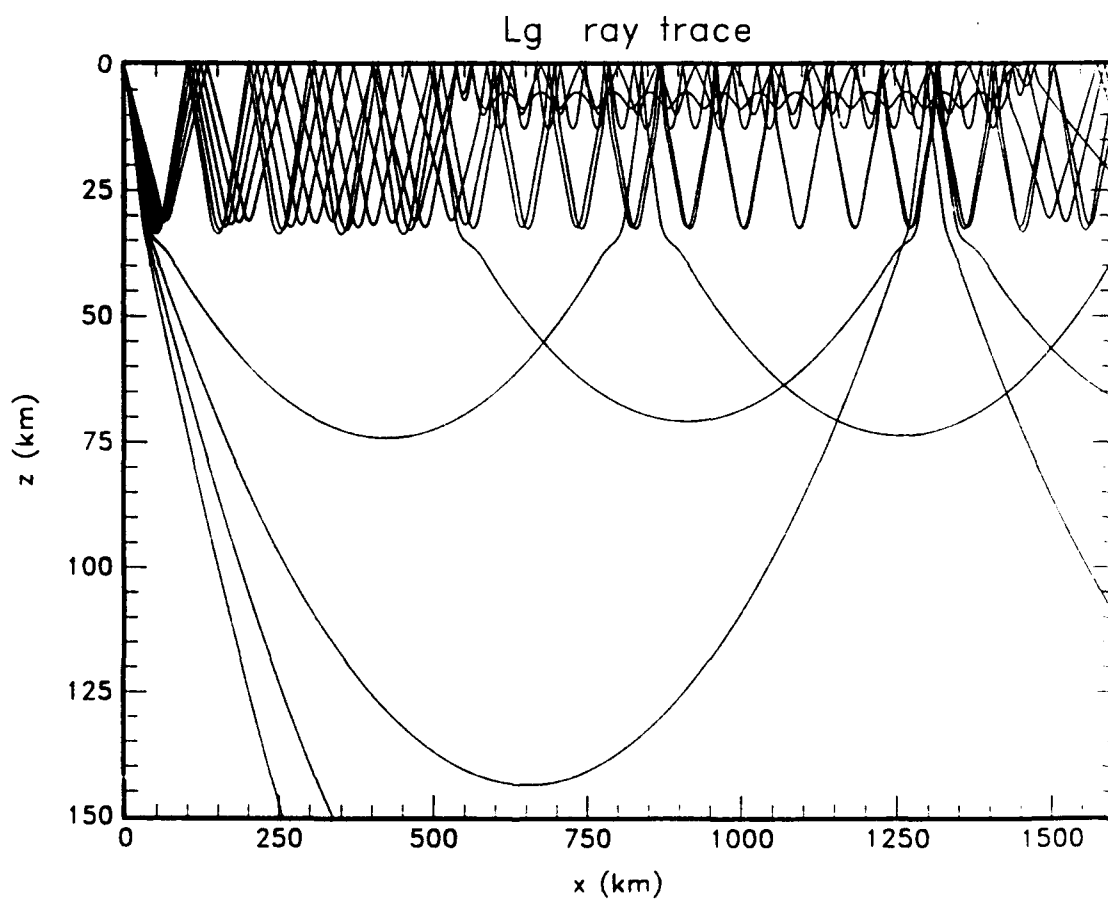
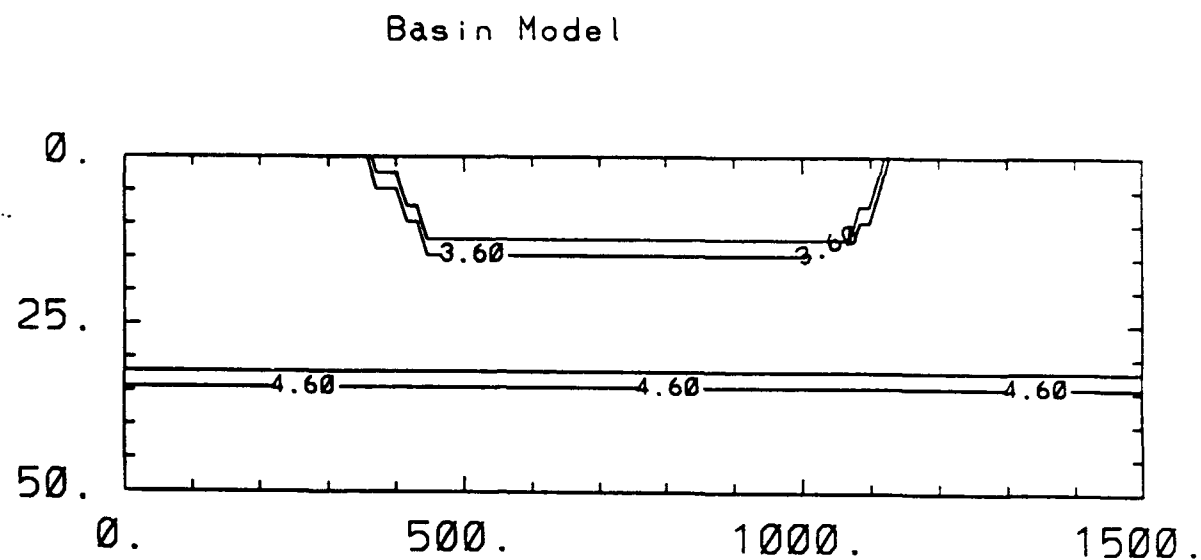


Figure 1

Top: Iso-S velocity contours defining a deep sedimentary basin (Z and X-co-ordinates are in kilometers.) Bottom: ray trace of S waves trapped in the crustal waveguide (Lg). Note that the effect of the basin will be to attenuate Lg at stations 1400 km and greater range.

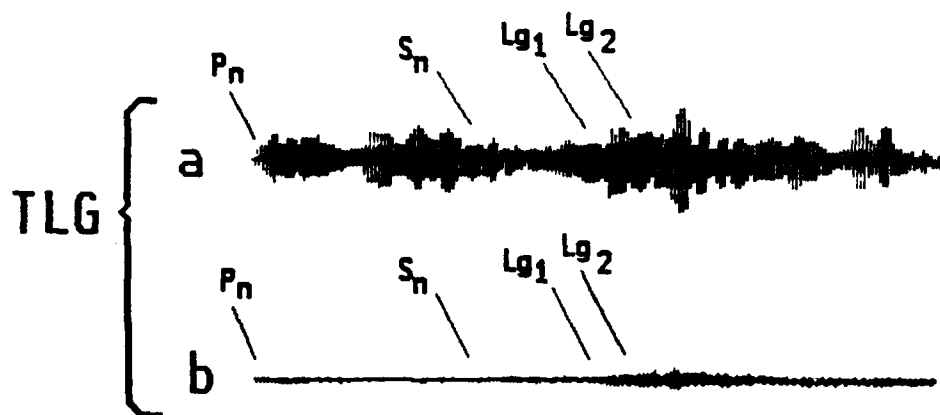


Figure 2a. Central Asia strong path seismograms. The seismograms recorded from the left earthquake of figure 7a show clear Lg energy in both the top (1.25-2.0 second period) and bottom (2.5-5.0 second) traces.

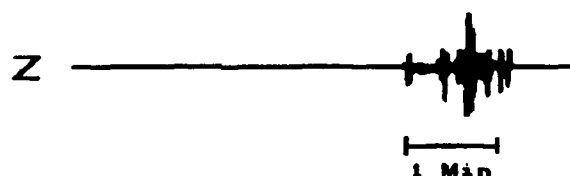
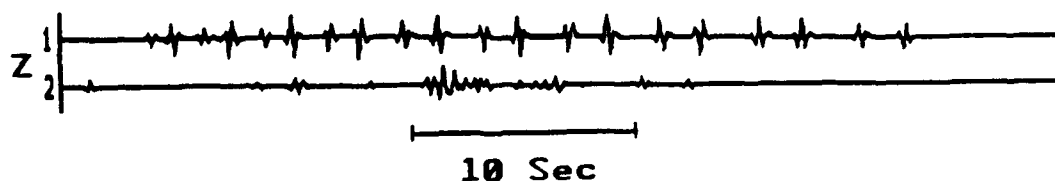


Figure 2b. Scaled strong path synthetic. The synthetic seismogram is scaled to the dimensions of the actual seismogram and shows a good recreation of Lg.



Trace 1 = Non-attenuated Lg
Trace 2 = Strong path synthetic

Figure 2c. Detailed strong path synthetic. These synthetic seismograms are not scaled to the recordings and allow determination of the level of attenuation. Ray modeling through a homogeneous crust predicts significant attenuation over this path.

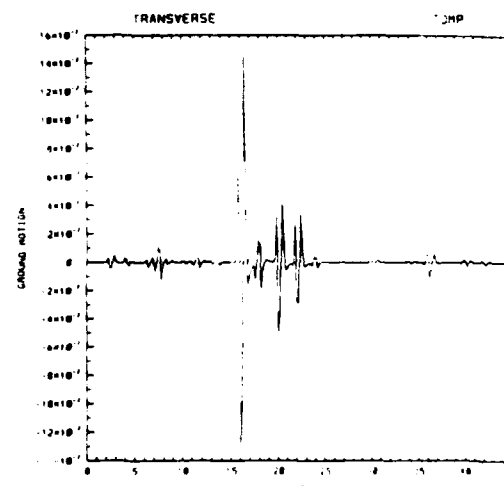
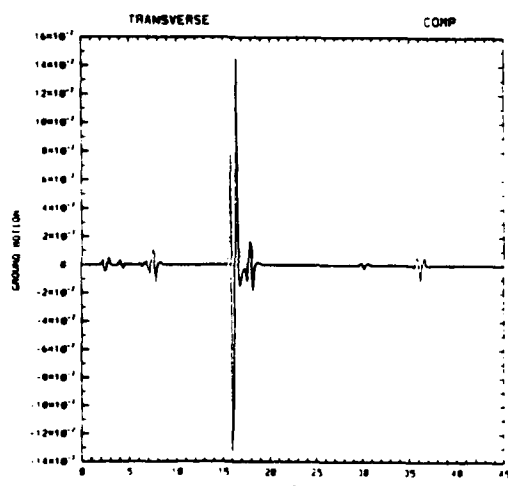
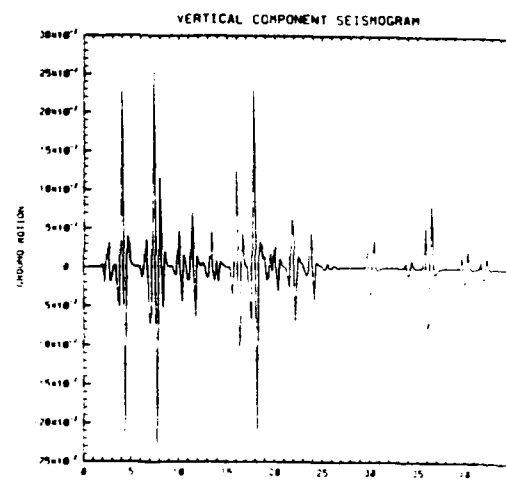
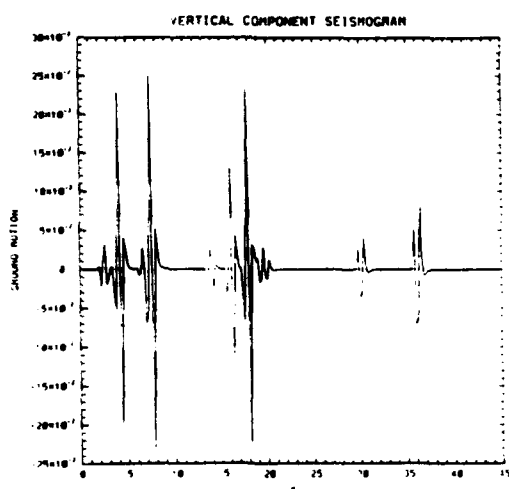
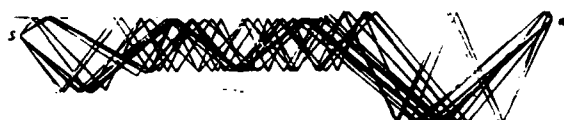


Figure 3

Left: Lg rays and ray theoretical seismograms for the vertical and transverse components for vertical and horizontal depth Moho. Right: ray theoretical seismograms including rays at top left and scattered rays at top right.

AN X-WINDOWS GRAPHICS TOOL TO COMPUTE SYNTHETIC SEISMOGRAMS FOR 2-D MODELS USING GAUSSIAN BEAMS

J. P. Davis and I. H. Henson

Teledyne Geotech Alexandria Laboratory,
314 Montgomery Street, Alexandria, VA 22314-1581

Contract No. F29601-91-C-DB04

1. OBJECTIVE

The principal goal of this project is to create an X-Windows-based graphics tool to compute rapidly and efficiently, synthetic seismograms for laterally heterogeneous, two-dimensional (2-D), isotropic velocity models using the Gaussian beam method. Existing Gaussian beam software is written in Fortran code and is often very cumbersome to use. By constructing an X-Windows Graphical User Interface (GUI) to augment the original code, much of the tedium of introducing lateral heterogeneity into 2-D velocity models can be eliminated. The tool can be used to aid the interpretation of waveforms or to study how lateral structure and the source's location within that structure impact arrival times and waveform shape. When completed, this code will be integrated into the software environment at the Center for Seismic Studies (CSS).

This report begins with an outline of the system architecture and how the modules interface with software already developed under the NMRD. Figures illustrating some of the graphical displays and explanations of the functions those displays serve are included to give the reader some appreciation of the project's purpose. Appended is a list of references in which applications of the original Fortran code to seismological problems of interest are described.

2. FUNCTIONAL OUTLINE

The functional flow for computing Gaussian beam seismograms and/or calculating traveltimes through heterogeneous media is shown in Figure 1. The first step is either to create an input model *ab initio* or to access a fully 2-D model which has been created previously. Whether created *ab initio* or read in and modified, the model may be stored at the end of this step.

Each model is parameterized by fixing v_p , v_s , and ρ at a series of knotpoints in space. The velocity is fully specified in two dimensions by assuming a linear gradient between each knotpoint. Knotpoints are grouped into triplets to form triangles, and values for Q_α and Q_β , the P - and S -wave attenuation, are assigned to the space enclosed by each triangle. The program tracks which triangles share knotpoints and are therefore "neighbors."

Under this linear gradient assumption, there is an analytical solution for the raypath across a triangle. Raytracing through the model is accomplished by stepwise tracing analytically through each component triangle along the raypath. Anelasticity is accounted for by

Functional Analysis

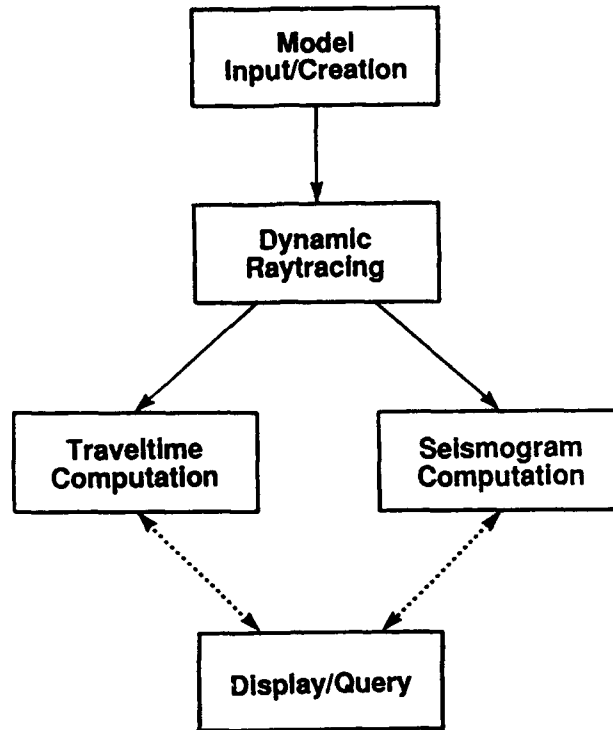


Figure 1.

System Architecture

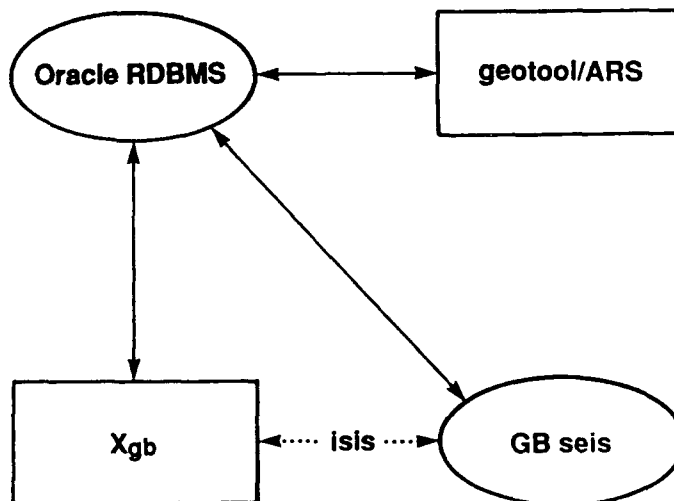


Figure 2.

computing a t^* operator using Q_α and Q_β from the triangles. This is the second step shown in Figure 1. Results from this step are also stored for later reference.

The essentials for traveltimes calculation or seismogram computation are now complete. One should remember that in the Gaussian beam method, it is not necessary to compute rays which travel directly from source to receiver. Rather, it is sufficient to compute a number of rays which originate at the source and terminate within several wavelengths of the receiver. Therefore, to obtain a traveltimes or seismogram, one must first specify the source-receiver geometry and phase, or component phases in the latter case.

This is represented by the display/query box at the bottom of Figure 1. Since at this point the prerequisite quantities have all been computed, one may repeatedly access the model and ray information to obtain traveltimes and seismograms for different receivers and focal mechanisms. The seismogram computation is performed by a second, non-graphic module which runs in background and reads in the raytracing results. Synthetics are written out in standard CSS 3.0 database format and can therefore be displayed by any of several graphics packages available through CSS.

3. SYSTEM ARCHITECTURE

How the functional capabilities are realized is outlined in Figure 2. In this diagram, rectangles represent programs with an X-windows graphical component, ellipses enclose the names of background processes, and ISIS is the name of the interprocess communication (IPC) module employed by the NMRD system. The modules being developed for this project are *Xgb* and *GBseis*.

It is *Xgb* which is at the heart of this system. *Xgb*'s X-windows interface allows the user to create or modify 2-D earth models. If a velocity structure is to be assembled from scratch, the user is presented with a suite of 1-D models, either global, regional, or customized by the user. The 1-D model is recast into triangles extending laterally. Alternatively, the user may read in a model created with *Xgb* on a previous run. This is accessed from where it is stored on disc via the Oracle Relational Database Management System (RDBMS) running at CSS.

Once a model is input, alteration can be accomplished by: (1) repositioning a knotpoint with a mouse "drag-and-drop;" (2) selecting a model point or triangle and changing its parameter values; and (3) applying a filter to some or all knotpoints to change their position and/or velocity values. The three may be done repeatedly and in any sequence. The program provides bookkeeping functions to maintain consistent internal relationships between triangles while knot translation is taking place.

Once the model is adjusted to the satisfaction of the operator, raytracing may be performed with *Xgb*. This is accomplished by specifying the initial ray parameter of the ray and by describing the discontinuity interactions, namely what discontinuities the ray encounters and whether it is reflected, transmitted, or converted there. The graphical interface enables the user to reposition the source within the model: The user merely translates the source across the screen with a mouse "drag-and-drop." Because rays are updated for the new source location in a matter of a few seconds at most, source translation can be

performed repeatedly while the user observes the effects of the position changes on the ray-paths. This has proven to be a valuable aid to intuition. Like the model, raytracing results are stored in a file for later reference, and a pointer to this file location is passed to the Oracle RDBMS.

The computational functions of *Xgb* are complete at this stage. Traveltime calculation and synthetic seismogram computation are performed by the non-graphic server process *GBseis*. This is accessed via IPC messages instructing it what function, traveltime or synthetic seismogram, to fulfill. If that function is traveltime calculation, *GBseis* returns its results via IPC reply. If seismogram computation, the results are written to disk, registered in the database, and an IPC acknowledgment sent. When completed, *Xgb* will be able to form the proper IPC messages to prompt *GBseis* to perform the described calculations.

By design, there is no capability in either *Xgb* or *GBseis* to display the resulting synthetic seismograms. In keeping with the NMRD goal of modular design and distributed processing, this task is left to modules such as the Analyst Review Station (ARS) or Geotool, both under NMRD development.

4. EXAMPLES

Several figures are included here to illustrate some of the features of *Xgb* discussed above. Figure 3 shows the display presented to a user who wishes to construct a 2-D model from one of the starting 1-D models, shown on the lists at left. The 1-D global model selection *jb* (for Jeffreys-Bullen) is highlighted in inverse video, and the appropriate v_p , v_s , and ρ are plotted on the right. The vertical dimension of the space to be modeled extends from the free surface to a depth controlled by the horizontal line segment shown on each of the three functions. The line may be slid vertically by the mouse or, alternatively, the bottom depth may be entered into the space labeled "Depth" at the lower left. By setting a minimum lower depth and the number of horizontal knots (at the lower right), one can control model size and therefore performance speed. The breadth of the model is controlled by entering the maximum number of degrees (or kilometers for regional models) in the bottom center window.

Figure 4 shows two views of how the model of Figure 3 is presented to the user. Figure 4a is the default earth flattened view. Major discontinuities appear as horizontal lines, and the vertical dimension is exaggerated by the effect of the earth flattening transformation. Rays emanate from the source whose location is denoted by a star. Rays for *PcP* radiate to the right, those for *P* and *PKP*, to the left. These same rays are presented in a non-flattened view in Figure 4b. Here the inner concentric ring represents the model bottom. The user may toggle between the two views as convenient. In both cases, view of the component triangle borders has been suppressed leaving only the discontinuities.

Figure 5 illustrates a regional model into which a salt dome has been introduced via the mouse. All component triangles are displayed in Figure 5a. In the actual display, color is used to distinguish between *P*- and *S*-rays, model borders, discontinuities and normal triangles. To limit confusion in a black-and-white figure, the triangles are again suppressed in Figure 5b to leave only the source and discontinuities showing. Finally in Figure 5c, rays are drawn emanating from the source. The user may translate the source position through

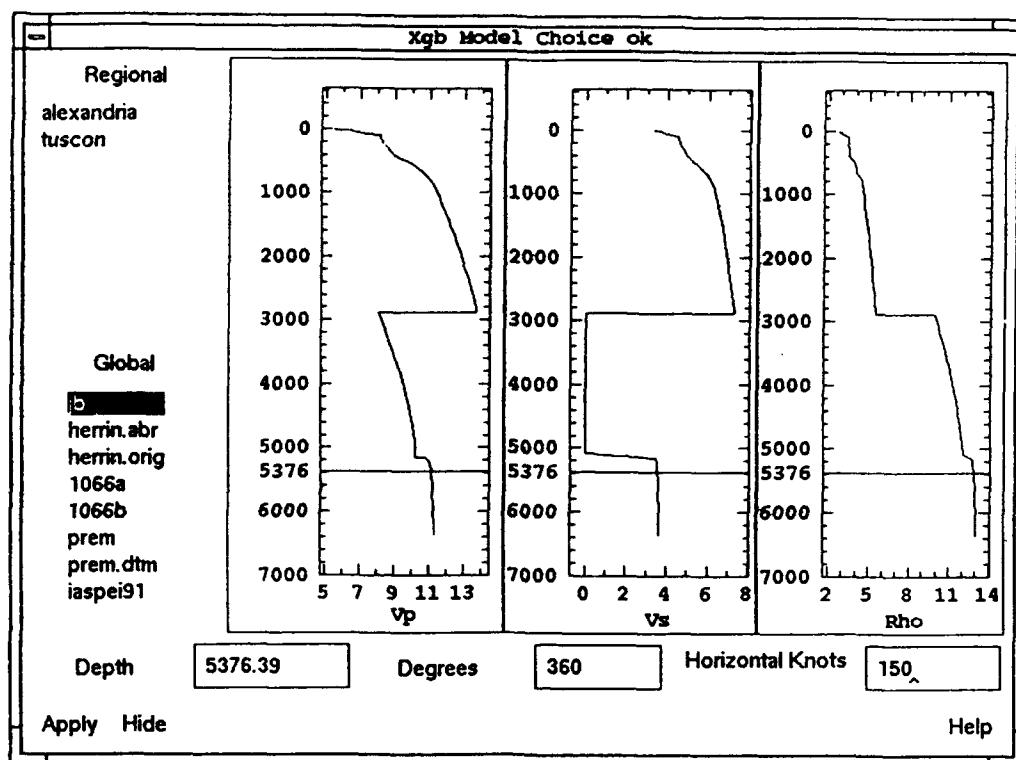


Figure 3.

the heterogeneity and watch the program rapidly update the raypaths.

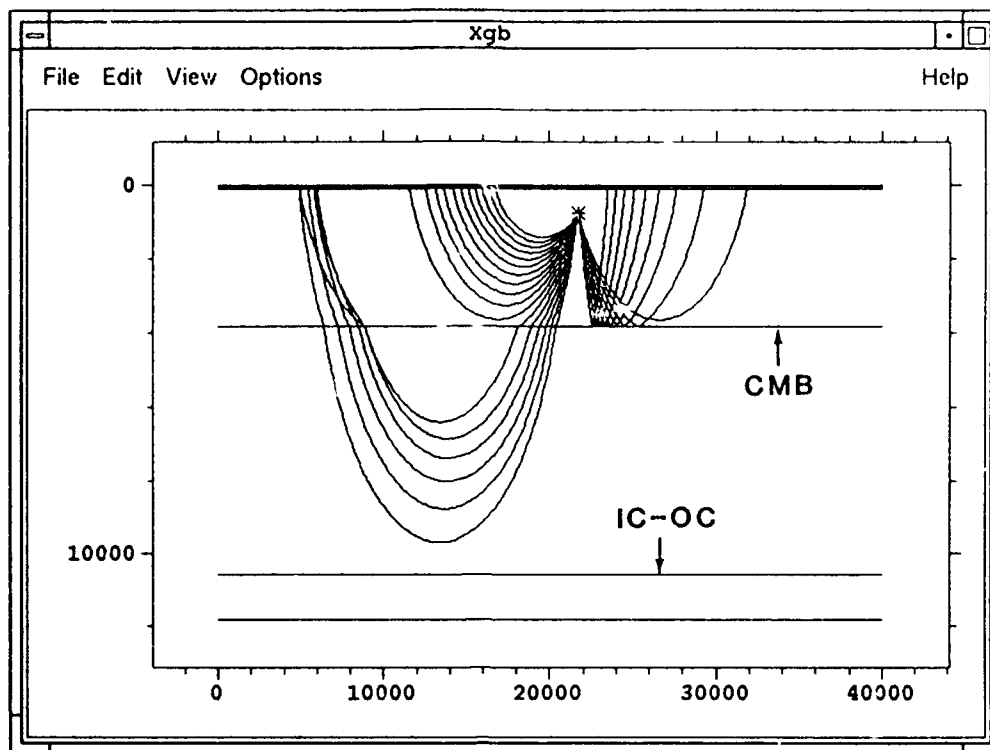
5. CONCLUSIONS

When completed, the software described here should provide analysts and researchers with a powerful tool to allow them to explore the effects of lateral structure on seismic waves. The capability to change iteratively the velocity model and source position can greatly aid intuition and will stimulate modeling of structures previously considered too complex for direct forward modeling.

6. REFERENCES

- Davis, J. P., R. Kind, and I. S. Sacks (1989), Precursors to $P'P'$ re-examined using broadband data, *Geophys. J. Internat.*, **99**, 595--604.
- Weber, M. (1988a), Computation of body-wave seismograms in absorbing 2-D media using the Gaussian beam method: comparison with exact methods, *Geophys. J.*, **92**, 9-24.
- Weber, M. (1988b), Application of the Gaussian beam method in refraction seismology -- Urach revisited, *Geophys. J.*, **92**, 25-31.
- Weber, M. (1990), Subduction zones -- their influence on traveltimes and amplitudes of P -waves *Geophys. J. Internat.*, **101**, 529-544.
- Weber, M., and J. P. Davis (1990), Evidence of a laterally variable lower mantle structure from P - and S -waves, *Geophys. J. Internat.*, **102**, 231--255.

(a)



(b)

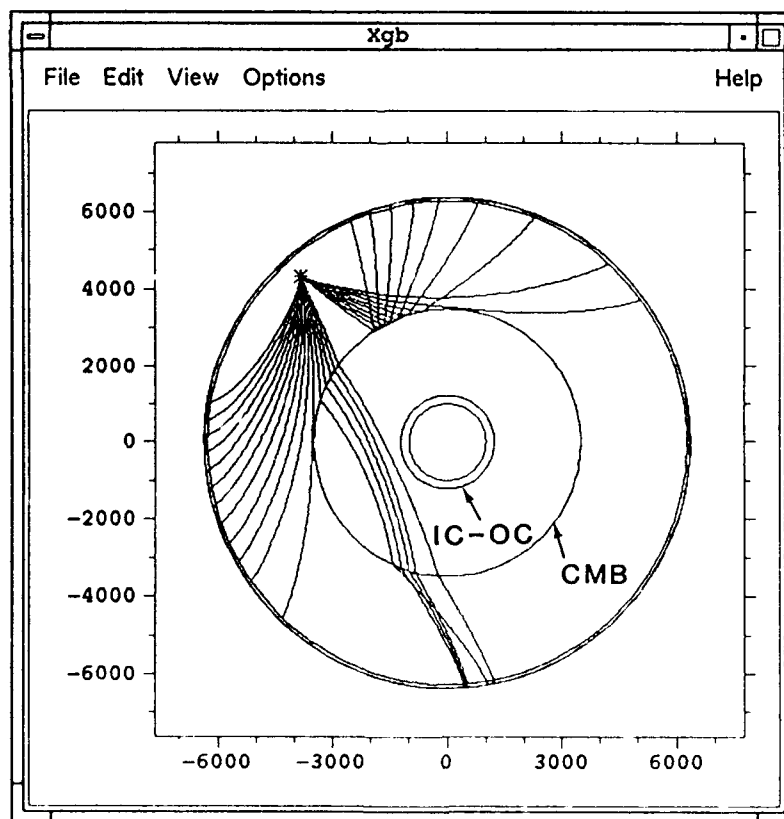
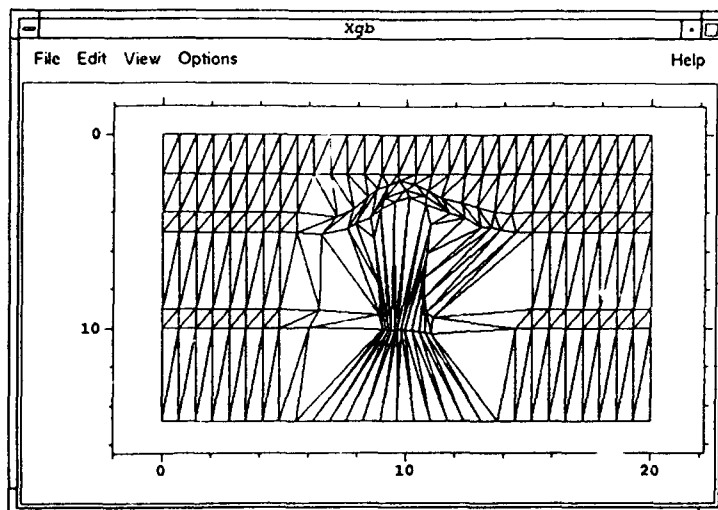
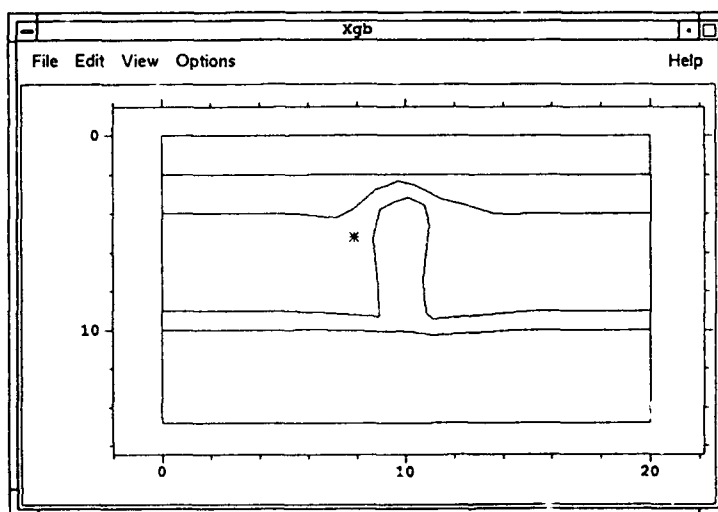


Figure 4.

(a)



(b)



(c)

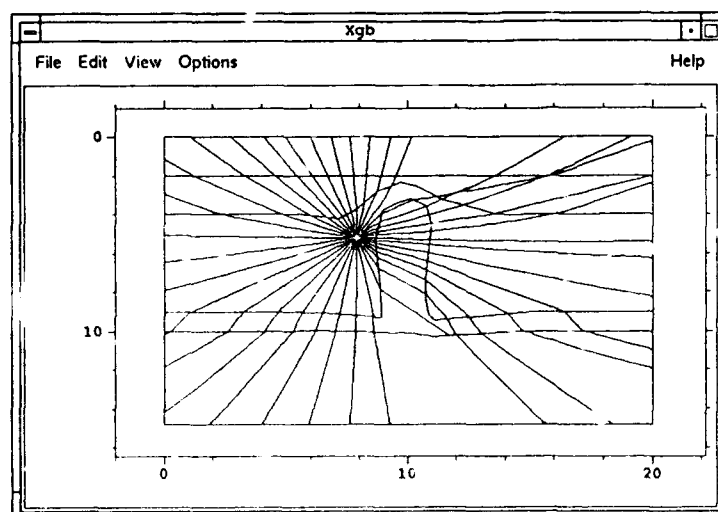


Figure 5.

Seismic Array Study of the Baikal Rift Zone, Siberia

**Paul M. Davis
Shanxing Gao
Hong Liu
Philip D. Slack**

*Department of Earth and Space Sciences
The University of California, Los Angeles
Los Angeles California 90024-1567*

Contract No. F29601-91-K-DB17

Objective:

The objective is to measure seismic propagation effects in south central Siberia across three geologic provinces. These include the Siberian craton, the Baikal rift zone (the site of the IRIS/DARPA seismograph site at Talaya) and the Cenozoic fold belt to the south. In particular, we investigate lateral variations in the seismic properties of the crust and mantle, including phase delays caused by the lithosphere-asthenosphere transition, attenuation, and generation of converted phases in P and surface wave coda by scattering.

Introduction

There are geophysical indications from seismic, gravity, magnetotelluric studies and modeling that the asthenosphere upwarps beneath the Baikal rift relative to the adjacent regions. However, the size and shape of this upwarp are not clear. Some argue that the peak of the asthenospheric diapir reaches the Moho, i.e., the lithosphere is thinned to the thickness of the crust, while others believe it is much deeper (Zorin et al., 1989; Logatchev and Florensov, 1978; Logatchev and Zorin 1987; Zamarayev et al., 1978; Zorin et al., 1989).

The teleseismic P-wave method for investigating crust and upper mantle structure has been applied to a number of rift zones (Davis, 1991; Davis et al., 1984; Parker et al., 1984; Dahlheim et al., 1989; Halderman et al., 1991; Green et al., 1991; Glahn et al., 1992). The method consists of timing P-wave arrivals from distant earthquakes and comparing observed arrival times with those expected for a laterally homogeneous earth model. The residuals are then explained in terms of local lateral heterogeneity in the velocity field. Given enough angles of incidence and azimuths of incoming rays to an observational network, the residual pattern can be used in a linearized inversion to determine velocity variations. We compare those results with data collected on lake Baikal and also associated variation in waveforms.

Research Accomplished

In the summer of 1991, we installed 26 seismic stations (10 PASSCAL Reftek and 16 U. Wisconsin recorders) about Lake Baikal (Figure 1). All the stations were equipped with 1 Hz 3-D sensors and five of the stations were co-sited with broadband vertical (4 Guralp and 1 STS2) seismometers. All seismographs synchronize internal clocks to signals from the Omega navigation system which ensured that the timing error for most of the data was less than 20 ms.

The network ran from early July to early October 1991. 118 teleseismic events with good signal-to-noise ratio were recorded. Theoretical arrival times were calculated by using the IASPEI 1991 earth model (Kennet and Engdahl 1991). Residuals were found by subtracting computed arrival times from observed ones, and relative residuals were formed for each event by subtracting the mean residual from the raw residuals (Figure 2). Examples are shown in Figure 2 where events are separated into clusters having similar azimuths and epicentral angles. The relative residual curves from nearby events have similar variation pattern. The strong dependance of relative residuals upon hypocentral location suggests

that the asthenosphere-lithosphere boundary varies 3-dimensionally within the studied area.

Inversion of the travel time data

We use a 3D downward projection method developed from a previous 2D procedure (Davis et al., 1984; Halderman and Davis 1991) to estimate the configuration of the lithosphere-asthenosphere interface. The method assumes a straight ray and plane wave approximation for the teleseismic waves. The raw residuals are then proportional to the length of the ray in the anomalous velocity zone. By taking into account the azimuth and angle of incidence of the incoming ray to a station, the geometry of the interface is determined. The interface is found by minimizing the sum of squares of residuals to a six order polynomial fit in both x and y directions, varying depth of the interface and velocity contrast. The best fit model is shown in Figure 3. The inversion used 554 travel times from 118 earthquakes to determine the 36 polynomial coefficients.

The overall misfit is 0.12 seconds, which is larger than the observational error range, but is presumed to arise from over simplification of the transition as an undulating boundary separating two regions of constant but different velocity. The resultant velocity contrast is -5.6% in the asthenosphere. If we use deep seismic sounding results that the P wave velocity in the lithosphere immediately beneath the Moho is 8.1 km/s in the region (Puzyrev et al., 1978), we get an asthenospheric velocity $V_a = 7.65$ km/s. Figure 4 is a cross section from Figure 3 along our array. It shows that the depth of the interface ranges from 130 km in the West beneath the craton, and increases up to 75 km at the east end of the profile in the fold belt. The upwarp is asymmetrical. The Baikal rift zone is not seated above its summit but lies above a local upwelling.

The result (Figure 4) correlates well with gravity observations (Figure 5). The raw Bouguer gravity anomaly was separated into a local anomaly which is related to shallow heterogeneity (surface to Moho) and a regional anomaly which is related to deep heterogeneity (Moho to 250 km) by using the decompensative method developed by Zorin et al (Zorin et al., 1989). To perform the separation, deep seismic sounding estimates of crustal thickness were used to remove crustal effects. The rms difference between the resulting regional anomaly and the calculated anomaly from our teleseismic model is 3.3 mgal. Density contrasts were adjusted in the calculation in order to get an optimized fit and gave values of -269 kg/m^3 for the crust and -60 kg/m^3 for the low velocity zone. The contrast of P wave velocity and density across the lithosphere-asthenosphere boundary is -5.6% and -1.8% respectively. A large velocity contrast and small density contrast may indicate a small fraction of partial melt within the upper asthenosphere (Davis et al., 1984), .

Attenuation

Relative T^* were calculated from spectra of P coda using the procedure discussed in Halderman and Davis (1991). Relative T^* (i.e. travel time divided by Q) values along the profile support the view that the delays in the asthenosphere are caused by partial melt.

The T^* values increase eastward with a peak to peak difference up to 0.1 second, and at the rift region, a 0.06 second local anomaly was clearly observed (Figure 6).

Broad-band Recordings

Figure 7a shows records from an earthquake in northern California recorded on 4 Guralp seismometers, 2 each side of the lake. Station 1 was about 300 km west of the lake at the end of the profile; 5, about 20 km west of the lake; 7, 100 km to the east and 10, 250 km to the east. The great circle path crosses lake Baikal from east to west, but at an acute angle. The western surface waveforms show similar characteristics, in contrast to the eastern waveforms. Figure 7b shows waveform spectra. The eastern signals have peak amplitudes at about 22 seconds whereas the western peak at about 16 seconds. Also the phase of the buildup of eastern energy is earlier than that in the west. Since the crust is similar on either side of the lake, these differences are probably explained by effects encountered in crossing the rift zone itself. Excitation of the rift zone lake and sediments may have generated trapped modes which absorbed energy from selective frequencies on crossing. We propose to use our structural models to explain these differences as more examples are gathered from the data.

Converted Phase in East P wave Coda

We used beam steering methods to attempt to identify local (near-receiver) scatterers either in the upper mantle or in the crust. We searched for secondary waves in the P wave coda which were identified by their contrasting apparent velocity to the direct arrivals. By stacking the arrivals for a given event we generated a mean waveform for the array (figure 8a). Then subtracting this from the record section gives a differential record section (figure 8b). A secondary arrival is clearly identifiable in the eastern stations. We have performed tests to interpret this arrival as a reflection from an upper layer in the crust.

Conclusion and Recommendations

Our 26-station teleseismic array, spread 700 km across the Siberian craton, the Baikal rift zone and the Trans Altai Baikalian Fold Belt, has detected travel time delays of about 1.0 seconds which increase from the craton into the fold belt. Azimuthal dependence of the delays has been used to map the variation in the lithosphere-asthenosphere boundary after removing crustal effects determined from deep seismic sounding. The boundary lies at a depth of about 130 km beneath the Siberian craton in the northwest rises beneath lake Baikal to about 75 km, and remains elevated towards the southeast. The travel time delays are about 50% of the variation we recorded across the east African rift in a similar experiment, and 66% of those recorded across the Rio Grande rift. The value of dt/dt^* of 0.1 secs/sec is slightly larger than the value on the Rio Grande rift of 0.075 secs/sec and is significantly less than we observed in east Africa 0.20 secs/sec. We have identified scattered energy in the teleseismic P wave coda on the eastern side of the lake by forming a differential record section which entails removing the primary waveform. We have also found evidence for significant filtering of surface waves after crossing the rift.

Recommendations and work to be completed are listed below:

1. A larger array with more broad-band stations is required to determine the geographical extent of the variation in each province. This is presently under way in 1992. We have installed a 1200 km long, 25 station, linear array stretching from well into the Siberian craton and extending to the Gobi desert in Mongolia. A further 25 station 2D array has been installed in the Baikal rift zone. The array includes 10 broad-band stations.

2. The initial 1991 experiment recorded 4GB of data. Another 8GB will be recorded this summer. Further analysis of these data include extracting local and regional earthquakes, and mining explosions; receiver function studies; birefringence studies; S-wave delays and scattering studies as well as extending the surface wave and converted phase analysis undertaken so far.

3. Data from the Talaya station and the Russian and Mongolian networks should be integrated into the study as well as the results of the multi-channel reflection work of the USGS in the summer of 92 including wide-angle shore recordings at our stations.

4. Ultimately an assessment will be made of the aliasing of the teleseismic wavefield recorded on a 50 element array in a region of extreme geological variation. Preliminary indications show that P-wave coda show good coherence over hundreds of km either side of the lake once arrivals from coherent local scatterers have been removed. Surface waves show similar coherence but are less well correlated one side to the other. Attenuation results show that explosions detonated in the area are likely to give low estimates of yield.

References

Dahlheim, H-A., P.M. Davis and U. Achauer, Teleseismic Investigation of the East African Rift - Kenya, *J. African Earth Sciences*, 8, 2-4, 461-470, 1989.

Davis, P.M., E.C. Parker, J.R. Evans, H.M. Iyer and K.H. Olsen, Teleseismic deep sounding of the velocity structure beneath the Rio Grande rift, New Mexico, *Geol. Soc. Guide Book*, 35th Field Conf., 29-38, 1984.

Davis., P.M., Continental rift structures and dynamics with reference to teleseismic studies of the Rio Grande and East African Rifts, In :A.F. Gangi (Editor), *World Rift Systems, Tectonophysics*, 197, 309-325, 1991.

Glahn, A., Granet, M., Achauer, U., Liotier, Y., Wittlinger, G., and Slack, P. Dynamics of the Lithosphere - Asthenosphere system beneath the southern Rhinegraben area from a small-wavelength tomographic study. (submitted) 1992.

Green, W. V, U Achauer and R. P. Meyer, A three-dimensional seismic image of the crust and upper mantle beneath the Kenya rift, *Nature*, 354, 199-203, 1991.

Halderman, T.P., and P.M. Davis, Teleseismic estimates of asthenospheric Q beneath

the Rio Grande and East African Rift zones., J. Geophys. Res., B6, 10,113-10,128, 1991.

Kennet, B.L.N. and E.R. Engdahl, Travel times for global earthquake location and phase association, Geophys. J. Int. 105, 429-465, 1991.

Logatchev, N.A., and N.A. Florensov, The Baikal system of rift valleys, In N.A. Logatchev and P.A. Mohr (editors), Geodynamics of the Baikal rift zone, Tectonophysics, 45, 1-13, 1978.

Logatchev, N.A. and Y.A. Zorin, Evidence and causes of the two-stage development of the Baikal rift, tectonophysics, 143, 225-234, 1987.

Parker, E.C., P.M. Davis, J.R. Evans, H.M. Iyer and K.H. Olsen, Upwarp of anomalous asthenosphere beneath the Rio Grande rift, Nature, 312, 354-356, 1984.

Puzyrev, N.N, M.M. Mandelbaum, S.V. Krylov, B.P. Mishenkin, G.V. Petrik, and G.V. Krupskaya, Deep structure of the Baikal and other continental rift zones from seismic data, In N.A. Logatchev and P.A. Mohr (editors), Geodynamics of the Baikal rift Zone, Tectonophysics, 45, 15-22, 1978.

Zamarayev, S.M., V.V. Ruzhich, On the relationships between the Baikal rift zone and ancient structures, In N.A. Logatchev and P.A. Mohr (editors), Geodynamics of the Baikal rift Zone, Tectonophysics, 45, 41-47, 1978.

Zorin, Yu, Recent structure and isostasy of the Baikal rift zone and adjoining territories, Nauka, Moscow, 168 pp, 1971.

Zorin, Yu. A., V.M. Kozhevnikov, M.R. Novoselova, and E.K. Turutanov, Thickness of the lithosphere beneath the Baikal rift zone and adjacent regions, tectonophysics, 168, 327-337, 1989.

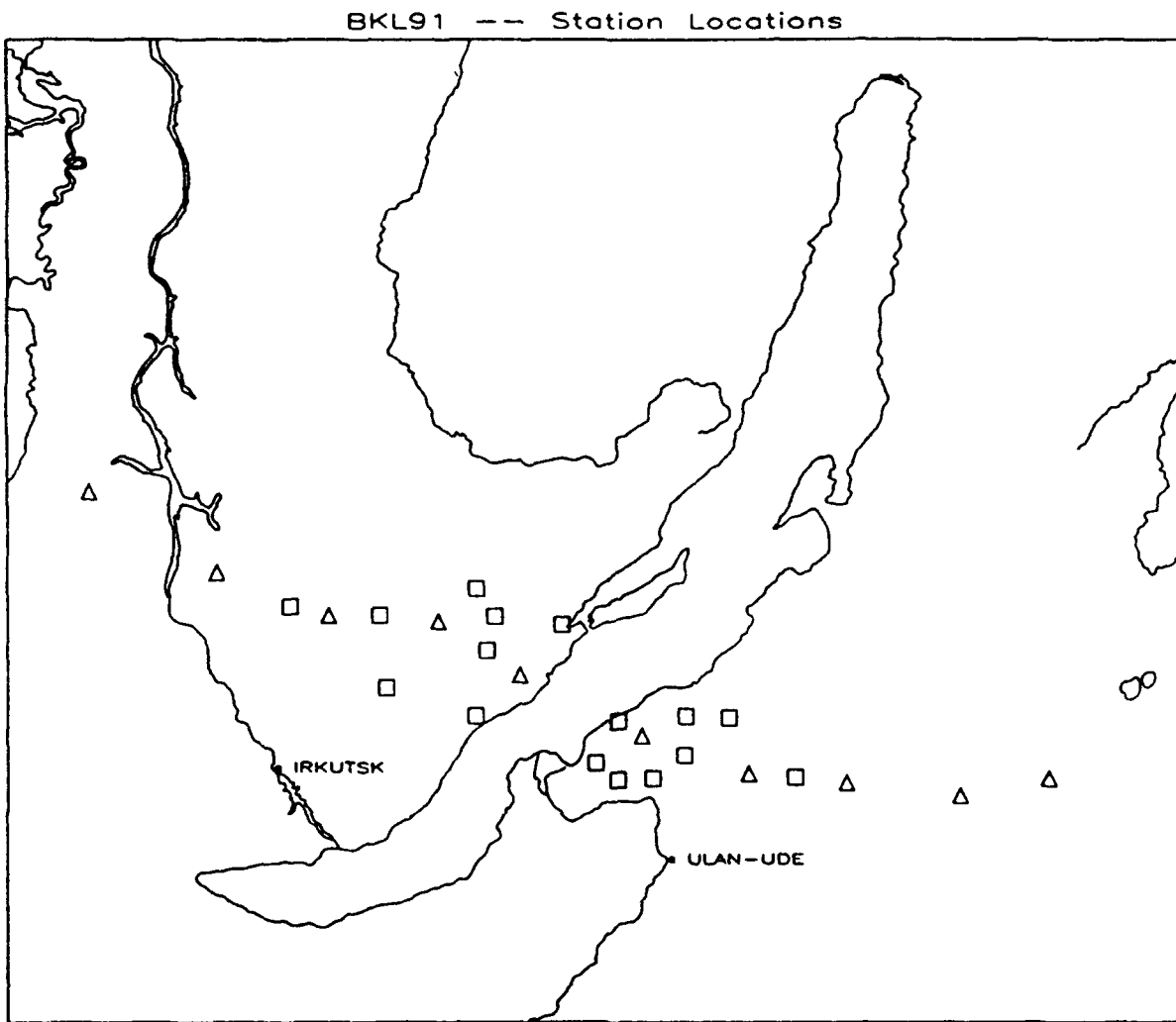


Figure 1. Station locations for the Baikal 1991 Experiment. Triangle - PASSCAL stations; squares - U. Wisconsin stations.

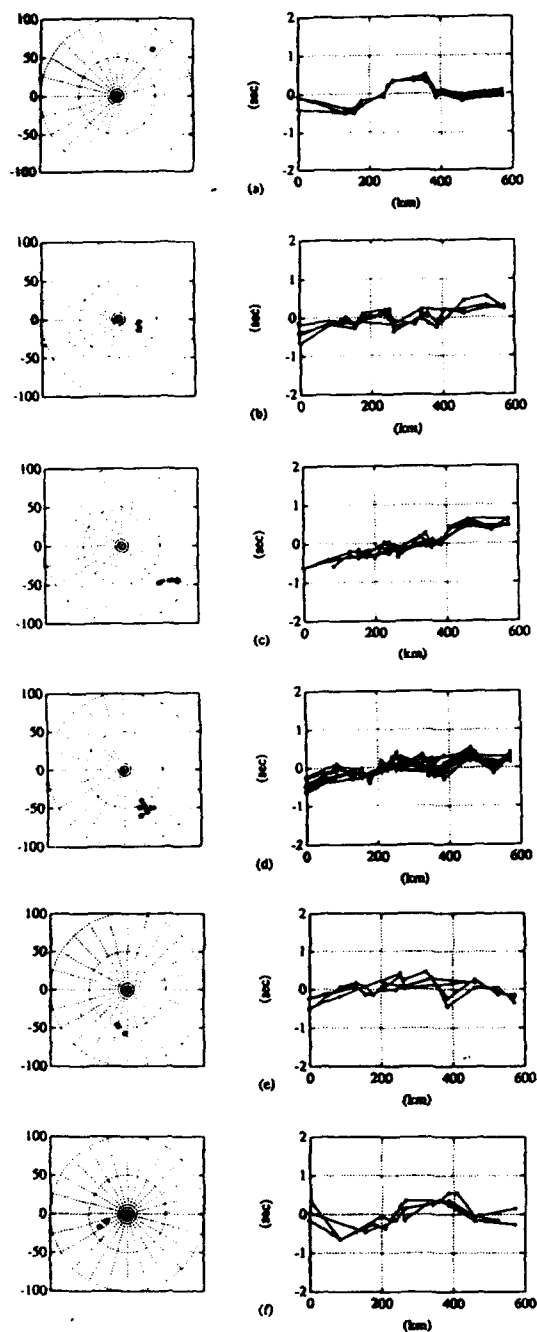


Figure 2a. - 2f. Telescismic travel time residuals relative to the IASPEI 91 Earth Model. Events are separated into clusters having similar azimuths and epicentral angles (left diagrams: center of polar map is center of the array).

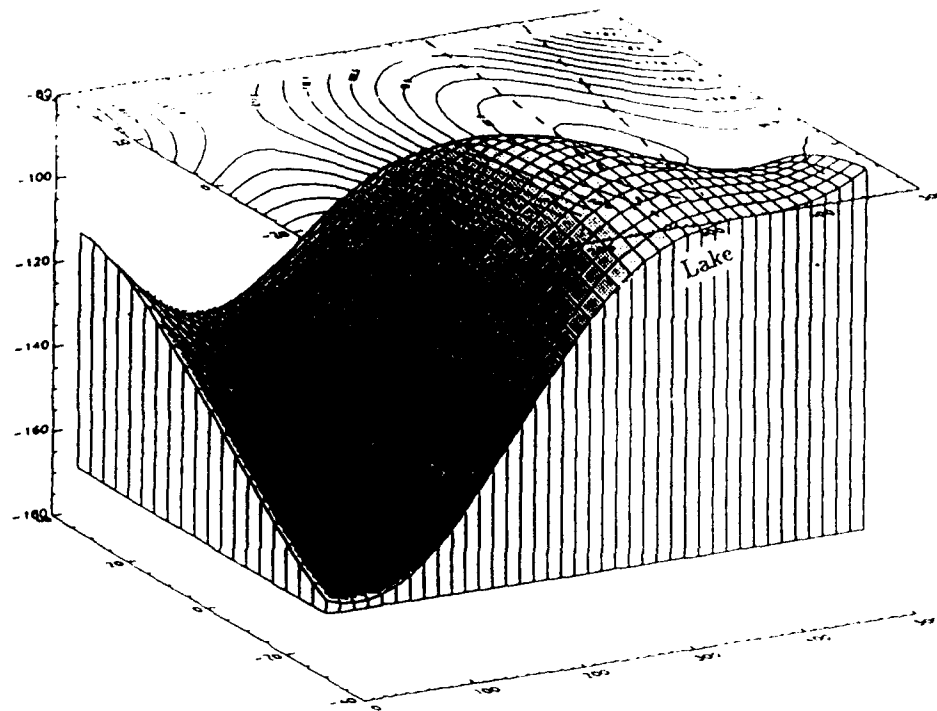


Figure 3. Downward projection of the residual patterns of Figure 2. P-wave velocity contrast from the inversion is -5.6

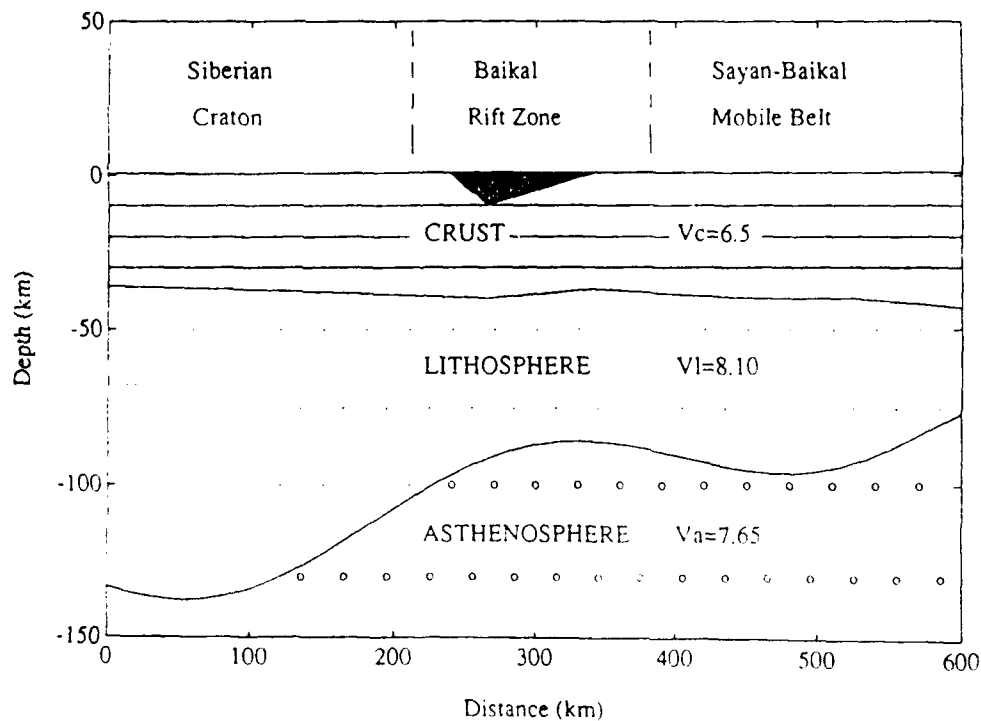


Figure 4. Cross-section of Figure 3 along the profile. Variation in thickness of crustal layers and crustal velocities are taken from DSS (Puzyrev et al., 1978).

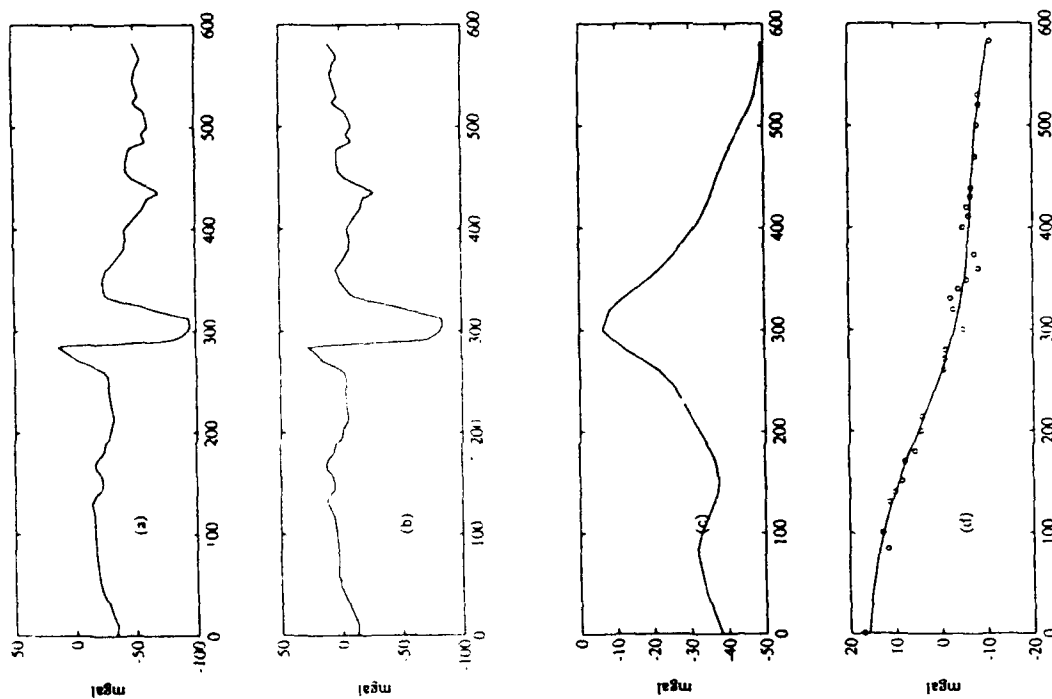


Figure 5. Measured and calculated gravity anomaly. Total Bouguer gravity anomaly (a) was separated into: local anomaly (b); anomaly from variation of the Moho as determined from DSS (c); and anomaly related to mantle heterogeneity (d), by using DSS results and a decompensative method. Calculated anomaly from inverted deep structure agrees with measured anomaly. Density contrast is -0.57%.

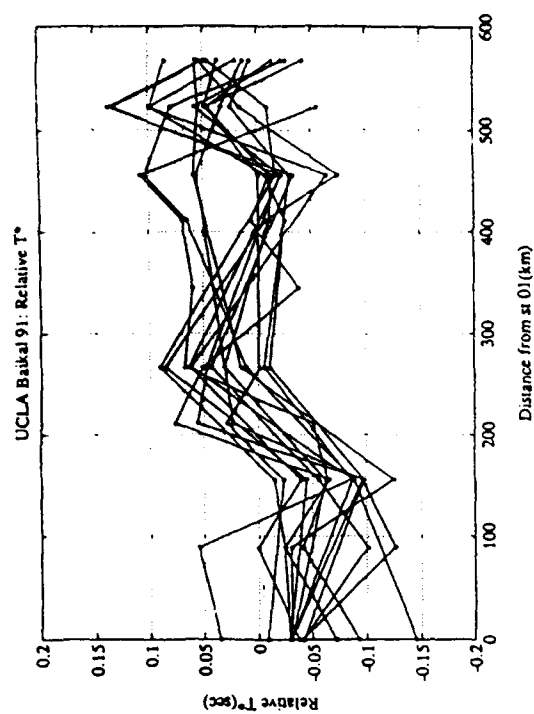


Figure 6. Variation of T^* from west to east across the array

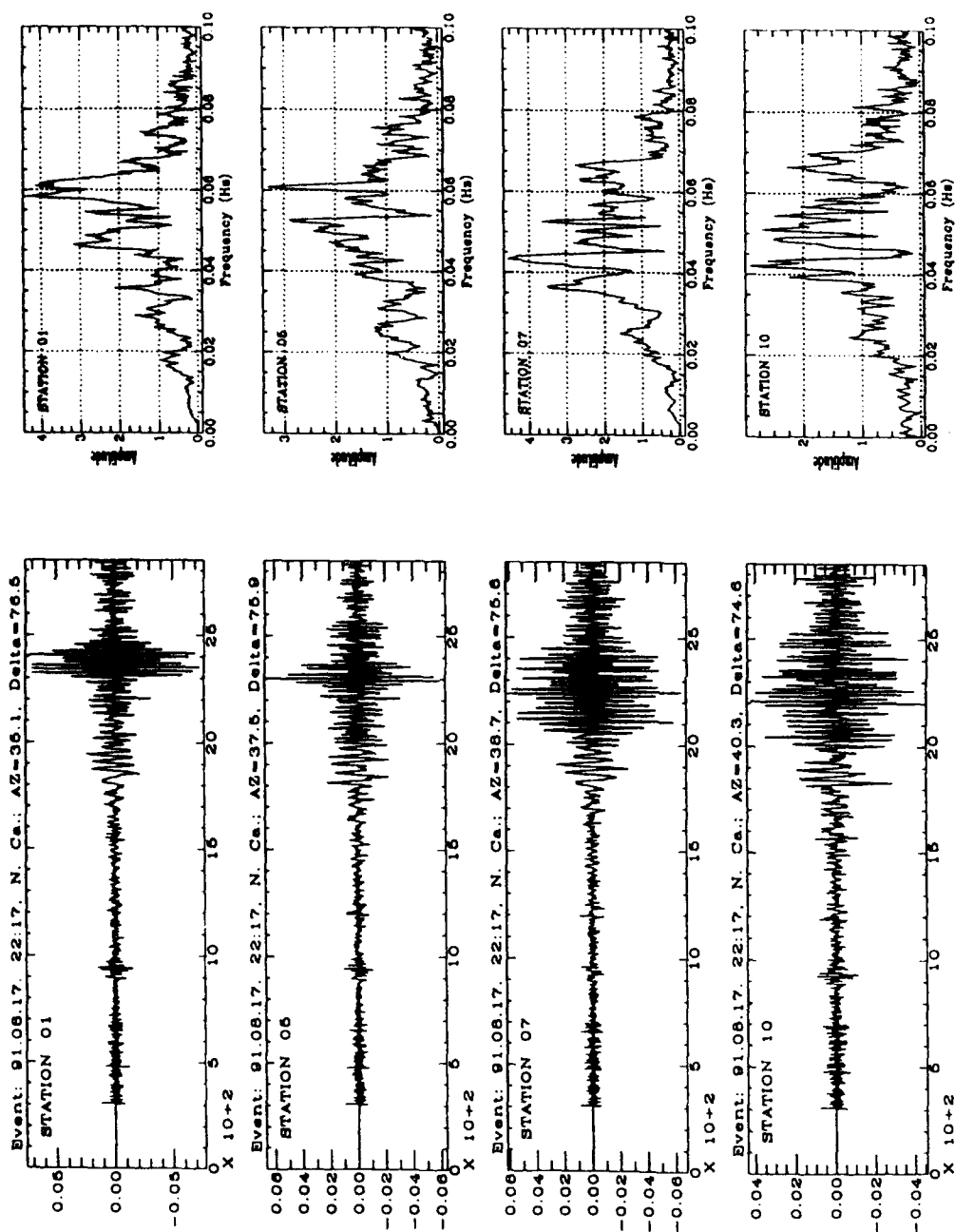


Figure 7a. Broad-band seismograms from Guralp seismometers for a northern California earthquake at stations 1, 5, 7 and 10 located at 0, 270, 410 and 560 km (west to east see Figure 6). 1 and 5 are west of lake Baikal and show strikingly different waveforms from 7 and 10 on the east.

Figure 7b. Spectra of broad-band recordings showing higher frequencies at the western (craton) stations (1 and 5).

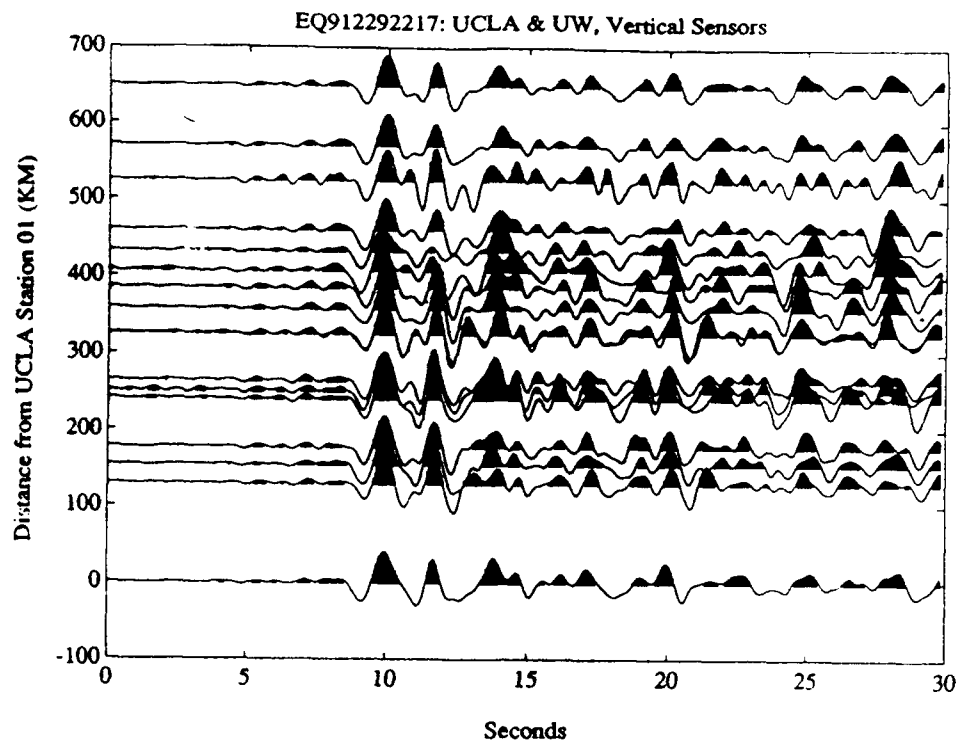


Figure 8a. Seismic section for northern Californian earthquake. Top trace is stacked trace.

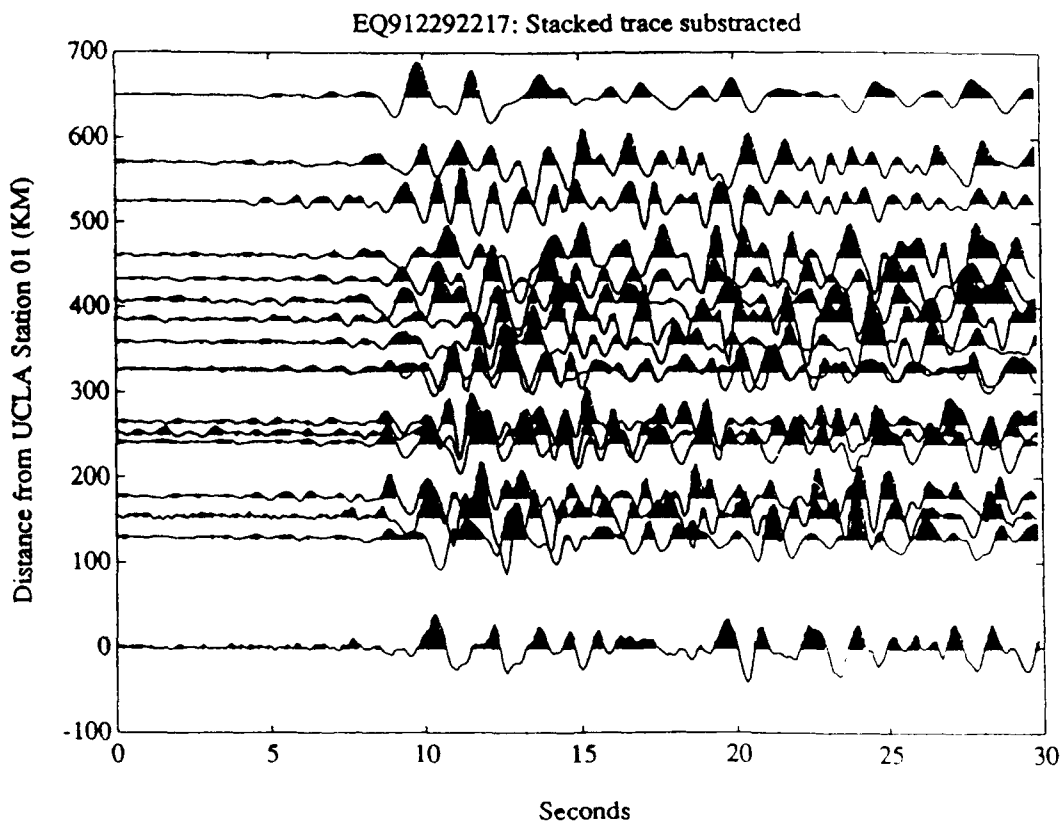


Figure 8b. Differential section for Figure 8a after stacked trace has been removed. Coherent energy between 300 and 450 km at about 13 secs may be due to a coherent scatterer in the upper crust in the east.

Numerical Simulation of Nonlinear Attenuation Using an Endochronic Formulation

Steven M. Day*, J. Bernard Minster†, Lois Yu†

* San Diego State University, San Diego, CA

† Scripps Institution of Oceanography, University of California, San Diego

Contract No. F19628-88-K-0039

OBJECTIVES

Near-source seismic observations of stress wave attenuation, in rock and soil, show evidence of significant nonlinearity. This nonlinear attenuation is also evident in cyclical loading experiments in the laboratory, often emerging at strain amplitudes as low as 10^{-6} , and gives rise to an amplitude dependence of the apparent Q . Moreover, recent quasistatic laboratory testing of rock at low strain has permitted the detailed observation of hysteresis loops giving rise to amplitude-dependent attenuation. These issues have been recently reviewed by *Minster et al.* (1991) and summarized by *Martin and Minster* (1992). Nonlinear wave propagation in rocks and soils has also been observed and modeled in a different context by *Bonner and Wannamaker* (1990, 1991), and by *Johnson et al.* (1987, 1991), and *Johnson and Shankland* (1989). Our objective is to identify and validate a rheological model (constitutive equation) for rocks, valid at moderate strains, that explains satisfactorily these various observations, and is appropriate for incorporation in numerical source and wave propagation codes.

RESEARCH ACCOMPLISHED

A capability for numerical modeling of stress waves in rock, in the strain regime in which the loss mechanism is nonlinear, but the rock remains undamaged, is important for addressing a number of seismological issues. These include the quantification of seismic coupling from underground explosions and the understanding of strong motion from earthquakes. We propose a phenomenological model for nonlinear attenuation based on the endochronic framework developed by *K. Valanis* (e.g. *Valanis and Read*, 1979). This constitutive formulation is characterized by the following features:

- (1) It is inherently rate-independent, and therefore automatically preserves seismic scaling relationships deduced from analysis of underground explosions.
- (2) It automatically ensures hysteresis loops which close, are cusped, and have tangent modulus approximating the elastic modulus at points of strain-path reversal.
- (3) The model generates hysteresis even in the absence of a yield surface.
- (4) The constitutive functional is strain-path dependent, but can be readily converted to a differential form.

The first three properties are consistent with laboratory observations in the strain amplitude range from roughly 10^{-6} to 10^{-3} . The fourth one renders the method suitable for application to numerical simulations of stress wave propagation. In this report, we will compare endochronic model hysteresis loops with data for a granite and a sandstone, kindly made available by Dr. R. Haupt of New England Research. The features of stress-strain curves that we seek to emulate include:

- They are (of course) dissipative

- They become nonlinear at moderate strain levels, and in particular, they become "cusped" instead of elliptical
- No yield surface is evident, at least for strains up to $\sim 10^{-4}$
- The tangent modulus is close to the elastic modulus upon reversal of the strain path.
- Hysteresis loops are closed
- The materials exhibit memory

A class of material models of interest in this context is that of "simple materials", which for present purpose we define in the following terms: Given the strain history $e(t')$ over the time interval $0 \leq t' \leq t$ the stress at time t is given in the form:

$$\sigma(t) = \mathcal{F}[e(t'), 0 \leq t' \leq t] \quad (1)$$

Here \mathcal{F} is a functional, relating the stress $\sigma(t)$ to the strain history. For example: if \mathcal{F} is linear and time invariant, equation (1) reduces to a convolution, and we have the usual formulation of viscoelasticity:

$$\sigma(t) = M(t) \star e(t) \quad (2)$$

Rate-independent simple materials are an important subclass which is conveniently introduced by rewriting (1) as:

$$\sigma(t) = \mathcal{F}[e(\xi), \dot{\xi}, 0 \leq \xi(t') \leq \xi(t)] \quad (3)$$

The concept of "rate-independence" implies that there is no dependence of the rheology on the rate $\dot{\xi}$:

$$\sigma(t) = \mathcal{F}[e(\xi), 0 \leq \xi(t') \leq \xi(t)] \quad (4)$$

where

$$d\xi = (de : g : de)^{1/2} \quad (5)$$

In other words, ξ is the strain path length, measured in terms of the metric g .

K. Valanis proposed a special rheological model, called the *Endochronic Material Model*, by specializing the formulation to the case in which \mathcal{F} is a linear, shift-invariant functional in the plastic strain path length z

$$dz = (d\theta : g : d\theta)^{1/2} \quad (6)$$

where

$$d\theta = de - \frac{d\sigma}{2\mu} \quad (7)$$

is specified to be the plastic strain increment. (μ is the elastic modulus.) The linear, shift-invariant assumption then guarantees that we can write σ as a convolution over z , that is:

$$\sigma(z) = K(z) \star \frac{d\theta}{dz} \quad (8)$$

If the kernel $K(z)$ is chosen to have an integrable singularity at $z = 0$, then all the features noted above are realized:

$$K(z) \sim z^{-\alpha}, \quad 0 < \alpha < 1 \quad (9)$$

This model results in an explicit amplitude dependence of Q^{-1} , which can be derived by noting that

$$\sigma \propto \int_0^{z_m} z^{-\alpha} \frac{d\theta}{dz} dz \quad (10)$$

Restricting the treatment to the simple case of uniaxial loading, we have

$$\left| \frac{d\theta}{dz} \right| = 1 \quad (11)$$

so that, in terms of the maximum plastic strain

$$\sigma \propto z_m^{\alpha+1} \quad (12)$$

From the definition of Q^{-1} in terms of the area of the hysteresis loop, we obtain:

$$\begin{aligned} Q^{-1} &\propto \frac{\sigma_m z_m}{\sigma_m^2} \propto z_m^{-\alpha} \\ Q^{-1} &\propto \sigma_m^{\alpha/(1-\alpha)} \propto \epsilon_m^{\alpha/(1-\alpha)} \end{aligned} \quad (13)$$

Note that for $\alpha = 1/2$, we have an approximately linear dependence on strain amplitude, in agreement with a large body of laboratory observations. The endochronic model appears thus capable of emulating laboratory observations of hysteretic behavior, and of amplitude dependence of attenuation at moderate strain amplitudes.

In order to validate the use of the endochronic model to simulate the rheology of rocks at moderate strains, we have conducted simulations of hysteresis loops measured at several strain amplitudes in uniaxial tests on Sierra White granite and Berea sandstone. These data have been collected by New England Research Inc., and have been kindly made available to us by Drs. R. Martin and R. Haupt.

Figure 1 shows a comparison of such simulations (left hand side) with three observed loops in Sierra White (right hand side), at stress levels of 3, 6, and 12 bars, respectively. The numerical simulations (which are symmetrical in stress and strain histories) match well the overall character of the observations; this includes in particular the increase in attenuation with increasing strain. The extra simulation for a stress amplitude of 40 bars shows how Q^{-1} continues to increase at large strain levels.

Figure 2 shows a similar comparison for Berea sandstone, for which the attenuation levels are much higher, as illustrated by the loop areas. Again, the comparison is quite favorable, including the amplitude dependence of Q , and the non elliptical loop shapes, with apparent cusps at the ends. It should be emphasized that, unlike many nonlinear models, the model used in these simulations depends only on a small number of parameters, once the kernel singularity is specified.

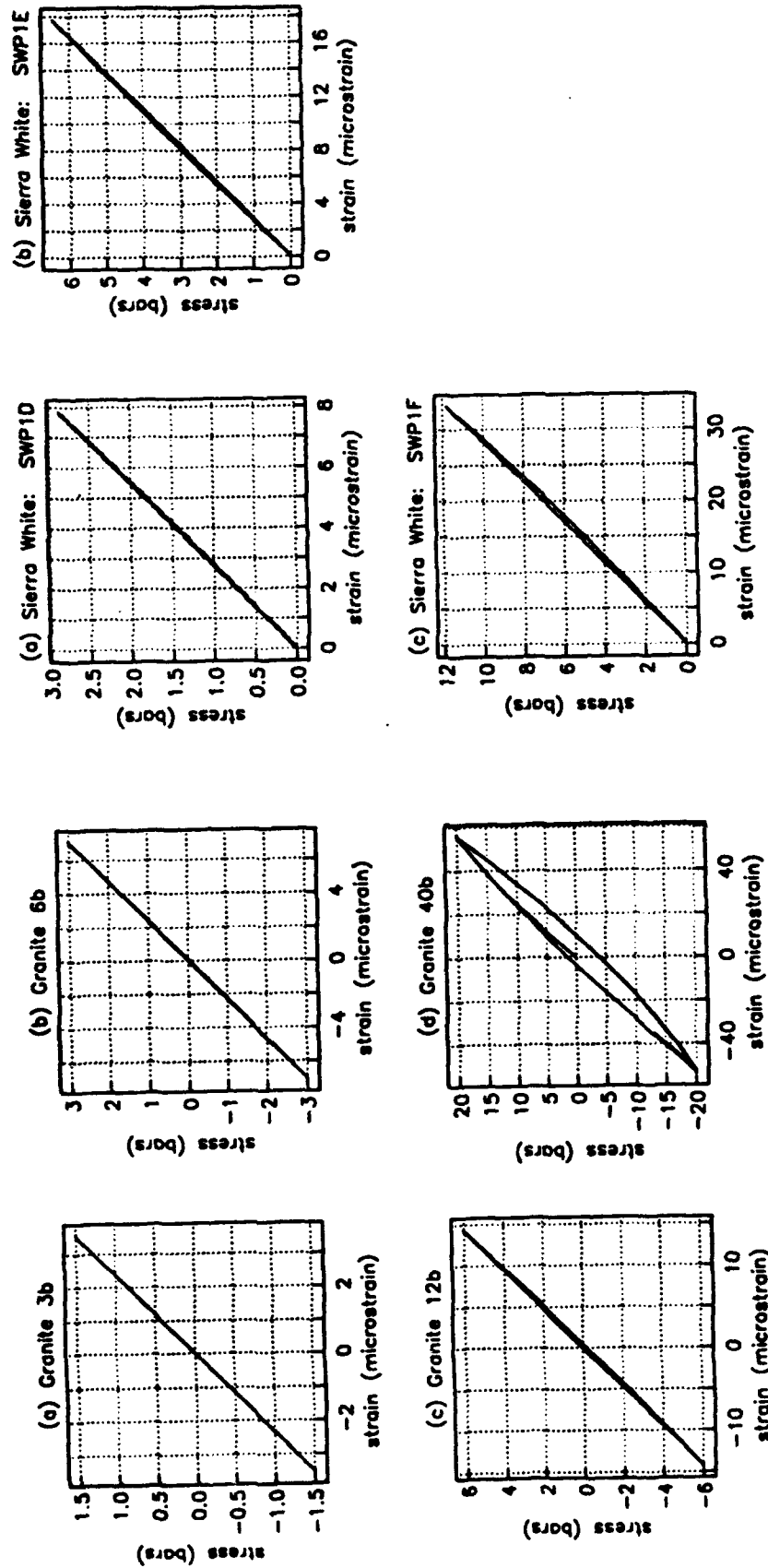


Figure 1: Comparison of numerical simulations of hysteresis loops calculated with an endochronic model for granite (left) and observations collected by NER, Inc. on Sierra White granite (right), for several stress levels.

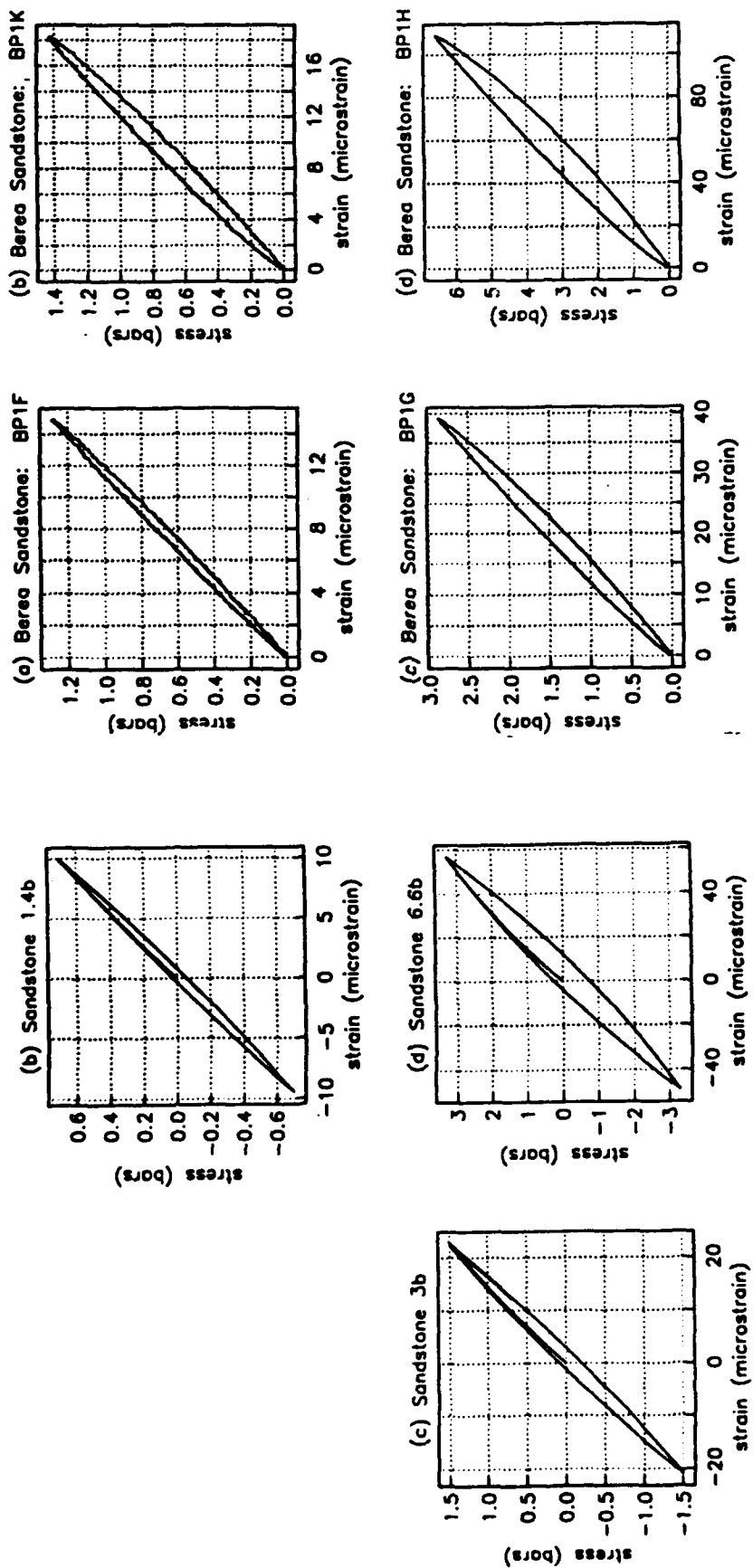


Figure 2: Comparison of numerical simulations of hysteresis loops calculated with an endochronic model for sandstone (left) and observations collected by NER, Inc. on Berea sandstone (right), for several stress levels

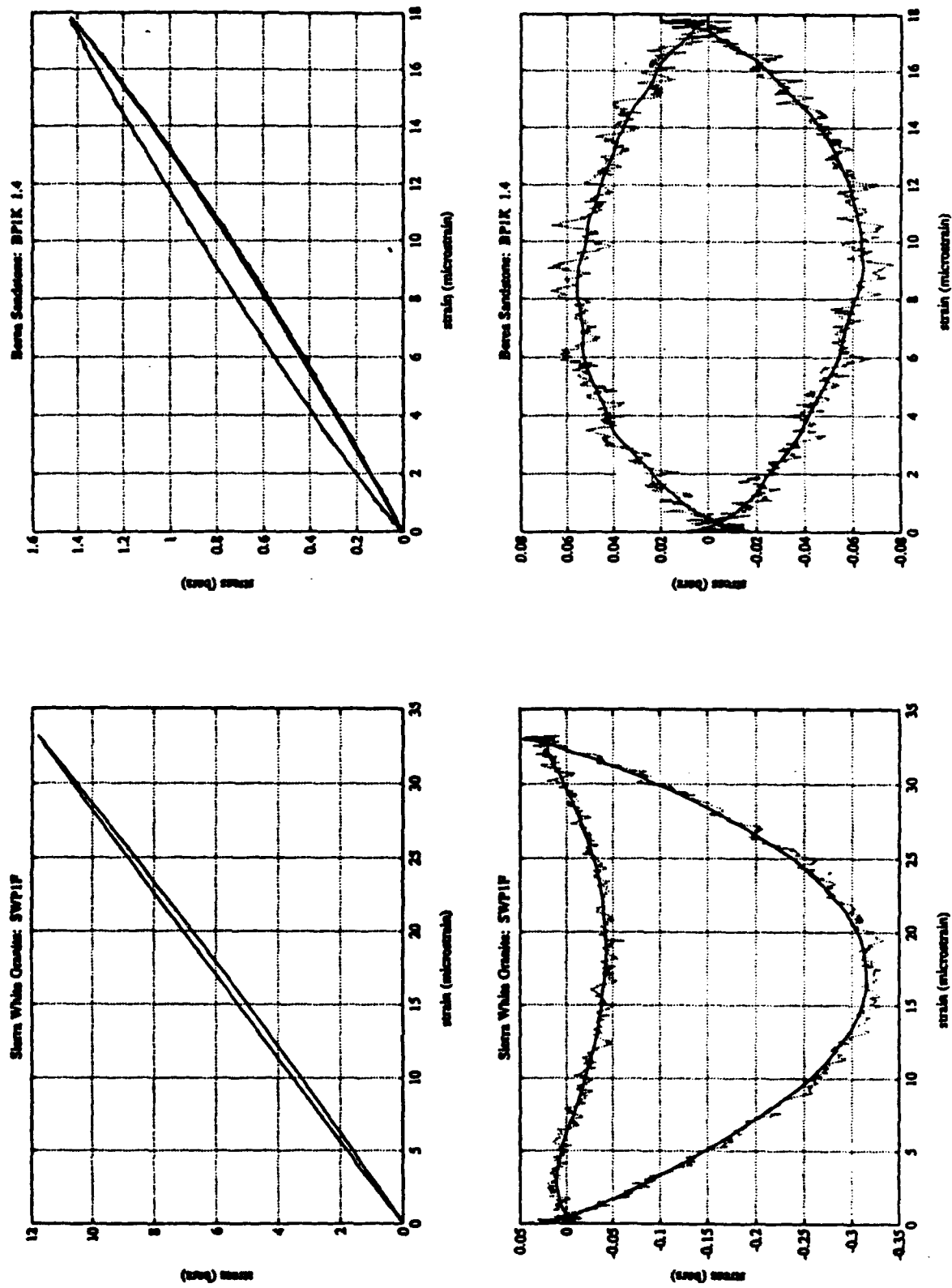


Figure 3: Processing of hysteresis data for Sierra White granite and Berea sandstone, by removing a mean slope, and filtering loading and unloading portions of the loop separately. This method emphasizes the departures from elliptic loops.

CONCLUSIONS AND RECOMMENDATIONS

In order to examine the details of hysteresis loops, and particularly the shapes of the cusps at both ends, we show on Figure 3 selected data for both types of materials, where a mean slope (modulus) is removed. Note that the raw data (dotted lines) are somewhat noisy, and require filtering (solid lines). Because simple low-pass filtering smooths the cusps, we have begun experimenting with a technique to filter separately the loading and unloading portions of the loops. This requires constructing a longer time series out of a half-loop by appropriate symmetries in order to remove the end effects of the filtering operation. The technique appears to give satisfactory results, and in particular, appears to facilitate the estimation of the elastic modulus. If this process can be validated and is successful, it should provide the necessary input for adjusting the parameters of the endochronic model using an inversion approach.

The results illustrate clearly the non-elliptical (nonlinear) character of the hysteresis loops at such moderate strain levels, and brings out clearly the strain hardening in granite. A successful rheological model should be capable of matching such features, which are often difficult to see in the raw data. But it should, as much as possible, avoid introducing a large number of additional model parameters for this purpose. We hope that our simulations will reach that level of success before we consider wave propagation problems.

REFERENCES

- Bonner, B.P., and B.J. Wannamaker, Nonlinear acoustic effects in rocks and soils, *Rev. Prog. in Quant. Nondestructive Eval.* **9**, 1709, 1990.
- Bonner, B.P., and B.J. Wannamaker, Acoustic nonlinearities produced by a single macroscopic fracture in granite, *Rev. Prog. in Quant. Nondestructive Eval.* **10B**, 1861, 1991.
- Johnson P.A. and T.J. Shankland, Nonlinear generation of elastic waves in granite and sandstone: Continuous wave and travel time observations, *J. Geophys. Res.*, **94**, 17,729, 1989.
- Johnson P.A., T.J. Shankland, R.J. O'Connell and J.N. Albright, Nonlinear generation of elastic waves in crystalline rock, *J. Geophys. Res.* **92**, 3597, 1987.
- Johnson P.A., A. Migliori and T.J. Shankland, Continuous wave phase detection for probing nonlinear elastic wave interactions in rocks, *J. Acoust. Soc. Amer.*, **89**, 598, 1991.
- Martin R.J., and J.B. Minster, *Rheology of rocks at moderate strains with application to attenuation and source characterization*, NER conference report, Jan. 8, 1992.
- Minster, J.B., S.M. Day, S., and P.M. Shearer, The transition to the elastic regime in the vicinity of an underground explosion, *AGU monograph XX* (Proceedings of the 1989 DOE workshop on explosion seismic sources.), 229-238, 1991.
- Valanis K.C., and H.E. Read, A new endochronic plasticity theory for soils, S-Cubed Rept. SSS-R-80-4294, 1979.

APPLICATIONS OF ARRAY SPECTRAL FACTORIZATION METHODS TO REGIONAL SEISMIC DISCRIMINATION AND THREE-COMPONENT PROCESSING

Zoltan A. Der, Michael R. Hirano, Douglas R. Baumgardt (ENSCO, Inc.),
and Robert H. Shumway (University of California at Davis)

OBJECTIVES

The objective of the research presented is to utilize detailed waveform information contained in regional arrivals recorded at seismic arrays for discrimination and fine location of closely spaced events. The technique of decomposition of three-component regional signals into source spectral factors and empirical intersensor transfer function factors enables one to identify and label regional arrivals automatically despite the three-dimensional complexities of particle motion not describable by analytical models.

RESEARCH ACCOMPLISHED

Theoretical Background

We can consider a suite of seismograms recorded at an array as a result of two kinds of processes:

- a) Filtering the source inputs for each component of a moment tensor with filters corresponding to the Green's functions.
- b) Filtering the (random) Green's functions with the six independent source time function components of the moment tensor.

It is advantageous to look at the problem using the second interpretation since the Green's functions are extremely variable and we shall probably never know them adequately to model waveforms in detail. We know, however, that they tend to remain similar for multiple events along closely situated paths. Any information we gain from the seismograms should depend only on the existence of linear transfer function relationships, i.e., coherence relationships, among the various suites of seismograms (e.g., Bendat and Piersol, 1966; Kaveh and Wang, 1991). In order to see how this concept can lead to something useful, we must consider some known facts and special situations. Various scenarios lead to different types of measurable interrelationships among seismograms recorded at various sensors for various events.

For instance, for collocated events with identical source mechanisms but different source time functions the site functions will be identical for all the events, since the modal makeup of the wave types for a given regional phase for collocated events with the same mechanism and depth are expected to be the same. The two sets of seismogram outputs will then be pairwise coherent, since it will be possible to transform one into the other (at all sensors) with a digital filter. The coherence is defined as

$$\gamma_{ij}(\omega) = \frac{|P_{ij}(\omega)|}{\sqrt{P_{ii}(\omega) P_{jj}(\omega)}} \quad (1)$$

between two events i and j , in the case of low background noise. Note that high coherence does not necessarily imply strong waveform similarity. On the contrary, the waveforms may still have a low or even zero correlation coefficient. In this respect, our methods differ fundamentally from analyses utilizing time domain correlation matrices (Jurkevics, 1988; Riviere-Barbier and Grant, 1992).

Central to our ideas is the estimation procedure for the power spectral components, P_{ij} . These are computed by some smoothing procedure, such as smoothing and averaging the dot products of the signal Fourier transforms denoted as vectors f , such that

$$P_{ij}(\omega) = \sum_s \overline{f_i(\omega)} f_j^*(\omega) \quad (2)$$

where the overbar denotes spectral smoothing, the star denotes complex conjugation, and the summing of smoothed products is performed over sensors. In our case, we use the combination of spectral smoothing and averaging over array sites. The equivalent time-bandwidth product (TBWP) of the result can be computed by multiplying together the spectral averaging bandwidth B , the total time length of the data used for each array site T , and the number of array sites N .

In the case of collocated events with different source mechanisms, multiple coherence groups with lesser number of events than the six moment sensor components may attain relatively high values that are significantly different from zero. Multiple coherences are defined as (Bendat and Piersol, 1966)

$$\gamma_{i,x}^2 = 1 - [P_{ii}(\omega) P^{ii}(\omega)]^{-1} \quad (3)$$

where the subscripted and superscripted $P(\omega)$ are the i -th diagonal elements of the interevent spectral matrix and its inverse, respectively. Multiple coherences give the proportion of power predictable in the i -th input from the rest of the inputs x . When the number of inputs exceeds the number of independent Green's functions making up the data and the background noise can be neglected, then the $\gamma_{i,x}$ must be close to unity, and additional events near the same location will also have high values of multiple coherence. Thus, no matter how complex the source mechanisms may be, it will be possible to "calibrate" parts of a quarry with a small number of events and the high multiple coherences or the ability to span multiple events with some master events (Der et al, 1990; 1991; Harris, 1991) will identify all subsequent events which are roughly at the same depth and location within that quarry. The advantage of applying simple linear system analysis methods is that one does not need to know the Green's functions or the moment tensor time functions either. We simply test the multi-sensor data, treated as independent realizations of the same process, for the existence of interevent linear transfer function relationships of the various types described above.

DATA ANALYSES

Multiple Coherence Analyses of Regional Events

These analyses were performed to detect spatial groupings of events with possible differences in source mechanisms which cannot be detected by simple-minded waveform or waveform envelope correlation methods.

Analyses of Titania Explosions Recorded at NORESS

It has been postulated above that low multiple coherences are less prone to be caused by differences in source mechanisms than by decorrelation of the Green's functions by large event spacings, while low pairwise coherences can be caused equally by both. The reason is that the frequency domain Green's functions appropriate to the various moment tensor components will comprise a complex vector space into which all frequency domain seismograms corresponding to various source mechanisms and source time functions lie, i.e., the vector space spans all possible seismograms originating from sources at the same physical location. An additional necessary refinement we have added is to estimate the maximum attainable coherence by considering the background noise.

Computing multiple coherences among groups of events should enable one to rank them hierarchically with respect to relative spacing and mechanisms. We have found that there is a well defined grouping among events, some have high multiple coherences relative to the others in the group of events while others do not. The relative ranking is the same regardless of the particular regional phases analyzed. We have found the same rankings for P_n , S_n , and L_g analyzed independently and high coherence values tended to remain high over wide frequency ranges. In Figure 1, we have consistently low multiple coherences for all phases of the Titania Event 860452, while in Figure 2 we have consistently high coherences for Titania Event 86045 relative to the whole Titania group of eight events analyzed. *This indicates clearly that we are not dealing with accidental correlations but rather with inherent internal consistencies (multichannel linear filter relationships) in the fine details of waveforms that behave consistently for all phases.* The events can thus be ranked with respect to coherence relative to the group (Der et al, 1990).

Investigation of Clustering in Kola Peninsula Events Recorded at ARCESS

We have performed similar analyses on Kola Peninsula events recorded at the ARCESS array from the HD8 and HD9 mines. The events located at the same mine are all coherent but there is a variability in the falloff of coherences with frequency (Figure 3). Again, it was found that the multiple coherence patterns were similar regardless which phase, P_n , S_n , or L_g , was analyzed. Given the gradual decorrelation of Green's function with interevent distance (Harris, 1990), this may be the manifestation of differences in the mutual distances of the events, since we expect that the waveform similarity will decrease with distance at high frequencies. Regional waveforms tend to decorrelate significantly within a few km displacement in sensors or sources but not as fast as the "quarter wavelength" argument would suggest.

Three-Component Processing Results

Most approaches to three-component processing are based on simplistic models of particle motion derived from either elastic halfspace or flat layered crustal models. The properties of real signals do not agree with such models. For instance, significant transverse motion is present in most P waves, the P motion is not linear but has complex three-dimensional orbits (Menke and Lerner-Lam, 1992; Jepsen and Kennett, 1990; Kennett, 1991). Indeed, it is often difficult to recognize P and S waves based on the "rectilinearity" or "ellipticity" criteria (Kvaerna and Ringdal, 1992).

In our work we only assume that complex frequency dependent multichannel transfer function relationships exist between the three components that remain the same for the same source region and are characteristically different for each regional arrival. We have assembled ARCESS three-component data for nine high S/N Kola Peninsula events at the HD9 mine for testing this idea. We have computed an event-compounded (instead of sensor-compounded as in Equations 1 and 2) 3×3 spectral matrix for the three sensors. From this, we computed a single set of two-channel filters for predicting the vertical component from the two horizontals as

$$\begin{bmatrix} f_e(\omega) \\ f_n(\omega) \end{bmatrix} = \begin{bmatrix} S_{ee} & S_{en} \\ S_{ne} & S_{nn} \end{bmatrix}^{-1} \begin{bmatrix} S_{ez} \\ S_{nz} \end{bmatrix} \quad (4)$$

where the $f_i(\omega)$ are the filters and the $S_{ij}(\omega)$ are the elements of the event-compounded intersensor spectral matrix. Figure 4 shows that this was done successfully at the ARA0 site of ARCESS even though the motion is distinctly non-linear as evidenced by the differences between the east (approximately radial) and vertical components and the often observed transverse trace excursions on the horizontal for the same events. Many transient features unique to the vertical components are faithfully reproduced on the predicted vertical

components even though these are not apparent on the horizontals. Although we have applied only a single set of two-channel filters, the performance in reproducing the vertical component from the two horizontals is uniformly good for all nine events. When compared to the actual verticals, there is some numerical noise added by the process in the predictions. At this stage of the work, no attempt was made to optimize the process with respect to background noise although this can be easily done. The verification of our multichannel transfer function idea for groups of nearly collocated events opens the way for designing automatic phase recognition algorithms for regional seismograms. Using the prestored multichannel filters they will identify a phase, (P_n , P_g , S_n , or L_g) by successfully predicting one component from the two others and the intercomponent prediction will be successful only for the appropriate phase.

CONCLUSIONS AND RECOMMENDATIONS

Our work indicated that linear system analysis methods can be successfully used for diagnosing various scenarios involving closely spaced events. These include groupings with respect to relative source location and detecting differences in mechanism. The interevent distances involved are commonly smaller than one could detect by standard location analysis. Although many facts about the events analyzed are not known, complementary work by Harris (1991) confirms the validity of the ideas proposed here. Transfer function-based three-component analysis can be used for automatizing the recognition of regional phases arriving from limited source regions. The peculiarities of particle motion can be used as unique signatures to recognize various regional arrivals. Based on various observables, such as spectral modulation patterns, pairwise and multiple coherence measurements, and transfer function relationships, numerous rules can be derived for obtaining information regarding the circumstances of industrial blasting and possible evasion. These rules could be included into various monitoring systems including seismic arrays and single three-component stations.

REFERENCES

- Bendat, J.S. and A.G. Piersol (1966). *Measurement and Analysis of Random Data*, John Wiley & Sons.
- Der, Z.A., M.R. Hirano, and R.H. Shumway (1990). Coherent processing of regional signals at small seismic arrays, *Bull. Seism. Soc. Am.*, **80**, 2161-2176.
- Der, Z.A., M.R. Hirano, K.A. Ziegler, and R.H. Shumway (1991). Broad-band studies of seismic sources at regional and teleseismic distances using advanced time series analysis methods, PL-TR-91-2059 (I), ENSCO, Inc. ADA239201
- Harris, D.B. (1991). A waveform correlation method for identifying quarry explosions, *Bull. Seism. Soc. Am.*, **81**, 2395-2418.
- Jepsen, D.C. and B.L.N. Kennett (1990). Three-component analysis of seismograms, *Bull. Seism. Soc. Am.*, **80B**, 2032-2052.
- Jurkevics, A. (1988). Polarization analysis of three-component array data, *Bull. Seism. Soc. Am.*, **78**, 1725-1743.
- Kaveh, M. and H. Wang (1991). Threshold properties of narrow-band signal subspace array processing methods, in "Advances in Spectrum Analysis and Array Processing," S. Haykin Editor, Prentice Hall.

Kennett, B.L.N. (1991). The removal of free-surface interactions from three-component seismograms, *Geophys. J. Int.*, **104**, 163.

Kvaerna, T. and F. Ringdal (1992). Integrated array and three-component processing using a seismic microarray, *Bull. Seism. Soc. Am.*, **82**, 870-882.

Menke, W. and A. Lerner-Lam (1991). Observations of the transition from linear polarization to complex polarization in short-period compressional waves, *Bull. Seism. Soc. Am.*, **81**, 611-621.

Riviere-Barbier, F. and L.T. Grant (1992). Cluster analysis of closely spaced mining blasts as a method of location, PL-TR-92-2006, *Science Applications Intl. Corp.*, Arlington, VA. ADA248935

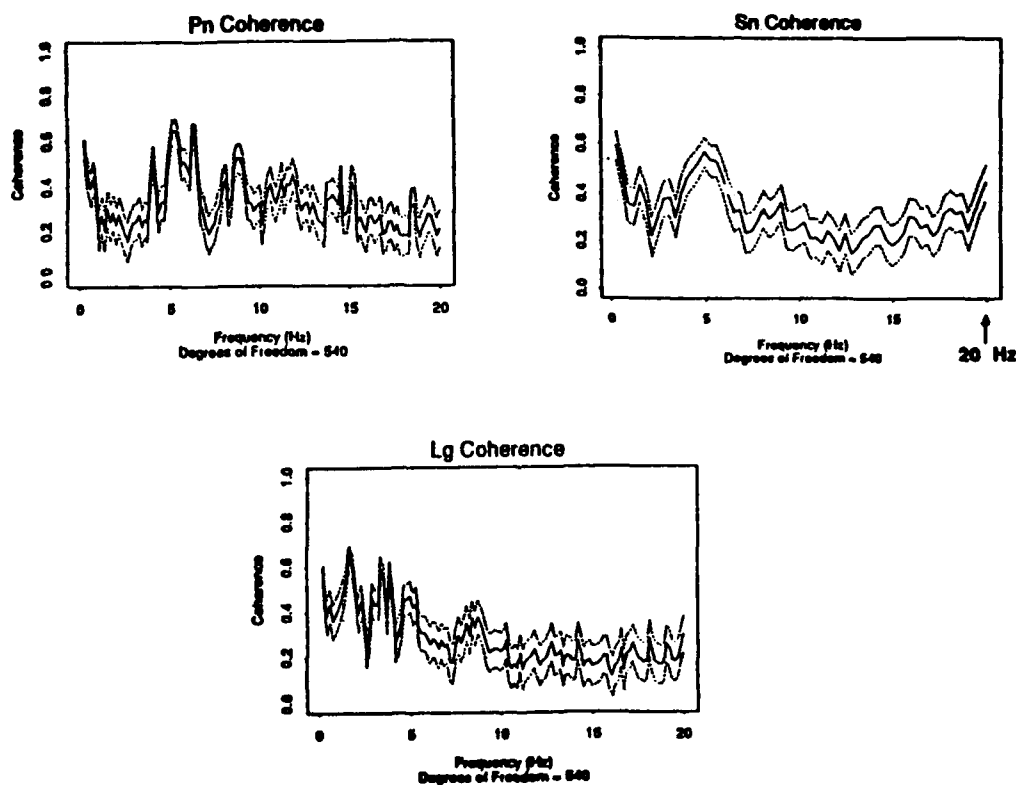


FIGURE 1: Representative plots of high multiple coherences for Event 860452 from the group of Titania mine events recorded at NORESS. Note that these coherences are low regardless of which phase (*Pn*, *Sn*, or *Lg*) was analyzed independently. The expected coherences based on the observed *S/N* ratios should have been high for this event. Since time shifts do not affect coherences, these results indicate the lack of multichannel transformability in the respective groups of waveforms.

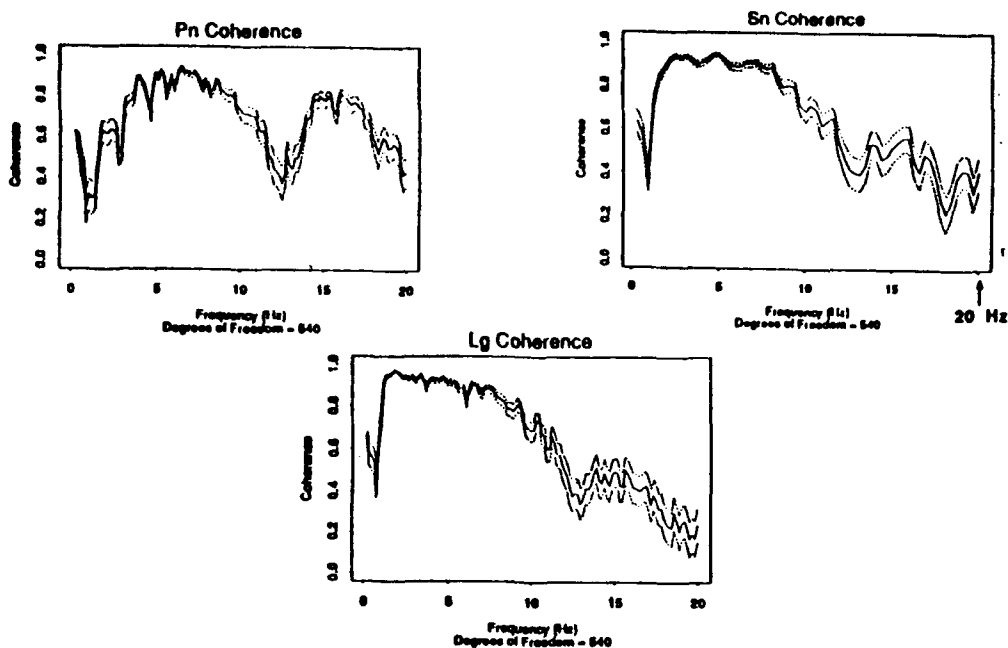


FIGURE 2: Representative plots of high multiple coherences for Event 86045 from the group of Titania mine events recorded at NORESS. Note that these coherences are high regardless of which phase (*Pn*, *Sn*, or *Lg*) was analyzed (independently). Since time shifts do not affect coherences, these results measure the multichannel transformability in waveforms only.

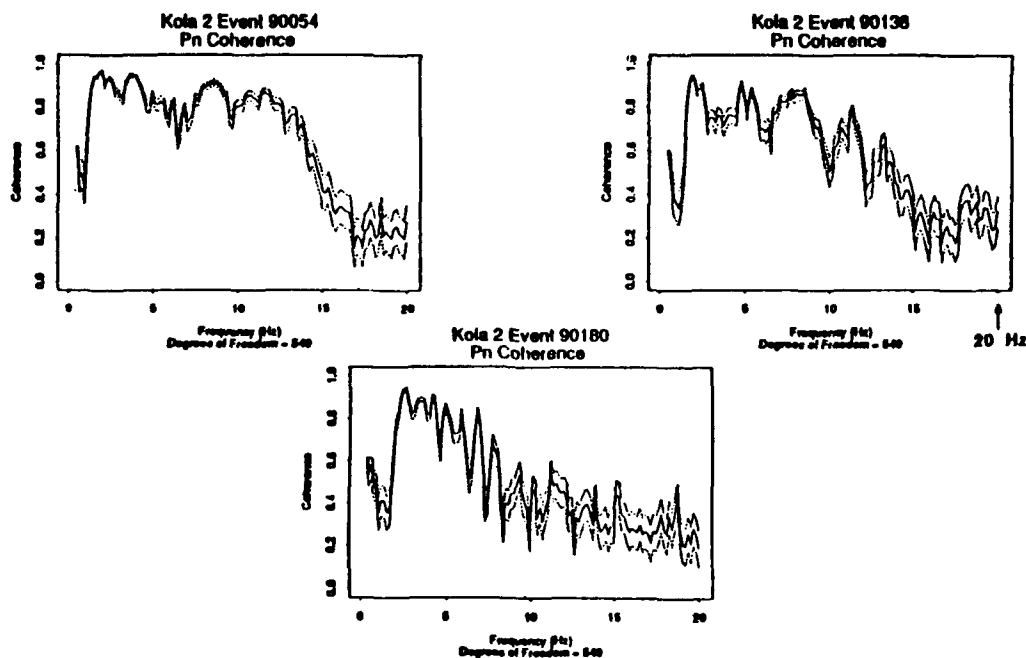
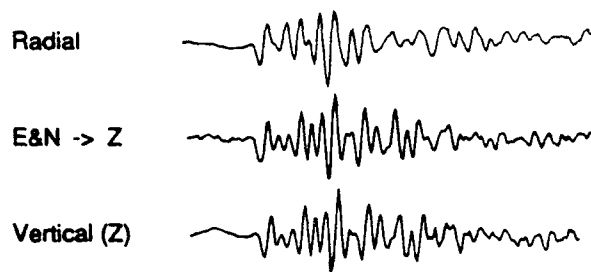
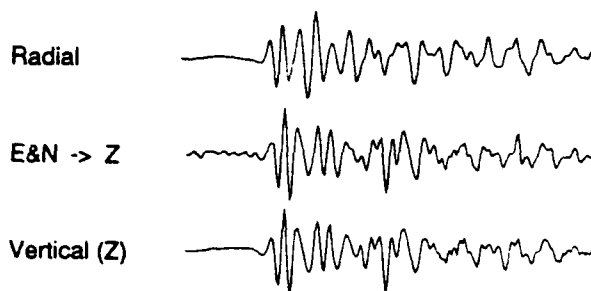


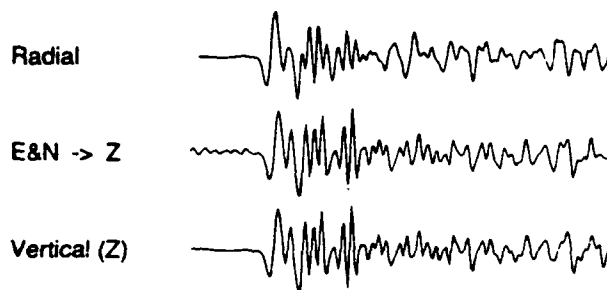
FIGURE 3: Plots of multiple coherences for *Pn* phases from several events from the group of Kola mine events recorded at ARCESS. Note that the high frequency falloff rates of these coherences vary considerably within the group even though the expected coherences (not shown) should be high throughout. This may be a result of decorrelation at high frequencies with increasing spacing of the events. Such interpretations need independent verification.



Event 1990219



Event 1990147



1.3 SEC

Event 1990054

FIGURE 4: Three-component processing results at ARCESS for P_n phases from HD9 mine blasts on the Kola Peninsula. The results are shown for only three events but the rest of the data fit just as well. Two-channel filters designed from nine blasts are used to derive the vertical component motion from the two horizontals. The derived traces (in the middle) closely resemble the actual vertical traces (lowermost traces). The inverted east components which are closest to the radial in orientation (top traces) are different indicating that the particle motion is not linear. Thus, spectral factoring extracting intersensor transfer functions can be used to characterize complex, three-dimensional particle motion and use this information for automatic phase recognition.

A Network-Accessible Geological and Geophysical Database for Eurasia

Eric J. Fielding, Bryan L. Isacks, and Muawia Barazangi

Institute for the Study of the Continents (INSTOC)
Cornell University, Ithaca, NY 14853
E-mail: "eric@geology.cornell.edu" -or- "fielding@seismo.css.gov"

Contract #F29601-91-K-DB08

OBJECTIVE

The topography and lateral variations in crustal structure along seismic propagation paths and at the source and receiver sites are crucial information to understand the excitation and propagation of regional seismic phases and other aspects of the problems of detection, verification, and estimation of the yield of nuclear explosions. Our objective is to collect and organize available topographical, remote-sensing, geological, and geophysical datasets for Eurasia into a digital information system that can be accessed by display programs running at the Center for Seismic Studies (CSS) and by other DARPA researchers. We plan to expand the area of data coverage to include China, the Middle East and North Africa. We store the data in an information system (GIS) with a network-accessible server to which can connect X Window System client modules of future versions of the Intelligent Monitoring System (IMS) running at CSS and other DARPA researchers. The information system is organized to extract and usefully display the information most relevant to verification and yield estimation. The work includes assembly of available digital datasets such as topography, satellite imagery, and crustal reflection and refraction profiles and digitization of available geological and geophysical map information on sedimentary basins and crustal thicknesses and other details of crustal structure.

RESEARCH ACCOMPLISHED

Work in progress has now realized useful datasets for Eurasia, including a set of crustal seismic structure maps, at a scale of approximately 1:15,000,000. These include maps of crustal thicknesses (depth to Moho) and sedimentary basin depths (depth to seismic basement). We have created regularly spaced grids of the crustal and sediment thickness values from these preliminary maps that can be used to create profiles of crustal structure. These profiles can be compared by an analyst or an automatic program with the crustal seismic phases received along the propagation path to better understand and predict the path effects on phase amplitudes, a key to estimating magnitudes and yields. The gridded data could also be used to model propagation of crustal phases in three dimensions. We are utilizing the rapidly accelerating Internet (formerly ARPAnet) network to share datasets with CSS and other DARPA researchers. We have begun development of a "server" system at Cornell to allow "client" modules of the IMS to directly connect to databases that we are generating and improving. This would allow IMS users to utilize data as soon as it is available. We have completed a preliminary version of a network "raster server" program that allows "client" programs to access our topography

datasets over the Internet. We have collaborated with DARPA Researcher Bill Menke at Lamont to design a raster addition to the Lamont "view-server" protocol (Menke and others, 1991), and our server is compatible with the new protocol. We encourage DARPA researchers to contact us about gaining access to our databases at the computer mail addresses listed on the first page of this paper.

We continue to expand our database of digital topography for Eurasia. We have processed and analyzed a large volume, more than four gigabytes (GB), of high-resolution Digital Terrain Elevation Data (DTED—Level 1) that we received through our first contract for a large area of Central Asia. We are now processing a larger DTED volume for the Middle East and North Africa that we received a few weeks ago, and we hope to soon receive the DTED that we requested for Europe and western Asia (Figure 1). The basic processing of the raw DTED into an accessible format included the creation of mosaics of the full resolution data for each 5° by 5° block, a file of manageable size for manipulation on a workstation and storage on optical media.

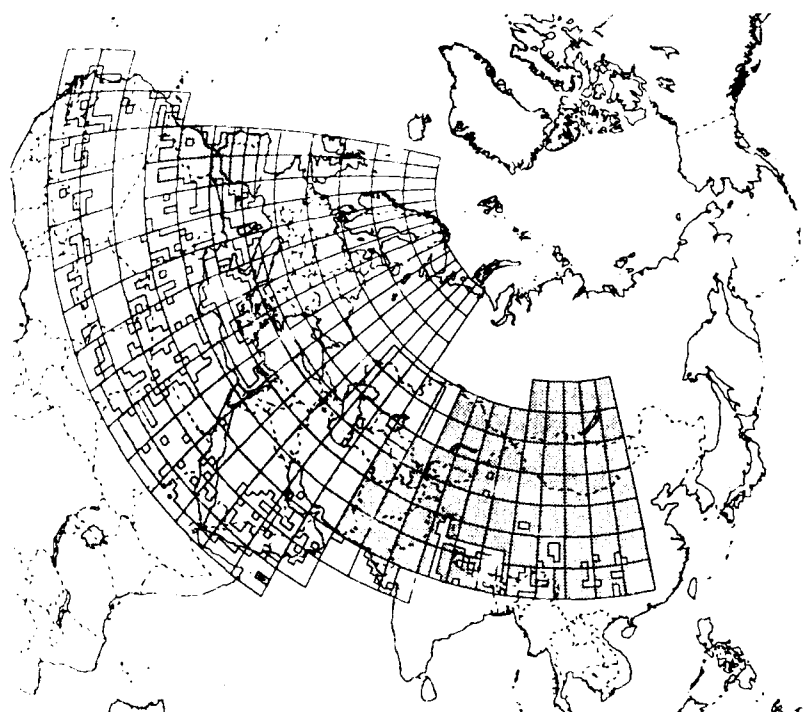


Figure 1: Map of Eurasia, the Middle East and North Africa showing area covered by our present databases of digital topography. Coastlines of oceans, seas, and major lakes are *solid lines* and country borders are *dashed lines*. Acquired and processed DTED cells are *filled light gray* and outlined with a *black line*. Missing and "unavailable" cells are *irregular white holes*. Blocks 5° by 5° of acquired and requested DTED are outlined with *dark gray lines*. Map is an azimuthal equidistant projection centered in north central Eurasia.

All of our topography, including both the reduced resolution mosaics and the full resolution topography blocks, and other archived datasets, such as the digitized geological and geophysical datasets shown in Figures 2 and 3, are being

stored in our recently acquired Epoch-1. The network-based Epoch file server includes an optical disk jukebox system with a library unit that contains 60 GB of "semi-online" storage and unlimited off-line storage of rewritable optical cartridges. The Epoch-1 provides unattended access, usually within less than a minute to any of the disks in the library unit. Our server program is able to load any part of the dataset in a short time.

In addition to the mean elevations, maximum and minimum elevations have also been calculated from the full resolution data for different sized moving windows. The calculations maintain the full range (maximums and minimums) of

values in the original data but result in a more manageable dataset that can be easily stored on-line and manipulated for the whole area of coverage, e.g., to generate topographic profiles along great-circle paths (Figures 4 and 5). These derived datasets can be used for the interpretation of surface roughness on a variety of scales for comparison to the propagation paths of L_g and other regional phases.

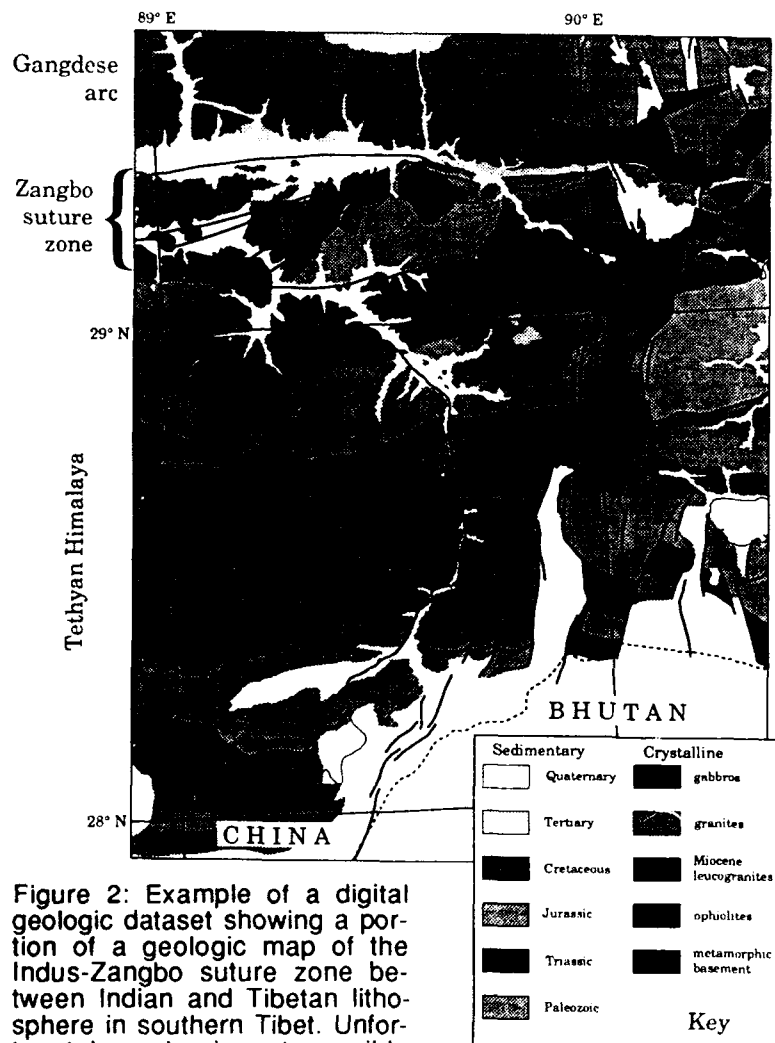


Figure 2: Example of a digital geologic dataset showing a portion of a geologic map of the Indus-Zangbo suture zone between Indian and Tibetan lithosphere in southern Tibet. Unfortunately, color is not possible here to fully portray units. Digitized from J. P. Burg's map of southern Tibet (1977). See box on Figure 4 for location.

We have begun to digitize available geophysical, geologic and tectonic maps for Eurasia. The polygons that enclose geologic units are not straightforward to digitize, so considerable effort has gone into defining a methodology for doing the work. An example of a digitized geologic map is shown in Figure 2. The Arc/Info GIS provides a powerful "toolbox" for selecting and combining the various types of data and overlaying them on top of raster imagery. One can easily select features, such as geologic polygons, by their assigned attributes, such as rock type or age.

This geologic map (Figure 2 shows only a portion of the full map) covers one of the major crustal boundaries of Central Asia, the Indus-Zangbo suture zone between the Indian and Tibetan plates in southern Tibet. This is a relatively detailed geologic map, published by J. P. Burg in 1977, that we can combine with

the digital topography that we have for the area. We digitized both the geologic units and faults from the 1:500,000 scale map. Polygons are assigned a code value within Arc/Info via their labels that encodes information on the interpreted age and type of rock for the unit. The faults similarly have attributes indicating the fault type (e.g., normal) and interpreted age (e.g., Neogene). These attributes allow one to select rock geologic units or faults of a certain age and then color or otherwise mark the different units on a workstation display or on a hardcopy map. The portion of

the map shown in Figure 2 covers the area of the seismic reflection and refraction experiments running this summer in southern Tibet.

We started our digitization of lithospheric structure with a set of crustal seismic structure maps of Eurasia, at a scale of approximately 1:15,000,000. These include maps of crustal thicknesses (depth to Moho) and sedimentary basin depths (depth to seismic basement), both prepared by Professor Kunin's group at the Institute for Physics of the Earth in Moscow from a large amount of Deep Seismic Sounding (DSS) profiles and other data and published in 1987. Using the attributes capability of the Arc/Info GIS, we recorded which contours are dashed (inferred or interpolated) and which are solid. Arc/Info was used to edit the resulting databases and project the unusual projection data into latitude-longitude coordinates. We then created regularly spaced grids of the crustal and sediment thickness values from these preliminary maps. An example of a portion of the gridded dataset of depths to "seismic basement" is shown in Figure 3.

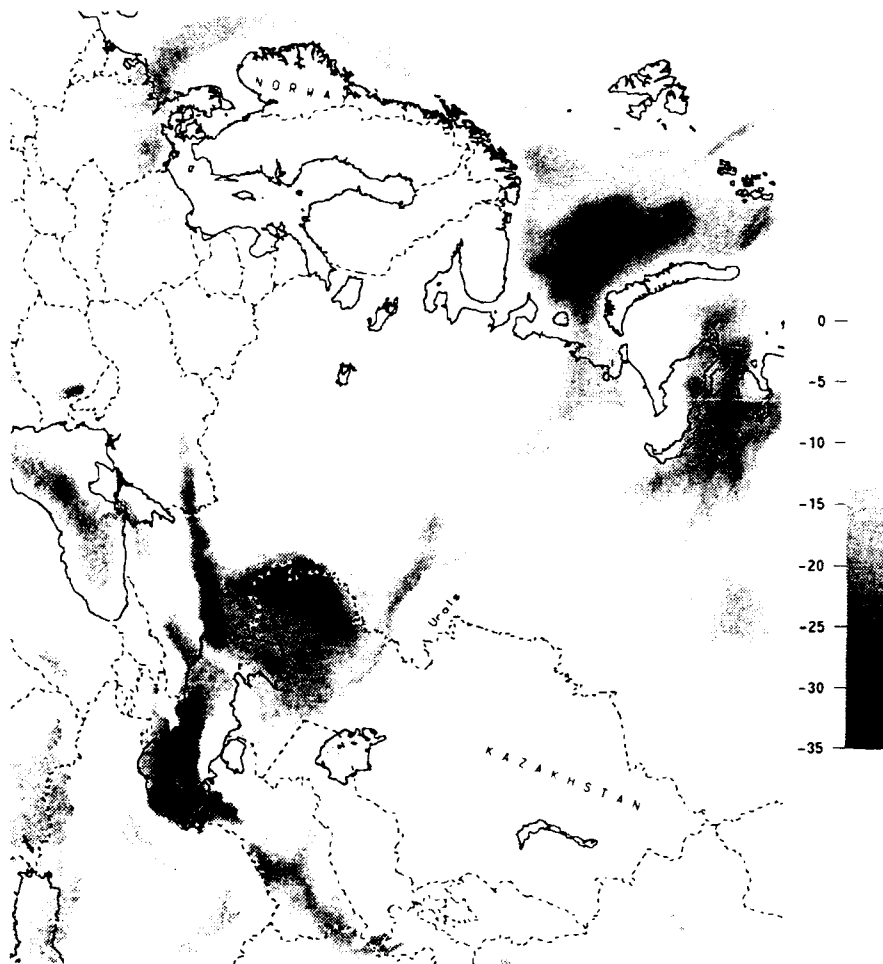


Figure 3: Map of a portion of the gridded database of depth to "seismic basement" showing eastern Europe, northern Middle East and west central Asia. Dataset was digitized for all of Eurasia, the Middle East and North Africa from a map by IPE, Moscow. *White areas* are areas of basement at the surface on the map. *Gray scale* shows depth in km. This gridded dataset, along with similar dataset of depth to Moho can be used for three-dimensional modeling of crustal phase propagation. *Solid black lines* mark coastlines and major lakes. *Dashed lines* mark country boundaries and former USSR republic borders. Map projection is the same as in Figure 1.

The two crustal structure datasets were combined with our topographic dataset to produce Figure 4 which shows the crustal structure along a

great circle path from station NIL in Pakistan and the Chinese nuclear test site at Lop Nor. Figure 5 shows a similar crustal structure profile along the great circle path from the NORSAR array in Norway to the Matochkin Shar test site on Novaya Zemlya. This type of profile of crustal structure can be compared by an analyst or an automatic program with the crustal seismic phases received along the propagation

path to better understand and predict the path effects on phase amplitudes, a key to estimating magnitudes and yields. These profiles could also be used for two-dimensional modeling of crustal phase propagation, so we will gladly make them available to other DARPA researchers.

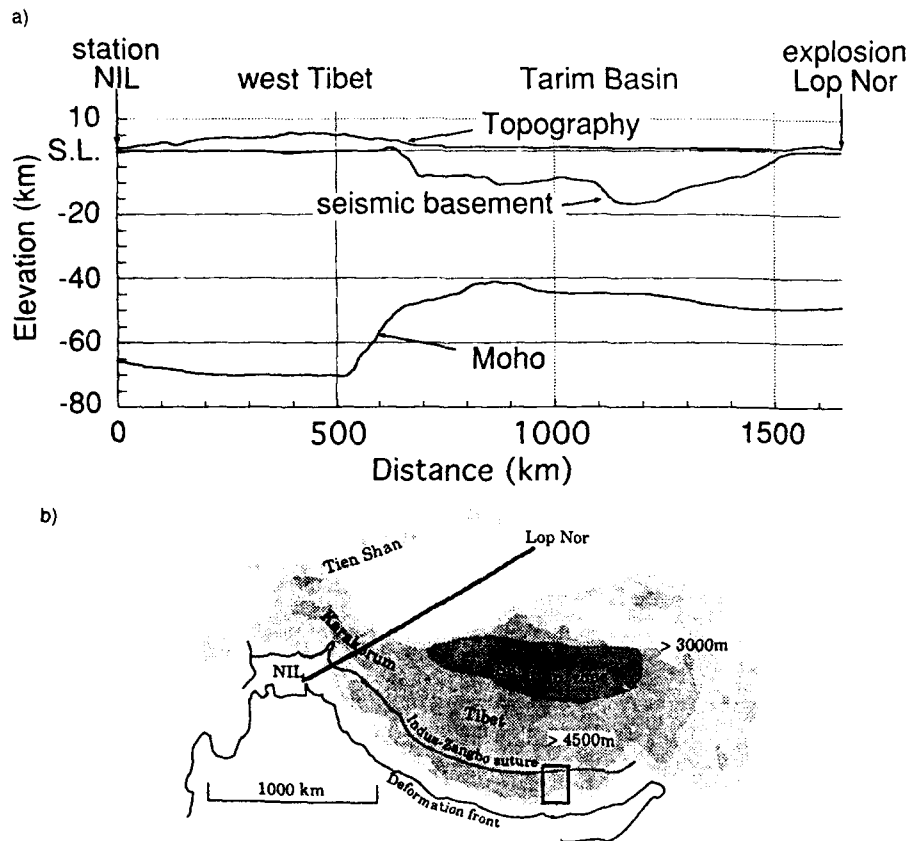


Figure 4: a) Profiles of topography, basement depth, and Moho databases along great circle path from station NIL in Pakistan to the Chinese nuclear test site at Lop Nor. Note the extreme variations in topography and crustal thickness that will affect the propagation of crustal phases, such as L_g . b) Map showing great circle path (thick black curve) and location of geologic map of Figure 2 (black outline box) with geographic and major tectonic features.

These datasets of digital geological and geophysical information when incorporated into

future versions of the IMS at the CSS will be extremely useful for the interpretations of seismic data. Several workers, for example, have noted or modeled the effects of three-dimensional heterogeneities within the crust along the propagation paths of regional seismic phases, especially L_g (e.g., Kennett and Bostock, 1989; Baumgardt, 1990; Bennett and others, 1991; Cormier, 1991; Kennett, 1991; Kennett and others, 1990; Lynnes and others, 1990). Qualitative studies have noted the lack of propagation of high-frequency L_g waves across major mountain ranges, such as the Central Andes (Chinn, Isacks, and Barazangi, 1980), Himalaya-Pamirs (Ni and Barazangi, 1983; Francis Wu, pers. comm. 1992), Turkish and Iranian Plateaus (Kadinsky-Cade, Barazangi, Oliver, and Isacks, 1981), and other ranges in Central Asia (Ruzaikan and others, 1977).

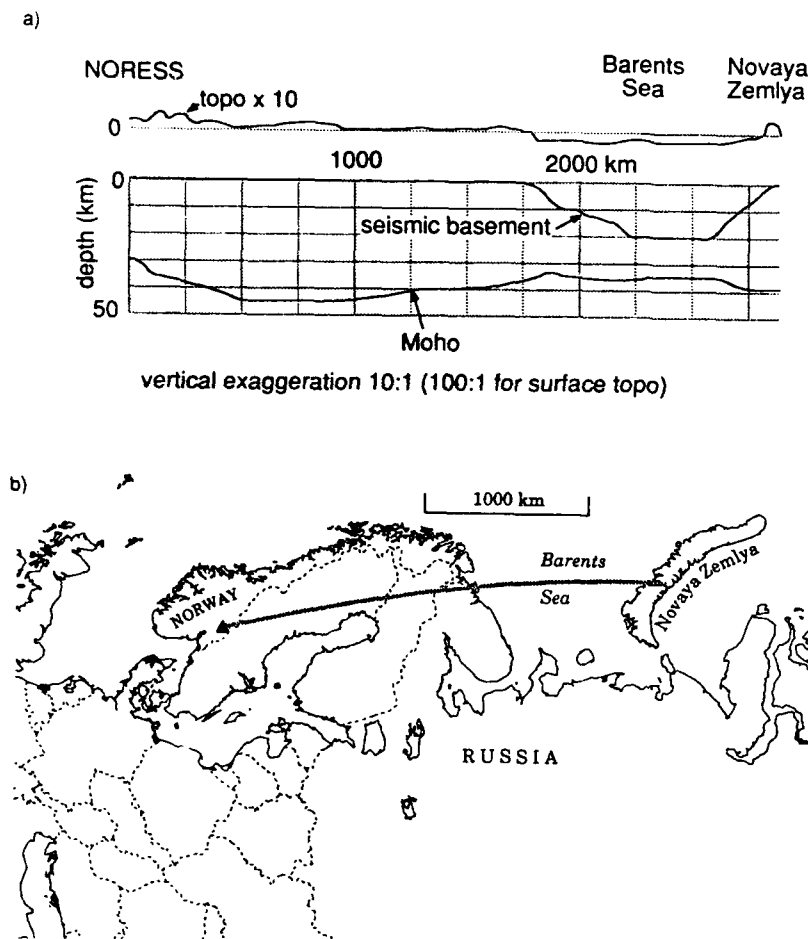


Figure 5: Crustal profile generated along great circle path between NORESS array and the Novaya Zemlya test site, similar to Figure 4. a) profiles of topography, depth to seismic basement, and depth to Moho. b) Map of the area in an azimuthal equidistant projection with symbols similar to Figure 1. Researchers have found a significant blockage of L_g along this path, probably caused by the crustal thinning under the Barents Sea.

Other features also seem to at least partially block L_g such as the Caspian Sea-Caucasus mountains (Kadinsky-Cade et al., 1981; Given, 1991) and the Barents Sea between Novaya Zemlya and Norway (see Figure 5; Baumgardt, 1990). Extreme surface roughness caused by fluvial and glacial erosion and sharp changes in sedimentary basin and Moho depths (e.g. Figures 3-5) may significantly contribute to

explaining the lack of L_g propagation across high mountain ranges. Use of L_g amplitudes along such paths for discrimination or yield estimation could be invalid or require correction factors. Surface roughness images can be used to map out areas of significant topographic relief, and basement and Moho relief images can similarly be used to map significant relief on those crustal boundaries.

CONCLUSIONS AND RECOMMENDATIONS

Geophysical and geological datasets can provide important ancillary information on the propagation of seismic phases through the continental lithosphere. In turn, this bears on the detection, discrimination, and yield estimation of nuclear explosions. The rapidly changing geopolitical situations in Eurasia, North Africa, and the Middle East make it imperative that databases are extended to areas outside the former Soviet test sites. The types of datasets that we are compiling can be used to compare well studied propagation paths, such as between NORESS and the Kazakhstan test sites, with paths to events in other locations that have not been studied in great detail to enhance the monitoring of nonproliferation treaties.

We will continue to work closely with CSS personnel to develop an interface that is best for cooperation with systems in use at CSS. We will continue to make our databases available via Internet (ARPAnet) connections to CSS and other

DARPA researchers. We will continue close contact with the DARPA researchers at Lamont to avoid duplication of effort and make our network database system compatible with their view-server system. We have proposed some modifications to the protocol of their system to make some data types more accessible, especially high-resolution "raster" or gridded data. The fast connection of Cornell to the NSFnet (T3 backbone) makes communication between Cornell and the Internet especially rapid. As described above, we will make the processed topography data available to the CSS and others, beginning with the reduced resolution mosaics that will be most useful to other DARPA researchers

REFERENCES

- Baumgardt, D. R., 1990, Investigation of teleseismic L_g blockage and scattering using regional arrays, *Bull. Seism. Soc. Am.*, v. 80, p. 2261-2281.
- Baumgardt, D. R., 1990, Causes of L_g amplitude variations and scattering in the Eurasian continental craton, *Proceedings of the 12th Annual DARPA/GL Seismic Research Symposium, 18-20 September 1990*, p. 224-233. GL-TR-90-0212, ADA226635
- Bennett, T. J., A. K. Campanella, J. F. Scheimer, and J. R. Murphy, 1991, Regional discrimination of Soviet nuclear explosions, earthquakes, and mine blasts, *Proceedings of the 13th Annual DARPA/PL Seismic Research Symposium, 8-10 October 1991*, p. 78-84. PL-TR-91-2208, ADA241325
- Cormier, V. F., 1991, Ray modeling of L_g attenuation across mountainous regions, *Proceedings of the 13th Annual DARPA/PL Seismic Research Symposium, 8-10 October 1991*, p. 145-151. ADA241325
- Chinn, D. S., B. L. Isacks, and M. Barazangi, 1980, High-frequency seismic wave propagation in western South America along the continental margin, in the Nazca plate and across the Altiplano, *Geophys. J. R. astr. Soc.*, v. 60, p. 209-244.
- Given, H., 1991, Heterogeneous propagation and blockage of L_g in the Caspian Sea-Caucasus mountain area of the USSR, *Proceedings of the 13th Annual DARPA/PL Seismic Research Symposium, 8-10 October 1991*, p. 211-217. PL-TR-91-2208, ADA241325
- Kadinsky-Cade, K., M. Barazangi, J. Oliver, and B. Isacks, 1981, Lateral variations of high-frequency seismic wave propagation at regional distances across the Turkish and Iranian Plateaus, *J. Geophys. Res.*, v. 86, no. B10, p. 9377-9396.
- Kennett, B. L. N., 1991, The distance dependence of regional seismograms, *Proceedings of the 13th Annual DARPA/PL Seismic Research Symposium, 8-10 October 1991*, p. 305-312. ADA241325
- Kennett, B. L. N., M. G. Bostock, and J. R. Bowman, 1990, Processes contributing to the coda of regional seismograms, *Proceedings of the 12th Annual DARPA/GL Seismic Research Symposium, 18-20 September 1990*, p. 98-104. GL-TR-90-0212, ADA226635
- Kennett, B. L. N., and M. G. Bostock, 1989, The effects of three-dimensional structure on crustally guided waves, *Proceedings of the 11th Annual DARPA/AFGL Seismic Research Symposium, 2-4 May 1989*, p. 213-220. GL-TR-90-0301, ADA229228
- Menke, W., P. Friberg, A. Lerner-Lam, D. Simpson, R. Bookbinder, and G. Karner, 1991, Sharing data over Internet with the Lamont view-server system, *EOS, Trans. AGU*, v. 72, no. 38, p. 409 ff.
- Ni, J., and M. Barazangi, 1983, High-frequency seismic wave propagation beneath the Indian Shield, Himalayan Arc, Tibetan Plateau and surrounding regions: high uppermost mantle velocities and efficient S_n propagation beneath Tibet, *Geophys. J. R. astr. Soc.*, v. 72, p. 665-689.
- Ruzaikan, A. I., I. L. Nersesov, V. I. Khalturin, and P. Molnar, 1977, Propagation of L_g and lateral variation in crustal structure in Asia, *J. Geophys. Res.*, v. 82, p. 307-316.

MULTIVARIATE SEISMIC CALIBRATION FOR THE NOVAYA ZEMLYA TEST SITE

Mark D. Fisk
Mission Research Corporation
and
Henry L. Gray and Gary D. McCartor
Southern Methodist University

CONTRACT NO: F19628-90-C-0135

OBJECTIVE

Recently, yield data have been made available for the underground nuclear tests conducted at the Novaya Zemlya Test Site between 18 Sep 1964 and 24 Oct 1990. The yields, determined from a Soviet graph, are compared to previously published estimates of the yields, and some discrepancies in the new data set are noted. Seismic magnitude data, NORSAR Lg and P coda, Gräfenberg Lg, a Soviet network Lg, and a world-wide m_b , were recorded for 18 of these events. Using these data, multivariate calibration of the linear magnitude-log yield relations is performed.

RESEARCH ACCOMPLISHED

Yield and Magnitude Data. Accurate seismic calibration for the Novaya Zemlya Test Site (NZ) has been hindered in the past by the lack of yield information. Within the last year, yield data for 42 underground nuclear tests conducted at NZ have been made available to DARPA by an official of the former Soviet Union. The original bar graph of the yield data is shown in Figure 1. The year and the number of events tested in that year (in parentheses) are labeled along the x -axis, and the month and accumulated number of events tested during a particular month are labeled along the left and right edges of the y -axis, respectively. The dates of each event are listed at the top of the graph. We have determined the yields by comparison of the lengths of the bars with the 150 KT scale at the left edge of the graph.

Table 1 lists the dates provided with the original data, our determination of the yields, as well as previous estimates of some of the yields by Nuttli (1988), Sykes and Ruggi (1988), and Burger et al. (1986). The yield estimates by Nuttli (1988) were based on a quadratic fit of Lg to the log yields of NTS events. The fit was then transported to NZ with no corrections. The yields from Sykes and Ruggi (1988) were estimated from a linear regression model for m_b , assuming bias corrections relative to NTS and Amchitka. The yields from Burger et al. (1986) were estimated by scaling relative to an Amchitka event. These and other yield estimates of NZ events have been compiled by Lay (1991); we present them here for comparison. Jih and Wagner (1992) also estimate

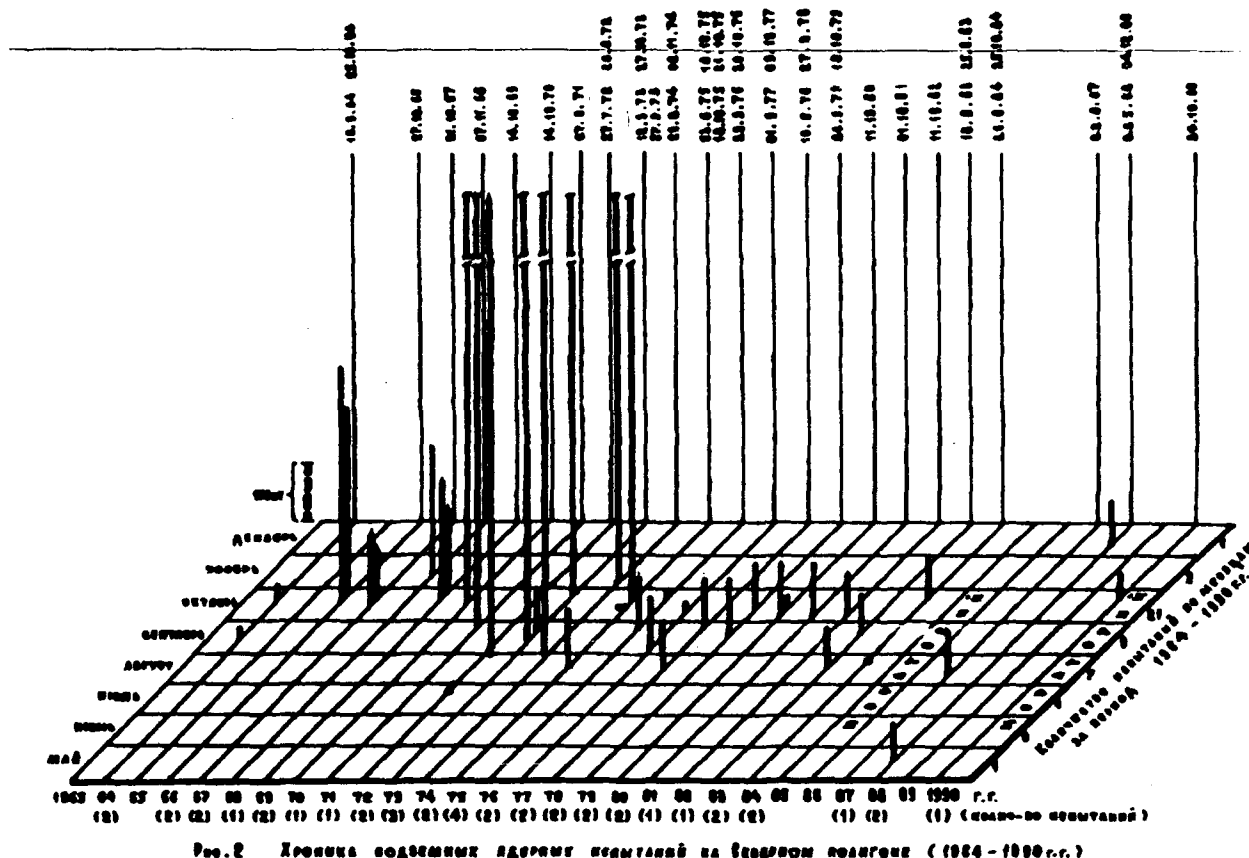


Figure 1. Original bar graph of Soviet yield data for 42 underground nuclear tests conducted at Novaya Zemlya.

the yields of 28 of these events based on path corrected short-period teleseismic P-wave amplitudes and experience at Semipalatinsk and NTS.

There are several points regarding the new yield set that should be noted. First, there are breaks in the bars of 7 of the 8 largest events. These events are larger than 1 MT, as confirmed by the other yield estimates, but the bars do not provide accurate measures of the yields. Second, our estimates of the very small events (12, 20, 21, 37) have limited accuracy; in fact, we do not currently know the accuracy with which any of the yields were recorded on this graph. Third, the graph in Figure 1 shows a small event on 27 July 1972, which is not present in any of the other data sets we have examined. We have also learned from Richards (1992) that a Soviet official believes that this event never occurred. Third, the two events on 18 October 1975 are known to be double explosions at SNZ (southern site) (e.g., Lay, 1992), and all available yield estimates suggest that these were large events, on the order of a megaton or more. This has been confirmed by a Soviet official (Richards, 1992). These events are, however, represented as very small on the bar graph (Figure 1). Last, many of the yields agree with the previous estimates; however, there are several events for which the yields differ significantly. Clearly, these discrepancies need to be resolved. Hence,

Table 1. Yield estimates of Novaya Zemlya tests.

| Event | Date | Y (FGM) | Y (Nuttli) | Y (SR) | Y (BBL) |
|-------|--------|---------|------------|--------|---------|
| 1 | 640918 | 29 | 2.5 | 2 | --- |
| 2 | 641025 | 40 | 16.4 | 8 | --- |
| 3 | 661027 | 603 | 644 | 422 | 600 |
| 4 | 661027 | 485 | --- | --- | --- |
| 5 | 671021 | 184 | 180 | 93 | 61 |
| 6 | 671021 | 126 | --- | --- | --- |
| 7 | 681107 | 334 | 253 | 119 | 110 |
| 8 | 691014 | 302 | 399 | 140 | 183 |
| 9 | 691014 | 219 | --- | --- | --- |
| 10 | 701014 | >1000 | 1970 | 1001 | 1714 |
| 11 | 710927 | >1000 | 1500 | 586 | 973 |
| 12 | 720727 | 14 | --- | --- | --- |
| 13 | 720828 | 1183 | 580 | 329 | 426 |
| 14 | 730912 | >1000 | 3510 | 2099 | 2824 |
| 15 | 730927 | 102 | 129 | 100 | 36 |
| 16 | 731027 | >1000 | 4990 | 4055 | 3886 |
| 17 | 740829 | >1000 | 1110 | 497 | 629 |
| 18 | 741102 | >1000 | 2840 | 2099 | 1624 |
| 19 | 750823 | 152 | 690 | 477 | 604 |
| 20 | 751018 | 10 | 2220 | 1281 | 1166 |
| 21 | 751018 | 10 | --- | --- | --- |
| 22 | 751021 | >1000 | 600 | 497 | 554 |
| 23 | 760929 | 131 | 91 | 70 | --- |
| 24 | 761020 | 22 | 19 | 13 | --- |
| 25 | 770901 | 134 | 122 | 55 | --- |
| 26 | 771009 | 27 | 10 | 4 | --- |
| 27 | 780810 | 121 | 91 | 89 | --- |
| 28 | 780927 | 125 | 61 | 44 | --- |
| 29 | 790924 | 144 | 81 | 55 | --- |
| 30 | 791018 | 120 | 79 | 70 | --- |
| 31 | 801011 | 139 | 76 | 55 | --- |
| 32 | 801011 | 30 | --- | --- | --- |
| 33 | 811001 | 136 | 116 | 113 | --- |
| 34 | 821011 | 107 | 79 | 44 | --- |
| 35 | 830818 | 105 | 145 | 89 | --- |
| 36 | 830925 | 97 | 99 | 70 | --- |
| 37 | 840826 | 10 | --- | --- | --- |
| 38 | 841025 | 101 | --- | 89 | --- |
| 39 | 870802 | 121 | --- | 70 | --- |
| 40 | 880507 | 97 | --- | --- | --- |
| 41 | 881204 | 112 | --- | --- | --- |
| 42 | 901024 | 64 | --- | --- | --- |

Table 2. Yield and magnitude data for 18 tests at NNZ.

| Event | Y (kt) | NORSAR Lg (m1) | Grafenberg Lg (m2) | Soviet Net Lg-Jui (m3) | NORSAR P-coda (m4) | World-Wide mb (m5) |
|-------|--------|-------------------|-----------------------|---------------------------|-----------------------|-----------------------|
| 23 | 131 | 5.770 | 5.799 | 5.606 | 5.732 | 5.77 |
| 24 | 22 | 5.071 | 5.022 | 0.000 | 4.969 | 4.89 |
| 25 | 134 | 5.757 | 5.872 | 5.672 | 5.750 | 5.71 |
| 26 | 27 | 4.845 | 0.000 | 0.000 | 4.637 | 4.51 |
| 27 | 121 | 5.783 | 5.759 | 5.707 | 5.952 | 6.04 |
| 28 | 125 | 0.000 | 5.660 | 5.529 | 0.000 | 5.68 |
| 29 | 144 | 5.779 | 5.825 | 5.692 | 5.782 | 5.80 |
| 30 | 120 | 5.737 | 5.664 | 5.674 | 5.821 | 5.85 |
| 31 | 139 | 5.784 | 5.732 | 5.694 | 5.776 | 5.80 |
| 33 | 136 | 5.782 | 5.783 | 5.760 | 5.882 | 5.91 |
| 34 | 107 | 5.603 | 5.585 | 5.515 | 5.551 | 5.52 |
| 35 | 105 | 5.807 | 5.739 | 5.750 | 5.769 | 5.84 |
| 36 | 97 | 5.797 | 5.777 | 5.722 | 5.723 | 5.71 |
| 38 | 101 | 5.805 | 5.837 | 5.690 | 5.743 | 5.77 |
| 39 | 121 | 5.806 | 5.810 | 5.712 | 5.769 | 5.71 |
| 40 | 97 | 5.719 | 5.654 | 5.630 | 5.614 | 5.52 |
| 41 | 112 | 5.800 | 5.811 | 5.723 | 5.822 | 5.79 |
| 42 | 64 | 5.605 | 5.550 | 0.000 | 5.618 | 5.60 |

although there are no known discrepancies associated with the events used to obtain the calibration results, given below, our results are preliminary, and contingent on the accuracy of the original data.

NORSAR Lg and P coda, Gräfenberg Lg, and a world-wide m_b have been published by Ringdal and Fyen (1991) for 18 of the underground nuclear tests at NNZ (northern site). Due to the complicated topography of the northern site, these tests were mainly emplaced in near-horizontal tunnels in the mountains. (Leith et al. (1990) and Lay (1991) provide reviews of the test site geology, topography, tectonic release and complex surface interactions and propagation effects.) Table 2 lists the event numbers, yields and magnitudes of those tests. A set of Soviet network Lg measurements are also listed. Some of the magnitudes were not recorded for events 24, 26, 28 and 42.

Regression Analysis Results. Figure 2 shows scatter plots of the data and lines of best fit for all but the Soviet network Lg. Three lines of best fit were computed using all of the available data (solid), all except event 26 (dashed), and all except events 24 and 26 (dotted). Events 24 and 26 are represented by the solid square and triangle markers, respectively. The corresponding estimates of the intercepts, slopes and standard deviations are given in the legends above each frame. Estimates of the

Table 3. Correlation coefficient estimates using all available data.

| Magnitude | NAO Lg | GRF Lg | NAO P coda | m_1 |
|------------|--------|--------|------------|-------|
| NAO Lg | 1.000 | 0.523 | 0.844 | 0.782 |
| GRF Lg | | 1.000 | 0.294 | 0.298 |
| NAO P coda | | | 1.000 | 0.982 |
| m_1 | | | | 1.000 |

Table 4. Correlation coefficient estimates excluding event 26.

| Magnitude | NAO Lg | GRF Lg | NAO P coda | m_1 |
|------------|--------|--------|------------|-------|
| NAO Lg | 1.000 | 0.755 | 0.664 | 0.560 |
| GRF Lg | | 1.000 | 0.423 | 0.383 |
| NAO P coda | | | 1.000 | 0.951 |
| m_1 | | | | 1.000 |

Table 5. Correlation coefficient estimates excluding event 24 and 26.

| Magnitude | NAO Lg | GRF Lg | NAO P coda | m_1 |
|------------|--------|--------|------------|-------|
| NAO Lg | 1.000 | 0.740 | 0.579 | 0.511 |
| GRF Lg | | 1.000 | 0.332 | 0.308 |
| NAO P coda | | | 1.000 | 0.957 |
| m_1 | | | | 1.000 |

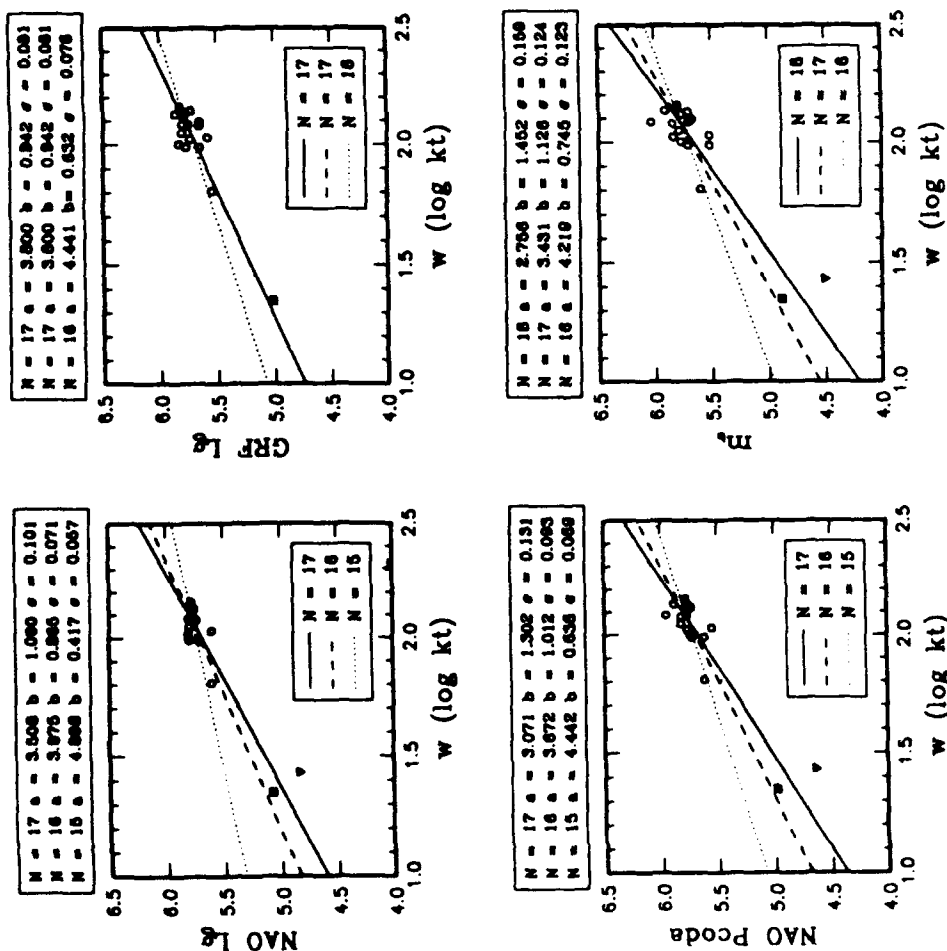


Figure 2. Scatter plots of NORSAR Lg, Gräfenberg Lg, NORSAR P coda, and world-wide m , magnitudes versus the yields of 18 nuclear explosions at NNZ. The solid, dashed and dotted lines in each frame represent the linear regression analysis fits using all available data, all except event 26 (denoted by the solid triangle), and all except events 26 and 24 (denoted by the solid square). The corresponding estimates of the parameters are given in the legends above the plots.

correlation coefficients associated with the random error covariance matrix are given in Tables 3-5 for the three cases.

We have several comments regarding these results. First, the set of Soviet network Lg magnitudes does not include the 3 smallest events, and the remaining 15 events are too tightly clustered to yield reliable estimates of the calibration parameters; the intercept, slope and standard deviation estimates are 5.538, 0.065 and 0.075, respectively. Second, the NORSAR and Gräfenberg Lg measurements exhibit the least random scatter of the remaining 4 magnitudes considered in Figure 2. Third, the slope estimates for these 4 magnitudes are somewhat larger than expected, particularly for NORSAR P coda and the world-wide m_b . As a result, the intercepts are also smaller than expected. Note that the slopes are highly dependent on the data values for the 2 smallest events. For example, when either event 26 or events 24 and 26 are omitted, the slopes decrease significantly (Figure 2). This is referred to as the "lolly pop" effect in regression analysis literature. The standard deviations also decrease when these events are omitted, and the correlation coefficient estimates change significantly (Tables 3-5). One might suspect that event 26, in particular, could have been a decoupled explosion, although we currently lack any concrete evidence.

Future Yield Estimation. A classical multivariate confidence interval to estimate future yields is presented by Fisk et al. (1992a). Estimates of the F-number, based on this interval, are also given. This interval, derived by Brown (1982), has been considered previously by Shumway and Der (1990) for yield estimation at Semipalatinsk. Fisk et al. (1992a) also discuss application of Bayesian methods (e.g., Fisk et al., 1992b; Gray et al., 1992; Shumway and Der, 1990). A Bayesian approach, that integrates expert opinion and calibration data, might be useful here since there is considerable uncertainty in the slopes.

CONCLUSIONS AND RECOMMENDATIONS

The yield data set presented here provides the first published set of actual yields for Novaya Zemlya tests. We have also provided the first direct estimates of the associated calibration parameters for several seismic magnitudes. There are several remaining discrepancies that must be resolved before a high level of confidence should be placed in these results. With the possibility of resumed testing at NNZ in late 1992, the calibration results may prove to be useful.

REFERENCES

- Brown, P.J. (1982). Multivariate Calibration, *J. R. Statist. Soc. B* **44**, 287-321.
- Burger, R.W., L.J. Burdick and T. Lay (1986). Estimating the relative yields of Novaya Zemlya test by waveform intercorrelation, *Geophy. J. R. Astr. Soc.*, **87**, 523-537.

Fisk, M.D., H.L. Gray and G.D. McCartor (1992a), Multivariate Seismic Calibration for the Novaya Zemlya Test Site, MRC-R-1402, Mission Research Corp. (to appear as a Phillips Laboratory Technical Report).

Fisk, M.D., H.L. Gray, G.D. McCartor and G.L. Wilson (1992b), A Constrained Bayesian Approach for Testing TTBT Compliance, PL-TR-91-2170, Phillips Laboratory, Hanscom AFB, MA. ADA253288

Gray, H.L., J. Baek, G.D. McCartor and W.A. Woodward (1992). A Bayesian Method for Testing TTBT Compliance with Unknown Intercept and Slope, SMU Technical Report.

Jih, R.-S. and R.A. Wagner (1992). Path-Corrected Body-Wave Magnitudes and Yield Estimates of Novaya Zemlya Explosions, PL-TR-92-2042, Phillips Laboratory, Hanscom AFB, MA. ADA251240

Leith, W., J.R. Matzko and J. Unger (1990). Geology and image analysis of the Soviet Nuclear Test Site at Matochkin Shar Novaya Zemlya, U.S.S.R., in *Proceedings of the 12th Annual DARPA/GL Seismic Research Symposium*, 18-20 September 1990, Key West, FL, Report GL-TR-90-0212 (Eds. J. Lewkowicz and J. Mcphetres), Phillips Laboratory, Hanscom AFB, MA. ADA226635

Lay, T. (1991). Yield estimation, free-surface interactions, and tectonic release at Novaya Zemlya, in *Proceedings of the 13th Annual PL/DARPA Seismic Research Symposium*, 8-10 October 1991, Keystone, CO, Report PL-TR-91-2208 (Eds. J. Lewkowicz and J. Mcphetres), Phillips Laboratory, Hanscom AFB, MA. ADA241325

Nuttli, O.W. (1988). Lg magnitudes and yield estimates for underground Novaya Zemlya nuclear explosions, *Bull. Seis. Soc. Am.*, **78**, 873-884.

Richards, P.G. (1992). Personal Communication.

Ringdal, F. and J. Fyen (1991). RMS Lg analysis of Novaya Zemlya explosion recordings, Semiannual Technical Summary, 1 Oct 1990 - 31 Mar 1991, *NORSAR Scientific Report No. 2-90/91*, NTNF/NORSAR, Kjeller, Norway.

Shumway, R.H. and Z.A. Der (1990). Multivariate Calibration and Yield Estimation for Nuclear Tests, University of California, Davis.

Sykes, L.R. and S. Ruggi (1989). Soviet nuclear testing, in *Nuclear Weapon Databook* (Volume IV, Chapter 10), Natural Resources Defense Council, Washington, D.C.

Ground-Truth Data for Seismic Discrimination Research

Lori Grant and John Coyne
Center For Seismic Studies
1300 North 17th Street
Arlington, VA 22209

Contract No. F29601-92-C-0005

Objective

To facilitate research on the seismic discrimination problem, there is a need for a standardized database of events of known type. This select suite of events could be used to develop, test and compare various algorithms and systems that identify the source type of seismic events. The objective of this project is to develop such a standard set of events. A key aspect of this project is that the resulting database will contain parameter and waveform data linked to "ground-truth" about the event. By this we mean non-seismic information that identifies source type and location is available for each event. This paper describes the database under development and makes an appeal for contributions of data.

Research Accomplished

Target Attributes of Database

The first step in this project has been to define goals for the content of the database. At this point, the emphasis is not to collect new data from field observations, but rather to locate and retrieve existing information from various institutions. Target attributes of the database are as follows:

- Events that are well-documented with supporting evidence for identification of source type. For example, felt earthquake reports have been used to identify earthquakes, while blaster's logs from mine operators have been used in the case of industrial explosions. The intention is to exclude events identified by seismic analysis alone.
- A variety of source types including: industrial shots (quarry and mine blasts, ripple-fired and single shots), earthquakes, exploration activity, nuclear explosions, collapse from nuclear explosions, mine collapse, rockbursts and other unusual sources.
- A variety of geographic regions, preferably where earthquakes and explosions are co-located.
- Waveforms in the distance range between 2 and 15 degrees. Waveforms from any distance will be included, but the emphasis is on events with regional data.
- Events with magnitude between 2 and 4.

The waveform and ground-truth data in this database will come from a variety of sources. The approach taken in this project is to identify interesting events and then collect the waveform data necessary to make the event useful in a seismic discrimination project. Once the database is popu-

lated with a diverse set of events meeting the target attributes, the entire dataset will be carefully analyzed in a consistent manner. Eventually, all waveform data in this database will be stored on-line at the Center for Seismic Studies (CSS).

Data Sources - An Appeal for Data

This section outlines the type of data available at CSS and the different types of data being requested from other institutions and researchers. In addition to the database described in this paper, other distinct databases exist at CSS that could be used for discrimination research. One of these is the Sereno and Patnaik dataset where the event identifications are based on seismic bulletins and analysis (1991). Another significant dataset contains all waveforms at CSS for known nuclear explosions. Appropriate events in these datasets will be included in the discrimination dataset.

When an event is identified that should be installed in the discrimination database, the approach for collecting the data depends on which of the following categories the event is in. The first two categories account for most of CSS's data holdings. Events in the last two categories require collection of waveform data and ground-truth information from sources outside CSS in order to expand the database to new areas.

- (1) Waveform data with no link to seismic event origin.
- (2) Focal parameters (origins) and waveform data with unknown event type.
- (3) Focal parameters (origins) only - no waveform data in the CSS's holdings.
- (4) Waveform and parameter data from controlled experiments.

In category 1, waveform data exists at CSS but is not linked to specific origins because it has not been analyzed. Examples are the IRIS/NRDC data on tape, data from the Scandinavian high-frequency arrays before IMS start-up, and other network tapes: GDSN, CDSN, and RSTN. Category 2 includes database accounts with analyzed events where waveform data is linked to origins and arrivals, but there is no event type recorded. Example database accounts in this category are IMS and GSETT-2. Table 1 is a partial listing of CSS's data holdings for categories 1 and 2. For any origin occurring in the time-period covered by data in categories 1 and 2, it is straightforward to retrieve the data and load it into the database. However, the ground-truth information about the event still has to be added. An example of new ground-truth information that could be linked to events already in CSS databases is the refined event locations for Shagan River nuclear explosions obtained by analysis of SPOT photos (C. Thurber and H. R. Quin, 1991). As we become aware of new information about events in this database, the appropriate database tables will be updated.

The extent of data in the discrimination database should not be limited to CSS's data holdings. An example of category 3 events are those that appear in a journal article or report, with documented ground-truth, for areas of the world where we do not have direct access to the waveform data. Adding these events to the discrimination database requires input from other researchers. Simi-

Table 1: Partial List of CSS's Data Holdings

| Network | Description | type | start date | end date | storage type |
|-----------|----------------------------|------------|------------|----------|--------------|
| NORSAR | pre-IMS array data | segments | 1976 | 1987 | tape |
| ARCESS88 | pre-IMS array data | segments | 1988 | 1988 | tape |
| NORESS | pre-IMS array data | continuous | 1984 | 1989 | tape |
| NORSSHf | pre-IMS; high frequency | continuous | 1984 | 1988 | tape |
| RSTN | Regional Seis. Test Net. | segments | 1982 | 1988 | tape |
| IRIS/NRDC | Territory of former USSR | continuous | 1987 | present | tape |
| GDSN | Global Digital Seis. Net. | segments | 1976 | present | tape |
| CDSN | Chinese Digital Seis. Net. | segments | 1986 | present | tape |
| IMS | 2-arrays | segments | 10/1/89 | 11/3/90 | on-line |
| IMS2 | 3-arrays; 4 arrays | segments | 11/4/90 | present | on-line |
| GSETT-2 | 58 station global network | segments | 4/22/91 | 6/2/91 | on-line |

larly in category 4, we have neither the event nor the waveform data recorded. Examples in this category are controlled experiments where temporary seismic networks are often deployed (e.g., Reamer and Stump, 1992a). In this case a complete dataset related to an experiment could be installed into the discrimination database with the cooperation of the experimenter.

New Relations

While developing the discrimination database, extensions have been added to the CSS Version 3.0 Database Schema (Anderson *et al.*, 1990) for handling more detailed shot information and for storing and quickly retrieving technical references, general comments, and ground-truth information. An attempt has been made to draw from the experience of others in designing new schema, relying on standard CSS Version 3.0 schema where possible.

In addition to database extensions, the scope of the ETYPE (event type) attribute in the CSS origin relation has been expanded as shown in Table 2. A distinction is made between quarry blasts with different levels of information. The designation **qb** indicates that the mine or quarry has verified the shot and there is no other "ground-truth" information available (e.g., Wüster, 1992). The **qb+** designation means the quarry has verified the shot and has given at least some specifics of the blast design from the blaster's logs (e.g., Chapman *et al.* 1991). The **qb++** designation is reserved for the few experimental quarry or mine shots that have been observed and fully documented by seismologists or mining engineers for research purposes (e.g., Reamer *et al.*, 1992b).

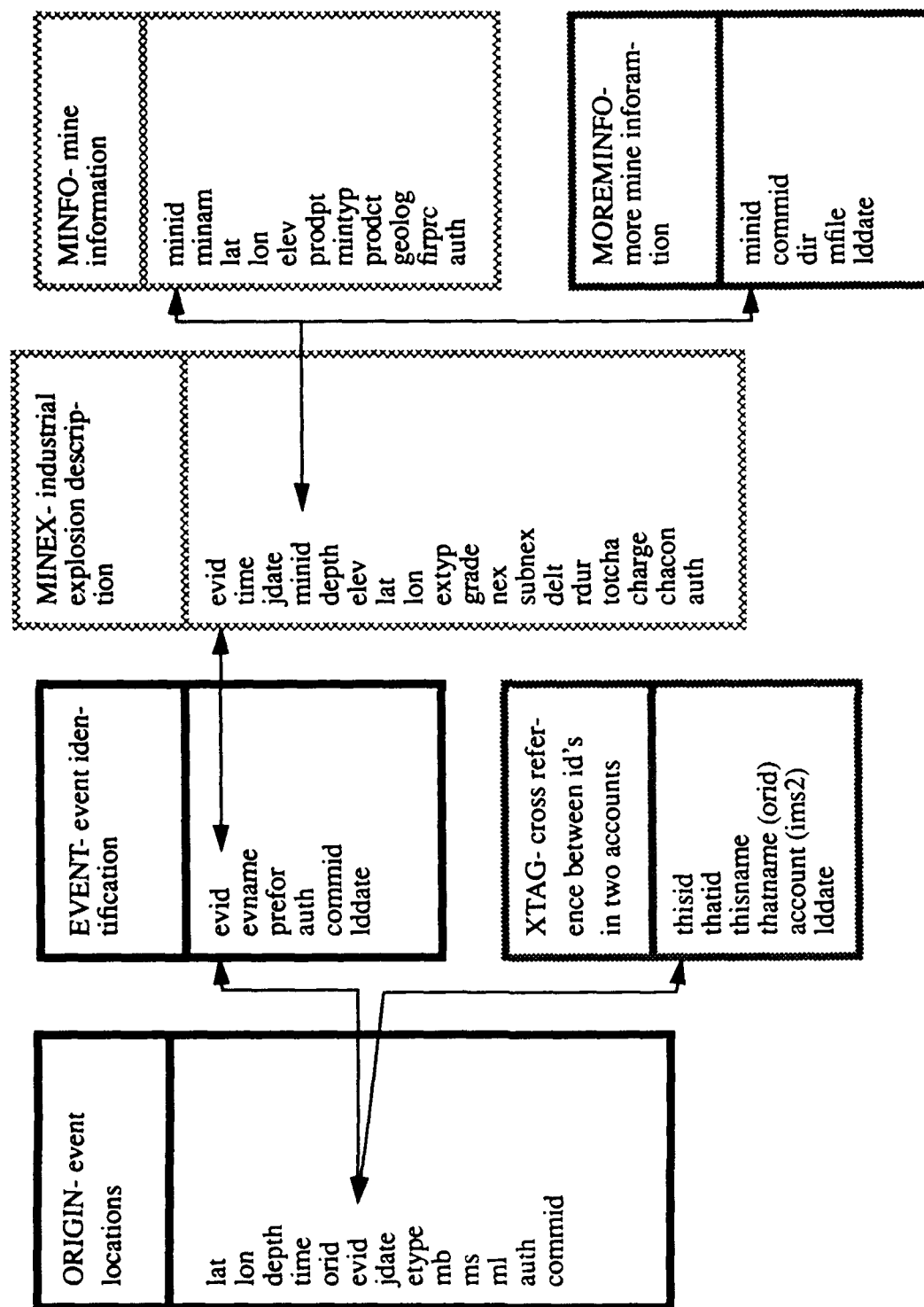
Tables related to known industrial explosions, MINEX, MINFO, MOREMINFO, and XTAG are shown in Figure 1. The MINEX and MINFO tables were proposed by Dahle *et. al* (1989). The MINEX relation lists shot information for specific explosions gathered from mine and quarry operators, with one record for each charge in the ripple-fire. Updated versions of these tables have

Table 2: RANGE OF ETYPE ATTRIBUTES IN ORIGIN RELATION

| ETYPE | DESCRIPTION |
|-------|------------------------------------------------------------------------|
| qb | Quarry blast or mining shot confirmed by quarry |
| qb+ | Quarry blast or mining shot with designed shot info- ripple fired |
| qb++ | Quarry blast or mining explosion with observed shot info- ripple fired |
| qbx | Quarry blast or mining explosion- single shot |
| qrb | Rockburst in quarry |
| ex | Explosion of known origin; i.e. exploration, construction, calibration |
| nu | Nuclear explosion |
| nc | Nuclear cavity collapse |
| eq | Earthquake |
| eq+ | Earthquakes in a swarm or aftershock sequence |
| eq++ | Felt earthquake |
| o | Other source of known origin |
| u | Undetermined or conflicting information |

been loaded into the database. Currently, the MINEX table holds over 400 individual shots documented between 1986 and 1992 (Dahle, personal communication). Where the time-period in MINEX overlaps with data in other database accounts at CSS, the events are cross-referenced through the XTAG relation. The MINFO relation contains mine-specific information, such as typical shooting practices (e.g. time of day and frequency), production depth and product. The MINFO table currently describes 50 mines in Scandinavia and additional mines in Central Europe (K.-G. Hinzen, personal communication). The new relation, MOREM-INFO, points to a flat file containing free-form text about a particular mine or mining district. These tables will be updated with mining events from other areas of the world including Germany, France, Russia and the United States. Some of the information will come from blaster's logs (qb+) and some of it will result from field observations (qb++).

Tables related to note-keeping, NOTEBOOK, NOTELINK, REFERENCE, TRUTH, and TRUTHLINK are shown in Figure 2. The NOTEBOOK relation is a "menu" of standard notes or statements about events. Use of a set "menu" of statements about events will aid in data retrieval. The REFERENCE relation tracks journal articles and scientific reports. The NOTEBOOK and REFERENCE relations are linked to other CSS relations through the COMMID attribute in NOTELINK. This NOTELINK relation is designed to be very general and track many types of information such as observations made during analysis or data quality. The TRUTH relation is another "menu" of statements that give the basis for the seismic source identification of an event. The TRUTHLINK table links truth statements to the origins. Sample truth statements are: "reported as felt earthquake in Helsinki Bulletin"; "reported as felt earthquake in Bergen Bulletin"; "location determined from SPOT photos".



PROPOSED

PROPOSED by Dahle *et al.* 1989

CSS Version 3.0 Database

Figure 1: Tables related to industrial explosions.

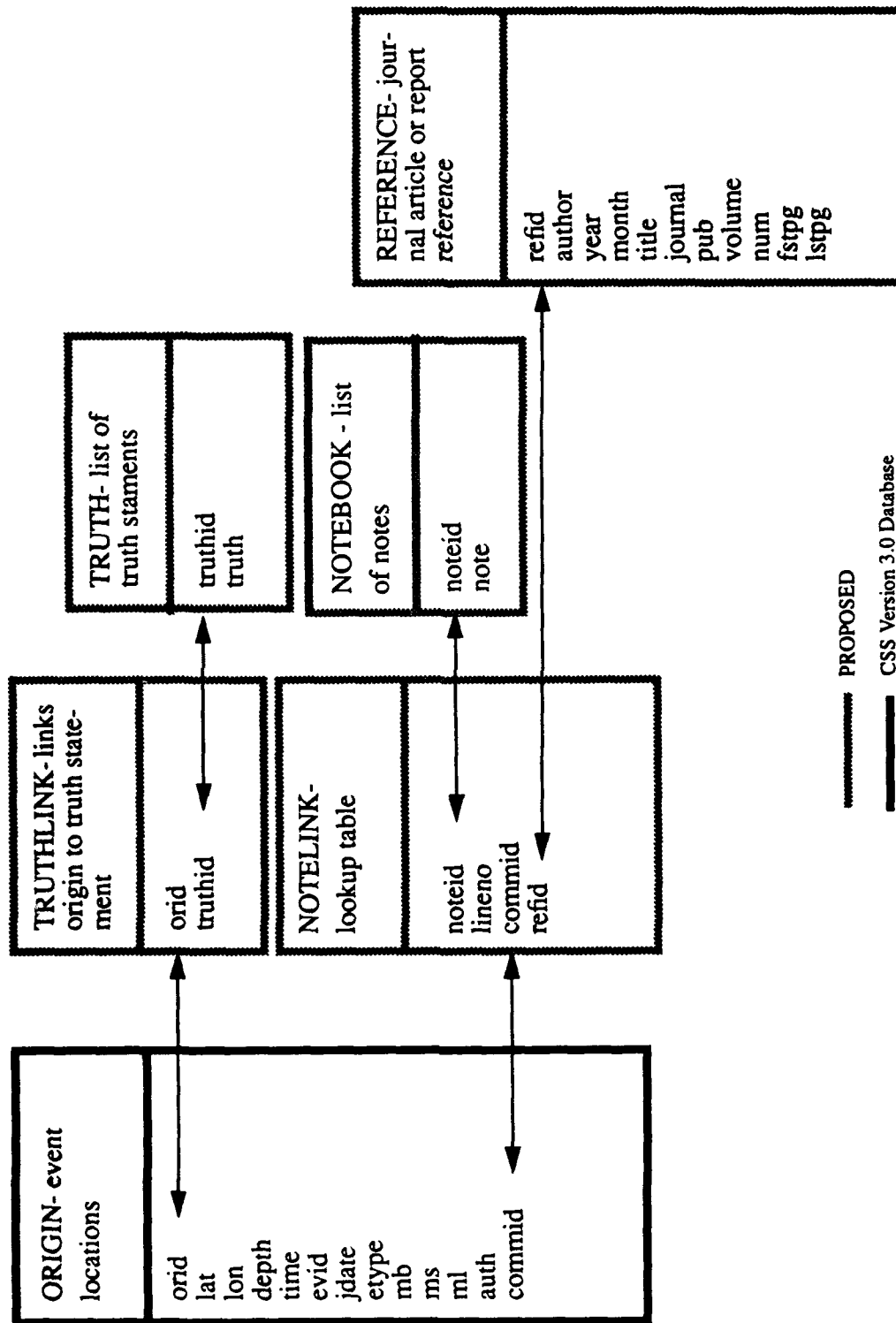


Figure 2: Tables related to note-keeping.

Conclusions

A plan for identifying and collecting a standardized set of events for discrimination research has been presented. The focus has been to develop new schema that is both easy to use and general enough to house a large variety of information. Many researchers who have data fulfilling the above criteria have been contacted with requests for specific data. Other researchers with relevant information are encouraged to participate. In-coming data is being incorporated into the database. When complete, this database will give researchers access to a large set of events of known type with links to ground-truth information.

For more information on this database or if you wish to make suggestions, please contact the authors at grant@seismo.CSS.GOV or coyne@seismo.CSS.GOV.

Acknowledgments

We thank the following contributors to the database: Doug Baumgardt, Bob Blandford, Hilmar Bungum, Tom Carter, Anders Dahle, Klaus-G. Hinzen, Hans Israelsson, Tormod Kværna, Tom Sereno, Marja Uski, and Jan Wüster.

References

- Anderson, J., W. E. Farrell, K. Garcia, J. Given, and H. Swanger (1990). Center for Seismic Studies Version 3 Database: Schema Reference Manual, *SAIC Tech. Rep. C90-01*, Arlington, VA., 61 pp.
- Champan, M. C., G. A. Bollinger, and M. S. Sibol (1991). Spectral studies of the elastic wave radiation from Appalachian earthquakes and explosions - explosion source spectra modeling using blaster's logs, *Proceedings of the 13th Annual PL/DARPA Seismic Research Symposium*, Keystone, Colorado, 138-144. PL-TR-91-2208, ADA241325
- Dahle, A., A. Alsker, S. Mykkeltveit (1989). Establishment of a mining explosion database, *NORSAR Sci. Rep. 1-89/90*, NORSAR, Kjeller, Norway, 83-102.
- Reamer, S.K. and B. W. Stump (1992a). Source parameter estimation for large, bermed, surface chemical explosions, *Bull. Seism. Soc. Am.*, 82, 406-421.
- Reamer, S. K., K.-G. Hinzen, and B. W. Stump (1992b). Analysis of spatial and temporal finiteness observed in the seismic wavefield radiated from quarry blasts, *Bull. Seism. Soc. Am.*, submitted for publication.
- Sereno, T. J. and G. B. Patnaik (1991). Data to test and evaluate the performance of neural network architectures for seismic signal discrimination, *Phillips Laboratory Tech. Rep. PL-TR-92-2110(I)*, Hanscom Air Force Base, MA, 53 pp.
- Thurber, C. H. and H. R. Quinn (1991). Teleseismic and regional seismic event location: constraints from master events, satellite images, and synthetic seismograms, *Proceedings of the 13th Annual PL/DARPA Seismic Research Symposium*, Keystone, Colorado, 438-441. ADA241325
- Wüster, J. (1992). Discrimination of chemical explosions and earthquakes in Central Europe - a case study, *Bull. Seism. Soc. Am.*, submitted for publication.

HIGH-PRECISION RELATIVE EVENT LOCATION WITH CROSS-SPECTRAL ANALYSIS AND RELATED STUDIES

I. N. Gupta and J. P. Davis
Teledyne Geotech Alexandria Laboratory,
314 Montgomery Street, Alexandria, VA 22314-1581

Contract No. F29601-91-C-DB07

OBJECTIVE

Analyze regional data from closely located explosions to improve relative locations and investigate the influence of path differences and the near-source environment.

RESEARCH ACCOMPLISHED

Location relative to a reference event is often more useful and precise than absolute event location. The use of relative location compensates for most of the errors arising from path effects. Such location requires relative arrival times for pairs of events observed at common stations, which can be obtained with high precision for similar events by waveform cross-correlation. The precision can be further boosted by applying the cross-spectral analysis method, which can yield relative delay times with resolution up to an order magnitude better than the seismogram sampling interval.

Relative locations are limited primarily by the precision with which the phase arrival times can be measured. For two events that occur close together, the waveforms at a common recording station are often similar. In such cases, a cross-correlation of the two waveforms can provide a much improved estimate of the relative time, since the full waveform is used rather than a subjective pick of the initial phase arrival. Conventional cross-correlation slides one waveform past another, and the lag with the optimum correlation coefficient is taken as the relative time. However, the cross-spectral analysis method can yield improved relative time estimates. Following Ito (1985), the cross-spectrum, $Sc(f)$, of two signals A and B is:

$$Sc(f) = \frac{F_a(f) F_b^*(f)}{T} = \text{Re}(f) - i \text{Im}(f), \quad (1)$$

where $F(f)$ is the Fourier transform of $f(t)$ and $*$ indicates the complex conjugate. Then the phase spectrum $\phi(f)$ is

$$\phi(f) = \tan^{-1} \frac{-\text{Im}(f)}{\text{Re}(f)} \quad (2)$$

If the two seismograms are similar in shape but have different amplitudes, then

$$f_b(t) = k f_a(t+\tau), \quad (3)$$

and by the application of the shift theorem, the phase spectrum becomes

$$\phi(f) = 2 \pi f \tau \quad (4)$$

Thus the delay time τ can be obtained by simply by fitting a straight line through the phase of the cross-spectrum with zero intercept. In fitting this slope, the values are weighted based on the coherence $C(f)$:

$$C(f) = \frac{\sum_{f'=f-\Delta f}^{f'=f+\Delta f} S_c(f')}{\sum_{f'=f-\Delta f}^{f'=f+\Delta f} \sqrt{S_a(f') S_b(f')}} \quad (5)$$

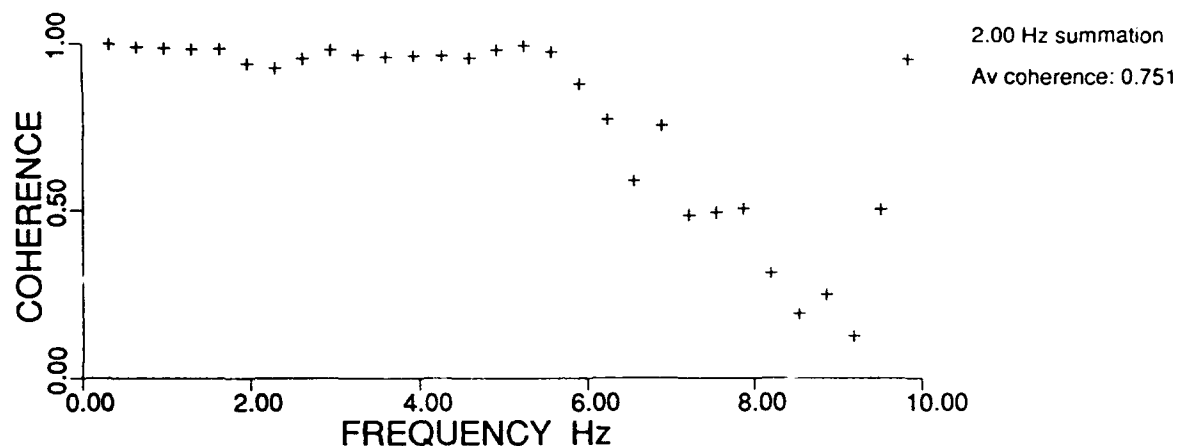
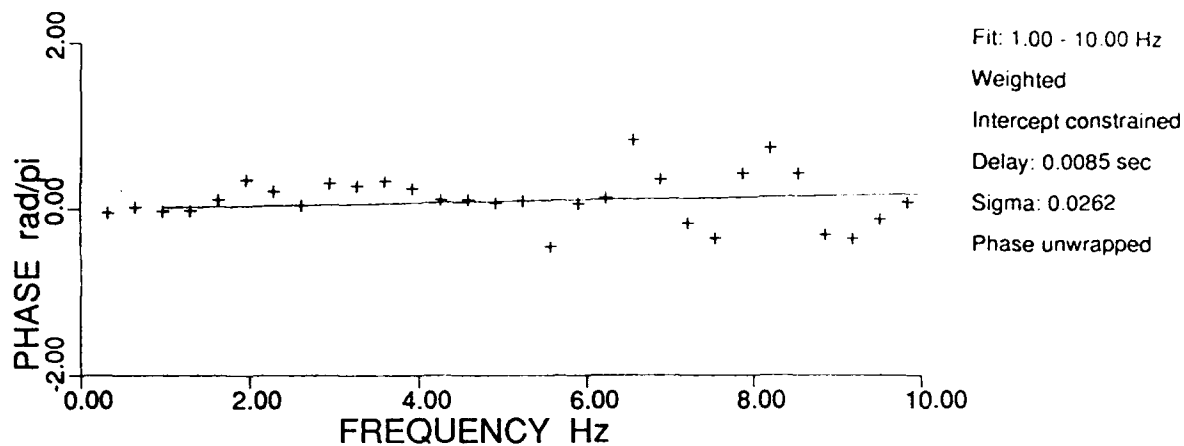
where $S(f)$ is the signal power. The weighting factor, $W(f)$ in the linear fit is based on the Hannon-Thomson processor (Knapp and Carter, 1976), *i.e.*

$$W(f) = \frac{C^2(f)}{1 - C^2(f)} \quad (6)$$

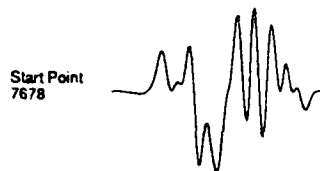
The slope of the line has a continuum of possible values, rather than discrete values, with the result that estimates of delay time for highly coherent pairs can actually be an order of magnitude more precise than the sample rate. This technique has been applied successfully to local sequences of earthquakes with impressively precise locations (Ito, 1985; Fremont and Malone, 1987).

Regional data from closely spaced underground nuclear explosions at the Nevada Test Site (NTS), recorded at the four broadband digital stations, ELK, KNB, LAC, and MNV, have been analyzed to determine how the cross-spectral method may best be used to improve relative locations. For these explosions, with precisely known locations, the near-source geological and geophysical properties are also known so that the influence of parameters such as shot depth and geological environment can also be investigated. Software for determining the delay time between two waveforms has been developed and tested. The relative arrival times between two events recorded at a common station are determined with a precision of 0.001 sec. As an example, results from the vertical component ELK records of the Yucca Flat explosions ROUSANNE and BASEBALL are shown in Figure 1. The digital data are sampled at about 42 samples/sec. Figure 1 (bottom) shows the input waveforms which may be selected to be of any desired duration. The signal window over which a cosine taper applies is also variable. The top plot shows the phase of the cross-spectrum varying between -2π and $+2\pi$. The lower plot shows the coherency, varying between 0 and 1, derived by using a bandwidth of 2.0 Hz. As expected from theory, the coherency is generally observed to decline with increasing frequency. The delay time is simply the slope of the phase of the cross-spectrum over the specified range of 1.0-10.0 Hz and is obtained by fitting a slope through 0, using a weighting scheme based on coherence of the cross-spectrum (see equation 6).

Assuming BASEBALL to be the reference shot with known location and its first peak at each station as the reference time, the corrected arrival times (such as the one indicated on Figure 1) for each explosion recorded at the four stations are determined. For each explosion, the four arrival times are used as input to the LOCATE feature of the Analyst Review Station (ARS) to obtain its epicentral location and the origin time. The arrival times (without any delay correction) for BASEBALL recorded at the four stations are also used to compute the corresponding ARS location. The ARS computed locations and the actual (known) locations of six explosions are shown in Figure 2a. The ARS computed locations for the five shots (paired with BASEBALL) are shifted by the amount of shift between the ARS computed and actual locations of BASEBALL. A comparison of the shifted locations of each of the five shots with its actual location provides the location error associated with each shot (Figure 2a).

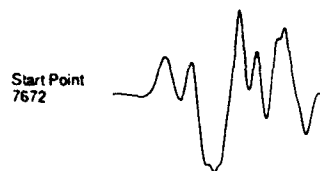


1187.8 nm 0-P Seis 1 ELK BASEBALLelk
 Start time: 15 Jan 81 20:25:57.8181



128 pts
 42.010 samp/sec
 Cosine Taper
 Backup: 21 pts
 Arrival:
 20:25:58.3180

751.9 nm 0-P Seis 1 ELK ROUSANNEelk
 Start time: 12 Nov 81 15:0:57.6873



Corrected Arrival:
 15:0:58.1956

0.0 5.0 Sec

PROGRAM CSA vers 1.7 Tue Jul 28 16:11:34 1992

Figure 1. Cross-spectral analysis for measuring delay times. The two input waveforms (bottom), each 128 points long, provide the phase of the cross-spectrum (top) and coherence based on bandwidth of 2.0 Hz for frequencies up to 10 Hz. The slope of the phase spectrum, computed by fixing the intercept to 0 and applying weights related to the coherence, provides the delay time used to obtain the corrected arrival time for ROUSANNE recorded at ELK.

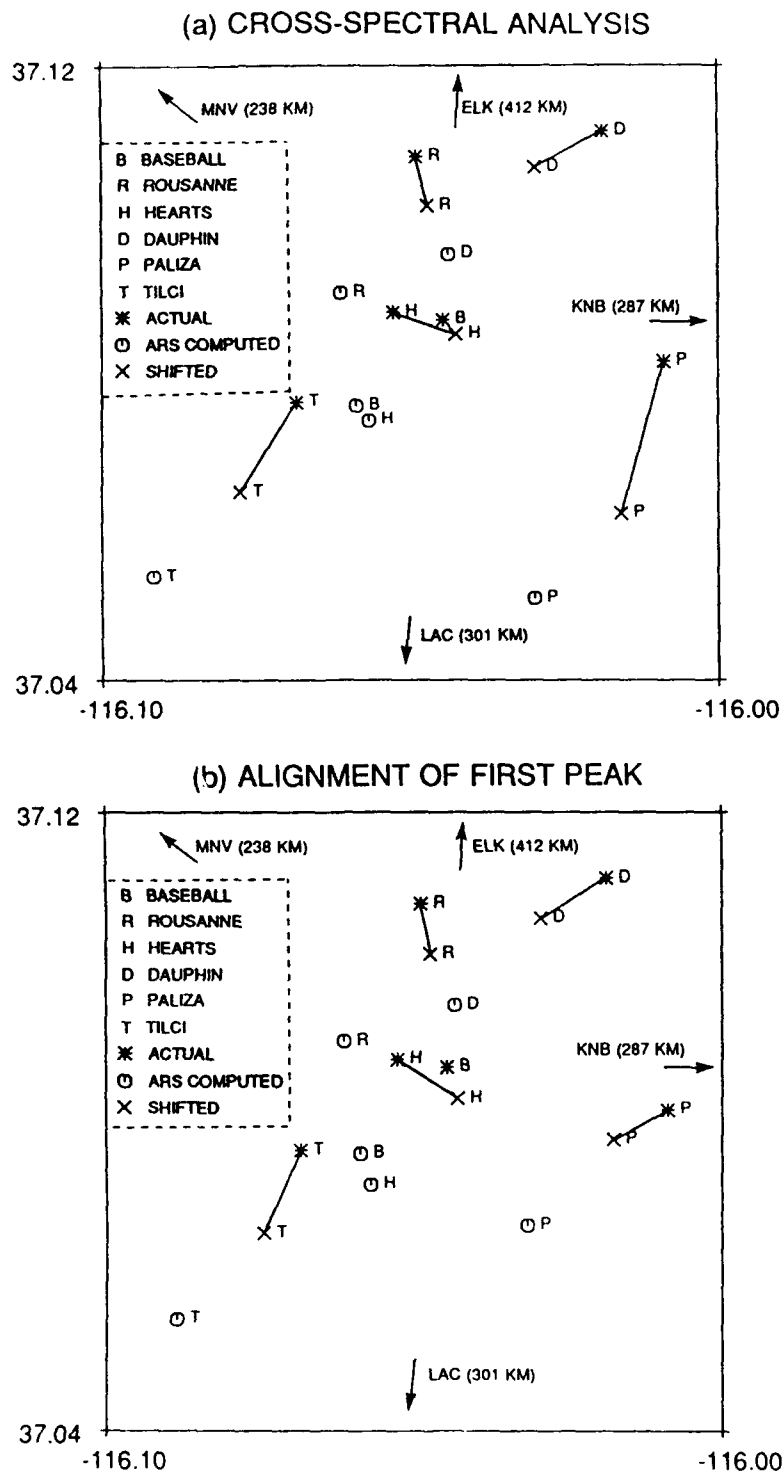


Figure 2. Location results for six Yucca Flat explosions from arrival times based on use of (a) cross-spectral analysis and (b) alignment of the first peaks. Actual locations, ARS computed locations, and locations with shift based on BASEBALL are shown; the five lines indicate the error between the actual and computed locations. Directions and distances from BASEBALL to the four recording stations are indicated.

The mean location error is only 1.32 km with one standard deviation of 0.61 km. Cross spectral analysis based on the use of longer (256 points) windows was also carried out for the same six explosions. Using a bandwidth of 1.0 Hz for deriving coherency and a frequency range of 0.5-5.0 Hz for computing the delay time, the location results were found to be very similar to those in Figure 2a in both the magnitude and azimuthal direction of the location errors; the mean location error was 1.22 km with a standard deviation of 0.61 km. These results appear to be impressive if one considers the large epicentral distances (about 200 km to 320 km) and the complex geology of the Nevada test site.

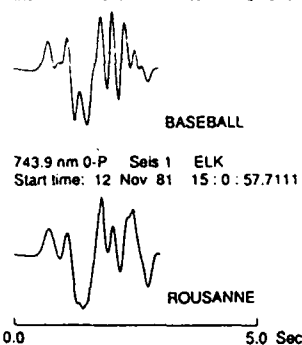
Locations based on use of arrival times determined by simple alignment of the first peaks at common stations are shown in Figure 2b. A comparison with locations derived by using the cross-spectral analysis (Figure 2a) shows significant improvement, especially for the two shots PALIZA and TILCI. The mean location error is only 1.02 km with a standard deviation of 0.22 km. Possible reasons for the smaller accuracy of the cross-spectral analysis are the spectral leakage and variability for the estimates expected when cosine taper is used on rather short time series (Vernon *et al.*, 1991). We plan to try later the multiple-taper spectral analysis technique devised by Thomson (1982).

Analysis of regional data from Yucca Flat explosions also provided valuable information regarding inter-source coherence, the coherence between Pn or Lg arrivals from pairs of closely located explosions recorded at common stations. The shorter signal windows of Pn indicated significantly better coherency over a much larger range of frequency than the longer windows, suggesting that the first arrivals in Pn are considerably more alike than the later arriving phases, perhaps due to greater contamination by later-arriving scattered energy. Inter-source coherence for Pn was found to be significantly greater when the two sources lay along the direction of wave propagation than when perpendicular to it. This is illustrated by results from the three explosions BASEBALL, ROUSANNE and PALIZA recorded at ELK and KNB (Figure 3). For BASEBALL and ROUSANNE, ELK and KNB are nearly along and perpendicular to the direction of wave propagation, respectively. On the other hand, for BASEBALL and PALIZA, ELK and KNB approximate directions perpendicular to and along the wave propagation. These results are similar to the inter-sensor coherence of regional phases generally observed to be greater along the radial direction than along the transverse direction. An attempt will be made to exploit these coherency differences to improve locations. Analysis of the Lg phase showed the inter-source coherence to be significantly smaller than for Pn, again similar to the observed inter-sensor coherence results for Lg and Pn. Furthermore, coherency appeared to vary significantly from one station to another.

In order to understand what causes the discrepancy between the actual locations and those computed from observations of Pn from the Yucca Flat explosions, we examined the lateral variations in the Pn velocity under the test site. Pn arrival times from closely spaced explosions can be used to estimate average velocities to various stations if the spatial locations of the explosions are precisely known and data from at least two shots are available.

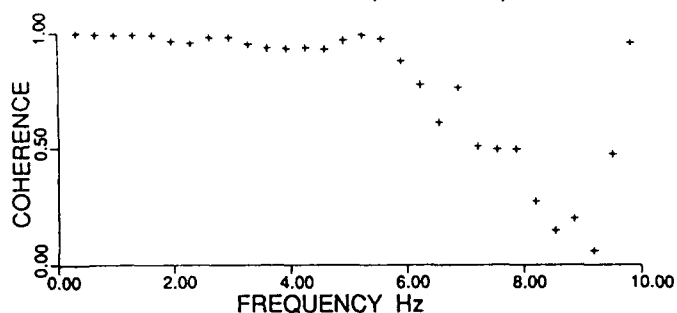
Let us consider a number of closely located sources, S_i recorded at a number of well-separated receivers, R_j . Let the average P-wave velocities from the limited source region to the relatively distant receivers be α_j . If r_{ij} represents the distance from source S_i to the receiver R_j and z_i are the origin times of the various sources, then the P-wave arrival times, T_{ij} are given by

1187.8 nm 0-P Seis 1 ELK
Start time: 15 Jan 81 20:25:57.8181



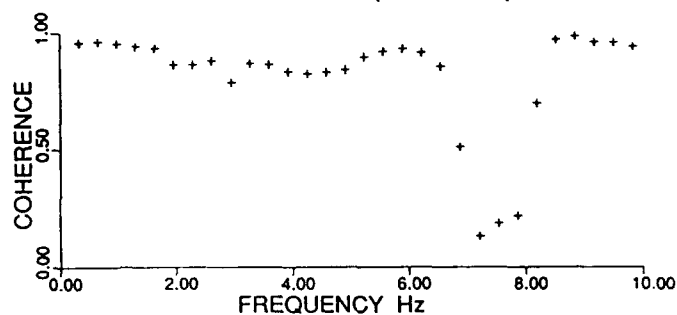
(a)

AVERAGE COHERENCE (0.1 - 3.0 HZ) = 0.982

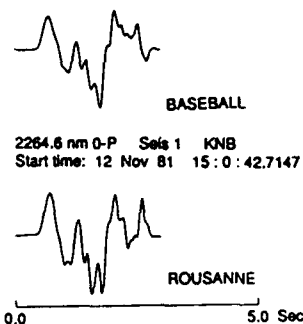


(b)

AVERAGE COHERENCE (0.1 - 3.0 HZ) = 0.911

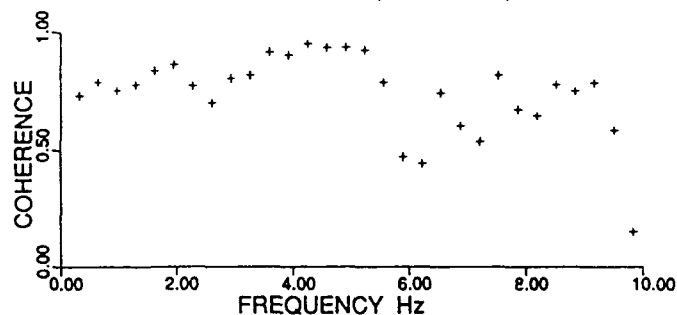


3972.5 nm 0-P Seis 1 KNB
Start time: 15 Jan 81 20:25:42.6075

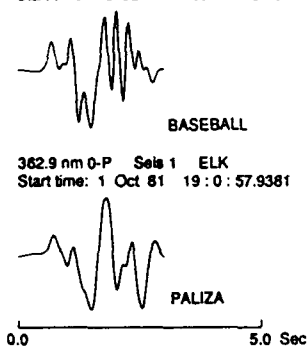


(c)

AVERAGE COHERENCE (0.1 - 3.0 HZ) = 0.777

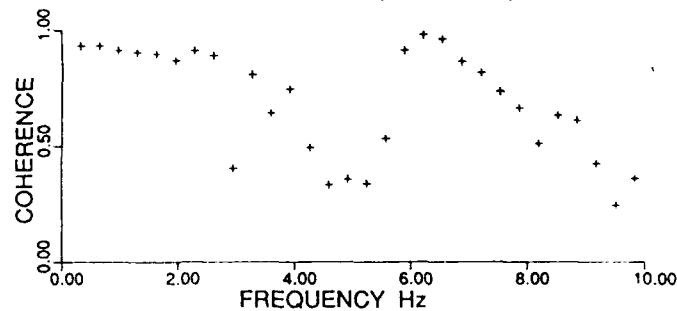


1187.8 nm 0-P Seis 1 ELK
Start time: 15 Jan 81 20:25:57.8181



(d)

AVERAGE COHERENCE (0.1 - 3.0 HZ) = 0.855



3972.5 nm 0-P Seis 1 KNB
Start time: 15 Jan 81 20:25:42.6075

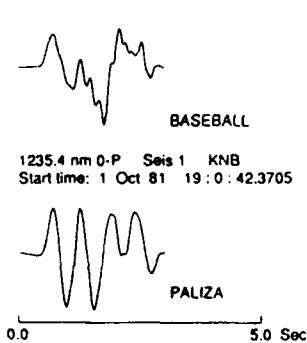


Figure 3. Waveform and coherency plots indicating the inter-source coherency approximately along the direction of wave propagation (such as BASEBALL and ROUSANNE at ELK or BASEBALL and PALIZA at KNB) to be larger than perpendicular to it (such as BASEBALL and ROUSANNE at KNB or BASEBALL and PALIZA at ELK).

$$T_{ij} = \frac{r_{ij}}{\alpha_j} + z_i \quad (7)$$

Having data from two or more sources at two or more receivers, we can solve for α_j by using the method of least squares.

Using Pn arrival times from the six explosions used earlier (listed on Figure 2) recorded at the four stations and basing the arrival times on the alignment of the first peak, the mean velocities to the four stations ELK, KNB, LAC, and MNV were determined to be 7.051 (0.006), 6.636 (0.007), 6.767 (0.007), and 6.469 (0.008), respectively. The quantities within parentheses denote one standard deviation value and are remarkably small. These velocity values indicate significant anisotropic variation (about 9%) around the test site and appear to suggest velocities along the north-south direction to be somewhat larger than those along the east-west direction, in general agreement with the tectonics of the region and the velocity measurements of Harmsen (1992). It follows that at least a part of the observed location errors are due to the assumption of a uniform velocity model under the test site.

CONCLUSIONS AND RECOMMENDATIONS

Cross-spectral analysis of regional data from Yucca Flat explosions with precisely known locations provides relative locations that are accurate to within about 1 km. However, locations based on arrival times determined by alignment of the first peaks appear to be somewhat better. A possible reason is the use of cosine taper on rather short signal windows; the use of multiple-taper is recommended for the future. Our analysis also provides valuable information regarding inter-source coherence of Pn and Lg which may be useful for improving locations.

REFERENCES

- Fremont, M. J. and S. D. Malone (1987). High precision relative locations of earthquakes at Mount St. Helens, Washington, *J. Geophys. Res.* 92, 10223-10236.
- Harmsen, S. C. (1992). Regional-scale velocity anisotropy inferred from Nevada Test Site nuclear test P-arrivals, *Seismol. Res. Lett.* 63, 39 (abstract).
- Ito, A. (1985). High resolution relative hypocenters of similar earthquakes by cross-spectral analysis method, *J. Phys. Earth* 33, 279-294.
- Knapp, C. H., and G. C. Carter (1976). The generalized method for estimation of time delay, *IEEE Transactions on Acoustics, Speech, and Signal Processing* 24, 320-327.
- Thomson, D. J. (1982). Spectrum estimation and harmonic analysis, *Proc. IEEE* 70, 1055-1096.
- Vernon, F. L., J. Fletcher, L. Carroll, A. Chave, and E. Sembera (1991). Coherence of seismic body waves from local events as measured by a small-aperture array, *J. Geophys. Res.* 96, 11981-11996.

Depths of Upper Mantle Discontinuities Beneath Broad Band Seismic Stations by Velocity Spectrum Stacks of Receiver Functions

Harold Gurrola¹, Bernard Minster¹, and Tom Owens²
(1-IGPP, UCSD; 2-University of South Carolina)
CONTRACT NO: AF F19628-90-K-0045

OBJECTIVES

A commonly used technique to estimate crustal structure from a single three-component seismographic station is to compute and interpret "receiver functions" (e.g., Langston 1989, 1981; Owens, Crosson and Hendrickson 1988; Owens, Taylor and Zandt 1987; Owens, Zandt and Taylor 1984), wherein the horizontal components are deconvolved by the vertical component to produce a trace consisting primarily of Ps conversions and converted S-wave reverberations. The technique has been successfully extended to arrays of broadband portable stations by Owens et al. (1988). To improve the signal to noise ratio, receiver functions can be binned by ray parameter and back azimuth and stacked (Owens, Taylor and Zandt 1983). In areas with flat geological structure the receiver functions show little or no azimuthal dependence and can be stacked at common ray parameter for all azimuths. However, if we wish to stack traces with different ray parameters, we must first correct for the differences in relative arrival times. We have adapted the velocity spectrum stacking technique used extensively in reflection seismology (Yilmaz, 1987) to be applicable to receiver functions. For reasons discussed below this method is most applicable to the study of upper mantle discontinuities. We have produced VSS for IRIS/IDA stations AAK, ALE, ARU, ERM, ESK, GAR, KIV, NNA, OBN, PFO, SUR, and TLY, and for the RSTN stations RSNT, RSNY, RSCP, RSSD, and RSON. Due to space limitations in this paper, we focus our attention to the VSS illustrating the 670 km discontinuity at each station.

METHOD

Figure 1 illustrates the geometry of the most significant type of phase observed in receiver function studies — the P to S conversion (Ps) generated when the wave crosses an interface — for a layer over a half space. The time delay for the Ps arrival relative to that of the P arrival $\Delta T_{Ps}(p)$ (moveout) is given by:

$$\Delta T_{Ps}(z, p, V_S, V_P) = z(\sqrt{V_S^2 - p^2} - \sqrt{V_P^2 - p^2}) \quad (1)$$

In the above equations: V_S and V_P are the average S and P velocities in the layer, respectively; p is the ray parameter; and z is the depth to the interface. In terms of the vertical travel time of Ps relative to P (ΔT_{Ps0}) through the layer and the velocity ratio $R_V = V_P / V_S$, we have:

$$\Delta T_{Ps}(\Delta T_{Ps0}, V_S, R_V) = \frac{R_V \Delta T_{Ps0} (\sqrt{1 - p^2 V_S^2} - \sqrt{R_V^{-2} - p^2 V_S^2})}{R_V - 1} \quad (2)$$

Note that this equation depends only on ΔT_{Ps0} , p , V_S and an assumed value for R_V (which will be held constant for an entire velocity spectrum stack, e.g. $R_V = \sqrt{3}$ for a Poisson solid). Figure 2 depicts a set of synthetic receiver functions generated for PREM (Dziewonski and Anderson, 1981) over a range of ray parameters. We see that all the Ps phases are delayed with increasing ray parameter relative to the initial P-wave. In this paper we are

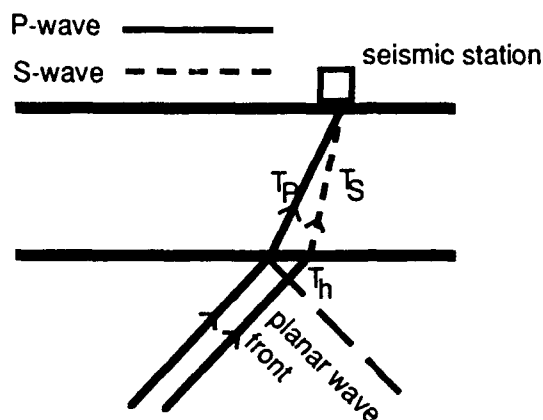


Figure 1. Ray paths for the Ps phase relative to the P phase for a layer over a half space. T_P and T_S are the travel times of the P and S phases with the same ray parameter through the layer respectively. T_h is the travel time differential in the half space for the two rays assuming a planar wave front.

only concerned with the Ps phase and refer the reader to Gurrola and Minster (1991) for additional applications of VSS.

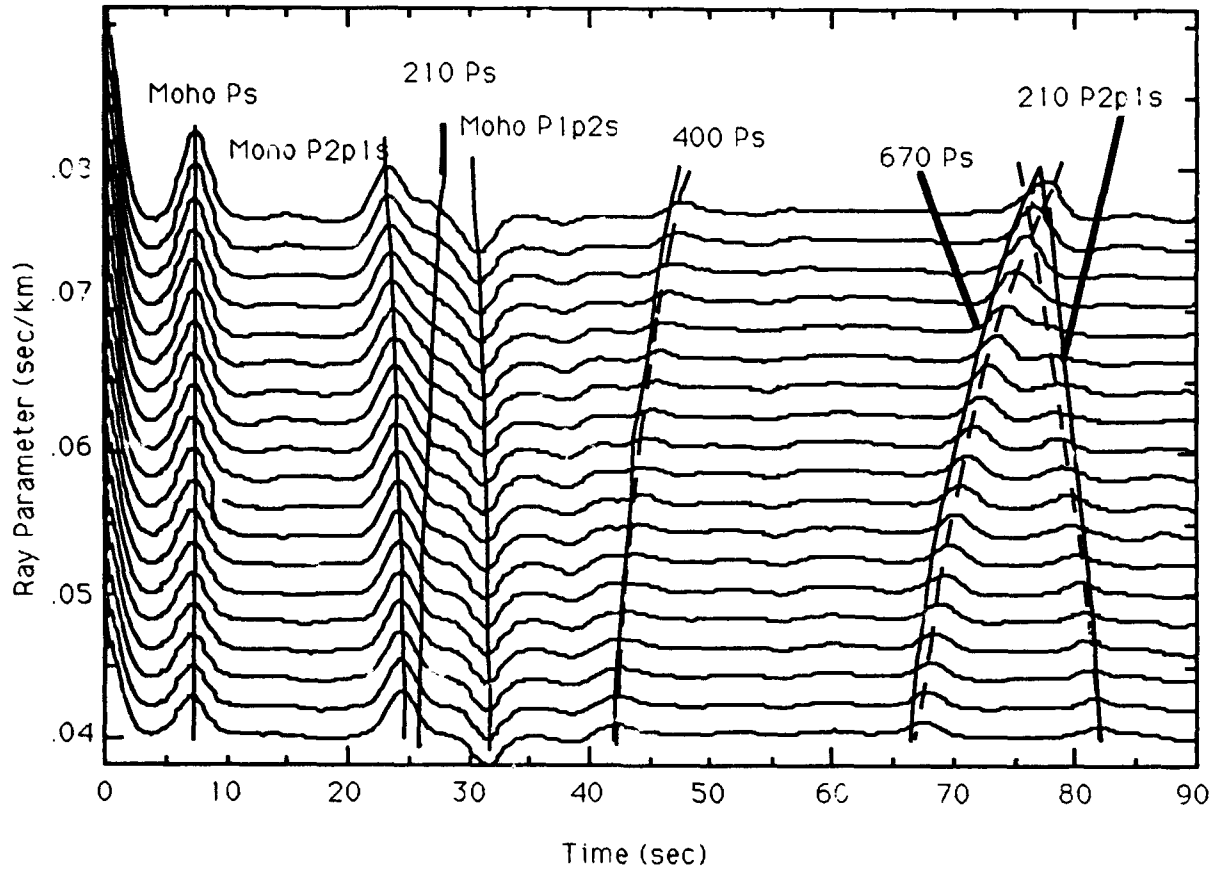


Figure 2. A representative display of the 80 low pass filtered PREM synthetic receiver functions used to compute the VSS in later figures. The moveout curve associated with Moho and upper mantle discontinuities are labeled. Dashed lines are the moveout curves computed for a curved ray path. The solid lines were computed for a single layer of equal vertical travel time and depth as the structure used to compute the respective dashed line.

Constant velocity stacks are produced by averaging along the moveout curve the amplitudes of N receiver functions with various ray parameters.

$$S(\Delta T_{\Phi 0}, V_s) = \frac{1}{N} \sum_{i=1}^N f_i(\Delta T_{\Phi}(\Delta T_{\Phi 0}, p_i, V_s, R_v)) \quad (3)$$

Where F is the type of phase (i.e. Ps); $S(\Delta T_{\Phi 0}, V_s)$ is the averaged amplitude at a given zero offset time and S-wave velocity; $f_i(\Delta T_{\Phi}(\Delta T_{\Phi 0}, p_i, V_s, R_v))$ is the amplitude of the i^{th} trace at the computed moveout time, $\Delta T_{\Phi}(\Delta T_{\Phi 0}, p_i, V_s, R_v)$, for a given wave type (Φ). If the moveout time falls between two samples we linearly interpolate a value for $f_i(\Delta T_{\Phi}(\Delta T_{\Phi 0}, p_i, V_s, R_v))$. After producing constant velocity stacks for the range of all reasonable velocities, we contour the amplitudes in the velocity-time plane to produce the VSS. The Ps conversion will appear as a positive ridge (negative for a velocity inversion) elongated parallel to the velocity axis. The velocity structure beneath a station can then be inferred by selecting the time and velocity of the highest amplitude on each ridge.

Figure 2 depicts the shapes of the Ps and P2p1s (reverberation) moveout curves computed for various depths using the PREM velocity model over the range of ray parameters typical of P-arrivals used in receiver function studies (0.04 to 0.08 sec/km for epicentral distances of 30° to 90°). The above procedure outlined the method of producing VSS for receiver functions analogous to that of the reflection method in which the structure to any given depth is replaced by a layer with vertical travel time equal to that of the "true" layered structure. However, from Figure 2, we observe that for upper mantle depths the "true moveout curves" (dashed lines) computed by ray tracing through PREM exhibit a greater amount of moveout than those computed by replacing the PREM structure above the interface with a single layer of equivalent average vertical slowness (solid lines). Because the amount of moveout is directly proportional to increases in velocity, it is clear that computing moveout using the single layer assumption outlined above will result in a high estimate of velocity when applied to data from layered structure. We notice in Figure 2 that the "true moveout curves" and the single layer moveout curves merge to the same zero offset time delay. As a result the time delays observed are true zero offset travel times but the velocities are overestimated which would result in an overestimate of the depths to the upper mantle discontinuities. This should affect observed data and synthetics in the same way, so that the procedure should be adequate to compare synthetics and observed data; it will of course work well for shallow layers. VSS computed with a time vertical axis are most useful for comparisons with PREM synthetics to determine which discontinuities are observable at a particular station. As a result, we can compute the time domain VSS more quickly using the method outlined above (equations 1 through 3). To estimate more accurately the velocity structure directly from VSS, we have refined our method of producing VSS by applying normal moveout corrections computed for curved ray paths and converting the vertical axis to depth (VSS_C).

The curved ray path normal moveout correction can be computed by ray tracing through a reference model. Because we do not need the amplitude information provided by ray tracing, it is quicker to compute moveout corrections by integrating the relative time delay (equations 1) due to each infinitesimally thin layers (dz) to the given depth (z₁).

$$\Delta T_R(z, p, V_S, V_P) = \int_0^{z_1} (\sqrt{V(z)_S^2 - p^2} - \sqrt{V(z)_P^2 - p^2}) dz \quad (4)$$

Equation (4) is used to compute the ΔT_R values required by equation (3) to produce "reference velocity model stacks" (RVMS) in the same manner that constant velocity stacks were produced in previous sections. By multiplying all velocities of the reference model by a constant fraction we compute a "fractional reference model". A VSS_C is then constructed by contouring RVMS produced for a range of different fractional reference models. The axes of the VSS_C are depth versus "fraction of reference model", therefore a phase identified on the VSS_C is characterized as a certain fraction or percentage above or below the reference model.

A SYNTHETIC EXAMPLE OF VSS APPLIED TO RECEIVER FUNCTIONS

Traditionally, receiver functions are used to model crustal structure but when used to interpret upper mantle structure we violate the following two approximations typical of most studies: the Ps converted phase arrives with the same ray parameter as the incoming P phase; and that the curvature of the earth is negligible.

Because all the moveout equations derived above were based on a flat-layered earth, we may use a classical earth flattening transformation (EFT, Aki and Richards, 1980) to map a flat earth structure into the spherical earth structure that will yield the equivalent seismograms. The transformation is not exact for P-SV waveforms, but it is exact for their travel times (Chapman 1973). Because the purpose of VSS is to sum the amplitudes of the receiver functions along the moveout curves in order to find the velocity and time delay for which the pulse of any given shape stacks most coherently, travel time preserving transformations will not reduce the effectiveness of the VSS method. In the following discussion all VSS will include a spherical earth correction. We will use the notation VSS_{sph} for the time domain VSS but we will continue to use the notation VSS_C for spherical earth depth domain VSS.

The assumption that the P and the Ps phases have the same ray parameter results in a slight error in the estimate of the shape of the moveout curve. This error behaves similarly to that described above for the curved ray path correction but results in only about a fifth as much error in the estimated velocity. We note that the absolute depth to the 670 km discontinuity will be shallow by about 5 km in the VSS to follow, however the relative depth, estimated between two stations will not be effected greatly by this error. We are currently working on a method using ray tracing to estimate moveout thereby avoiding the assumption of a constant of ray parameter.

In VSS_{sph} computed for the PREM synthetics, we observe Ps conversions from the 400 and 670 km discontinuities at about 41 seconds and 63 seconds time delays respectively. Because the Ps phase from the 220 km discontinuity is on the trailing edge of the Moho reverberations at 20 seconds there is no distinct arrival for it on the VSS; however the corresponding P2p1s phase appears strongly at 76 seconds on the P2p1s VSS_{sph} (see Figure 2).

Figure 3A shows a Ps VSS_c computed using PREM P and S velocities applied to the synthetics depicted in Figure 2. The peak associated with the arrival on the VSS_c lines up along the value of 1.0 on the horizontal axis and appear at the expected 670 km depth (the synthetics were produced using a constant ray parameter therefore the depth bias described above does not arise). The elongation of the peak from the low velocity—shallow depth corner toward the high velocity—greater depth corner demonstrates the trade off between these combination of parameters in producing similar moveout curves. Throughout the rest of this paper we will, therefore, refer to this peak as the "trade off peak".

By following the steps outlined above to generate the VSS_c but holding the model constant and varying the velocity ratio (R_v), we can produce a spectrum of stacked receiver functions (R_vSS) which will be most coherent at the proper value of R_v . Figure 3B depicts the R_vSS computed from the above PREM synthetics using PREM as the reference model. Though the resolution is poor, for this synthetic example, we observe the encouraging result that the expected value of $R_v = 1.82$ to 1.825 produces the greatest amplitude on the R_vSS .

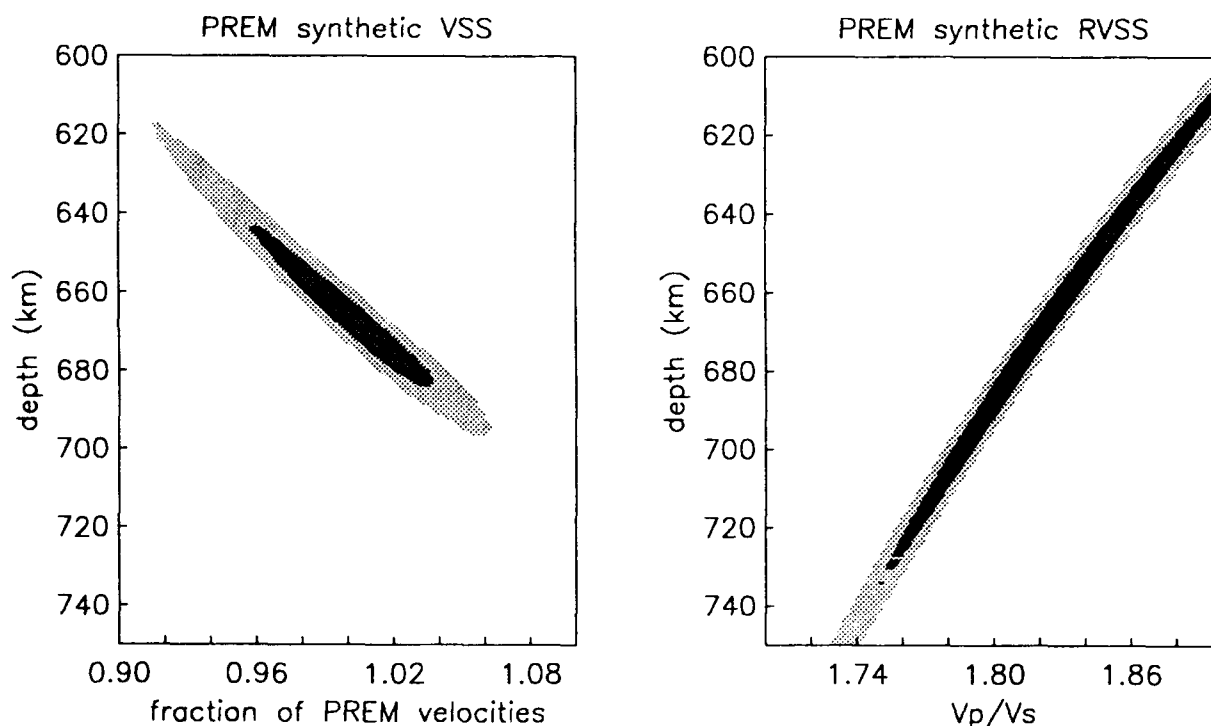


Figure 3. A) The VSS_c produced from the PREM synthetics depicted in Figure 2 using PREM for the reference model and R_v equal to 1.825. B) Velocity ratio spectrum stacks (R_vSS) computed using PREM for the reference model.

UPPER MANTLE DISCONTINUITIES BENEATH BROAD BAND STATIONS AROUND THE WORLD

We computed VSS_{sph} for all the stations listed earlier, with the following results: In general we do not see the reverberation from the 210 km discontinuity observed in PREM synthetics. The Ps conversion from the 410 km discontinuity is observed at most of the stations we have studied. At most of the stations the amplitude of the Ps conversion from the 410 km discontinuity is about half that of the 670 km discontinuity, however at both OBN and ARU the amplitude of Ps from the 410 km discontinuity is greater than that of the 670 km discontinuity. The Ps from the 670 km discontinuity at OBN and ARU are as prominent as that of PREM, therefore we believe that the

unusual amplitude relationship between these discontinuities is more the result of variation of the 410 km discontinuity rather than the 670 km discontinuity. The Ps from the 670 km discontinuity is the only upper mantle phase observed consistently at all the stations for which we have produced VSS_{sph} . We will focus our attention to the Ps phase from the 670 km discontinuity (P670s) for the remainder of the paper.

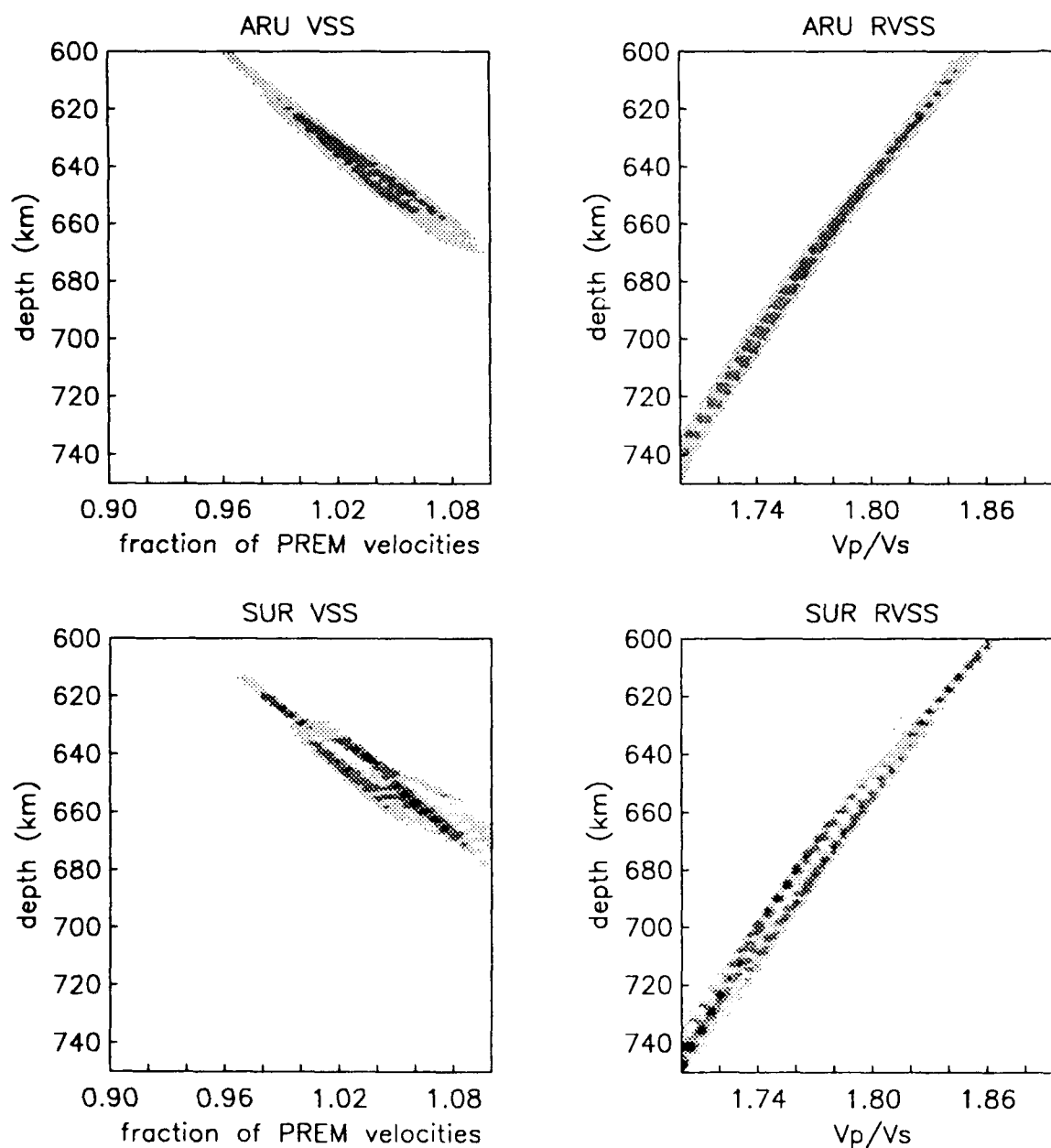


Figure 4. VSSc (left column) and R_{vSS} (right column) for data from receiver functions computed for ARU (top row) and SUR (bottom). The darker contour level is about 90 percent of the peak amplitude and the intermediate shade is from 80 to 90 percent of the peak amplitude.

Figure 4 shows VSSc and R_{vSS} for data from receiver functions computed for ARU (the VSS of this station has the sharpest peaks of those studied) and SUR (an average quality VSS). From the ARU VSSc we pick a depth

for the upper mantle discontinuity of about 640 km and a fractional velocity as compared to PREM of 1.03. The peak on the R_v SS is much broader and, in general, we prefer to use it to infer a bias (i.e. to infer whether V_p/V_s (R_v) is higher or lower than the approximate PREM value of 1.825), however for the sake of discussion we pick a value for R_v of 1.78 at a depth of 660 km. One would expect that the depths would match on these plots when we have the appropriate moveout correction. The fact that they do not indicates that we must search the three dimensional space (V_s , R_v , and depth) more thoroughly in order to find the velocity structure that will best stack these data.

We have tabulated estimates of the depth to the discontinuity (always taken from the VSSc), the fractional adjustment to PREM, and the V_p/V_s ratio from VSSc and R_v SS computed for each station (first three columns of Table 1). The last three columns are, respectively (from left to right) the depth to the discontinuity taken from Figure 4 of Shearer and Masters (1992), followed by the fraction of the PREM velocity and the V_p/V_s ratio measured using this depth on the VSSc and R_v SS. Comparing columns one and four of Table 1 we conclude that our depth estimates differ from those of Shearer and Masters' (1992) in a random manner. As mentioned earlier the VSSc and R_v SS are two slices of a three dimensional trade off peak and it is unlikely that the correct combination lies on either one. Upon inspection of the last two columns of Table 1 we see that all the stations with the exception of GAR require velocities higher than PREM but a lower V_p/V_s ratio than the 1.825 value computed from PREM. Considering that as a global model PREM is probably biased toward oceanic mantle structure, it is reasonable that the upper mantle beneath stations located primarily on continents would have a higher average velocity and it is even more likely that the V_p/V_s ratio beneath the continents would be lower than PREM.

Table 1

| Station | Depth (km) | Fraction of PREM velocity | V_p/V_s (R_v) | Shearer and Masters (1992) depth (km) | Fraction of PREM velocity 2 | V_p/V_s (R_v) 2 |
|---------|------------|---------------------------|---------------------|---------------------------------------|-----------------------------|-----------------------|
| AAK | 625 | 0.96 | 1.84 | 660 | 1.04 | 1.80 |
| ALE | 656 | 0.99 | 1.84 | 640 | 1.03 | 1.81 |
| ARU | 640 | 1.03 | 1.78 | 658 | 1.06 | 1.78 |
| ESK | 630 | 0.98 | 1.84 | 660 | 1.04 | 1.81 |
| ERM | 620 | 0.95 | 1.85 | 670 | 1.02 | 1.82 |
| GAR | 645 | 0.93 | 1.86 | 660 | 0.96 | 1.85 |
| OBN | 640 | 1.03 | 1.78 | 658 | 1.06 | 1.78 |
| RPN | 660 | 1.04 | 1.76 | 658 | 1.04 | 1.81 |
| RSCP | 645 | 1.04 | 1.75 | 650 | 1.05 | 1.81 |
| RSNT | 630 | 0.97 | 1.85 | 652 | 1.03 | 1.79 |
| RSNY | 652 | 0.98 | 1.85 | 652 | 1.00 | 1.82 |
| RSSD | 630 | 0.95 | 1.85 | 652 | 1.03 | 1.80 |
| SUR | 640 | 1.03 | 1.75 | 650 | 1.04 | 1.80 |
| TLY | 620 | 0.93 | 1.85 | 660 | 1.02 | 1.80 |

By recomputing the VSSc for ARU using a value for R_v of 1.78 derived from the last column of Table 1 (Figure 5), arrived at a depth estimate for the discontinuity much closer to that found by Shearer and Masters (1992). Though we are encouraged by this result, we are developing a technique to search the three dimensional space for the appropriate combination of parameters which best stacks the data. We hope that when it is possible to constrain one of the three parameters, a reasonable estimate of the other two can be made.

CONCLUSIONS AND RECOMMENDATIONS

Through the use of velocity spectrum stacks we can stack data from different ray parameters, and by doing so infer velocity structure beneath the seismographic station. The method looks most promising for the interpretation of upper mantle structure. The shape of the moveout curve for a particular phase is dependent on the depth of the interface from which it originates and the velocity structure above the interface. In order to compute moveout for the curved ray path of Ps phases for upper mantle discontinuities, we trace rays through a reference model and infer a fractional difference between the reference model and the structure necessary to satisfy the data. It should be clear

from the examples above that the depth of an interface from which the phase of interest originated is poorly constrained by the VSS method unless reasonable assumptions are made about the velocity structure or R_v .

We are continuing to develop the technique. We are working on a method to compute moveout corrections by ray tracing through a modified version of PREM (modified only directly beneath the receiver) in order to reduce errors as a result of assumptions basic to the receiver function method (not significant when modeling shallow structure). We will expand the VSSc method to include a full search of the model space and develop a method to assess the errors of our estimates.

REFERENCES

- Aki, K. and P. G. Richards, 1980, Quantitative Seismology Theory and Method, W. H. Freeman and Co., volume 1.
- Chapman, C. H., 1973, The Earth flattening transformation in body wave theory, *Geophys. J. Royal Astron. Soc.*, **35**, 55-70.
- Dziewonski, A.M. and D.L. Anderson 1981, Preliminary reference Earth model, *Phys. Earth Plan. Int.*, **25**, 297-356.
- Gurrola, H. J.B. and Minster, 1991, Single-Station Estimates of Crust and Upper Mantle Velocity Structure at Broadband IRIS/IDA Stations in the USSR, 13th annual Darpa/GL Seismic Research Symposium, Geophysical Laboratory Hanscom AFB, Mass. PL-TR-91-2208, ADA241325
- Langston, C.A., 1989, Scattering of teleseismic body waves under Pasadena, California, *J. Geophys. Res.*, **94**, 1935-1951.
- Langston, C. A., 1981, Evidence for the subducting lithosphere under southern Vancouver Island and western Oregon from teleseismic P wave conversions, *J. Geophys. Res.*, **86**, 3857-3866.
- Owens, T. J., R. S. Crosson, and M.A. Hendrickson, 1988, Constraints on the subduction geometry beneath western Washington from broadband teleseismic waveform modeling, *Bull. Seismol. Soc. Amer.*, **78**, 1319-1334.
- Owens, T. J., S. R. Taylor, and G. Zandt, 1987, Crustal structure at regional seismic test network stations determined from inversion of broadband teleseismic P waveforms, *Bull. Seismol. Soc. Amer.*, **77**, 631-662.
- Owens, T.J., G. Zandt, S.R. Taylor, 1984, Seismic evidence for an ancient rift beneath the Cumberland plateau, Tennessee: a detailed analysis of broadband teleseismic P waveforms, *J. Geophys. res.*, **89**, 7783-7795.
- Owens, T. J., S. R. Taylor, and G. Zandt, 1983, Isolation and Enhancement of the Response of Local Seismic Structure from Teleseismic Structure from Teleseismic P-waveforms, *internal report*, Lawrence Livermore Laboratory.
- Yilmaz, O., 1987, Seismic data processing. *Society of Exploration Geophysicists, investigations in geophysics* volume 2.

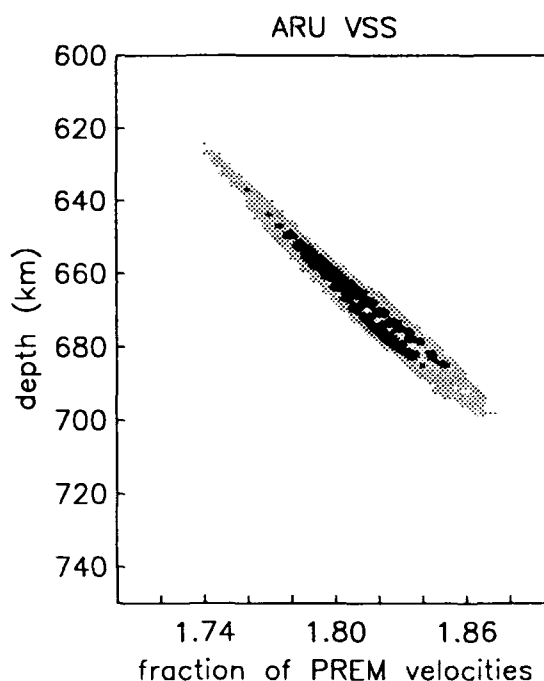


Figure 5. VSSc for ARU recomputed using a value for V_p/V_s of 1.78.

Site Effects, Regional Wave Path and Source Characteristics at GERESS

H.-P. Harjes, N. Gestermann, M. L. Jost, J. Schweitzer and J. Wüster

Institute of Geophysics, Ruhr-University Bochum, Germany

Grant AFOSR-90-0189

Objective

The German Experimental Seismic System (GERESS) array project is a cooperative research program of Southern Methodist University Dallas (USA) and Ruhr-University Bochum (Germany). GERESS is the newest member of a multi-array network that includes NORESS, ARCESS, and FINESA in Scandinavia (Harjes, 1990). The objective of research activities carried out at the data center in Bochum included the characterization of the array by looking at its ability to increase the signal to noise ratio (SNR) by beamforming. Another research objective centered on the assessment of regional path effects and the correlation to the complex geotectonic environment in Europe. Finally, we focussed on source effects in the waveforms of regional events observed at GERESS.

Research accomplished

a) GERESS P-wave detectability

Following a similar study at NORESS, a quantitative assessment of the SNR improvement by beamforming at GERESS was done for P-phases of strong local, regional, and teleseismic events at various frequencies and for different array subgeometries (Jost, 1992.)

DATA ANALYSIS

1. 13 partially overlapping band-pass filters were defined following Kvaerna (1989).
2. Using the 25 short-period vertical components of GERESS, 11 subgeometries were defined. Stations showing a large site effect, i.e., A0, A3, and B3, were omitted. A2-sz was chosen as reference station.
3. 28 strong events were selected. Since the GERESS array has not been fully acceptable (Golden et al., 1991), data of many strong events could not be used in this study.
4. For each event, wide-band frequency-wavenumber analysis (Kvaerna and Doornbos, 1986) was carried out.
5. For all events, detection processing was applied using the RONAPP on-line program system (Mykkeltveit and Bungum, 1984; Fyen, 1987). The SNR, short term average (STA), and long term average (LTA) detection values for all beams and single channels were determined. From these values, the SNR gain, noise suppression, and signal loss values were calculated.

$$NOISE\ SUPPRESSION = \frac{MEAN\ LTA\ OF\ CHANNELS\ IN\ BEAM}{BEAM\ LTA}$$

$$SNR\ GAIN = \frac{BEAM\ SNR}{MEAN\ SNR\ OF\ CHANNELS\ IN\ BEAM}$$

$$SIGNAL\ LOSS = \frac{MEAN\ STA\ OF\ CHANNELS\ IN\ BEAM}{BEAM\ STA}$$

$$SNR\ GAIN\ (db) = NSUP\ (db) - SLS\ (db)$$

The STA values were determined by averaging absolute values over 1 sec intervals. The LTA values were calculated by averaging over 30 seconds. Kvaerna (1989) has shown that the specific choice of these values does not influence the beamforming results.

RESULTS

The mean values for 5 of the 11 configurations (AB, ABC, ABCD, CD, and D) indicate that the full array has the highest SNR gain from 1 - 6 Hz and configuration ABC (inner 3 rings) from 6 - 10 Hz. Figure 1 compares the mean curves for GERESS and NORESS (Kvaerna, 1989) for the full array (ABCD) which is based on 25 channels at NORESS (14.0 db) and 22 channels at GERESS (13.4 db).

The differences between NORESS and GERESS can be explained by the noise characteristics at both arrays (see Harjes, 1990). At NORESS, low frequent noise (around 1 Hz) shows an order of magnitude higher peak spectral displacement values than at GERESS ($10\ nm^2/Hz$ versus $0.7\ nm^2/Hz$, respectively). From 3 - 6 Hz, GERESS records show cultural noise that varies with time of day. Cultural noise at NORESS is observed in the frequency range of 5 - 9 Hz. At high frequencies (around 10 Hz), the noise values at GERESS are significantly higher than at NORESS ($2.5 \cdot 10^{-4}\ nm^2/Hz$ versus $0.6 \cdot 10^{-4}\ nm^2/Hz$). These differences in noise level may serve as one explanation of the observed poorer SNR gains at GERESS in the frequency range of 6 - 10 Hz.

b) Regional path effects

Since the GERESS array became fully operational in 1991, numerous events at regional distances have been recorded. To assess the influence of structure on the waveforms recorded at GERESS, we divided the area around GERESS into 6 sectors (I - VI, Figure 2) in order to separate events from different azimuthal directions. The investigation was restricted to distances less than 800 km, because there are no events with greater distances from northern directions which can be compared with events from the south.

Most of the events from the same epicentral region show typical characteristics. It is observed that the S_n and L_g phases are most suitable to extract these characteristics (Gestermann, 1992.) The amplitudes of P_g or P_n seem to be more influenced by different source mechanisms and orientations. Investigations with synthetic seismograms confirm these observations.

Figure 3 shows events from sector III, grouped according to increasing epicentral distance from top to bottom. This sector is a very active zone especially at the Dinarides in the south with many earthquakes at the transition to the Adriatic Sea. No L_g wavetrain could be identified in the seismograms of events with epicentral distance of more than 500 km. At the same time, S_n is visible for epicentral distances greater than 350 km and is the dominant onset in the seismograms above 500 km.

Nearly the same situation can be reported from sector IV. The L_g wavetrain is missing for events with epicentral distances greater than 500 km and a corresponding dominant S_n phase can be observed which indicates a drastical change in crustal properties. In sectors V and VI the L_g wavetrain is prominent to several hundred kilometers with no visible decrease of amplitude in opposite to sector III and IV.

The explanation of this observed waveform variability is the very complex geotectonic situation. The Moho depth shows dramatic variations. Following Meissner et al. (1987), the most obvious

features are: The sharp boundary between the East European Platform and Palaeozoic Europe along the Teisseyre-Tornquist Zone, forming a deep graben (with a Moho depth of about 60 km). The deep mountain roots of the Cenozoic orogenies (Alps, Pyrenees, and Hellenides with Moho depths larger than 50 km). The rather uniform and small thickness of Phanerozoic Europe with the absence of any Caledonian and Variscan mountain roots (crustal thickness 29 km). The smallest continental depth correlating with areas of recent subsidence (Pannonian Basin, Black Sea, and North German Lowlands with Moho depths partially less than 20 km). Continental basins show substantial sedimentary coverage (e.g. the Pannonian Basin of sector II) that leads to very unusual waveforms with a large P_n onset followed by a long coda.

c) Source effects

Aside from natural seismicity, GERESS recordings are dominated by artificial events like quarries in near regional distances. A wide variety of sources resulting in different waveform signatures is observed and can be used for event classification.

As an example, both natural and artificial seismicity is observed in the Vogtland area, about 180 km NW of GERESS. The region extends on both sides of the German/Czechoslovakian border between 50°- 50°30' N and 12°- 13°E. Several German and Czech institutions operate seismic stations in or near the area and a common earthquake bulletin is being published.

Natural seismicity occurs mainly in the form of earthquake swarms. Two smaller swarms and several single events have been recorded since the GERESS array became operational in 1990. Artificial seismicity occurs in the form of mine and quarry blasts, mostly near the town of Karlovy Vary in Western Bohemia.

Figure 4 compares a typical Vogtland earthquake and a typical mine blast recorded at GERESS (GEC2, GS13 sampled at 120 Hz). The most striking differences between the two seismograms are:

- the amplitudes of P-wave impulses (much lower for earthquakes)
- the frequency content of the S-wave group (maximum at higher frequencies for earthquakes)
- the excitation of surface waves (very clear for blasts.)

In a CTB context as well as in the daily routine of a sensitive regional array such as GERESS, robust procedures are most desirable to identify different types of artificial seismicity (mine and quarry blasts, mining induced events) and to discriminate them from natural seismicity. Regions like the Vogtland area offer the opportunity to test various discrimination criteria with a uniform data set of high frequency high resolution digital recordings from GERESS in a setting, which minimizes wave-path and distance effects that usually complicate discrimination studies.

In a case study (Wüster, 1992), several discrimination techniques – obtained by quantification of heuristic criteria – were applied to a data set comprising 39 earthquakes and 22 chemical explosions from the Vogtland region. Discriminants employed included L_g/P_g and L_g/R_g maximum amplitude ratios, spectral peaks and slopes extracted by ARMA-modelling, master-event correlation and the search for time-independent frequency structures in sonograms. Master-event correlation was found to be the most effective single discrimination method. Under a joint discrimination scheme using simple majority voting, the two event populations could be separated with a misclassification ratio of only 2 %.

Conclusions and Recommendations

Following a study at NORSAR, an evaluation of the P-wave detectability was undertaken for GERESS. In the frequency range between 1 Hz and 3 Hz the full GERESS array reaches a higher SNR

gain than expected by \sqrt{N} . In the same frequency range, the SNR gain is also higher than at NORESS. GERESS shows a SNR gain similar to NORESS in the frequency band from 3 Hz to 6 Hz. At higher frequencies, the SNR gain at GERESS is significantly lower than at NORESS. The differences in P-wave detectability, observed at GERESS and NORESS, clearly correlate with the noise characteristics at both array sites. The study will be extended to address the S-waves which gain importance for automatic event location.

In contrast to the regional arrays in Scandinavia, GERESS is located in a complex geotectonic environment. The Alpine-Mediterranean earthquake belt to the South or the Tornquist-Teisseyre (TTL) suture to the Northeast are prominent examples (e.g., Tornquist, 1911; Meissner et al., 1987). As a consequence, regional phases show remarkable azimuthal variation. This study of the regional characteristics reveals that L_g and S_n are the most sensitive phases to separate the different propagation paths. In a further step, waveform modeling will be applied to look at effects of regional path.

There are regions in Central Europe, where both natural and artificial seismicity coexist. Events in these regions offer the opportunity to develop and test discrimination methods. In a case study, chemical explosions and earthquakes from the Vogtland region were separated effectively. Future research should focus on possible generalization and the physical basis of the discriminants used.

Literature

- Fyen, J. (1987). Improvements and modifications, Semiannual Technical Summary, 1 October 1986-31 March 1987, NORSAR Sci. Rep. No. 2-86/87, Kjeller, Norway.
- Gestermann, N. (1992). Characteristics of regional phases recorded at GERESS. In: Harjes et al. (1992)
- Golden, P., E. T. Herrin, and C. Hayward (1991). Results of the GERESS verification test, in: Development of an intelligent seismic facility and preparation for participation in the conference on disarmament group of scientific experts technical test, Quarterly Technical Report, Southern Methodist University, Dallas, Texas.
- Harjes, H.-P. (1990). Design and siting of a new regional array in Central Europe, *Seism. Soc. Am.* **80**, 1801-1817.
- Harjes, H.-P., N. Gestermann, M. Jost, J. Schweitzer and J. Wüster (1992). *Advanced Waveform Research Methods for GERESS Recordings, Annual Report: 15 Feb 1991 - 14 Feb 1992* Grant AFOSR-90-0189. Submitted to DARPA for distribution. PL-TR-92-2142
- Jost, M. L. (1992). GERESS P-Wave Detectability. In: Harjes et al. (1992)
- Kvaerna, T. (1989). On exploitation of small-aperture NORESS type arrays for enhanced P-wave detectability, *Bull. Seism. Soc. Am.* **79**, 888-900.
- Kvaerna, T. and D. J. Doornbos (1986). An integrated approach to slowness analysis with arrays and 3-component stations, Semiannual Technical Summary, 1 October 1985-31 March 1986, NORSAR Sci. Rep. No. 2-85/86, Kjeller, Norway.
- Meissner, R., T. Wever, E. R. Flüh (1987). The Moho in Europe - Implications for crustal development, *Ann. Geophys.* **5B**, (4), 357-364.
- Mykkeltveit, S. and H. Bungum (1984). Processing of regional seismic events using data from small-aperture arrays, *Bull. Seism. Soc. Am.* **74**, 2313-2333.
- Tornquist, A. (1911). Die Tektonik des tieferen Untergrundes Norddeutschlands, *Sitzungsberichte der königlich preussischen Akademie der Wissenschaften* **38**, 27.7.1911, 822-836.
- Wüster, J. (1992). Discrimination of chemical explosions and earthquakes in Central Europe - A case study. Submitted to *Bull. Seism. Soc. Am.*

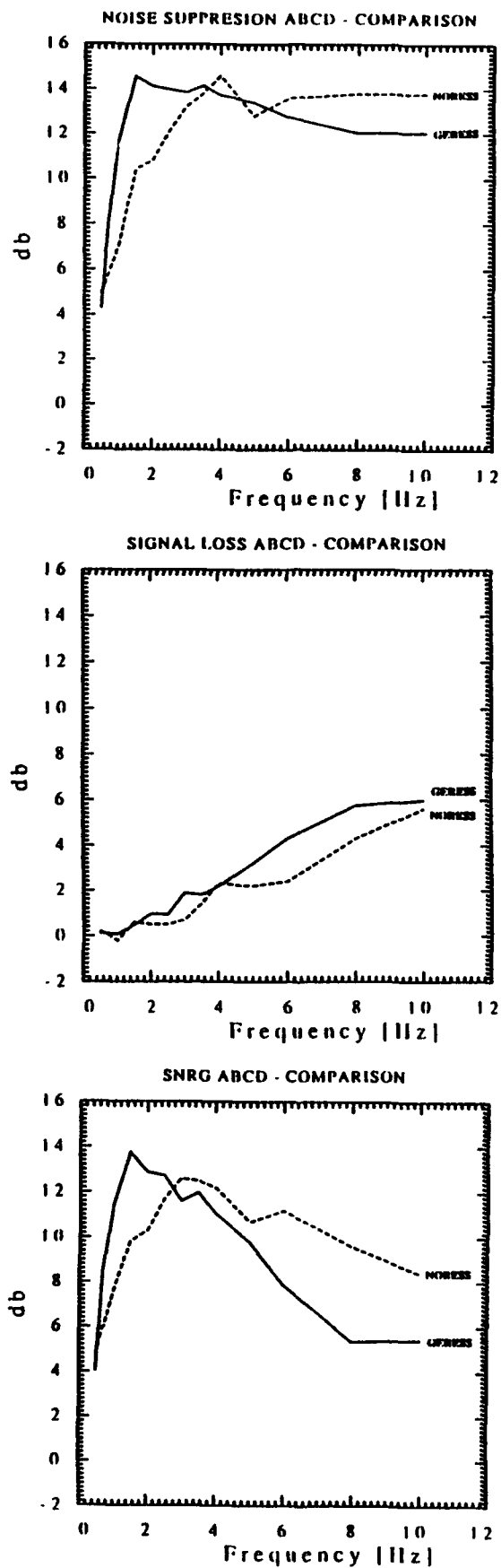


Figure 1: Mean curves of noise suppression, signal loss, and SNR gain for configuration ABCD of GERESS (solid line) and NORESS (dashed line; from Kværna, 1989).

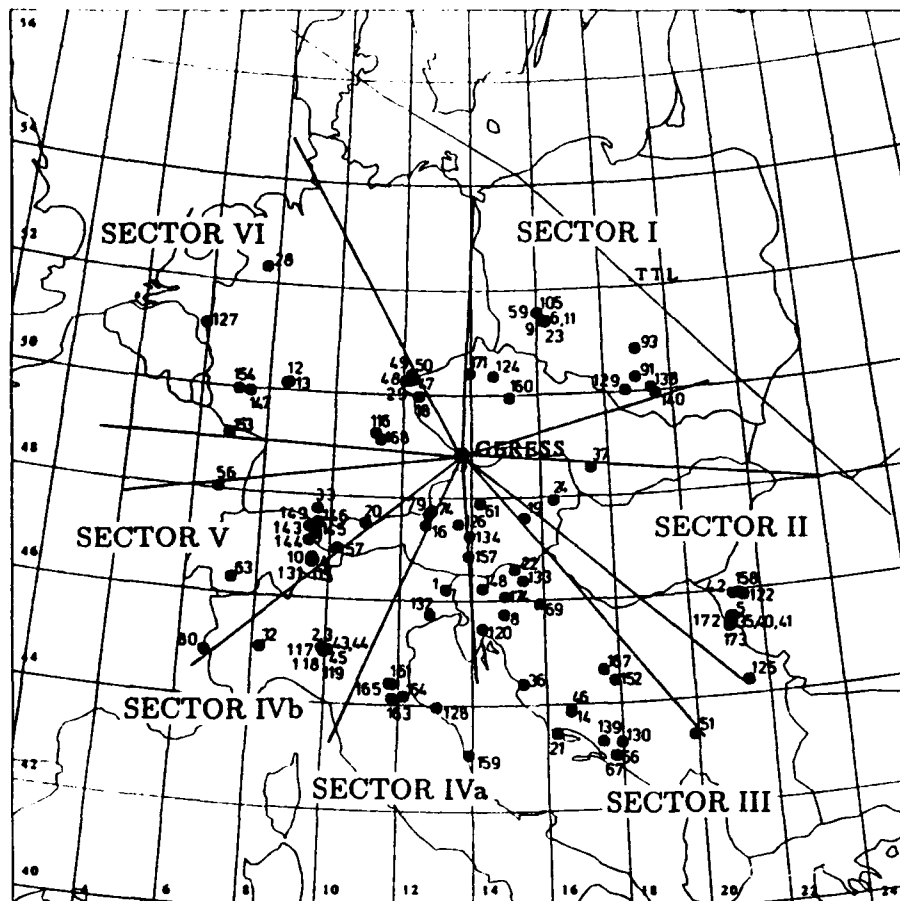


Figure 2: Map of epicenters.

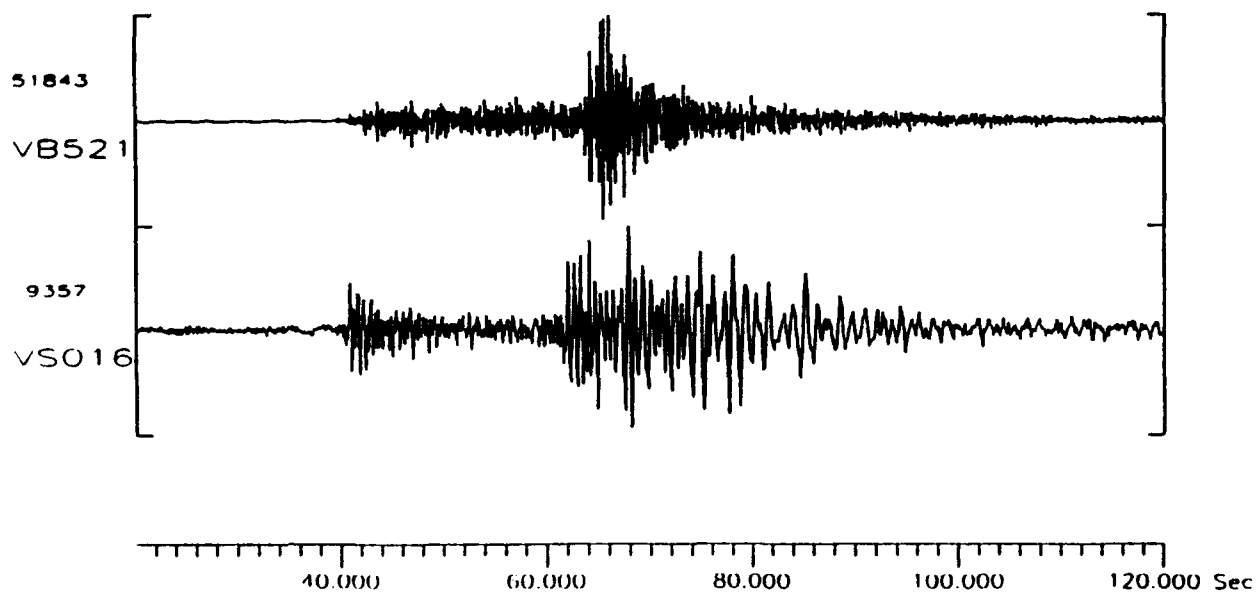


Figure 4: A typical Vogtland earthquake (VB521) and a typical mine blast from Karlovy Vary (VS016) recorded at GEC2.

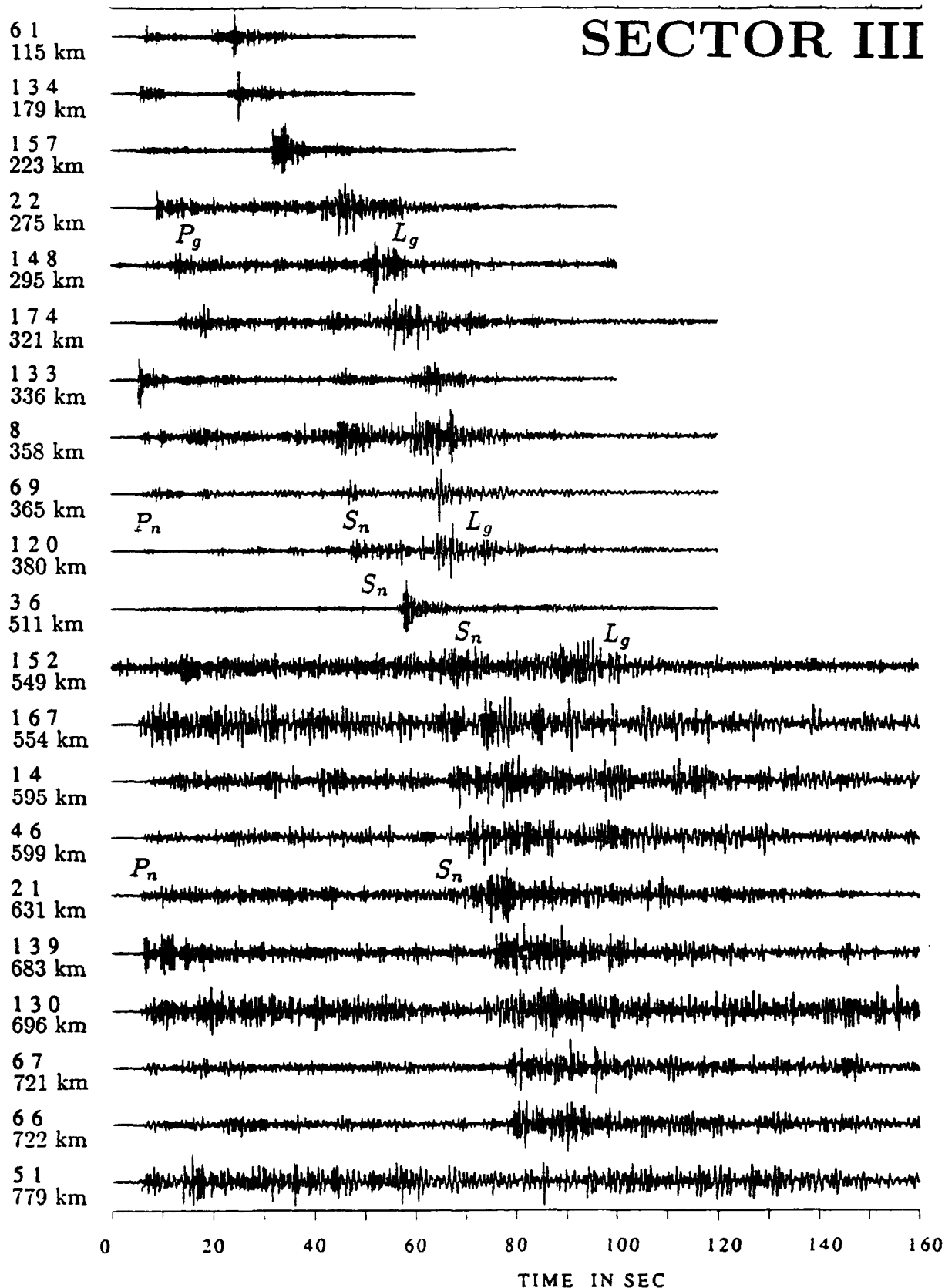


Figure 3: Seismograms of several events in sector III (GEC2). The numbers refer to the event numbers on the map (Fig. 2.) Distances are specified with respect to the GERESS array.

SINGLE STATION TIME DOMAIN TIME ESTIMATES OF SEMPALATINSK MOMENTS

D. G. HARKRIDER

Seismological Laboratory, California Institute of Technology,
Pasadena, California, 91125
F19628-90-K-0049

OBJECTIVE

The objective of this research is to determine surface wave magnitudes or moments from regional stations, which may have the only seismic data available for small events. Surface wave magnitudes or equivalent moments are especially important in estimating biases at new test sites for which there may be no calibration event.

RESEARCH ACCOMPLISHED

We have obtained from CSS over 40 Shagan River and 8 Degelen Mountain long period analogue Russian recordings. This data was part of the exchange of historical data between the USA and USSR. The most useful long-period data was from NVS, a distance of over 600 km from the Russian test site (Figure 1). The Russian instrument was very close in response to the Pasadena 30-90 Press Ewing and the Russian events appeared very similar to NTS events recorded at Pasadena. Time domain estimates are especially useful for analog seismograms in that the most common long period non-linearity can be corrected for in a straight forward manner. This instrumental non-linearity is frequently seen on the Caltech 30-90 recordings of NTS events.

Since the Rayleigh and Love wave-forms show little variation over the different events at this Russian test, we decided to restrict this study to time domain measurements of the moment. We do this by comparing the observed largest peak to trough amplitude to that of a theoretical Rayleigh or Love wave of known moment. In order for this to give realistic results, one needs to estimate the "so-called" path correction or theoretical wave-form. In Figure 2, we show the vertical seismogram for the Shagan River event of 25 April 1982. Below it we display the theoretical fundamental Rayleigh wave at the same distance for the Langston (personal communique) structure for stations to the northwest of the Semipalatinsk test site. The shear wave velocity in the model is an estimate based on the Leith P-wave velocity model in Priestly et al (198x). The fit is exceptional especially for the early arriving large amplitudes. We also show the two superimposed at the bottom.

The log moment determined from this path correction is 15.93 using the Langston model as source region model or 16.09 if we use Kazakh structure of Stevens (1986) for the source region. This agrees fairly well with the teleseismic surface wave value of 15.85 determined by Stevens (1986). The tectonic release mechanism determined from teleseismic surface waves by Given and Melman (1986) is given in Figure 3. The solid curve is the observed radiation pattern. The dashed curve is the corrected explosion relative to the observed amplitudes. For this event, the tectonic release effect should reduce the explosion amplitude by a factor of two. They obtained an explosion log moment of 16.17 and an F factor of 0.33. Their estimates use somewhere between 5 and 10 stations compared to our one.

The log moments for all the events are given in the Tables. Since NVS is almost due North of the test site, the horizontal instruments are almost naturally rotated so that the Love wave is essentially isolated on the E-W instrument and shows little contamination from the Rayleigh wave. Therefore a similar procedure can be used to estimate the Love wave moment with "canonical" assumptions concerning source mechanism.

CONCLUSIONS AND RECOMMENDATIONS

It is not our intention to use these near regional M_0 or M_s values to determine the tectonic release of small events but to establish a regional magnitude or moment relation to yield for events with small tectonic release. As mentioned above, the degree of tectonic release is easily determined from the SH waves seen on these regional 3 component stations. We also want to verify that the mb_M_s relation for Semipalatinsk agrees with the JVE determined mb bias because of its importance in transporting mb versus yield to regions where there may be no other calibration data.

References

- Given, J. W., and G. R. Mellman, 1986. Estimating explosion and tectonic release source parameters of underground nuclear explosions from Rayleigh and Love wave observations, SIERRA GEOPHYSICS, INC Final Report 1985-87, AFGL-TR-86-0171(I) for Contract No. F19628-85-C-0028. ADB110040
- Stevens, J. L., 1986. Estimation of scalar moments from explosion-generated surface waves, *Bull. Seism. Soc. Amer.*, **76**, 1233-152.

| Log Moments For Balapan Region | | | | | |
|--------------------------------|------------|-----------|--------|------------|-----------|
| Date | location | log M_0 | Date | location | log M_0 |
| mmddyy | | log(N-m) | mmddyy | | log(N-m) |
| 122869 | Av-KO | 15.27 | 122781 | Balapan SW | 16.06 |
| 090577 | Balapan NE | 15.50 | 042582 | Balapan SW | 15.93 |
| 061178 | Balapan SW | 16.04 | 070482 | Balapan SW | 16.14 |
| 082978 | Balapan NE | 15.80 | 120582 | Balapan SW | 15.96 |
| 110478 | Balapan NE | 15.16 | 121382 | Balapan SW | 15.98 |
| 062379 | Balapan SW | 16.03 | 122682 | Balapan NE | 15.41 |
| 070779 | Balapan NE | 15.98 | 061283 | Balapan SW | 16.12 |
| 080479 | Av-SR | 16.06 | 102683 | Balapan SW | 15.93 |
| 081879 | Balapan SW | 15.76 | 030784 | Balapan NE | 15.24 |
| 102879 | Av-SR | 15.99 | 052684 | Av-SR | 16.10 |
| 122379 | Av-SR | 15.84 | 102784 | Balapan SW | 16.12 |
| 091480 | Balapan SW | 15.80 | 120284 | Balapan NE | 15.54 |
| 101280 | Balapan NE | 15.95 | 121684 | Balapan SW | 16.06 |
| 121480 | Balapan SW | 15.71 | 021085 | Balapan SW | 15.89 |
| 122780 | Balapan NE | 15.63 | 040387 | Balapan SW | 16.24 |
| 032981 | Balapan NE | 15.06 | 080287 | Balapan SW | 15.60 |
| 042281 | Balapan SW | 15.87 | 122787 | Balapan SW | 15.95 |
| 091381 | Balapan SW | 15.98 | 021388 | Balapan SW | 16.04 |
| 101881 | Av-SR | 14.46 | 040388 | Balapan SW | 16.09 |
| 112981 | Balapan NE | 15.50 | 050488 | Balapan SW | 16.03 |

| Log Moments For Degelen Mountain | | | | | |
|----------------------------------|----------|-----------|--------|----------|-----------|
| Date | location | log M_0 | Date | location | log M_0 |
| mmddyy | | log(N-m) | mmddyy | | log(N-m) |
| 060875 | D.M. | 14.93 | 122683 | D.M. | 14.76 |
| 032977 | D.M. | 15.06 | 041584 | D.M. | 15.36 |
| 032678 | D.M. | 15.63 | 022687 | D.M. | 14.76 |
| 072878 | D.M. | 15.06 | 050687 | D.M. | 15.24 |

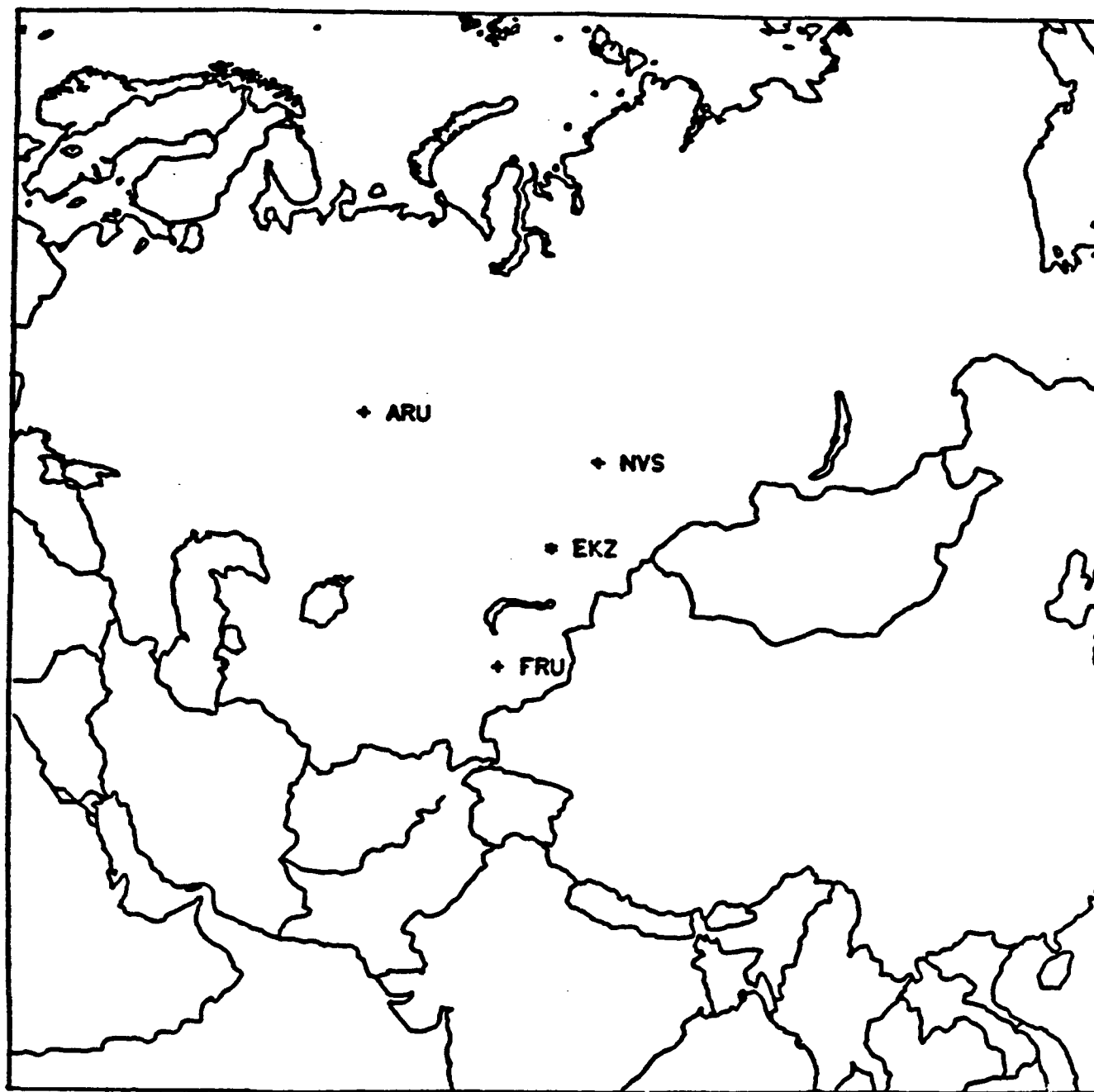


Figure 1. Map of Asia with the the East Kazakh test site and seismic station locations marked. Stations range between 580 and 850 km distant from the test site.

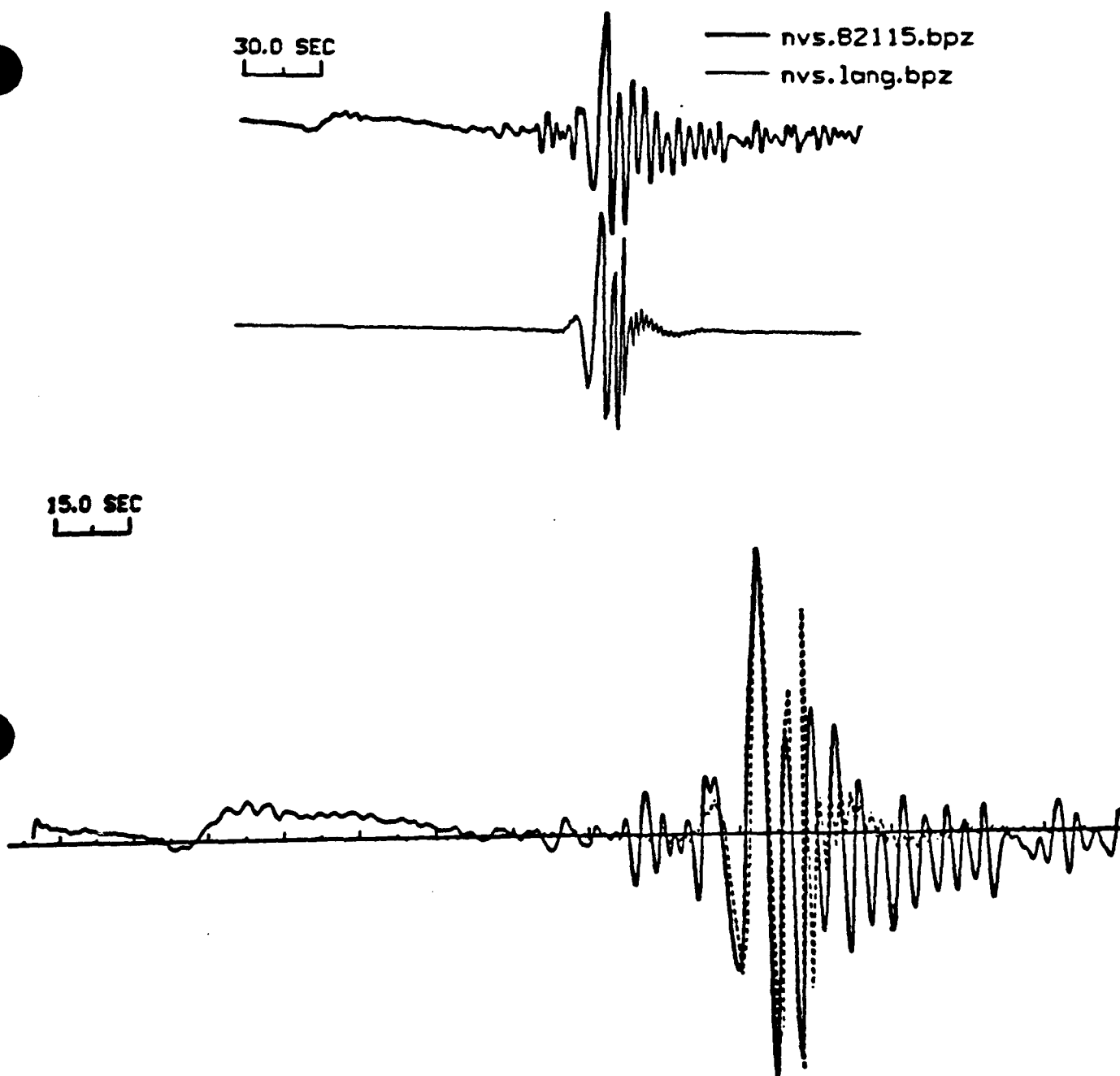
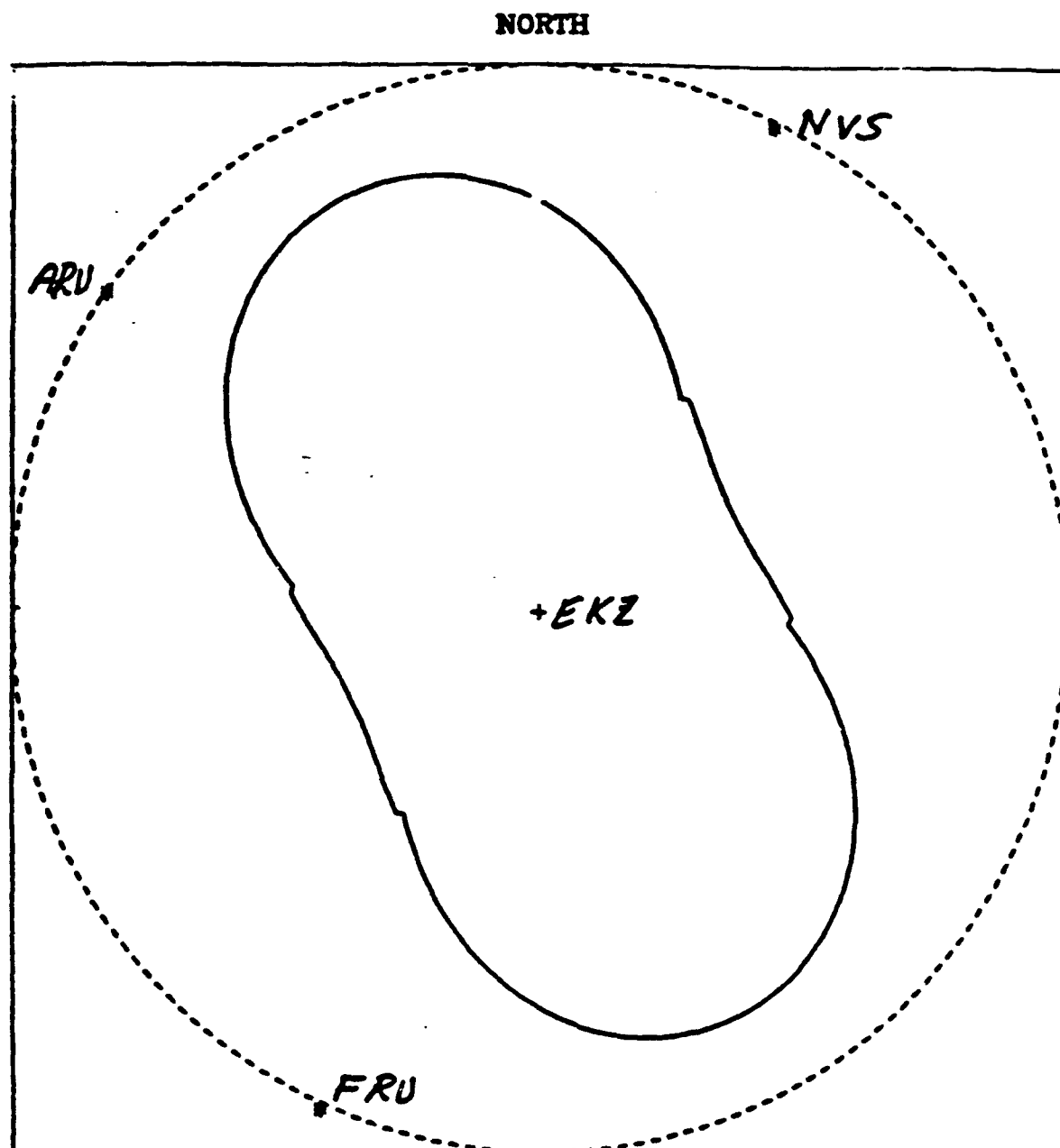


Figure 2. Comparison of a synthetic seismogram modeling the fundamental Rayleigh to the data wave-train of an Semipalantinsk explosion (4/25/82) recorded at NVS (distance=580 km). In the upper figure, the top trace is the data and the the lower trace is the synthetic. The lower figure is an overlay of the two traces , with the dashed trace being the synthetic. Time scales are displayed in the upper left-hand of each figure. The front portion of the Rayleigh wave-train, is modelled well by the synthetic. It is this longer period energy which is used to calcute M_0 and/or seismic moments.



radiation pattern

Figure 3. Radiation pattern for an explosion (dashed line). The addition of a reverse-thrust mechanism double couple with an equal seismic moment (F -factor=1) is given by the solid line radiation pattern. This mechanism is characteristic of events displaying tectonic release at the East Kazakh test site (Given and Mellman, 1986). Station azimuths for the historical network are marked along the dashed line; North is to the top of the paper. The network has good azimuthal coverage for having only three stations.

Source Estimation from Regional Seismograms

D. Helmberger, L. Zhao, and D. Dreger
California Institute of Technology

Contract No. F29601-91-K-DB14

Objective: One of the fundamental reasons why seismology is contributing to the monitoring of nuclear weapons is its prediction capability. That is, given a set of seismograms we can predict the nature of the source and its location. This has been demonstrated with both teleseismic body waves and well dispersed long period surface waves. To retrieve source information from regional phases requires an understanding of complicated path effects and the generation of Green's functions. This study addresses the issue of source estimation in this environment when modern instrumentation is available.

Research accomplished: With the installation of broad-band, high dynamic range instruments, it has become possible to compare the regional waveforms of different sized events. In many cases, events in the range of $M_L=3$ to 6 for a particular source region have similar waveforms indicating the prominence of regional Green's functions. Once these functions are established it becomes possible to estimate source parameters for small events from just one station. These functions can be established by forward modeling a regional record from a known source, master event, determined from a local array or from teleseismic observations ($M>5.5$).

Results : Results of our studies to date are either published or in press, i.e. Helmberger et al. (1992a and b), Zhao and Helmberger (1992), Zhao et al. (1992), and Dreger and Helmberger (1992). This review will primarily cover the last two which are concerned with source retrieval from the Garm station (GAR), and the structural complexity of the Hindu-Kush-Tibet tectonic belt. But, first we discuss our source inversion results from the recent Yucca Mountain event, where we will also review the basic method.

(a.) Yucca Mountain event

On June 29, 1992, a $M_w=5.5$ event occurred at 36.6° north latitude and 116.3° west longitude at 10:14:22 UT (NEIC). This event was recorded by the Caltech TERRAScope array and at several stations of the National Broadband Network. Five stations, PAS (320 km), PFO (332 km), BKS (544 km), ANMO (908 km) and COR (1065 km), were used to determine the fault plane solution and seismic moment by inverting the three-component regional waveforms. A solution of strike= 178° , rake= 119° , dip= 48° , and $M_0=2.5 \times 10^{24}$ dyne-cm was obtained. Observations of teleseismic P-waves at HRV and COL agree with the normal-motion mechanism and give a source depth of approximately 12 km. Figure 1 compares simulated Press-Ewing data and synthetic waveforms.

This inversion scheme uses only the long period bodywave portion of the regional records (surface waves are removed in the first pass) and assumes a 1D standard southern California model. A catalog of Green's function, as a function of range and depth is used to estimate four parameters; strike, dip, rake, and M_0 . The inversion results are given at the top of figure 1 along with the observations and predicted synthetics at the bottom.

For the TERRAScope stations (PAS and PFO) there is good agreement in both amplitude and waveform. Note that the polarity of the SH waves reverses between 211° and 182° azimuth. The P_{nl} and SV-wave fit at BKS is remarkable, considering that the same velocity model was used for this station as was for PAS and PFO. Only the P_{nl} waves were used at the more distant stations. The fit at ANMO is good using synthetics computed with a layer over a half-space crustal model, see Helmberger and Engen (1980) for details. The fit at long-periods at COR are

adequate, but the simple layer over a half-space model fails to produce the strong P-wave arrival observed in the data. This arrival is probably produced by a P-wave which turns in the upper mantle as modeled by Bent and Helmberger (1991). Note that the onset of the P-wave at COR is negative, which is also predicted by the synthetic.

The general procedure and resolution issues are discussed in detail in Dreger and Helmberger (1992). One station proves effective in source estimation in many situations if P, SV and SH body waves are available. The depth phases such as sS are particularly important. In the next section we apply this technique to recovering source information in the Hindu-Kush region.

b.) Source Retrieval from the GAR station

The crustal velocity is established by modeling the regional waveform data from a master event. This master event is large enough to be recorded teleseismically and modeled in detail, both short period and long period, and relocated using the depth phases, see Zhao and Helmberger (1991). The mechanism used here is for event 89205, an event at a depth of 85 km, see the map in figure 2 along with the focal mechanism (tele). The preferred four layered crustal model is given in Table 1. A comparison of the synthetics predicted from this model assuming the (tele) mechanism is displayed against the GAR observations. The tangential motion is not used since it proves to be nodal. Also, included in this figure is the source inversion results. The mechanism and location information is given in Tables 2 and 3.

Most of the smaller events are not well constrained in depth, i.e., depth=33 km. But from the experience gained in relocating events beneath Tibet, Zhao and Helmberger (1991), we expect the location to be quite good in comparison. Essentially, the depth trades off with origin time. This means that we must explore the depth and to a lesser extent the range to GAR before attempting an inversion. Thus we compare a catalog of Green's functions with the waveforms to make these adjustments, see figure 3 for an example set of Green's functions at a distance of 355 kms. Since we do not know the mechanism initially we must begin by exploring with the three fundamental faults. For example, we find that the 45° dip-slip synthetics fit the observations of event 90064 reasonably well on the vertical and radial components, while the strike-slip looks more like the tangential observation, see figure 4a. Adjusting the timing and waveshapes by varying the depth and range we obtain the fits in figure 4a. The bottom portion of the figure contains the inversion results, figure 4b.

Two solutions for this event are available since this event can be seen teleseismically; namely strike 169°, dip 30° and rake -57° and moment 2×10^{25} dyne-cm from NEIC; and strike 192°, dip 36° and rake -46° and moment 2×10^{25} dyne-cm given by the CMT solution (Harvard), see Table 3. The source depth ranges from 3-60 km from different agencies (see ISC bulletin for details). Figure 4b gives the comparison of data with the synthetics predicted by the different source mechanisms. The top darker traces are the data. The second set of traces are the synthetics of the source mechanism, strike 85°, dip 77°, rake 4°, $M_0 = 8.8 \times 10^{24}$ dyne-cm obtained by the whole waveform inversion and the third trace uses only a portion of the waveforms denoted by arrows. The bottom traces are the synthetics of the CMT source mechanism.

Inversion results from the third trace are very close to the Harvard solution and are almost the same as the mechanism given by NEIC. This solution and the CMT solution give very nice surface wave fits to the data. However, the partial waveform solution predicts the wrong polarity of both P_n and S_n (SH component) phases. The whole waveform solution is almost a pure strike-slip, however the partial waveform solution is the summation of pure strike-slip, dip-slip and 45° with about same strength for the P-SV waves. The source mechanisms from inversion and others are given in Table 3, along with magnitude information. It is clear that the source mechanism that predicts the best fit to the whole waveforms of one station may not be the same as the source mechanism from more stations and points out the limitation of the one-station waveform inversion. Results for some other events are given in figures 6 and 7. These inversions yield

quick good fits and are probably useful in establishing smaller "master events". That is they can be used to calibrate other systems, case-based event characterizations, etc.

Conclusions and Recommendations

A basic problem in the above approach is that we are mapping 3D structural variations into mislocations. That is, in making adjustments in (Δ, d) we probably produce incorrect locations. Perhaps allowing some (δt) timing corrections between P_n and S_n determined by calibration events could help as suggested by Helmberger et al. (1992b). Still another method for estimating such corrections could come from a detailed regionalized of P_n and S_n , see figure 8.

Generally, we find it relatively easy to model the entire SH motion but consistently have problems with the Rayleigh waves which appears to show considerable distortion caused by the shallow structure. This is observed in southern California and is probably universal. However, by simply comparing the amount of observed Rayleigh wave energy to that in synthetics in conjunction with the SH results we can probably produce meaningful depth estimates routinely.

References

- Bent, Allison L. and Donald V. Helmberger, (1991). Seismic characteristics of earthquakes along the offshore extension of the western transverse ranges, California, *Bull. of the Seismol. Soc. of America*, **81** 2, 399-422.
- Dreger, D. S. and D. V. Helmberger, (1992). Determination of Source parameters at Regional Distances with Three-Component Sparse Network Data, *J. Geophys. Res.*, in press.
- Helmberger, D. V., R. Stead, P. Ho-Liu, D. Dreger, (1992b). Broadband modeling of regional seismograms; Imperial Valley to Pasadena, *Geophys. J. Intern.*, in press.
- Helmberger, D. V., L. S. Zhao, D. Dreger and V. LeFevre (1992a). Exploration of the lower Lithosphere; Northeastern United States, *Phys. Earth Planet. Intr.*, **70**, 22-38.
- Zhao, L. S. and Helmberger, (1991). Geophysical implications from relocations of Tibetan earthquakes: Hot lithosphere, *Geophys. Res. Lett.*, **18**, 2205-2208.
- Zhao, L. S., D. V. Helmberger, and Harkrider, D. G., (1991). Shear-velocity structure of the crust and upper mantle beneath the Tibetan Plateau and southeastern China, *Geophys. J. Int.*, **105**, 713-730.
- Zhao, L. S., J. Xie and D. Helmberger (1992), Lateral variations in compressional velocities beneath the Tibetan Plateau from P_n travel time tomography, submitted to *Geophys. J. Res.*

Table 1. Models

| Thickness (km) | One-Layer | | Four-Layer | |
|-------------------|-----------|---------|------------|---------|
| | α | β | α | β |
| 2.5 | 6.35 | 3.70 | 4.55 | 2.55 |
| 17.5 | 6.35 | 3.70 | 6.16 | 3.50 |
| 20.0 | 6.35 | 3.70 | 6.55 | 3.70 |
| 25.0 | 6.35 | 3.70 | 6.70 | 3.80 |
| 20.0 | 8.00 | 4.80 | 7.98 | 4.57 |
| - | 8.50 | 4.85 | 8.50 | 4.85 |

Table 2. Information of Earthquakes

| PDE | | | | | | Relocation | | | |
|-------|--------|-------------|----------|-------|-----|-------------|----------|-------|------------------|
| Event | Date | origin time | Location | | | origin time | Location | | |
| | mmddyy | hhmm sec | Δ | Depth | | hhmm sec | Δ | Depth | |
| 89205 | 072489 | 0327 | 49.1 | 328 | 97 | 0327 | 48.9 | 325 | 85 ^M |
| 89124 | 060489 | 2225 | 25.0 | 200 | 40 | 2225 | 19.3 | 200 | 20 ^S |
| 89146 | 062689 | 0108 | 44.8 | 439 | 30 | 0108 | 49.2 | 445 | 35 ^S |
| 90036 | 020590 | 0516 | 45.1 | 230 | 131 | 0516 | 44.5 | 235 | 100 ^M |
| 90038 | 020590 | 0516 | 45.1 | 230 | 131 | 0516 | 42.8 | 245 | 100 ^S |
| 90064 | 030590 | 2047 | 3.5 | 336 | 33 | 2047 | 4.5 | 320 | 10 ^S |
| 90065 | 032690 | 2219 | 29.5 | 324 | 33 | 2219 | 29.0 | 315 | 10 ^S |
| 90091 | 040190 | 0046 | 51.0 | 364 | 96 | 0046 | 48.0 | 365 | 80 ^S |
| 90111 | 042190 | 0206 | 28.5 | 321 | 111 | 0206 | 27.4 | 295 | 100 |
| 91026 | 012691 | 0814 | 4.6 | 226 | 33 | 0814 | 1.5 | 225 | 10 ^S |

^M is master event, ^S is the event whose source mechanism is obtained by waveform inversion.

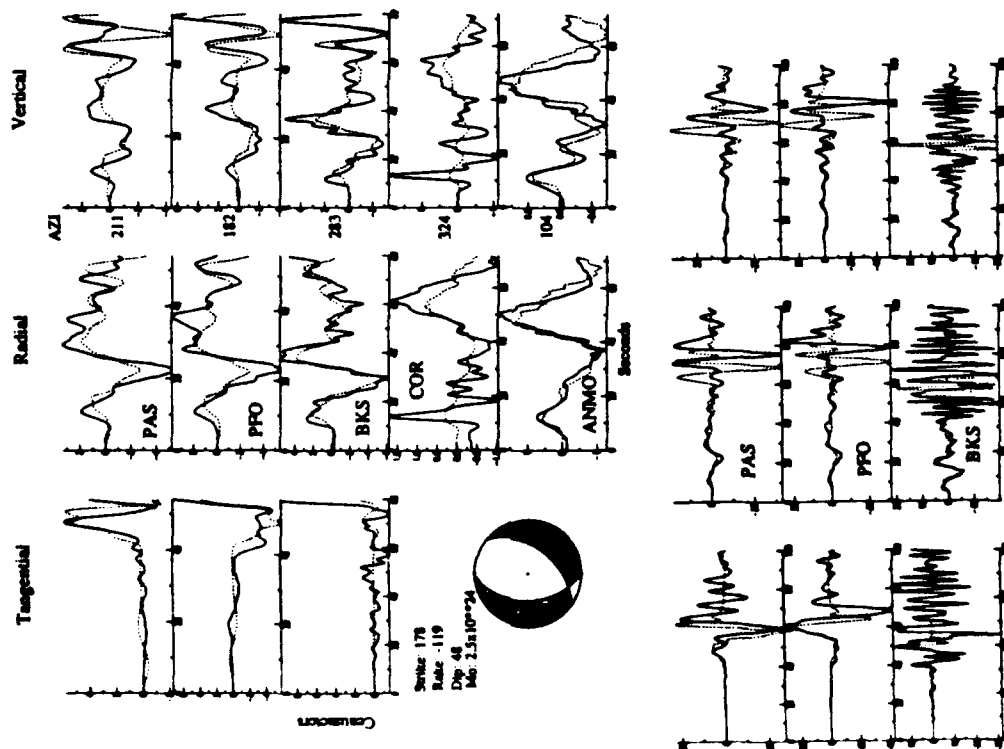


Figure 1.) Comparison of observed and synthetic waveforms for the recent Yucca Mountain event. The upper portion displays the bodywave inversion results at two TERRAscope stations along with a few more distant stations. The lower panel shows the whole seismogram predictions. The latter portions of the comparisons show little agreement which indicates the importance of lateral variations in the shallow structure.

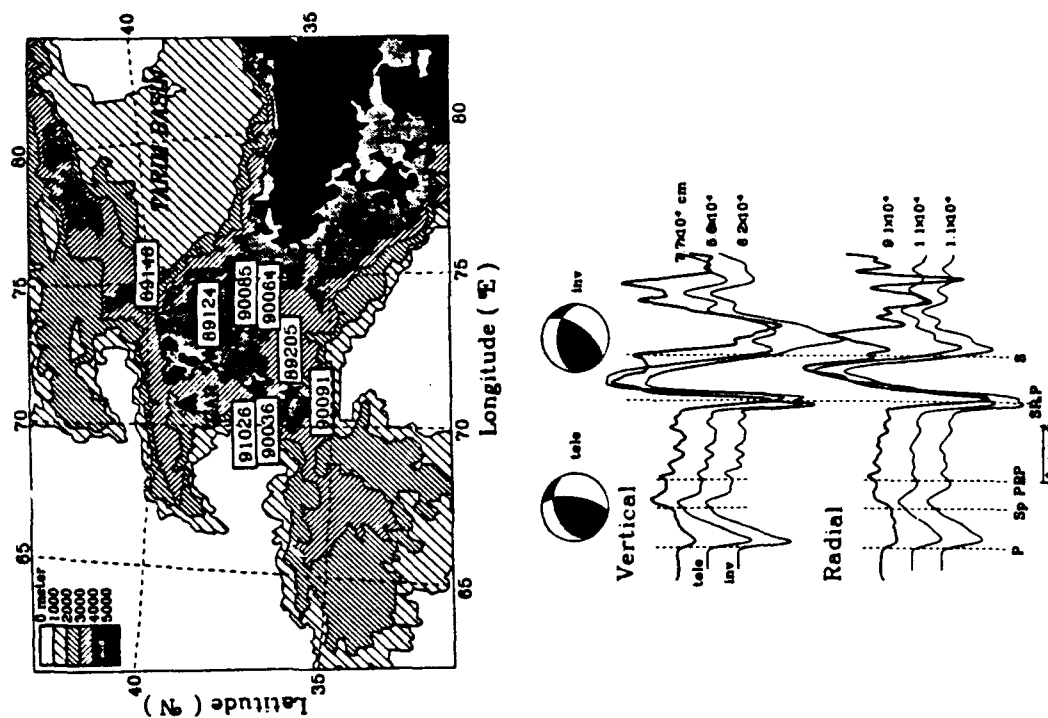


Figure 2.) Upper map displays the events and geometry relative to the GAR station. The lower panel displays the comparisons between observations and synthetics. The lower synthetic was obtained by inversion while the middle trace corresponds to a prediction assuming the teleseismic mechanism and moment. Motions are in cms of displacement.

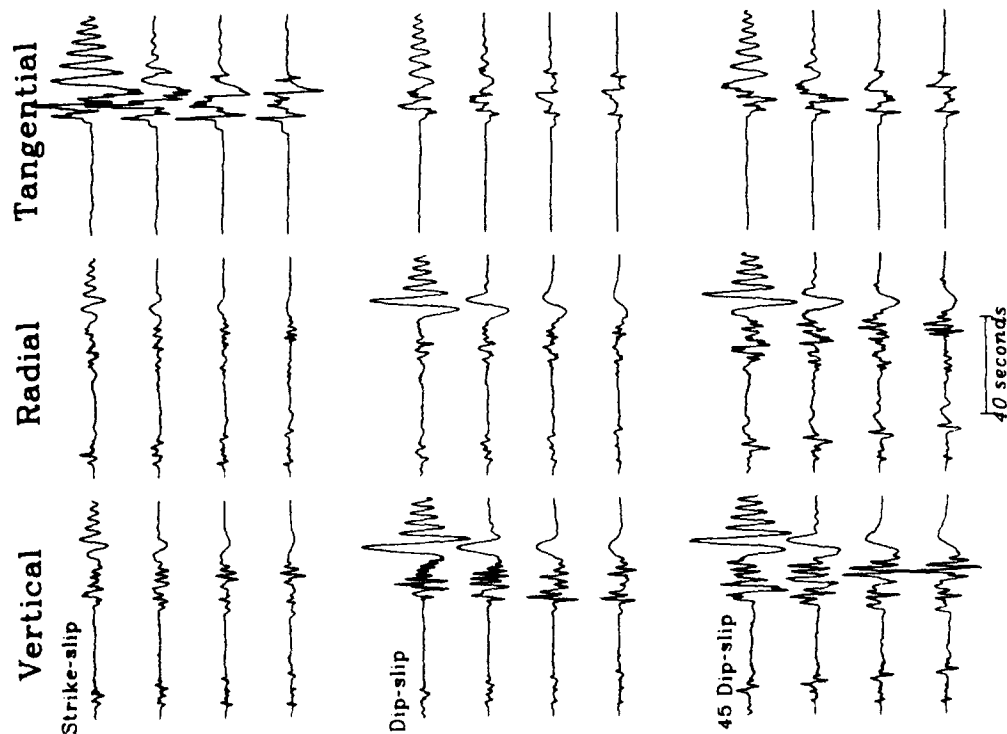


Figure 3.) Set of synthetics assuming the model given in Table 1 at a distance of 355 km for the fundamental fault orientations. The motions are on the same scale for an assumed moment.

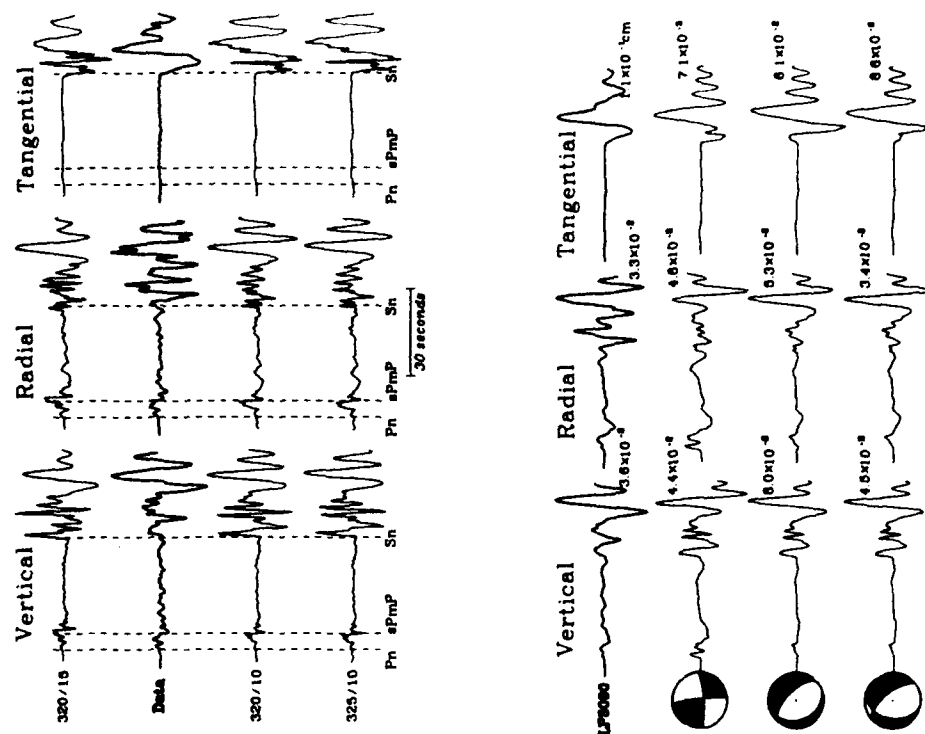


Figure 4a.) Determination of the source depth and source-receiver distance for the 90064 event. For the vertical and radial components, 450 dip-slip synthetics are used, and for the tangential, strike-slip is used. "320/15" means distance 300 and depth 15 km. The best fit is obtained with "320/10". The comparison of the 90064 data with the synthetics of the resulting source mechanism from inversion is given in figure 4b. The second traces are the synthetics of the resulting source mechanism from the whole waveform inversion, the third from the waveform after S_n and the fourth, the Harvard moment tensor solution.

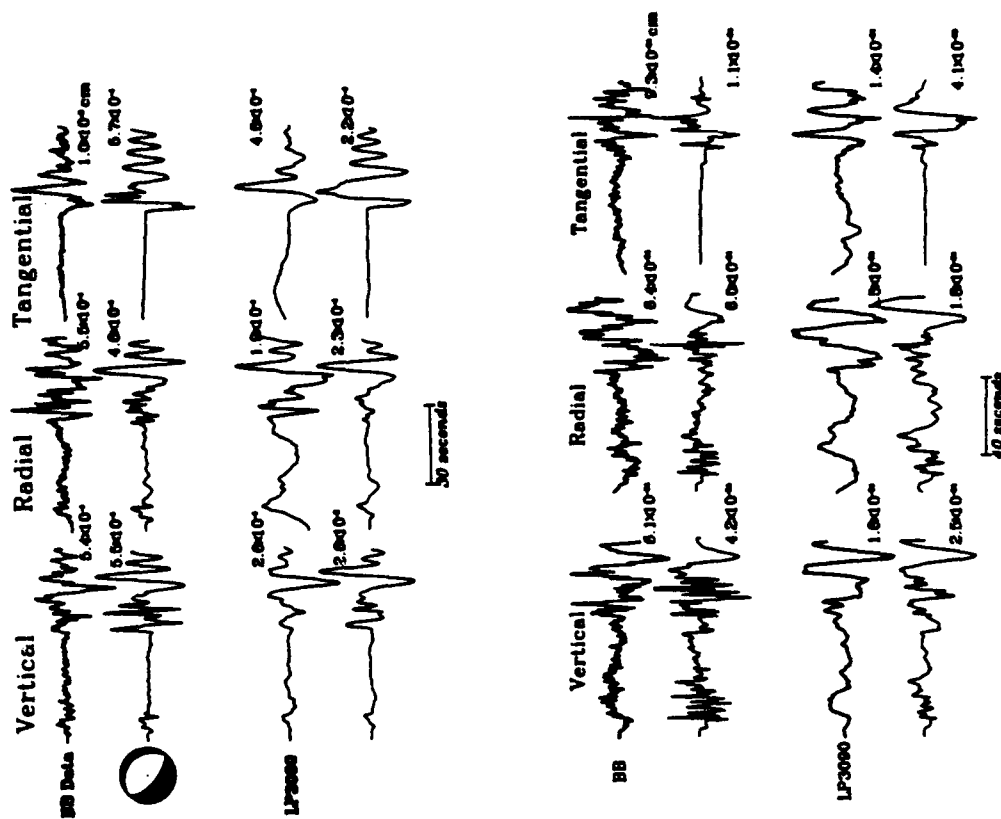


Figure 6. Upper panel displays a comparison of the 90085 event with inverted synthetics both BB and long period. A source depth of 10 km was used in the inversion. The lower panel displays a similar result for event 89146 which occurred at a depth of 35 km relative to our Green's functions.

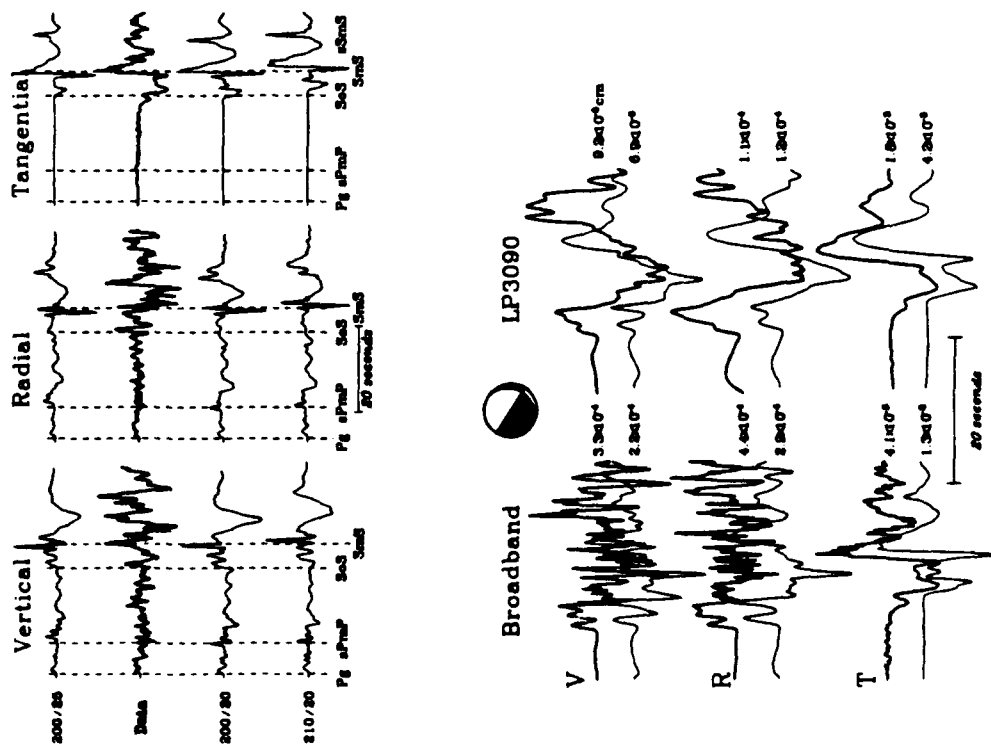


Figure 5. Determination of the source depth and source-receiver distance for the 89124 event, "20025". For the vertical and radial component, the 450 dip-slip synthetics are used and for the tangential, the dip-slip. The source function is a 0.5 0.5 triangle. The lower panel contains a comparison of the 89124 data with the inverted synthetics and associated mechanism.

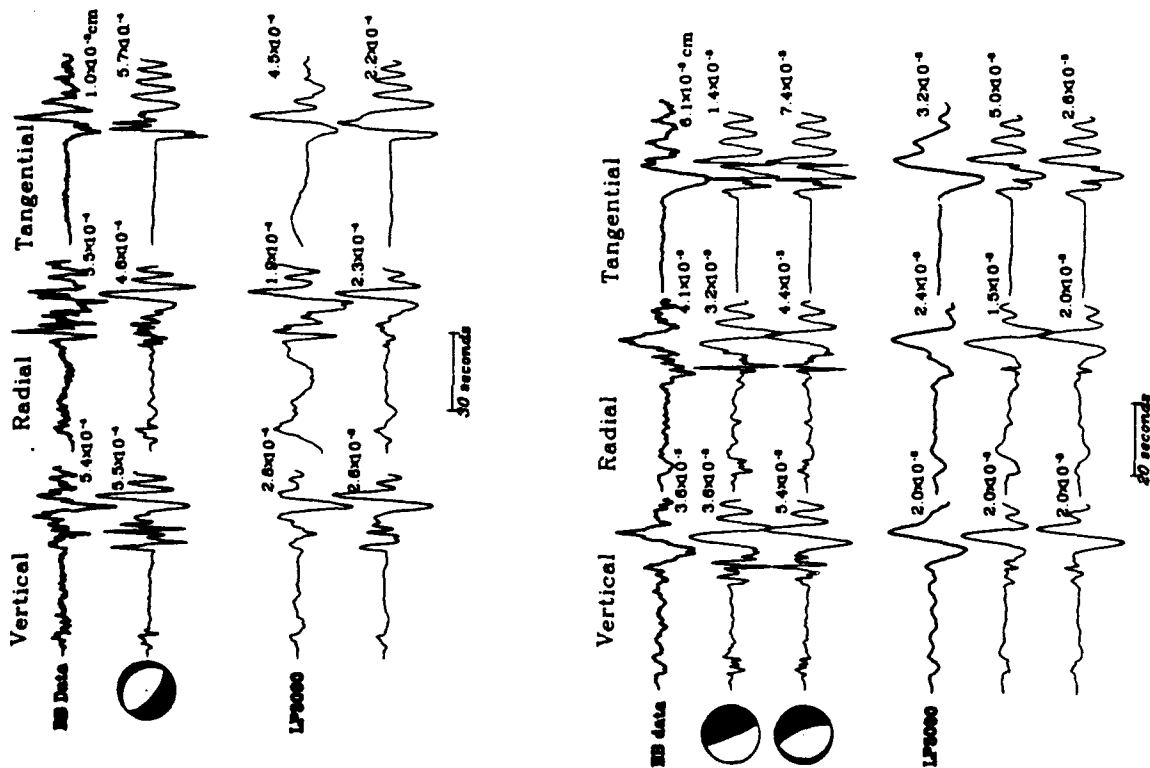


Figure 7. Upper panel displays a comparison of the 90085 data with inverted synthetics, both BB and long period. The lower panel displays the comparison of the 91026 data with inverted synthetics of the resulting source mechanisms from whole and part waveform inversion.

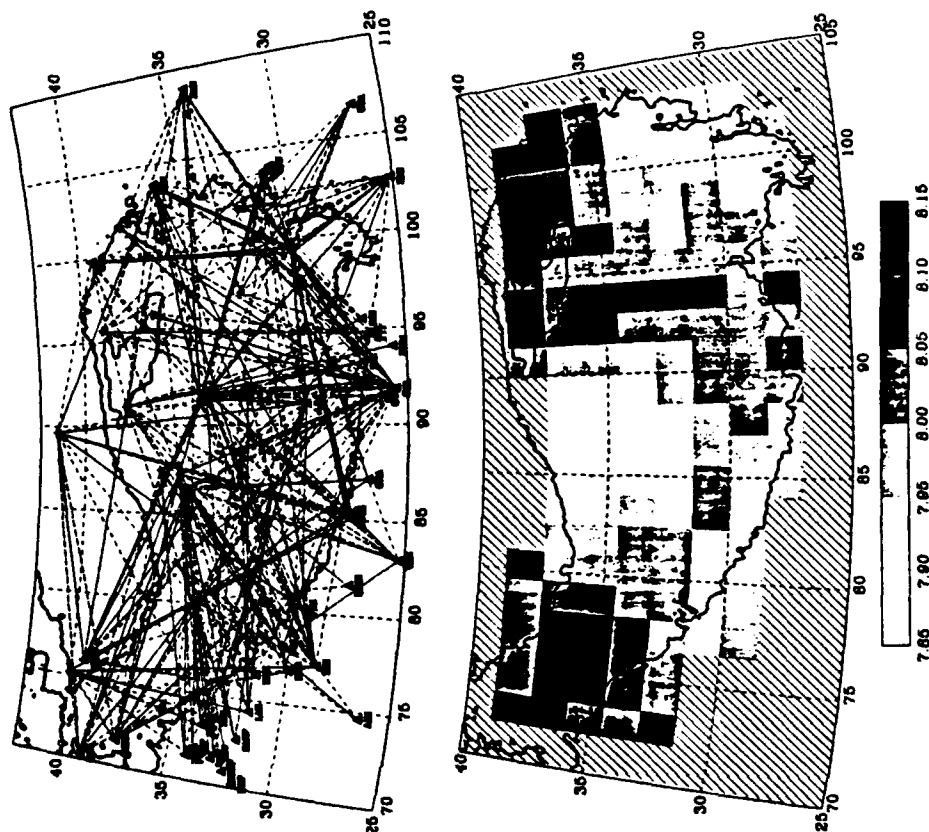


Figure 8. The upper panel displays the P_n paths from 'relocated events' (Zhao and Helmberger, 1991) to regional stations. The bottom panel indicates the P_n velocities obtained by a tomographic inversion.

Source Multiplicity Examined with Minimum Entropy Deconvolution

Ivan Henson and Robert Cessaro
Teledyne Geotech Alexandria Laboratory,
314 Montgomery Street, Alexandria, VA 22314-1581

Contract No. F29601-91-C-DB02

OBJECTIVE

The objective of this project is to investigate the feasibility of using minimum entropy deconvolution (MED) as a technique for discriminating ripple-fired explosions from other seismic events. The effectiveness of this approach under varying conditions, including shot delay times, data sampling rate, frequency content and signal to noise ratio will be determined.

RESEARCH ACCOMPLISHED

First introduced by Wiggins (1977, 1978), minimum entropy deconvolution is a method of generating a linear filter capable of transforming its input signal into a signal with its energy concentrated into as few spikes as possible. This is referred to as maximizing the spikiness of the signal, which is equivalent to minimizing its disorder, or minimizing the entropy. If the the input signal can be characterized as the convolution of a seismic source wavelet with a series of spikes, MED represents a deconvolution operation. We assume that the seismic signal from a multiple shot blast can be modeled as the superposition of time delayed replications of the signal from a single shot. This implies that a deconvolution method could be used to extract the shot delay times from the multiple shot signal.

The design of the MED filter centers around a mathematical measure of the spikiness of a signal. For example, the varimax norm suggested by Wiggins (1978) is

$$V = \frac{\sum_i y_i^4}{(\sum_i y_i^2)^2},$$

where y_i represents the seismic signal. Maximizing V with respect to the filter coefficients leads to an equation which can be iteratively solved for the MED filter coefficients. The solution of the equation is particularly simple, since it involves a toeplitz autocorrelation matrix. Filter designs based on other norms have also been suggested. Ooe and Ulrych (1979) investigated the use of an MED norm including an exponential transformation with a damping coefficient to control the effect of noise. We have experimented with both of these norms. Several parameters in the specification of these filters, such as filter length and exponential damping coefficient, can be adjusted to fine tune the filters.

The MED algorithm has been integrated into an interactive X Windows program for seismic data analysis, where the effects of the filter parameters and the effects of the data window length and position can easily be tested. This program permits display of the MED

filter along with the resulting filtered signal after each iteration. Using synthetic data, we have found that the filter which actually maximizes a particular norm frequently does not deconvolve the data as well as one of the filters from an earlier step in the iterative solution.

We have tested the algorithm on data from known and suspected quarry blasts. Figure 1 shows vertical component short-period data recorded at station KK of the Soviet/NRDC data set, at a distance of 180km from the source. Many events from this data set are suspected to be mining blasts, and its high sample rate (250sps) make it an appropriate choice for attempting to deconvolve sources separated by time delays on the order of tens of milliseconds. The middle waveform in Figure 1 is the first 6 seconds of the signal shown on the top. A 2.8-second (700 point) MED filter was generated for this data window. The filtered or deconvolved data is shown on the bottom of Figure 1. The output of the filter operation is typically time shifted by an arbitrary amount, because the MED algorithm does not constrain the phase of the filter. The deconvolved data consists of three pairs of impulses separated by 380 and 170 msec. The time between the impulses of each doublet is a nearly constant 47 msec. We suspect that the three doublets represent three different phase arrivals. The doublet nature could be due to source multiplicity, although this was the only record for which we obtained such a result from more than 50 records that were examined.

The algorithm has also been tested on data from a known quarry blast, for the case of a shot separation time smaller than the data sampling interval. The shot layout and time delays for a quarry blast about 32 km from the Oklahoma Geophysical Observatory are shown in Figure 2. The average delay time between shots is approximately 9 msec. There were a total of 27 shots spanning approximately .25 seconds. Figure 3 shows a vertical component borehole recording of the signal from this quarry blast at station LNO. The sample rate for this record is 60 sps, i.e. a sample interval of 17 msec. An MED filter was generated for the first second of the signal, shown in the middle of Figure 3. The deconvolved data is shown at the bottom of the figure. The first three impulses span less than .25 second, and thus may represent the primary deconvolution result from the 27-shot signal.

To determine if the MED algorithm can actually deconvolve shots where the shot separation time is less than the data sampling interval, we have tested the method on synthetic seismograms. A simplistic synthetic seismogram was generated by summing a record from this event, with time shifts equal to the shot delay times plus a 10 percent random deviation in time. The MED algorithm failed to recover any of the simulated shot impulses. To determine the resolution of the algorithm, synthetic seismograms were generated with shot separation times equal to an integral multiple, from 2 to 5, of the actual shot separation times. The algorithm was unable to recover any shot impulses until the shot separations were 5 times the original values, or the average shot separation was 45 msec. The method recovered 10 of the 27 shots when it was applied to a high-pass filtered synthetic (10 to 30hz), shown in Figure 4.

CONCLUSIONS AND RECOMMENDATIONS

Our experience with applying this deconvolution method to synthetic and real data from quarry blasts leads us to several observations about the nature of the technique. In general, the algorithm is not robust, but is very sensitive to the filter parameters, filter length and filter damping coefficient. It is also sensitive to the data window length and position. Tests with synthetic data indicate that the filter which performs the best deconvolution frequently does not correspond to that which maximizes the data norm, but occurs earlier in the iterative solution for the maximum. In addition, the deconvolution of individual shots is not possible when the shot separations are less than approximately three times the data sampling interval. For cases where the data sampling interval is adequate, the sensitivity of the algorithm will remain as the chief obstacle hindering attempts to develop the method into an automatic discriminant.

REFERENCES

- Wiggins, R. A. (1977). Minimum entropy deconvolution, *Proc. Int. Symp. Computer Aided Seismic Analysis and Discrimination*, IEEE Computer Society, 7-14.
- Wiggins, R. A. (1978). Minimum entropy deconvolution, *Geoexploration*, **16**, 21-35.
- Ooe, M., and T. J. Ulrych (1979). Minimum entropy deconvolution with an exponential transformation *Geophys. Prosp.*, **27**, 458-473.

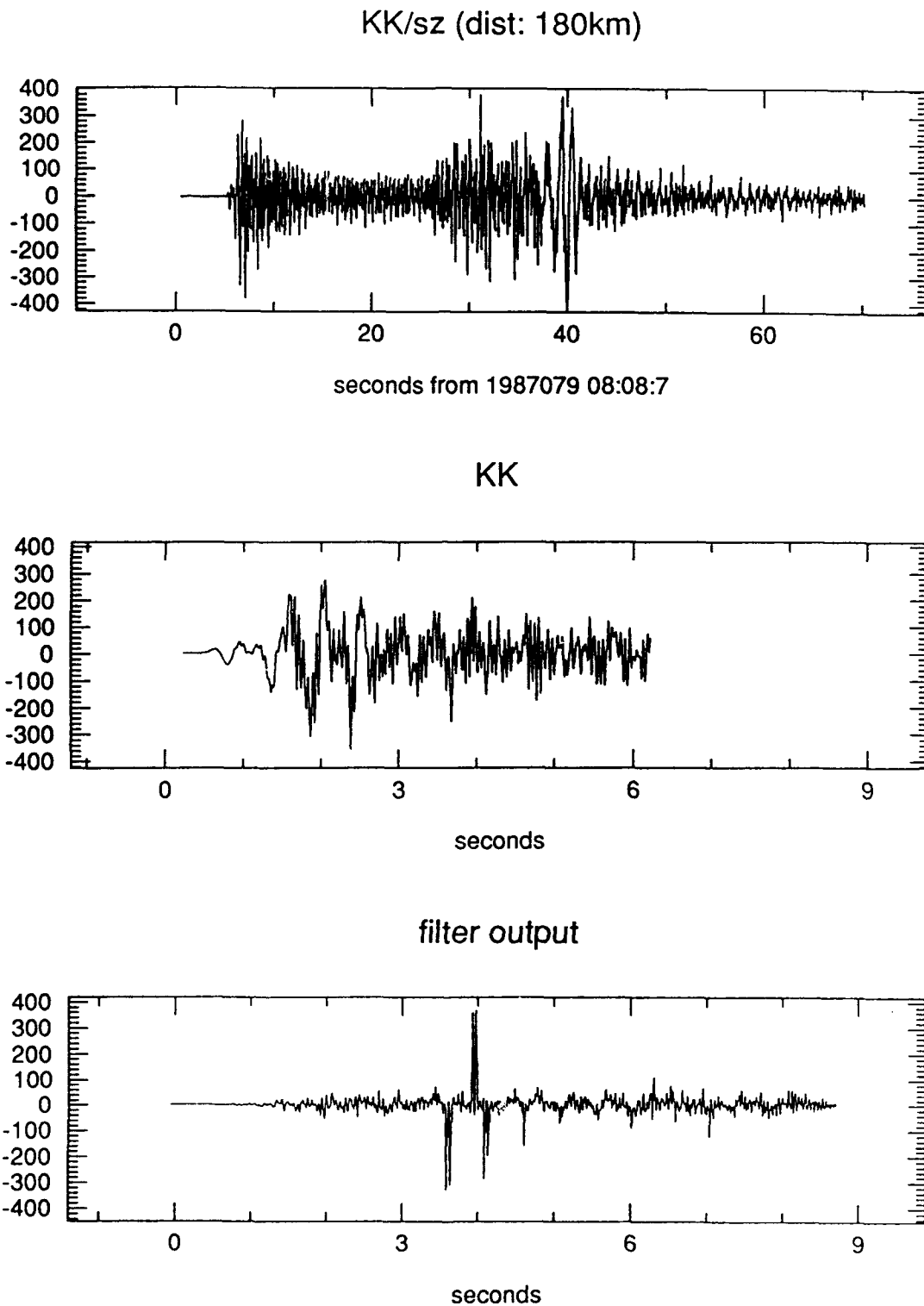
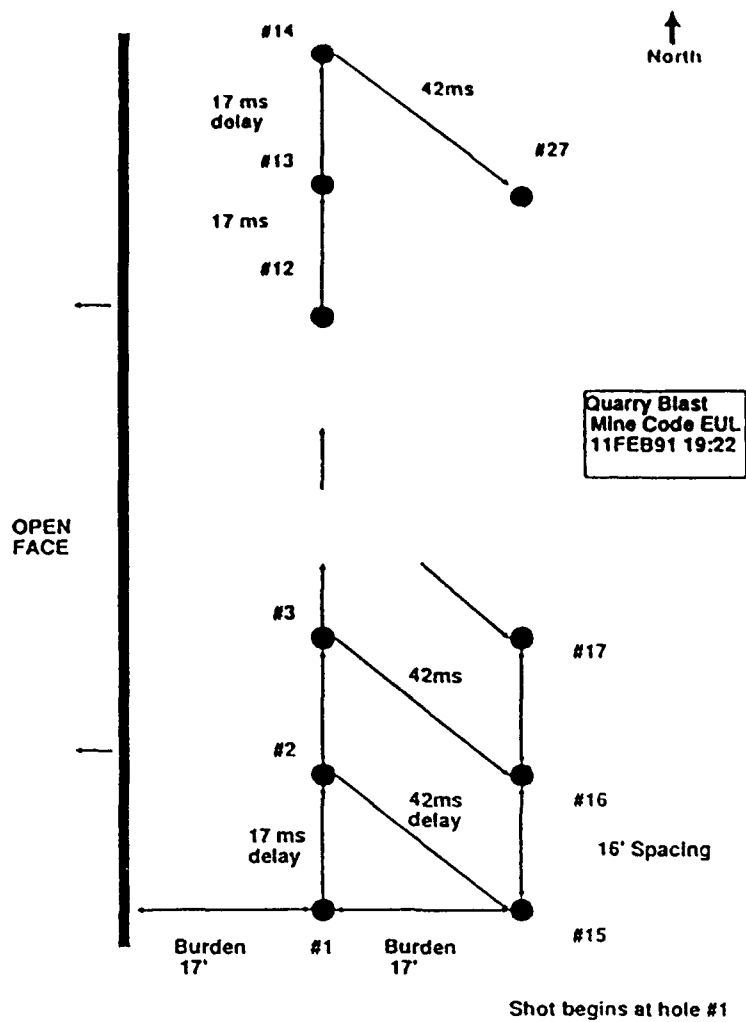


Figure 1. top: Vertical component record from station KK for an event at (49.9N, 73.1E). middle: Data window at the beginning of the signal for which an MED filter was generated. bottom: The deconvolved data window. The time between the impulses in each of the three doublets is a nearly constant 47 msec.



shot times

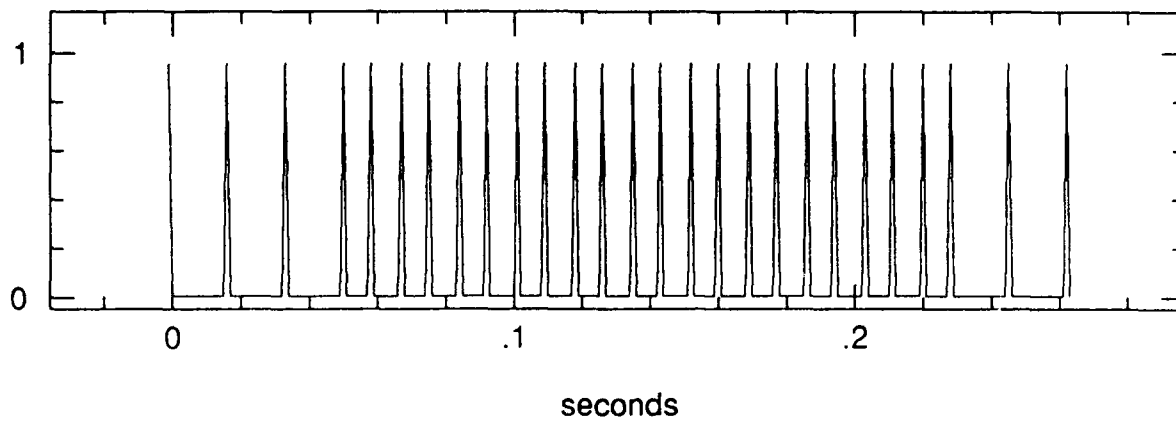
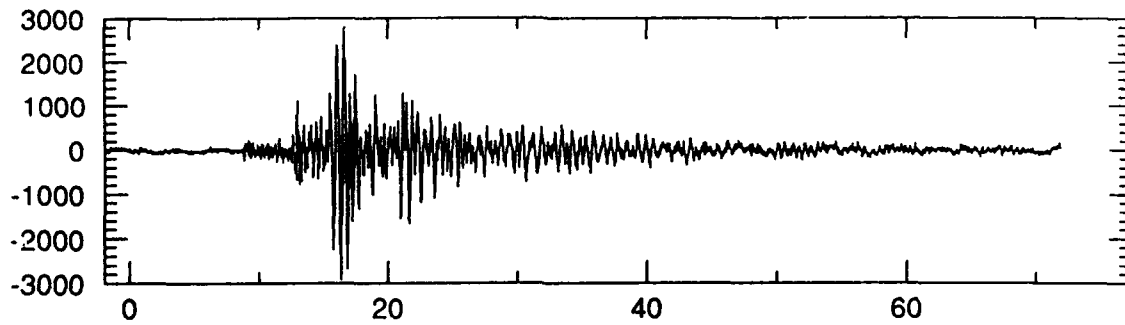


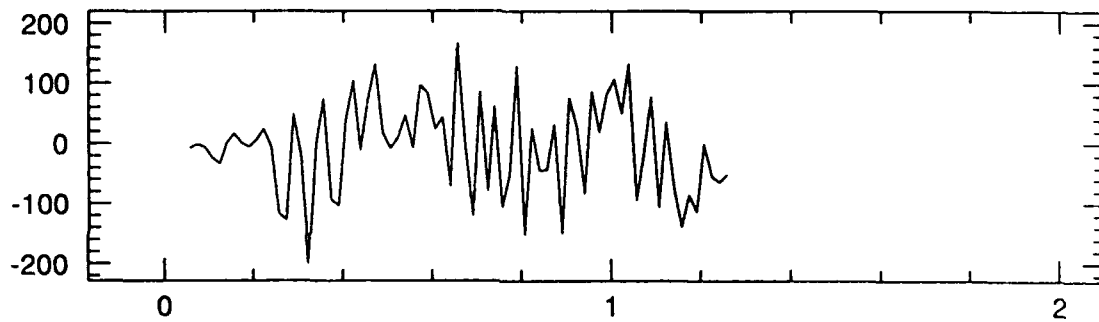
Figure 2. top: Quarry explosion timing and layout. bottom: The shot times.

LNO/sz1 (dist: 40km)



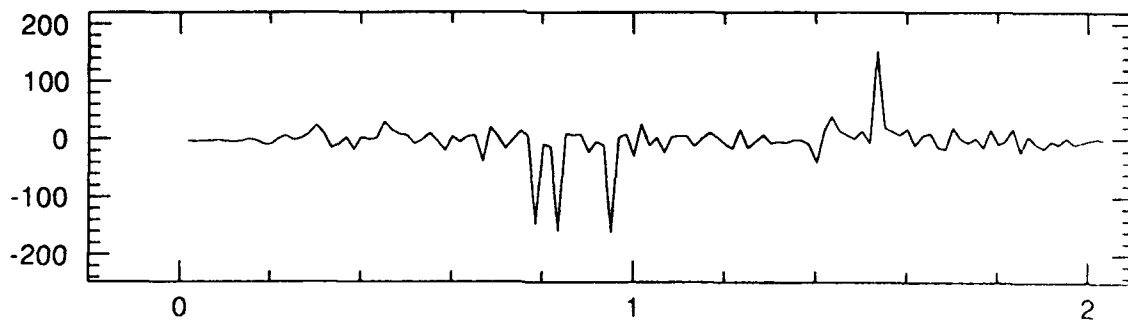
seconds from 1992042 20:31:0

input data: LNO/sz1



Seconds from 1992042 19:23:16

filter output



Seconds

Figure 3. top: Vertical component borehole record of a quarry blast with the shot layout shown in Figure 2. middle: Data window at the beginning of the signal for which an MED filter was generated. bottom: The deconvolved data window.

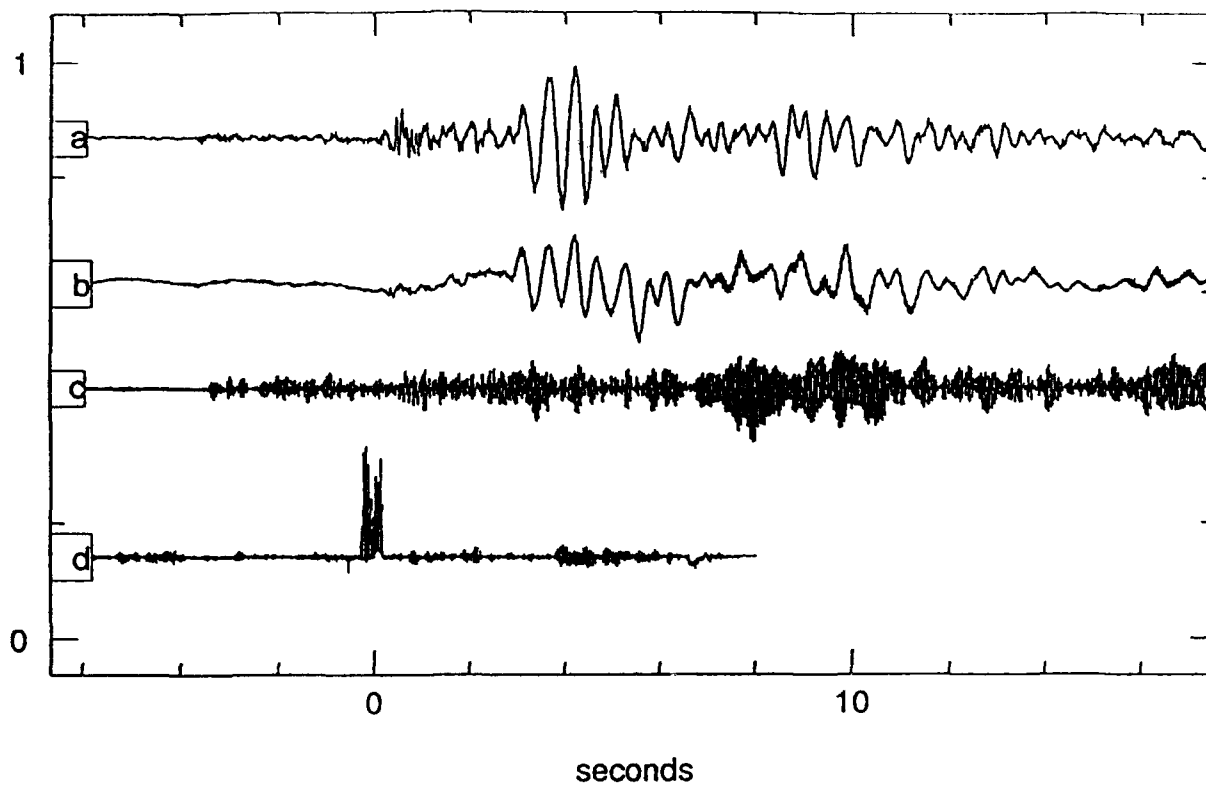


Figure 4. a) LNO/sz recording for a quarry blast at a distance of 32 km. b) Synthetic record made from 27 time shifted copies of a), using delay times equal to 5 times the actual delay times. c) high-pass filtered synthetic (15-30hz), d) deconvolution of c.

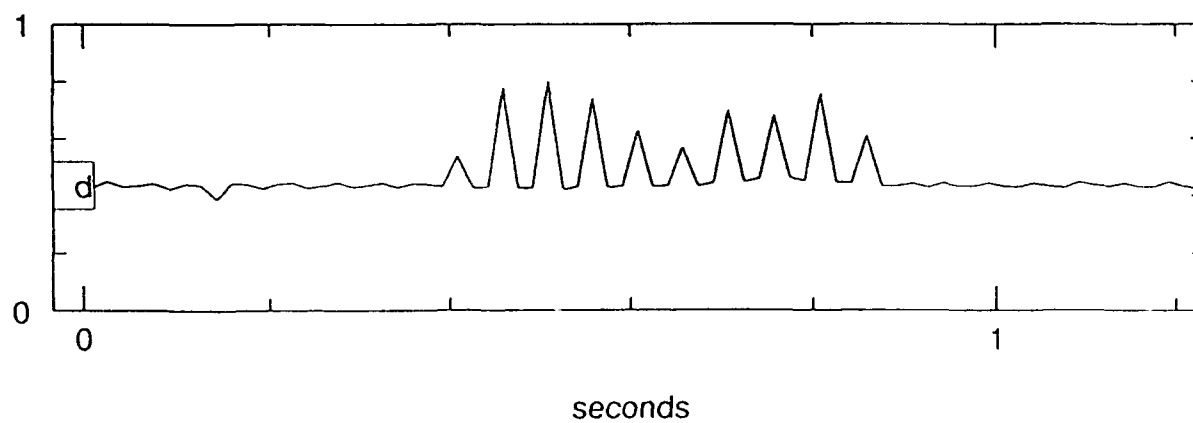


Figure 5. The deconvolved data window from Figure 5d shown at an enlarged scale.

HIGH FREQUENCY WAVE PROPAGATION

R. B. Herrmann, G. Al-Eqabi, K. Hutchensen
Department of Earth and Atmospheric Sciences
Saint Louis University

Contract No. F19628-90-K-0040

OBJECTIVE

The objective of the research effort is to understand aspects of high frequency wave propagation that relate to the quantification of explosion size. Initial work on the L_g phase has been followed by research on high frequency surface waves, e.g., in the 1 Hz band because of the need to establish some basis for ground truth.

RESEARCH ACCOMPLISHED

High frequency surface wave studies

The most recent results were published in the report *Quantification of m_{Lg} for small explosions*, PL-TR-92-2109, dated 23 April 1992.

The report showed the results for inverting for a laterally varying shear-wave velocity model in the upper 2 km, obtained by inverting short-period vertical component Rayleigh waves excited by shallow one ton shots of a refraction survey. The profiles examined were both perpendicular and parallel to the strike of the Appalachian Mountains in the U. S. state of Maine. In addition to the shear-velocity, average shear-wave Q along the 30 km long profiles and the isotropic moment of shot were also obtained.

The relation between isotropic moment and the one ton explosion size fit the regressions of Denny and Johnson (1991) which had chemical explosion data up to 1/2 ton and nuclear explosion data at much higher yields. The incorporation of our results into theirs is not fully possible because of our lack of knowledge of shot placement, and material parameters, such as porosity, at the shot depth. On the other hand, our inferences from data in the 5 - 30 km range are quite good.

The only outlier in our isotropic moment - yield data set is from a shot set off in a lake, for which the signals are very complicated, and for which the inferred moment (not taking into account the water layer about the source) differs by a factor of eight from that expected for shots in hard rock.

There is one other significant outcome of our study. The region studied consists of folded, metamorphic Paleozoic sedimentary rocks, for which we have observed correlations between the shallow shear-wave velocities and specific rock type. To the extent that this part of the Appalachian Mountain range is similar in geology to the Urals and to Novaya Zemlya, we thus have estimates of shear-wave velocities in those rocks.

Wave propagation theory

Because of a need to incorporate point force source representations into our wavenumber integration code for synthetic seismograms, the Haskell (1964) theory for point sources in layered elastic media, has been revisited. In doing so, the

previous code has been generalized to permit elastic, rigid or stress-free boundary conditions at the top and bottom of the layer stack, to permit a stack of fluid layers, and to permit the receiver to be buried anywhere in the model. Thus the code could handle atmospheric explosions as well as buried, and also provide complete synthetics for VSP problems. The draft paper will hopefully be the last review of the Haskell (1964) technique because of its completeness and its use of Fourier-Bessel integrals, and because recent advances in wave propagation in flat layered media incorporate anisotropy and thus generally required two-dimensional spatial Fourier transforms and also require recursive techniques rather than 6x propagator matrices.

The essence of the generalization is simple. Wang and Herrmann (1979) showed that the Haskell (1964) formulation for a wavefield due to a buried point source in cylindrical coordinates could be expressed as

$$\begin{aligned} \mathbf{B}_{N-1} = & a_{N-1}(d_{N-1})a_{N-2}(d_{N-2}) \cdots a_m(d_m - h_m)\Delta\mathbf{B} \\ & + a_{N-1}(d_{N-1})a_{N-2}(d_{N-2}) \cdots a_1(d_1)\mathbf{B}_0 \end{aligned} \quad (1)$$

where the layering convention of Haskell (1964) is followed. The transformed motion-stress vector \mathbf{B}_k is evaluated at the k' th interface. For P-SV waves $\mathbf{B}_k = (U_r, U_z, T_z, T_r)^T$ and for SH waves $\mathbf{B}_k = (U_\phi, T_\phi)^T$. The medium properties of the k' th layer are between the $k-1'$ th and k' th interfaces. The layer thickness of the k' th layer is d_k , the compressional and shear wave velocities are α_k and β_k , respectively, and the density is ρ_k . The source is at a depth of h_m in the m' th layer.

Equation (1) states that the wavefield at some position beneath the source is a function of the wavefield discontinuity at the source and also the wavefield at the top boundary. There is nothing in this formulation restricting the 0'th interface to be a free surface, or the N' th medium to be a halfspace. The source is at a depth h_m in the m' th layer.

Haskell (1964) expressed (1) in terms of upgoing and downgoing P- and SV-potential coefficients, giving a total of four coefficients for each layer. At the top and bottom boundaries, the boundary conditions require only two unknowns. This observation is used below.

P-SV Problem

Let us assume that there are matrices \mathbf{G} and \mathbf{H} such that

$$\begin{bmatrix} 0 \\ 0 \\ a \\ b \end{bmatrix} = \mathbf{G}\mathbf{B}_{N-1} \quad (2)$$

and

$$\mathbf{B}_0 = \mathbf{H}(c, d, 0, 0)^T \quad (3)$$

Multiplying (1) on the left by \mathbf{G} and defining

$$\mathbf{X} = \mathbf{G}a_{N-1}(d_{N-1})a_{N-2}(d_{N-2}) \cdots a_m(d_m - h_m)$$

and

$$\mathbf{R} = \mathbf{G}a_{N-1}(d_{N-1})a_{N-2}(d_{N-2}) \cdots a_1(d_1)\mathbf{H},$$

and using (2) and (3)

$$\begin{bmatrix} 0 \\ 0 \\ a \\ b \end{bmatrix} = \mathbf{XS} + \mathbf{R} \begin{bmatrix} c \\ d \\ 0 \\ 0 \end{bmatrix} \quad (4)$$

where we have set $\mathbf{S} = \Delta \mathbf{B}$.

Consider the first two equations in this linear system of four equations. The left side is zero, and we can solve directly for the unknowns c and d :

$$\begin{bmatrix} c \\ d \end{bmatrix} = \frac{-1}{R_{11}R_{22} - R_{12}R_{21}} \begin{bmatrix} R_{22} - R_{12} \\ -R_{21} & R_{11} \end{bmatrix} \begin{bmatrix} X_{1i}S_i \\ X_{2i}S_i \end{bmatrix} \quad (5)$$

$$= \frac{-1}{R \mid_{12}^{12}} \begin{bmatrix} R_{22}X_{1i}S_i - R_{12}X_{2i}S_i \\ R_{21}X_{1i}S_i - R_{11}X_{2i}S_i \end{bmatrix} \quad (6)$$

$$= \frac{-1}{R \mid_{12}^{12}} \begin{bmatrix} X_{2j}Z_{j2}X_{1i}S_i - X_{1j}Z_{j2}X_{2i}S_i \\ -X_{2j}Z_{j1}X_{1i}S_i + X_{1j}Z_{j1}X_{2i}S_i \end{bmatrix} \quad (7)$$

$$= \frac{-1}{R \mid_{12}^{12}} \begin{bmatrix} S_i X \mid_{ij}^{12} Z_{j2} \\ -S_i X \mid_{ij}^{12} Z_{j1} \end{bmatrix} \quad (8)$$

where we have used $\mathbf{R} = \mathbf{XZ}$, and the compound matrix definition $R \mid_{kl}^{ij} = R_{ik}R_{jl} - R_{il}R_{jk}$. Note that the repeated indices represent summations in the range 1 - 4.

This is essentially the derivation given in Wang and Herrmann (1979), where the \mathbf{G} matrix was designed to give the upward and downward potentials in the halfspace, and the \mathbf{H} matrix was such to make the free surface stress free, with $c = U_r$, and $d = U_z$, the displacements at the top boundary.

The formulation of (8) has proven to be numerically stable. To get the wavefield at points above the source, it is obvious through the use of propagator matrices that at a depth h_k in the k' th layer, which is above the source,

$$\mathbf{B}_k = a_k(h_k) \cdots a_1(d_1) \mathbf{H} \begin{bmatrix} c \\ d \\ 0 \\ 0 \end{bmatrix} \quad (9)$$

$$= \mathbf{y} \begin{bmatrix} c \\ d \\ 0 \\ 0 \end{bmatrix}. \quad (10)$$

One may be tempted to use (6) first, and then (9) to evaluate the wavefield of a buried receiver directly, but this is not numerically stable, due to possibly increasing exponential terms in y . (In the extreme case of a layered wholespace, the whole space solutions indicate that an exponentially decreasing solution is required in the z -direction away from the source).

To work around this problem, we note that $R = XZ = Xxy$, where we define

$$x = a_m(h_m) \cdots a_k(d_k - h_k) \quad (11)$$

and

$$y = a_k(h_k) \cdots a_1(d_1)H, \quad (12)$$

where the propagator matrix property $a(h_1) \cdot a(h_2) = a(h_1 + h_2)$ is used. Combining equations (8 - 12), we have, after some algebra,

$$B_k = \begin{bmatrix} U_r \\ U_z \\ T_z \\ T_r \end{bmatrix}_k = \frac{-1}{R \mid \begin{smallmatrix} 12 \\ 12 \end{smallmatrix}} \begin{bmatrix} S_i X \mid \begin{smallmatrix} 12 \\ il \end{smallmatrix} x_{lm} y \mid \begin{smallmatrix} 1m \\ 12 \end{smallmatrix} \\ S_i X \mid \begin{smallmatrix} 12 \\ il \end{smallmatrix} x_{lm} y \mid \begin{smallmatrix} 2m \\ 12 \end{smallmatrix} \\ S_i X \mid \begin{smallmatrix} 12 \\ il \end{smallmatrix} x_{lm} y \mid \begin{smallmatrix} 3m \\ 12 \end{smallmatrix} \\ S_i X \mid \begin{smallmatrix} 12 \\ il \end{smallmatrix} x_{lm} y \mid \begin{smallmatrix} 4m \\ 12 \end{smallmatrix} \end{bmatrix} \quad (13)$$

The complete theory will be given in the Final Report under this contract, and will represent a complete exposition of wave theory solutions for the whole space, halfspace, and layered models, as well as a documentation of numerical techniques required to make the code work correctly.

Random process theory

We have recently rewritten modified the random process theory techniques of Ou and Herrmann (1990a, 1990b) in order to better use ray theory. The concept of random process theory is that the peak amplitude of windowed, band limited white noise, $s(t)$ is related to the Fourier transform of the signal, $S(f)$, by Parseval's theorem a suitable definition of signal duration. Ou and Herrmann (1990a, 1990b) indicated how the duration and observed site spectra are related to the earth model by simple ray tracing techniques.

The improvements correctly use high frequency ray theory to account for wave transmission and reflection at boundaries. The assumption of only using shear-wave to shear-wave conversions is born out by comparison with ω - k simulations. The resulting code is significantly faster than the ω - k integration techniques and is adequate for understanding the effect of crustal structure on high frequency Lg wave propagation.

There are applications to the research program. Even though the explicit generation of the Lg wave by explosions is not understood, the Lg phase has proven to be useful. The modification to random process theory can be easily used with ray-tracing in other than flat layered media to model the effect of laterally varying crustal structure on Lg wave propagation, in a computationally fast manner.

Use of short period surface waves as a depth discriminant

It is accepted that the observation of a short period surface wave is an indication of a shallow source depth. There is no discrimination between earthquake or explosion in this statement. The real question is whether this theoretical statement can be used as a depth discriminant.

In order to combine this observation with theory to quantify the use of the observed surface wave as a depth discriminant, assumptions must be stated, and a methodology proposed. Assume that

- a) the regional surface-wave propagation characteristics are known, e.g., the crustal velocity and Q model is known.
- b) there is an independent estimate of the seismic source size, e.g., a moment-magnitude relationship.

Now construct some theoretical curves, such as those in Figure 2. These curves relate the expected amplitude on a specified seismogram to seismic moment, source, source depth.

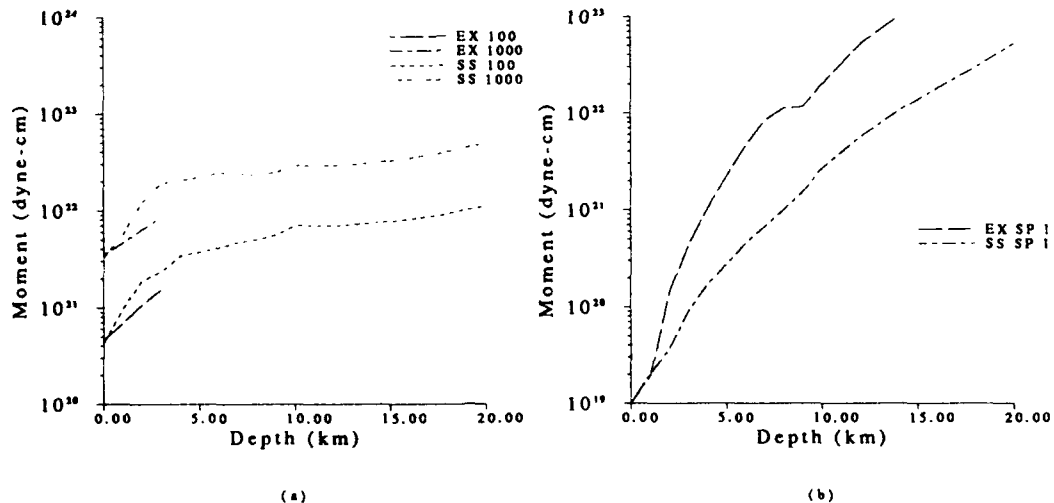


Fig. 2. Curves showing seismic moment required for a given focal depth and source (EXplosion or SS strike slip earthquake at an azimuth of 22.5°) in order to observe a 1mm high surface wave amplitude on a vertical component instrument. a) 15-100 WWSSN long period seismograph with peak gain of 1500 with curves for 100 and 1000 km. b) for a WWSSN short period seismograph with a peak gain of 50000 and distance of 100km.

Now assume that we know that the source moment was 1.0×10^{21} dyne-cm. If we do not resolve any surface wave arrival at 100 km on the long period seismogram, this means that the source must be greater than 1.0 km deep if it is an earthquake or 2.0 km deep if it is an explosion. In other words, for a given source size, a lack of observation of the surface wave would indicate a depth to the right of the curve. For a short period seismogram and the same moment, we would know that an explosion source would have to be deeper than 3 km, and a strike slip source would have to be deeper than 8 km.

Such a binary threshold is not possible with real data. Since earthquakes in a region monitored may have different focal mechanisms, these curves would be replaced by distributions, thus making this criteria more applicable for "fuzzy logic." Other curves could be generated for other instruments and other threshold criteria.

This example shows the need to know regional velocity structure and to have a regional magnitude scale that can be correlated with with moment. It also shows

that there is not much to distinguish between explosions and earthquakes in surface-wave excitation for shallow sources if a simple amplitude criteria is used.

The purpose of this exercise is to indicate how the presence or absence of short period Rayleigh waves could be used in making decisions. The absence of a surface-wave means nothing, however, its presence will provide an extra constraint on depth, and together with assumptions of maximum possible depths of explosion, it will be useful as a discriminant between earthquakes and explosions.

CONCLUSIONS AND RECOMMENDATIONS

We have completed extensive studies on the quantification of explosions using high frequency data, primarily using the Rayleigh wave from refraction data sets. This permitted independent estimates of anelastic attenuation and source excitation.

Future work should attempt to understand the relation between seismic measures of size and yield of chemical explosions for larger events, for which the frequency shaping effects of the large source dimensions would be a useful discriminant between extended (chemical) and point (nuclear) explosions.

Regional knowledge of high frequency surface-wave propagation can also be used in a depth determination scheme.

REFERENCES

- Denny, M. D. and L. R. Johnson (1991). The explosion seismic source function: models and scaling laws reviewed, Lawrence Livermore national Laboratory, UCRL-JC-107941, preprint.
- Haskell, N. A. (1964). Radiation pattern of surface waves from point sources in a multi-layered medium, *Bull. Seism. Soc. Am.* **54**, 377-393.
- Ou, G.-B., and R. B. Herrmann (1990a). Estimation theory for peak ground motion, *Seism. Res. Letters* **61**, 99-107.
- Ou, G.-B., and R. B. Herrmann (1990b). A statistical model for peak ground motion from local to regional distances, *Bull. Seism. Soc. Am.* **80**, 1397-1417.
- Wang, C. Y., and R. B. Herrmann (1980). A numerical study of P-, SV-, and SH-wave generation in a plane layered medium, *Bull. Seism. Soc. Am.* **70**, 1015-1036.

**EURASIAN SEISMIC SURVEILLANCE:
2D FD SEISMIC SYNTHETICS AND EVENT DISCRIMINATION**

E.S. Husebye¹⁾, B.O. Ruud²⁾ and S. Hestholm³⁾

¹⁾ NTNF/NORSAR, P.O. Box 51, 2007 Kjeller, Norway

²⁾ Dept. of Geology, Oslo Univ., Oslo, Norway

³⁾ IBM Bergen Environmental Sciences and Solutions Centre, Bergen, Norway

Contract no. F49620-89-C-0038

Objectives:

The major challenge in seismic surveillance in the context of a potential test ban treaty is that of classifying small seismic events as either an earthquake or man-made explosion at local distances. Signal features commonly explored in event discrimination experiments are P/Lg amplitude ratios and P and Lg spectral ratios (Baumgardt et al, 1991). As is well known, none of the proposed discrimination schemes is globally applicable, and the reasons for their regionalization are attributed to lithospheric structural differences. Also source depths, topography, and sedimentary basin crossings are important elements in this context.

Part of our classification strategy is to gain a better insight into propagation effects at local distance ranges. The principal tool here is the 2-dimensional (2D) finite-difference (FD) numerical solution of the elastic wave equation (Hestholm et al, 1992). The corresponding synthetics are calculated for both P- and S-type sources, varying focal depths and a wide range of lithospheric models. The latter ranges from a homogeneous single-layered medium to multilayered, inhomogeneous (von Kármán type) media, even including free-surface topography and Moho undulations. Notice that a limitation in using 2D models is that coherencies even for coda waves are relatively high in comparison with real data.

The overall objective is to develop a better theoretical rationale for local event discriminants and their relation to various crustal environments within Eurasia using 2D FD synthetics. We will also undertake classification analysis of local events within this region using schemes similar to those described by Tsvang et al (1992).

Research accomplished

In this section we first describe briefly extension of our 2D FD technique to "handle" models with a non-planar free surface, that is, incorporating topographic scattering effects. The Rg-phase, if observed, would constrain the focal depth to at most 3 km. We demonstrate that its general elusiveness is due to topographic effects and scattering in the top crustal low velocity layer. P-coda waves are important for teleseismic event classification. In this context we explore various scattering mechanisms for coda generation at the source side and also whether Pn- and/or Pg-coda could be useful in an event classification context.

Finite-difference scheme for handling free-surface topography in 2D

The basic equations governing wave propagation in an isotropic elastic medium are the momentum conservation and the stress-strain relations (Hooke's law). An (x, z) -coordinate system is used which is stretched in the vertical direction. The stretching is done in such a way that below the surface the x axis is parallel with the topography. The undulations on the x axis are then decreased linearly with depth until the bottom of the grid, where the x axis is plane.

By applying the chain rule, the elastic equations in the (x, z) -system are transferred into a rectangular (ξ, η) -system. The relations between the two system are given by

$$x(\xi, \eta) = \xi$$

$$z(\xi, \eta) = \frac{\eta}{\eta_{max}} z_0(\xi)$$

where η_{max} is the maximum value of the vertical coordinate in the (ξ, η) -system, and $z_0(\xi)$ is the topography function. Both systems have positive direction of the vertical coordinates upwards. This way of numerical handling of a non-planar free surface is due to Tessmer et al (1992).

We want to retain our previous boundary conditions for a free surface, consisting of a closed system of particle velocities (Hestholm et al, 1992). Since it is here presumed that the vertical coordinate is normal to the local surface, we have to introduce a new (x', z') -coordinate system at each point on the surface fulfilling this requirement. The boundary conditions are enforced in each of these systems. However, the numerical computations are done in the (ξ, η) -system so that the original boundary conditions have to be rotated back to the (ξ, η) -system in order to retain their validity. Knowing the angles between the (x', z') and the (ξ, η) -systems this rotation is described by:

$$\tilde{v} = A \bar{v}'$$

where \bar{v}' is the velocity vector in the rotated system (x', z') , \tilde{v} is the velocity vector in the (ξ, η) -system and A is the rotation matrix. Important, the free surface has to vary smoothly to ensure numerical stability. This implies that both the topography function $z_0(\xi)$ and its derivative $(\partial_{z_0}(\xi)) / \partial \xi$ have to exist at all points. In order to avoid Gibb's phenomenon, the derivative should not vary too much over a short distance. Also, practical experience dictated that the medium should be kept homogeneous at least for the top 4 "vertical" node points.

The above extension of our 2D FD technique for synthetic seismogram calculation is now in use. The outcome of some experiments aimed at simulating topography wavefield effects will be given below, while the numerical algorithm is described separately (Hestholm, 1992).

Rg propagation in the inhomogeneous crust

As is well known, Rg excitation for sources at focal depths exceeding 2-3 km is essentially non-existent, and thus this phase has the potential of being a good event discriminant. Classical schemes for Rg synthetics are tied to homogeneous crustal models, often including a top crust low velocity layer (LVL). For such models the Rg wavetrains are clear with clear Airy-phases of periods at ca 1 sec. In contrast, real Rg records seldom exhibit clean Airy phases, and for stations in hilly areas like NORESS Rg phases are seldom observed beyond source distances of 100 km. Across GERESS we have seen clear Rg waves at one sensor, but at nearby ones 0.5-1.0 km away there were no Rg recordings. The outcomes of our Rg synthetic experiments with the basic homo-

geneous model being an LVL over a half space and P-source were as follows: Replacing the LVL with a positive velocity gradient "destroyed" the Airy phase. In another model with an inhomogeneous (von Kármán type) LVL, S-type scattering wavelets partly masked the Rg wavetrain, having no clear Airy phase. Additional structural complexities like free surface topography and half-space interface corrugations (1D von Kármán shaped) resulted in even more complex and attenuated Rg wavetrains (Ruud et al, 1992). However, most of the above scattering distortions are related to signal frequencies above ca 0.8 Hz, explaining why Rg is seldom reported from local, high-frequency recordings. Some instructive results are displayed in Figs. 1 and 2.

P-slowness estimates -- topographic effects

Three-component (3C) P-slowness estimates are accurate when based on low-frequency recordings (Ruud et al, 1988). The reason is simply that long-wavelength phases are insensitive to lithospheric inhomogeneities. However, around 1 Hz P-signals are sensitive to the above-discussed top crust low velocity layer (Lokshtanov et al, 1991). Another likely bias effect is that stemming from topographically related interferences in the station siting area. To mimic such effects, we used a very simple 2D FD model of a homogeneous half-space with a P-source located at 50 km depth. The free surface topography was similar to that across NORESS, but dampened by a factor of 2 because of tricky non-planar free surface boundary conditions. The topographical relief ranged from 30-50 meters unevenly distributed along two profiles of length 1200 m and with a sensor spacing of 200 m. Polarity characteristics of the corresponding synthetics were then used to estimate the apparent P-velocities. These were within ± 0.3 km/sec relative to the "true" ones around 8 km/sec. Outliers amounted to ± 1.0 km/sec and were observed for sensors in an area with relief change of 30 m over a 300 m stretch. The corresponding angular variations were within ± 10 deg. In another experiment the free surface was planar. There we introduced RMS velocity fluctuations of 3 per cent in the half space. For this model the apparent P velocity variations were within ± 0.3 km/sec, equivalent to angular fluctuations of 3-4 deg.

If we presume that the above angular fluctuations in the vertical plane would be representative for those in the horizontal plane, then azimuth fluctuations should roughly be in the range of ± 15 deg. In cases of Moho corrugations, this range may be a few degrees larger. These predictions compare favorably to the Suteau-Henson (1990) azimuth results for the four 3C stations within NORESS. Three of these, A0, C2 and C4, had similar distributions of azimuth differences relative to the "true" ones and with corresponding standard deviations of 15 to 16 deg. Station C7 was somewhat different and exhibited standard deviations of 25 deg. Similar kinds of azimuth fluctuations have also been reported for 3 stations in Eurasia (Riviere-Barbier et al, 1992).

Our synthetic experiments have demonstrated the importance of topography also as regards the incoming P-wave itself. Furthermore, such effects are deterministic and thus would justify introduction of azimuth corrections for 3C stations as also recommended by Suteau-Henson (1990) and Riviere-Barbier et al (1992).

Topography, mode conversions and scattering

Recent studies of teleseismic coda waves across NORESS have amply demonstrated the importance of P-to-Rg conversions at hills close to the array siting area (Bannister et al, 1990; Gupta et al, 1991). Also, from stacking analysis it is obvious that a considerable amount of coda energy originated near the source in view of wavelet slowness estimates being comparable to that of the preceding P-wave. An outstanding feature here is the long duration of the coda which amounts to 1-2 minutes or more for events with m_b around 5.5 or larger. The standard explanation of this phenomenon is S and/or Rg conversions to teleseismic P due to structural heterogeneities within a few hundred kilometers of the source. At local distance we should then observe both part of the "unconverted" S, hardly much "unconverted" Rg due to attenuation as discussed above, and natu-

rally some S and/or Rg conversions to P. So far the coda explanations are mainly quantitative; below we describe synthetic seismogram experiments aimed at more qualitative understanding of the above wave phenomenon.

The models used have the following characteristics. The free surface topography is representative of the NORESS siting area, but strongly smoothed. At the time of writing we have only considered half-space media which are either homogeneous or inhomogeneous. The sensor clusters of 10 pair each of radial and vertical instruments are located both on the surface and at depths of 25 and 50 km. The latter sensor synthetics would be indicative of Pn or teleseismic P coda excitation.

In Fig. 3 synthetics are shown for a homogeneous half space and with a surface topography similar to that discussed above. The P-type source (Hestholm et al, 1992) is located at a depth of 2 km. P- and Rg-waves dominate the seismograms. The FO-trace at a depth of 25 km is interesting in the sense that coda waves are weak. In Fig. 4 synthetics are shown for a more complicated model, that is, a low velocity layer of thickness 1.4 km is overlaying a homogeneous halfspace. The seismograms are in this case rather complicated, although the coda waves on the deep FO sensor remain weak. Other interesting features are the smearing in time of the pS-phase, but less pronounced for the pP-phase.

The synthetics presented above demonstrate that even simple crustal models could profoundly affect high-frequency seismic wave propagation. However, so far we have been unable to mimic P-coda excitation in a realistic wave. Obviously, the current crustal models are too simple. Future work will include models with von Kármán velocity fluctuations of the order of 3 to 5 per cent, Moho corrugations and both P- and S-type of sources at a wide range of focal depths.

Conclusions and recommendations

We have here demonstrated that a heterogeneous top crust low velocity layer including topographical relief profoundly affects Rg wave propagation. Topography clearly biases the 3-component type of P-slowness estimation and in this respect appears to be more important than crustal heterogeneities. At this stage of work we have been unable to qualitatively synthesize coda wave excitation, but apparently the whole range of crustal heterogeneities has to be included to ensure realistic modelling. A recommendation for future work is to aim at a better understanding of the relative merits of various kinds of event classification features in terms of a priori known crustal structures along the propagation path and the source environments.

References:

- Bannister, S.C., E.S. Husebye and B.O. Ruud (1990). Teleseismic P-coda analyzed by three-component and array techniques -- deterministic location of topographic P-to-Rg scattering near the NORESS array, Bull. Seism. Soc. Am., 80, 1969-1986.
- Baumgardt, D.R., G.B. Young and K.A. Ziegler (1991). Design and development of the intelligent event identification system: Design considerations and processing for regional event identification, Sci. Rep. No. 1, PL-TR-91-2211, Ensco, Inc., Springfield, VA, USA. ADA246793
- Gupta, I.N., C.S. Lynnes, T.W. McElflesh and R.A. Wagner (1990). F-k analysis of NORESS array and single-station data to identify sources of near-receiver and near-source scattering, Bull. Seism. Soc. Am., 80, 2227-2241.

- Hestholm, S.O., B.O. Ruud, E.S. Husebye and B.O. Kosland (1992). Synthesizing 2D wave propagation in a heterogeneous lithosphere using finite difference techniques, Submitted for publication.
- Hestholm, S.O. (1992). 2D finite difference modelling of seismic responses of surface topography, manuscript in preparation.
- Lokshtanov, D.E., B.O. Ruud and E.S. Husebye (1991). The crustal transfer function in seismic 3-component slowness estimation, *Geophys. Res. Lett.*, 18, 1393-1396.
- Riviere-Barbier, F., A. Suteau-Henson, V.Z. Ryaboy and J.A. Carter (1992). Analysis of three-component data from IRIS/IDA stations in the USSR, *Bull. Seism. Soc. Am.*, 82, 192-220.
- Ruud, B.O., E.S. Husebye, S.F. Ingate and A. Christoffersson (1988). Event location at any distance using seismic data from a single, three-component station, *Bull. Seism. Soc. Am.*, 78, 308-325.
- Ruud, B.O., E.S. Husebye and S.O. Hestholm (1992). On crustal, short period Rg-propagation using array records from 4 continents, Submitted for publication.
- Suteau-Henson, A. (1990). Estimating azimuth and slowness from three-component and array stations, *Bull. Seism. Soc. Am.*, 80, 1987-1998.
- Tessmer, E., D. Kosloff and A. Behle (1992). Elastic wave propagation simulation in the presence of surface topography, *Geophys. J. Int.*, 108, 621-632.
- Tsvang, S.L., V.I. Pinsky and E.S. Husebye (1992). Enhanced seismic source discrimination using NORESS recordings from Eurasian events, *Geophys. J. Int.* (in press).

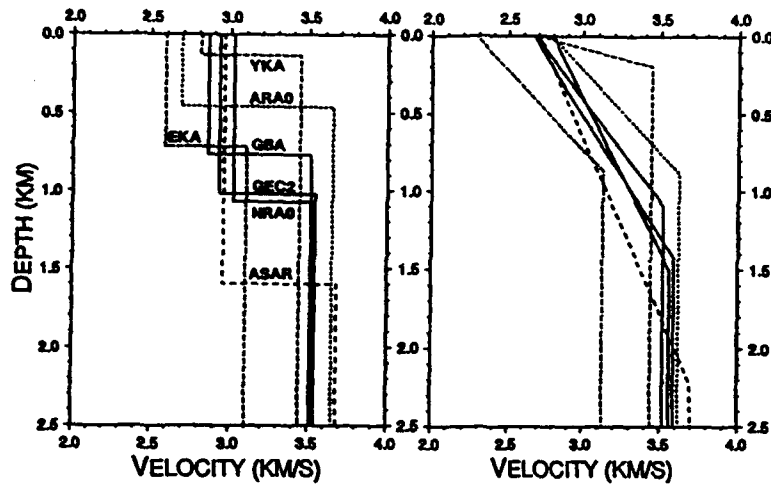


Fig. 1. S-velocities versus depth for the two types of models considered. On the left side results from Model 1 inversion are shown (constant velocity layer over a halfspace), while Model 2 results (gradient layer over a halfspace) are shown to the right. The array markings are the same for the two models.

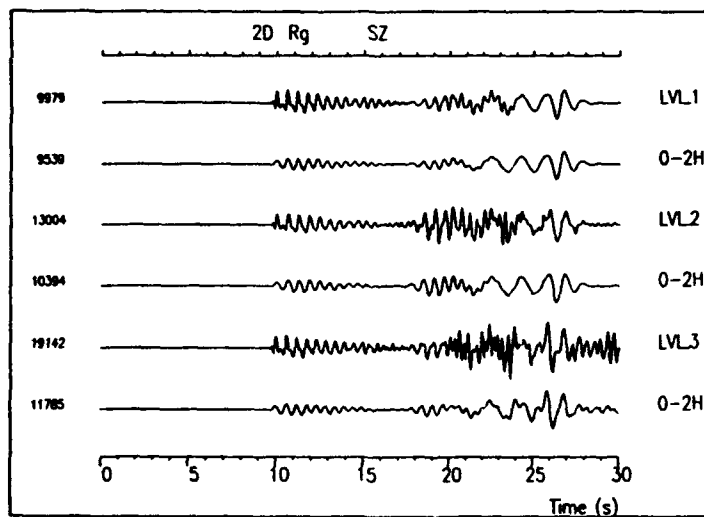


Fig. 2. Synthetic seismograms computed by our 2D finite difference scheme for different models. In all three cases the explosion source is located at 60 km distance and 2 km depth. The trace labelled LVL_1 was produced with a flat homogeneous low velocity layer. LVL_2 is for a model with random variations in layer thickness, while LVL_3 is for a flat layer with random variations in layer velocity. Further model details are given in Ruud et al, 1992. Below each of the three traces, a low-pass filtered (0-2 Hz) version is shown. Note that the low frequency Rg waves are almost unaffected by the random variations.

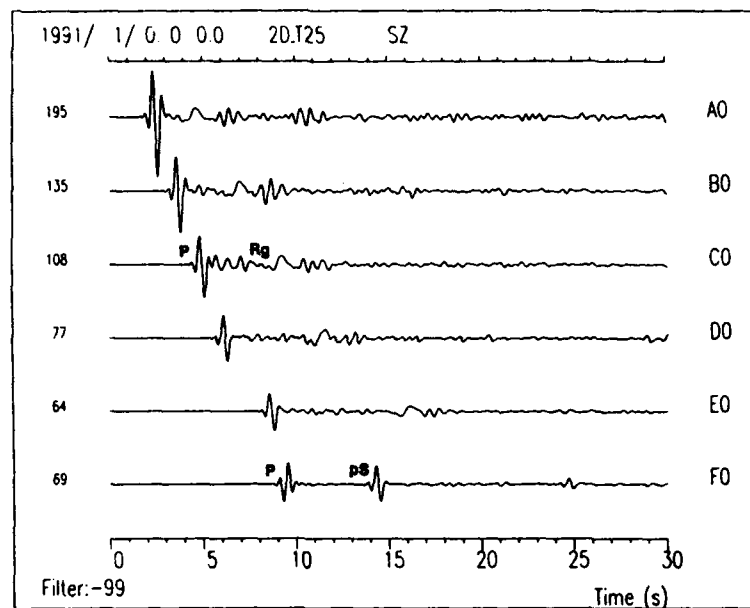


Fig. 3. 2D finite difference synthetic seismograms (vertical) for a homogeneous halfspace but with a non-planar free surface. The latter represents a strongly smoothed cross-section of the NORESS siting area. A P-type source is used and the focal depth is 2 km. The sensors are on the surface, and interspacing is 7.5 with A0 being 15 km from the source. The exception is FO being at a depth of 25 km and like EO being 52.5 km from the source. Major phase arrivals are marked, while the small FO wavelet at 25 sec appears to be an "edge" reflection artefact. Notice that the P-coda excitation must be small as the FO trace is dominated by the P- and pS-phase arrivals.

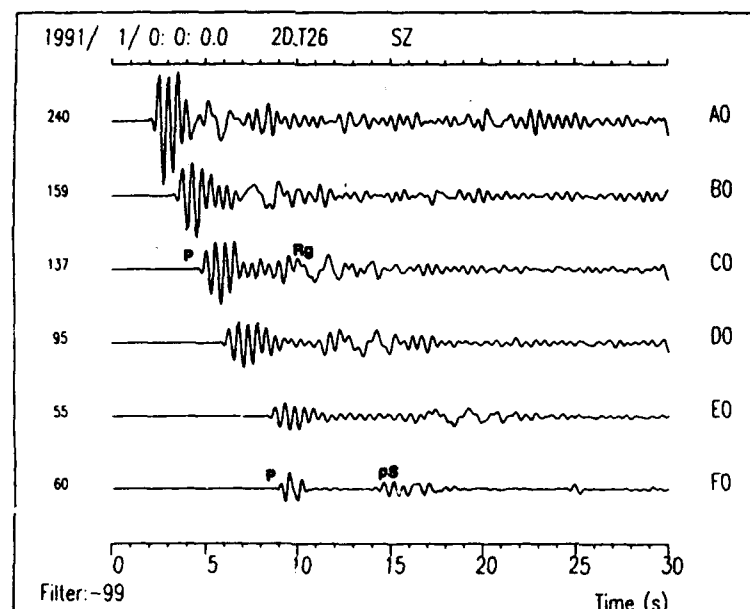


Fig. 4. 2D finite difference synthetic seismograms (vertical) for a homogeneous halfspace with an overlaying 1.4 km thick low velocity layer. Caption otherwise as for Fig. 3. The synthetics are rather complex, although coda excitation of the FO trace remains weak. A noticeable feature here is the "smearing" in time of the pS-phase, and this also applies to the preceding pP-phase, which partly coincides with the P-phase itself.

RE-EXAMINATION OF REGIONAL L_g Q VARIATION IN IRANIAN PLATEAU

Rong-Song Jih
Teledyne Geotech
314 Montgomery Street
Alexandria, VA 22314

Christopher S. Lynnes
Hughes STX
7601 Ora Glen Dr., Suite 300
Greenbelt, MD 20770

Contract Number: F19628-90-C-0158

Project Objective

The primary objective of this project is to improve our fundamental understanding of regional phase propagation in Eurasia. Both forward and inverse modeling studies are conducted at different stages during the contract period. Following the travel-time analysis of Central Asian events with regional phases (Lynnes and Jih, 1991), we recently examined a general procedure which incorporates the independently derived information of localized path effects into the magnitude determination. The goal of this task is to quantify the bias in the seismic magnitude (such as $m_b(L_g)$) that would be inherent in a scheme without fully coupling the regional propagational characteristics into the magnitude determination procedure. Iran was chosen as a test case in this study because of the growing nuclear proliferation concern in the Middle East.

Research Accomplished

To characterize correctly the propagation of regional phases due to explosion sources in regions of high proliferation concern (such as Iran) would require fairly accurate crustal models. Iran lies on the Alpine-Himalayan seismo-tectonic belt, within a wide band of seismic activity connecting the Hindu Kush and eastern Mediterranean highly seismic regions. The Zagros Main Thrust Fault constitutes the boundary between the Iranian and Arabian Plates. Central Iran, northwest Iran, and the south Caspian areas have low levels of seismicity compared to those of the narrow belts surrounding them (Figure 1). This is regarded as a highly heterogeneous and complicated geological environment (Leith, 1992).

A tentative zoning partitioning Iranian Plateau into six regions (*viz.*, the Zagros Range, the Lut Block, East Iran Range, Central Iran Range, the Elburz/Caspian area, and the Great Kavir/Esfahan/Rezaiyeh region; *cf.* Figure 2) has been used in our block inversion to reveal the spatial pattern of the L_g attenuation parameter, Q . We used 109 observations recorded at 3 WWSSN stations in Iran (*viz.*, Meshed, MSH; Tabriz, TAB; and Shiraz, SHI) for which the γ was readily measured by Nuttli (1980) (Figure 3). The weighted average γ of these paths is 0.0044 km^{-1} , very close to the 0.0048 for coastal California derived by Herrmann (1980). It is also largely in agreement with the L_g coda Q map recently compiled by Xie and Mitchell (1992) for Eurasia. In our inversion with a more detailed regionalization, both the Zagros Range and the Lut Block show a large γ of 0.005 km^{-1} , roughly corresponding to a Q of 181 ± 12 and 183 ± 18 , respectively. The Kopet Dag, Shahrud Doruneh, and the Qom region also seem to have a Q slightly smaller than the average. On the other hand, the Elburz Province and central Iran have a Q of about 250 for 1 Hz L_g waves, which could be the highest Q value in Iran.

For the purpose of calculating $m_b(L_g)$, Nuttli's (1986) original formula for Eastern North America and Central Asia regions can be rewritten in an equivalent form:

$$m_b(L_g) \equiv 4.0272 + \log A(\Delta) + \frac{1}{3} \log(\Delta) + \frac{1}{2} \log \left[\sin \left(\frac{\Delta(\text{km})}{111.1(\text{km/deg})} \right) \right] + \frac{\gamma(\Delta - 10\text{km})}{\ln(10)}, \quad [1]$$

$$\text{where } \gamma \equiv \frac{\pi}{Q \cdot U \cdot T}, \quad Q(f) = Q_0 \cdot f^\zeta,$$

Δ is the epicentral distance in km, $A(\Delta)$ is the observed L_g amplitude measured in the time domain in μm [microns] at the epicentral distance of Δ km. For instance, a seismic source with 1-sec L_g amplitude of 110 μm at 10 km epicentral distance would correspond to a $m_b(L_g)$ of $4.0272 + 2.0414 + 0.3333 - 1.4019 + 0.0000 = 5.0000$, same as what Nuttli's (1986) formula would give. It is clear from [1] that an erroneous path γ would yield a $m_b(L_g)$ bias which increases with the distance. Figure 4 shows the spatial pattern of apparent $m_b(L_g)$ corrections that would be needed at WWSSN station SHI and IRIS station ASH (Ashkhabad), respectively, if a constant γ of 0.0044 km^{-1} (viz., the average γ across Iran) was assumed in computing $m_b(L_g)$ at these two stations. For each hypothetical epicenter, the $m_b(L_g)$ correction required is independent of the amplitude actually observed (cf. Equation [1]). Partitioning Iran into 21 regions (Figure 5) as proposed by Nowroozi (1976) would yield more profound spatial variation in Q , and hence a stronger variation in $m_b(L_g)$ residual as well.

3. Conclusions

Although the whole Iranian Plateau can be briefly described as a region of very low Q , applying a simple averaged attenuation coefficient (Q) for the whole plateau would be inappropriate. The regional variation of the anelastic attenuation parameter is significant enough that it needs to be taken into account in calibrating each monitoring station for a reliable magnitude scale in monitoring possible clandestine tests from a vast area. Unless this has been done, adding more stations/arrays to the monitoring network may not provide substantial improvement in reducing the error in the network-averaged magnitude based on regional phases. In fact, the bias in $m_b(L_g)$ would be much smaller if the magnitude was solely based on the nearest station alone (as compared to using a network of sparse stations for simple averaging). This situation is very different from that of monitoring a specific nuclear test site for which the empirical site-dependent correction term can be applied afterwards to the station magnitudes even when the path Q s are not fully known in advance. A regionalized γ map (e.g., Singh and Herrmann, 1983, for North America; and that in Kadinsky-Cade *et al.*, 1982, for S_n) for each crustal phase of interest should be established and applied to the routine magnitude computation procedure.

Nuttli (1980) suggested that a seismic source in Iran with the ISC bulletin m_b 5.0 should excite L_g amplitude of 270 microns at a 10-km extrapolated distance, whereas the seismic sources in Central Asia and North America with comparable ISC bulletin m_b would excite a L_g amplitude of 110-150 microns (Nuttli, 1986). Possible explanations for this apparent bias of 0.26 m.u. include [1] the uncertainty in the ISC bulletin m_b values (Nuttli, 1981), [2] the difference in L_g excitation relative to m_b , or [3] the difference in the upper mantle property which causes a bias in m_b . While we agree that, without careful re-processing, the ISC

bulletin m_b values typically would be associated with large uncertainty, it is very important to adopt a better m_b in calibrating the crustal phases in Iran (or any other area) in the first place.

4. Recommendations

Fault-plane solutions for many suitably located earthquakes in the Middle East have been determined by McKenzie (1972) and Jackson and McKenzie (1984). We recommend to assemble events recorded at regional as well as at teleseismic distances according to the clustering of earthquakes with similar focal mechanism. Preferably at least 10 events in each clustered area should be measured. The redundancy of data in each group will provide better constraints for inferring the empirical station and region-specific path corrections (Jih and Wagner, 1992a, 1992b), and it will thereby result in more precise magnitude scales for both regional and teleseismic phases. The determination of seismic magnitudes for events occurring in isolated suspected spots will also benefit from this exercise significantly, since more accurate station corrections will be available. Although several crustal models of the Middle East have been suggested during the past three decades, the identification of small seismic events has raised a need to refine the available models for more detailed and more accurate regionalized profiles. More tomographic inversions of the Middle East would be very useful.

5. References

- Herrmann, R. B. (1980). Q estimates using the coda of local earthquakes, *Bull. Seism. Soc. Am.*, **70**, 447-468.
- Jackson, J. and D. McKenzie (1984). Active tectonics of the Alpine-Himalayan belt between western Turkey and Pakistan, *Geophys. J. R. astr. Soc.*, **77**, 185-264.
- Jih, R.-S. and R. A. Wagner (1992a). Path-corrected body-wave magnitudes and yield estimates of Novaya Zemlya explosions, *PL-TR-92-2042 (=TGAL-91-09)*, *Scientific Report #1*, Phillips Laboratory, Hanscom Air Force Base, MA. **ADA251240**
- Jih, R.-S. and R. A. Wagner (1992b). Path-corrected body-wave magnitudes and yield estimates of Semipalatinsk explosions, *TGAL-92-05*, *Semi-annual Technical Report #1*, Teledyne Geotech, Alexandria, VA.
- Kadinsky-Cade, K., M. Barazangi, J. Oliver, and B. L. Isacks (1981). Lateral variations of high-frequency seismic wave propagation at regional distances across the Turkish and Iranian Plateaus, *J. Geophys. Res.*, **86**, 9377-9396.
- Leith, W. (1992). Geological factors affecting seismic monitoring in countries of nuclear proliferation concern, *Seismo. Res. Lett.*, **63**, 26.
- Lynnes, C. S. and R.-S. Jih (1991). Regional phase propagation in Central Asia, in *Special Report PL-TR-91-2208*, *13th PL/DARPA Seismic Research Symposium*, (8-10 October, 1991, Keystone, CO.), Phillips Laboratory, Hanscom AFB, MA. **ADA241325**
- McKenzie, D. (1972). Active tectonics in the Mediterranean region, *Geophys. J. R. astr. Soc.*, **30**, 109-185.
- Nowroozi, A. (1976). Seismotectonic provinces of the Persian Plateau, *Bull. Seism. Soc. Am.*, **66**, 1249-1276.

- Nuttli, O. W. (1980). The excitation and attenuation of seismic crustal phases in Iran, *Bull. Seism. Soc. Am.*, **70**, 469-485.
- Nuttli, O. W. (1981). On the attenuation of L_g waves in Western and Central Asia and their use as a discriminant between earthquakes and explosions, *Bull. Seism. Soc. Am.*, **71**, 249-261.
- Nuttli, O. W. (1986). Yield estimates of Nevada Test Site explosions obtained from seismic L_g waves, *J. Geophys. Res.*, **91**, 2137-2151.
- Singh, S. and Herrmann, R. B. (1983). Regionalization of crustal coda Q in the continental United States, *J. Geophys. Res.*, **88**, 527-538.
- Xie, J. and B. J. Mitchell (1991). L_g coda Q variation across Eurasia, Chapter 3 in *Report PL-TR-91-2286, Final Report, Contract F19628-89-K-0021*, Phillips Laboratory, Hanscom AFB, MA. ADA251590

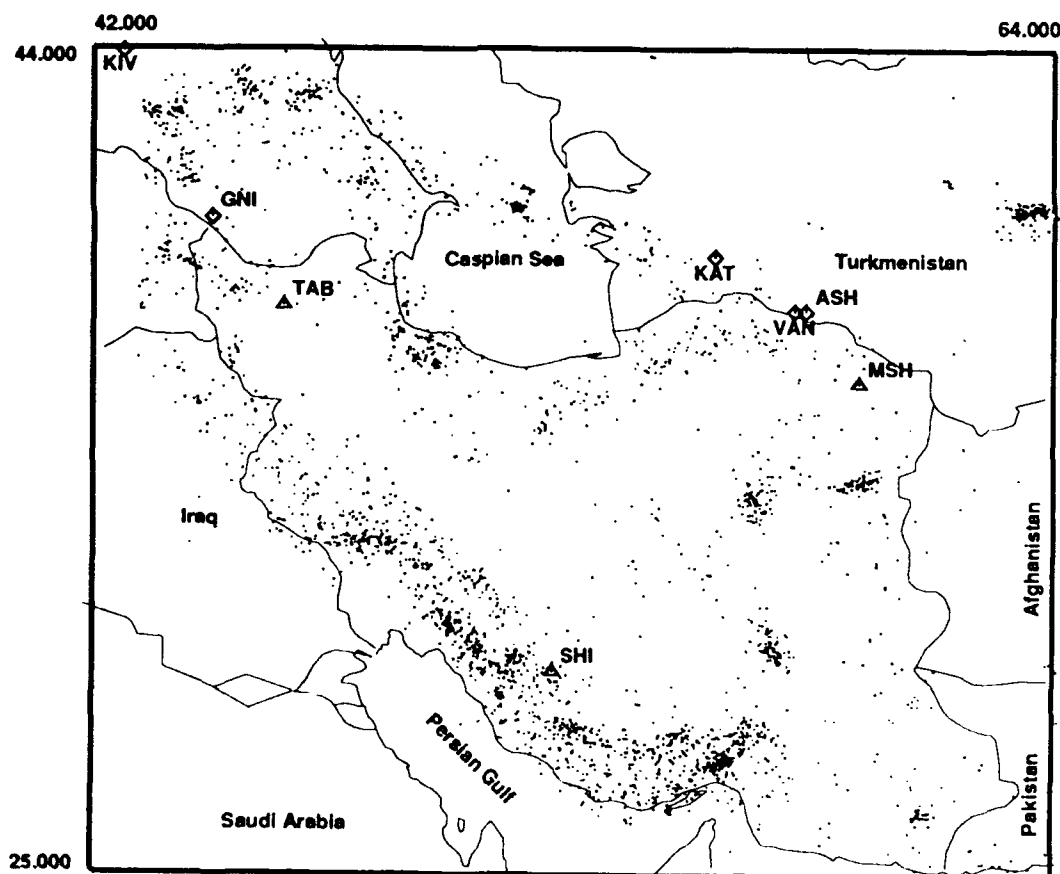


Figure 1. The seismicity map of Iranian Plateau showing all events with $m_b > 4$.

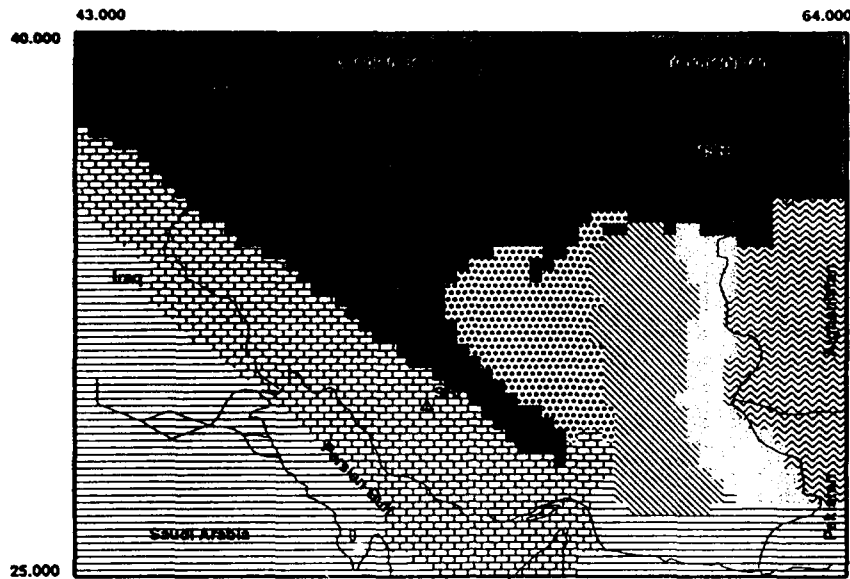


Figure 2. A preliminary regionalization which partitions Iran into 6 seismotectonic regions: Zagros Range, Lut Block, Eastern Iran Range, Central Iran Range, Elburz/Caspian region, and Great Kavir/Estaphan/Rezaiyeh. Block inversion indicates that both the Zagros Range and the Lut Block show a large γ of 0.005 km^{-1} , roughly corresponding to a Q of 181 ± 12 and 183 ± 18 , respectively. The Kopet Dagh, Shahrud Doruneh, and the Qom region also seem to have a Q slightly smaller than the average. The Elburz Province and central Iran have a Q of about 250 for 1 Hz L_g waves, which could be the highest Q value in Iran.

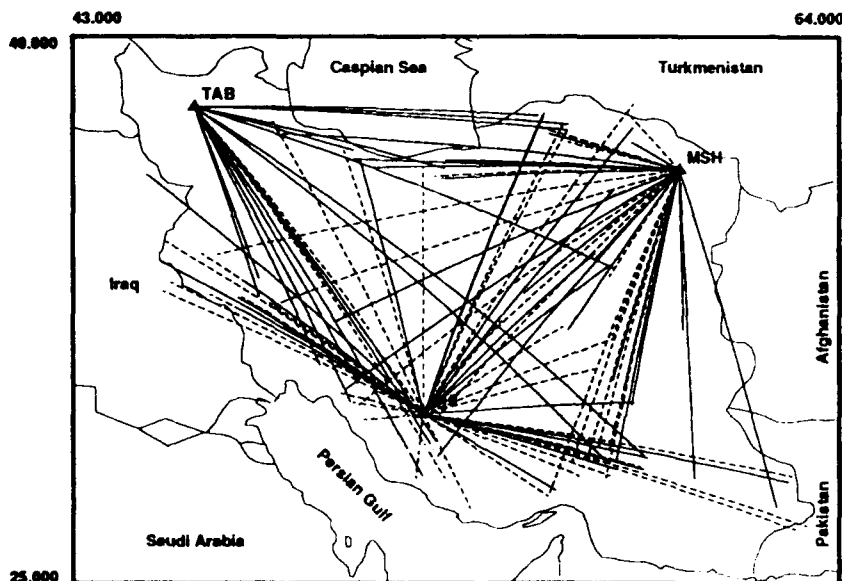


Figure 3. 109 L_g paths recorded at 3 WWSSN stations in Iran (MSH, TAB, and SHI) during 1972-1976 for which the attenuation parameter, γ , was readily measured by Nuttli (1980). Solid and dashed lines represent those with γ value smaller and larger than the average (0.0044 km^{-1}), respectively.

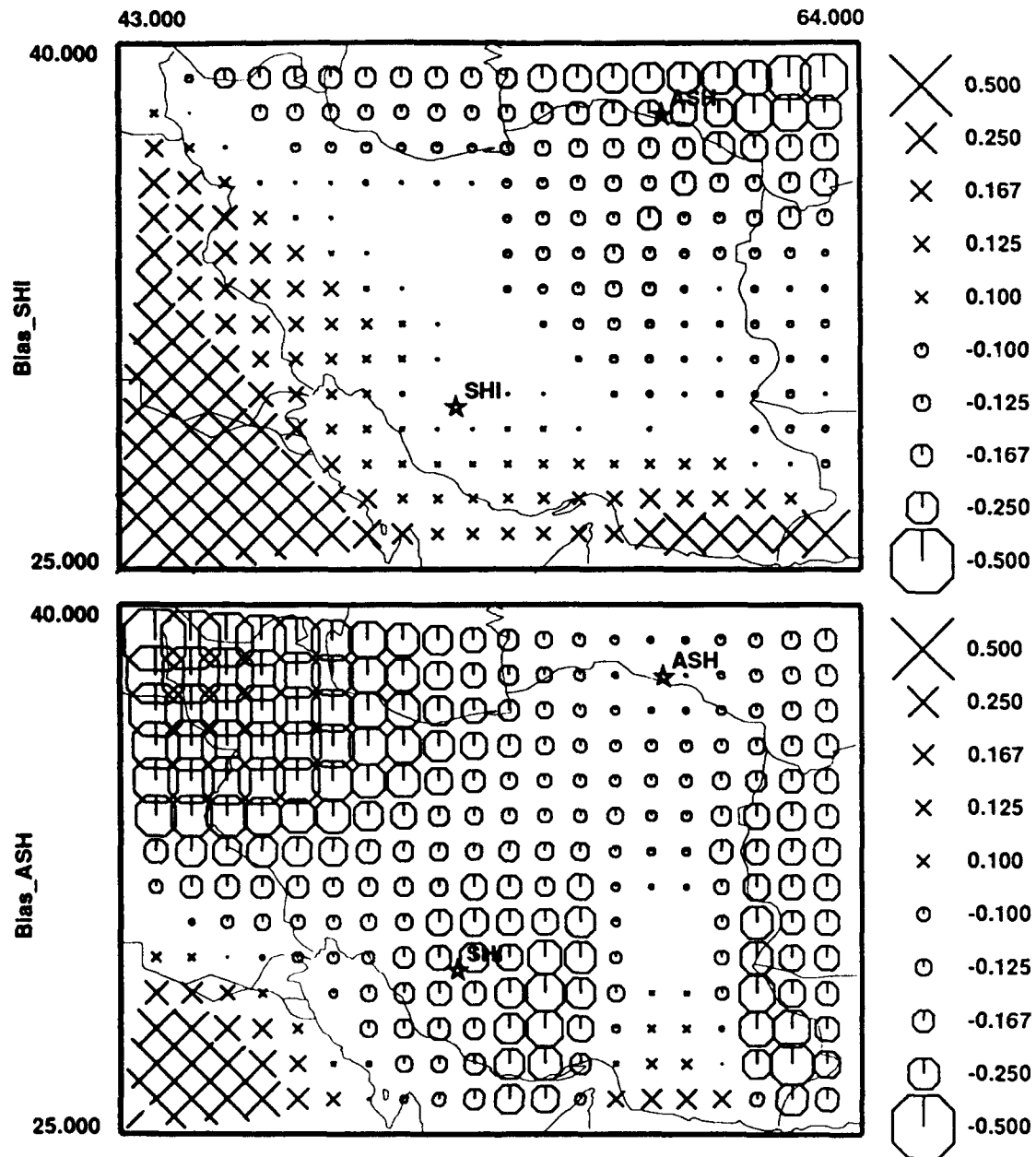


Figure 4. The spatial pattern of apparent $m_b(L_g)$ corrections as a function of hypothetical hypocenters that would be needed at WWSSN station SHI (top) and IRIS station ASH (bottom) if a constant γ of 0.0044 km^{-1} (viz, the average γ across Iran) was assumed in computing $m_b(L_g)$ at these two stations.

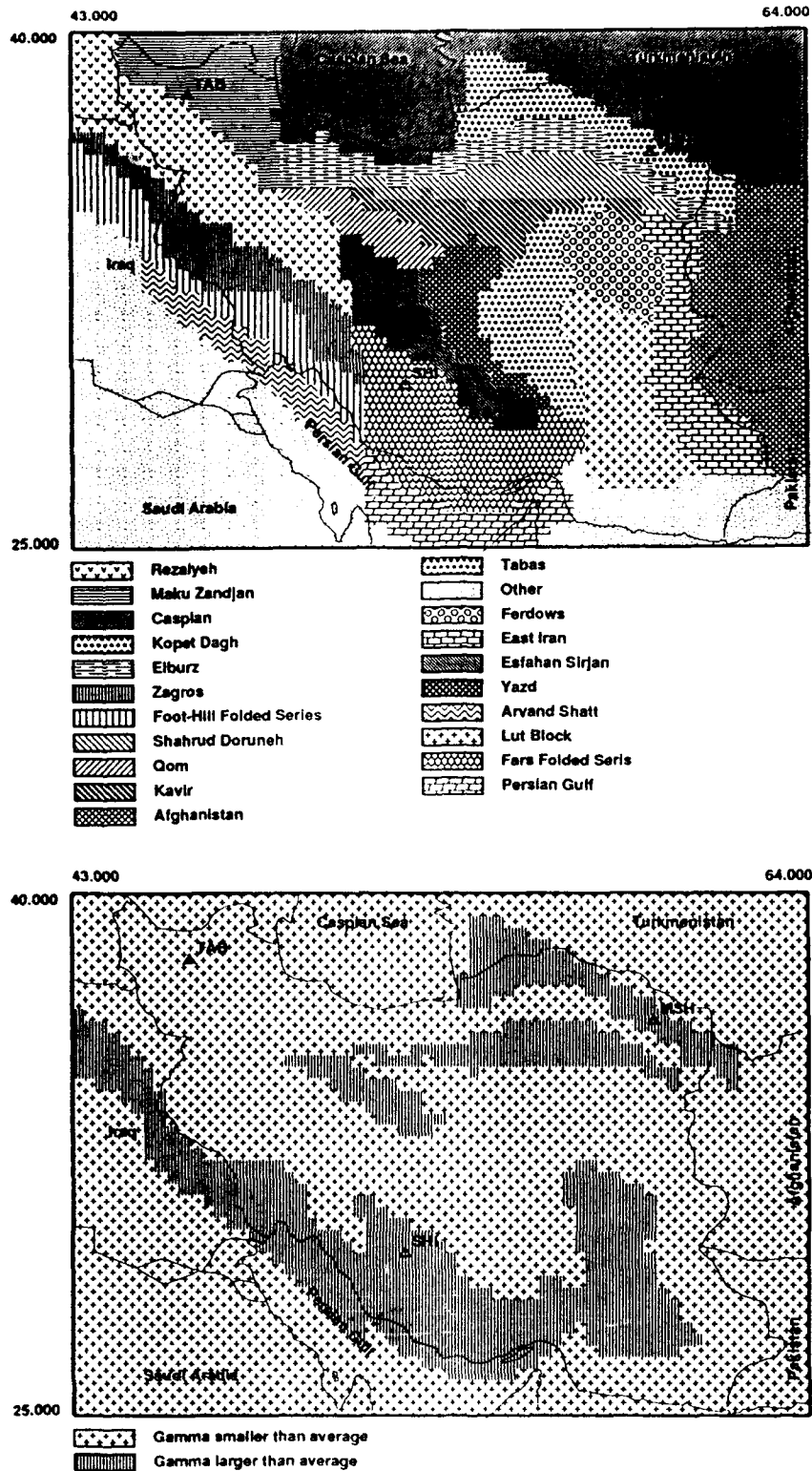


Figure 5. Partitioning Iran into 21 regions (top) as proposed by Nowroozi (1976) would yield more profound spatial variations in Q (bottom) as well as a more complicated pattern of $m_b(L_g)$ residual.

PATH-CORRECTED BODY-WAVE MAGNITUDES AND YIELD ESTIMATES OF SOVIET NUCLEAR EXPLOSIONS

R.-S. Jih, R. A. Wagner
Alexandria Laboratory
Teledyne Geotech
Alexandria, Virginia

R. H. Shumway
Department of Statistics
Univ. of California
Davis, California

Contract Number: F29601-91-C-DB23

Project Objective

The primary objective of this study is to develop and apply the improved statistical methodologies for relating the seismic magnitudes to the explosion yields, treating both the magnitudes and yields as uncertain variables and incorporating the censored information into the yield estimation procedure.

Research Accomplished

1. Methodological Improvement in m_b Determination: The standard procedure used in estimating the source size of underground nuclear explosions using m_b measurements has been to separate the station terms from the network-averaged source terms. The station terms thus derived actually reflect the combination of the path effect and the station effect, when only those events in a close proximity are utilized. If worldwide explosions are used in the inversion, then the path effect tends to be averaged out at each station. In either case, the effect due to the propagation path alone would not be obvious. In this study, we decompose the station magnitudes with the following joint model:

$$E(i) + S(j) + F(k(i),j) + \varepsilon(i,j) = \log_{10}[A(i,j)/T(i,j)] + B(\Delta(i,j)) \quad [1]$$

The right-hand side of [1] is the conventional raw station m_b of the i -th event observed at the j -th station where A , T , and $B(\Delta)$ are the displacement amplitude, the dominant period, and the distance-correction term, respectively. On the left-hand side, S represents the station correction, and $F(k(i),j)$ is the path correction at the j -th station for explosions from the $k(i)$ -th source region. The resulting new event magnitude (*viz.*, $E(i)$ in [1]) is hereby called $\bar{m}_{2.9}$ to avoid confusion with the m_3 defined in Marshall *et al.* (1979) that corrects for the source-region attenuation and station terms solely based on published P_n velocity. Short-period P -wave amplitudes of 217 worldwide underground nuclear explosions, including 28 blasts from Novaya Zemlya and 92 from Semipalatinsk, recorded at 118 seismic stations have been used in one single inversion. Table 1 gives a partial listing of the resulting station and path terms for the six subregions of these two major test sites in the former Soviet Union. Applying these path and station corrections to any individual explosions would yield a reduction in the fluctuational variation of station magnitudes with a factor ranging from 1.2 to 3. Most Novaya Zemlya events have a typical reduction factor of 2 (Figure 1).

2. Propagation Effects on Novaya Zemlya Events: The inferred path terms for Novaya Zemlya and Semipalatinsk explosions have been compared against the travel-time residuals to characterize the propagation paths. Our result indicates that paths from the northern test site in Novaya Zemlya to stations in North America have systematically faster arrivals and smaller amplitudes, suggesting a profound defocusing effect on the first arrivals; while stations in Ireland, Scotland, Spain, Bangladesh, northern India, Pakistan, Korea, and Kenya report slow arrivals and large amplitudes, suggesting a focusing effect. Amplitudes for paths to Greenland, Iceland, Alaska, Turkey, Germany, Luzon, Zimbabwe, Italy, Puerto Rico, Ethiopia, and Hawaii, however, seem to be controlled by the anelastic attenuation with slow rays also associated with small amplitudes, and fast rays associated with large amplitudes. Our empirical path corrections for Semipalatinsk explosions are in good agreement with those independently derived by Marshall *et al.* (1992) based on the digital data recorded at 4 U.K.-designed arrays.

Table 1. Partial Listing of Receiver and Path terms for Soviet Events

| Station | | | | Path Terms [F] | | | | | |
|---------|----------|--------|------------------|----------------|--------|--------|--------|--------|------------------|
| Code | Lon | Lat | Rcv ¹ | BSW | BTZ | BNE | Deg | Mzk | NNZ ² |
| AAE | 38.766 | 9.029 | -0.290 | -0.439 | -0.274 | -0.640 | -0.287 | -0.447 | 0.342 |
| AAM | -83.656 | 42.300 | 0.210 | 0.267 | 0.140 | 0.163 | -0.224 | -0.335 | -0.108 |
| AKU | -18.107 | 65.687 | -0.053 | 0.169 | 0.342 | 0.155 | 0.185 | 0.043 | -0.275 |
| ANP | 121.517 | 25.183 | -0.139 | -0.232 | -0.514 | | 0.123 | -0.301 | -0.164 |
| AQU | 13.403 | 42.354 | -0.102 | -0.167 | -0.141 | -0.159 | -0.051 | -0.104 | 0.602 |
| ATU | 23.717 | 37.972 | 0.171 | 0.050 | 0.088 | 0.040 | -0.312 | -0.176 | 0.063 |
| BAG | 120.580 | 16.411 | 0.030 | -0.189 | -0.148 | -0.064 | -0.213 | -0.273 | 0.157 |
| BEC | -64.681 | 32.379 | -0.120 | 0.160 | 0.216 | -0.072 | -0.087 | -0.289 | -0.176 |
| BKS | -122.235 | 37.877 | 0.104 | -0.008 | -0.015 | -0.116 | -0.026 | 0.112 | -0.202 |
| BLA | -80.421 | 37.211 | 0.022 | -0.165 | -0.158 | -0.184 | -0.217 | -0.410 | 0.173 |

1) the station bias which needs to be corrected (in addition to the path effect).

2) BSW = SW subsite, Balapan; BNE = NE subsite, Balapan; BTZ = transition zone, Balapan; Deg = Degelen Mountain; Mzk = Murzhik; NNZ = northern island, Novaya Zemlya.

3. Yield Estimates of Novaya Zemlya and Semipalatinsk Explosions: We have recomputed the yield estimates of Novaya Zemlya and Semipalatinsk explosions based on the path-corrected m_b values. Assuming the basic coupling and the mantle condition at Novaya Zemlya are comparable to those at Eastern Kazakhstan, the m_b bias relative to NTS at 50KT level using the path-corrected $m_b(P_{max})$ values is inferred as 0.25 and 0.36 magnitude unit for Novaya Zemlya and Semipalatinsk, respectively. The $m_b(P_{max})$ bias of 0.11 (at 50KT level) between Semipalatinsk and Novaya Zemlya (Table 2) is largely due to the difference in pP interference between these two test sites (cf. Table 4). The relative source size determined by Burger *et al.* (1986) and the theoretical $\log(\Psi_\infty)$ yield scaling are combined to extrapolate our m_b scaling to the higher end. The resulting yield estimates of northern Novaya Zemlya explosions range from 2 to 2100 KT, with peak values at 550 KT and 65 KT for events before and after 1976, respectively, which are in reasonable agreement with those in previous studies (*e.g.*, Burger *et al.*, 1986; Sykes and Ruggi, 1989). First motion (*viz.*, P_a) of the initial short-period P waves appears to be a very favorable source measure for explosions fired in hard rock sites underlain by a stable mantle such as Semipalatinsk.

Table 2. Expected m_b Bias Relative to NTS

| Phase/Site | $m_{2.2}$ | | | | $m_{2.9}$ | | | |
|----------------------|-----------|------|-------|-------|-----------|------|-------|-------|
| | 10KT | 50KT | 100KT | 150KT | 10KT | 50KT | 100KT | 150KT |
| $m_b(P_{max})$ (KTS) | 0.47 | 0.44 | 0.42 | 0.41 | 0.40 | 0.36 | 0.35 | 0.34 |
| $m_b(P_b)$ (KTS) | 0.50 | 0.47 | 0.46 | 0.45 | 0.42 | 0.40 | 0.39 | 0.39 |
| $m_b(P_a)$ (KTS) | 0.37 | 0.38 | 0.38 | 0.38 | 0.26 | 0.29 | 0.30 | 0.31 |
| $m_b(P_{max})$ (NNZ) | 0.41 | 0.35 | 0.32 | 0.30 | 0.27 | 0.25 | 0.25 | 0.24 |
| $m_b(P_b)$ (NNZ) | 0.44 | 0.41 | 0.40 | 0.40 | 0.33 | 0.34 | 0.35 | 0.35 |
| $m_b(P_a)$ (NNZ) | 0.37 | 0.38 | 0.38 | 0.38 | 0.26 | 0.29 | 0.30 | 0.31 |

1) KTS = all 5 subsites in Eastern Kazakh combined

2) $m_{2.2}$ = m_b with station terms corrected (Jih and Wagner, 1991); $m_{2.9}$ = m_b with station and path terms corrected (Jih and Wagner, 1992a, 1992b)

3) P_a = the first motion (0-to-peak); P_b = 'b' phase, first peak-to-first trough; P_{max} = the peak-to-peak amplitude within the first 5 seconds (Jih and Shumway, 1989).

4. m_b - L_g Bias at Various Test Sites: We followed the zoning of Ringdal *et al.* (1992) in partitioning Balapan test site into three regions: southwest (SW), transition zone (TZ), and northeast (NE). The $m_b(P_{max})$ - L_g bias of 0.11 m.u. between SW and NE we derived (cf. Table 3) is slightly smaller than that of previous studies. Regressing the RMS L_g furnished by Israelson (1992) and our $m_{2.9}$ on the yields

published by Bocharov *et al.* (1989) (and Vergino, 1989) show that NE explosions have positive L_g residuals and negative m_b residuals; whereas SW explosions show the opposite trend (Figure 3). A three-dimensional geological model of the Balapan test site by Leith and Unger (1989) shows a distinct difference between the NE and SW portions of the test site, with the granites closer to the surface and the alluvium thinner in the southwest. The thicker alluvium layer in NE region could increase the waveform complexity and reduce the magnitudes measured with P_{\max} . The first motion should be least affected by this factor, however. We suggest that the m_b-L_g bias between SW and NE Balapan can be tentatively decomposed into several parts:

[I] Difference in pP between SW and NE,

[II] Difference in m_b coupling, i.e., $m_b(\text{SW}) > m_b(\text{NE})$,

[III] Difference in L_g coupling, i.e., $L_g(\text{NE}) > L_g(\text{SW})$,

[IV] Effects due to the station-station correlation structure,

[V] Effects due to the uneven geographical clustering of stations, as well as any path effect which is not fully accounted for through the network averaging.

Based on our $\bar{m}_{2.9}$, [I] is about 0.03-0.06 m.u. (cf. Table 4), whereas [II] and [III] are about 0.02-0.03 m.u. each (Figure 3). The bias of 0.11 m.u. in Table 3 using $m_b(P_{\max})$ is essentially the sum of [I] through [III]. It reduces to 0.06 if m_b based on the first motion is used (Table 3.) For ISC data, we estimate that [V] is about 0.02 m.u. when the event $\bar{m}_{2.2}$ values derived by the conventional LSMF are used. If $\bar{m}_{2.9}$ were used instead, this term is eliminated, and hence a smaller m_b-L_g bias can be obtained, as it should. Our current m_b determination procedure as described in [1] may not not eliminate [IV] completely. However, the residual contribution of the inter-station correlation alone is believed to be relatively insignificant for WWSSN (as compared to ISC) after the (site-dependent) path terms are removed.

Table 3. $\bar{m}_{2.9}$ vs. RMS ! (NORSAR)¹ at Various Sites

| Site | $m_b(P_a) - m_b(L_g)$, # ² | $m_b(P_b) - m_b(L_g)$, # | $m_b(P_{\max}) - m_b(L_g)$, # |
|------|----------------------------------------|---------------------------|--------------------------------|
| BSW | -0.504±0.011 11 | -0.228±0.011 11 | +0.023±0.015 20 |
| BTZ | -0.523±0.045 6 | -0.243±0.020 6 | -0.041±0.015 14 |
| BNE | -0.565±0.023 8 | -0.304±0.014 9 | -0.092±0.012 14 |
| Deg | -0.484±0.046 5 | -0.207±0.042 5 | +0.012±0.034 5 |
| Mzk | -0.562±0.073 3 | -0.259±0.045 3 | -0.046±0.032 3 |
| KTS | -0.524±0.013 33 | -0.250±0.010 34 | -0.026±0.010 56 |
| NNZ | -0.519±0.020 14 | -0.296±0.023 14 | -0.121±0.024 14 |

1) from Ringdal and Fyen (1991) and Ringdal *et al.* (1992).

2) #: number of events.

Table 4. $m_b(P_{\max})$ and $m_b(P_b)$ vs. $m_b(P_a)$ (with $\bar{m}_{2.9}$)

| Test Site | $m_b(P_b) - m_b(P_a)$ | $m_b(P_{\max}) - m_b(P_a)$ | # |
|-----------|-----------------------|----------------------------|----|
| BSW | 0.290±0.012 | 0.524±0.013 | 14 |
| BTZ | 0.290±0.021 | 0.503±0.035 | 8 |
| BNE | 0.268±0.018 | 0.493±0.025 | 9 |
| Deg | 0.289±0.012 | 0.515±0.014 | 21 |
| Mzk | 0.300±0.017 | 0.531±0.020 | 13 |
| KTS | 0.289±0.006 | 0.516±0.008 | 65 |
| NNZ | 0.226±0.008 | 0.396±0.009 | 28 |
| Lop Nor | 0.133±0.042 | 0.328±0.063 | 12 |

Conclusions

Incorporating the path terms into the joint inversion scheme [1] significantly reduces the station m_b variation. For Novaya Zemlya events, the factor of reduction in m_b variation is typically about 2. The anomalous explosion of Oct 11, 1980 with little improvement turns out to be a double event. The simultaneously inferred path and station corrections show some relevance to known geological/geophysical features. The apparent bias of about 0.11 m.u. in $m_b(P_{\max}) - m_b(P_a)$ between Eastern Kazakhstan and Novaya Zemlya coincides with the $m_b(P_{\max}) - m_b(L_g)$ bias between these two sites, suggesting that the mantle conditions at Novaya Zemlya could be comparable to those at Eastern Kazakhstan if the basic coupling is about the same. Extrapolating our m_b scaling to the high-yield level with relative source sizes determined by Burger et al. (1986) suggests that yields of northern Novaya Zemlya explosions range from 2 to 2100 KT, with peak values around 550 KT and 65 KT for events before and after 1976, respectively. At 50 KT level, the m_b bias relative to NTS using path-corrected $m_b(P_{\max})$ values is inferred as 0.25 and 0.36 for Novaya Zemlya and Eastern Kazakhstan, respectively. The commonly quoted apparent $m_b - L_g$ bias between NE and SW regions of Balapan could have been overestimated somewhat due to the negative correlation between m_b and L_g residuals as well as the pP difference. This bias can be reduced to 0.06 m.u. when the procedure [1] is applied to the m_b based on the first motion.

References

- Bocharov, V. S., S. A. Zelentsov, and V. Mikhailov (1989). Characteristics of 96 underground nuclear explosions at the Semipalatinsk test site, *Atomic Energy*, **67**, 210-214.
- Bonham, S., W. J. Dempsey, J. Rachlin (1980). Geologic environment of the Semipalatinsk area, U.S.S.R. (*Preliminary Report*), U.S. Geological Survey, Reston, VA 22092.
- Burger, R. W., L. J. Burdick, and T. Lay (1986). Estimating the relative yields of Novaya Zemlya tests by waveforms intercorrelation, *Geophys. J. R. astr. Soc.*, **87**, 775-800.
- Israelson, H. (1992). L_g as a yield estimator in Eurasia, *PL-TR-92-2117(I)*, *Final Report*, Phillips Laboratory, Hanscom Air Force Base, MA.
- Jih, R.-S. and R. A. Wagner (1991). Recent methodological developments in magnitude determination and yield estimation with applications to Semipalatinsk explosions, *PL-TR-91-2212(I)* (=TGAL-91-05), *Final Report*, Phillips Laboratory, Hanscom Air Force base, MA. **ADA244503**
- Jih, R.-S. and R. A. Wagner (1992a). Path-corrected body-wave magnitudes and yield estimates of Novaya Zemlya explosions, *PL-TR-92-2042* (=TGAL-91-09), *Scientific Report #1*, Phillips Laboratory, Hanscom Air Force Base, MA. **ADA235959**
- Jih, R.-S. and R. A. Wagner (1992b). Path-corrected body-wave magnitudes and yield estimates of Semipalatinsk explosions, *TGAL-92-05*, *Semi-annual Technical Report #1*, Teledyne Geotech, Alexandria, VA.
- Jih, R.-S. and R. H. Shumway (1989). Iterative network magnitude estimation and uncertainty assessment with noisy and clipped data, *Bull. Seism. Soc. Am.*, **79**, 1122-1141.
- Jih, R.-S. and R. H. Shumway (1992). Magnitude-yield regression with uncertain data: a Monte-Carlo approach with applications to Semipalatinsk underground nuclear explosions, *TGAL-92-11*, *Semi-annual Technical Report #2*, Teledyne Geotech, Alexandria, VA.
- Leith, W. (1987). Tectonics of Eastern Kazakhstan and implications for seismic source studies in the Shagan River area, *Proceedings of DARPA/FGL Annual Seismic Research Review*, 34-37, 15-18 June, 1987, Nantucket, MA.
- Leith, W. and J. Unger (1989). Three-dimensional geological modeling of the Shagan River nuclear test site, paper presented at *DARPA/AFTAC Annual Seismic Research Review*, Patrick AFB, FL.

- Marshall, P. D., D. L. Springer, and H. C. Rodean (1979). Magnitude corrections for attenuation in the upper mantle, *Geophys. J. R. astr. Soc.*, **57**, 609-638.
- Marshall, P. D., D. Porter, and P. Peachell (1992). Analysis of seismograms from nuclear explosions of known yield at Degelen Mountain and Konystan in East Kazakhstan, USSR, *UKIAWE Report O-2/92*, HMSO, London, UK.
- Marshall, P. D., T. C. Bache, and R. C. Lilwall, R. C. (1984). Body wave magnitudes and locations of Soviet underground explosions at the Semipalatinsk Test Site, *UKIAWE Report O-16/84*, HMSO, London, UK.
- Ringdal, F. and J. Fyen (1991). *RMS L_p analysis of Novaya Zemlya explosion recordings*, Semiannual Technical Summary, 1 Oct 1990 - 31 Mar 1991, *NORSAR Scientific Report No.2-90/91*, NTNF/NORSAR, Kjeller, Norway (May 1991).
- Ringdal, F., P. D. Marshall, and R. Alewine (1992). Seismic yield determination of Soviet underground nuclear explosions at the Shagan River Test Site, *Geophys. J. Int.*, **109**, 65-77.
- Sykes, L. R. and S. Ruggi (1989). Soviet nuclear testing, in *Nuclear Weapon Databook (Volume IV, Chapter 10)*, Natural Resources Defense Council, Washington D. C.
- Vergino, E. S. (1989). Soviet test yields, *EOS, Trans. A.G.U.*, Nov 28, 1989.

VARIOUS WWSSN MAGNITUDES OF EVENT 791018Z

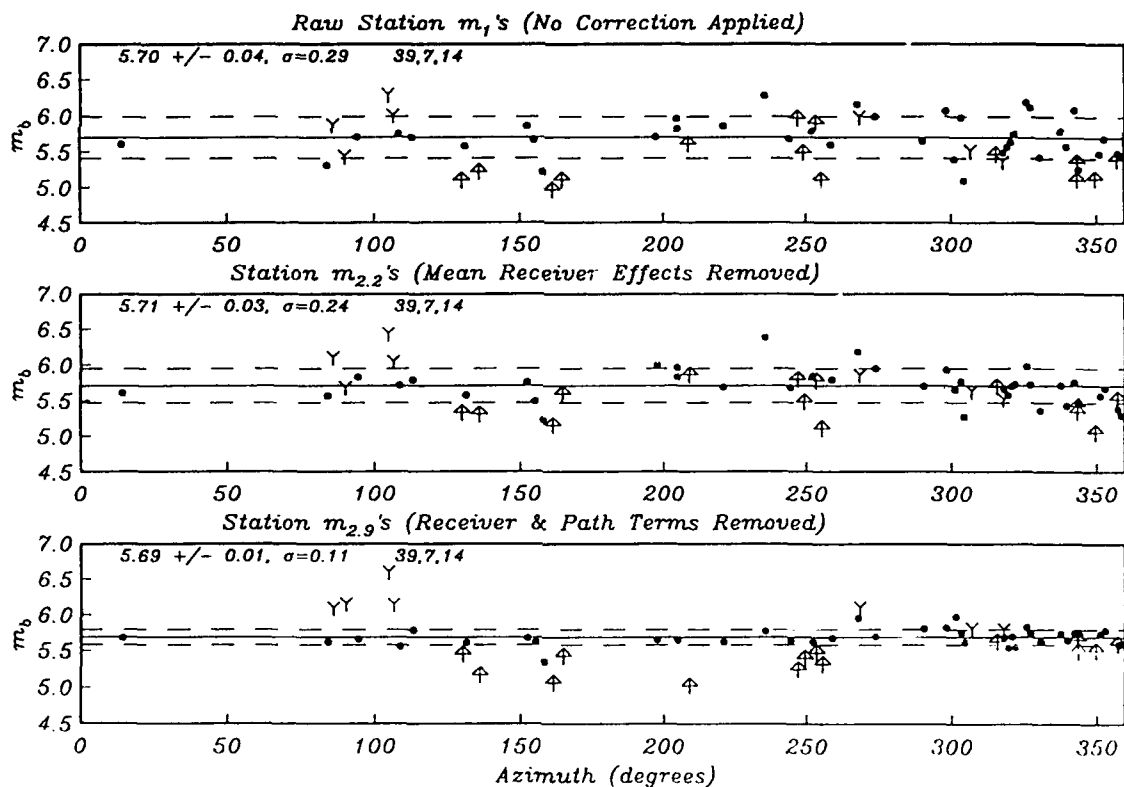


Figure 1. Scatter plot of 3 different types of station m_b 's for Novaya Zemlya explosion of Oct 18, 1979. The 39 good recordings, 7 noise, and 14 clips are shown with filled circles, Y-shaped downward arrows, and upward arrows, respectively. The raw station m_b 's (top) have a standard deviation of 0.29 m.u. Applying the station corrections reduces the scatter to 0.24 m.u. (middle). Applying the "secondary" corrections to count for the path effects (viz., the "F" term in [1] and Table 1) reduces the scatter further down to 0.11 m.u. (bottom). The dramatic reduction of variation from m_1 to $m_{2,9}$ shows a factor of nearly 2.7, as compared to the worst case of about 1.26 for the explosion of Oct 11, 1980, which turns out to be a double event (Jih and Wagner, 1992a). Novaya Zemlya and Semipalatinsk events typically exhibit a reduction factor around 2 (Jih and Wagner, 1992b).

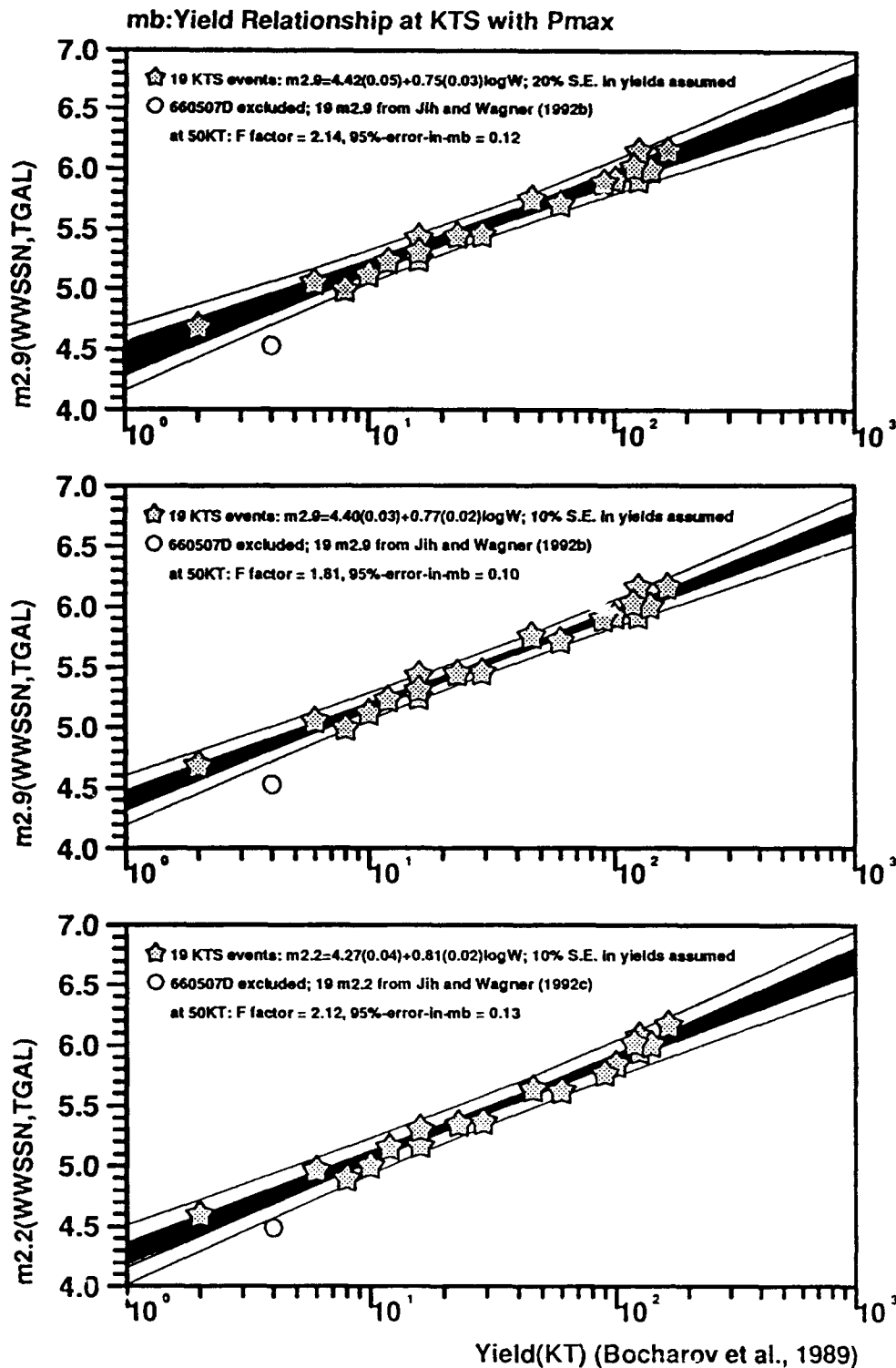


Figure 2. Regressing the $m_b(P_{max})$ on 19 Soviet published yields with various m_b and different levels of postulated uncertainties in the yields (from Jih and Shumway, 1992). The uncertainties in the m_b s and the yields are taken into account through 800 Monte-Carlo simulations. The darkened bundle is actually the collection of all 800 regressions, with each line represents the result using a possible realization of 19 $[m_b, \text{yield}]$ pairs perturbed by the postulated probabilistic distributions. The 95% confidence band (shown as 2 hyperbolic curves around the darkened bundle) is narrowest near the centroid, as expected. With the same postulated level of 10% standard errors in the yields, $m_{2.9}$ (middle) would provide higher confidence (i.e., smaller F factor) in the yield estimate as compared to $m_{2.2}$ (bottom) which only corrects for the station effects.

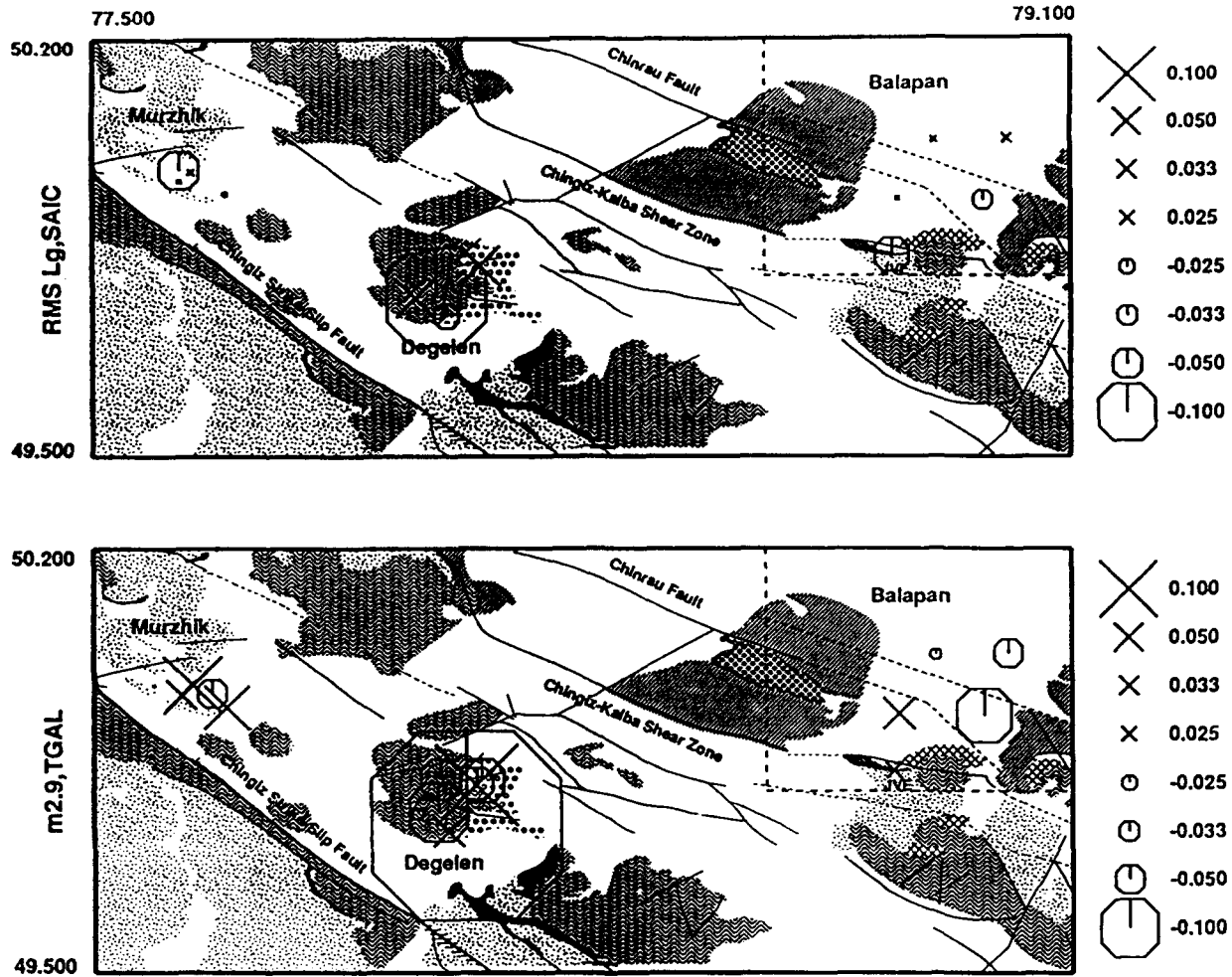


Figure 3. Regressions using yields published by Bocharov *et al.* (1989) indicate that BNE explosions have positive L_g residuals (top) and negative m_b residuals (bottom); whereas BSW explosions show the opposite trend. Thus it would seem plausible that the commonly quoted apparent m_b-L_g bias of 0.15 m.u. could have been overestimated somewhat due to the negative correlation between m_b and L_g residuals (Jih and Wagner, 1992b). There is a distinct difference in the source media between the NE and SW portions of Balapan test site, with the granites closer to the surface and the alluvium thinner in the southwest. The thicker alluvium layer in NE region could increase the waveform complexity and reduce the magnitudes measured with P_{max} .

- Sedimentary & volcanic rocks
- Devonian & Carboniferous rocks
- Granitic rocks
- Limestone
- Lower Metamorphic rocks
- Upper Paleozoic sedimentary rocks
- Migmatite
- Metamorphic rocks
- Cataclastic rocks

Top: RMS L_g (SAIC) - $0.78 \log(W)$ - 4.42

Bottom: $m_{2.9}$ (WWSSN) - $0.77 \log(W)$ - 4.40

L_g (top): RMS L_g based on Soviet waveforms (Israelson, 1992)

$m_{2.9}$ (bottom): WWSSN-network average of $[m_b(l,j)-S(i)-F(l,k(j))]$

Yield (W): Bocharov *et al.* (1989)

Locations: Bocharov *et al.* (1989), Marshall *et al.* (1984)

Tectonics: Bonham *et al.* (1980), Leith (1987)

WAVE PROPAGATION NEAR EXPLOSIVE SOURCES

Lane R. Johnson and T. V. McEvilly

Center for Computational Seismology, Lawrence Berkeley Laboratory,
and Seismographic Station, University of California,
Berkeley, California 94720

Contract No. F19628-90-K-0055

OBJECTIVE

The general objective of this research effort is directed toward the problems of detection and identification of underground explosions through the study of radiated seismic waves. Particular emphasis is on the collection and analysis of broad band seismic data at near and regional distances. In the past couple of years much of the research has focussed upon the physical processes which control the relationship between the yield of an explosion and the amplitude of seismic waves radiated into the far field. Of particular interest in this relationship is the role played by material properties in the vicinity of the source. A number of special experiments have been conducted for the purposes of testing the effects of source depth, source size, and source medium upon the seismic yield of explosions. This paper describes an attempt to model some of the data collected in these experiments. An equivalent elastic treatment has been investigated as a possible means of handling the important region between the original cavity radius and the elastic radius of an explosion.

RESEARCH ACCOMPLISHED

The relationship between the energy of an explosive source and the amplitude of the seismic waves which are radiated into the far field has been a primary interest of the verification program since its beginning (Latter et al., 1959). The problem is made difficult by the fact that the seismic energy represents only a small fraction of the total energy. Most of the energy of the explosion is deposited within the elastic radius by a series of complicated non-linear processes. Given that the wave propagation problem beyond the elastic radius is essentially solved, the primary difficulty concerns the treatment of the non-linear region surrounding the source. A number of computer codes have been developed for modeling this region, but they are fairly complicated, involving hydrodynamic effects, shock waves, and non-linear equations of state. Because of the basic numerical approach which is followed in these codes, they do not readily provide insight into questions about which parameters are playing the critical role in determining the radiated elastic waves. We have thus begun looking at alternative methods of modeling this region immediately surrounding an explosive source.

In the recent study of Denny and Johnson (1991) an extensive data base for explosions was analyzed in terms of the factors which control seismic scaling laws. Data on cavity size, seismic moment, and corner frequency were systematically regressed against explosion yield and such material properties as density, elastic constants, gas porosity, and overburden pressure. This type of analysis was successful in reconciling a wide variety of explosion data into fairly simple empirical scaling relationships. A single scaling relationship could be used over the entire range of explosion size and type, ranging from tiny chemical explosions in the laboratory to large nuclear explosions. A suggestion which emerges from these results is that, at least with respect to the energy radiated as elastic waves, a very basic approach to the explosion process might yield useful results. The fundamental problem is one of energy flux and the possibility exists that the basic principles of wave propagation might be sufficient even in the non-linear region surrounding the source. Consequently, an exploration of various alternative approaches which could possibly be used to model elastic wave generation by explosive sources has begun.

In order to minimize the computational effort and also retain a formulation which provides easy access to the basic physics of the problem, we have been particularly interested in analytical approaches to this problem. In this regard, there are a couple of recent publications that suggest that it might be possible to handle the non-linear region with approximate analytical solutions. Lamb et al. (1992) have obtained an approximate analytical solution for the hydrodynamic region that depends upon material properties in a simple way and seems to satisfactorily explain the basic features of shock waves generated by explosions. Majtenyi and Foster (1992) introduce a simple approximation that explains some of the features of shock waves in the hydrodynamic region and also facilitates a smooth transition to the elastic wave propagation in the elastic region. Glenn (1992) has also presented some interesting results which present an insight into the parameters which control the energy flow from the explosion cavity out to the elastic radius. We have been investigating these approaches and attempting to determine how they might be coupled to the elastodynamic equations that apply beyond the elastic radius.

We have also begun investigating another approach to this problem in which an equivalent elastic treatment is used for the region between the original cavity radius and the elastic radius. This concept of an equivalent elastic medium has been used quite successfully by earthquake engineers to model the non-linear behavior of soils that occurs during strong ground motion. In our present attempts we are using constraints on the energy flux as an aid in selecting the relevant elastic parameters. We have derived the complete solution for the case where the density and elastic constants vary in an arbitrary manner as a function of radius. Thus we can make the material properties a function of the stresses and strains in the outward propagating pressure pulse and obtain the results in the form of a simple numerical propagation of the analytical solutions. Our present formulation relates density and bulk elastic properties to the peak over-pressure in the pressure pulse and shear and anelastic properties to the maximum shear strain. The material properties are adjusted in an iterative process so

that the appropriate properties are present in the vicinity of the propagating pressure pulse. While this approach is only an approximation to calculations with hydrodynamic equation-of-state codes, it has the advantage of providing simple analytic results in which the role of various model parameters are easily investigated. This is important when one wants to conduct a sensitivity analysis over a wide range of explosion sizes and material parameters. It is also useful in investigating end member situations where the limits of the analytical solutions can often be obtained in forms that allow simple physical interpretations.

The basic ideas of the equivalent elastic treatment are illustrated by some initial calculations in Figure 1. The upper panel shows the first 10 msec of measured particle velocity within a few meters of a buried chemical explosion, while the lower panel shows the results of simulating these measurements with an analytical code that employs equivalent elastic material properties. In this case the shear modulus within 5 meters of the explosion was reduced as a means of simulating the finite strength of the tuff which was the emplacement media. In this distance range the peak radial stresses exceeded 0.1 Gpa, which is the range where it is generally considered that tuff begins to fail by plastic yielding. The agreement between the observed and calculated velocities in Figure 1 indicates some promise for this approach. The recordings at the two closest distances of 1.5 and 7.2 meters are somewhat suspect, so the comparison here may not be valid. The accelerations at the first gage was in excess of 8000 g and there is a suggestion on the acceleration record that the gage may have broken loose and gone into ballistic motion. The acceleration at the second gage was greater than 2500 g and the maximum acceleration occurs during the second pulse which is delayed by about 4 msec, which is very difficult to explain in terms of an outgoing pressure wave. At the three outer gages the observed records seem more reasonable, indicating an outward propagating wave that changes slowly with distance. The simulated records agree quite well in amplitude and period in this range, although the asymmetry in the waveforms is somewhat different for the observed and calculated results. One possible explanation for this difference is that the dispersion associated with the anelastic properties of the medium has not been properly modeled in the simulations. This, along with many other aspects of the simulation calculations, need considerably more investigation. We plan to apply this modeling approach to the free field measurements from other chemical explosions, as several other recordings such as shown in Figure 1 are available from recent recording experiments, and we also are in the process of applying this approach to free field measurements from nuclear explosions.

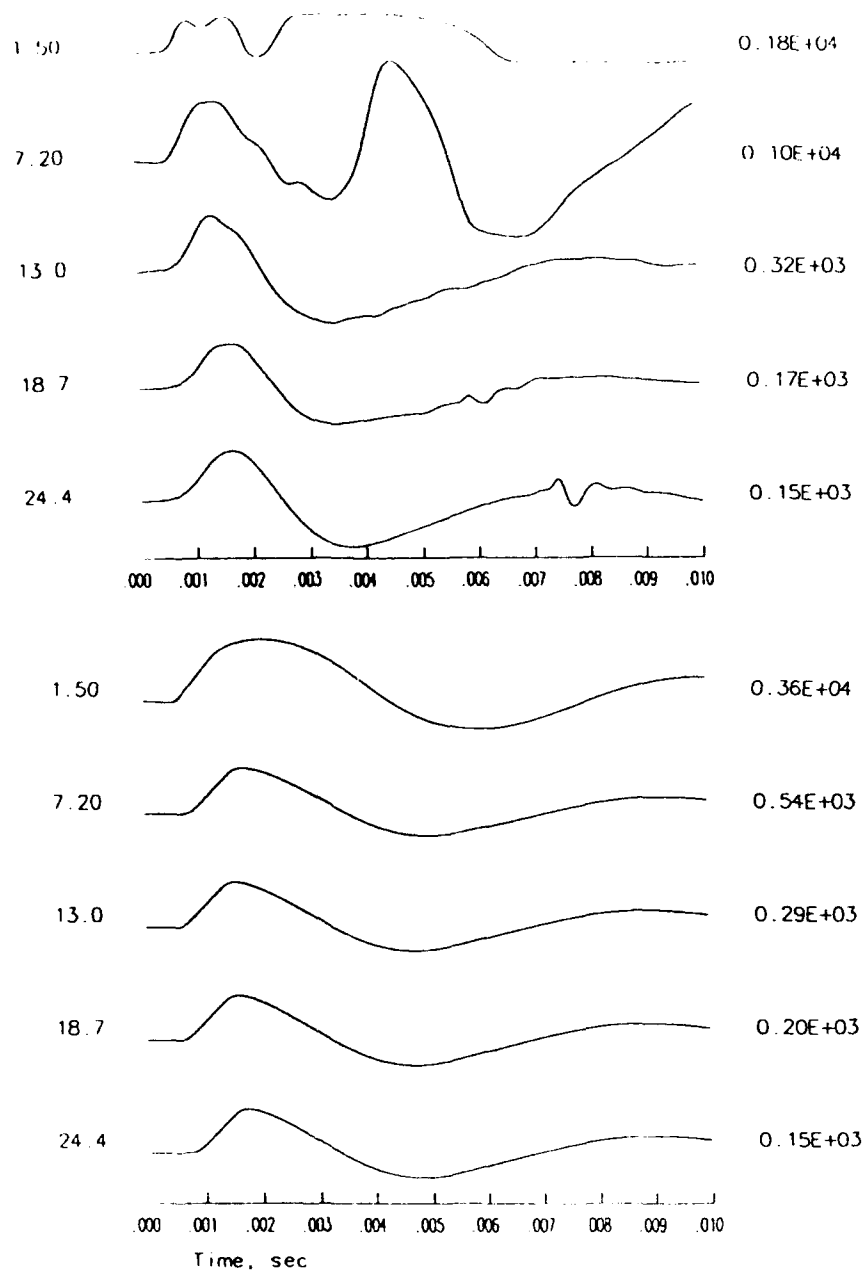


Figure 1. Recorded and calculated free field measurements for a chemical explosion. The explosion consisted of 100 pounds of C4 explosive which was detonated at a depth of 534 meters in Yucca Valley. The upper panel shows velocities that were recorded by a linear array of gages directly above the explosion. The number on the left of each trace is the radial distance of the gage from the center of the explosion in meters and the number on the right is the maximum velocity in cm/sec. The traces have been multiplied by distance from the explosion for the purposes of plotting. The lower panel is similar to the upper except that the traces were calculated using an equivalent elastic treatment of the material surrounding the source.

CONCLUSIONS AND RECOMMENDATIONS

We are still in the initial stages of this investigation, but the general approach which has been adopted appears to offer promise. The computer codes are all developed and are quite efficient, so that it is possible to run extensive simulation studies in which the role of various parameters is investigated. For instance, we are looking at the effect of source depth and investigating whether this can explain some interesting features of chemical explosions in quarries.

One characteristic of the equivalent elastic method is that it requires a relationship between material properties and the level of strain. Thus, we are putting together a data base of empirical relationships for equivalent elastic treatments and attempting to cover all of the different types of materials which might serve as source media for explosions. The literature contains considerable data of this type for various soils, but we are also searching for comparable data pertaining to hard rocks.

A situation which makes this study feasible is the availability of the seismic wave form data which can be used to check the modeling efforts. These data, which have been collected in recording experiments performed in recent years, cover a considerable range in source type, source size, source medium, and source distance. It is important to take advantage of any future opportunities to expand the size and variety of this data base.

References

- Denny, M. D., L. R. Johnson, The explosion seismic source function: models and scaling laws reviewed, Explosion Source Phenomenology, Geophys. Monograph 65, American Geophysical Union, Washington, 1991.
- Glenn, L. A., Energy-density effects on seismic decoupling, preprint, Lawrence Livermore National Laboratory, 27 pp, January, 1992.
- Lamb, F. K., B. W. Callen, and J. D. Sullivan, An approximate analytical model of shock waves from underground nuclear explosions, J. Geophys. Res., 97, 515-535, 1992.
- Latter, A. L., E. A. Martinelli, and E. Teller, Seismic scaling law for underground explosions, Phys. of Fluids, 2, 280-282, 1959.
- Majtenyi, S. I., and E. L. Foster, Propagation velocity of shock waves and pressure waves in soil and rock, Geophys. Res. Lett., 19, 865-868, 1992.

**VARIATION OF AMPLITUDES AND WAVEFORMS
OF SEISMIC PHASES RECORDED BY A SMALL-APERTURE ARRAY
SURROUNDING WESTON OBSERVATORY**

Alan L. Kafka and Matthew R. Jacobson-Carroll
Weston Observatory
Dept. of Geology and Geophysics
Boston College
Weston, MA 02193

Contract No. F19628-90-K-0035

OBJECTIVE:

A key issue in monitoring nuclear explosions is the extent to which details of the earth structure in the vicinity of a recording site can affect amplitudes and waveforms of seismic waves. In an effort to address this issue, we are analyzing data recorded by a seismic array that we installed in the area surrounding Weston Observatory (the WESTon Seismic Array, WESSA; Figure 1). The purpose of this experiment is to investigate the extent to which site effects in the vicinity of the Observatory cause variations in amplitudes and waveforms of seismic waves.

RESEARCH ACCOMPLISHED:

We installed an array of 1-Hz vertical seismometers at distances up to about 0.25 km from the main recording piers of station WES. In addition, we installed temporary field stations with 2-Hz seismometers at sites located about 1 km from the Observatory to temporarily extend the array. The array does not currently have an event trigger, so all events recorded on the array thus far are quarry and construction blasts (for which we have advance warning of the event time). We are in the process of installing an event trigger algorithm, and are also planning to extend the array to include at least one station at about 0.5 km from the reference station.

With the exception of site F and two recently installed sites, the array sites are located along two arms: one trending approximately NS and the other trending approximately EW. Site F is near the center of the triangle formed by the two arms. The Observatory has four seismic recording piers that are anchored into bedrock (sites A, B, C and D), with the greatest distance between those piers being 250 m. Site A is the same pier on which the short-period station of the New England Seismic Network is located, and that site was chosen as a reference site.

Part of this experiment involves comparing signals recorded by seismometers directly adjacent to each other to estimate the fundamental level of precision with which we are capable of measuring amplitudes and waveforms. Three seismometers are therefore located adjacent to each other at the reference site, and three seismometers are located adjacent to each other at site B (43 m from the reference site, and about 5 m from the WWSSN piers). Two seismometers are located at site D (122 m east of the reference site), and a single seismometer is located at site C (250 m south of the reference site). Four additional seismometers are buried in soil overlying the bedrock. The thickness of the soil cover at these sites is probably on the order of 10 to 30 ft (e.g. Koteff, 1964).

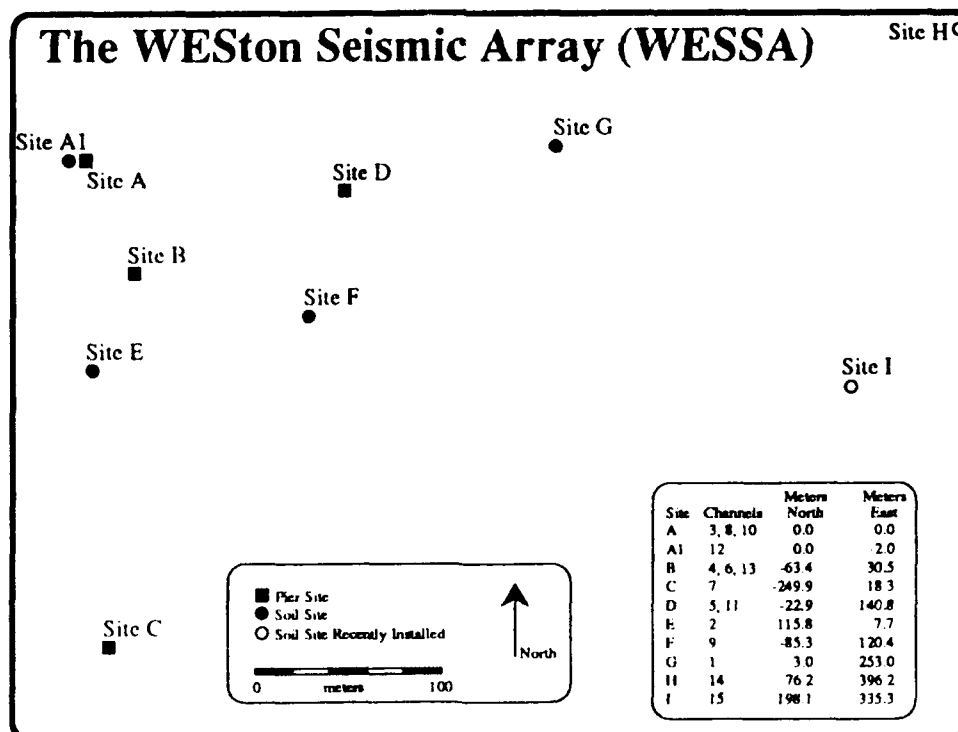
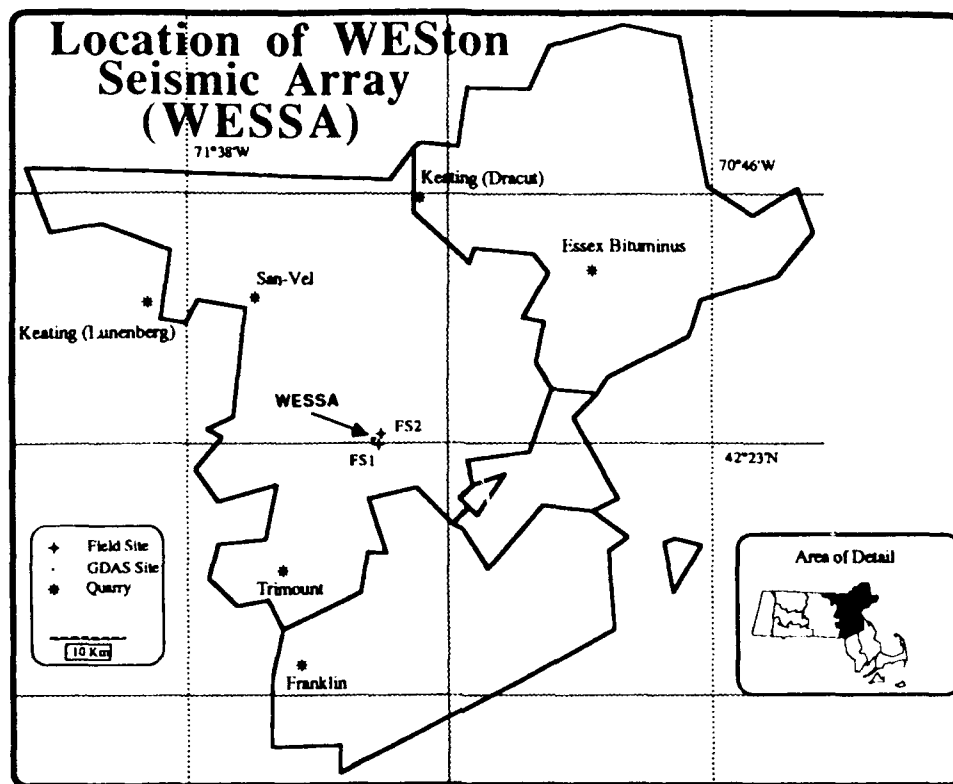


Figure 1: (a) Map of eastern Massachusetts showing location of the WESTon Seismic Array (WESSA) and locations of local quarries and field sites. (b) Geometry of the WESSA.

The data from the WESSA are recorded at 50 sps by the Geophysical Data Acquisition System (GDAS), which was developed at Weston Observatory (Blaney, 1990). All of the seismometers are connected to the GDAS recording system by cables. The system is calibrated with the seismometers deployed at their field sites by applying a known current to the calibration coils of the seismometers. Estimates of the system response were obtained by minimizing the least squares error between the observed calibration pulses and pulses determined from theoretical models of the system.

So far we have recorded 72 blasts on the array. Nearly all of the events recorded by the array are quarry blasts, although we have also recorded a relatively large construction blast detonated in Boston Harbor (located about 30 km from the array). Figures 2, 3 and 4 show examples of seismograms recorded by the array. Amplitudes and waveforms of the seismograms shown in those figures can be directly compared from one seismogram to the next because the signals have been processed to appear as if they were recorded by the same instrument. This was accomplished by first deconvolving the system response and then convolving the resulting ground motion through a theoretical instrument with a response similar to that of Channel 3 (located at the reference site): i.e. a 1-Hz seismometer, a damping constant of 0.77, a gain of 15,364 counts/micron at 1-Hz, and a 12.5 Hz anti-aliasing filter.

For a given event, we calculated spectral amplitudes for each site, and compared them with the amplitudes recorded on Channel 3. Specific results for three events recorded by the array are shown in Figures 2, 3 and 4. Figure 2 shows three examples of spectral ratios for a quarry blast detonated at the Keating quarry in Dracut, MA. The spectral ratios for the Dracut blast are the ratios of spectral amplitudes recorded on Channels 1, 7 and 8 relative to Channel 3. The results for Channel 8 show that after correcting for system response, the amplitudes are very similar for the two seismometers located adjacent to each other. For this event, the spectral ratios for pier site C vary by about the same amount as for soil site G (maximum deviation of about 60 to 80%).

Figure 3 shows three examples of spectral ratios for a quarry blast detonated at the San-Vel quarry in Littleton, MA. The spectral ratios for this blast are for the same channels as for the Dracut blast. The results for Channel 8 are nearly identical to the results for the previous example. For the San-Vel blast, the spectral ratios for pier site C vary by about the same amount as for soil site G between 4 and 7 Hz (maximum deviation of about 60%). At higher and lower frequencies, however, the soil site has much greater variations (more than 100%). The large maximum deviations at this soil site appear to be a result of background noise interfering with the signals.

Figure 4 shows three spectral ratios for the construction blast located in Boston Harbor, which has trace amplitudes that are about 3 times as great as those of the quarry blasts. The spectral ratios shown for this blast are for Channels 2, 7 and 8 relative to Channel 3. The results for Channel 8 are surprising because they are different from what we obtained in all of the cases of quarry blasts that we analyzed. For the Boston Harbor event, the variation between Channels 3 and 8 (located adjacent to each other) is about the same as that between Channels 3 and 7 (located 250 m from each other). Also, for this event, the spectral ratios for pier site C vary by about the same amount as for soil site G below about 3 Hz (maximum deviation of about 30%). At higher and lower frequencies, however, the soil site has much greater variations (more than 700%). Unlike the case for the (smaller) quarry blasts, the large deviations at the soil site do not appear to be a result of background noise interfering with the signal.

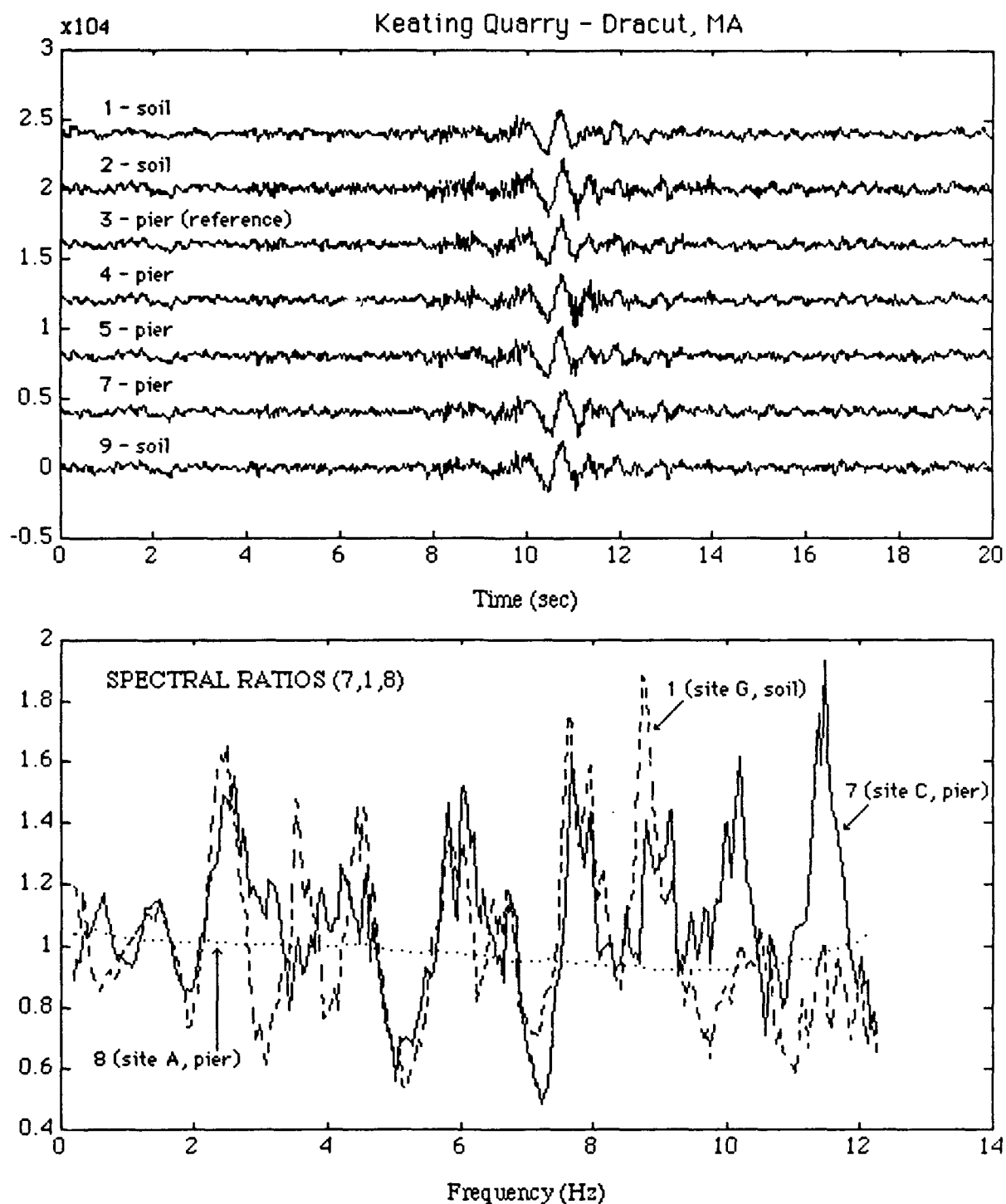


Figure 2: (a) Examples of seismograms recorded from a quarry blast detonated at the Keating quarry in Dracut, MA (event 91-227A). (b) Spectral amplitude ratios for Channels 1, 7 and 8 relative to Channel 3.

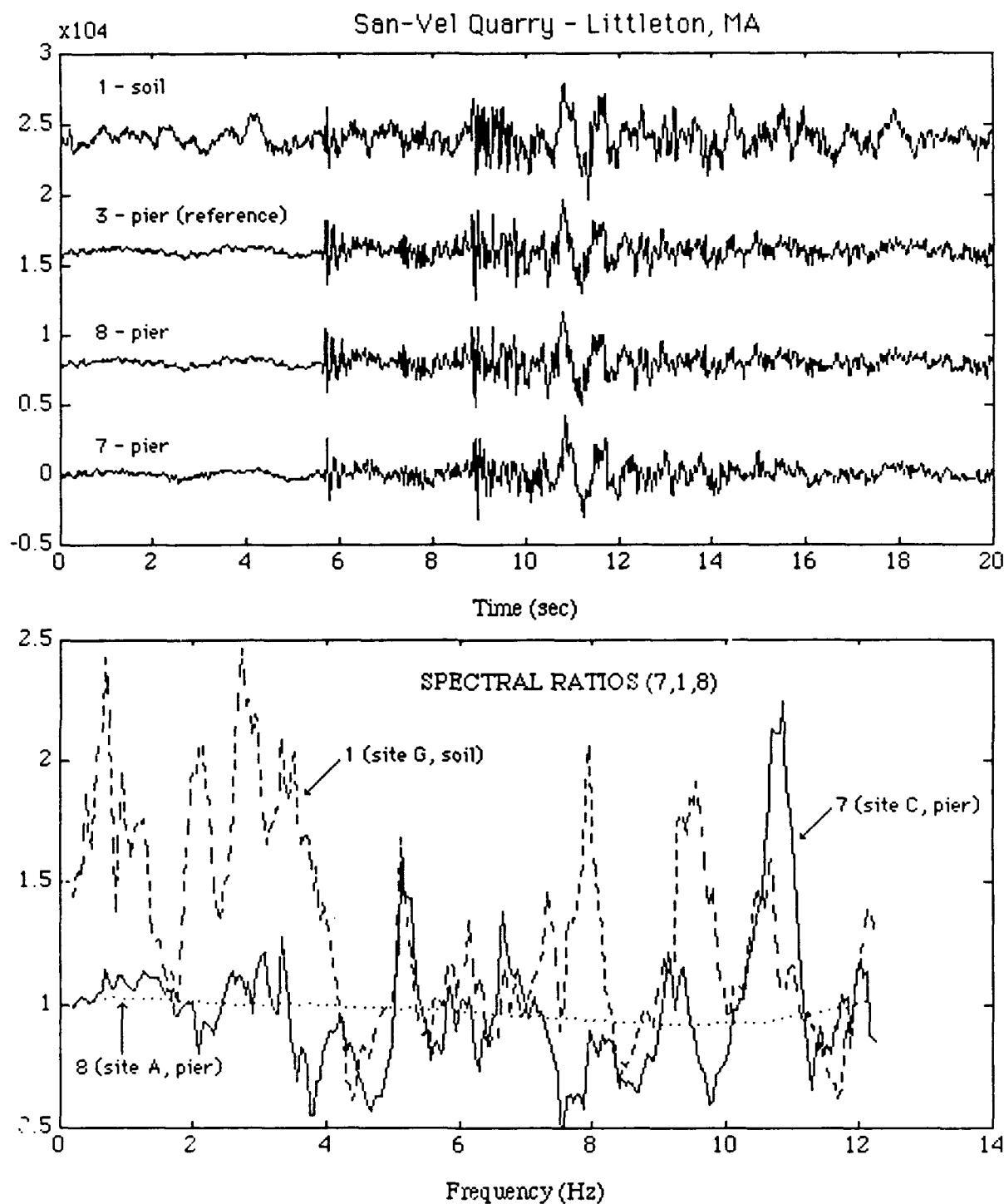


Figure 3: (a) Examples of seismograms recorded from a quarry blast detonated at the San-Vel quarry in Littleton, MA (event 91-234B). (b) Spectral amplitude ratios for Channels 1, 7 and 8 relative to Channel 3.

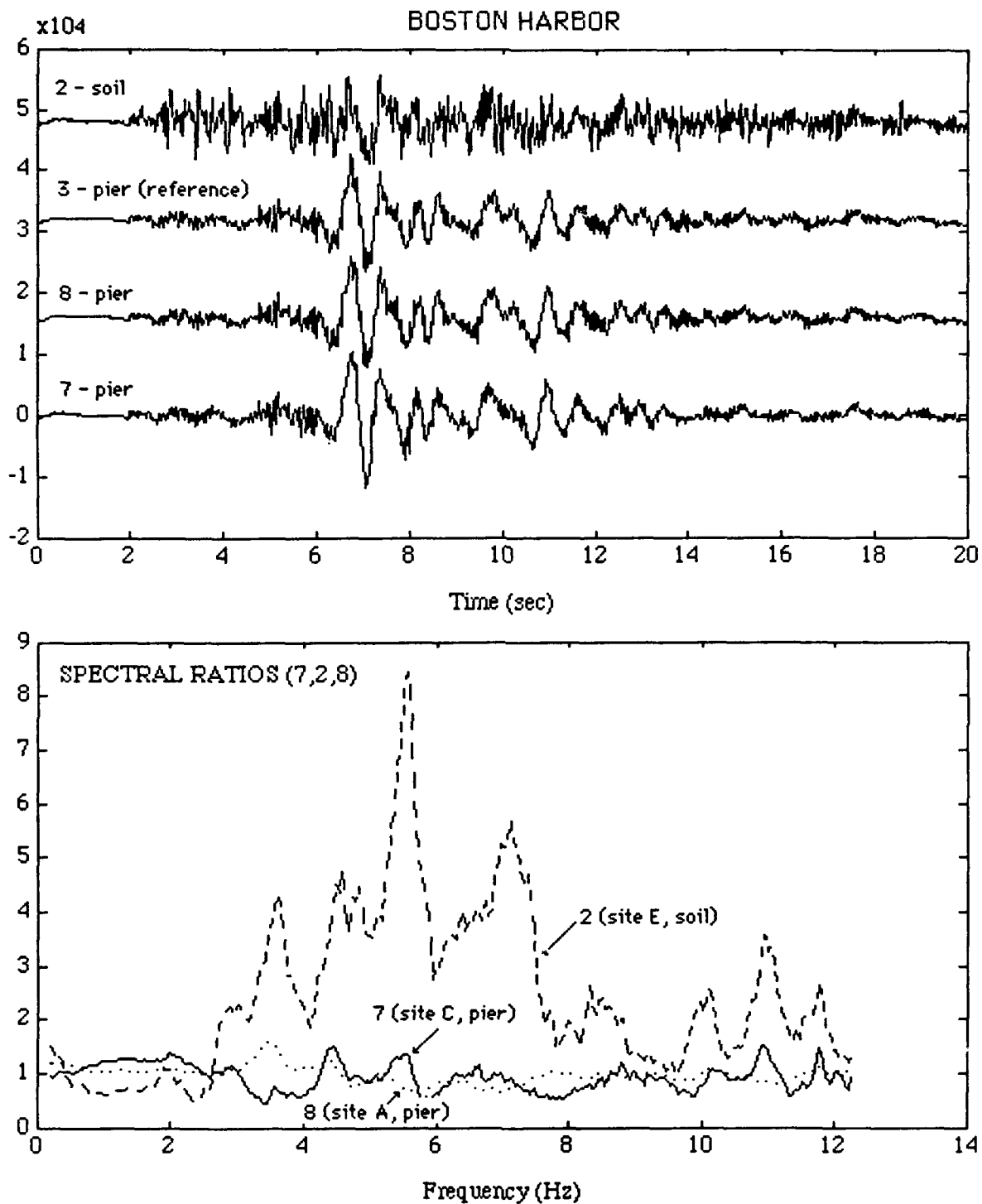


Figure 4: (a) Examples of seismograms recorded from a construction blast detonated in Boston Harbor (event 92-103A). (b) Spectral amplitude ratios for Channels 2, 7 and 8 relative to Channel 3.

CONCLUSIONS AND RECOMMENDATIONS:

Preliminary results of this study are summarized in Table 1, which shows conservative estimates of the maximum and average deviations of spectral amplitudes at the various sites (compared to the amplitudes measured on Channel 3). These estimates are "conservative" in the sense that unusually large deviations were ignored in some cases, particularly if there was evidence of significant background noise at that site.

These preliminary results suggest the following general pattern of variation in spectral amplitudes: At 1-Hz, the maximum deviation from the amplitude measured at the reference site is at least 20% at the pier sites and at least 100% at the soil sites. Between 2 and 4-Hz, the maximum deviation is at least 50% at the pier sites and at least 200% at the soil sites. Between 6 and 10-Hz, the maximum deviation is at least 120% at the pier sites and at least 400% at the soil sites.

Results based on the Boston Harbor blast are strikingly different from the results based on the (smaller) quarry blast sources. In particular, the apparent difference between system responses based on the larger blast is hard to explain. It appears that the seismometers are responding quite differently to the stronger ground motion than to the weaker ground motion. Although for quarry blasts some of the large maximum deviations at the soil sites appear to be a result of background noise interfering with the signals, that does not appear to be the case for the Boston Harbor blast. The relatively strong signals recorded from the Boston Harbor blast suggest that at higher frequencies, amplitudes can be greatly amplified at the soil sites relative to pier sites.

There is no obvious indication of a trend toward greater variation in amplitudes for sites separated by greater distances. Based on these observations it appears that (at this scale) site effects play a larger role than propagation effects in determining the variation in spectral amplitudes.

TABLE 1
Estimates of Maximum and Average Deviation of Spectral Amplitudes

| <u>Frequency Range</u> | <u>Maximum Deviation</u> | | <u>Average Deviation at a Given Site</u> | |
|------------------------|--------------------------|-------------|------------------------------------------|-------------|
| | <u>Pier</u> | <u>Soil</u> | <u>Pier</u> | <u>Soil</u> |
| 1 Hz | 20% | 100% | 9% | 80% |
| 2-4 Hz | 50% | 200% | 35% | 130% |
| 6-10 Hz | 120% | 400% | 40% | 130% |

REFERENCES:

Blaney, J.I., 1990, A functional description of the Geophysical Data Acquisition System, Scientific Report, GL-TR-90-0202, August 10, 1990. **ADA230032**

Koteff, C., 1964, Surficial geology of the Concord quadrangle, Massachusetts, MAP GQ-331, U.S. Geological Survey, Washington, DC.

High Resolution algorithms for adaptive Beam-Forming and adaptive Polarization Analysis.

Simon Katz and Keitti Aki

University of Southern California
Department of Geological Sciences

Contract No. F29601-91-K-DB06

Objective

Our objective has been to develop asymptotically linear algorithms of adaptive beam-forming and adaptive polarization analysis which may be used for high resolution estimation of azimuth of signal arrival, estimation of angle of incidence of an incoming seismic ray, and separation of signals arriving from different azimuths. These algorithms are called asymptotically linear, because, being strongly nonlinear in the case of low SNR, they produce nonlinear distortions tending to zero with increasing value of SNR. Thus, the signals characterized by high SNR are subjected to minimal nonlinear distortions. The algorithms of this type are devised as a combination of linear and nonlinear signal processing techniques in such a way that they retain the best properties of both linear and nonlinear methods: they have high resolution in the time domain typical for linear methods, and at the same time, they will be characterized by high resolution in the parameter space and by high stability with respect to random noise.

Research Accomplishments.

We developed and tested algorithms of adaptive beam-forming and adaptive polarization analysis that are characterized by high resolution in time and with respect to azimuth of the signal arrival and allow for high precision estimate of a signal arrival time.

1. Adaptive Beam-Forming.

In this section we give a brief description of the algorithm of adaptive beam-forming based on the joint use of the results of linear beam-forming and local estimates of the SNR.

Let the coordinates of sensors in the array be defined by the vector \vec{u}_k

$$\vec{u}_k = (x_k, y_k)$$

and v be a trial velocity of signal's propagation through the array. Then the output of linear beam-forming for the trial azimuth defined by the angle α is

$$Z(t, v, \alpha) = \sum_{k=k_1}^{k_2} y_k(t - \tau_k(v, \alpha)) \quad (1)$$

where the time delays $\tau_k(v, \alpha)$ are

$$\tau_k(v, \alpha) = \frac{(x_k - x_0) \cos(\alpha) - (y_k - y_0) \sin(\alpha)}{v} \quad (2)$$

The output of adaptive beam-forming is defined as:

$$G(t, v, \alpha) = F[\rho(t, v, \alpha)] Z(t, v, \alpha) \quad (3)$$

where $F[\rho(t, v, \alpha)]$ is the cost function defined as continuous monotonic function of the signal-to-noise ratio (SNR) ρ .

2. Adaptive Polarization analysis.

It is assumed that an input signal is of the form:

$$\vec{y}(t) = \vec{f}(t) + \vec{\xi}(t) \quad (4)$$

$$z(t, \alpha, \varphi) = (\vec{y}(t) * \vec{a}(\alpha, \varphi)) \quad (5)$$

Here $\vec{a}(\alpha, \varphi)$ is a trial vector with its direction in the three dimensional space defined by two angles α and φ ; $z(t, \alpha, \varphi)$ is the inner product of two vectors $\vec{y}(t)$ and $\vec{a}(\alpha, \varphi)$.

The output of the adaptive polarization analysis is defined by the equation (3).

One can see that the structure of adaptive algorithms of beam-forming and polarization analysis is very similar. The difference is in the linear component of the respective operator and in the way signal-to-noise ratio is calculated

3. Cost Function.

In both cases of beam-forming and polarization analysis the cost function is defined as monotone non-decreasing function of the SNR tending to zero with SNR tending to zero and tending to a constant with SNR tending to infinity. Example of this type cost function is defined by the following equation.

$$F[\rho(t, v, \alpha)] = \begin{cases} \frac{C \rho^n}{\rho_0^n + \rho^n} & \rho > 0 \\ 0 & \rho < 0 \end{cases} \quad (6)$$

Parameter ρ_0 in (6) plays a role of a threshold defining the region of the values of SNR estimates where the output of a linear component is suppressed at least in half by a cost function:

$$F[\rho(t, v, \alpha)] < 0.5 C; \quad \rho < \rho_0 \quad (7)$$

$$F[\rho(t, v, \alpha)] > 0.5 C; \quad \rho > \rho_0 \quad (8)$$

The parameter n defines the sharpness of the border between the region of suppression defined by (7) and a pass region where the cost function is close to 1.

The important property of the cost function (6) is that it converges to a constant with increasing SNR. Thus, the signals characterized by high SNR are subjected by the procedure (3) to minimal nonlinear distortion. The cost function (6) tends to zero if SNR tends to zero. Therefore, the use of the cost function (6) guarantees additional suppression of the output signal in the cases when the SNR corresponding to a given trial velocity or trial azimuth is small.

4. Multi-channel signal-to-noise ratio (SNR) estimates

Methods of adaptive beam-forming and adaptive polarization analysis are based on the use of SNR estimates calculated continuously in time for a given set of azimuths of signal arrivals. In both cases the SNR estimate is constructed as the ratio of two estimates - the estimate of the signal's energy and the estimate of the energy of the residual field:

$$\rho(t, v, \alpha) = \frac{\hat{\epsilon}_s(t, v, \alpha)}{\hat{\epsilon}_n(t, v, \alpha)} \quad (9)$$

Here

$$\hat{\epsilon}_s(t, v, a) = \sum_{u=t-T_1/2}^{t+T_1/2} [c_{1,1} A_1(u) + c_{1,1} A_2(u)] \quad (10)$$

$$\hat{\epsilon}_n(t, v, a) = \sum_{u=t-T_2/2}^{t+T_2/2} [c_{2,1} A_2(u) + c_{2,1} A_1(u)] \quad (11)$$

$$A_1(u) = \left[\sum_{k=k_1}^{k_2} y_k(t - \tau_k(v, \alpha)) \right]^2 \quad (12)$$

$$A_2(u) = \sum_{k=k_1}^{k_2} y_k(t - \tau_k(v, \alpha))^2 \quad (13)$$

In the case of adaptive beam-forming, $y_k(t)$ is the input signal recorded by the k -th sensor in the array, v is a velocity of an individual coherent signal, α is an angle defining a trial azimuth of a signal's arrival, $\tau_k(v, \alpha)$ is an arrival time delay corresponding to the trial azimuth.

In the case of polarization analysis $y_k(t)$ is the k -th component of the input vector signal.

The coefficients $c_{i,j}$ in (10) and (11) are chosen in such a way that if the input noise is uncorrelated for different input channels (it may still be correlated in time) then the following conditions hold:

1. The maximum value of the mathematical expectation of the signal energy estimate defined as a function of azimuth and velocity (in the case of adaptive beam-forming) or as function of azimuth and emergence angle equals an actual value of signal energy.
2. The minimum value of the mathematical expectation of the residual energy estimate defined as a function of azimuth and velocity (in the case of adaptive beam-forming) or as function of azimuth and emergence angle equals an actual value of the noise energy.

Conclusions.

Multi-channel processors for adaptive high resolution beam-forming and polarization analysis are built as combinations of two components: linear processor and a nonlinear processor called the 'cost function'. These two components have different advantages and disadvantages. The linear component has comparatively high resolution in time, but its resolution in parameter space and its stability with respect to random noise is low. The cost function has much higher resolution in parameter space and is more stable with respect to random noise, but its resolution in time is low. The signal processors discussed here are constructed in such a way that they retain advantages of their both components: its resolution in time is as high as resolution of the linear beam-forming; its resolution in a parameter space and stability with respect to random noise is as high as that of its nonlinear component. Additional advantage of these methods is that they are asymptotically linear: the higher the output signal-to-noise ratio is the smaller nonlinear distortions of the output signal are.

References.

- Duttweiler, D. L., 1982, Adaptive filter performance with nonlinearities in the correlation multiplier: IEEE Trans. Acoustics, Speech and Signal Processing, vol. 30, p. 578.
- Flinn, E. A., 1965, Signal analysis using rectilinearity and direction of particle motion: Proc. IEEE, 53, 1874-1876
- Honig, Michael L., and David G. Messerschmitt, 1984, Adaptive filters, structures, algorithms and applications: Kluwer Academic Publishers.
- Katz, S., Ershova, T., Mikhailova, N., Egorkhin, A., 1977, Analysis of seismic data from the crust and upper mantle by non-linear beam-forming: Physics of the Solid Earth, 6, Washington, American Geophysical Union.
- Katz, S., Shubik, B., 1977, Adaptive velocity filters: Physics of the Solid Earth, 8, Washington, American Geophysical Union.
- Katz, S., Henyey, T., 1989, High resolution velocity and slope analysis: Expanded abstracts of the 59 SEG meeting, Dallas, 1287-1290.
- Katz, A., Katz, S., 1990, Multichannel adaptive filters. Transactions of the 60-th SEG International Meeting. San Francisco 1697-1700.
- Katz S.A., 1991, Asymptotically linear velocity analysis with high resolution in time domain, Geophysics, V., 56, 11, 1840-1841.
- Kong, S. M., Phinney, R. A., Roy-Chowdhury, K., 1985, A nonlinear signal detector for enhancement of noisy seismic data, Geophysics, 19, 539-550.

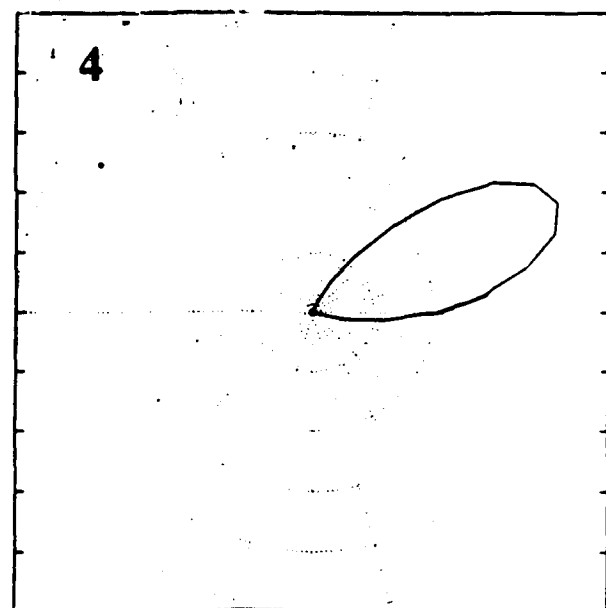
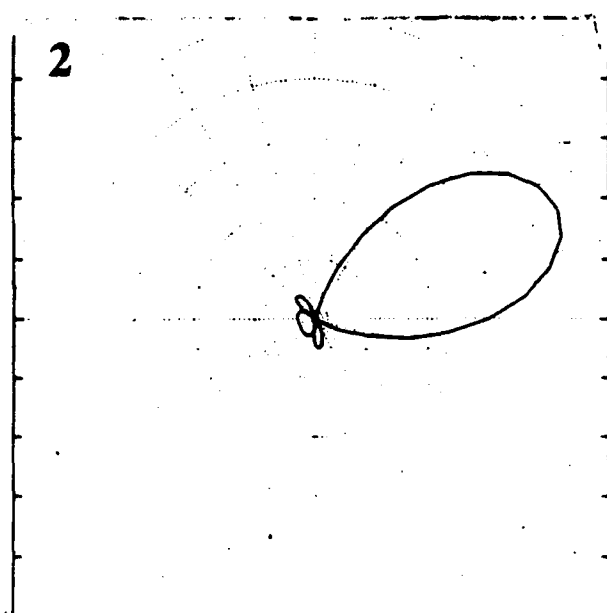
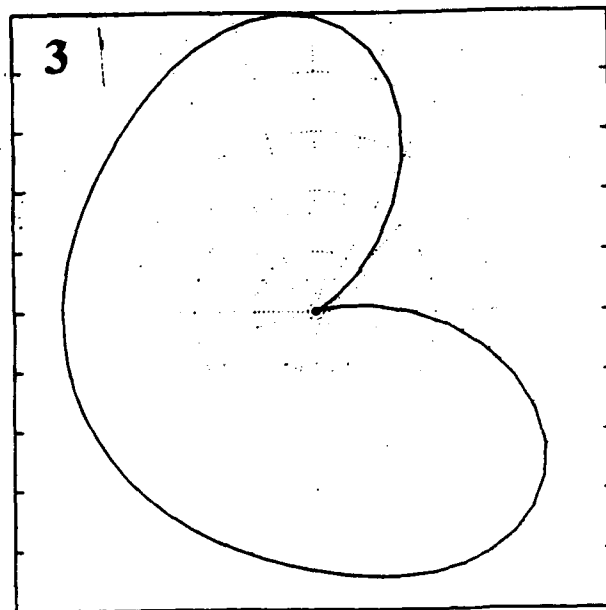
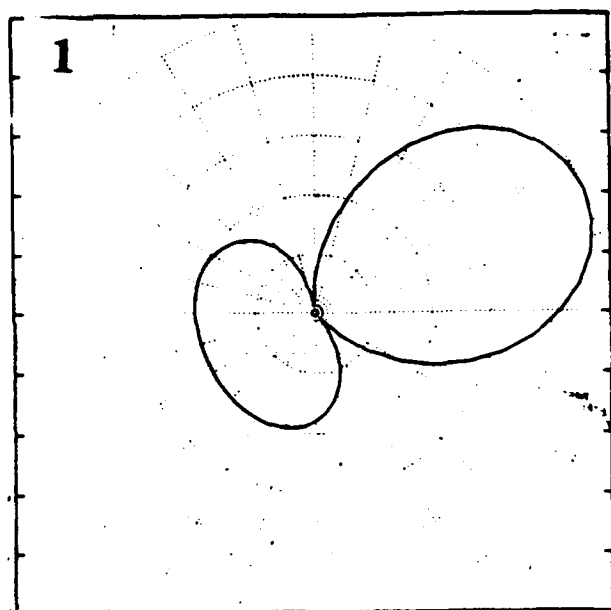


Figure 1. Resolving power of the various components in adaptive beam-forming.
 1 Linear beam- forming.
 2 Signal energy estimate.
 3 Residual energy estimate.
 4 Adaptive beam-forming.

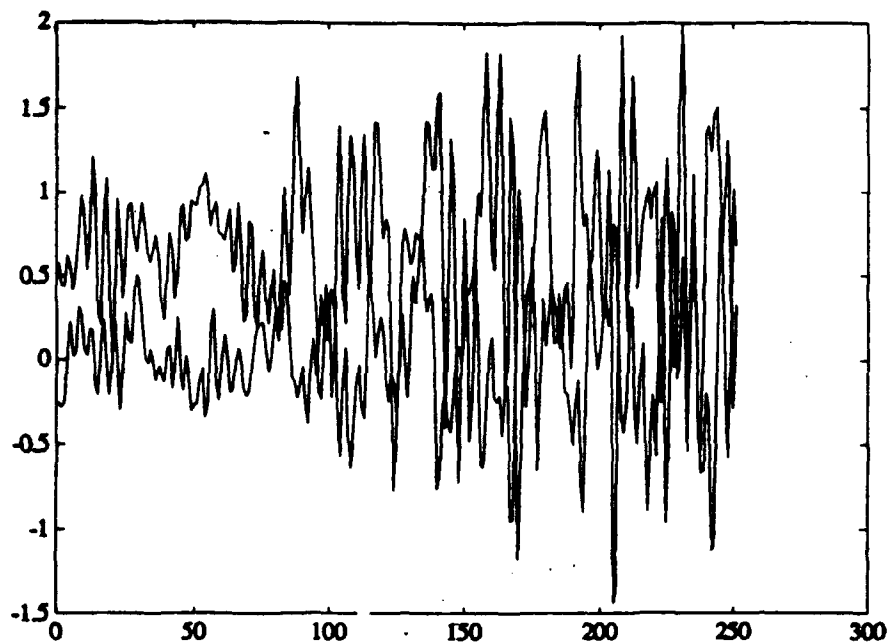


Figure 2. Horizontal components of the S wave recorded by ARCESS.

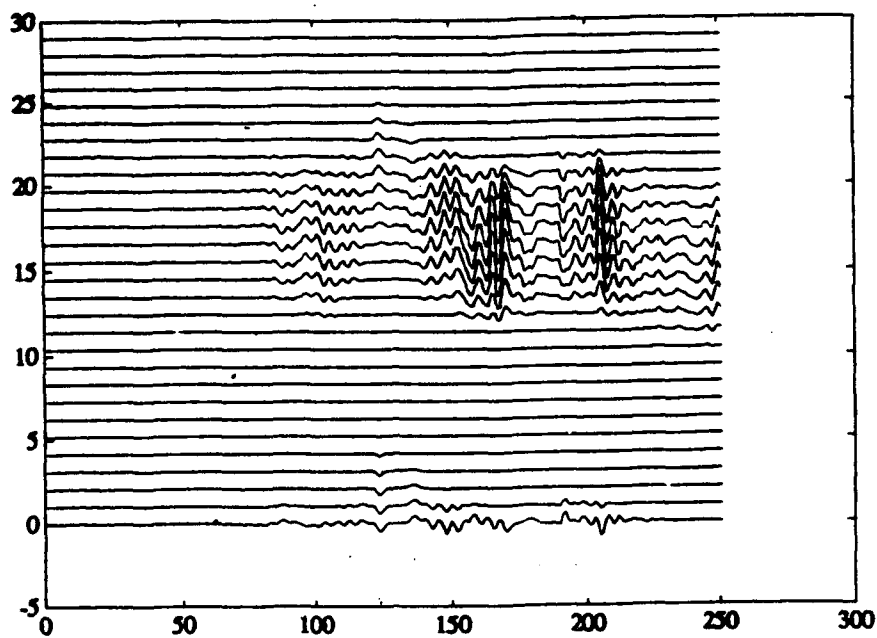


Figure 3. High resolution polarization analysis of the data shown in the Figure 2. Each trace corresponds to a certain azimuth of polarization vector. Azimuth step is 9° .

The Distance Dependence of Regional Discriminants

B.L.N. Kennett
Research School of Earth Sciences
The Australian National University
G.P.O. Box 4, Canberra A.C.T. 2601
Australia

Grant: AFOSR-90-0352

OBJECTIVE

A number of the techniques which have been proposed for discriminating between different types of seismic sources at regional distances depend on the relative amplitudes of different P and S phases. Ideally the P and S phases which are being compared should have similar propagation characteristics so that amplitude differences can be ascribed to the variation in the radiation at the source. The crustally guided waves Pg and Sg can be used to some extent out to 200 km from the source but Pg is frequently difficult to track to larger distances. For the distance zone from 200-1000 km away from the source, the main arrivals are Pn, Sn and the superposition of crustally guided S waves denoted by Lg in discrimination work. Lg is frequently the largest phase on seismic records out to 1000 km but it is known to be sensitive to variations in crustal structure and so can be only used as an S reference when the propagation paths from different sources are very similar.

The propagation characteristics of the Pn and Sn waves which travel in the uppermost mantle are observed to be rather complex on long range refraction profiles. Both phases show distinct and localised maxima in amplitude as a function of range but it is not yet clear how the ratio of Pn and Sn amplitudes would vary as a function of range in the interval from 200-800 km from the source.

In order to look at the patterns of P and S phase behaviour out to 1000 km we have used a used results from refraction profiles in Eurasia to look at the behaviour of the ratio of P and S wave velocities. We have also made a detailed study of 3-component data from the Fennolora long range seismic profile recorded in Sweden in 1979. As an adjunct to the observational work we have investigated modelling schemes for the upper mantle phases Pn and Sn which could taken into account the lateral variations in structure in the uppermost mantle revealed by the detailed surveys.

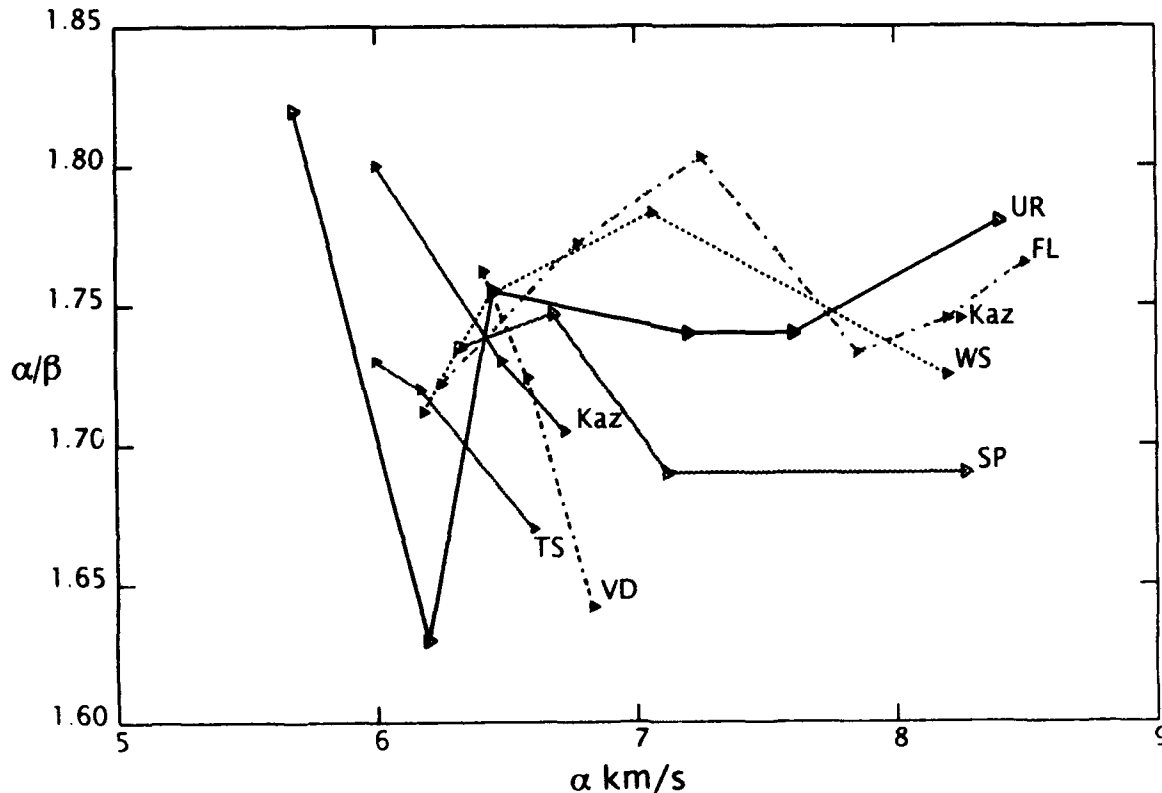
RESEARCH ACCOMPLISHED

In the first phase of this project we concentrated on the emergence of the Sn phase in the distance range 200-300 km with the aid of refraction profiles from Finland and Russia. In the Precambrian regions exceptionally efficient S propagation occurs from explosive sources (as is also seen on the regional arrays in Scandinavia), and Sn can be easily recognised as it separates from Lg. In Phanerozoic regions on the other hand Sn often has rather small amplitudes at

the crossover with Lg and the amplitude builds up towards 300 km (Gajewski et al 1990).

The second phase of work has concentrated on examining the relation of P and S wave structure with a view to understanding the way in which the distance dependance of ratios of different P and S waves may be influenced. A extensive program of long-range explosion seismology within the territory of the former U.S.S.R has produced a good deal of information on the crustal and upper mantle structure, P wave models have been published to depths of 200 km or more but also S wave models for the crust and uppermost mantle. However only a small fraction of the data has been presented in the form of record sections along a profile (especially for S). A notable exception is the paper by Tarkov & Basula (1983) which displays both P and S record sections out to 300 km from quarry blasts in the Voronezh shield to the south of Moscow. From this work and other Russian compilations (Alekseev et al 1988) we can build up a picture of the correlation of P and S wave velocities in the crust and upper mantle. Figure 1 illustrates the behaviour of the ratio of P wave to S wave velocities (α/β) as a function of P wave velocity (α) for a number of different regions of Eurasia. There are substantial differences in the S wave velocities for the same P wave velocity in both the crust and uppermost mantle even where the tectonic settings are comparable.

Fig. 1. Variation of the ratio (α/β) of P wave to S wave velocity as a function of P wave velocity (α) for different regions of Eurasia: UR- the Urals, Kaz - the Kazakh fold belt, TS - the Tien Shan, SP - the Siberian Platform, WS - west Siberian plate, VD - Vilyui depression, FL - the Fennolora profile in Sweden.



In the distance range beyond 200 km the mantle phases P_n, S_n have separated from the waves guided in the crust and the time interval between the main phases becomes quite large. Beyond 300 km there is only a limited amount of refraction data available and even less in digital form. We have therefore concentrated on an analysis of three-component data recorded during the Fennolora Profile in Sweden in the summer of 1979. Stangl (1990) has presented a compilation of all the data from the different shot points which provide detailed cover of crustal structure along a 1700 km profile the length of Sweden (Fig 2). The digital three-component data from shot point B to the south of Sweden was kindly provided to us by Prof. K. Fuchs from the University of Karlsruhe and our analysis has concentrated on the zone out 800 km from the source. The shots were fired in water and each shot was recorded on up to 152 recorders with a station spacing of approximately 10 km; the data quality is generally good because large charges were being used to secure propagation to beyond 1000 km.

Fig 2. The configuration of the 1979 Fennolora experiment in Sweden, the three-component digital data displayed in figure 4 is from shotpoint B to the south of Sweden.

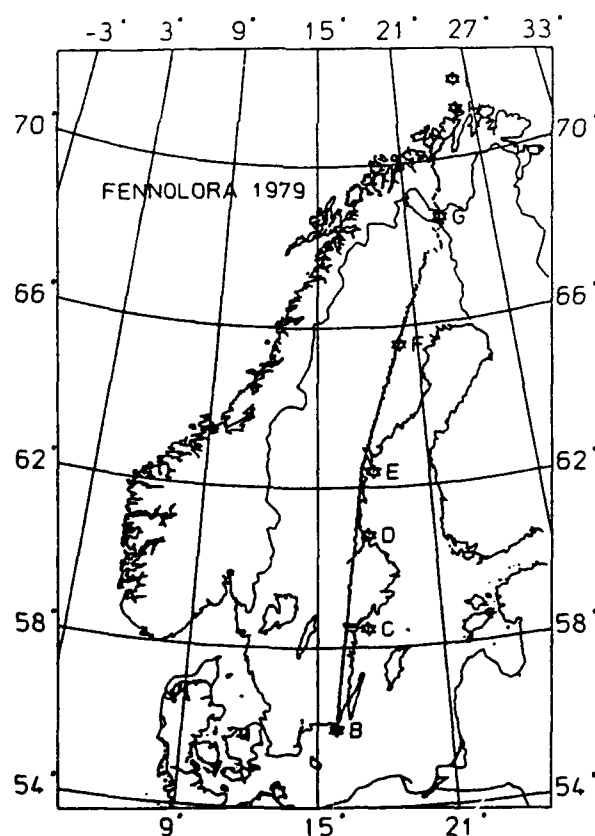
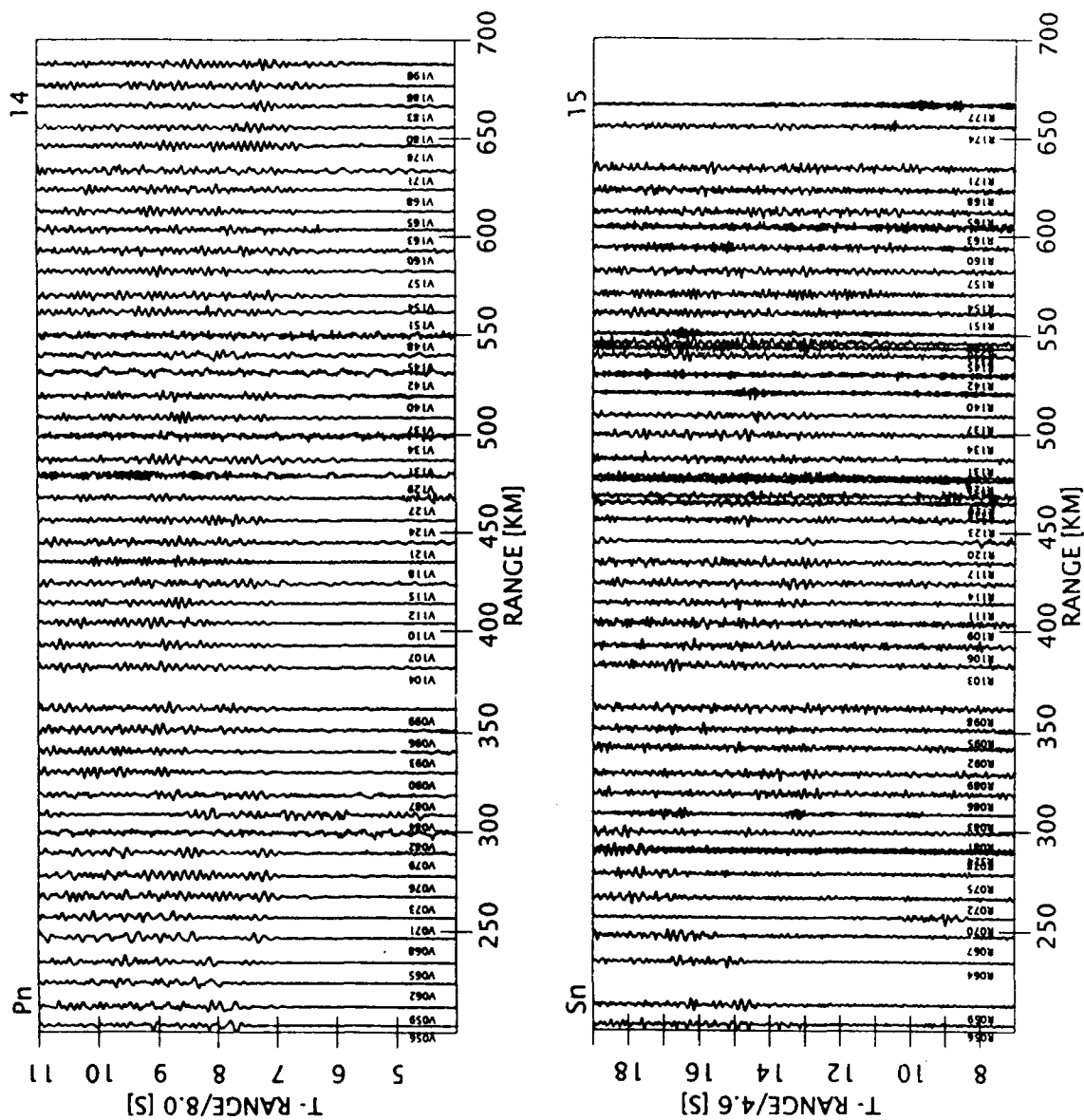
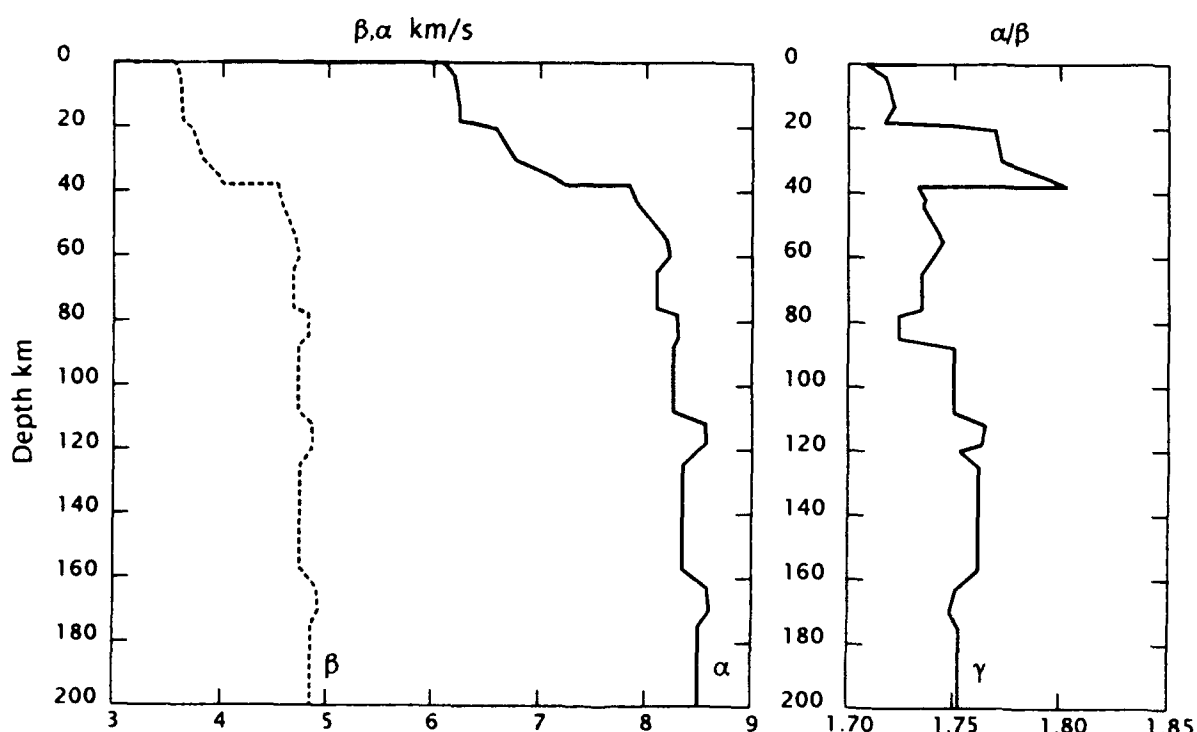


Fig 3. Comparison of P and S wave record sections for the time intervals corresponding to the mantle phases Pn, Sn indicating the complexity of the detailed propagation patterns in the uppermost mantle.



In figure 3, we display portions of the record sections which include the Pn phase from the vertical component and the Sn phase from the horizontal radial component. The traces are unfiltered and normalised to a common maximum amplitude. Within the Pn and Sn wave groups we see a significant variation in the patterns of the amplitude distribution in time and distance. These variations have been modelled by Stangl (1990) using the reflectivity method to produce a model of the variation of both P and S wave velocity with depth which is plotted in fig 4 along with the velocity ratio. The general character of the P and S wave distributions are similar but there is a noticeable difference between the P/S velocity ratio in the mantle above 80 km depth and that beneath. At larger distances (beyond 700 km) where the contribution to the onset of Sn comes from below 80 km there will be a change in the distance dependence of the Pn/Sn amplitude ratio. The actual situation is compounded by the existence of significant lateral variations in P wave velocity in the crust and uppermost mantle.

Fig 4 The depth variation of P and S wave velocities, and their velocity ratio, for the long range profile from shotpoint B on the Fennolora profile in Sweden (Stangl 1990)



We have considered a number of different ways to model the influence of the structure in the mantle on the Pn and Sn waves. All of these methods make use of results from horizontally stratified models of velocity variation. In many areas there is evidence for significant variation in the topography at the Moho which can introduce substantial modifications to seismic wave amplitudes due to focussing and defocussing effects. A limited allowance for topography can be made by modifying the boundary conditions at the Moho and then using a reflectivity calculation for the layers beneath the Moho. Velocity heterogeneity within the crust or the mantle can be included by using a modified reflectivity method in which coupling is introduced between different wavenumbers. For perturbations of 1-2 per cent a first order perturbation technique can be used in each major zone but then all interactions are allowed between zones. Such an approach can simulate the influence of stochastic velocity heterogeneity, and in principle could be combined with the modified boundary technique to include Moho topography.

CONCLUSIONS AND RECOMMENDATIONS

The observational studies from long-range refraction studies with simple source indicate that wave propagation through the uppermost mantle is much more complex than is assumed in simple phase interpretation. The Pn and Sn phases have a delicate sub-structure which reflects the velocity structure in the upper part of the mantle. Variations in the P/S velocity with depth will lead to changes in the amplitude ratio for Pn/Sn as a function of distance.

The current class of regional phase discriminants based on simple interpretations of seismic phases are likely to give misleading results in some distance ranges because of the way in which the peak amplitudes in the appropriate time windows shift between wave groups with different propagation paths.

REFERENCES

- Alekseev A.S., Egorkin A.S. & Pavlenkova N.I., (1988), Shear waves in lithosphere studies on the territory of the U.S.S.R., *Tectonophys.*, **154**, 227-239.
- Egorkin A.V., S.K. Zaganov, Pavlenkova N.A. & Chernyshev N.M. (1987) Results of lithospheric studies from long-range profiles in Siberia, *Tectonophys.*, **140**, 29-47.
- Gajewski D., Stangl R., Fuchs K. & Sandmeier K.J., (1990), A new constraint on the composition of the topmost continental mantle - anomalously different depth increases of P and S velocity, *Geophys. J. Int.*, **103**, 497-507.
- Stangl R., (1990), Die Struktur der Lithosphäre in Schweden, abgeleitet aus einer gemeinsamen Interpretation der P- und S-Wellen Registrierungen auf dem FENNOLORA-Profil, *Doktors der Naturwissenschaften Thesis*, University of Karlsruhe.
- Tarkov A.P. & Basula I.P., (1983), Inhomogeneous structure of the Voronezh shield lithosphere from explosion seismology data, *Phys. Earth. Planet. Int.*, **31**, 281-292

Phase Identification and Location for Regional and Teleseismic Events

B.L.N. Kennett

*Research School of Earth Sciences
The Australian National University
G.P.O. Box 4, Canberra A.C.T. 2601
Australia*

Grant: MDA972-91-J-1021

OBJECTIVE

The object of the current phase of research is to develop flexible and efficient procedures for the location of seismic events which can incorporate a wide range of information from a sparse global network of seismic stations. Such location procedures must be able to use many different phases from each seismic record, so that many different propagation paths from source to receiver compensate for a limited number of stations. The procedures need to be able to assign phase identifiers to the different seismic phases and then use the full range of available data (including array estimates of slowness and azimuth) in the location step. Particular attention needs to be given to the estimation of the depth of the event so that the procedures can be implemented in global seismic monitoring for discrimination purposes.

An important requirement is the development of techniques to improve the recognition and utility of later phases (especially S) at teleseismic distances using for example the vector characteristics of the wavefield.

RESEARCH ACCOMPLISHED

When attempting to locate and identify the nature of a seismic event from a limited number of seismic stations it becomes necessary to make use of as many phases on the seismic record as possible to compensate for the sparse recording network. The current phase identification and association schemes used for the analysis of regional arrays are designed to cope with the prominent phases (Pn, Sn, Lg) seen at regional distances out to 1000 km, and largely depend on the phase velocity information at arrays, with a limited dependence on polarisation. In the far regional range from 1000 to 2500 km the arrivals of the main P and S phases are complicated by the returns from upper mantle discontinuities and surface multiples also become identifiable as distinct arrivals on the seismic record. Beyond 3000 km recognising the onset of P is relatively straightforward but if accurate locations are to be obtained using teleseismic observations at a limited number of global monitoring stations then as many phases as possible must be identified on the seismogram and used in the location procedure.

The algorithms used by the major agencies (National Earthquake Information Centre [NEIC], International Seismological Centre [ISC]) are optimised for the determination of the location of seismic events using a large number of P wave arrivals. Very little later phase information is used even though a large number of later phases are reported by many stations. The ISC

routinely gives a depth estimate derived from pP-P differential times as well as the depth from the fitting of the P arrival times, but the agreement is often poor. This discrepancy rises in part from the use of the Jeffreys & Bullen travel times and also from the difficulty of identifying pP arrivals if the approximate location of the event is not known.

The first stage of our work has been to establish nonlinear location procedures which do not require any differentiation of seismic travel times and which can be used for arrival time, slowness and azimuth data on an equal footing. As a result any convenient measure of the misfit between observed and calculated quantities (arrival times, slownesses or azimuths) can be used. This has the major advantage that we can employ robust statistical measures which are not readily differentiated as for example the L1 misfit measure

$$C = \sum_i |t_i^{obs} - t_i^{calc}| / \sigma_i,$$

additional terms of similar form can be added to include array information. The nonlinear location procedures make use of the computational form of the *iasp91* travel time tables (Kennett & Engdahl 1991) to generate estimates of travel times and slowness for the passage between source and recording station. Modified tables designed to give improved representation of regional variations such as oceanic regions (Kennett 1992) can also be included.

We have considered two major classes of such nonlinear schemes. The first is based on the direct grid search of Kennett (1972) in which the smallest misfit on a four dimensional net is chosen as the centre for a finer scale search. The second is based on the application of Genetic Algorithm procedures (Kennett & Sambridge 1992), in which the global minimum of the misfit function on a fixed four-dimensional mesh is sort by a set of procedures originally developed in the context of automated decision making. We have found that in each case good locations can be found using multi-phase data in modest computing times on a workstation. Even for an initial search area as large as 20 degrees in both latitude and longitude, 600 km and 120 seconds in time it is possible to get better than 10 km constraints on the location (with good data) in a two stage location process.

The contracting grid search method is more computationally efficient than our current implementation of the genetic algorithm but we are working on ways to exploit the separation of the spatial and temporal components of the location and this should reduce the calculation time. However, the nature of the genetic algorithm procedure looks well suited to the process of refining the identification of later phases.

As an example of nonlinear inversion using a robust (L1) misfit measure we consider an event on the Iran/Iraq border (1988 Jan 26, 09:34, mb 5.4) for which the ISC bulletin lists a rich crop of later phases. There are numerous reports of S, especially from Soviet stations but also from Europe. The ISC location is at 32.70°N, 47.08°E with a depth of 40 km.

Since the event was of a significant size it was reported by over 300 stations. In order to simulate a limited network we have looked at various subsets of the data. We firstly concentrated on the 60 stations which reported the aftershock about 10 minutes later. Three separate location estimates were found using the P observations (including pP), the S observations (26 stations) and both P and S

Fig 1. Distribution of selected stations for an event on the Iran/Iraq border. The map is in linear polar projection centred on the epicentre with a radius of 90°.

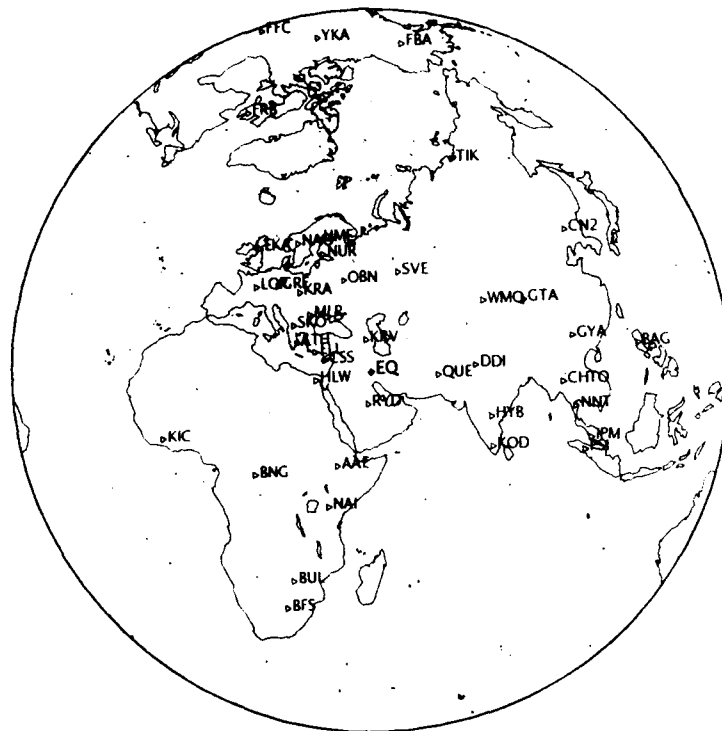
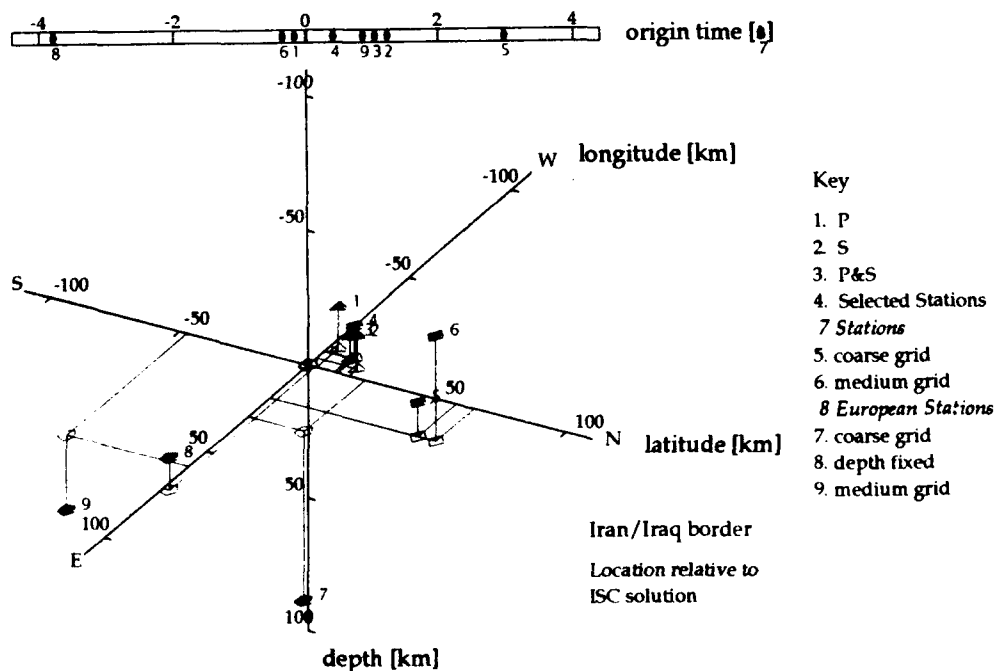


Fig 2. Location estimates from a contracting grid search scheme for an event at the Iran/Iraq border using a variety of different classes of observations. The location with S observations alone using the *iasp91* times is in quite close agreement with the solutions using a somewhat larger body of P wave information



observations, and a fourth using P readings from a selected set of stations as shown in fig 1.

The location estimates for these different data subsets are compared in figure 2 in a four-dimensional representation. Each hypocentre is plotted relative to the location given by the ISC using the full dataset which is placed at the centre of the display. There is about a 5 km shift in position between the P wave solution (1) and that using S waves alone (2), there is also an offset in origin time of 1.4 s. It is very encouraging that it is possible to get a satisfactory location estimate using just S wave phases. When the P and S data sets are combined, the location (3) is slightly closer to the S wave estimate (2) than that obtained using just P wave information (1). The hypocentre determined using the subset of P readings selected for good azimuth coverage (4) is in quite close agreement with the location using both P and S information (3). The zone about 10 km across within which all these location estimates lie, gives a good measure of the potential accuracy of location using teleseismic observations.

We have also considered two smaller network configurations: a) 7 stations with a good azimuthal distribution using both a medium (2°) grid and a coarse (20°) grid, and b) 8 stations just from Europe with both medium and coarse grids and also a constrained depth of 28 km, as for (4). These additional estimates are also plotted in figure 2. The locations from the limited networks are significantly displaced by 50 km or more from the tight cluster of the earlier estimates. With the 7 station network with good azimuthal coverage the two location estimates (5,6) are in close agreement, the discrepancy in the depth can be attributed to the differences in resolution inherent in the different sizes of starting grid. With a one-sided network (the 8 stations in Europe) the control on the location is rather poor

We have been able to demonstrate that the use of robust measure of misfit such as an L_1 norm allows satisfactory solutions to be found when very major discrepancies arise between observed and calculated values for some stations. Such large mismatches reduce the variation in the misfit function as a function of the variation of the spatial and temporal coordinates of the hypocentre. This makes it harder to find the minimum in the misfit unless we use procedures which can exploit rather small changes in the misfit function. We have found that errors of minutes in travel time and up to 180° degrees in azimuth can be accommodated in the contracting grid search procedure without a significant degradation in the quality of the solution.

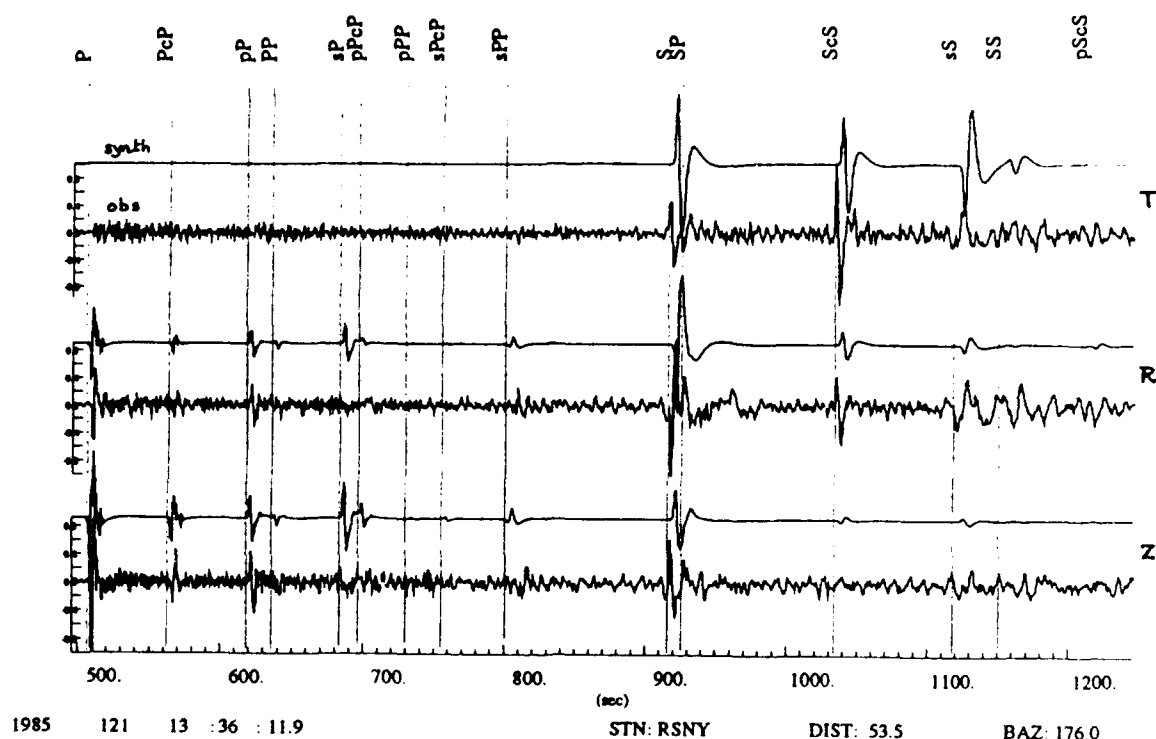
We have therefore modified the contracting grid method of Kennett (1992) to include an initial phase in which a coarse grid search is employed to determine an approximate location, once a likely zone for the event has been identified. This approximate location is then used to test the set of phase information against prescribed criteria and pieces of information with particular large difference between observed and calculated values are set aside. With the reduced data set the contracting grid procedure is then applied to a finer grid to generate the best estimate of the hypocentre based on the assumptions about likely location. The data which has been set aside is still available and once an improved location is found, it may be possible to provide an alternative phase association so that further constraints can be placed on the solution.

The experimental rules for excluding phase data are:
for arrival times - if the residual between observed and calculated times exceeds 25 s that time should not be used in the final stage of the location,
for slowness - if the residual exceeds 0.05 s/km, the slowness observation should be excluded, and
for azimuth - if the residual exceeded 25°, the azimuth observation should be set aside.

Such rules have worked well for phase data sets taken from the GSETT-2 e.g. for an event in Japan on 1991 June 6 we were able to exclude data associated with a small event in Poland and also to improve the use of azimuth information by dropping unreliable observations.

The next step in the procedure is to be able to improve the reliability of the labels attached to the pieces of phase information. If only time information is available this requires an adaptive procedure in which the location performance is compared using different choices for the phase identification. When waveform information is available and the location is known to within a couple of degrees it is possible to exploit direct comparisons of observed waveforms and the theoretical seismograms for a generic source at the postulated location. A efficient procedure for generating such seismograms is provided by symbolic manipulation of the algebra of ray path segments defining the propagation patterns as proposed by Clarke & Silver (1991) The resulting ray

Fig. 3. Comparison of a body wave seismogram for the major seismic phases computed for the *iasp91* reference model with an observed broad-band seismogram at the RSNY station for a deep event in South America



synthetics can be readily adapted to a wide variety of source types and source spectra. A combination of an isotropic component and a 45° dip slip component gives a reasonable balance of P and S radiation for an initial examination, so that the major seismic phases stand out on the theoretical seismogram. As an illustration of the potential of this approach we show in figure 3 a comparison of synthetic seismograms for the *iasp91* model with broadband observations from the station RSNY from a deep earthquake in South America. Even though the attenuation structure for S needs some adjustment the general character of the observations are well reproduced and there would be no ambiguity in phase association.

CONCLUSIONS AND RECOMMENDATIONS

Nonlinear location schemes with robust measures of misfit between observations (such as arrival times, slownesses and azimuths) and the corresponding quantities calculated for postulated hypocentral locations can be used to avoid problems associated with the misidentification of seismic phases. For limited seismic networks the inclusion of later phases can help to compensate for the number of stations because different propagation paths have different sensitivity to the depth and location of the source. Direct inclusion of phases such as pP, sP in the location scheme is desirable and profitable if a consistent set of travel times tables such as *iasp91* is employed.

The effective use of the available information for later seismic phases is dependent on the quality of phase identification. Techniques which make direct use of seismic waveforms look to offer the most promise for such identification procedures.

REFERENCES

- Clarke T.J. & Silver P.G. 1991, A procedure for the systematic interpretation of body wave seismograms - I. Application to Moho depth and crustal properties, *Geophys J. Int.*, **104**, 41-72.
- Kennett B.L.N. & Engdahl E.R., 1991, Travel times for global earthquake location and phase identification, *Geophys. J. Int.*, **105**, 429-465.
- Kennett B.L.N. (1992), Locating oceanic earthquakes - the influence of regional models and location criteria, *Geophys., J. Int.*, **109**, 848-854
- Kennett B.L.N. & Sambridge M. (1992) Earthquake location - genetic algorithms for teleseisms, *Phys. Earth Planet. Int.*, in press.

STUDIES OF RMS Lg DATA

Won-Young Kim, Paul G. Richards* and Jinghua Shi*
Lamont-Doherty Geological Observatory, Palisades, NY 10964

(*also, Dept. of Geological Sciences, Columbia University)

F19628-90-K-0048

OBJECTIVE

In recent years it has been shown that single-station measurement of Lg-wave amplitudes can be as stable, for purposes of estimating the strength of a seismic source, as the conventional P-wave magnitude measured by averaging several tens of stations in a global network. In light of this technical result, our objective has been to evaluate nuclear explosions in Central Asia (Soviet and Chinese), for which we have found new collections of Lg data.

RESEARCH ACCOMPLISHED

We have carried out three projects:

- an evaluation of digital Lg signals recorded in Kazakhstan at a regional distance from nuclear explosions at the Semipalatinsk test site;
- an analysis of Lg signals recorded in China for a large Soviet explosion for which Lg data was unavailable at stations in Europe and the Middle East; and
- a study of regional and teleseismic signals for the only explosion at Balapan that was carried out in the fractured rock of a deep fault zone.

RMS Lg measurements at Borovoye, Kazakhstan

RMS Lg measurements using digital seismograms recorded at the Borovoye Geophysical Observatory, Kazakhstan (station BRV) from explosions on the Balapan test site ($\Delta = 682 \sim 697$ km) show very good correlation with NORSAR ($\Delta \approx 4300$ km) $m_b(Lg)$ which is based on RMS Lg measurements (Ringdal *et al.*, 1992). It follows that BRV instrument calibrations (gains) are known and stable, over a period of years, to within a few per cent.

In this study, we used vertical component digital seismograms recorded on a low-gain channel (KSVM) of the STsR-TSG system at BRV (see, Adushkin & An, 1990; Fig. 2 of Richards *et al.*, 1992a; and Richards *et al.*, 1992b). The KSVM channel is derived from a short-period Kirnos seismometer and has low- and high-gain vertical components. The low-gain channel has been operating with a nominal gain of about 50 and has nearly flat response to ground displacement in the frequency band 0.8 - 5 Hz (3 db level). The seismic signal with frequencies up to about 6 to 8 Hz is useful for most of the explosions studied. This channel provides unclipped short-period seismograms for large underground explosions from eastern Kazakhstan test sites.

To measure the RMS Lg, we followed Hansen *et al.* (1990), except that we

used a gaussian window instead of the usual box-car window. We first bandpass filter the signal in the frequency band from 0.6 to 3 Hz with a 3rd order Butterworth filter. An RMS trace is obtained by calculating the RMS values of the signal with a moving time window. Each window is offset by 0.1 to 0.2 times the window length from the previous window. Noise in the signal is corrected as suggested in Ringdal & Hokland (1987) by taking RMS values of the trace (30 sec window) preceding the first arrival *P*-wave. However, noise correction was negligible for the explosions studied because signal-to-noise ratio on all seismograms were very high (above 200 and up to few 1000).

We used a gaussian window with $\sigma = 22.5$ s at a reference distance of 1000 km. This window covers the *Lg* phase in group velocity range 3.6 to 3.0 km/s. The gaussian is truncated at 2.58σ (99 % of unit area). The width of the gaussian window can be conveniently scaled as a function of distance (e.g., Butler *et al.*, 1987) allowing the RMS *Lg* measurements at many stations at different epicentral distance ranges to be combined to obtain a network $m_b(Lg)$ based on the RMS *Lg* measurements. The successive gaussian windows were shifted by 0.2 s relative to the previous window to sample the *Lg* waves smoothly.

Fig. 1 shows the \log_{10} of RMS *Lg* measurements in microns of ground displacement plotted against NORSAR $m_b(Lg)$. Regression of 12 measurements using BRV data yields a slope of 0.91 and a standard deviation of 0.036 magnitude units. This small scatter for 12 points indicates that one may have confidence in both RMS *Lg* (as a precise measure of signal strength), and in BRV calibration. The latter result is important for our current plans to work extensively with BRV data.

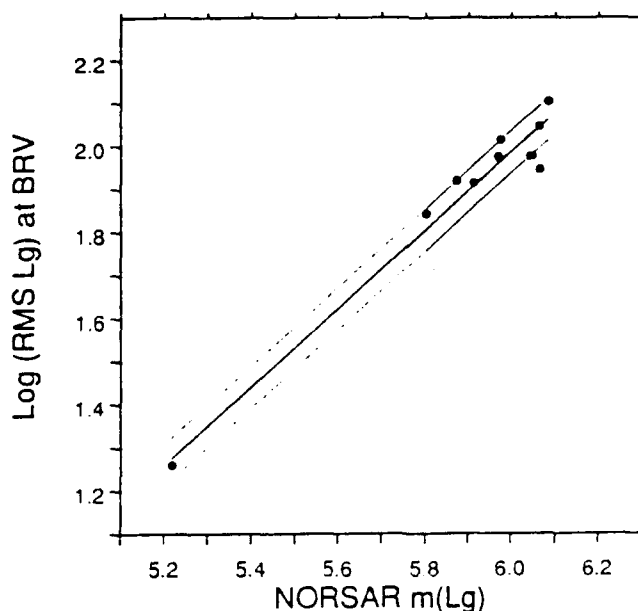


Fig. 1. Comparison of $\text{Log}(\text{RMS } Lg)$ measurements (in μ) at BRV with NORSAR $m_b(Lg)$. Solid line is a fitted slope of 0.91 and an orthogonal rms misfit of 0.036 magnitude units. The dotted lines correspond to ± 2 S.D.

A use of analog data to supply an important RMS Lg value

The Balapan underground nuclear explosion of 1980 September 14 had the largest P -wave magnitude, $m_b(P) = 6.21$, of any Soviet explosion since March 1976, according to Ringdal, Marshall and Alewine (1992). Unfortunately the usual sources of L_g data ran dry for this event: neither NORSAR nor the Gräfenberg arrays were operating at the time, and signals at some stations that normally record L_g well for Balapan explosions (e.g. Mashad, Iran) were clipped in this case. However, we were successful in obtaining good L_g data from the analog Kirnos instruments operated at Urumchi (station WMQ), for 10 Balapan explosions, 8 of which also had L_g signals that were measured at NORSAR. After hand-digitization and measurement of L_g at WMQ, and calibration against NORSAR for the 8 events in common, we conclude that the 1980 Sep 14 event had L_g magnitude corresponding to a value of about 6.094 at NORSAR, and thus was one of a number of events that cluster about this magnitude: it was not unusually large. Our results are shown in Table 1.

Table 1. RMS L_g measurements from analog records at WMQ

| date of Balapan expl. | mb(P) AWRE | mb(Lg) NOR & GRF | RMS Lg from Kirnos at WMQ: | | |
|-------------------------------------------------------|---------------|---------------------|--------------------------------|------------|------------|
| | | | frequency range, window length | | |
| | | | 0.3-3, 90 | 0.3-3, 120 | 0.6-3, 120 |
| 1980 Apr 25 | 5.45 | none | -4.3141 | -4.3502 | -4.5799 |
| 1980 Jun 12 | 5.52 | 5.63 | -4.0775 | -4.1238 | -4.4181 |
| 1980 Jun 29 | 5.69 | 5.71 | -3.9613 | -4.0060 | -4.2362 |
| 1980 Sep 14 | 6.21 | none | -3.4500 | -3.4952 | -3.8132 |
| 1980 Oct 12 | 5.88 | 5.93 | -3.7068 | -3.7242 | -4.0000 |
| 1980 Dec 14 | 5.93 | 5.94 | -3.6488 | -3.6894 | -4.0426 |
| 1981 Apr 22 | 5.94 | 5.93 | -3.6657 | -3.6946 | -4.0982 |
| 1981 May 27 | 5.30 | 5.46 | -4.3667 | -4.4030 | -4.7512 |
| 1981 Sep 13 | 6.06 | 6.11 | -3.4954 | -3.5370 | -3.8706 |
| 1984 Jul 14 | 6.10 | 6.05 | -3.4878 | -3.5279 | -3.8282 |
| mb(Lg) predicted at NORSAR, via WMQ measurements, for | | | | | |
| event of 1980 Sep 14 | | | 5.470 | 5.472 | 5.534 |
| event of 1980 Apr 25 | | | 6.099 | 6.091 | 6.092 |

event of 1980 Sep 14, average estimate of $mb(L_g)$: 6.094
 event of 1980 Apr 25, average estimate of $mb(L_g)$: 5.492.

The Balapan Nuclear Explosion of 1989 July 8 – effects of a fault zone?

We have begun a special study of the Balapan nuclear explosion of 1989 July 8, which is unique at this test site in having been conducted within the fractured rock of a major fault zone, the Kalba-Chingiz fault (Adushkin, paper given at SSA meeting, Santa Fé, 1992). ISC reports $m_b = 5.6$ and $M_s = 4.3$ for this explosion:

Table 2. List of explosions near Kalba-Chingiz f.z. at Balapan test site, Kazakhstan.

| Origin time | | latitude | longitude | $m_b^{(b)}$ | NORSAR | ISC | |
|----------------|--------------------------|---------------------|---------------------|-------------|----------------------|-------|-------|
| yy mm dd doy | hh:mm:sec ^(a) | (°N) ^(a) | (°E) ^(a) | | m(Lg) ^(b) | m_b | M_s |
| 87 03 12 (071) | 01 57 19.57 | 49.929 | 78.824 | 5.31 | 5.218 | 5.6 | 3.9 |
| 87 04 17 (107) | 01 03 07.09 | 49.874 | 78.663 | 5.92 | 5.910 | 6.0 | 4.7* |
| 87 08 02 (214) | 00 58 09.21 | 49.877 | 78.873 | 5.83 | 5.871 | 5.9 | 4.3 |
| 87 12 27 (361) | 03 05 07.15 | 49.867 | 78.718 | 6.00 | 6.042 | 6.1 | 4.5 |
| 88 09 14 (258) | 03 59 59.69 | 49.869 | 78.825 | 6.03 | 5.969 | 6.1 | 4.8 |
| 89 07 08 (189) | 03 47 00.03 | 49.869 | 78.775 | 5.55 | 5.418 | 5.6 | 4.3 |

(a) from Lilwall and Farthing (1990): (b) from Ringdal, Marshal and Alewine (1992);

(*) M_s is likely over-estimated due to an interfering earthquake.

For several explosions in the Kalba-Chingiz fault region (see above Table), we have examined signals at CDSN and IRIS/GDSN stations for waveform complexity, frequency content and possible variation in tectonic release.

Portions of the vertical component broadband seismograms from several explosions recorded at CDSN station WMQ (Urumqui, $\Delta \approx 955$ km, $\phi = 131^\circ$) are displayed in Fig. 2a. Explosions on 870802 and 880914 (Soviet JVE) are located north of the fault zone; the explosion on 890708 is located within the fault zone (which can be a kilometer or more in width); and an explosion on 871227 is located south. P_g and its coda from the explosion on 870802 have smallest amplitudes among the seismograms shown, while P_g and its coda from the explosion on 871227 have stronger amplitudes. Signal from the event on 890708 is similar to that from the event on 871227 which occurred south of the fault trace and its propagation path does not cross the fault. P_g and its coda from the JVE are similar to that from the explosion on 870802. This observation gives us an impression of signals that are weakened (or more scattered) along paths which cross the fault zone.

Fig. 2b indicates a similar result for the later phases in the whole wave train.

To see if signals from the fault zone explosion (890708) have frequency content differing from other explosions, we compared amplitude spectra of P_n , P_g , L_g waves and teleseismic P waves for a small number of explosions. We found an effect on regional waves, as noted by Adushkin (paper presented at SSA meeting, Santa Fé, April 1992). Amplitude spectra of P_n phases on broadband vertical component records from three explosions at station WMQ are shown in Fig. 3a. Spectra from two of the events are scaled to the JVE. The spectral amplitude shown corresponds to ground velocity in unit of μ/s . Amplitude spectra indicate that the P_n phase from the explosion on 890708 has higher frequency content than other

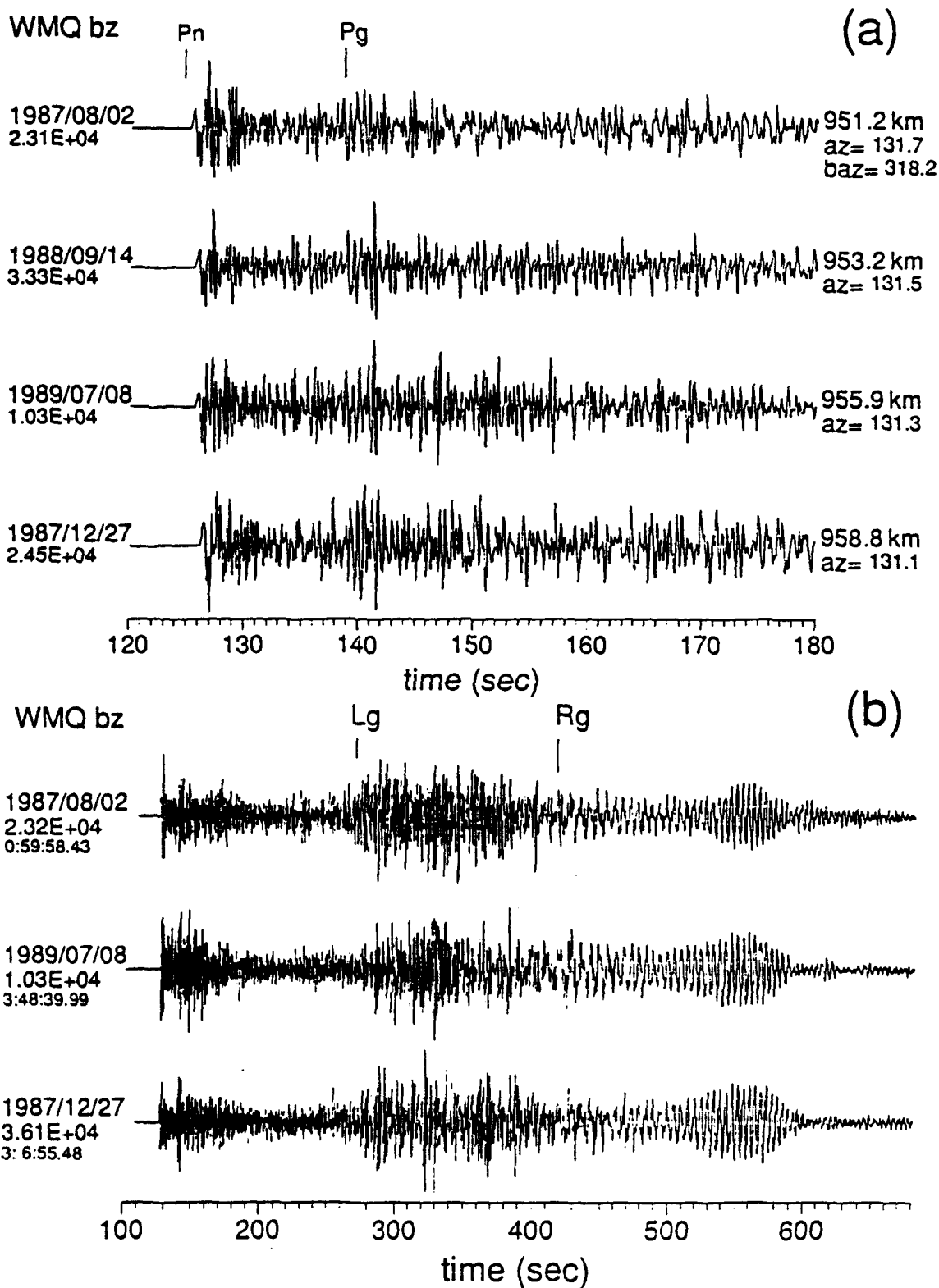


Fig. 2. a) P wave portion of broadband Z component seismograms at WMQ from several selected explosions located close to the Kalba-Chingiz fault, b) same as a) but complete seismogram is plotted. Time axis represents time after the origin.

explosions at frequencies above about 3 Hz (Fig. 3a). To check if this high frequency content is due to the source spectrum, we have also calculated amplitude spectra of one of the smallest explosions, on 870312 ($m_b=5.31$) in the same general area. A comparison is shown in Fig. 3a and 3c for signals recorded at WMQ. The higher frequency content of the signal from the explosion within the fault zone is also shown at other regional stations with broadband sensors, such as ARU and GAR.

CONCLUSIONS AND RECOMMENDATIONS

The regional seismic data now becoming available for Central Asia, digitally recorded at Borovoye, Kazakhstan, for virtually all nuclear explosions carried out in the last twenty-five years, appears to be of high quality. Amplitudes of Lg are stable, indicating good instrument calibration over many years.

Lg data for certain key explosions, for which Lg is not available at usually reliable stations in Europe, the Middle East, and South Asia, can be obtained from the Kirnos instrument operated in China at Urumqi (WMQ) since Sept. 20, 1962.

A large nuclear explosion at Balapan, on July 8, 1989, conducted in the fractured rock of a major fault zone, displays anomalously strong high-frequency (2 – 5 Hz) signal in the regional waves recorded in the range 1000 – 1500 km.

In these three conclusions, the common theme is new opportunities to work with regional signals from nuclear explosions conducted in geological structures very different from those at the Nevada Test Site. We recommend an expansion for efforts to study nuclear explosions recorded at regional distances in Central Asia, with attention turning in future to the data from *small* explosions and *small* earthquakes, and an emphasis on discrimination rather than yield estimation. The data may begin to become available in large amounts in the next 12 months.

References

- Adushkin, V. V. and V. A. An, Seismic observations and monitoring of underground nuclear explosions at Borovoye Geophysical Observatory, *Izvestiya Akademii Nauk SSSR: Fizika Zemeli*, 47-59, No. 12, 1990 (journal available in English as *Physics of the Solid Earth*).
- Butler, R., C. S. McCreery, L. N. Frazer and D. A. Walker, High-frequency seismic attenuation of oceanic P and S waves in the Western Pacific, *J. Geophys. Res.*, **92**, 1383-1396, 1987.
- Hansen, R. A., F. Ringdal and P. G. Richards, The stability of RMS Lg measurements and their potential for accurate estimation of the yields of Soviet underground nuclear explosions, *Bull. Seism. Soc. Am.*, **80**, 2106-2126, 1990.
- Lilwall, R. C. and J. Farthing, Joint epicenter determination of Soviet underground nuclear explosions 1973-89 at the Semipalatinsk test site, AWE Report No. O 12/90, Atomic Weapons Establishment, UK, 13pp, 1990.
- Richards, P. G., W. Y. Kim and G. Ekström, The Borovoye Geophysical Observatory, Kazakhstan, EOS, Transactions of the AGU, **73**, 201-206, 1992a.
- Richards, P. G., W. Y. Kim and G. Ekström, Initial visit to the Borovoye Geophysical Observatory, Northern Kazakhstan, companion paper at this Tucson meeting, 1992b.
- Ringdal, F. and B. Kr. Hokland, Magnitudes of large Semipalatinsk explosions using P coda and Lg measurements at NORSAR, in *Semiannual Technical Summary*, NORSAR Sci. Rept. 1-87/88, NTN/NORSAR, Kjeller, Norway, 1987.
- Ringdal, F., P. D. Marshall and R. W. Alewine, Seismic yield determination of Soviet underground nuclear explosions at the Shagan River test site, *Geophys. J. Int.*, **109**, 65-77, 1992.

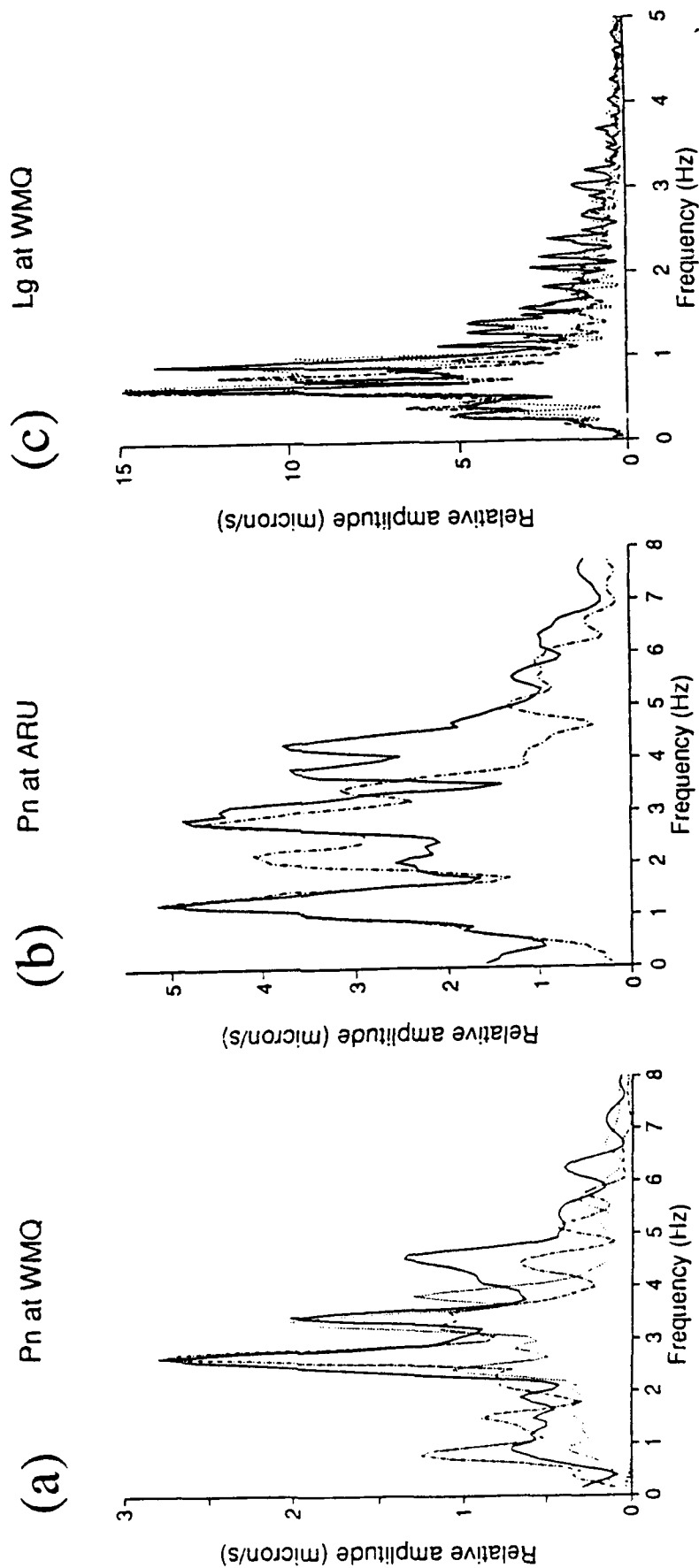


Fig. 3. a) A comparison of amplitude spectra of Pn phase recorded at WMQ from explosions on 870312 (dotted line), 880914 (dash-dot line) and 890708 (solid line), b) amplitude spectra of Pn phase recorded at ARU from explosions on 880914 (dash-dot line) and 890708 (solid line), c) a comparison of Lg wave spectra at WMQ same notations used as a).

FAR-REGIONAL SEISMOGRAM ANALYSIS FOR THE WESTERN UNITED STATES AND THE ROLE OF SHORT-PERIOD MANTLE S WAVES

Karl Koch, Brian W. Stump
Southern Methodist University, Dallas

Contract No: F19628-91-K-0016

OBJECTIVE

Modelling of seismograms at far-regional distances.

RESEARCH ACCOMPLISHED

DATA

The subject of this study is the constraint of a western U S regional shear velocity model (1-D) to depths that include the two upper mantle discontinuities with far-regional seismograms. In a previous study (Koch & Stump 1992), the upper mantle structure of the Basin and Range province was investigated with short period and broadband data. It was found that P phases turning in the upper mantle in the 200 km depth range, dominate the P waves at distances larger than 1200 km. In contrast, no corresponding S arrivals from the upper mantle could be unambiguously identified for distances <2000 km. Four magnitude 6 events in July/August 1991 supplemented by an event in January 1990, however, provided the first observable mantle S phases at Lajitas, TX (LTX) for distances from 2200 to 2400 km, or 20-22 degrees, respectively. As the events were in a small source region in the Cape Mendocino/Gorda plate area and data from a single station were used, their great circle paths are fairly close together, therefore sampling the same upper mantle region and allowing a 1-D interpretation.

The locations for the five earthquakes on the coast of Northern California and off the shore of Southern Oregon are summarized in Tab.1, along with moment tensor source parameters published by Harvard and the USGS. Two of the events at 2200 km were located on shore, while the epicenters of the 3 remaining events were about 200 km offshore. The station and event locations with their great circle paths are displayed with a schematic outline of the Basin and Range province

Table 1: Summary of event parameters ^{o)}

| No. | Date & Origin Time | | Latitude | Longitude | h | M _B | M _{sz} | Range ^{†)} |
|-----|--------------------|----------|----------|-----------|----|----------------|-----------------|---------------------|
| 1 | 01/16/1990(016) | 200822.0 | 40.232N | 124.138W | 2 | 5.1 | 5.5 | 2223 |
| 2 | 07/13/1991(194) | 025014.7 | 42.182N | 125.641W | 11 | 6.2 | 6.9 | 2431 |
| 3 | 08/16/1991(228) | 222617.2 | 41.697N | 125.385W | 10 | 5.5 | 6.3 | 2395 |
| 4 | 08/17/1991(229) | 192940.0 | 40.235N | 124.348W | 12 | 6.0 | 6.2 | 2219 |
| 5 | 08/17/1991(229) | 221714.7 | 41.821N | 125.397W | 14 | 6.2 | 7.1 | 2397 |

Harvard (USGS)- Centroid Moment Tensor Solutions

| No. | OT | Lat. | Long. | h | HD | Mo(DC)*e18 | α | δ | λ |
|-----|----------|--------|---------|----------|------|------------|----------|----------|-----------|
| 1 | 200830.6 | 40.06N | 124.94W | 15.0(-) | 2.2 | 0.2(-) | 37(-) | 90(-) | 0(-) |
| 2 | 025020.8 | 42.09N | 125.86W | 15.6(6) | 10.4 | 21.(19.) | 128(131) | 75(81) | 179(175) |
| 3 | 222618.9 | 41.23N | 125.56W | 15.0(13) | 6.1 | 3.1(3.8) | 40(218) | 68(82) | 6(82) |
| 4 | 192942.3 | 40.02N | 124.38W | 15.0(6) | 3.9 | 1.9(3.3) | 173(171) | 73(68) | 104(59) |
| 5 | 221720.8 | 41.71N | 125.63W | 15.0(12) | 13.1 | 44.(23.) | 46(47) | 86(82) | 28(-9) |

^{o)} NEIC : PDE - Monthly Listings

^{†)} Epicentral distance to Lajitas, TX (LTX) from QED's

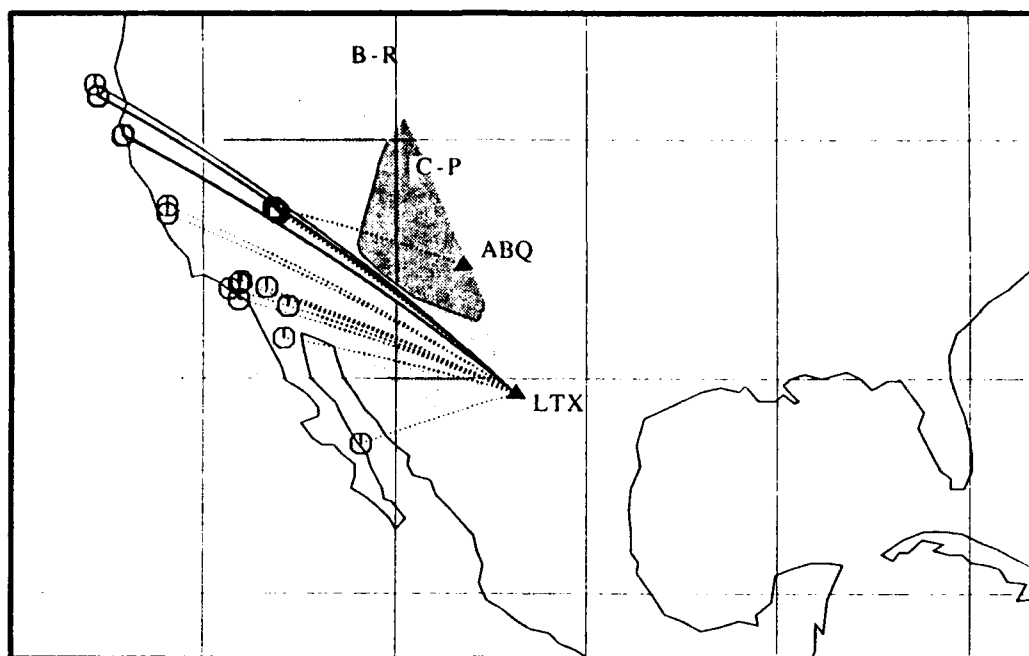


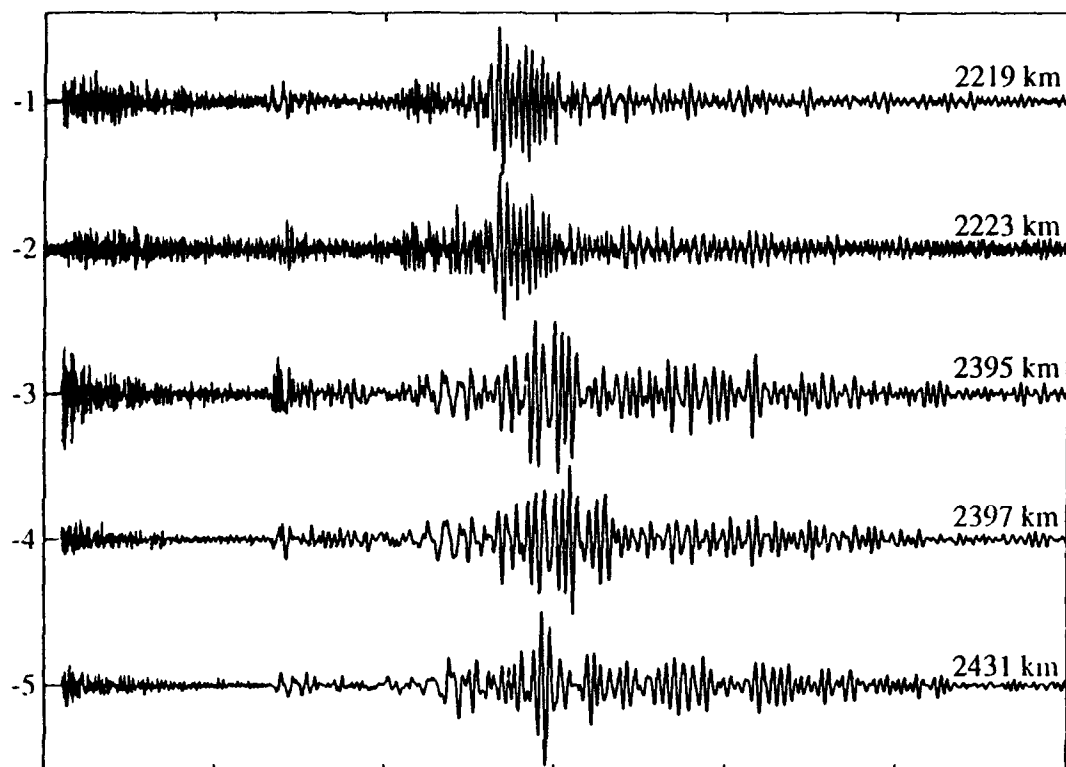
Fig.1 : Sketch map of station and epicenter locations; also shown are event locations used by Koch & Stump (1992)

in Fig.1. Previous events in California and the Nevada Test Site (NTS) studied earlier at distances less than 2000 km (Koch & Stump, 1992) are also shown. The primary motivation for our study was the fact that these earthquake data (2200-2500 km) are located so that their great circle paths to LTX coincides with the path from NTS to LTX, with the rays bottoming in the vicinity of NTS.

Both radial and transverse broadband records from all five events are plotted in Fig.2(a,b). These waveforms are characterized by the initial mantle P wave, some secondary arrivals, and surface waves. The top 2 traces in each sub-figure are for events on the coast of Northern California and show an emergent mantle S arrival as well as Lg waves on both components of motion. The bottom 3 traces which are from events offshore at distances of 2400 km and larger display mantle S arrivals which are impulsive on the transverse component and nonexistent Lg waves. The high-frequency nature of the mantle SH arrival for the closer distance suggests that this energy might be generated by scattering of the SV wave close to the receiver particularly since the mantle SV waves show a consistent emergent arrival throughout this distance range.

The Rayleigh waves from the two closest events (No.1 and 4, Table 1) are almost identical on the radial seismograms. The mantle S arrival and the Love wave energy following the fundamental mode arrival show large variations for these 2 events, which might be attributed to different source mechanisms, as the second event is a thrust event (Dengler et al., 1991, McPherson et al., 1991) while the other events are strike-slip. All 3 events in the 2400 km range show nearly identical seismograms from the onset of the mantle S wave to some 10 cycles into both Love and Rayleigh waves. Later arriving surface wave energy shows more significant differences. These variations may in part be due to the source itself, whether a source depth or spectral excitation effect. The complexity of the mantle S wave on the radial component might be associated with the source excitation as illustrated by the second and third trace from the top, which are relatively small events ($m_B < 6$). In these traces the mantle SV arrival is of relatively high frequency compared to the lower frequency character for larger events. The strong SH motion for distances larger than 2300 km appears to be unaffected by source differences as this S phase has the same simple waveform for all three distant events, even as the arrival for the third trace appears somewhat shorter in duration, with no strong secondary arrivals.

Radial Seismograms; Distance > 2000 km [BB]



Transverse Seismograms; Distance > 2000 km [BB]

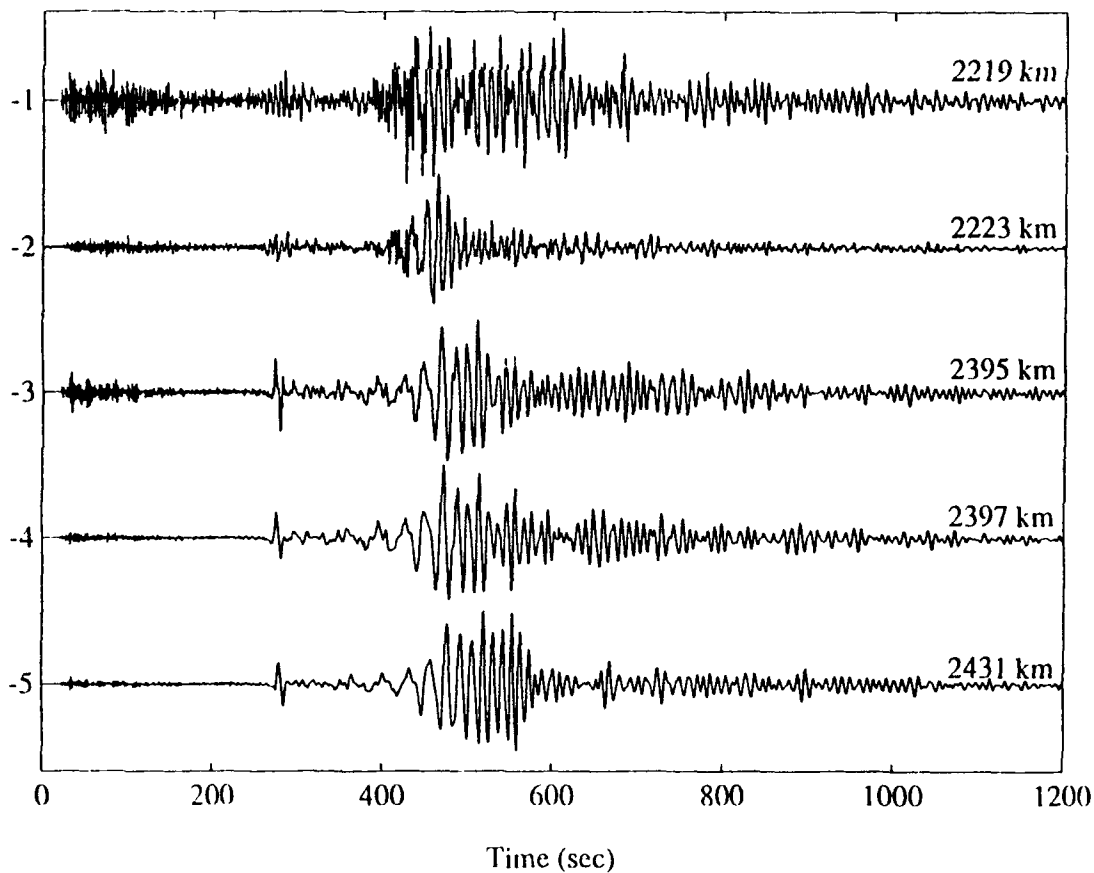


Fig.2 : Seismogram sections for radial (a) and transverse (b) seismograms showing mantle S wave development between 20° and 22°

TRAVEL TIMES AND SHEAR WAVE MODELS

The far-regional events of this study between 2200 and 2500 km (Tab.1) and the events from Koch & Stump (1992) provide a data set to investigate travel times across the Basin and Range from 800 to 2500 km. The travel times at these distances can be compared with predictions from a variety of upper mantle models, spanning regional to teleseismic wave propagation. We have considered standard travel time tables (Jeffreys-Bullen (JB), 1958; Herrin, 1968; Kennett & Engdahl, 1991), which are based on global travel time observations, and travel times from regional models for initial comparison with the data. Arrival times for P, L_g , and mantle S (S_m) phases were contrasted against standard travel time tables. The travel times of P follow the trend of JB as well as Herrin tables. Also, there is a significant delay, on the order of 10 seconds, for the mantle S arrivals relative to the JB model. A further comparison with the new IASPEI-91 tables (Kennett & Engdahl, 1991) reveals a similar result, with good prediction for the P times and a delay of nearly 15 sec for mantle S. It is important to note that the core-mantle reflection, PcP, crosses the mantle S wave travel time curve between 20–22°. Some of the complexity of the mantle SV arrivals was initially attributed to the interference of the S and PcP travel time branches, although PcP should be small at distance around 20° and for strike-slip mechanisms.

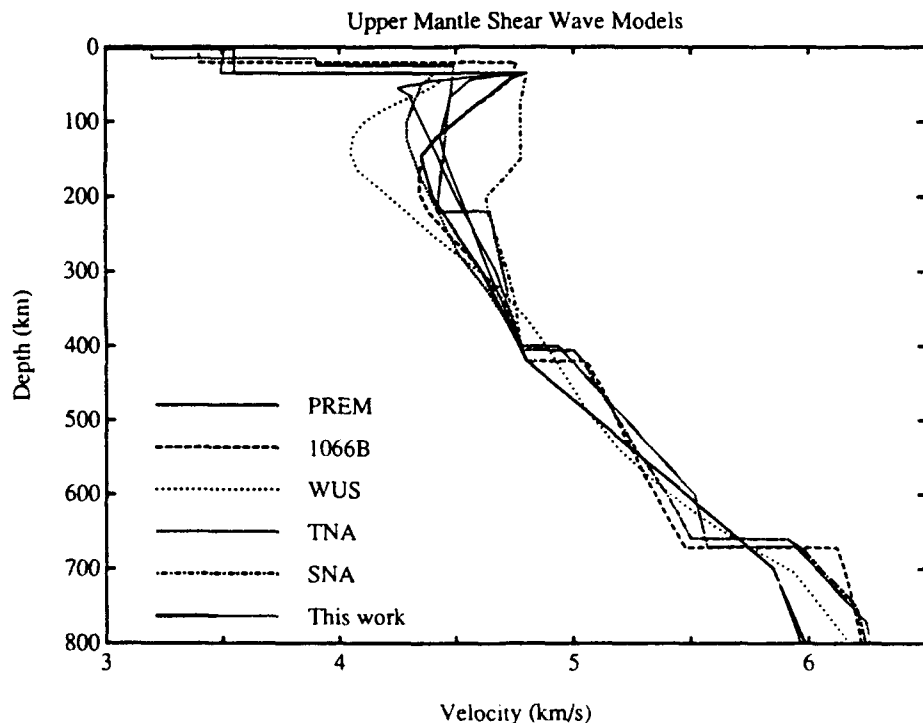


Fig.3 : Regional/teleseismic S wave velocity models tested for compatibility with far-regional mantle S wave observations

In order to explain the variations in observed travel times and ultimately model the mantle S waveforms, both global and regional velocity models were considered. The teleseismic models selected were PREM (Dziewonski & Anderson, 1981) and 1066B (Gilbert & Dziewonski, 1975), while the regional models were those from Cara (1979) (WUS) and Grand & Helmberger (1984) (TNA, SNA). These shear velocity models are summarized in Fig.3. The SNA model of Grand & Helmberger (1984) was included for completeness, but is not considered as adequate, as it was derived for the shield area of the Eastern U.S., while we are studying shear wave propagation in the tectonically active Western U.S. There is a large range for the velocity distribution in the uppermost mantle, but the velocities are similar near and below the 400 km discontinuity. Except for Cara's WUS model and the ones developed in this study, all other models are quite similar in

their structure between 400 and 700 km. Due to this similarity, we will emphasize models 1066B and WUS in the following discussion.

Travel times for these representative upper mantle shear models were calculated and are compared in Fig.4 to the observations. Both models include a single crustal layer with a velocity of 3.5 km/sec, which is consistent with the Lg arrivals to 2000 km. The upper mantle S wave arrival times are not well explained by either 1066B or WUS. Although 1066B shows several mantle S branches, none of these branches matches the trend of the mantle S arrivals. In addition, the first arrivals are too early. The S arrival times of WUS are 10-15 sec late between 2000-2500 km. But the slope of the branches appear to be in better agreement with the observations. As the travel time branches shown for WUS result from shear waves bottoming below the LVZ, the late arrivals suggest that the velocities for WUS are too low in the LVZ. The trend of the arrival times for the mantle S waves suggests, however, that the WUS model below the LVZ might be appropriate for modelling shear waves propagating in the upper mantle.

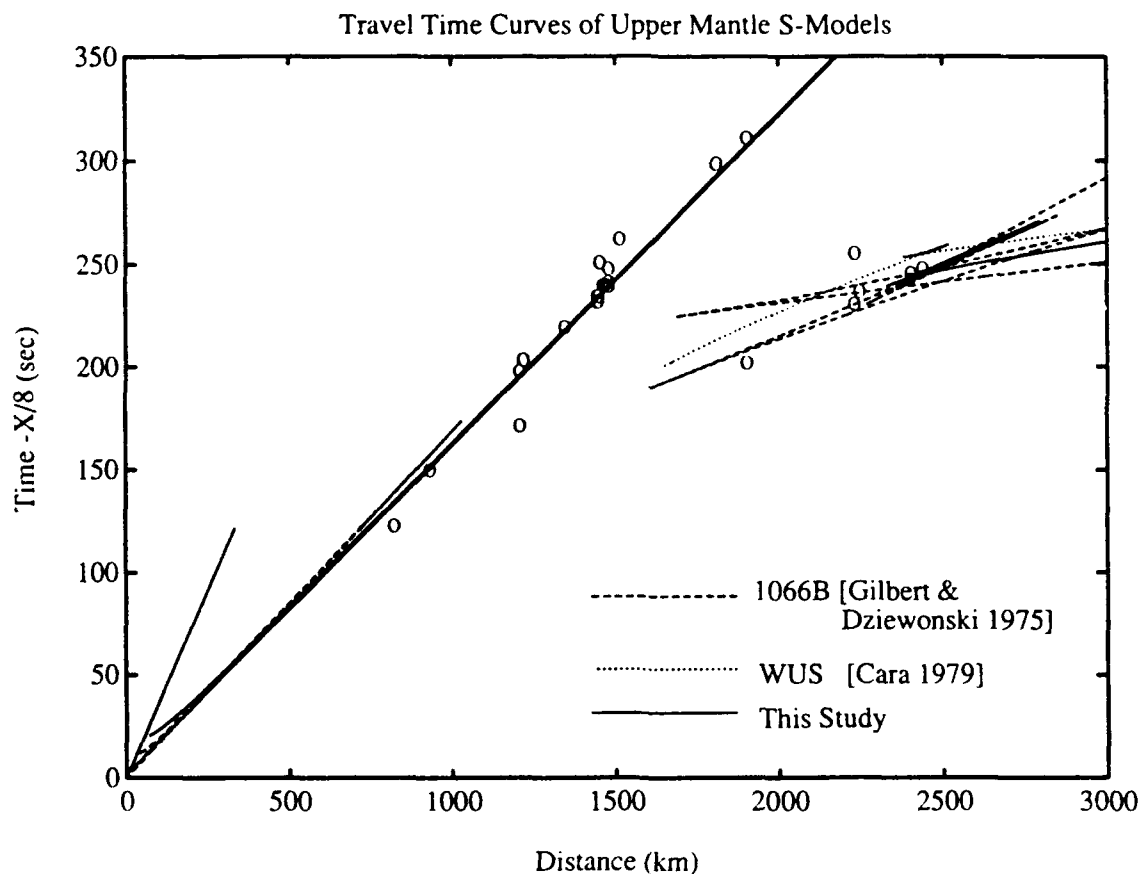


Fig.4 : Calculated S travel time curves (1066B, TNA, This study) and comparison with the observations.

MODELLING

For modeling the mantle S waves we used the reflectivity method (Müller 1985), which was used in a previous study to model far-regional data (Koch & Stump, 1992). We used a double couple source with fault parameters appropriate for the strike-slip mechanisms given in Tab.1. The source duration was set to 2 sec as a lower bound designed to include the higher frequency contributions from smaller events. Calculations were done at a sampling rate of 8 Hz with an effective bandwidth of 0.05-2 Hz. The source depth for all synthetic calculations was assigned to a fixed value of 5 km.

A first set of synthetic seismograms (Fig.5) was calculated for the 1066B velocity model (Gilbert & Dziewonski, 1975). A complex waveform pattern is found for the SH motion in the distance range between 2200 and 2400 km, as is suggested by the triplications in the travel time calculations. The most subtle feature of these seismograms are both the forward branch below 400 km as well as the reflection from the 700 km discontinuity causing an extended wavetrain. The reflections extend backwards in distance to well below 2000 km and hence the velocity distribution and the discontinuities in the shear wave model are inadequate for our observations. The $Q\beta$ values used for the shear waves were 200 in the crust and topmost mantle and 80 in the low velocity layer down to the 400 km discontinuity. Below 400 km $Q\beta$ was increased to between 300 and 400. These $Q\beta$ values are in the same range as those found by Al-Khatib & Mitchell (1991) from surface wave analysis or Lay & Wallace (1988) for multiple ScS phases.

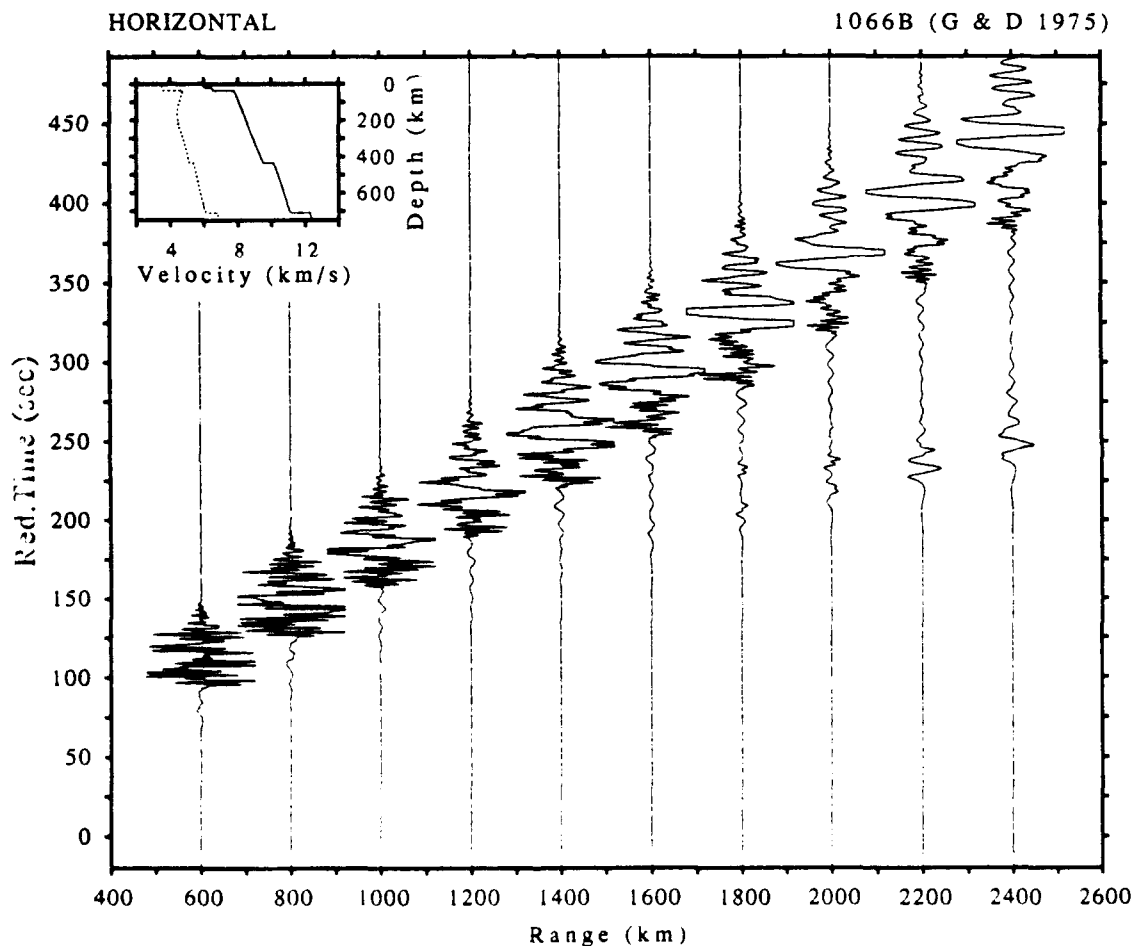


Fig.5 : Reflectivity seismograms for model 1066B at far-regional distances

These initial synthetic waveforms show that the velocity model between 400 and 700 km depth is critical to reproducing the mantle S phases observed between 20 and 22°. The WUS model of Cara (1979) offers an alternate velocity structure in this depth range incorporating a relatively smooth gradient above the 700 km discontinuity without any first order discontinuities. This second model was also tested and it is capable of producing a simple and impulsive shear arrival near 2400 km, while arrivals for shorter distances are emergent. Besides the large delay of the S arrivals relative to the observations, this model also generates some S energy in the synthetic seismograms near 1600 km from its strong positive gradient around 300 km depth.

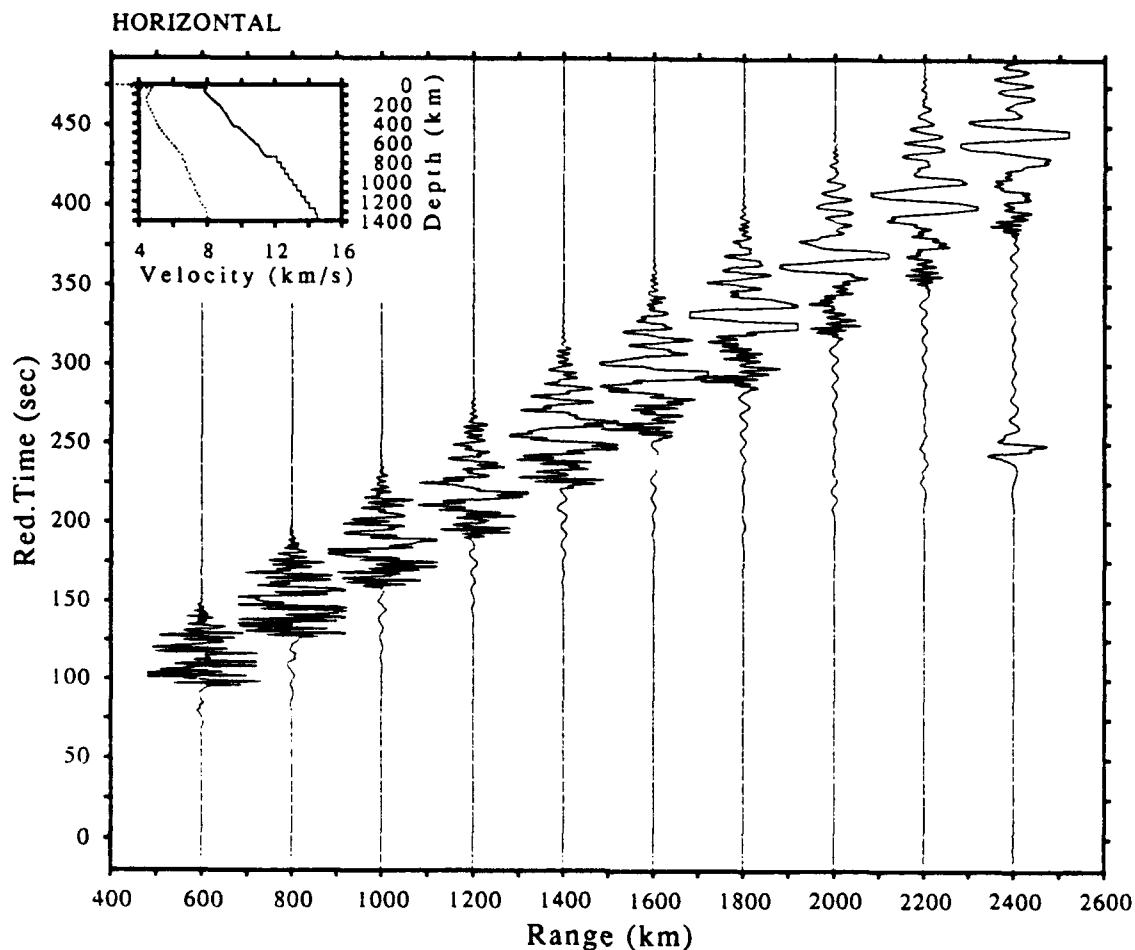


Fig.6 : Synthetic seismograms for upper mantle model developed in this study with a velocity gradient between 400 and 700 km similar to that of Cara (1979).

Based on these results, we revised the model proposed by Koch & Stump (1992) extending the shear velocities to greater depths. Previously a constant velocity in the LVZ of the upper mantle was assumed due to the lack of mantle S energy for distances less than 1500 km. The complexities in the shear waves introduced by velocity discontinuities in the 400-700 km depth range of 1066B are not found in our observations. Thus the discontinuities in the shear model were removed and a simple velocity gradient for S below 400 km was introduced into the regional model. This model however delayed the shear arrivals of the synthetics by more than 30 sec. As both 1066B and WUS include a negative gradient zone below the Moho, we developed an alternate model, where the transition to the low velocity zone in the upper mantle is represented by a negative gradient zone to about 150 km and the velocity turns smoothly to positive values. This procedure compensates for the travel times of phases propagating through the deeper upper mantle, while the smaller positive gradient above 400 km will not produce significant amplitudes for turning rays. The gradient in the 400-700 km depth range was held constant. The SH component synthetic seismograms are shown in Fig.6. They show very small mantle S contributions for all distances less than 2400 km, where the strong mantle S arrival appears.

CONCLUSIONS AND RECOMMENDATIONS

We have been able to identify mantle S arrivals at Lajitas for events at distances greater than 2000 km. For distances less than 1800-2000 km, Koch & Stump (1992) could not identify any coherent arrivals between the initial P waves and Lg. New observations between 20 and 22° show large amplitude, simple phases on the transverse component of motion between these phases.

These mantle shear phases can be attributed to the shear velocity structure between 400-700 km, which is best modelled by a strong positive gradient. Our data suggest that there is no evidence that the S velocity discontinuities at 400 and 700 km, incorporated in standard teleseismic Earth models are present for the S structure of the upper mantle beneath the Western U.S. These discontinuities if present would produce much more complicated shear arrivals than those observed at Lajitas. In contrast, the simple observed pulses argue for smooth velocity changes in both vertical and horizontal directions. It further indicates that the 1-D modeling applied in this study is fully adequate for our observations in the distance range of 20-22°.

The Q_β structure adopted throughout this work incorporated Q_β of 100 below the Moho and about 70-80 in the low-velocity zone to 400 km depth. These values were taken from standard earth models and are consistent with other studies (Al-Khatib & Mitchell, 1991, Lay & Wallace, 1988). Using higher values for Q_β produces significant arrivals from the mantle in the depth range between 200-400 km. Only the model used in Fig.6 produces a less pronounced increase of these mantle S amplitudes for higher Q_β . This apparent trade-off between upper mantle shear structure and low Q_β values needs to be further addressed through a detailed quantitative study of the absolute amplitudes for our mantle S waves. Additional work appears to be warranted including the P-velocity structure for the quantitative interpretation of radial and vertical seismograms.

REFERENCES

- Al-Khatib, H. & B. Mitchell (1991): Upper mantle anelasticity and tectonic evolution of the western United States from surface wave attenuation, *J. Geophys. Res.*, **96**, 18129-18146
- Cara, M. (1979): Lateral variations of S velocity in the upper mantle from higher Rayleigh modes, *Geophys. J. R. astr. Soc.*, **57**, 649-670
- Dengler, L. A., G. Carver & B. McPherson (1991): Potential sources of large Earthquakes in North coastal California, (abstract), *EOS*, **72(44)**, 315
- Dziewonski, A. M. & D. L. Anderson (1981): Preliminary reference Earth model, *Phys. Earth Planet. Int.*, **25**, 297-356
- Gilbert, F. & A. Dziewonski (1975): An application of normal mode theory to the retrieval of structural parameters and source mechanisms from seismic spectra, *Phil. Trans. Roy. Soc.*, **A278**, 187-269
- Grand, S. P. & D. V. Helmberger (1984): Upper mantle shear structure of North America, *Geophys. J. R. astr. Soc.*, **76**, 399-438
- Herrin, E. T. (1968): Introduction to "1968 seismological tables for P-phases, *Bull. Seism. Soc. Am.*, **58**, 1193-1195
- Jeffreys & Bullen (1958): Seismological tables, British Association Seismological Committee, London
- Kennett, B. L. N. & E. R. Engdahl (1991): Travel times for global earthquake location and phase identification, *Geophys. J. Int.*, **105**, 429-465
- Koch, K. & B. Stump (1992): Upper mantle structure of the Western United States from far-regional seismograms, submitted to *J. Geophys. Res.*
- Lay, T. & T. C. Wallace (1988): Multiple ScS attenuation and travel times beneath western North America, *Bull. Seism. Soc. Am.*, **78**, 2041-2061
- McPherson, B. C., L. Dengler & D. Oppenheimer (1991): Evidence of compressional tectonics in the Kings range, California: the 1991 Honeydew earthquake, (abstract), *EOS*, **72(44)**, 315
- Müller, G. (1985): The reflectivity method: a tutorial, *J. Geophys.*, **58**, 153-174

CONCEPTS FOR PROCESSING OF DATA FROM A NETWORK OF REGIONAL ARRAYS

Tormod Kværna, Svein Mykkeltveit, Frode Ringdal and Jan Fyen
NTNF/NORSAR, P.O. Box 51, N-2007 Kjeller, Norway

Contract No. F49620-89-0038

Objective:

The basic objective of NORSAR's regional array program is to provide data for use in seismological verification research. Specifically, the research in seismic data processing focuses on development and testing of methods to improve the detection, location and identification of low-magnitude events, and techniques that may be useful in the further development of the Intelligent Monitoring System (IMS) are of particular interest. In this regard, much attention has been devoted during this year to the concepts of Generalized Beamforming (GBF) and Threshold Monitoring (TM).

This paper summarizes the status of development of the regional network in northern Europe that contributes seismic data in real time to the NORSAR Data Processing Center and the IMS. Also summarized are plans for expansion of this network with two new small-aperture arrays in the very near future. Furthermore, the feasibility of the GBF and TM methods using regional array data is demonstrated in two separate studies.

Research accomplished:

Status of development of the regional network

The network contributing continuous data to NORSAR is shown in Fig. 1 and currently comprises the NORESS and ARCESS arrays in Norway, the FINESA array in Finland, the GERESS array in Germany, and the two 3-component stations at Ksiaz and Stary Folwark in Poland. A comprehensive description of NORESS and ARCESS is given by Mykkeltveit et al (1990). These 3-kilometer aperture arrays have been in stable and continuous operation since they were installed in 1984 and 1987, respectively. The somewhat smaller FINESA array in Finland has been described by Uski (1990). The GERESS array in the Bavarian Forest area of Germany (aperture 4 km) has been described by Harjes (1990).

A new version of IMS that accepts input data from arbitrary numbers of arrays and single, three-component stations has been installed at NORSAR, following a period of extensive testing at the Center for Seismic Studies in Washington D.C. This new version enables joint processing of data from the NORESS, ARCESS, GERESS and FINESA arrays and the two three-component stations in Poland. The new version of IMS has been operated in a research and evaluation mode at NORSAR since October 1991. The data from the two new small-aperture arrays in Apatity and on Spitsbergen (see below) will be integrated into the IMS.

A three-component station was installed in Apatity on the Kola Peninsula of Russia in June 1991, in cooperation with the Kola Science Center, and preliminary analysis has shown that this station is very valuable for near-field studies of mining explosions in the Khibiny Massif. The field work for the installation of a small-aperture (1 km) 10-element array near Apatity is nearing completion,

with expected data availability in September. Site preparation work as well as noise surveys for a similar array on the Arctic island of Spitsbergen have been carried out, and the installation of the electronic components and the satellite link to bring the data to NORSAR is also scheduled for September this year. The deployment of these two new arrays is expected to enhance the monitoring capability and also provide valuable new insight regarding propagation characteristics of regional phases, especially in the northernmost areas covered by the network.

The Generalized Beamforming method applied to data from a network of seismic microarrays

The applicability of the Generalized Beamforming method (Ringdal and Kværna, 1989) for automatic phase association and event location has been evaluated using detection data from a network of three microarrays (Kværna, 1992a). The center instrument and the A-ring of each of the existing Fennoscandian regional arrays NORESS, ARCESS and FINESA (see Fig. 1) were used to represent microarrays. The NORESS microarray is shown in Fig. 2.

For all three microarrays we conducted automatic detection processing and post-detection analysis for a period of 12 days (9-20 April 1992). The processing, which included broadband f-k analysis, was similar to that used in the study of Kværna and Ringdal (1992).

To obtain a data base against which to evaluate our results, we extracted all seismic phases detected by the three full arrays and associated with regional events for the 12-day period. *P*-coda detections and multiple *S*-phases were ignored, so that each event provided a maximum of 3 phases (*P*, *S* and *L_g*) for each array. These phases were then matched to the detection lists produced by the microarrays, and the apparent velocity and azimuth estimates were compared.

Fig. 3 shows the apparent velocity estimates derived from vertical sensors of the ARCESS microarray for *P* phases (circles) and *S* phases (asterisks) for the reference data set of phases associated with regional events. In this context, both *S* and *L_g* were counted as *S* phases. A summary of the results obtained from f-k analysis of the microarrays is given in Table 1. The first row gives the percentages of correctly classified phases, whereas the next four rows show statistics on the azimuth estimates of the verified *P* and *S* phases.

In the operation of the Fennoscandian array network we have found it important to isolate so-called noise detections (false alarms) at as early a stage in the processing flow as possible. This will prevent false events to be declared and also improve the performance of the phase association and event location procedure. In the processing of the full arrays, the noise detections are identified from low apparent velocities in the f-k spectra. Similarly, we defined all microarray detections (both associated and unassociated phases) with apparent velocities < 3.2 km/s as noise. The percentages are given in the 6th row of Table 1. The last row of the table gives the percentage of verified phases (*P*, *S* or *L_g*) classified as noise. These statistics implied that for the ARCESS and NORESS microarrays, noise detections could be effectively discarded from further analysis, practically without losing any of the real seismic phases. On the other hand, in the case of FINESA, we did also miss some of the real *P* and *S* phases, implying that the total benefit from discarding the low-velocity detections was very moderate.

The detection data from the microarrays were subsequently processed with the GBF method to form regional events. To check the robustness of the algorithm, we avoided tuning of the GBF parameters towards processing microarrays, and except for one change we used the same parameter setting as in the routine processing of the full array network.

The events declared by the GBF algorithm from processing of the full regional arrays ARCESS, FINESA and NORESS were used as a reference data set for the 12-day period, and a detectability study was conducted for events within 600 km of the closest array. A maximum likelihood estima-

tion of event detectability (Ringdal, 1975) of the region defined above is presented in Fig. 4. From the number of detections/no detections at each magnitude, the 50% and 90% incremental detection thresholds are inferred. The 90% threshold is about $M_L = 1.8$, whereas the 50% threshold is found to be about $M_L = 0.8$. These numbers are further confirmed by comparing with the seismic bulletin of the University of Helsinki, Finland.

For 249 events located within 600 km of the closest array, the median difference between automatic locations by the full array network and by the microarray network was only 47.4 km. Out of a total of 353 events formed after automatic GBF processing of the microarray network, only 92 (26%) were found to be false, a number that is easily handled in an analyst review situation. All events with 4 or more defining phases were real. The vast majority of the false events were associated with detections at the FINESA array.

These results demonstrate that automatic phase association and event location using the GBF algorithm can be successfully conducted using data from a sparse network of seismic microarrays (interstation distance ~ 1000 km). The apparent velocity and azimuth estimates of the detected phases found by f-k analysis of the 4 vertical-component sensors of each microarray place strong constraints on the use of the detected phases. This enables subsequent GBF processing of the detection data to be performed with good event detectability combined with a low number of false events.

Continuous seismic Threshold Monitoring of the northern Novaya Zemlya test site, long-term operational characteristics

The applications of the continuous Threshold Monitoring method (TM) for monitoring the northern Novaya Zemlya test site has been evaluated. Again using the three regional arrays NORESS, ARCESS and FINESA as data sources, detailed monitoring statistics for the full month of February 1992 were compiled (Kværna, 1992b).

During normal conditions when the background noise dominates the seismic amplitude level, ARCESS is clearly the most important array, followed by NORESS and FINESA. This is illustrated in Fig. 5, where we have plotted 4-hour medians of the magnitude thresholds for each individual array.

On the other hand, during time periods when the ARCESS noise level is high, or when there are interfering events, the relative contribution of NORESS and FINESA increases significantly. This is illustrated in Fig. 6, where we for the month analyzed have counted the number of threshold peaks exceeding a given magnitude, both for the network and for the best array (ARCESS). The figure shows that at a threshold of 2.6, the number of network threshold peaks are reduced by a factor of five in comparison to the threshold peaks at ARCESS alone (i.e., from 293 to 56). At a threshold of 3.0 the improvement is better than a factor of ten (i.e., from 41 to 3).

We have further identified all 56 peaks in the network magnitude thresholds exceeding $m_b = 2.6$ as resulting from interfering signals from an identified seismic event (teleaseismic or regional), or a short outage of the most important array (ARCESS). The total time span when these peaks exceeded 2.6 was only 43 minutes during the month of February (0.12% of the time). In practice, this implies that at the given confidence level, there has been no seismic event of $m_b \geq 2.6$ at the northern Novaya Zemlya test site during February 1992.

Conclusions and recommendations:

In our view, the deployment of advanced regional arrays and the associated development and implementation of automated and increasingly powerful data processing techniques (as exempli-

fied by the IMS) represents one of the major advances in seismic monitoring in recent years. In our judgement, the TM technique, the applicability of which has been demonstrated in this paper, represents a significant step forward in practical monitoring of underground nuclear explosions. Nevertheless, much research remains to be done to further develop this technique and other methods for integrated processing of data from a regional network of arrays and 3-component stations, in order to exploit the full potential of such data.

References:

- Harjes, H.-P. (1990). Design and siting of a new regional array in central Europe, *Bull. Seism. Soc. Am.*, 80, Part B, 1801-1817.
- Kværna, T. (1992a). Automatic phase association and event location using data from a network of seismic microarrays. NORSAR Semiannual Tech. Summary 1 Oct 91 - 31 Mar 92, Kjeller, Norway.
- Kværna, T. (1992b). Continuous seismic threshold monitoring of the northern Novaya Zemlya test site; long-term operational characteristics. Sci. Rep. No. 12, PL-TR-92-2118, Phillips Lab., Mass., USA. **ADA252890**
- Kværna, T. and F. Ringdal (1992): Integrated array and three-component processing using a seismic microarray, *Bull. Seism. Soc. Am.*, 82, 870-882.
- Mykkeltveit, S., F. Ringdal, T. Kværna and R.W. Alewine (1990). Application of regional arrays in seismic verification research, *Bull. Seism. Soc. Am.*, 80, Part B, 1777-1800.
- Ringdal, F. and T. Kværna (1989): A multi-channel processing approach to real-time network detection, phase association, and threshold monitoring, *Bull. Seism. Soc. Am.*, 79, 1927-1940.
- Ringdal, F. (1975): On the estimation of seismic detection thresholds, *Bull. Seism. Soc. Am.*, 65, 1631-1642.
- Uski, M. (1990). Event detection and location performance of the FINESA array in Finland, *Bull. Seism. Soc. Am.*, 80, Part B, 1818-1832.

| | ARCESS | FINESA | NORESS |
|-------------------------------------------------------------|--------|--------|--------|
| Percentage of correctly classified phases | 79.2% | 78.6% | 93.3% |
| Median azimuth error for P-phases | 10.4° | 13.4° | 14.0° |
| Percentage of P-phases within 25° | 78.5% | 73.0% | 86.1% |
| Median azimuth error for S-phases | 6.8° | 8.5° | 6.5° |
| Percentage of S-phases within 25° | 98.2% | 88.0% | 94.6% |
| Percentage of all microarray detections classified as noise | 36.3% | 26.0% | 11.2% |
| Percentage of verified phases classified as noise | 0.0% | 13.5% | 0.6% |

Table 1. This table contain a summary of the success rates for initial phase identification and the median errors in the azimuth estimates for the three microarrays considered.

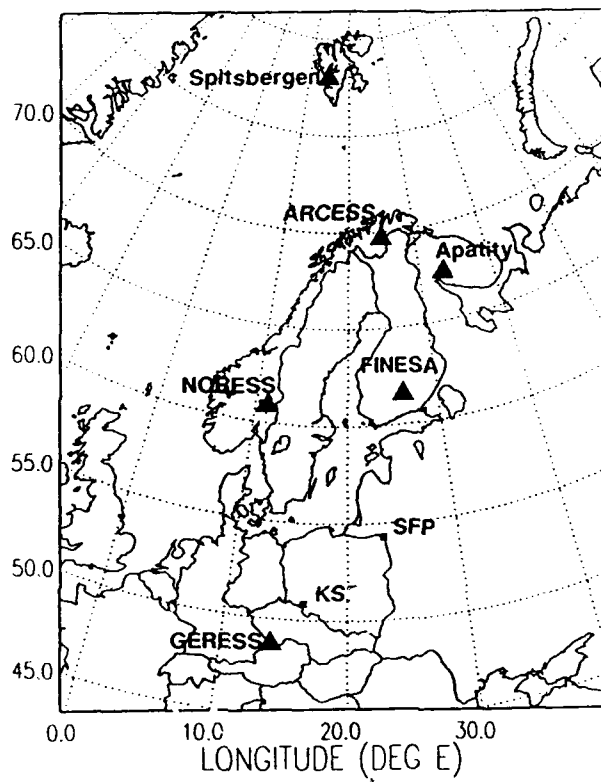


Fig. 1. The map shows the location of the existing regional arrays NORESS, ARCESS, FINESA and GERESS, as well as the 3-component stations KSP and SFP in Poland. The location of the new arrays at Apatity in Russia and on the island of Spitsbergen are also shown.

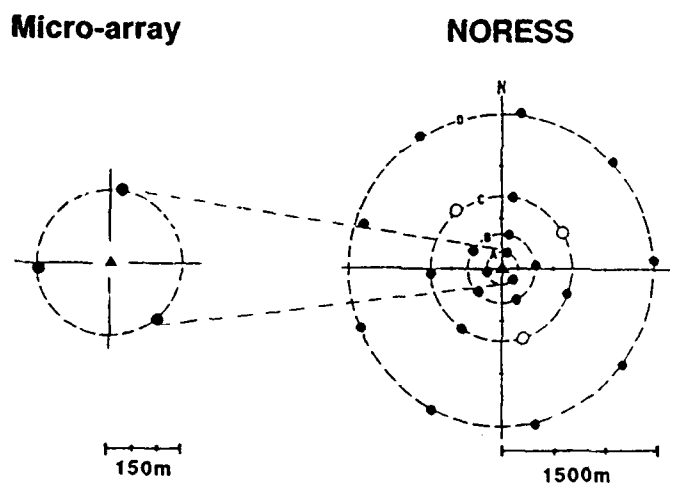


Fig. 2. Geometry of the NORESS array and the corresponding microarray used in this study. The vertical-component sensors are indicated by circles, whereas the triangles represent 3-component sensors. Similar microarray configurations were used at ARCESS and FINESA.

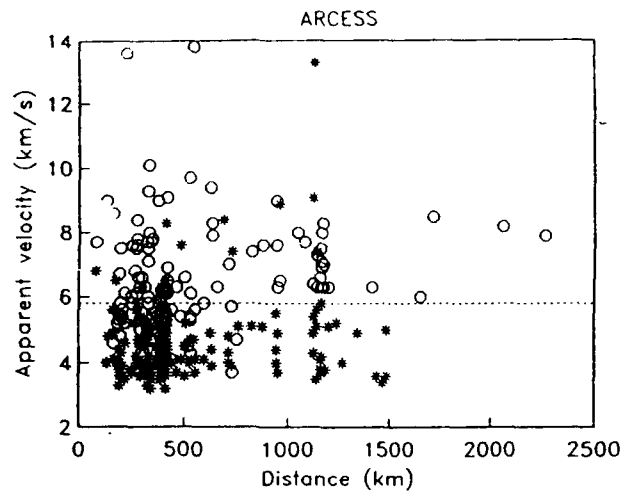


Fig. 3. Estimated apparent velocities from applying broadband f-k analysis to the vertical components of the ARCESS microarray for *P* phases (circles) and *S* phases (asterisks). An apparent velocity of 5.8 km/s (dashed line) has been used to classify the phases as *P* or *S*. The success rate is 79.2%.

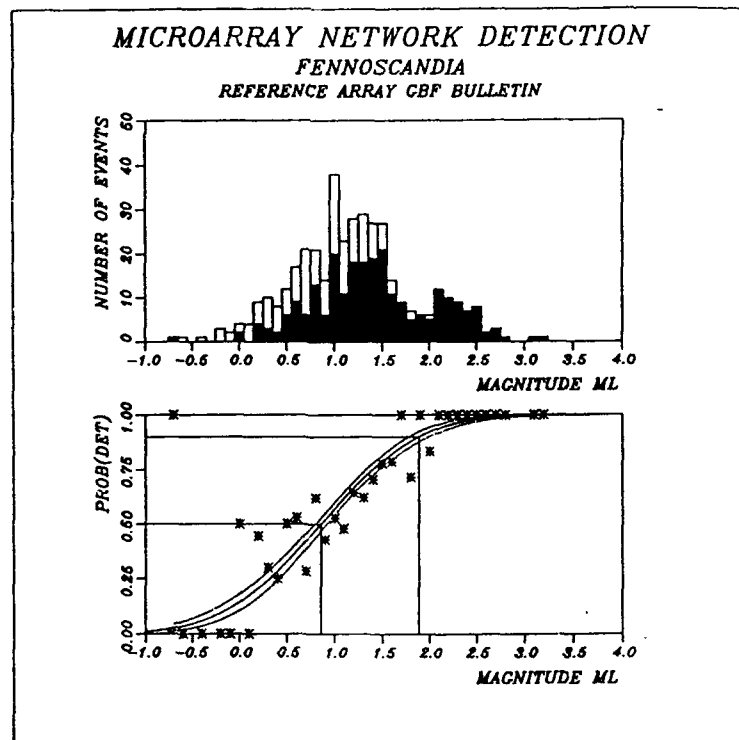


Fig. 4. Maximum likelihood detectability estimation of the microarray network for Fennoscandia-NW Russia using the GBF bulletin as a reference. The upper half shows the reference set and the number of events found by the microarray network for each magnitude. The lower half shows the maximum likelihood detectability curve and its confidence limits. The actual percentage of detected events at each magnitude is also shown.

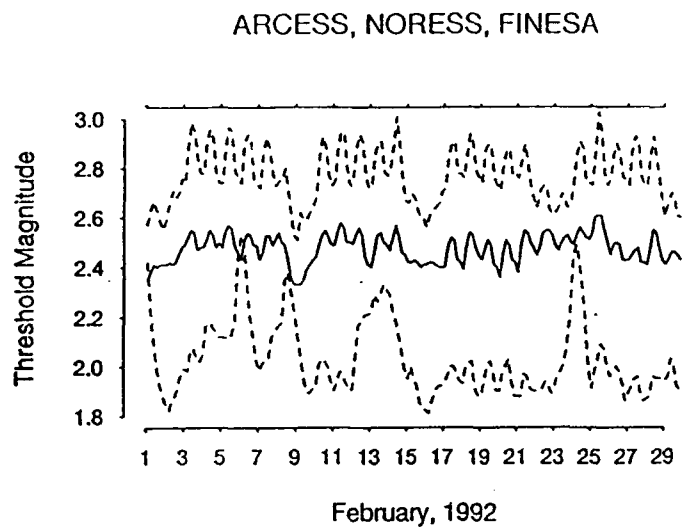


Fig. 5. Four-hour medians of the magnitude thresholds for each array for the month of February 1992. Lower dashed line: ARCESS; Middle solid line: NORESS; Upper dashed line: FINESA.

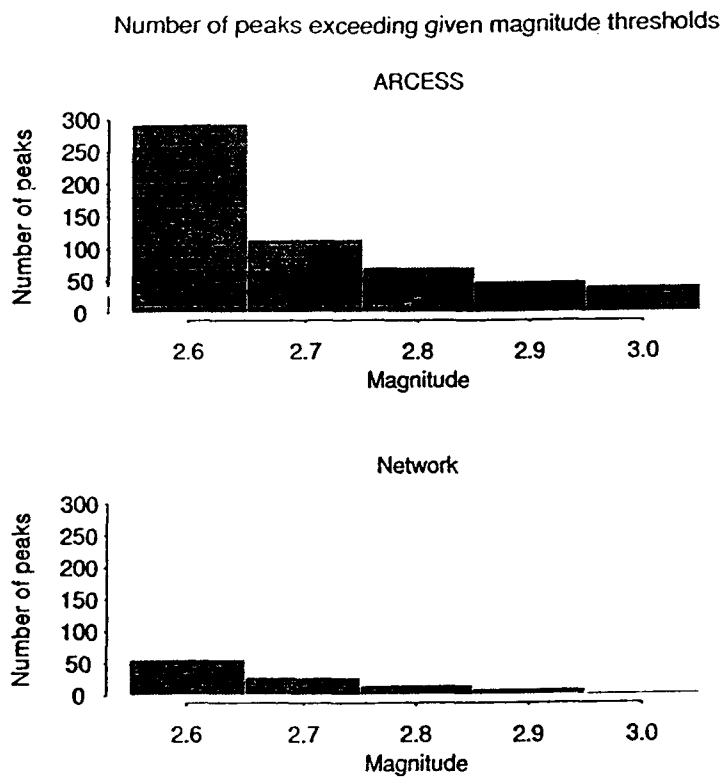


Fig. 6. Number of peaks exceeding given magnitude thresholds. Upper part: ARCESS; Lower part: Network.

SEISMIC PHASE AND EVENT RECOGNITION USING ALGORITHMS THAT LEARN FROM EXAMPLES*

R. T. Lacoss, S. R. Curtis, R. K. Cunningham
M.I.T. Lincoln Laboratory
CONTRACT: F19628-90-C-0002

July 31, 1992

1 OBJECTIVE AND INTRODUCTION

The project objective is to develop algorithms that learn to perform specialized recognition functions for nuclear test monitoring systems such as the DARPA Intelligent Monitoring System (IMS). Work this year has included refinement and evaluation of phase labeling networks for IMS and experiments with mining event recognition based upon autoregressive signal models. We have also begun experimenting with generalized beamforming to see how it might learn from experience and if more complex signal features and relationships can be incorporated to make it function as an event recognition aid.

2 RESEARCH ACCOMPLISHED

An important task within the IMS system is to attach phase labels (e.g. Pn, Pg, etc) to signal detections. This is done at two levels: (1) for each array or three-component station in isolation, taking only single-station information into account, and (2) at the network level where information from all stations is used, and some of the labels assigned at the single-station level may be modified.

Last year we reported on the development of single-layer perceptron networks that improved upon the single-station phase labeling done in IMS [5]. The neural network took the IMS expert system labels plus other parameters as inputs and produced a revised label with a reduced error rate. Training and testing were performed with IMS parametric data obtained from the on-line database at the Center for Seismic Studies (CSS).

During this year the networks have been refined and tested by integrating them into an IMS system and evaluating performance with and without the networks. This was done cooperatively with Tom Sereno and Gagan Patnaik of SAIC. We also evaluated phase labeling performance as a function of signal to noise ratio and developed methods for the network to provide an estimate of the probability of a label being correct. The results are reported in the Section 2.1.

We also have investigated other classifiers to see if they might improve the phase labeling performance. All the classifiers that we experimented with performed at about the same level, although the perceptron was slightly better than the others. Specific results are reported in Section 2.2.

We have also continued our investigation of autoregressive models for regional event labeling. Results from this work are given in Section 2.3.

Generalized beamforming results are not yet available and will be reported at a later date.

*This work was sponsored by the Department of the Air Force

2.1 Evaluation of Perceptron Phase Labeling Networks

In the past, our evaluation of the perceptron phase labeling networks concentrated on the percentage classification error in various situations. During the past year, we provided a copy of our phase labeling network to SAIC for evaluation in the overall IMS system. The goal was to determine to what extent our improvements in the initial single-station phase IDs translated into improvements in the final expert system phase IDs (after network processing) and in the location estimates computed for the seismic bulletin.

The experiment was conducted by SAIC using data from the entire month of April 1991. During this time period there were 5306 event-associated arrivals, of which 3125 were analyzed by the neural network. (Arrivals were not analyzed only if some of the parameters needed by the network were missing.) The neural network phase ID was different from the expert system phase ID approximately 9% of the time. A comparison of the neural network phase ID accuracy with the expert system phase ID accuracy is given in the Table 1.

Table 1. Performance of Neural Net Phase ID

| | % correct | |
|-------------------------|--------------------|-----------------|
| | without neural net | with neural net |
| single-station phase ID | 85.4 | 88.7 |
| final phase ID | 85.1 | 86.1 |

As can be seen in the table, in single-station processing, the neural network phase ID is 3.3% better than the expert system. After network processing, the system containing the neural network is 1.0% better than the system without the neural network. Thus, the neural net does improve the final results, but not by as much as was originally hoped based on the single-station improvement.

Further analysis suggests that there are two common scenarios that account for the smaller-than-expected improvement. In the first scenario, the (single-station) expert system mistakenly labels some Sn phases as Sx. The neural network corrects this error, but the IMS network processing can also correct this error if the neural net is not used. Thus, the correction provided by the neural net does not actually translate into an improvement in the final bulletin. In the second scenario, the expert system mistakenly labels some Lg phases as Sx. The neural net corrects this error, but the IMS network processing then changes it back to Sx, thus negating the gain of the neural network. Our conclusion is that for IMS to make best use of the neural network phase ID, some changes would have to be made in the IMS network processing.

We also compared the seismic bulletins generated with and without the neural network. This comparison is given in the Table 2.

Table 2. Comparison of Seismic Bulletins

| | without neural net | with neural net |
|------------------------------|--------------------|-----------------|
| correct events found | 2135 | 2137 |
| incorrect events found | 22 | 17 |
| median location error (km) | 43.8 | 28.2 |
| % closer to analyst solution | 47 | 53 |
| median time error (s) | 5.1 | 2.9 |
| # events perfect | 252 | 254 |

By every measure the system with the neural net produced more accurate bulletins than the system without the neural net. In many cases the gains were small, but there were no losses. We expect that if the IMS network processing was modified slightly to take advantage of the improved initial phase IDs, the improvements in the final bulletin would be even larger.

Since the output of the neural net is not simply a classification but is an activation level, we can use the output to estimate a confidence level, or probability that the classification is correct. For this problem, we have chosen to use a linear function of the difference between the highest

activation level (i.e. corresponding to the selected phase) and the second-highest activation level. We have found experimentally that on this data, this technique is as good or better than the method of using the activation levels directly. Specific results are given in Table 3.

Table 3. Evaluation of Confidence Measure

| network confidence | % correct |
|--------------------|-----------|
| 0.35-0.45 | 37 |
| 0.45-0.55 | 49 |
| 0.55-0.65 | 65 |
| 0.65-0.75 | 74 |
| 0.75-0.85 | 81 |
| 0.85-0.95 | 91 |
| 0.95-0.97 | 96 |

As can be seen from the table, the confidence levels provide a good estimate of the probability that the phase classification is correct. We have provided these confidence levels to SAIC as part of the IMS experiment described earlier. However, the IMS network processing does not currently take advantage of the confidence levels because the expert system does not provide them with its single-station phase ID. We expect that if the neural network phase ID is used, the network processing portion of IMS could be improved by using these confidence levels to decide which phase labels to change first.

We have also performed some experiments of our own to determine the phase classification accuracy at various signal-to-noise ratios (SNRs). A comparison of the neural net and the expert system single-station ID at various SNRs is given in Table 4.

Table 4. Performance at Different SNRs

| SNR(STA/LTA) | % correct | |
|--------------|---------------|------------|
| | expert system | neural net |
| < 5 | 83 | 82 |
| 5-10 | 85 | 89 |
| 10-20 | 90 | 92 |
| > 20 | 91 | 93 |

At very low SNRs, the parameter estimates used as inputs to the neural net are unreliable, and neither the neural net nor the expert system performs very well. However, the neural net performance begins to improve noticeably at SNRs of 5 or higher, whereas the expert system begins to improve at SNRs closer to 10. Thus, the biggest gain in using the neural network is for arrivals with SNRs in the range 5-10.

2.2 Alternative Phase-labeling Classifiers

Additional classifiers, feature sets, and feature normalizations were investigated to see if the perceptron phase classification results could be improved. The data used for these experiments were the measurements for a set of 9105 arrivals that were used for the initial development of the perceptron network.

For this experiment, we selected the most useful set of features as follows. Each possible feature was first used singly to find the one giving best performance with a nearest neighbor classifier. Then each other feature was used with that one to find the best pair. This continued until no further performance improvement was achieved. We then formed another feature set by starting with all the features and removing features one by one until performance began to deteriorate. The union of the two feature sets was used for all subsequent experiments with different classifiers and normalizations.

Classifiers can be sensitive to feature normalization. As part of the effort to improve phase-labeling results, we explored three different normalizations. The first normalization, labeled

simple normalization, involves computing the mean and variance of each feature and then linearly scaling the entries so that they have a mean of zero and a variance of one. The second normalization, labeled [-1:1], has each feature scaled to be between -1 and +1. (This normalization was used to select the best feature vector.) The scaling was either linear or logarithmic, based on an informal statistical analysis. The domain point which mapped to zero was similarly selected. Finally, components that represented N-way choices were split into N Boolean components. The third normalization, labeled [0:1], has each feature scaled to the range 0 to 1. The chief difference between [-1:1] normalization and [0:1] normalization is that [0:1] normalization further splits some features into multiple components, each indicating the distance from known seismologically-important values. Although the sign of the component is lost, this representation nevertheless improves the performance of some classifiers.

Several different types of classifiers were considered. One classifier was an explicit statistical model, three were error-minimization type classifiers, two were exemplar-based, one was a hybrid that stored exemplars that minimized coding error, and one was an ART type. The statistical classifier was a Gaussian classifier [3] (Gauss), for which the training data set is used to estimate the parameters of a Gaussian distribution. The error minimization classifiers were a single-layer perceptron [9] (Pcptrn), a two-layer perceptron (MLP2), and a Radial Basis Functions [6] (RBF) classifier. The exemplar-based classifiers were the K-Nearest Neighbor classifier [7] (KNN), and the Condensed K-Nearest Neighbor classifier [4] (CKNN). The hybrid classifier was the Hypersphere or Reduced Coulomb Energy Classifier [8] (Hyper). The ART-type classifier was Fuzzy ARTMap [1, 2] (FAM), which is a hybrid system that stores compound exemplars and computes similarity via a built-in distance metric, but incorporates an error-minimizing unit (called "Match Tracking") to determine when to mix new training data into existing exemplars and when to form a new exemplar.

Many experiments were performed to optimize parameter settings for each classifier for each of the three types of normalization. The percent correct classification using the best settings of each classifier for each normalization are shown in Figure 1. The error bars indicate the minimum and maximum percent correct, and the central point indicates the mean percent correct for the best parameter settings. These statistics were obtained using 3/4 of the data for training and 1/4 of the data for testing and repeating this four times with the four different testing sets.

The best and most robust performances were realized by the perceptron classifiers. The KNN classifier gave comparable performance with the [-1:1] normalization (the normalization used for feature set selection). In general, exemplar classifiers performed less well, and were more susceptible to effects of normalization. The Hypersphere classifier performed particularly poorly when simple normalization was used, because it internally normalizes its stored exemplars so that the input vector length is one. When input vector lengths are not fixed (as in the simple normalization case), the relative component values change. Although inter-component normalization is acceptable when an input consists of similar data (eg. coordinate directions), it is incorrect when an input consists of dissimilar data (eg. apple color and apple shape). Fuzzy ARTMap, like other networks that minimize coding error, was relatively immune to vector normalizations.

2.3 Autoregressive Models for Event Labeling

The goal of our event labeling research is to develop algorithms to aid in recognizing routine mining events, distinguishing earthquakes from explosions, and flagging unusual events. Last year we presented some preliminary results on discriminating earthquakes from explosions on the basis of autoregressive (AR) parameters. Recently we have examined these results in more detail and have performed additional experiments.

Our approach is to compute autoregressive parameters from the waveform data, and use these parameters as input to a neural network. The network then classifies the event as a mining explosion, another type of explosion, or an earthquake. The network output could be used in combination with another system, such as the SAIC event ID system, that takes into account

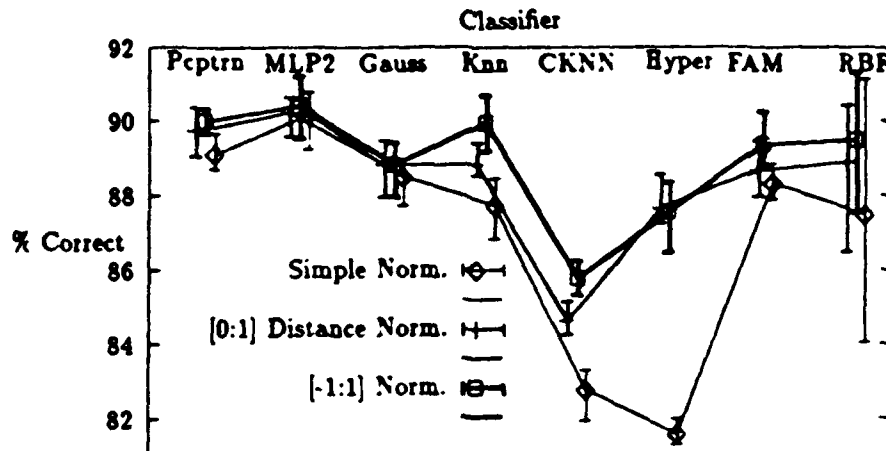


Figure 1: Percent Correct Classification for Eight Common Classifiers and Three Normalizations. The best performances were realized by classifiers that explicitly minimized coding error (Pcptrn, MLP2, FAM, RBF) or estimated parameters of a unimodal probability distribution (Gauss), while classifiers that used built-in distance measures (KNN, CKNN) and normalized vector length (Hyper) performed less well and were more susceptible to effects of normalization.

other information such as the event location, time of day, amplitude ratios, etc.

Two types of experiments have been performed. The goal in one case was to separate earthquakes from explosions of any type. In the other case the goal was to separate mining explosions from other types of explosions. Results reported here were obtained using a single-layer perceptron. Radial Basis Functions and multiple-layer perceptrons were also tried with no improvement in the results. All results were obtained with leave-one-out testing.

The waveforms and nominally correct event labels used for these experiments were obtained from SAIC. There were a total of 177 events at ARCESS (24 earthquakes, 133 mining explosions, and 20 other explosions) and 167 events at NORESS (26 earthquakes, 118 mining explosions, and 23 other explosions).

To compute the autoregressive parameters, we first formed 3-component beams (using data only from the 3-component seismometers at ARCESS and NORESS), steered with the azimuth and velocity measured for the first P phase associated with the event. The beams were then rotated to the estimated azimuth to obtain radial and transverse components. We then computed a 3-dimensional 2-pole autoregressive model (18 parameters) from about 7 minutes of data, encompassing the entire event. (In some cases, slightly improved results were obtained by using a subset of 4-8 autoregressive parameters rather than all 18.)

The performance of networks trained to distinguish earthquakes from explosions using autoregressive parameters are given in Tables 5 and 6 for ARCESS and NORESS, respectively.

Table 5. Event Identification at ARCESS

| SAIC label | neural net label | | |
|------------|------------------|-----------|-------|
| | earthquake | explosion | total |
| earthquake | 17 | 7 | 24 |
| explosion | 1 | 152 | 153 |

Total percent correct: 95%

Table 6. Event Identification at NORESS

| SAIC label | neural net label | | |
|------------|------------------|-----------|-------|
| | earthquake | explosion | total |
| earthquake | 11 | 15 | 26 |
| explosion | 2 | 139 | 141 |

Total percent correct: 90%

We examined the incorrectly-classified events in detail and found that they were often earthquakes from regions that have more explosions than earthquakes, or explosions from regions that have more earthquakes than explosions. Thus, we hypothesize that the autoregressive parameters may be as affected by the region in which the event occurred (or the propagation path), as by the source type. To test this theory, we tried using a classifier based on azimuth only, and found that it performed better than the AR-based classifier, and misclassified many of the same events.

We also performed a similar experiment to see if a neural network using the same AR parameters could distinguish mining explosions from other types of explosions. The results of this experiment are given in Tables 7 and 8.

Table 7. Explosion Identification at ARCESS

| SAIC label | neural net label | | |
|------------|------------------|-------|-------|
| | mining | other | total |
| mining | 129 | 4 | 133 |
| other | 10 | 10 | 20 |

Total percent correct: 91%

Table 8. Explosion Identification at NORESS

| SAIC label | neural net label | | |
|------------|------------------|-------|-------|
| | mining | other | total |
| mining | 114 | 4 | 118 |
| other | 11 | 12 | 23 |

Total percent correct: 89%

About half of the other explosions were incorrectly labeled as mining explosions. Unfortunately, we cannot really be sure the network is incorrect. The events identified by SAIC were usually labeled as mining explosions only if they were located at a known mine site. Thus, many of the explosions labeled "other explosion" may in fact be explosions from as-yet-unknown mines.

As before, we examined the events misclassified by the neural net to see if they are typically from regions where most of the events are of the other type. In this experiment, this was true for some of the events but there were also regions that had both types of explosions equally often. However, once again, a classifier based on azimuth alone out-performed the AR-based classifier.

We have concluded from these experiments that our current autoregressive model is not very powerful by itself in distinguishing source characteristics (as opposed to characteristics of signals coming from a particular region). It may still be useful when combined with other discriminants. Higher-order autoregressive or autoregressive-moving-average (ARMA) models may work better, since they capture more details of the spectra shape. Also, since the spectral shape changes significantly from one phase to the next, it may make more sense to compute phase-specific AR parameters rather than one set of event-wide parameters.

3 CONCLUSIONS AND RECOMMENDATIONS

Simple neural networks have been developed that improve upon the single-station phase-labeling performance of the current IMS expert system. The networks were integrated into an experimental IMS and performance scored. By every measure, the system with the networks gave superior

performance, but not by as much as was initially hoped. One reason is that the network-level expert system in IMS undoes some of the correct decisions made by the neural network. Also, the network-level expert system does not take advantage of the confidence measures provided by the neural network for its phase labels. Consideration should be given to modifying the expert system to use the confidence measures. This might be one way to avoid having it change single-station phase labels that are correct.

Phase-labeling experiments with other types of classifiers show no significant improvement over a single-layer perceptron.

Continued experiments with autoregressive parameters have not produced very encouraging results and suggest that the classification may be based on a combination of path and source differences. Strong conclusions are difficult to draw because of uncertainty in the ground truth information.

References

- [1] Carpenter, G. A., Grossberg, S., and Reynolds, J. H. "ARTMAP: Supervised Real-Time Learning and Classification of Nonstationary Data by a Self-Organizing Neural Network" *Neural Networks*, Vol. 4, pp. 565-588, (1991).
- [2] Carpenter, G., Grossberg, S., Markuzon, N., Reynolds, J. H., and Rosen, D. B. "Fuzzy ARTMAP: A Neural Network Architecture for Incremental Supervised Learning of Analog Multidimensional Maps" Boston University Technical Report, Boston, New York, (1991).
- [3] Duda, R. O., and Hart, P. E. *Pattern Classification and Scene Analysis*. John Wiley and Sons, New York, (1973).
- [4] Hart, P. E., "The Condensed Nearest Neighbor Rule," *IEEE Transactions on Information Theory*, Vol IT-14, No. 3, pp. 515-516, (May 1968).
- [5] Lacos, R. T., S. R. Curtis, R. K. Cunningham, and M. Seibert, "Seismic Phase and Event Labeling Using Artificial Neural Networks", Proceedings of the 13th Annual PL/DARPA Seismic Research Symposium, 8- 10 Oct. 1991, Phillips Laboratory report PL-TR-91-2208. ADA241325
- [6] Ng, K., "A Comparative Study of the Practical Characteristics of Neural Network and Conventional Pattern Classifiers," Master's thesis, Massachusetts Institute of Technology, Department of Electrical Engineering and Computer Science, Cambridge, MA, (May 1990).
- [7] Patrick, E. A. and Fischer, F. P. III, "A Generalized k-Nearest Neighbor Rule", *Information and Control*, V 16:2, pp. 128-152, (April 1970).
- [8] Reilly, D. L., Cooper, L. N., and Elbaum, C., "A neural model for category learning", *Biological Cybernetics*, Vol 45, pp. 35-41, (1982).
- [9] Rumelhart, D. E., Hinton, G. E. and Williams, R. J., Learning internal representations by error propagation. In Rumelhart, D. E. and McClelland, J. L., editors, *Parallel Distributed Processing*, Volume 1: Foundations, chapter 8. MIT Press, Cambridge, MA (1987).

Lg Propagation in Eurasia

Thorne Lay, Xiao-bi Xie and Tianrun Zhang
University of California, Santa Cruz

Contract No. F29601-91-K-DB21

Objective:

The Lg phase plays a critical role in the monitoring of underground nuclear testing and non-proliferation treaties. On specific paths various amplitude measures of the Lg phase, such as $m_b(Lg)$ and $RMS(Lg)$ give very precise measures of relative explosion yield, provided that relative yield calibration (e.g. the $RMS(Lg).vs.log(Yield)$ slope) is available. Absolute yield estimation further requires a determination of the intercept value. Lg spectral measures also play a role in many proposed regional discriminants, such as Pn/Lg ratios. Since a complete understanding of the excitation and propagation effects of Lg is not presently in hand, it is not yet possible to proceed to direct yield estimation or reliable discrimination using the Lg phase. We address one of many unexplained characteristics of the Lg phase, which is that despite the remarkable stability in its relative scaling, there are often variations in scaling slope between paths. We examine this problem with a combined observational and theoretical approach, to attain an improved understanding of how multi-station measurements of Lg should be incorporated in yield estimation and discrimination procedures.

Research Accomplished:

Systematic variations in Lg-yield scaling are observed between some paths, as shown for Kazakhstan explosions recorded at regional and upper mantle distance stations in Figure 1 (Ringdal, 1990). It is not clear how the highly precise nature of the measurements can be preserved in the presence of the large relative amplitude variations. Procedures which estimate separate source, path and receiver terms from suites of events and stations will be contaminated by these variations, unless they are accounted for by either a distant dependent measurement effect or by a systematic (burial depth, or source volume) source effect. Under this contract we will seek to isolate the source and propagation effects causing this behavior.

The first year of effort has involved two thrusts. The first, now largely completed, was to implement various techniques for calculating accurate regional distance seismograms. The second thrust involved consideration of the historic data digitized by DARPA to provide further empirical understanding of Lg. In our computational effort we have initially focussed on one-dimensional and two-dimensional algorithms, as these provide sufficient flexibility to explore many aspects of Lg propagation. With an eye toward eventually performing more realistic three-dimensional calculations we are separately developing several new synthesis techniques in collaboration with Ru-Shan Wu. Figure 2 shows a comparison of regional distance synthetics generated by three different methods. The structure is laterally homogeneous, with a 32 km thick layer over a half space. The source is at 8 km depth, and involves an explosion plus CLVD source, which exercises the full moment tensor excitation. For distances less than 200 km the 2D finite difference method of Xie and Yao (1988) is used for both layered and laterally varying models. The synthetics for this model are in close agreement with those of a reflectivity program, based on Yao and Harkrider (1983). Comparisons are also shown between reflectivity and the normal mode program of Herrmann (1985). The latter program has been the most extensively used in the first year, since it is best suited to computing Lg over long propagation paths.

Synthetic seismograms computed with the mode code are shown in Figure 3, for explosion and spall (Barker et al., 1990) sources buried at depths from 0.2 to 1.0 km. The structure used is the 'standard' model of Figure 4, which is adapted from a receiver function model for East-Kazakh from Priestley (1988). The synthetics are shown in the passband 0.5-3.0 Hz, over which most Lg

measurements have been made (e.g. Israelsson, 1992). The spall model is essentially an explosion plus CLVD source, or extensional crack. For simplicity in these initial calculations, we have simplified the source time function by treating it as the derivative of a Gaussian source, rather than a more physical system of opening and closing phases. The explosion and spall synthetics show many characteristics in common with previous calculations, with relative enrichment of the overtone energy for the CLVD component of the spall source (e.g. Barker et al., 1990). We see little variation in the signals over the narrow source depth range considered. The primary issue related to source depth will involve whether the variation in frequency content of Lg with source depth varies substantially from one structure to the next. One-dimensional synthetics are sufficient to address an issue such as this because the propagation effects are intrinsically held constant over the suite of sources. We are currently exploring this behavior.

The influence of different propagation structures on the Lg phase can also be assessed with one-dimensional models, and then combined with varying source characteristics to try to explain observations like those in Figure 1. Figure 4 shows mode synthetics for four different velocity structures, involving perturbations of the standard model. The perturbations involved removing the shallow low velocity layer, removing a mid-crustal low velocity layer, and introducing thin layer lamination in the deep crust. The synthetics are shown in two different passbands of 0.3-3.0 Hz and 1.0-4.5 Hz. Both passbands show appreciable differences in the excitation of Lg and Rg phases, as well as the partitioning of energy in the Lg window. Despite the time-domain differences in appearance, calculation of the RMS Lg amplitudes for each of the models shows relatively subtle variations with distance. The 0.3-3.0 Hz band shows the more variable behavior, as indicated by the crossing of the curves as a function of distance. If these subtle differences can be augmented by yield or depth dependent source characteristics we may be able to explain some of the observations. However, the higher frequency band of 1.0-4.5 Hz shows surprisingly little variation with distance, despite the differences in the interference apparent in Figure 4. We have only begun to explore these issues, but the synthetic approach appears to be useful.

To assess whether the RMS Lg measurement procedure is itself responsible for the trends in Figure 1 we have been analyzing the DARPA-digitized data set of historic Soviet recordings of explosions. These data have been extensively analyzed by Israelsson (1992), who has shown that for the most part, the data from these stations are actually very well explained by a simple model of geometric spreading and anelastic decay. We are further analyzing the data with both sonogram and RMS determinations in various frequency bands, to gain insight into the stability of these data. Clearly the examples in Figure 1 still require explanation.

Conclusions and Recommendations:

This effort is now fully underway, with all of the initial analytical tools and data sets now in place. Our immediate focus will be to explore combinations of source and path effects to assess how strong the variations in RMS Lg can become within the context of these one-dimensional models. As efficient three-dimensional capabilities come on-line we will explore more realistic characterizations of the crustal waveguide, to assess whether scattering properties can explain the variable yield-scaling behavior as well as gross differences in crustal structure. We will continue the data analysis as well, expecting to confirm Israelsson's findings of the stability of Lg for the Soviet data, but then pulling it apart in more detail in different frequency bands to gain insight into the Lg phase. We will then consider the observations from some of the more variable paths like those to the CDSN stations shown in Figure 1.

Barker, T. G., S. M. Day, K. L. McLaughlin, B. Shkoller, and J. L. Stevens, 1990. An analysis of the effects of spall on regional and teleseismic waveforms using two-dimensional numerical modeling of underground explosions, Air Force Geophysics Laboratory Report, GL-TR-90-0126. ADA226921

Herrmann, R. B. (editor), 1985. Computer programs in seismology, Vol. 3, St. Louis University.

Israelsson, H., 1992. RMS Lg magnitudes and path corrections for U.S.S.R. explosions, Bull. Seism. Soc. Am., submitted.

- Priestley, K. F., 1988. Crustal structure in eastern Kazakh, U.S.S.R. from teleseismic receiver functions, *Geophys. Res. Lett.*, 613-616.
- Ringdal, F., 1990. NORSAR detection and yield estimation studies, Papers presented at 12th Annual DARPA/GL Seismic Research Symposium, Geophysics Laboratory, Hanscom AFB, MA 01731-5000, pp. 145-151. GL-TR-90-0212, ADA226635
- Yao, Z. X., and D. G. Harkrider, 1983. A generalized reflection-transmission coefficient matrix and discrete wavenumber method for synthetic seismograms, *Bull. Seism. Soc. Am.*, 73, 1685-1699.
- Xie, X. B., and Z. X. Yao, 1988. P-SV wave responses for a point source in two-dimensional heterogeneous media: finite-difference method, *Chinese J. Geophys.*, 31, 473-493.

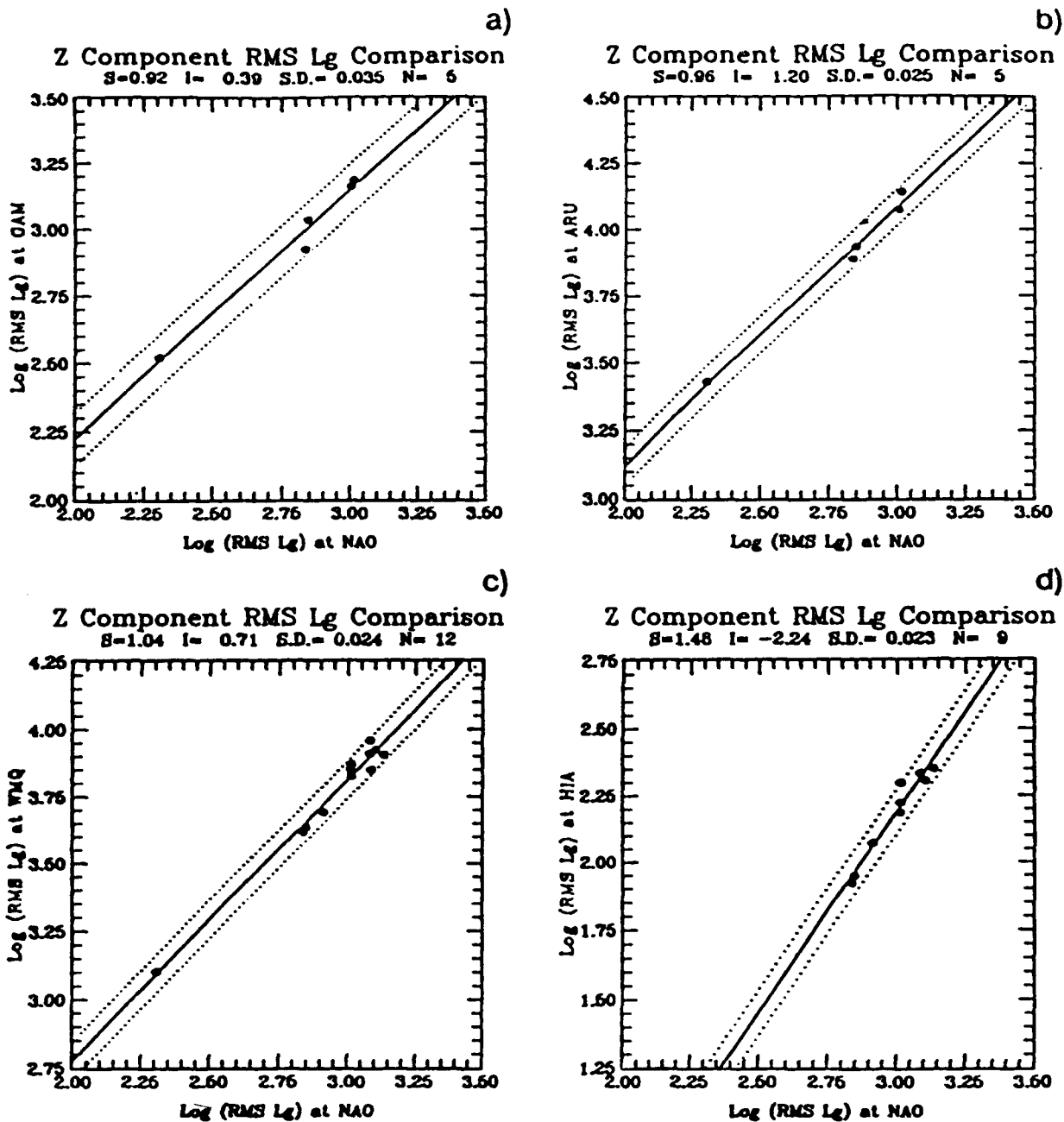
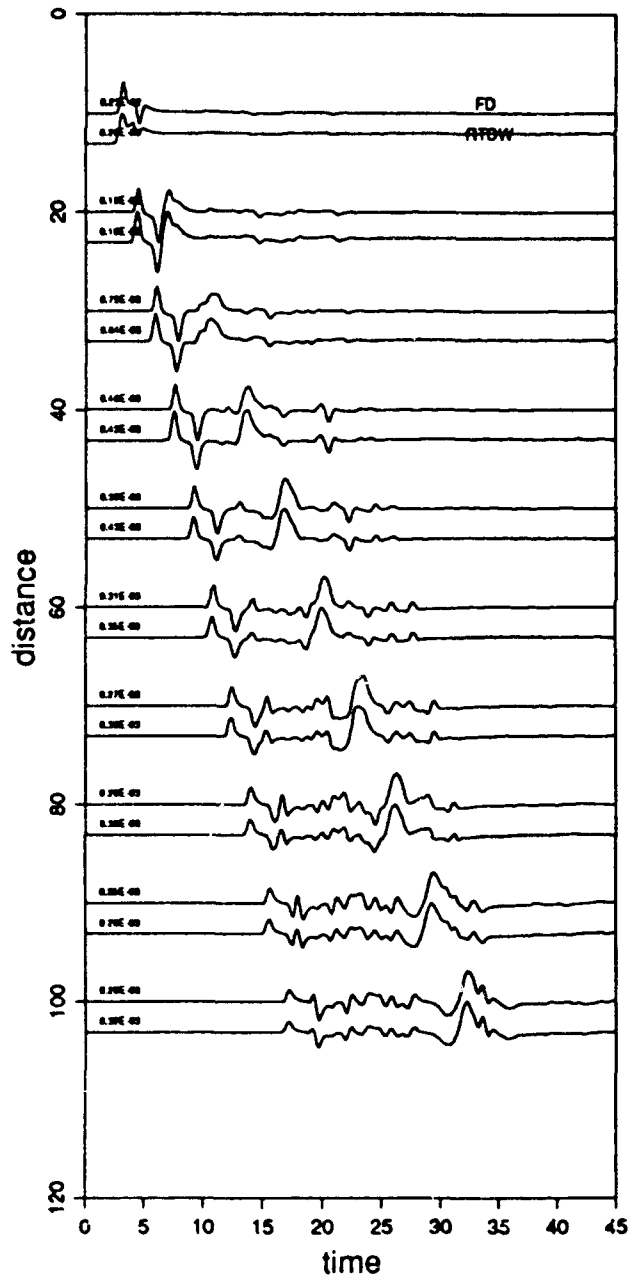


Figure 1. Comparison of RMS Lg scaling for several Shagan River explosions at IRIS, CDSN and NORSAR stations. Note the variability in relative amplitude scaling despite the remarkably high precision of the Lg variations. Our objective is to understand the path dependent Lg scaling behavior, to improve our ability to combine Lg measurements from various paths in yield estimation and discrimination procedures.

FD vs. Reflectivity



Reflectivity vs. Mode

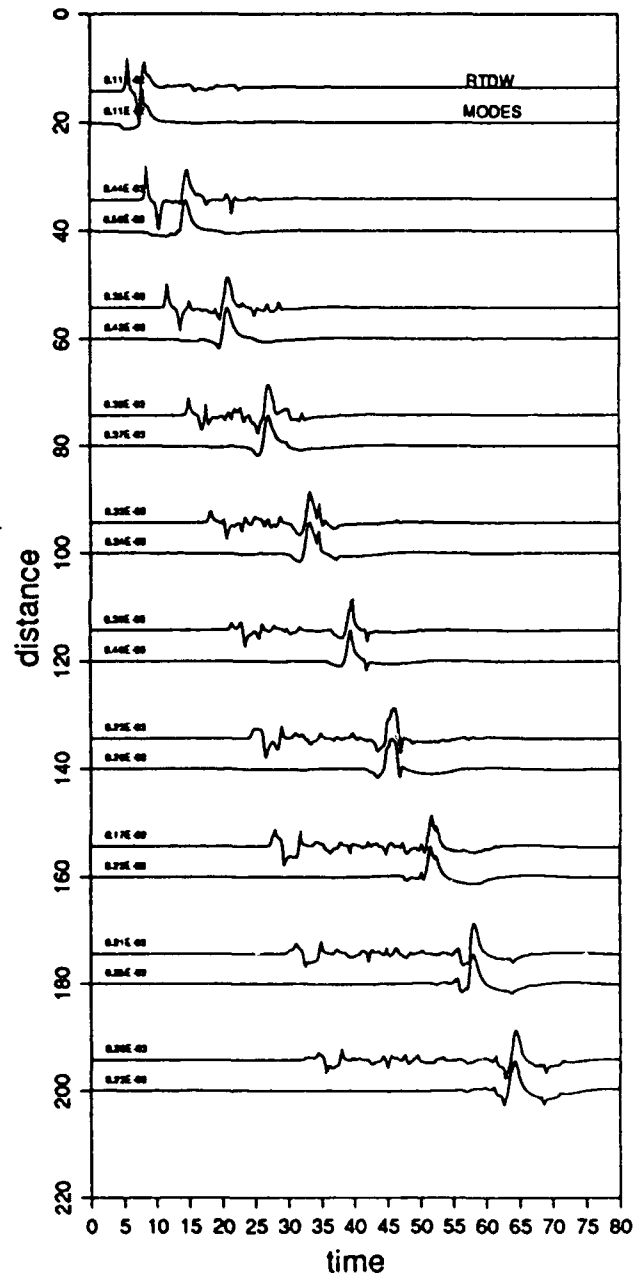


Figure 2. Comparison of regional distance synthetic seismograms for laterally homogeneous structures. The velocity model is a 32 km thick crustal layer over a half space. The source is a spall source (CLVD+explosion) at a depth of 8 km. The left panel shows 2D finite difference (FD) versus reflectivity (RTDW) calculations, and the right panel shows reflectivity versus modes method of Hermann (1985). Exploring the excitation of Lg in various crustal models for varying source depth and combination of explosion plus spall is part of this research effort.

Explosion

Spall

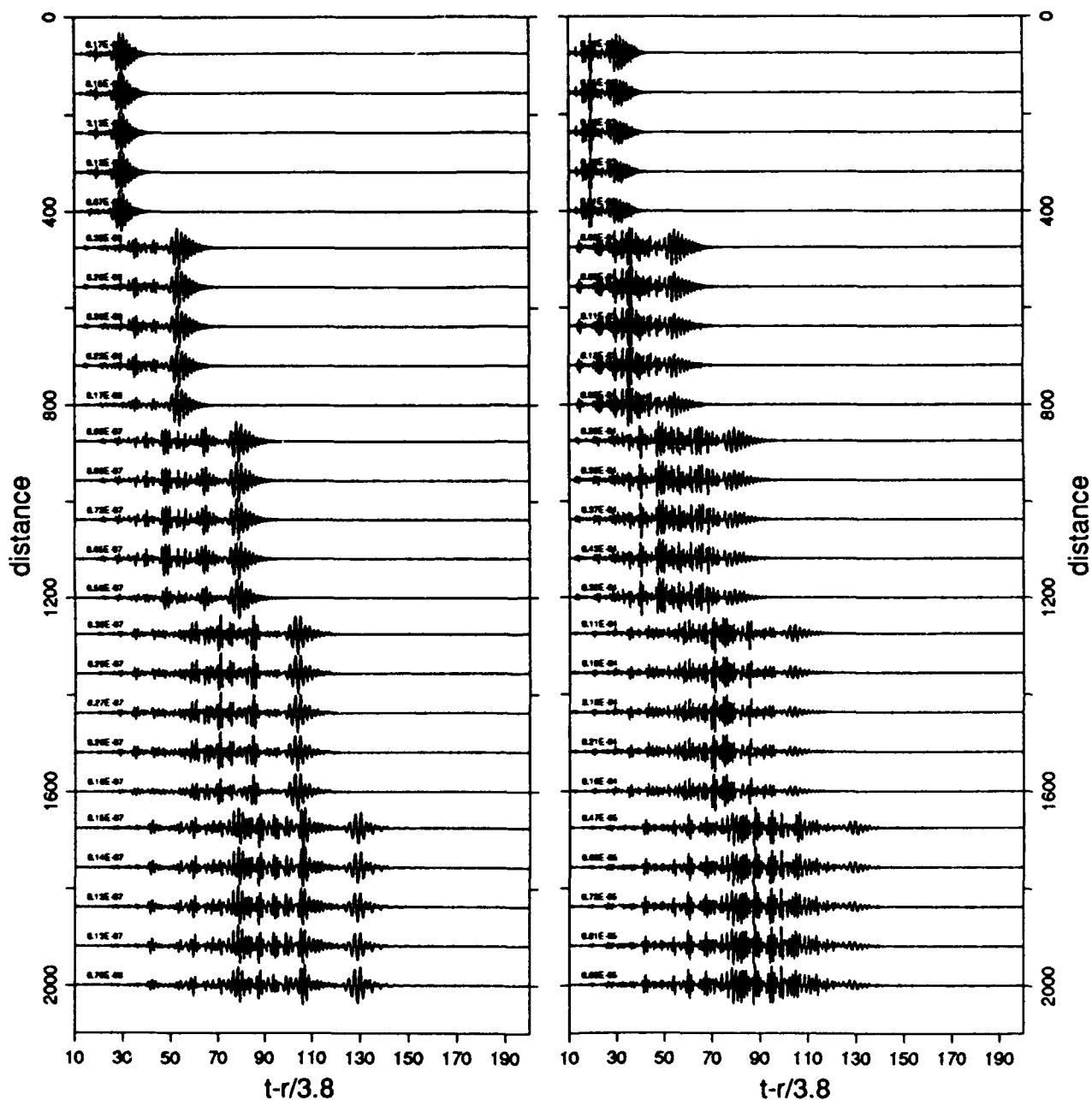


Figure 3. Mode-generated synthetic seismograms at 400 km distance intervals for source depths of 0.2, 0.4, 0.6, 0.8, and 1.0 km. The seismograms are bandpass filtered between 0.5 and 3.0 Hz. Explosion synthetics are shown on the left, with a Gaussian wavelet being used as a source function. Synthetics for a model of spall (CLVD+explosion) with a Gaussian derivative wavelet are shown on the right. The structure is the standard model shown in Figure 4. Very modest variations as a function of burial depth are observed, and the CLVD component of the spall model, along with the more complex source time history preferentially excite the Lg energy.

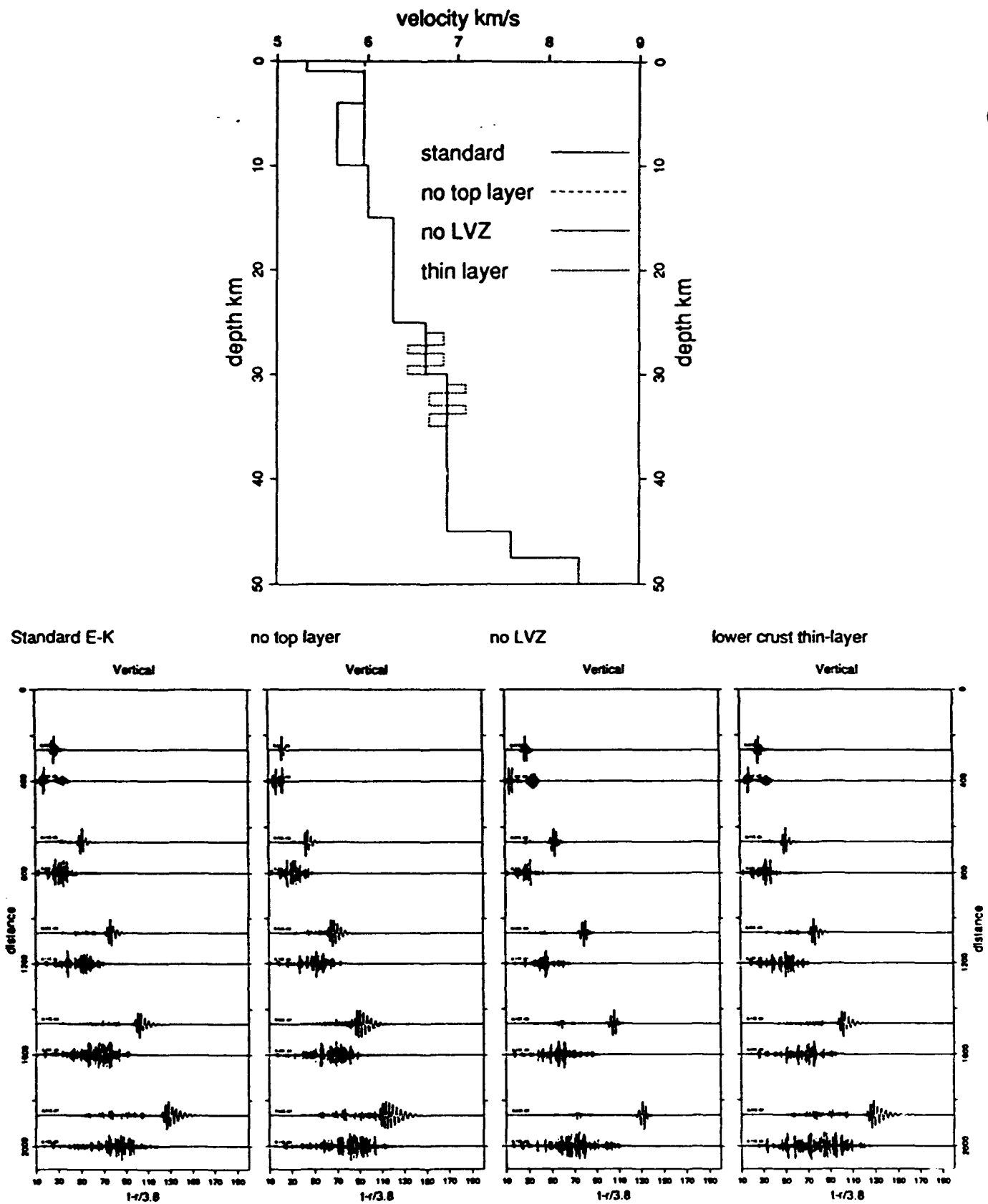


Figure 4. Top: several velocity models used in the preliminary modeling. The standard structure is that of Priestley (1988), determined by receiver function analysis. We explore the excitation and propagation of Lg in the various models below. Bottom: mode-generated synthetic seismograms for the 4 structures shown at the top at 400 km distance intervals. The synthetics at each distance are filtered into two passbands (0.3-3.0 Hz) and (1.0-4.5 Hz). The source is an explosion at 0.6 km depth, with a 0.2 sec triangular source time function.

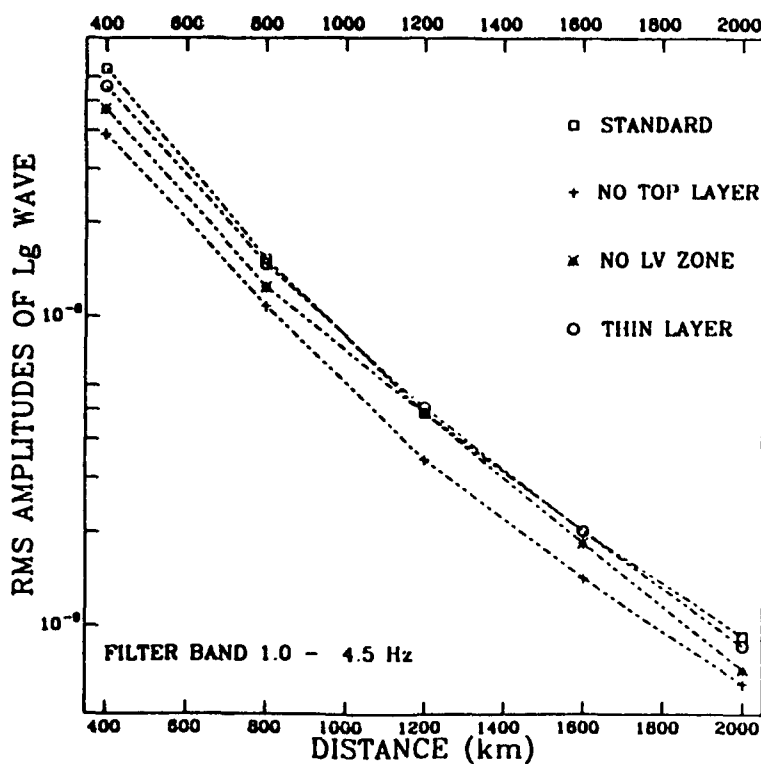
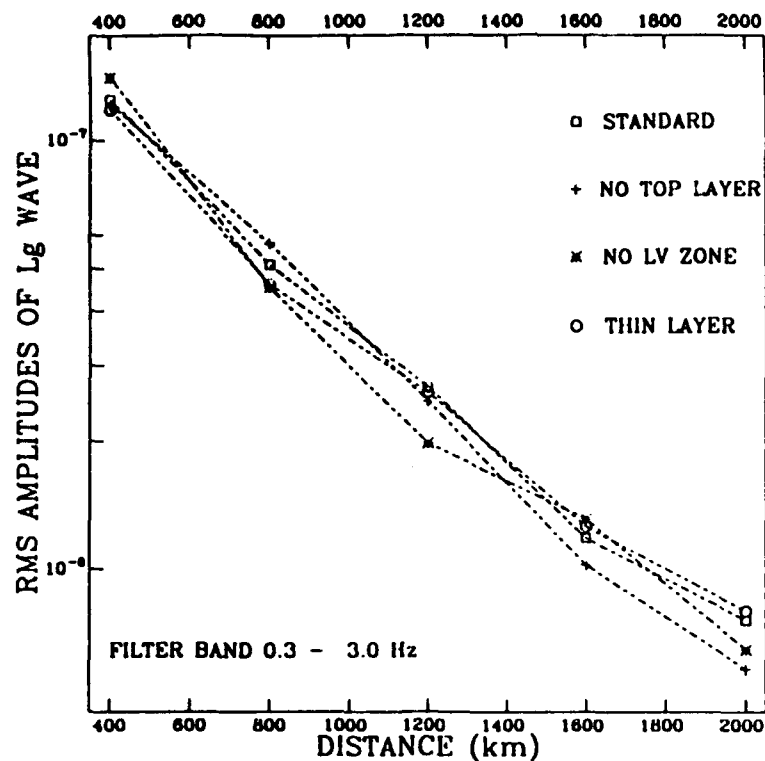


Figure 5. RMS L_g amplitudes measured from the synthetic seismograms in Figure 4 for 4 different structures. The RMS calculations were for the 3.1-3.7 km/s group velocity window in the indicated filter bands. There are small systematic differences as a function of distance which indicate the structural effects. Further analysis for various source depths and explosion/spall source combinations will be conducted in order to understand the patterns in Figure 1.

Finite Difference Modeling of Scattering by a Minimal Grid Technique

S.A. Magnier, J.B. Minster and J.A. Orcutt
Institute of Geophysics and Planetary Physics
Scripps Institution of Oceanography, La Jolla, CA. 92093-0225

Contract Number: F29601-91-K-DB13

1 Objective

An important aspect of understanding wave propagation through the Earth's crust is the deployment of effort into controlling forward modeling techniques. It is obvious that to compare real data obtained from artificial or natural sources with synthetic data we need to have excellent modeling routines in which the physical properties of the Earth may be input and their effects understood. It was within that perspective that a new finite difference algorithm was developed. Although finite differences encounter strong opponents due to the generally cited high cost of computation, its validity in complete wavefield computation needs not be demonstrated. Numerous wave propagation algorithms exist (Fisk, Charette and MacCortor, 1991, Mora, 1990, Mora and Rodrigues, 1990, Tal Ezer et al., 1987). In strongly heterogeneous media such as scattering media the method most commonly used is the finite difference technique which provides knowledge on the entire wavefield. The aim of this work is to show that new finite difference techniques may provide better controlled solutions to the wave propagation problem in full elastic media (Magnier, 1992 and Magnier et al., 1992). The question of high computing cost will not be raised as the development that follows was done on a massively parallel super computer (32 K processor CM-2 of Thinking Machines) so that time does not enter computation considerations. This supercomputer is owned by the Institut de Physique du Globe de Paris where this work was first developed. Although, the examples that will be presented result from 2D computation on the CM-2, the 3D application is straightforward and transport to other machines is in progress. The work presented here covers the theoretical development of the technique. The modeling of highly heterogeneous media and surface scattering effects is straightforward and remains one of the objectives for the future.

2 Research Accomplished

One of our aims in redefining the finite difference approximation is to use fewer points in the calculation than are classically required. To achieve this we will define a minimal second order discretization. A Cartesian discretization requires $2N$ (Aki and Richards, 1980) points to define a set of first derivatives, while the minimal technique will only use $N + 1$ points where N is the number of dimensions of the problem. This should generate different stability

properties for the numerical method (Bamberger et al. 1980). Most finite difference schemes in elastic media use staggered grids (Virieux, 1986) and the scheme presented here is based on those ideas.

The principle of the method is as follows: Given the point where the gradient of a function is to be computed, let us center a simplex around that point, project it in the appropriate space domain, and retroproject the coordinate points of this simplex onto the original function, hence defining a secant application. This procedure is illustrated in figure 1.

Once the secant is defined, the slopes of this linear application are easily computed. These slopes will be the minimal grid finite difference approximation to the gradient of the function. As grid spacing tends to zero, then obviously, the linear secant mapping tends to the tangent mapping which is the gradient of the function.

In order to emphasize the differences between this technique and classical finite difference methods, the classical scheme is also illustrated in figure 1 for a 2D problem. To compute the slopes of the function by these centered finite difference schemes $2N$ points are required.

Clearly, the medium may be discretized according to simplexes and since only $N + 1$ points are needed to compute the gradient instead of $2N$ as in classical schemes, then this may be called a minimal grid.

The method is applied for the full elastic wave equation which may be decomposed in a series of simple steps requiring computations of first derivatives only. The algorithmic steps and a typical 2D grid are schematically represented in figure 2.

Characteristics of the grid

The grid introduced is a 2D mesh composed of equilateral triangles. It is clearly staggered and will thus allow the modeling of various interfaces including the liquid-solid transition. One of its major characteristics is that all elastic parameters are input at the same spatial positions thus avoiding any disconnected solutions for isotropic media hence reducing memory waste. This is illustrated by figure 3. Obviously any elastic medium may be simulated including anisotropic or highly heterogeneous media. Free surface conditions are easily implemented and absorbing boundaries may be included.

Numerical results

In order to test the accuracy of the method, a comparison is presented between a solution obtained using a 2D minimal grid algorithm and an analytical solution computed by Virieux (1986) and Noble(1992) for an infinite acoustic homogeneous medium of constant velocity (see figure 4). The numerical solution converges very clearly to the analytical solution. Other tests with analytical solutions have been done and validate this method (see Magnier, 1992).

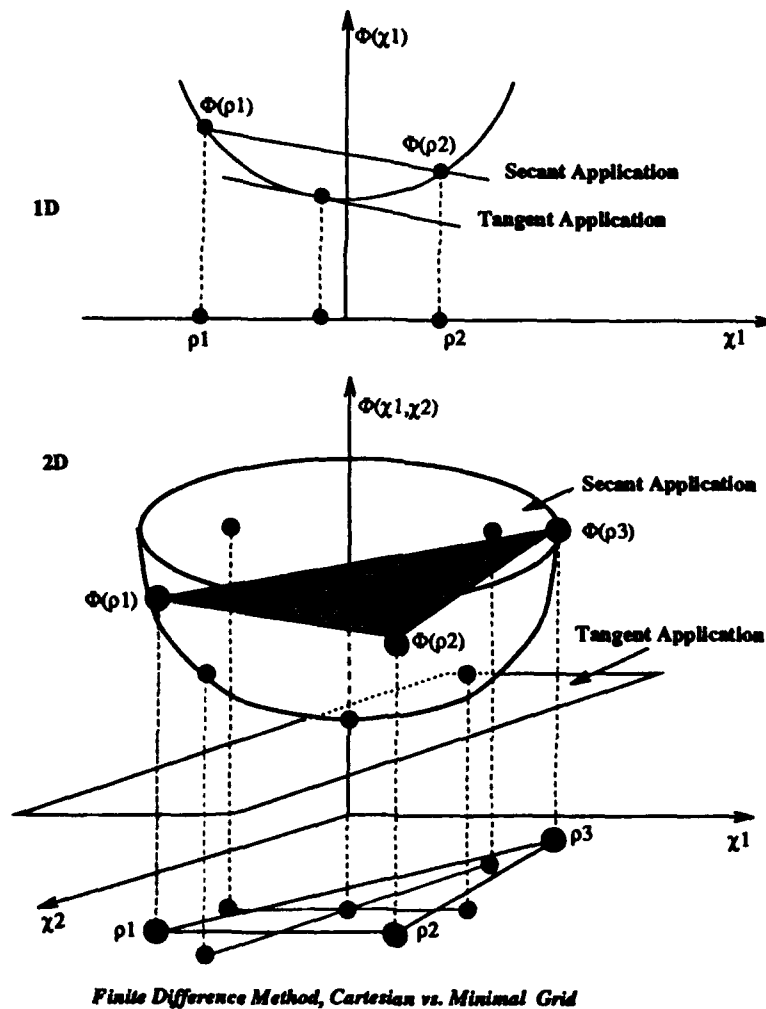
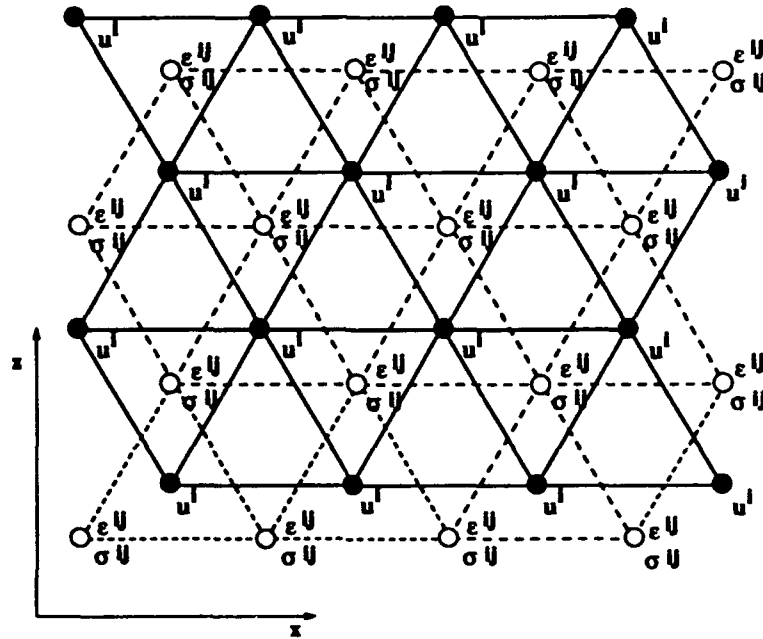


Figure 1: (From Magnier et al. 1992) The principle of defining the gradient of a function to be the slopes of the secant application to that function is illustrated in the 1D and 2D problem. Given the point where the gradient is wanted surround it by a simplex (segment in 1D and triangle in 2D), the points forming the simplex may then be retroprojected onto the function and clearly define the secant application to the function. In the 2D case the classical finite method is also illustrated whereby the point where the gradient is wanted is surrounded along all dimensions of the problem by 2 points for a second order scheme (black dots). This then gives 4 points on the original function (i.e. $2N$) and not 3 (i.e. $N+1$).



2D MINIMAL GRID

Figure 2: (From Magnier, 1992) 2D minimal grid for central finite differences. At an instant of time, the displacements, accelerations and mass densities are known at the positions represented by black dots. Strains, stresses and the elastic parameters are known at the positions represented by white dots. The centered finite differences are computed at the center of the equilateral triangles. The computational grids are staggered as shown by the continuous and broken lines. A white circle is surrounded by three black circles and vice-versa so that the center of a triangle becomes a node in the staggered grid. Then, a function and its first spatial derivatives are not known at the same node.

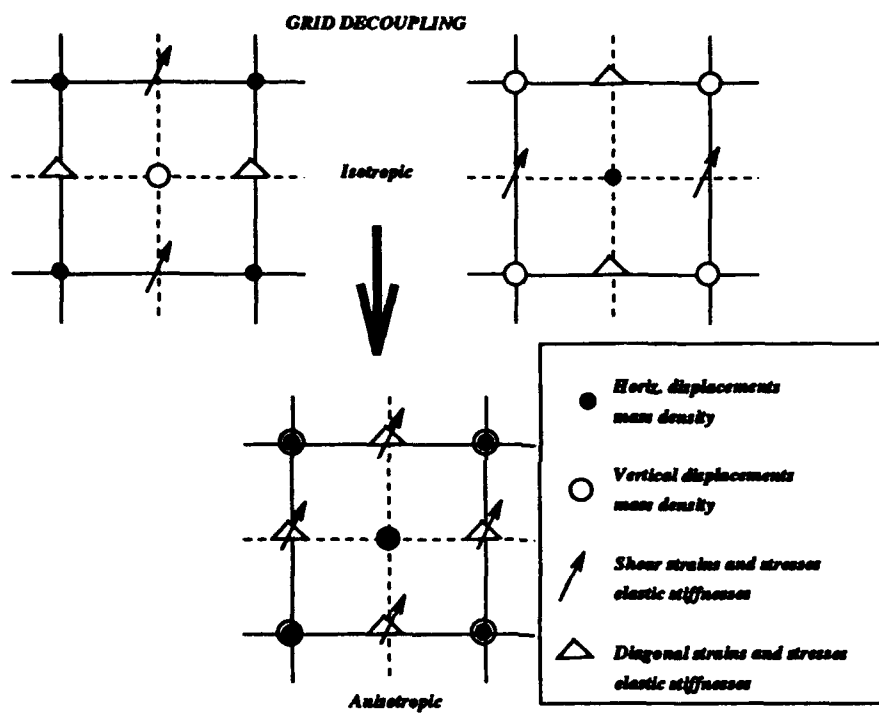


Figure 3: (From Magnier, 1992) Grid splitting in a homogeneous isotropic medium when using Cartesian staggered grids

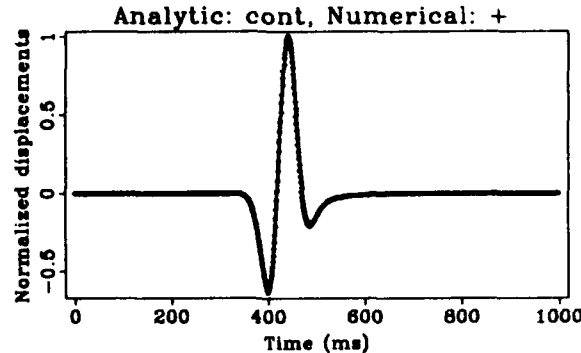


Figure 4: (From Magnier, 1992) Comparison between an analytical solution and the 2D minimal grid finite difference solution. The computation is done for an infinite homogeneous acoustic medium with a constant velocity of 2000 m/s. The source is a Ricker wavelet with a central frequency of 10 Hz. The recording geophone is 500 m away from the source. The analytical solution is plotted in a solid line while the numerical solution is plotted with crosses. Obviously, the numerical solution converges to the analytical solution.

3 Conclusions and recommendations

It has been shown with the numerical example previously given that this method is valid and gives precise results. Series of tests have been run which emphasize that modeling of complex media is possible (Magnier, 1992, Magnier et al. 1992) and give results which are as accurate as other finite difference techniques. In some cases the additional axis of symmetry of this new method constrains the numerical solution and provides a better method of calculation (Virieux and Madariaga, 1982). The domain to which this method should be applied is the modeling of scattering media (Aki, 1969) in order to see if fine effects may be detected and compared with real data sets obtained in Pinyon Flat, CA. (Vernon 1989, Vernon et al. 1991). One of the ultimate goals of data processing is to obtain images of the subsurface to be compared with synthetic data (Crase, 1989). If with processing algorithms (Hedlin et al, 1991) we can image surface scatterers then we will have the basis of comparison with a modeling routine.

4 References

- Aki, K., Analysis of the seismic coda of local earthquakes as scattered waves, *J. Geophys. Res.*, **74**, pp.615-631, 1969.
- Aki, K., Richards, P.G., *Quantitative Seismology, Theory and Methods, volumes I et II*, W.H. Freeman and Company, 1980.

- Bamberger, A., Chavent, G., Lailly, P., Etude de schémas numériques pour les équations de l'élastodynamique linéaire, *INRIA, Rapports de Recherche N° 41*, 1980.
- Crase, E., *Robust elastic nonlinear inversion of seismic waveform data*, Ph.D Thesis, University of Houston, 1989.
- Fisk, M.D., Charette, E.E., and McCartor, G.D., A comparison of phase screen and finite difference calculations for elastic waves in random media, *J. Geophys. Res.*, **96**, 1991.
- Hedlin, M., Minster, J.B., and Orcutt, J.A., Beam-stack imaging of crustal scatterers, *Geophys. Res. Lett.*, **18**, 1771-1774, 1991.
- Magnier, S. A., *Différences finies sur des grilles minimales et étude géothermique du Rift d'Asal*, Ph.D. Thesis Université Paris 7, 1992.
- Magnier, S. A., Tarantola, A. and Mora, P., Finite differences on minimal grids, *Submitted to Geophysics*, 1992.
- Mora, P., Modelling waves in the Earth, *The Seismic Simulation Project*, Tech. Rep. 1, *Inst. de Phys. du Globe de Paris*, 1990.
- Noble, M. S., *Ph.D Thesis Paris VII*, 1992.
- Tal Ezer, H., Kosloff, D., and Koren, Z., An accurate scheme for seismic forward modelling, *Geophysical Prospecting*, **35**, pp. 479-490, 1987.
- Rodrigues, D., and Mora, P., Analysis of a finite differences solution to the three dimensional elastic wave propagation, *The Seismic Simulation Project*, Tech. Rep. 2, *Inst. de Phys. du Globe de Paris*, 1991. Internal report, 1991.
- Vernon III, F.L., *Analysis of data recorded on the ANZA seismic network*, Ph. D. Thesis, U.C. San Diego, 1989.
- Vernon III, F.L., Fletcher, J., Haar, L., Chave, A., and Sembera, E., Coherence of seismic body waves from local events as recorded by a small aperture array, *J. Geophys. Res.*, **96**, 11981-11996, 1991.
- Virieux, J., PSV wave propagation in heterogeneous media velocity stress finite difference method, *Geophysics*, **51**, pp.889-901, 1986.
- Virieux, J. and Madariaga, R., Dynamic faulting studied by a finite difference method, *Bulletin of the Seismological Society of America*, **72**, 345-369, 1982.

The Receiver Structure Beneath the Chinese Digital Seismograph Network (CDSN) Stations: Preliminary Results

S. Mangino and J. Ebel
Department of Geology and Geophysics
Boston College Weston Observatory
381 Concord Road
Weston, MA 02193

Contract F19628-91-K-0009

Objective

Determination of the seismic velocity structure near the source, along the path and beneath the seismograph station has important applications for monitoring existing nuclear weapon treaties and detection of clandestine testing. Accurate knowledge of Earth structure at the station can be an important factor in refining yield estimates of nuclear explosions (Hanson et al. 1990). Accurate source locations require a detailed knowledge of the seismic velocity structure of the earth, something which is not well known in potential areas where clandestine testing could take place (Blandford, 1982). Some of the variability in amplitude and waveshape measurements of the body waves (typically the P waves) from underground nuclear explosions are due to scattering and body-wave conversions beneath the receiving stations (e.g. Bannister, 1990).

This study provides preliminary model estimates of the crust and upper mantle velocity structure in China beneath the Chinese Digital Seismograph Network. The one-dimensional models are derived from receiver functions obtained from teleseismic data recorded at each station. Individual models are used to investigate the effects of the receiver structure on regional waveforms recorded at each station.

Research Accomplished

In this report we describe the response and present preliminary models of the seismic velocity structure beneath five China Digital Seismograph Network (CDSN) stations. Operated by the State Seismological Bureau Peoples Republic of China in cooperation with the Albuquerque Seismological Laboratory US Geological Survey, the CDSN stations record high quality broadband digital data. In this report we examine the 20 sps BB/BH STS-1 data band (Peterson *and others*—Kexin *and others*, 1987). The CDSN represents 12% (as of March 26, 1992) of all stations consistently providing data to the Global Digital Seismic Network. Across mainland China from east to west shown in Figure 1 are CDSN stations: Mudanjiang, Heilongjiang province (MDJ); Hailar, Neimenggu Province (HIA); Beijing, Baijatan (BJI); Kunming, Yunnan Province (KMI); Lanzhou, Gansu Province (LZH); and Urumqi, Xinjiang Province (WMQ).

We present preliminary inversion results of the receiver structure for each CDSN station using the procedure given in Ammon et al. (1990). Over 100 receiver functions are examined from the CDSN network-day tapes. For a rigorous description of time domain teleseismic P-waveform inversion and on receiver functions in general, refer to Ammon et al. (1990); Owens et al. (1988); Langston (1979). In practice, once an initial model of the crust and upper mantle is obtained from previous work or forward modeling, we run a set of receiver function inversions with a range of smoothness values in order to minimize both model roughness and RMS error between the model synthetic and the data. With the pseudo-monte-carlo technique (Ammon et al. 1990), the initial model is randomly perturbed into 24 different starting models by adding a random cubic polynomial function as well as a random component for each layer. This allows a larger range of starting models to test the sensitivity of solution models on the initial model. A

total of 48 starting models are inverted, and all model synthetics that do not fit the most coherent arrivals within the variance of the stacked data are discarded.

Of primary concern is the contamination of a radial receiver function with waves generated by the interaction of the P-wavefield and lateral velocity variations. Differences between stacked azimuthal clusters may be attributed in part to variations in the local structure as a function of azimuth and in part by contamination with off-azimuth arrivals. The amount of scattering is represented by the observed motion on the tangential receiver function. Unlike interactive trial-and-error modeling the inversion scheme is unable to qualitatively judge the importance of a given arrival in a receiver function. Mangino et al. (1992) demonstrate a pitfall in interpretation of a receiver function inversion in the presence of significant scattering. To avoid potentially biased inversion results from small scale (relative to wavelength) heterogeneities we initially analyze CDSN data up to about 0.4 Hz. Longer period data tend to smooth over the effects of small scale crustal heterogeneities, so we should expect to obtain simpler and potentially less biased solution models.

Our goal here is to determine model estimates of the receiver structure by forcing *only the most prominent phases* in the synthetic receiver functions to be within the ± 1 standard deviation bounds obtained from the variance of the true amplitude stacked data. Current modeling efforts focus on relaxing the smoothness constraint, shifting layer thickness and upper mantle velocity in order to fit the smaller amplitude arrivals in the data. However, in some cases the lower amplitude arrivals on the radial component are close to the energy level present on the tangential component. Therefore, we stress that caution must be used whenever matching such energy solely with P to S conversions generated within the vertical-radial plane. For those stations where the tangential response is small the initial model solutions should provide a good 1-D estimate of the velocity structure beneath the station.

Beijing, BJI

Station BJI is located in the Sino-Korean block in the northern end of the Jizhong Depression approximately 20 km north of Beijing. Shown in Figure 2 are preliminary model results for station BJI. The starting model was estimated from previous refraction models near the station. In general the crust west of station BJI appears relatively simple in structure. The upper 6 km is characterized by a strong positive gradient. Between 10 to 33 km depth the average crustal P wave velocity is 6 km/s, and a small low velocity zone is present at about 15 km depth. Between 33-39 km depth a strong positive gradient is present, and the top of the upper mantle is at 39 km depth.

Kunming, KMI

Station KMI is located along the southwestern edge of the Yangtze or South China Block in the southern Yunnan province. Shown in Figure 2 are preliminary model estimates for KMI. No models have been selected based on synthetics that fit the data within one standard deviation. The starting model was estimated from previous refraction models near the station. The wide range of solution models at KMI is not surprising given the variability of the radial receiver function and the large tangential energy as a function of azimuth.

Lanzhou, LZH

Station LZH is located on the northeastern margin of the Tibetan Plateau along the Qinling fold belt in the Gansu Province. Shown in Figure 2 are preliminary model estimates for LZH. The synthetics are strongly dependent on changes in the near-surface velocity. Model synthetics from a high velocity shallow crust fall on and above the upper resolution bound, while synthetics from lower velocity shallow crustal models fall on and below the lower resolution bound. Shown in Figure 3 spanning 45° great circle arc are all LZH-SE radial and tangential receiver functions. Differences within each data bin suggest a difference in crustal structure. As the ray parameter decreases the radial response approaches the energy level on the tangential response.

The amplitude fall off of the 5-7s pulse and moveout of the pulse between 13-14s (inset) are consistent with a conversion from a common interface beneath LZH.

Hailar, HIA

Station HIA is the northern most CDSN station located on the Sino-Korean Block in the Neimenggu Province outside Hailar City adjacent to the Hailar River. Preliminary results for station HIA are shown in Figure 2. The model synthetics provide an excellent fit to the data. The starting model was estimated from surface wave estimates near HIA. The upper-crust has a shallow jump in velocity followed by a negative gradient to ~7.5 km depth. The mid-crust has a relatively constant velocity of ~6.0 km/sec to a depth of 28 km, and overlies a transitional crust-mantle boundary between 30-37 km depth. The top of the upper mantle is at 37-38 km depth. Shown in Figure 3 are all HIA-SE stacks. The strong similarity of the radial response in each bin indicates the crustal structure is similar over the azimuthal range sampled. The decreasing overall amplitude and the moveout of the PpP_{ms} Moho multiple as a function of epicentral distance is clearly present. Moveout of the P-S multiple from a common interface can provide additional constraint to the velocity structure beneath HIA.

Urumqui, WMQ

Station WMQ is located between the Junggar and Tarim Basin along the eastern Tien Shan of the Xinjiang Province. Shown in Figure 2 are preliminary results at station WMQ for data arriving from northwest of the station. The upper crust shows a strong positive gradient to about 6-8 km depth. The absence of a prominent converted phases from the Moho results in a smoothly varying velocity structure with increasing depth.

Azimuthal variation in response for all stacks about the station indicates a laterally varying velocity structure beneath the station. Close examination of the radial response reveals an offset of the direct arrival for all azimuths. This observation coupled with a significant variation in polarity within the initial 0-4s of the tangential response suggest the presence of a dipping structure beneath WMQ. Owens and Crosson (1988) show that the time lag of the direct arrival on the radial response is related to a Ps conversion from a dipping structure, provided that velocity increases with depth. A Ps conversion traveling up-dip has the largest delay because of a longer travel path through a slower medium. Langston (1977) shows that the initial motion on the tangential response is reversed across a line parallel to the dip direction.

Shown in Figure 4 are the observed time-lags measured from all stable WMQ radial receiver functions. A consistent pattern with an average delay of 0.8s is clearly present between 310°—15°. Figure 4 also shows the tangential response about WMQ. Arrows indicate the backazimuths we can constrain a line parallel to the dip direction. The time delays of the direct arrival and the polarity reversals are consistent with a north-northwest dipping structure beneath this station. The effects of this feature are most likely diverting converted shear wave energy out of the vertical-radial plane and therefore could lead to biased inversion results.

Implications for Monitoring

The source-receiver distances between the JVE2 and the CDSN are: WMQ - 950 km; LZH - 2530 km; HIA - 2926 km; BJI - 3106 km; and KMI - 3432 km. The effects of the crust and upper mantle structure beneath these stations on the waveforms from this event are explored in Figure 5. Synthetics were computed by taking the Mueller-Murphy source pulse shape for a 118 kt explosion in granite and convolving it with the STS-1 instrument response and the vertical and radial responses computed from an average model determined in this study for each station. These synthetics are quite simple. They do not include important upper mantle triplications which must be present in most of the seismograms, nor do they include free surface reflections (pP), spall, source structure or tectonic release. Their purpose is to document how much variability in the P waveforms can be expected due to differences in the receiver structure found

beneath each station. Figure 5 shows the same major effects documented by Bannister et al. (1990) in P-wave observations at NORESS. Motion on the radial component are much more affected by the receiver structure than the vertical component. However, even for the vertical component, the width of the second peak for the P wave (the so-called "c" peak) varies from station to station. Furthermore, the relative amplitude of the "c" peak to the first (or "a") peak differs somewhat among the stations for the vertical P component. The radial ground motion show variations among the width of the "c" peaks as well as in the waveforms about 5 seconds after the P-wave. The latter, hints of which may be observed in the data, reflect differences in the crustal structure.

Conclusions

Receiver function modeling of the CDSN has revealed new information on the seismic velocity structure of the crust and upper-mantle beneath each station. The preliminary velocity estimates can be used to model wave propagation from earthquake and nuclear explosion sources in Eurasia. Preliminary modeling of the Soviet JVE explosion data recorded by the CDSN has revealed some differences in the recorded waveforms which can be explained by the receiver structure at the recording station. The most significant receiver effects documented in this report are due to P to S conversions within the shallow crust, at the crust-mantle boundary, and due to dipping structures.

Acknowledgements

We would like to thank C. Ammon and G. Zandt for providing the inversion codes used in this report. We also thank K. Priestley for help with the JVE2 source time function, and R. Woodward for help with extracting data from the network-day tape archive.

References

- Ammon, C.J., G.E. Randall, and G. Zandt, On the resolution and non-uniqueness of receiver function inversions, J. Geophys. Res. v 95, 15303-15318, 1990.
- Bannister, S.C., E.S. Husebye, and B.O. Ruud, Teleseismic P coda analyzed by three-component and array techniques: deterministic location of topographic P-to-Rg scattering near the NORESS array, Bull. Seism. Soc. Am., 80, 1969-1986, 1990.
- Blandford, R.R., Seismic event discrimination, Bull. Seism. Soc. Am., 72, S69-S87, 1982.
- Gilder, S.A., G.R. Keller, M. Luo and P.C. Goodell, Timing and spatial distribution of rifting in China, Tectonophysics, 197, p 225-243, 1991.
- Hansen, R.A., F. Ringdal and P.G. Richards, The stability of RMS Lg measurements and their potential for accurate estimation of the yields of Soviet underground nuclear explosions, Bull. Seism. Soc. Am., 80, 2106-2126, 1990.
- Hsu, K.J., L. Jiliang, C. Haihong, W. Qingchen, S. Shu, and A.M.C. Sengor, Tectonics of South China: Key to understanding West Pacific geology, Tectonophysics, 183, p 9-39, 1990.
- Langston, C.A., The effect of planar dipping structure on source and receiver responses for constant ray parameter, Bull. Seismol. Soc. Am., V. 67, 713-724, 1977a.
- Langston, C.A., Structure under Mount Rainier, Washington, inferred from teleseismic body waves, J. Geophys. Res. 84, 4749-4762, 1979.
- Mangino, S.G., G. Zandt, and C.J. Ammon, The crustal structure beneath MNV, Mina Nevada, submitted January 1992.
- Owens, T.J., and R. S. Crosson, Shallow Structure effects on Broadband Teleseismic P Waveforms, Bull. Seismol. Soc. Am. 78, 96-108, 1988b.
- Owens, T.J., C. Zandt, and S.R. Taylor, Crustal structure at regional seismic test network stations determined from inversion of broadband teleseismic P waveforms, Bull. Seismol. Soc. Am. 77, 631-662, 1987.
- Peterson J., and others—Kexin, Q., and others, The China Digital Seismograph Network, A joint report by the Institute of Geophysics, State Seismological Bureau and the Albuquerque Seismological Laboratory, U.S. Geological Survey; 91 pp, 1987.

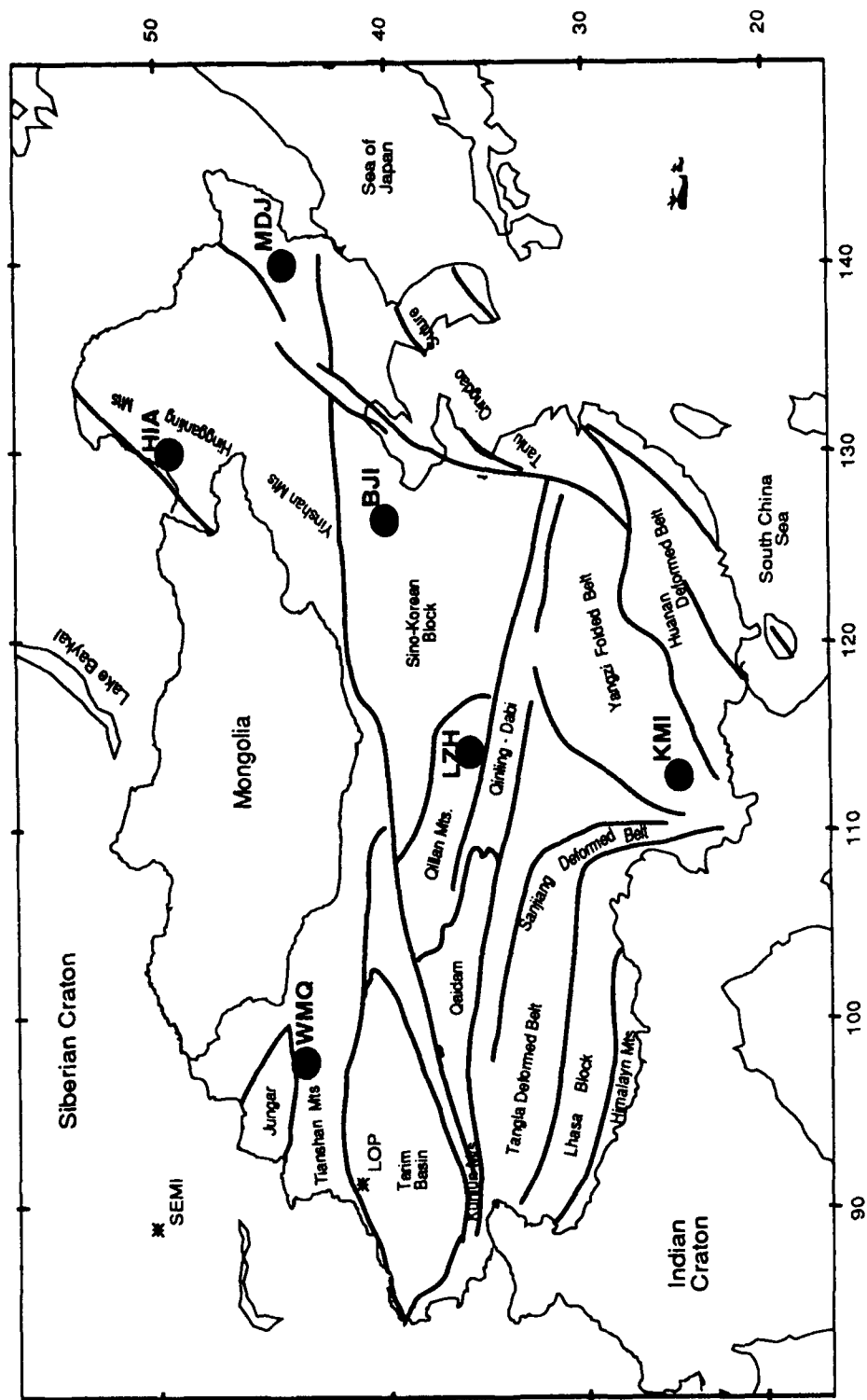


Figure 1. Mercator projection of mainland China with the most prominent physiographic features and CDSN station locations. From east to west the stations are: Mudanjiang (MDJ), Hailar (HIA), Beijing (BJI), Kunming (KMI), Lanzhou (LZH), and Urumqi (WMQ). Figure compiled from Gilder et al. (1991) and Hsu et al. (1990).

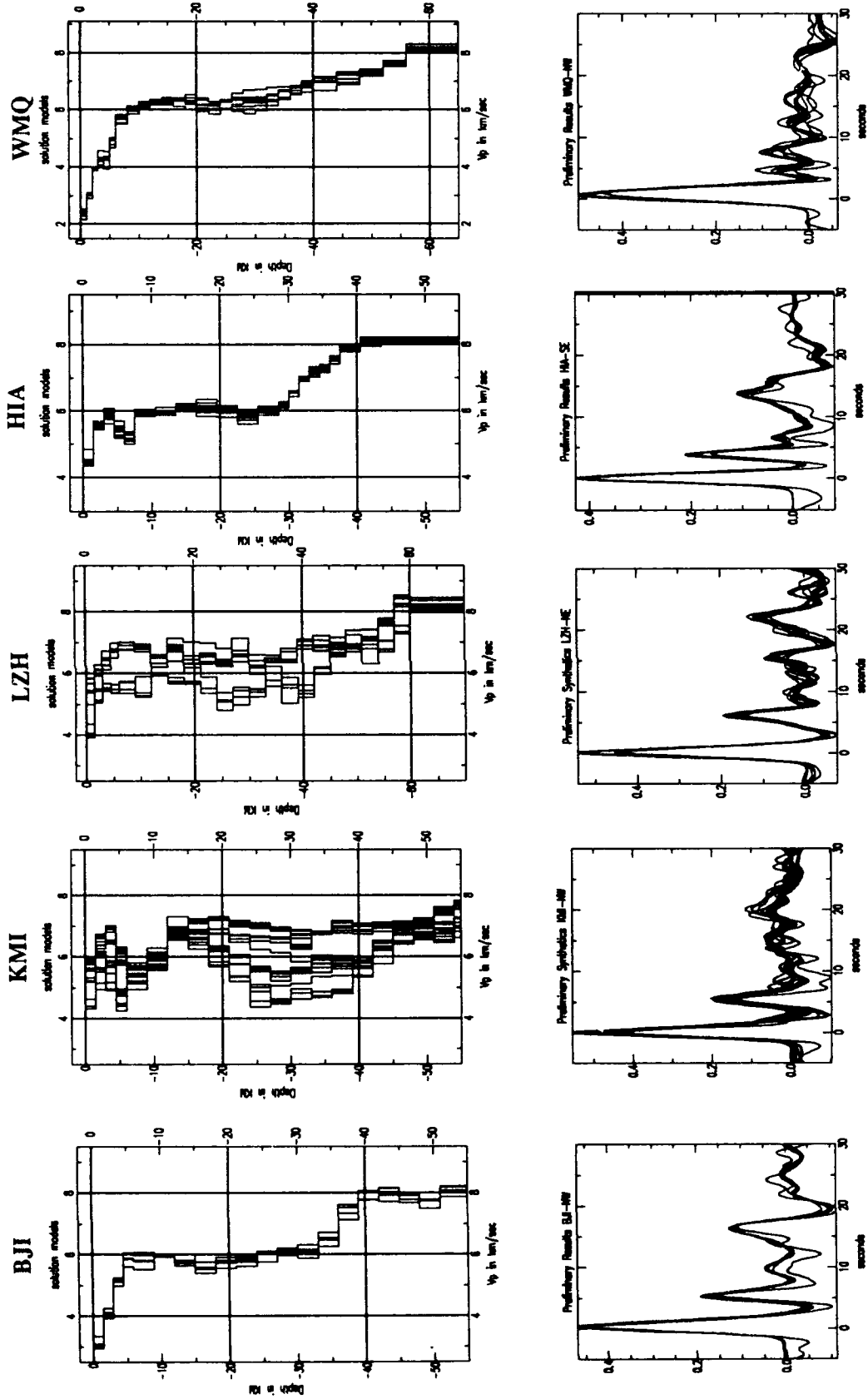


Figure 2. Preliminary modeling results for the CDSN stations and synthetic waveform fit to the stacked data.

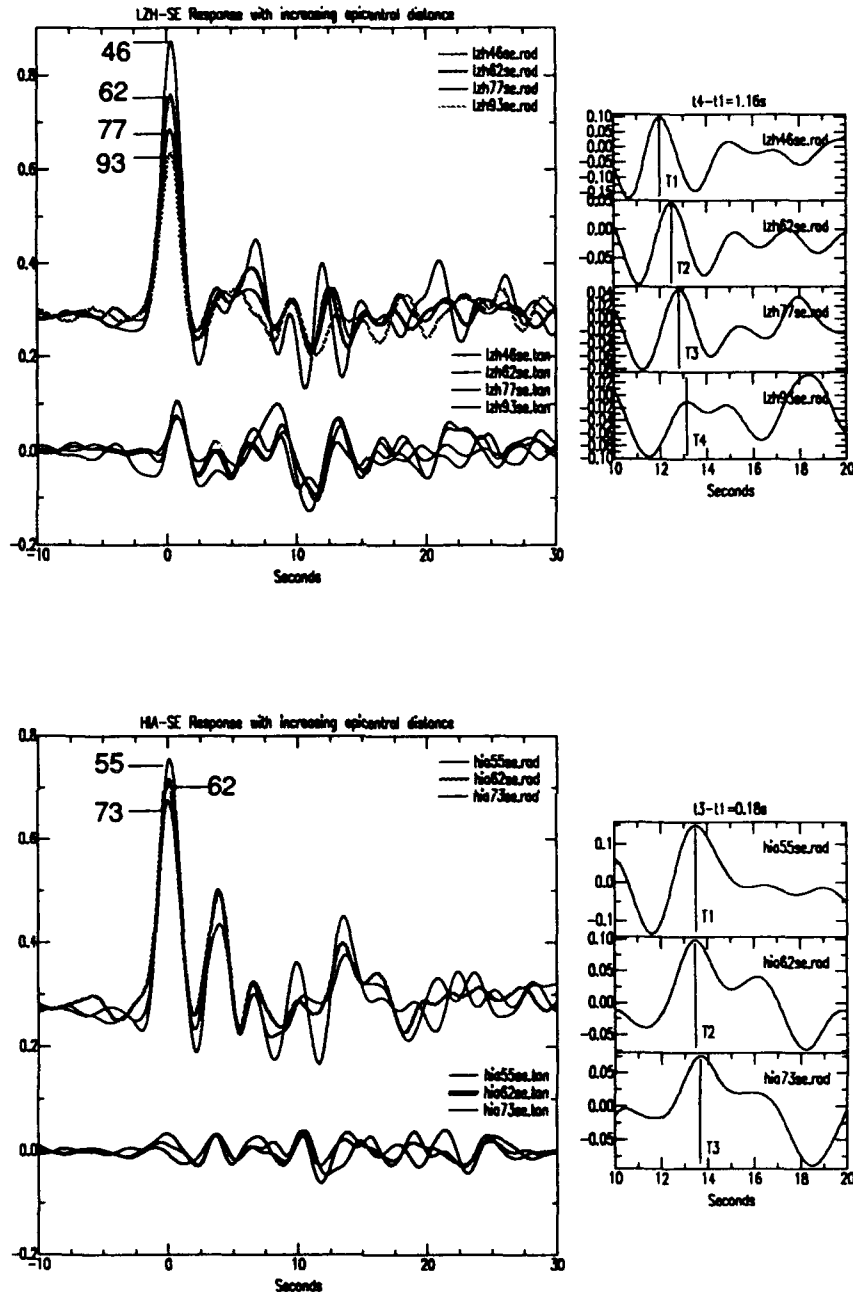


Figure 3. LZH-SE (top) and HIA-SE (bottom) radial vs tangential stacked receiver functions. The receiver structure at HIA is laterally consistent over the 45° azimuth sampled by the three stacks, while differences in the response suggest a more complex receiver structure over the 40° azimuth of sampling at LZH. Consistent in both figures is the moveout of a PpPmS Moho multiple between 12-14 seconds.

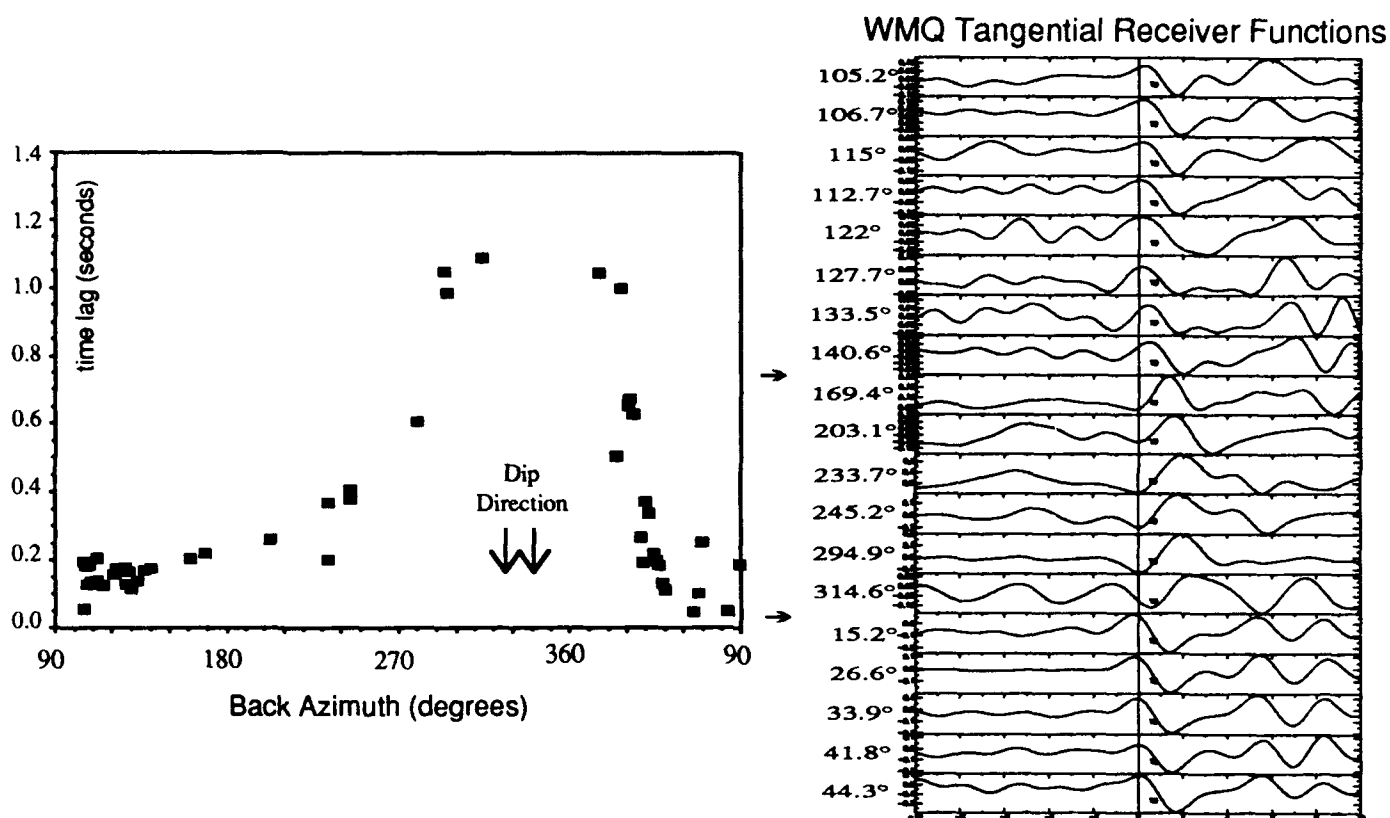


Figure 4. Shown above (left) are the time lags for all first arrivals of WMQ radial receiver functions. The time delay as a function of azimuth suggests a structure dipping toward the NW of the station. Shown at right is the distribution of tangential receiver functions about WMQ. Polarity reversals occur along a line parallel to the dip direction (Langston, 1977) as indicated by arrows and consistent with the time lag observations.

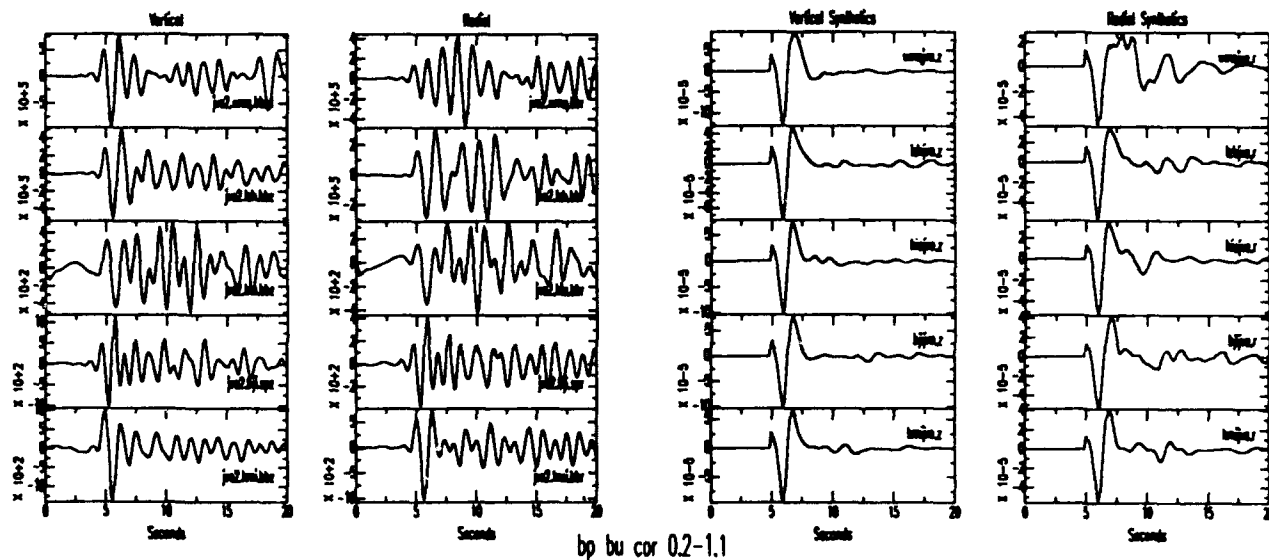


Figure 5. Shown at left are the vertical and radial component JVE2 data as recorded across the CDSN. Shown at right are synthetic seismograms from an average model for each station convolved with an appropriate JVE2 source time function and STS-1 instrument response to estimate the site effects at each station.

**TITLE: Geology of the Chinese Nuclear Test Site
Near Lop Nor, Xinjiang Province, China**

AUTHOR AND AFFILIATION: R. Matzko (*U.S. Geological Survey, Reston, VA 22092*)

CONTRACT: ARPA Order No. 5672

OBJECTIVE:

The collection, documentation and presentation of these data is undertaken to arrive at an understanding of the geology and physical properties of the Chinese nuclear test site as part of a larger, continuing effort to investigate the physical environment at underground nuclear test sites worldwide. This paper presents the currently available geologic, geophysical, and geohydrologic data on part of the Chinese test site, that is of interest to groups involved with monitoring and verification of nuclear tests through seismic methods.

RESEARCH ACCOMPLISHED:

Geology

The presumed Chinese nuclear test site (see Figure 1) is located in an intermontane basin and surrounding hills. The basin has a thin cover of unconsolidated material, (probably sand, silt and clay), a few meters thick; outcrops of hard rock also occur. The terrain is slightly uplifted and hilly. The hard rock consists of Devonian (360-390 million years) metamorphosed conglomerate and sandstone and Carboniferous (290-360 million years) granite. A geologic map of the site, published in the Chinese literature (Che, 1987), is shown in Figure 2. The lithologic units depicted on this map permit new geologic interpretations of Landsat and SPOT imagery of the area. The two Chinese-supplied test locations on the map (Explosions I and II, carried out in vertical shafts) help to locate this map on the satellite imagery. The structure in the region of the map is folded and faulted, with at least some fractures aligned to the northeast and northwest. Two high-angle faults, referred to by the Chinese as "pressure fractures," run east-west through the area and are identified as F2 and F3 on the geologic map. The nature and origin of these fractures is not addressed in the Chinese data. Small scale, short axis fold structures occur between these two fractures and X-shaped joints are common in the region. Table 1 presents a list of 15 presumed underground nuclear tests at the Chinese test site, occurring between 1969 and 1992.

Although Che (1987) does not specify the dates of Explosions I and II, reasonable estimates can be made through the process of elimination, focusing on those events that occurred prior to 1987, and which did not occur in the mountains. This procedure yields a date of 6 Oct. 1983 for Explosion I (if this one occurred first), and a date of 3 Oct. 1984 for Explosion II. Two other possible dates are 13 Sept. 1979 and 5 October 1982; however, no locations are available for these two events. Explosion I was reportedly carried out at a depth of 280 m, in Carboniferous granite (Che, 1987). Granite from a vertical shaft in the test area (presumably the same granite body in which Explosion I occurred) is described by Zhao (1986) as a "black mica" plagioclase granite, dark gray in color, with a fine crystal texture. The mineral composition consists of 60 percent feldspar, 27 percent quartz, 10 percent biotite, and minor white mica and pyrite. Explosion II was carried out at a depth greater than 200 m in metamorphosed sandstone of Upper Devonian age. Steel casing was reported to have been used in the shaft for this test, probably to protect the hole against excessive inflow of groundwater, or from caving and slumping of weak, loose material from the drill hole wall. Another geologic unit on the map in Figure 2 is "metamorphic rock" (D2a), of Middle Devonian age, which is described as sandstone and quartzite from a hydrologic observation well located in this unit, about 4 km south of Explosion I.

The geologic environment of a tunnel test site is described by Zhao (1986) as a black mica granite, light grayish-red in color, with large crystals and porphyritic texture. The constituent minerals are feldspar, 60 percent, and quartz, 30 percent; plus biotite, amphibole, and pyrite. The location of this site is not further identified, however, possible tunnel sites are suggested by plotting twelve events from Table 1 onto the topographic map in Figure 3 (the 4 May 1983 event plots beyond the limits of the figure).

Physical Properties

The Moho occurs at a depth of about 46 km in this area. The Pn velocity is estimated to average about 8.1 km/sec. The lithosphere in the Tarim continental block, which encompasses the test site, is 100 km thick (Ma, 1987). While no data have yet been found specifically addressing a low velocity zone (LVZ) in the area of the eastern Tien Shan Mountains or the test site, some references do mention the occurrence of LVZs elsewhere in China. Crustal discontinuities are indicated in North China (112° to 122° E, 36° to 42° N), at depths of 12 to 14 km beneath mountain ranges and 11 to 12 km beneath thick sediments (about 4 to 6 km below these discontinuities the velocity decreases by 0.1 to 0.2 km/sec). Low velocity layers are also indicated in the upper mantle of the Eastern China platform (Wu and Yu, 1987; Ma, 1988). In comparison, no low velocity zones are presently known under the Soviet test sites, but one does exist under the US test site in Nevada. Although the Tien Shan mountains are seismically and tectonically active, no recent volcanic activity in the area surrounding the test site has been noted in the geologic literature. Quaternary volcanism is known about 650 km to the southwest, along a portion of the major, seismically active Altun Tagh fault belt (Zheng, 1991). Northward-dipping thrust faults are typical of the southeastern Tien Shan area, although fault-plane solutions for some recent earthquakes in the area show a component of strike slip. The Kuruktag fault, which occurs near the southern margin of the Kuruktag mountains, is a large, right-lateral, strike-slip fault (Tapponnier and Molnar, 1979).

Some pre- and post-test physical properties of a biotite-plagioclase granite from a single vertical shaft are presented and compared in Table 2 (after Chu, 1986). In addition, two porosity values are given for the rock in this test area; 0.85 to 2.80 percent for the sandstone, and 0.80 to 2.60 percent for the granite (the porosity values of the granite described in a horizontal test area are probably similar). Although fractures in the granite are acknowledged, there are no values given for fracture porosity or fracture density and spacing. As seen in Table 2, the longitudinal wave velocities (v_p) of granite in a vertical shaft range from 4.1 km/sec near the surface (probably reduced by fracturing and weathering), to 5.3 km/sec at a depth of around 200 to 260 m. Apparent fracturing in the hole was indicated by acoustic logs at 130-150 m and 199 m depth. Corresponding compressive strengths range from 105 MPa near the surface to 178 MPa at about 200 to 260 m depth. The longitudinal velocity of undisturbed granite in a tunnel site is 5.2 km/sec, which is comparable to the pre-explosion average velocity of 4.7 km/sec for the granite at depth, in the vertical site (Chu, 1986).

Post-test investigations of the shaft characterized in Table 2 show that the stability of the granite rock mass was greatly reduced by the explosion. The post-test longitudinal wave velocity, above 60 m depth, was 20 percent lower than the pre-test wave velocity, while the wave velocity decrease was 43 percent in between 217 and 304 m depth. The "maximum boundary of influence" of the nuclear test emplaced in this shaft was 2.5 km from the (projected) center of the explosion. The maximum boundary of "severe" disturbance was about 200 m, and the maximum region of instability was 84 m from the projected explosion center. One of the conclusions reached in this test area is that degree and depth of post-test "spallation" of the land surface are related to the extent of the weathered layer, which reduces the tensile strength of the rock. Water leakage into this shaft was also a problem, even though the matrix porosity is low (0.8 to 2.6 percent for granite, as mentioned above). Although no pre-explosion physical properties data are given below

259 m, it is likely that the rock was weaker or more porous, due to fracturing and/or weathering between 242 and 279 m because steel casing was used to protect the shaft at that depth interval; below 279 m, cement was injected for protection in an apparent weaker zone, which would account for the low post-explosion velocity below 279 m. In comparing the pre and post-test data (Table 2), it is seen that as the longitudinal wave velocity decreases, the elastic and mechanical parameters of the rock also decrease.

A rock sampling program undertaken to determine the effect of a nuclear explosion on rock velocity indicated that the rock velocity gradually increases with increasing distance from the test emplacement point until it reaches the pre-explosion value beyond a certain distance (which is about $38 \text{ m/kt}^{1/3}$ in the case of the shaft studied in Table 2). Rock sampling for velocity studies was also conducted in a horizontal test area. As expected, the samples taken closer to the emplacement point were more fragmented than the samples taken from a greater distance. Near a horizontal emplacement tunnel, at a scaled distance of $16 \text{ m/kt}^{1/3}$ from the emplacement point, the longitudinal velocity (v_p) averages 4.4 km/sec, while beyond a scaled distance of $40 \text{ m/kt}^{1/3}$ from the emplacement point, the v_p is essentially unchanged from the pre-explosion value, averaging 5.2 km/sec. The difference between these two average values is about 15 percent.

Ground Water

In the area of Explosions I and II, data from hydrologic observation wells (Che, 1987), indicate that the depth to water ranges from about 3 m near the granite body, to a maximum of 34 m within the granite. The depth to water in the adjacent sandstone and conglomerate unit ranges from about 3 m nearer to the granite intrusion, to a maximum of 28 m in an observation well further west of the explosions. Due to this shallow water table, all events in this area are assumed to be emplaced below the water table. Because of the low porosity and permeability inherent in granite, excessive water inflow into holes drilled in this unit is not likely to be a problem, except in those areas where a drilled shaft may intersect a highly fractured or weathered zone. Che (1987) also describes two types of water-bearing zones in the area of Explosions I and II - a *fractured bedrock* water bearing zone, and a *fault or intrusive fracture* water bearing zone, both of which are under water table (unconfined) conditions. The ground water, which is replenished by snow melt to the southwest, flows generally N35° to 40° E, with a hydraulic slope of 0.9 to 2 percent. When the ground water encounters the east-west "pressurized" faults (labeled F2 and F3 on the geologic map in Figure 2) the water table rises and, in the low lying areas, can intersect the land surface to form springs. Shafts drilled within the *fractured bedrock* water bearing zone may see inflow rates of 100 cubic meters per day (a "small amount"), while those drilled within the water-bearing *fault or intrusive fracture* zone may see inflows of several hundred cubic meters per day. The ions contained in the ground water are primarily sulphate, sodium, and chlorine, with mineralization of 1 to 5 grams per liter. The mineralization increases from the southwest to the northeast.

Abrupt rises in the ground water level were recorded in two hydrologic observation wells during Explosion I, and six wells during Explosion II, at the zero-hour of the nuclear explosions. The water level rose quickly in the wells, then decreased more slowly. This abrupt rise may have been caused by elastic compression deformation of the aquifer due to the passage of the shock wave. Because the matrix porosity of the aquifer is low (0.85 to 2.80 percent in the sandstone; 0.80 to 2.60 percent in the granite), the water in the fractures was squeezed out and seen as a rise in the water level of the observation wells. As the pressure in the explosion cavity is disseminated quickly (within less than one minute), the rising water levels also drop quickly, probably due to filling of the collapsed cavity and the rubble chimney. The ground water table recovers slowly; observations indicate that re-establishing initial levels by regional ground water replenishment may require up to 280 days. This phenomenon of a rise in the water table, due to the expulsion of water during abrupt closure of fractures in a dense, low-porosity rock, may not be unique to the Chinese test sites.

CONCLUSIONS AND RECOMMENDATIONS:

Underground nuclear testing at the Chinese site near Lop Nor has occurred in Paleozoic-aged igneous rocks and metasediments. Testing has taken place both in vertical shafts and horizontal tunnels in granite; vertical shafts are also described in metasandstone and conglomerate. Tests conducted in the vertical shaft area are emplaced below the water table; casing is apparently used to protect the hole from weak or wet zones, when necessary. In at least one shaft in the vertical test area, the upper 50 m or so are weathered and fractured, and characterized by lower seismic velocities and tensile and shear strengths, than the intact rock. This weathered and fractured zone also appears to influence the degree and depth of spallation of the land surface after an explosion.

The geologic map and physical properties presented here are the first site-specific data made available by the Chinese for this test site. The map appears to precisely overlay remote sensing units discernable on Landsat MSS imagery, and can be the basis for future, detailed geologic mapping of the entire test site, based on Landsat and SPOT imagery. The small amount of vegetation cover, inherent in a desert climate, and the thin overburden make this a favorable area for mapping the bedrock geology through satellite imagery. Imagery analysis may also prove useful to more precisely locate the individual test sites, either through surface expressions of underground tests, or through surficial scars made during site preparations.

REFERENCES:

- Arora, S. K., and Basu, T. K., 1984 A source discrimination study of a Chinese seismic event of May 4, 1983, In: *Tectonophysics*, vol. 109, no. 3-4, Elsevier, Amsterdam, p. 241-251.
- Che, Yongtai, 1987, Response of ground water levels in wells to underground nuclear explosions, In: *Shuiwendizhi Gongchengdizhe (Hydrology and Engineering Geology)*, no. 4, p. 7-12.
- Chu, Yucheng, 1986, Observations of unstable rock mass under underground nuclear explosions, In: *Chengdu Baozha Yu Chongji (Explosions and Shockwaves)*, Vol. 6, No. 3, July, p. 261-267.
- Dahlman, O., and Israelson, H., 1977, *Monitoring underground nuclear explosions*, Elsevier, Amsterdam, 440 p.
- Defense Mapping Agency, 1983, Qinggir, China, scale 1:250,000, Series 1501, sheet NK 45-9, edition 2 (June).
- Fieldhouse, R. W., 1991, Chinese nuclear weapons: A current and historical overview, *Natural Resources Defense Council, Nuclear Weapons Databook, Working Papers*, Washington, D.C., p. 50-52.
- Gertz, B., 1992, Nuclear blast was test for new Chinese ICBM, *The Washington Times*, May 23.
- Ma, Xingyuan, (compiler), 1988, *Explanatory notes for the Lithospheric Dynamics Map of China and Adjacent Seas*, scale 1:4,000,000, Geological Publishing House, Beijing, China.
- National Defense Research Institute, 1978, Seismological recordings of nuclear explosions in 1976 obtained at the Hagfors Observatory in Sweden, *FOA Rapport C 20275-T1*, Nov. 1978, Stockholm, 71 p.
- National Defense Research Institute, 1981, Seismology 1980, Nuclear test ban verification, earthquake and earth resources investigations, *FOA Rapport C 20427-T1*, Oct. 1981, Stockholm, 68 p.
- National Earthquake Information Center, Preliminary Determination of Epicenters (PDE), 1973-1992, Monthly listing, U.S. Geological Survey, USGPO, Washington, D. C.
- Seiff, M., 1992, China explodes megaton bomb, *The Washington Times*, May 22.
- Tapponnier, P., and Molnar, P., 1979, Active faulting and Cenozoic tectonics of the Tien Shan, Mongolia, and Baykal regions, *Journal of Geophysical Research*, Vol 84, No. B7, AGU, p. 3425-3459.
- The Washington Times*, 1990, Nuclear blast detected in China, May 31.
- Wu, Gongjian, and Yu, Pan, 1987, Types of China's crusts and their geophysical characteristics, In: *International symposium on tectonic evolution and dynamics of continental lithosphere*, The third all-China conference on tectonics, Abstracts (II), Beijing, p. 157.
- Zhao, Wenrui, 1986, Effects of shock waves from underground nuclear explosions on sonic velocity of surrounding rock, In: *Chengdu Baozha Yu Chongji (Explosions and Shockwaves)*, vol. 6, no. 3, July, p. 267-270.
- Zheng, Jiandong, 1991, Significance of the Altun Tagh fault of China, In: *Episodes*, Vol. 14, No. 4, December, p. 307-312.

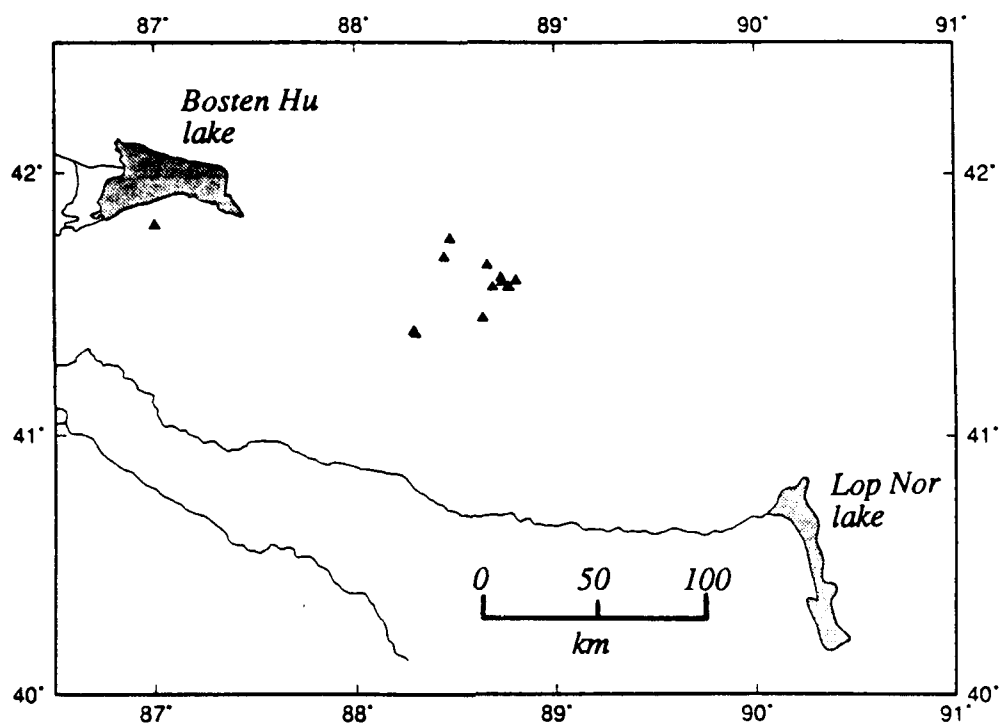


Figure 1. Location of the presumed Chinese nuclear test site in Xinjiang Province, between Bosten Hu and Lop Nor lakes. The triangles represent the seismic locations of events that are presumed to be underground nuclear explosions. Event locations are given in several references (Arora and Basu, 1984; Dahlman and Israelson, 1977; Fieldhouse, 1991; National Defense Research Institute, 1978, 1981) and plotted in collaboration with the U.S. Geological Survey's Preliminary Determination of Epicenters database. All thirteen events with coordinates, listed in Table 1, are plotted here; however, two triangles are doubled up and are not easily distinguishable.

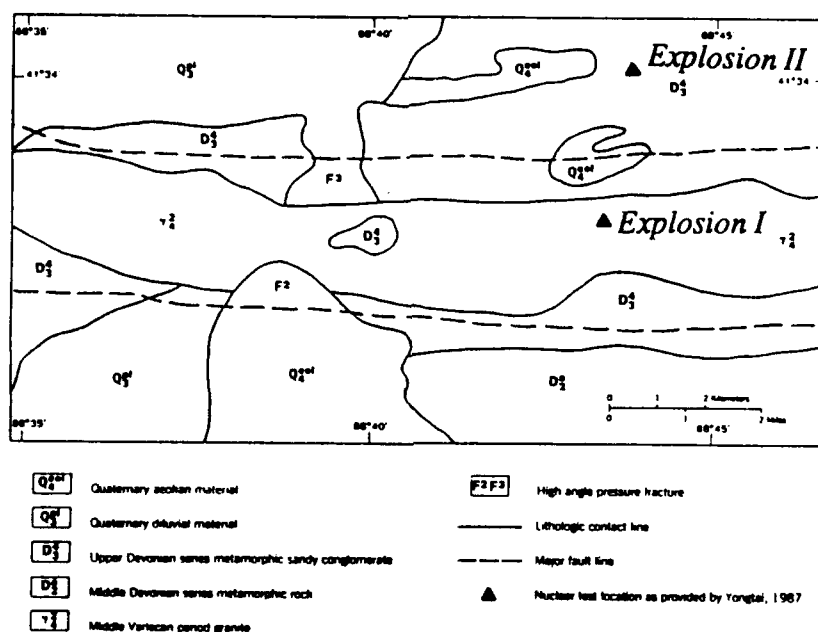
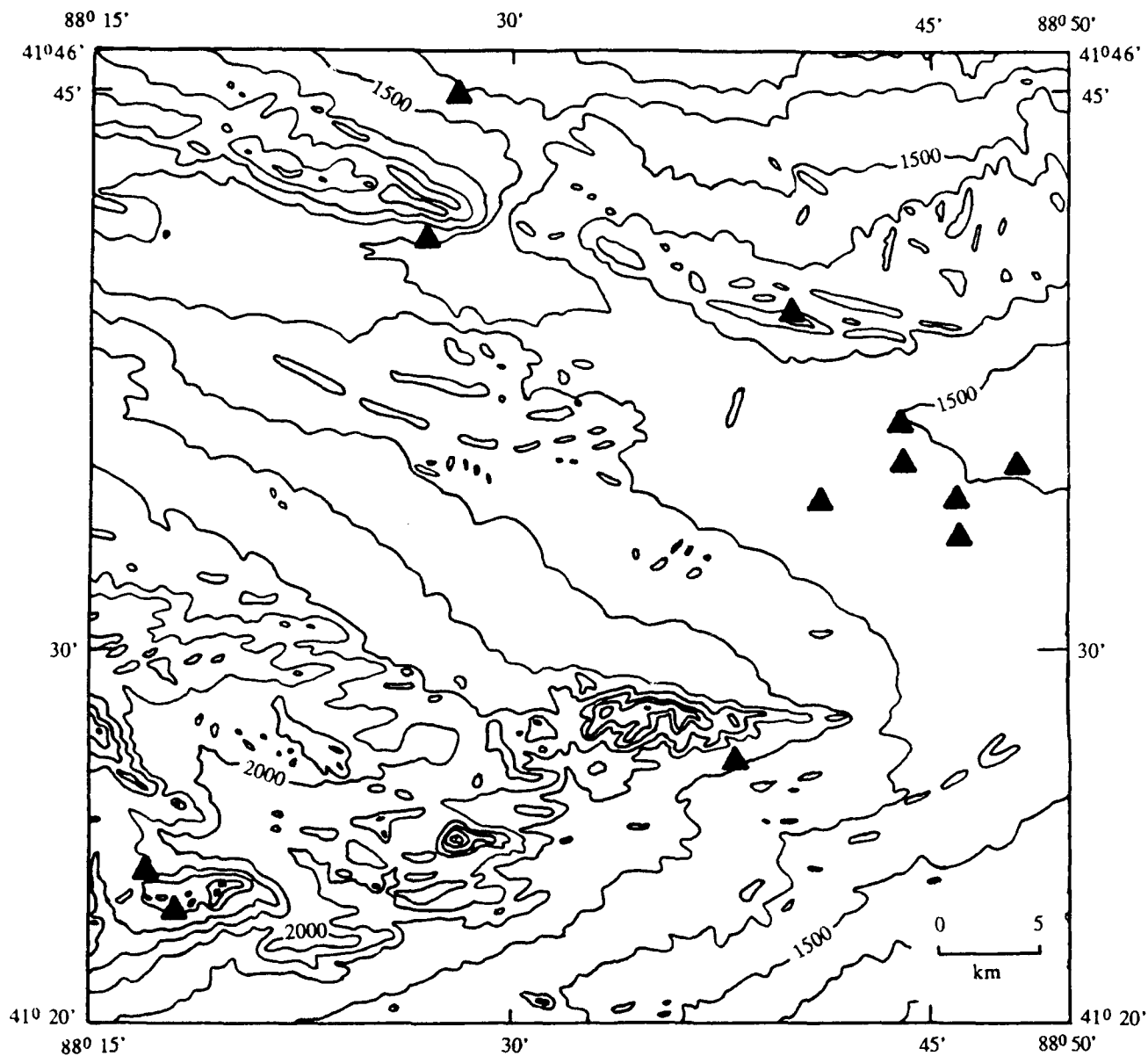


Figure 2. Geologic map of part of the Chinese nuclear test site near Lop Nor. After Che Yongtai, 1987.



*Contour interval 100 meters
Supplementary contours at
50 meter intervals*

Figure 3. Topographic map of the area of the Chinese nuclear test site. The triangles represent the locations of the events listed in Table 1. The 4 May 1983 event plots beyond the limits of the figure. After DMA, 1983.

Table 1
Chinese underground nuclear tests

| mo | day | yr | Time (GMT) | Latitude | Longitude | m_b | Yield (kt) |
|----|-----|----|------------|----------|-----------|-------|-------------|
| 09 | 22 | 69 | 16:14:58.8 | 41-23 | 88-18 | 5.1 | 25 |
| 10 | 27 | 75 | 01:00:03.5 | 41-24 | 88-17 | 5.0 | <10 |
| 10 | 17 | 76 | 05:00:03.7 | 41-39 | 88-40 | 4.9 | low (10-20) |
| 10 | 14 | 78 | 01:00:02.7 | 41-27 | 88-38 | 4.9 | <20 |
| 09 | 13 | 79 | | | | | |
| 10 | 05 | 82 | | | | | |
| 05 | 04 | 83 | 05:00:00.0 | 41-48 | 87-00 | 4.4 | |
| 10 | 06 | 83 | 10:00:02.8 | 41-33 | 88-46 | 5.5 | 20-100 |
| 10 | 03 | 84 | 05:59:57.8 | 41-36 | 88-44 | 5.3 | 15-70 |
| 12 | 19 | 84 | 06:00:04.2 | 41-41 | 88-27 | 4.7 | 5-50 |
| 06 | 05 | 87 | 04:59:58.3 | 41-35 | 88-44 | 6.2 | |
| 09 | 29 | 88 | 07:00:03.1 | 41-45 | 88-28 | 4.7 | 1-20 |
| 05 | 26 | 90 | 07:59:57.8 | 41-34 | 88-41 | 5.4 | 15-65 |
| 08 | 16 | 90 | 04:59:57.6 | 41-34 | 88-46 | 6.2 | 50-200 |
| 05 | 21 | 92 | 04:59:57.4 | 41-35 | 88-48 | 6.6 | 700-1800 |

Dates and yields are from Fieldhouse, 1991, who lists the 1969 event as 9-23; all other sources list it as 9-22. Date and yield of the 5-21-92 event is from Gertz, 1992

Times, latitudes, longitudes, and m_b 's are from the USGS PDE. The time and location of the 5-4-83 event comes from Arora and Basu, 1984, who list this as a possible earthquake.

Table 2
Physical properties of granite at the vertical test area

| Depth (meters) | Compressive strength (10^5 Pa) | Tensile strength (10^5 Pa) | Shear strength (10^5 Pa) | Elastic modulus (10^{10} Pa) | Shear modulus (10^{10} Pa) | Poisson ratio | V_p (m/s) | V_s (m/s) | Degree of weathering |
|-----------------------|-----------------------------------------|-------------------------------------|-----------------------------------|---------------------------------------|-------------------------------------|------------------|----------------|----------------|-------------------------|
| Pre-explosion | | | | | | | | | |
| 26-50 | 1,048 | 45.1 | 37.2 | | | | 4,080 | | weak |
| 50-85 | 1,412 | 61.2 | 50.5 | | | | 4,752 | | slight |
| 85-117 | 1,634.2 | 70.4 | 58.1 | | | | 5,108 | | none |
| 117-176 | 1,776.3 | 76.5 | 63.1 | | | | 5,208 | | none |
| 176-259 | 1,776.3 | 76.5 | 63.1 | 6.76 | 2.81 | 0.21 | 5,295 | 3,276 | none |
| Post-explosion | | | | | | | | | |
| 28-40 | 667.3 | 29.2 | 23.9 | | | | 3,287 | | |
| 40-60 | 1,003.1 | 43.2 | 35.6 | | | | 4,000 | | |
| 60-80 | 1,444.4 | 62.2 | 51.3 | | | | 4,800 | | |
| 80-217 | 1,776.3 | 76.5 | 63.1 | | | | 5,297 | | |
| 217-242 | 564.2 | 24.2 | 20.2 | | | | 3,000 | | |
| 242-279 | | | | | | | 5,200* | | |
| 279-304 | | | | | | | 1,800 | | |

*Longitudinal velocity of steel casing used to protect hole.
After Chu Yucheng, 1986.

Yield Estimation Research

J. R. Murphy, B. W. Barker, J. N. Jenab and M. E. Marshall
S-CUBED
11800 Sunrise Valley Dr., Suite 1212
Reston, Virginia 22091
Contract Nos. F19628-89-C-0026 and F29601-92-C-DB01

Objective

The objectives of both these research investigations are directed toward the development of improved seismic yield estimation procedures for Soviet underground nuclear explosions. The first project centers on the development and implementation of a state-of-the-art software system (YES) for the determination and evaluation of seismic yield estimates for explosions at the Soviet Shagan River and Novaya Zemlya test sites. The second deals with the application of network-averaged spectral analysis techniques to teleseismic P wave data recorded from Soviet PNE explosions for purposes of defining a more generally applicable yield estimation methodology for explosions occurring at arbitrary locations within the former Soviet Union.

Research Accomplished

Development of the Yield Estimation System (YES) has continued with principal focus on tasks related to the completion of the seismic databases for explosions at the Shagan River and Novaya Zemlya test sites, implementation of a semi-automatic report generation module and documentation of the software system. With regard to the seismic databases, short-period and long-period data from all known explosions at the two test sites recorded at stations of the GDSN, USAEDS, CDSN, IRIS and internal Soviet networks have been assembled into a uniform, validated database at the DARPA CSS. These data include the recently acquired 178 hand-digitized waveforms recorded at ten different Soviet stations from selected explosions at the two test sites. We are currently developing a plan with DARPA to distribute unclassified versions of these comprehensive databases to the research community on CD-ROM.

The YES has also been expanded to include a semi-automatic report generation module which can be used by the analyst to produce full color reports documenting the results of the yield estimation analyses conducted for selected

explosions. This module has been built around the FrameMaker™ desktop publishing software running on a Sun SPARCStation and features a graphical user interface which permits the operator to produce the finished reports in a nearly fully automatic environment. This has been accomplished by establishing templates for the reports which automatically adjust to the particular test site and event selected and to the types of seismic data available for that event. Thus, once an event analysis has been completed, the analyst can initiate the report preparation by selecting the "Event Report" option from the YES main FUNCTION menu. This action opens a FrameMaker document and automatically imports all the event specific information (e.g., location, date, magnitude values, yield values, etc.) from the database into the appropriate places in the pre-specified text. It also brings up a menu which instructs the operator how to select the graphics which are to be included in the report. Once the appropriate screen corresponding to a required figure has been displayed, the operator simply selects the "Copy" button from the menu line and the image is automatically captured, resized and imported into the final report. The report module menus and a sample page from a finished FrameMaker document are displayed in Figure 1. Once the listed figures have been captured, a draft version of the document can be viewed and edited using the "View Report" menu option. In this process, text can be inserted or modified and figures can be replaced using simple procedures which require no knowledge of the FrameMaker software. When the final version of the report is saved using the "Save Report" option, the text and graphics are automatically reformatted to accommodate any such changes. A specified number of full color copies of this finished report can then be printed using the "Print Report" menu option.

The second project, which deals with the application of network-averaged spectral analysis techniques to teleseismic P wave data recorded from Soviet PNE events, is in its initial phase, and work to date has focused on the compilation of event parameter and seismic databases and on the development of a workstation-based, graphical user interface to facilitate access, analysis and display of these data. Since its inception in the mid 1960's, the Soviet PNE program has utilized nuclear explosions in a variety of commercial and scientific applications. Over 100 such explosions have now been conducted in this series and these tests have been widely dispersed throughout the territories of the former Soviet Union. We have selected a preliminary sample of 63 of these events and have collected GDSN and USAEDS short-period data recorded from these explosions into a uniform database at the DARPA CSS.

In order to provide convenient access to these diverse data, a map-based, graphical user interface has been developed which permits the analyst to select, view and analyze them in a workstation environment. The top level display of this interface is shown in Figure 2 where the locations of the selected 63 events

are shown as overlays (large squares) to a color-coded topographic map of the former Soviet Union and surrounding countries. A wide variety of other information has been assembled for use in conjunction with this map interface, as is illustrated by the overlay of seismicity (small squares) shown on this figure. Available information regarding the source characteristics of these explosions (e.g., origin time, location, purpose, m_b value, etc.) has also been collected into an on-line database which can be accessed by the user by simply selecting a particular explosion location symbol with the mouse.

In an attempt to systematize the estimation of yields, pP parameters and t^* values for individual PNE tests, an analytical module has been added to the data access and visualization system described above. This module permits the analyst to compute the network-averaged P wave spectrum for a selected explosion and to then interactively invert this spectrum to obtain the required source and propagation path parameters. In applying this inversion procedure, the operator first selects a specific seismic source model (e.g., Mueller/Murphy granite) from a menu and the system then automatically computes the theoretical P wave spectrum and associated source parameters which provide the best overall fit to the observed spectrum over the frequency band 0.5 to 2.5 Hz, under the assumption that the upper mantle attenuation beneath the selected PNE site is the same as that beneath the Shagan River test site. At this point, the module provides the analyst with the option to interactively refine the automatically determined values of the yield (W), pP/P amplitude ratio (A), pP-P delay time (t_0) and t^* in order to resolve any remaining discrepancies in the fit to the observations. The final results of applying these inversion procedures to the two PNE events identified in Figure 2 are shown in Figure 3, where it can be seen that the simple model provides very precise descriptions of the observed spectra. In the case of the 7/18/85 explosion (top) which was located in the stable continental interior north of Archangel, the data are well described using the same t^* value which was found to be applicable at the Shagan River test site (i.e., $t^* = 0.53$ sec). However, for the 8/15/73 explosion (bottom), which was located in a region of active seismicity north of Tashkent, it was found that a higher t^* value of about 0.69 sec was required to fit the data. Thus, the final inferred value of t^* for this PNE test location is intermediate between those which have been found to be characteristic of the Shagan River ($t^* = 0.53$ sec) and NTS ($t^* = 0.75$ sec) test sites, which is qualitatively consistent with what would be expected on the basis of the tectonic environments in which these tests were conducted.

Conclusions and Recommendations

The development of a software system (YES) which can be used to estimate state-of-the-art seismic yields for underground nuclear explosions at the Shagan River and Novaya Zemlya test sites is nearing completion. The seismic database for explosions at these two test sites is now essentially complete and a

sophisticated, semi-automatic report generation capability has been implemented to permit the analyst to document the results of the yield estimation analyses of specific explosions. Current efforts are focusing on full implementation of the Oracle DBMS and documentation.

The initial analysis of network-averaged, teleseismic P wave spectra corresponding to Soviet PNE explosions has focused on the development of source parameter and seismic databases for a preliminary sample of 63 well-distributed events. A new, map-based graphical user interface has been developed to improve the analyst's capability to access, analyze and display these data. Results of initial tests of the associated source inversion module indicate that the selected seismic source and propagation models can provide excellent fits to the observed spectral data. Work is currently in progress to analyze spectral data from a large sample of these PNE explosions in order to define the variation of t^* and other seismic yield estimation parameters as a function of location throughout the territories of the former Soviet Union.

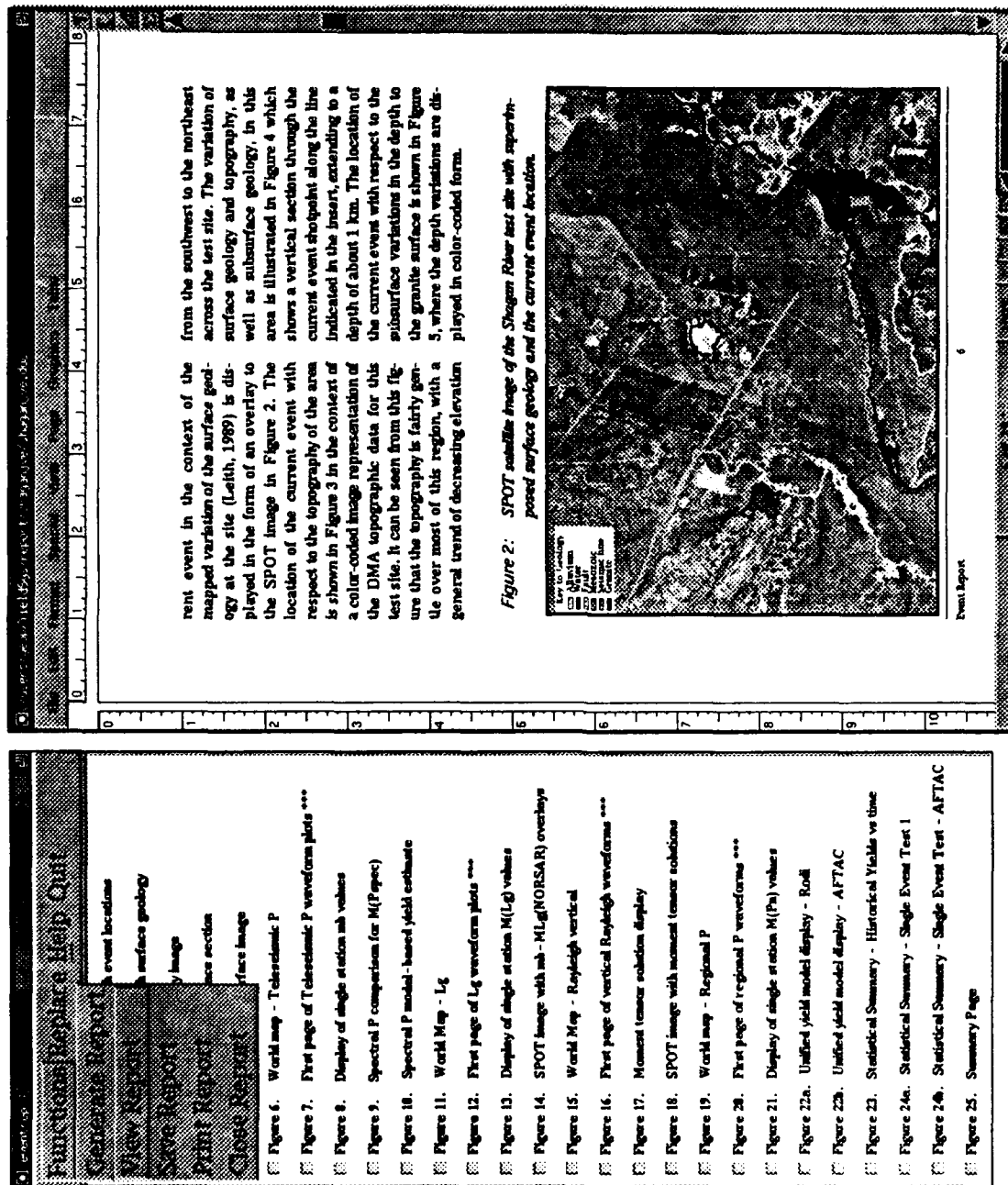


Figure 1. Yield Estimation System Event Report module menu and associated sample FrameMaker page display.

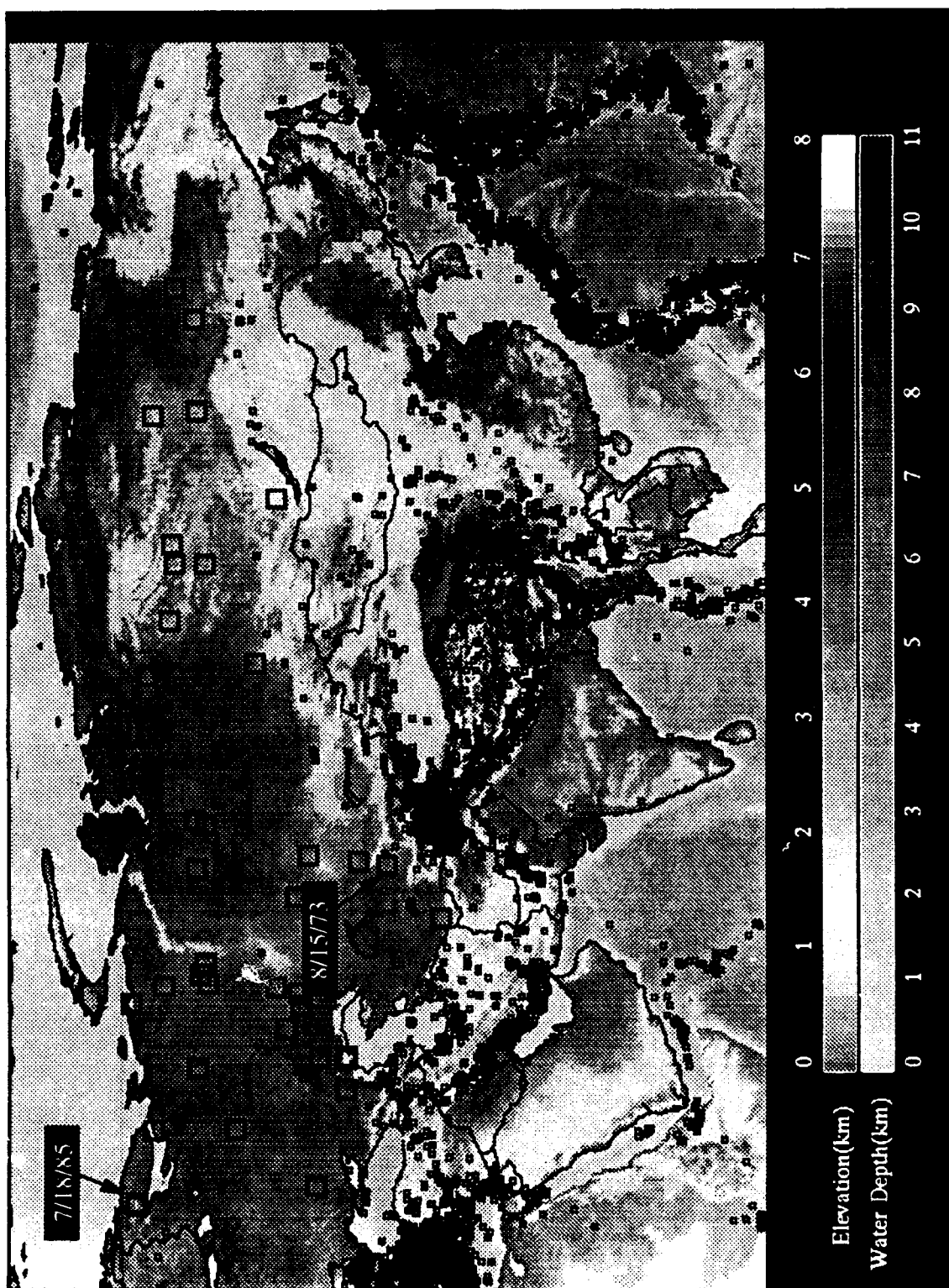


Figure 2. Color-coded topographic map of former Soviet Union and surrounding countries showing locations of selected PNE events (large squares) with respect to the distribution of seismicity in the region (small squares).

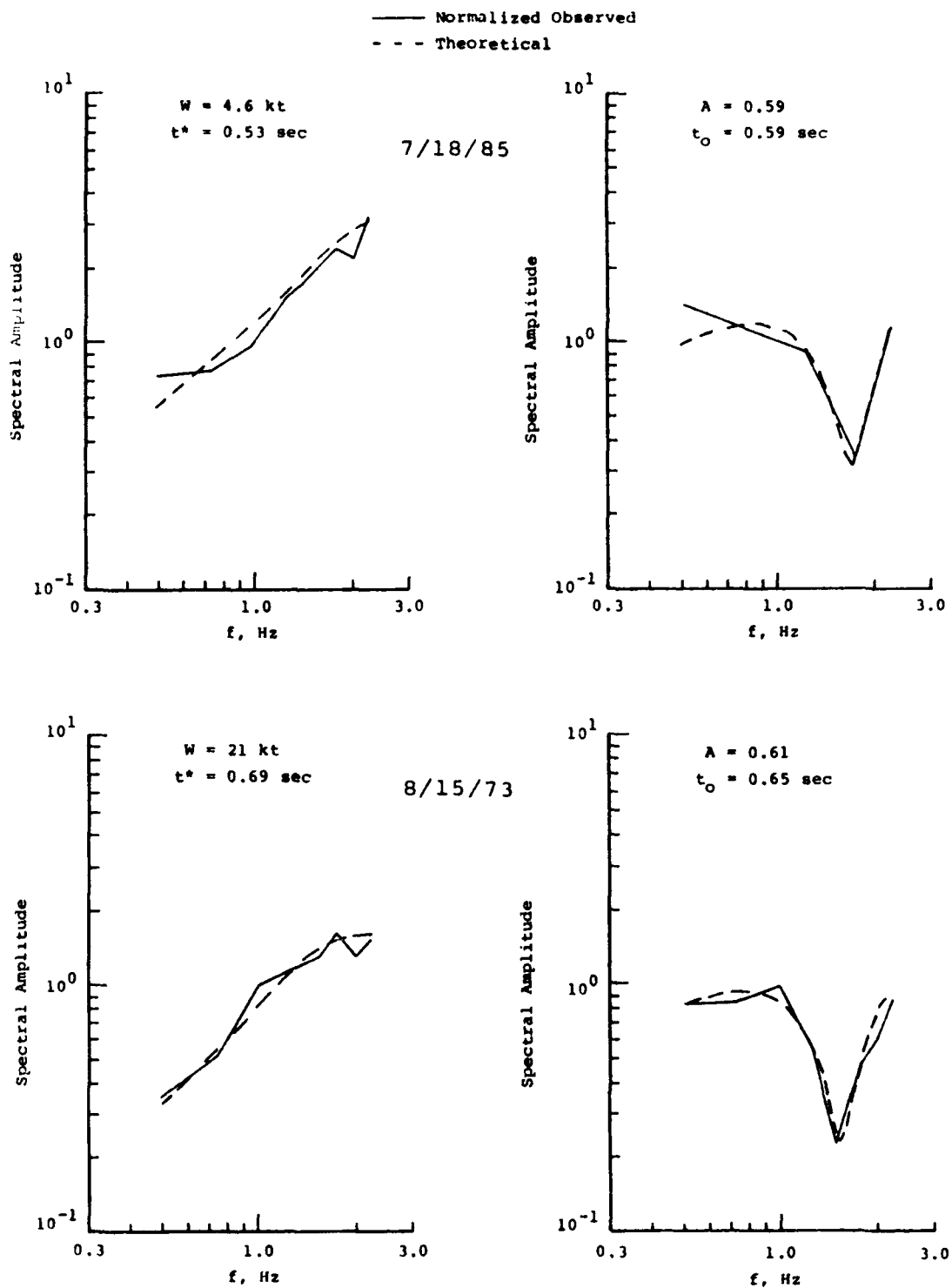


Figure 3. Comparison of observed and best-fitting theoretical network-averaged P wave spectra (left) and pP (right) for the Soviet PNE events of 7/18/85 (top) and 8/15/73 (bottom).

Lg CODA Q ACROSS NORTHERN EURASIA

**Y. Pan, B. J. Mitchell, J. Xie,
and J. Ni**

**Department of Earth and Atmospheric Sciences
Saint Louis University
3507 Laclede Avenue
St. Louis, MO 63103**

Contract No. F29601-91-K-DB19

OBJECTIVE

The primary objective of this research is to determine the regional variation of 1-Hz Lg waves across the northern portion of Eurasia, including the continental shelves of northern Europe and northwestern Asia. That information is of primary importance in determining yields of nuclear events and in estimating detection thresholds for various parts of Eurasia.

RESEARCH ACCOMPLISHED

We have applied a tomographic method to map the regional variation of Lg coda Q across a portion of Eurasia extending between about 40 and about 80 degrees north latitude and between about 0 and 120 degrees east longitude (Figure 1). This region includes much of northern Europe, including the Barents shelf, almost all of eastern Europe, and all of the mainland portion of northern Asia except for a broad region of northeastern Siberia and a fringe of eastern Asia north of, and including Korea. When combined with our earlier results for southern Eurasia (Xie and Mitchell, 1990a) Lg coda Q values are now mapped for all of Eurasia except for the regions cited above in northern Eurasia, most of western Europe, much of the Middle East, Pakistan, India, and a small region of southeastern Asia (Figure 2).

The results for northern Eurasia were obtained from the analysis of 95 Lg coda records from 18 IRIS, GDSN, WWSSN, and Russian Kirnos stations. These were combined with more than 200

records from earthquakes and underground nuclear explosions in southern Eurasia to produce the map in Figure 2.

The process assumes that $Q(f)=Q_0f^\eta$ where Q_0 is Lg coda Q at 1 Hz and η is its frequency dependence. These values were obtained using a stacked spectral ratio (SSR) method (Xie and Nuttli, 1988) on digital data obtained from the stations in the region of study. The SSR method yields values of Q_0 and η with smaller variances than those associated with earlier methods and reduces tradeoffs between Q_0 and η which have plagued some studies. Figure 3 shows approximate scattering ellipses associated with a late portion of the coda of Lg in northern Eurasia. Because of the areal nature of that scattering, spatial coverage is much better than it would be if we assumed that the Q_0 and η values merely represent a path average between a seismic event and a recording station.

The variances of Q_0 and η are small enough so that we can apply the back-projection tomographic technique of Xie and Mitchell, 1990b) to obtain regionalized images of Q_0 and η for continental regions where a sufficient quantity of Lg coda Q data are available. Our Q_0 maps in Figures 1 and 2 reveal the following pattern of regional variation:

1. A broad swath of high values (700-1100) extends from the Barents shelf, across Scandinavia, and into northeastern Siberia.
2. Another high- Q region occurs in northeastern Siberia. This region, like that in the preceding paragraph, is an old cratonic region which is 1700 My or more in age.
3. The Q_0 values show a general trend of decreasing values from north to south.
4. The lowest values (~ 200) occur through a west-northwest east-southeast trending band extending along the southernmost part of the map from Turkey, through northern India, and into southern China.
5. Preliminary estimates of η indicate that that parameter increases with increasing values of Q_0 through northern and central China having values between about 0.2 and about 0.7.

In other regions, however, it decreases with increasing values of Q_0 , having values between about 0.7 and 0.0.

The pattern of Q_0 values is consistent with the results of earlier studies (e.g. Mitchell, 1975; Cheng and Mitchell, 1981) where it was found that crustal values of shear wave Q are lowest in regions which have undergone tectonic activity most recently and are highest in the old stable shield regions.

CONCLUSIONS AND RECOMMENDATIONS

The patterns of Q_0 (Figures 1 and 2) show clear relationships with tectonic features in Eurasia. The highest values (1000 or more) are associated with old stable regions and the lowest values (200 or less) are associated with the regions of most recent tectonic activity.

The frequency dependence values, in some regions, vary directly with Q_0 , and in others, vary inversely with it. They appear to take on a wide span of values from 0.0 to 0.7 or more.

Although we now have a Q_0 map which covers most of Eurasia, there are several gaps in key areas. In particular, we need to obtain information on most of the Middle East, on India and Pakistan, and Korea. Other areas where information is lacking is western Europe, a corner of southeast Asia, and northeastern Siberia. Lg coda data should be available for all of these areas except northeastern Siberia, so it should be possible to obtain a map of Lg coda Q which is complete except for that region.

REFERENCES

- Cheng, C.C., and B. J. Mitchell, Crustal Q structure in the United States from multi-mode surface waves, *Bull. Seism. Soc. Am.*, 71, 161-181, 1981.
- Mitchell, B. J., Regional Rayleigh wave attenuation in North America, *J. Geophys. Res.*, 35, 4904-4916, 1975.
- Xie, J., and O.W. Nuttli, Interpretation of high-frequency coda at large distances: stochastic modelling and method of inversion, *Geophys. J.*, 95, 579-595, 1988.

- Xie, J., and B. J. Mitchell, A back-projection method for imaging large-scale lateral variations of Lg coda Q with application to continental Africa, *Geophys. J. Int.*, 100, 161-181, 1990a.
- Xie, J., and B. J. Mitchell, Lg coda Q variation across Eurasia, Spec. Rpts., No. 261, *Proc. Twelfth Ann. DARPA/GL Seismic Res. Symp.*, 198-203, 1990b. GL-TR-90-0212, ADA226635

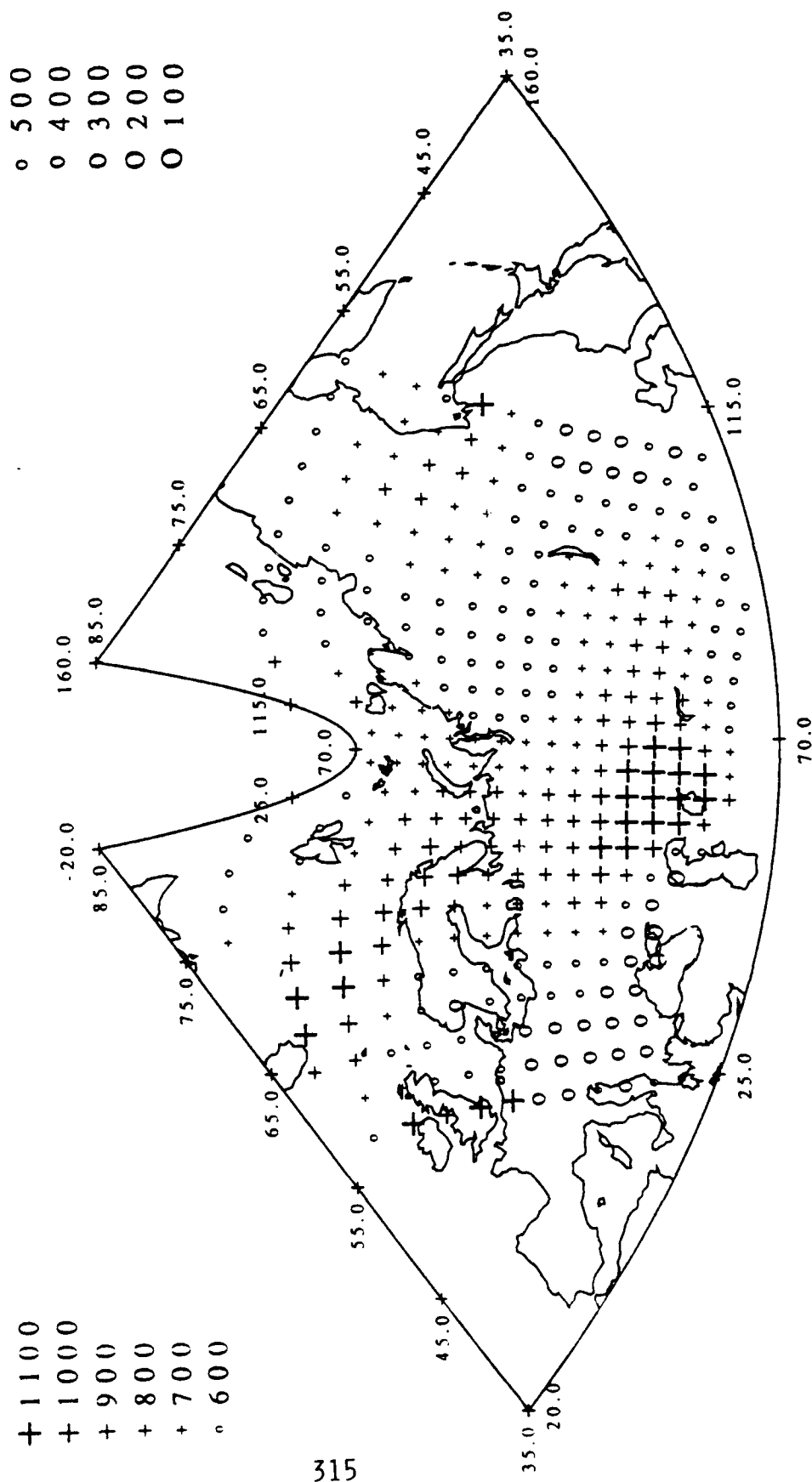


Figure 1. Regionalized values of Q_0 from tomographic inversion of data in only northern Eurasia.

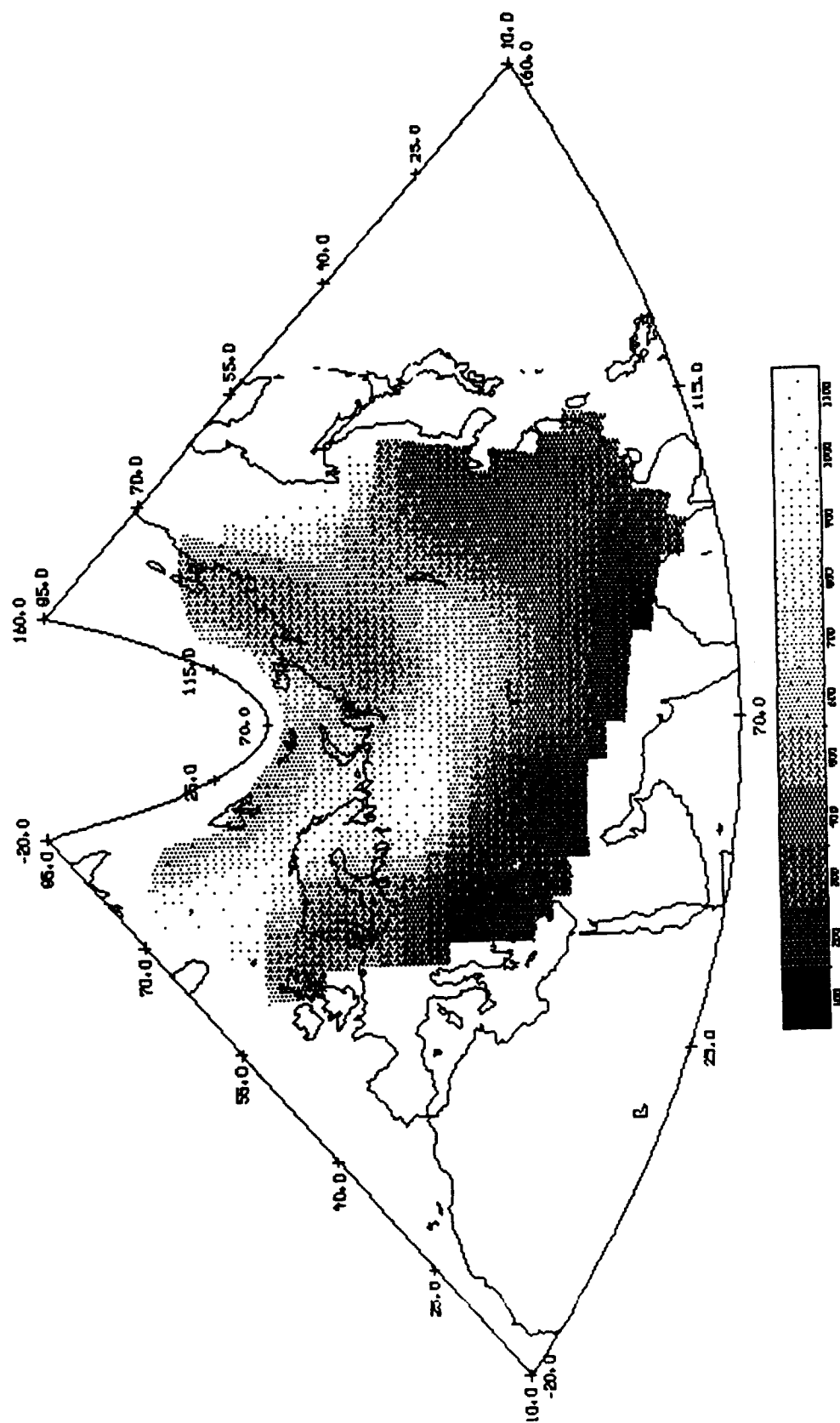


Figure 2. Tomographic image of Lg coda Q_0 values in Eurasia from data processed to date.

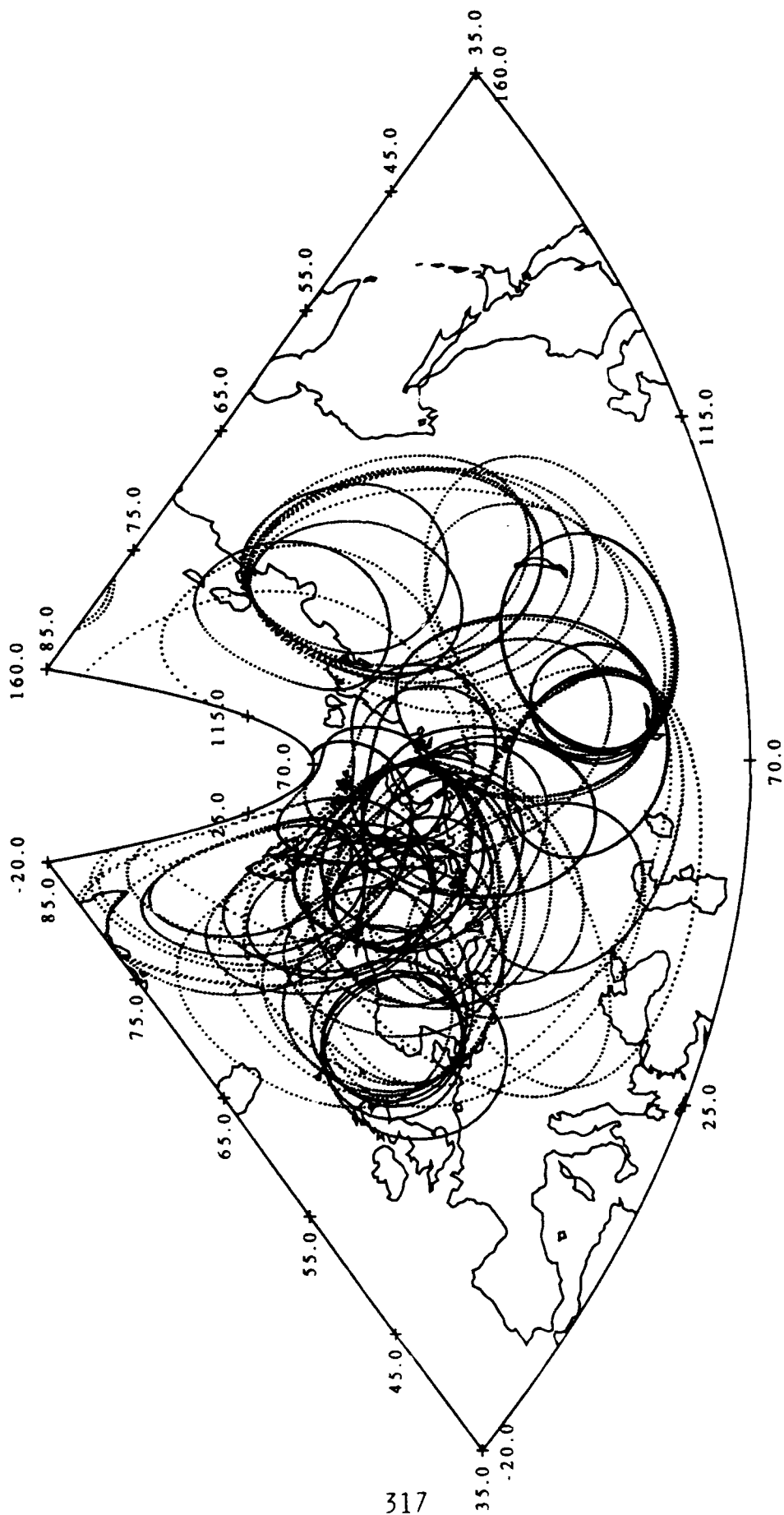


Figure 3. Sampling pattern of Lg coda for data compiled in northern Eurasia. Each record of Lg coda is assumed to sample an elliptical area corresponding to the maximum lapse time used in the analysis.

TITLE: A Regional Seismic Data Set, and Results on Automated Interpretation of Seismic Data Using Neural Networks

AUTHORS &

AFFILIATION: Gagan B. Patnaik, Thomas J. Sereno, Jr.,
Mari J. Mcztell, and Richard D. Jenkins

*Science Applications International Corporation
10260 Campus Point Drive
San Diego, California 92121*

CONTRACT NO: F-19628-90-C-0156

OBJECTIVE:

One of the goals of DARPA's Artificial Neural Network Technology program is to determine whether or not neural networks can improve upon current methods for seismic monitoring of underground nuclear explosion testing. Since the current emphasis is on low yields, the primary interest is on events at regional distances (e.g., $\leq 20^\circ$).

The objectives of our DARPA project are: (1) Assemble a data set to test and evaluate the performance of neural networks for processing and interpretation of seismic signals, and (2) Evaluate neural network applications for automated interpretation of seismic data by integrating them into DARPA's *Intelligent Monitoring System (IMS)*.

RESEARCH ACCOMPLISHED:

A Regional Seismic Data Set

We assembled a data set that includes waveform and parametric data from >500 regional events recorded by the NORESS and ARCESS arrays in Norway, and the GERESS array in Germany (Figure 1). The epicentral distances are 50-2000 km, and the magnitudes are 1.0-5.0. Most of the events are mining explosions in the western part of the CIS, Sweden, Finland, Poland and Germany. This data set also includes 22 presumed underwater explosions, and 51 earthquakes in Fennoscandia that were identified in a regional bulletin produced by the University of Helsinki. Other earthquakes (for which independent bulletin information was not available) are also included in this data set. For example, there are many presumed earthquakes located to the south of GERESS.

The events in this data set are shown in two groups in Figure 1. The first group (shown in the map to the left) consists of 241 regional events that were recorded by the NORESS and ARCESS arrays in Norway. The epicentral distances to NORESS and ARCESS are 200–1800 km, and the M_L magnitudes are 1.5–3.2. Most of the events are mining explosions but there are also 22 underwater explosions, and 51 presumed earthquakes in this group (most of these were reported in a bulletin produced by the University of Helsinki). This data set also includes parametric data (without waveforms) from 249 other events that were recorded during a continuous 10-day period. This first group is described in detail by *Sereno and Patnaik* (1991). The second group (shown in the map to the right in Figure 1) consists of 255 regional events recorded by the GERESS array in Germany. The epicentral distances are 200–1600 km, and the M_L magnitudes are 1.5–5.0. Many of these events are presumed to be earthquakes (particularly to the south of GERESS). However, most of the events to the north of GERESS are mining explosions (e.g., from an active mining region in Lubin, Poland).

The parametric data include results from automated *IMS* processing and subsequent analyst/seismologist review (*Sereno and Patnaik*, 1991). These include the estimated event origin (latitude, longitude, depth, magnitude, and origin time), and detection and association data (e.g., phase identification, arrival time, azimuth and phase velocity estimated from $f-k$ processing, amplitude, signal-to-noise ratio, frequency, and polarization data). The waveform data include 7-minute segments from each short-period array element. These segments start 30 seconds before the theoretical P_n arrival time based on the final event origin. In addition to these single-channel waveforms, the data set includes the *detecting beam* for each associated arrival and three coherent beams formed from the 3-component elements of each array (vertical, north-south, and east-west).

Evaluation of Neural Network Applications

As part of our second project objective, we integrated MIT Lincoln Laboratory's neural network for regional final phase identification (e.g., P_n , P_g , S_n , L_g , and R_g) into the *IMS* (*LaCoss, et al.*, 1991). Under operational testing, this module performed 3–5% better than the rule-based *Expert System for Association and Location* (ESAL) in *IMS* station processing. However, after network processing (where data from all stations are combined), the gain obtained from the neural network dropped to about 1.0%. It is possible that higher gains could be realized if network processing was improved by including the final-phase confidence estimates from the neural network in the rules for network processing.

We also developed a neural network application which automates the initial identification (P or S) of seismic phases recorded by 3-component stations based on polarization and detection attributes. This technique (*Patnaik and Sereno*, 1991) is found to perform better than either the *IMS* rule-based approach, or a multivariate statistical approach applied to the same data (particularly for signals with low signal-to-

noise ratio). This approach is also much easier to develop than a more traditional rule-based system because of the high-dimensionality of the input data, and because the data are station-dependent. The ease in rapid adaptability and the automated interpretation capability of this new technique makes it amenable to machine-learning.

An improved version of the neural network module, that also uses context parameters as input was implemented in *IMS* (Figure 2). It replaced the previous version that only used eight polarization attributes as input. One of these context parameters is the number of detections before the arrival in question minus the number of detections after it for a fixed time window. The other context parameter is the mean time difference between the detection in question and detections before and after it for a fixed time window. The window length, which is dependent on the seismicity observed at a station, is determined empirically for each station to maximize identification accuracy. Neural network weights were obtained by using polarization data and context from six IRIS/IDA stations in the CIS (Figure 1). The results after analyst review were used as the *ground truth*. As in the earlier version, the implementation of these neural networks includes provision for station-dependent weight tables (e.g., separate neural networks are trained for each station). However, only two of the IRIS/IDA stations had enough analyst-reviewed data for reliable training and testing (AAK and GAR). These neural networks perform better than the latest rule-based system in *IMS* by about 3–6%. The identification accuracy is at least 97% for each individually-trained station. Figure 3 shows a schematic 3-layer network with weights derived for the station GAR.

Since only two of the stations had enough analyst-reviewed data for training and testing, we developed an average weight table by training and testing with data combined from all 6 IRIS/IDA stations. This average weight table will be replaced with station-specific tables as more analyst-reviewed data become available. Figure 4 shows the matrix for adaptability testing for these IRIS/IDA stations. The diagonals show the percentage of identification accuracy for each station where training and testing was done using data from the same station. The off-diagonals show the results of cross-testing (i.e., adaptability testing). A trained neural network generally showed about 84% correct identification of phases if applied to data from a different site. The identification accuracy is about 10–15% higher if training and testing used data from the same station. This increase in accuracy (after retraining) may be attributed to the site-specific characteristics of the different regions.

A new application of a neural network technique for the identification of regional events that uses the shape of the broadband envelope of regional seismograms and estimates of their ARMA coefficients is in progress. *Wuster* (1992) uses a similar parameterization in a linear classification scheme. We are developing and testing this new application with data from the events recorded at GERESS.

CONCLUSIONS AND RECOMMENDATIONS:

We assembled a regional seismic data set to test and evaluate the performance of neural networks for automated processing and interpretation of regional seismic data, which may also be valuable for other studies related to seismic monitoring at regional distances. This data set is available at the CSS in the Oracle database, or in UNIX tar format on Exabyte tapes. It consists of waveform and parametric data from >500 regional events recorded by the NORESS and ARCESS arrays in Norway, and the GERESS array in Germany.

We developed and implemented a neural network technique for initial phase identification (*P* or *S*) using polarization measurements and detection attributes (*context*) from 3-component data. This technique (1) is easier to develop than rules, (2) performs 3-7% better than a linear multivariate discriminant analysis method (particularly for low *snr* data), (3) incorporates station-specific characteristics, and (4) is easily adapted to data from new stations. For example, about 80-85% identification accuracy is achieved for data from a new station using a neural network derived from data from a different station. After retraining, the identification accuracy increases to >90%. This initial phase identification neural network module was implemented in *IMS* for station processing of 3-component data.

REFERENCES:

- LaCoss, R., R. Cunningham, S. Curtis, and M. Seibert. "Artificial Neural Networks for Seismic Data Interpretation", *Semiannual Tech. Rep.*, ESD-TR-91-058, Lincoln Laboratory, MIT, ADA239673, 1990.
- Patnaik, G.B. and T.J. Sereno. "Neural Computing For Seismic Phase Identification", PL-TR-92-2110(II), Sci. Rep. No.1, 27 September 1991. ADA252442
- Sereno, T.J. and G.B. Patnaik. "Data To Test And Evaluate The Performance Of Neural Network Architectures For Seismic Signal Discrimination", PL-TR-92-2110(I), Sci. Rep. No.1, 27 September 1991.
- Wuster, J. "Discrimination of Tectonic Earthquakes and Quarry Blasts at Regional Distances from GERESS", in Harjes, *et. al.*, *Advanced Waveform Research Methods for GERESS Recordings*, PL-TR-92-2142, Sci. Rep. No.2, p.92-136, 15 April 1992.

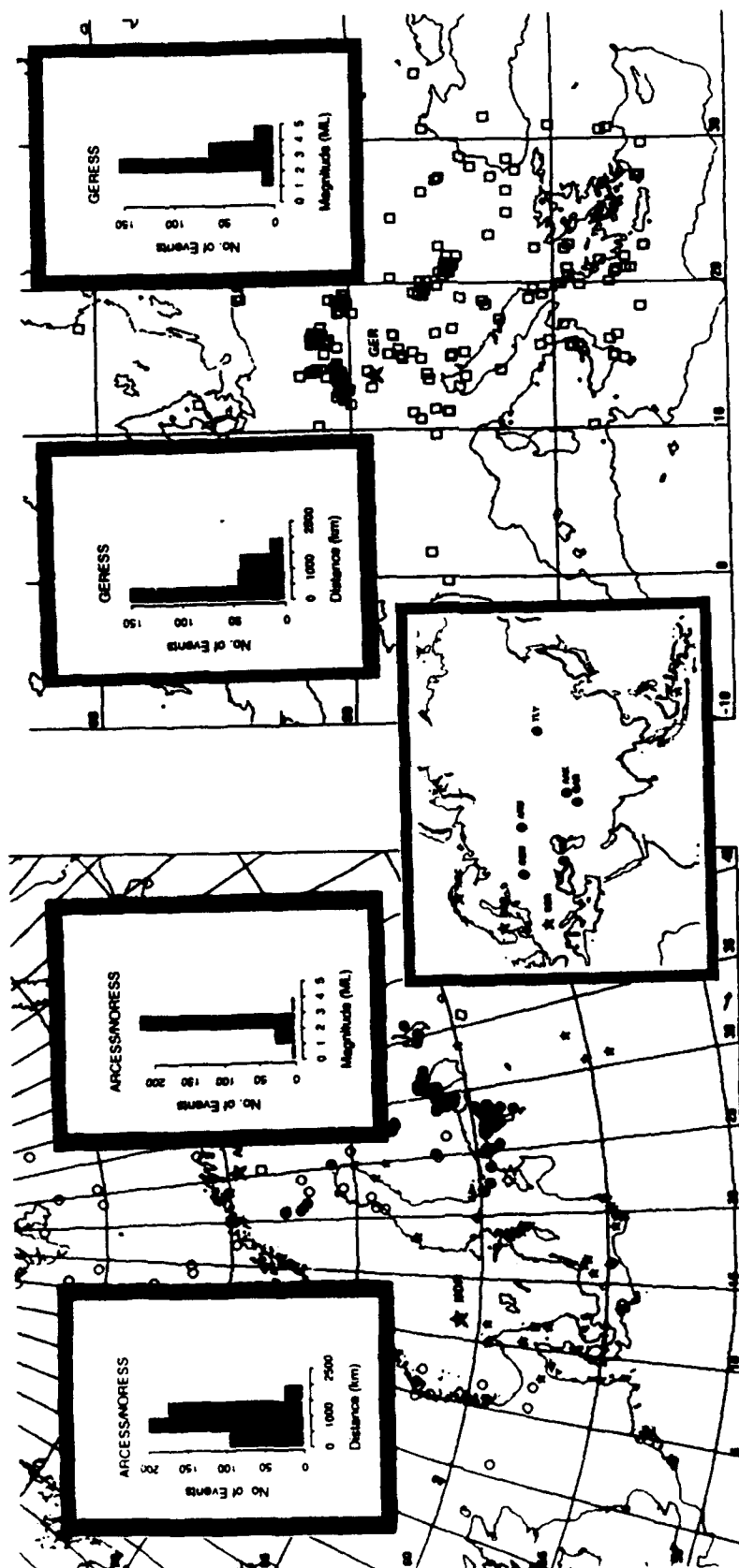


Figure 1. The middle inset shows the location of the arrays (ARCESS, NORESS, and GERESS; denoted by star symbols), and IRISIDA 3-component stations in the CIS (AAK, ARU, GAR, KIV, OBN, and TLY; denoted by solid circles). The map on the left shows the location of earthquakes (open circles), mine blasts (closed circles), other explosions (stars) and two other unidentified events (open squares). Also shown in this map are the combined distance and magnitude distribution of the events (insets) for ARCESS and NORESS. Similarly, the map on the right shows the location, distance and magnitude distribution (insets) of the events recorded at GERESS.

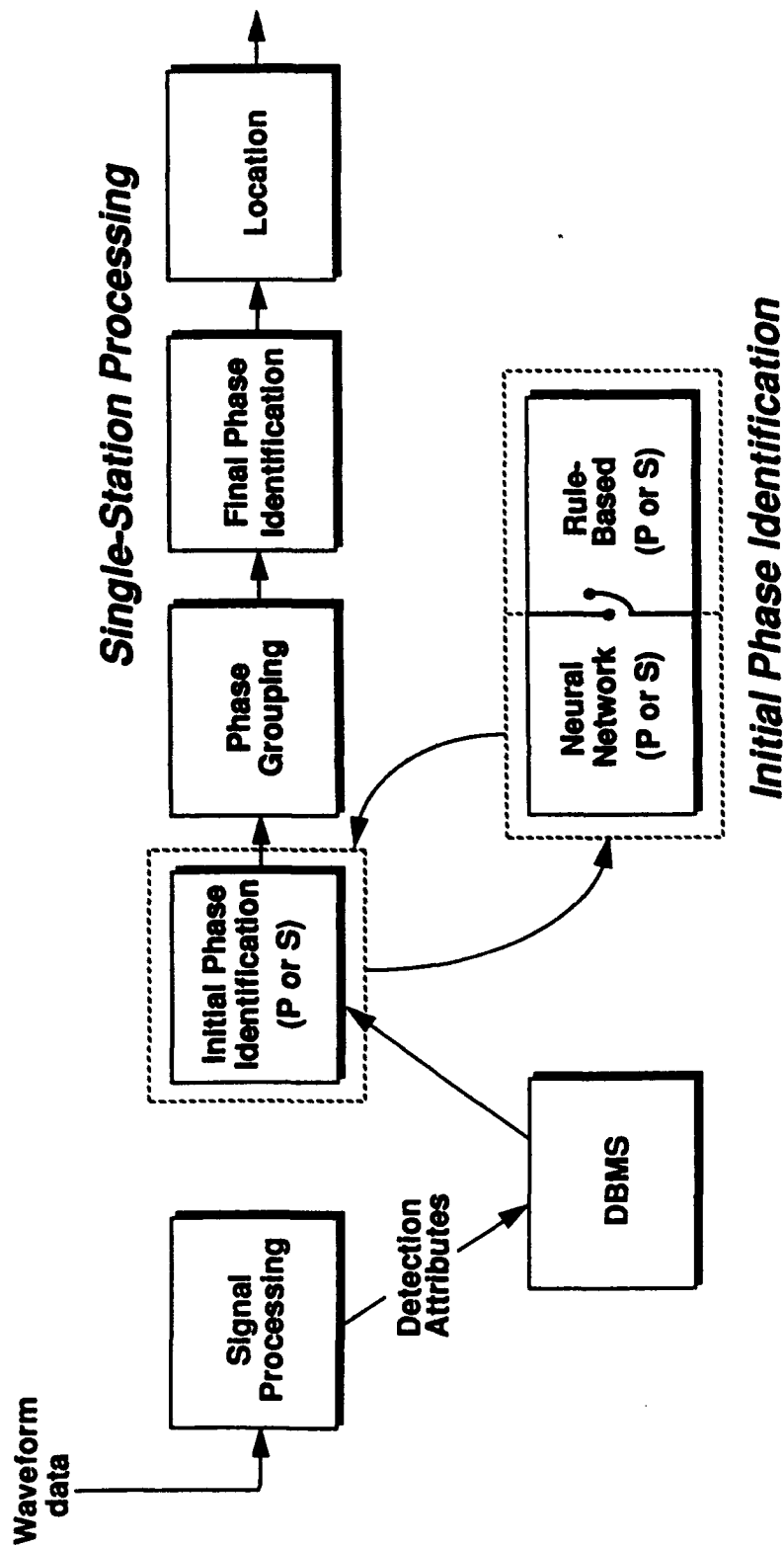


Figure 2. This diagram shows the integration of the neural network initial phase identification module into the rule-based expert system ESAL (Expert System for Association and Location, in IMS). The initial phase identification elements of ESAL (for 3-component stations like IRIS/IDA stations in the CIS) are replaced by trained neural networks.

SCHEMATIC THREE-LAYER "TRAINED" NETWORK

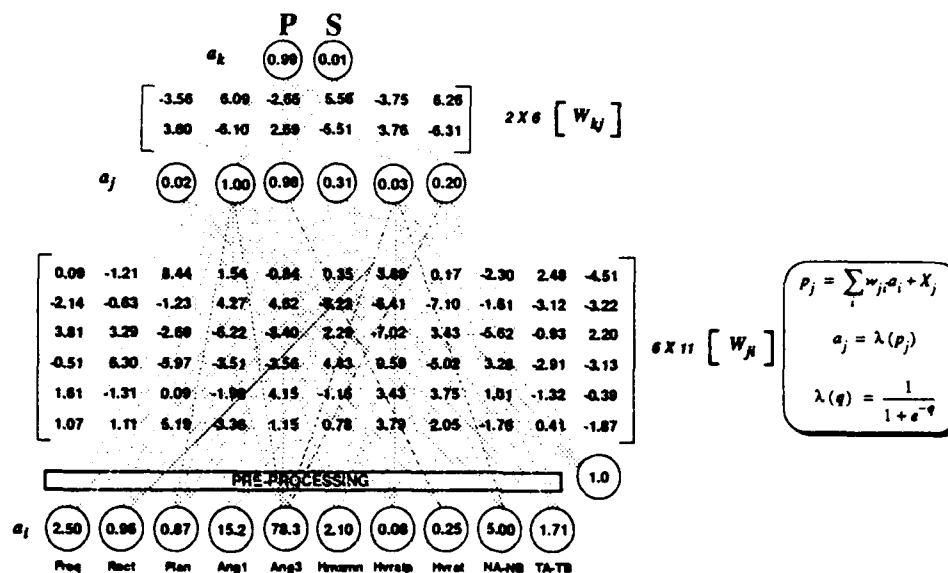


Figure 3. Schematic diagram of a trained, 3-layer, feed-forward neural network (10-6-2). The input nodes are a_i (polarization and contextual attributes); W_{ji} are the weights from input to middle (hidden) layer; a_j are the middle layer nodes; w_{kj} are the weights from middle to output layer; and a_k are the output nodes (P or S). This particular example shows the identification of a P-type phase at GAR.

ADAPTABILITY TESTING FOR IRIS STATIONS IN THE FORMER SOVIET UNION

Average Percentages of Correct Identification of Both P-type and S-type Phases

| Test Train | IRIS (2102) | AAK (805) | ARU (82) | GAR (740) | KIV (248) | OBN (78) | TLY (149) |
|------------|-------------|-----------|----------|-----------|-----------|----------|-----------|
| IRIS | 94.3 | 97.1 | 92.2 | 94.2 | 90.7 | 88.5 | 91.8 |
| AAK | 88.3 | 99.5 | 89.0 | 86.5 | 76.6 | 78.2 | 83.6 |
| ARU | 84.1 | 83.0 | 100.0 | 79.2 | 81.5 | 84.6 | 71.4 |
| GAR | 92.0 | 94.4 | 93.9 | 97.0 | 78.2 | 75.6 | 81.3 |
| KIV | 89.4 | 92.0 | 86.6 | 84.5 | 99.2 | 83.3 | 90.6 |
| OBN | 84.4 | 84.1 | 93.9 | 79.7 | 81.0 | 100.0 | 74.3 |
| TLY | 80.9 | 80.0 | 79.3 | 83.9 | 82.3 | 68.0 | 100.0 |

Figure 4. As shown in this matrix for adaptability, on the average, a trained network generally shows about 84% correct identification of phases if applied to data from a new station. After retraining with data from the same station, this accuracy increases by 10-15%. The perfect accuracy (100%) obtained for the stations ARU, OBN, and TLY are the artifact of too few training samples (ground truths). The numbers in parentheses below each station denote the number of analyst-verified training samples (P and S phases) available for that station.

REGIONAL MOMENT:MAGNITUDE RELATIONS FOR EARTHQUAKES AND EXPLOSIONS

Howard J. Patton and William R. Walter
Department of Earth Sciences, Lawrence Livermore National Laboratory

OBJECTIVE: The best known discriminants between earthquakes and explosions employ a comparison of seismic amplitudes in the long-period passband to amplitudes in the short-period passband. The $M_s:m_b$ discriminant was developed for teleseismic recordings in the early sixties, and has been successfully implemented globally for events with m_b greater than about 5.0. With the advent of broadband regional data, $M_s:m_b$ was extended to study smaller events. Taylor *et al.*, (1989) have demonstrated the excellent performance of the discriminant down to about m_b 4.0 in the western U.S. The main limitation is the ability to measure M_s for small events because of poor signal-to-noise ratios and the resulting need for long-period measurements at shorter epicentral distances. The seismic moment, M_o , could be used as the measure of long-period amplitude. As shown for $M_s:m_b$ by Stevens and Day (1985), a physical basis for a discriminant based on $M_o:m_b$ is desirable in order to make predictions for various source and receiver geologies. This predictive aspect is important in the present monitoring environment where non-proliferation is the principal concern, and we are met with the challenge of monitoring many different areas around the world. In this project, we are studying $M_o:m_b$ discriminants using regional data for both U. S. and Soviet explosions, and for earthquakes in both tectonic and stable areas. We are also studying $M_o:m_b$ scaling from a theoretical standpoint in order to identify key factors affecting the separation between earthquakes and explosions.

RESEARCH ACCOMPLISHED: We have derived relationships between M_o and m_b based on two regional phases, P_n and L_g . Magnitudes based on amplitudes of P_n waves, $m_b(P_n)$, were measured for Nevada Test Site (NTS) explosions and western U.S. earthquakes by Denny *et al.* (1987). The moments for explosions were estimated using combined datasets of higher-mode and fundamental-mode surface waves (Patton, 1991; unpublished data). The explosions are located above and below the water table with the majority fired in tuff on Pahute Mesa. We have included a few events from Yucca Flat fired in alluvium and tuff, among those being the smallest event in the dataset, Coalora, whose moment was estimated from near-field data by Stump *et al.* (1992). The moments for earthquakes in the western U. S. were estimated in the study of Patton and Zandt (1991) using fundamental-mode surface waves. A plot of M_o versus $m_b(P_n)$ data for both earthquakes and explosions is shown in Figure 1a.

Magnitudes based on the 3rd peak amplitudes of L_g waves, $m_b(L_g)$, for NTS explosions, were taken from the study of Patton (1988). For the earthquakes, we have only one event in the dataset of Patton and Zandt (1991) with an $m_b(L_g)$: the Massachusetts Mountain earthquake of 8/5/71 located on NTS, and its magnitude is 4.93. Consequently, we have resorted to using a dataset of eastern North American earthquakes from the study of Herrmann (1979), in which source mechanisms, moments, and $m_b(L_g)$ are estimated for 22 events. A plot of M_o versus $m_b(L_g)$ for both earthquakes and explosions is shown in Figure 1b. The Massachusetts Mountain earthquake is called out for reference on this plot and fits well with the population of eastern North American earthquakes.

Also shown on the plot of M_o versus $m_b(L_g)$ are data for presumed underground nuclear explosions fired on the Soviet test site (KTS) in eastern Kazakhstan. The $m_b(L_g)$ values for those explosions were taken from the study of Nuttli (1986b), and the seismic moments come from the work of Given and Mellman (1986). While this population of explosions is quite restricted in magnitude range, it is notable that they plot very well with the population of NTS explosions. Piledriver, a U.S. explosion in granite with an $m_b(L_g)$ of 5.84 (Nuttli, 1986a) and moment of 6.9×10^{15} N-m (Stevens, 1986), also fits well with these two explosion populations.

The observations in Figure 1 show good separation between earthquakes and explosions. The separation is best for $m_b(P_n)$, and it appears to be magnitude independent. The scatter in the

explosion populations for NTS is small for both $m_b(P_n)$ and $m_b(L_g)$, while the earthquake data has more scatter, especially at small magnitudes for $m_b(P_n)$. The small scatter for NTS explosions is remarkable because of the range of media in which these explosions are detonated. These NTS observations and the agreement with KTS explosions suggests a weak dependence of $M_o:m_b$ relations on source medium.

Regression lines of the form, $\log M_o = a m_b + b$, were computed for all earthquake and explosion populations, and the results are shown in Figure 1. The slopes for earthquakes and explosions are only marginally different at the one sigma level in the case of $m_b(L_g)$; they certainly are not different for $m_b(P_n)$. We decided to constrain the slope of the regression line for earthquakes to be the same as the slope estimated for the explosions. This permits the simple difference of intercept values, b , to be a measure of separation between earthquake and explosion populations. In the case of $m_b(P_n)$, the intercepts are 10.88 and 9.55 for earthquakes and explosions, respectively, giving a separation of 1.33 log moment units (lmu). For $m_b(L_g)$, the intercepts are 10.00 and 8.88 for a separation of 1.12 lmu. We also computed the intercept for KTS explosions using the slope obtained for NTS explosions. This intercept is 8.91, and the separation between Soviet explosions and NTS explosions is only 0.03 lmu.

A simple theoretical model, employing scaling similarity and conservation of energy, was developed to explain the causes of $M_o:m_b$ separation between earthquakes and explosions. For body waves in media where velocity varies only as a function of depth, we may use ray theory to write the expression for the P or S wave far-field displacement (Aki and Richards, 1980, p. 116):

$$u_c(t + T_c) = \frac{F_c \dot{M}_o(t)}{4 \pi \rho_s^{1/2} \rho_r^{1/2} c_s^{5/2} c_r^{1/2} R_c} \quad (1)$$

where T_c is the ray travel time, F_c is the point source radiation pattern, $\dot{M}_o(t)$ is the time derivative of the point source moment time function, ρ is the density, c is the wave velocity (P or S ; c subscripts indicate P or S dependent quantities), R_c is the geometrical spreading factor, and the subscripts s and r denote source and receiver material properties, respectively. In order to study $M_o:m_b$ scaling, we obtain a relation between the peak amplitude of the moment rate time function and the seismic moment using a similar-scaling model, where the scaling constants are independent of moment. In addition, we require that conservation of energy be satisfied. For details, we refer the interested reader to our recent paper (Patton and Walter, 1992). If one considers an earthquake and explosion with the same magnitude recorded at the same station, then by our analysis the difference in log moment is given by:

$$\Delta \log M_o = -\frac{1}{2} \log \left(\frac{F_c'^3 I_c}{F_c^3 I_c'} \right) + \frac{1}{4} \log \left(\frac{(\lambda' + 2\mu')^2 \rho_s' c_s'^5}{\mu^2 \rho_s c_s^5} \right) - \frac{1}{2} \log \left(\frac{\eta_c' \sigma' k_1 k_2}{\eta_c \sigma k_1' k_2'} \right) \quad (2)$$

where $I_c = \langle F^2 \rangle$ is the average squared radiation pattern, λ and μ are Lamé constants, σ is the average applied stress, k_1 and k_2 are scaling constants, and the explosion parameters are primed. The product, $(\eta_a + \eta_b)\sigma$, is called the apparent stress (Wyss, 1970), and η_a and η_b are the P and S wave efficiencies, respectively. We now examine each term on the right hand side of equation (2) separately.

Radiation Pattern Term. For a spherically symmetric explosion the radiation is independent of azimuth and $\langle F_a' \rangle = I_a' = 1$. For earthquakes the average P wave radiation pattern is $\langle I_a \rangle = 0.44$ and $I_a = 4/15$ (Boore and Boatwright, 1984). Using these values leads to a difference of about -0.25 lmu. However since $|F_a|$ can vary from 0 to 1 it also contributes scatter to the log moment versus magnitude plots.

Material Properties Term. For crustal earthquakes we assume $\rho_s = 2700 \text{ kg/m}^3$ and $c_s = \alpha_s = 6 \text{ km/s}$. These values are in sharp contrast to NTS explosions fired in tuff. Many of the explosions in Figure 1 were detonated in saturated tuff on Pahute Mesa. An example is Towanda (called out

in Figure 1) where $\rho'_s = 2000 \text{ kg/m}^3$ and $c'_s = \alpha'_s = 3.1 \text{ km/s}$. Using these values leads to a difference of about -0.51 lmu.

Source Term. We will assume that the general shape of the far-field displacement pulses from earthquakes and explosions are similar so that $k_1 k_2 = k'_1 k'_2$. Typical earthquake apparent stresses are about 3 MPa or 30 bars (e.g. Kanamori and Anderson, 1975). For earthquakes, S waves carry the majority of the radiated seismic energy, since the S wave efficiency is about 10 to 15 times the P wave efficiency (e.g. Wyss, 1970). Therefore the total apparent stress as used by Kanamori and Anderson (1975) is very nearly the S wave apparent stress, and the P wave apparent stress will be about 0.2-0.3 MPa. We will use 0.25 MPa as a typical earthquake P wave apparent stress value. For explosions, we again use Towanda as a representative Pahute Mesa event. The inferred yield of this event based on $m_b(L_g)$ and magnitude-yield relations of Patton (1988) is 116 kt. App and Brunish (1992) estimate the approximate upper bound on the percent of total energy that is seismically radiated to be 0.595% from near source modeling. Using the seismic moment of $8.5 \times 10^{15} \text{ N-m}$ (Patton, unpublished data) and the working point source properties above, we estimate the P wave apparent stress for this event to be about 6.5 MPa. Using these values leads to a difference of about -0.71 lmu.

Combining all three sources of difference in log moment for the same magnitude gives a total of -1.47, not too different from the value of -1.33 observed for $m_b(P_n)$. We expect a similar combination of radiation pattern, material differences and apparent stress differences cause the observed offset between explosions and earthquakes on the $\log M_o$ versus $m_b(L_g)$ plot in Figure 1b, although we recognize that the Green's function for $m_b(L_g)$ will be more complex than that used in equation (1).

CONCLUSIONS AND RECOMMENDATIONS: The results of this study are encouraging for the potential of discrimination at small magnitudes in different geologic environments. Based on theory, the separation between earthquakes and explosions should be magnitude independent, providing that scaling similarity holds and the bandwidth of the recording, on which magnitude is based, is sufficiently broad. Our observations of $m_b(P_n)$ appear to support this claim. Stevens and Day (1985) predict a major source of scatter will arise in the earthquakes due to variations in source mechanisms affecting amplitudes to stations of a monitoring network. We see significant scatter in the earthquake population for $m_b(P_n)$, as well as for other magnitudes such as M_L . We will be studying the scatter in the earthquake population caused by the source radiation patterns using the source mechanisms which are known for all of the earthquakes. Also, we have plans to study the effects of pP on the estimates of $m_b(P_n)$ and the effects of source depth on the excitation of L_g and the estimates of $m_b(L_g)$.

We also claim in this study that the effects of material properties in the source region and the effects of apparent stress tend to compensate for one another such that $M_o:m_b$ relations show relatively little variation (Patton and Walter, 1992). Explosions fired in a variety of media and emplacement conditions at NTS support this claim. Also, there are the observations of the Soviet explosions at KTS which plot very well with NTS explosions. We intend to study this claim further by supplementing our observations with addition results for KTS explosions using the Borovoye data and other sources of regional data. Also, we plan to investigate in greater detail whether this claim applies to weak media. Our preliminary results suggests that it does, but more explosions in alluvium at NTS must be analyzed.

Finally, the June 29, 1992 earthquake located on NTS generated a rich sequence of aftershocks with which to test the findings of this study on more events and extend the findings to smaller magnitudes. In particular, analysis of these aftershocks will offer the opportunity to study the causes of scatter in the earthquake population under controlled conditions of common paths and common recording sites with epicenters in close proximity to NTS explosions.

Acknowledgements. This research was performed under the auspices of the U.S. Department of Energy by the Lawrence Livermore National Laboratory under contract W-7405-ENG-48.

References

- Aki, K., and P. G. Richards, *Quantitative seismology*, W. H. Freeman and Co., San Francisco, 1980.
- App, F. N., and W. M. Brunish, Modeling surface motion and spall at the Nevada test site, Los Alamos National Laboratory, LAUR-92-500, Los Alamos, New Mexico, 1992.
- Boore, D. M., and J. Boatwright, Average body-wave radiation coefficients, *Bull. Seism. Soc. Am.*, 74, 1615-1621, 1984.
- Denny, M. D., S. R. Taylor, and E. S. Vergino, Investigation of m_b and M_s formulas for the western United states and their impact on the m_b/M_s discriminant, *Bull. Seism. Soc. Am.*, 77, 987-995, 1987.
- Given, J. W. and G. R. Mellman, Estimating explosion and tectonic release source parameters of underground nuclear explosions from Rayleigh and Love wave observations, Air Force Geophysics Laboratory Final Report, AFGL-TR-86-0171, Hascom Air Force Base, MA, 1986. ADB110040
- Herrmann, R. B., Surface wave focal mechanisms for eastern North American earthquakes with tectonic implications, *J. Geophys. Res.*, 84, 3543-3552, 1979.
- Kanamori, H. and D. L. Anderson, Theoretical basis of some empirical relations in seismology, *Bull. Seism. Soc. Am.*, 65, 1073-1095, 1975.
- Nuttli, O. W., Yield estimates of Nevada test site explosions obtained from seismic L_g waves, *J. Geophys. Res.*, 91, 2137-2151, 1986a.
- Nuttli, O. W., L_g magnitudes of selected east Kazakhstan underground explosions, *Bull. Seism. Soc. Am.*, 76, 1241-1251, 1986b.
- Patton, H. J., Application of Nuttli's method to estimate the yield of Nevada test site explosions recorded on Lawrence Livermore National Laboratory's seismic system, *Bull. Seism. Soc. Am.*, 78, 1759-1772, 1988.
- Patton, H. J., Seismic moment estimation and the scaling of the long-period explosion source spectrum, in *Explosion Source Phenomenology*, American Geophysical Union Monograph, 65, 171-183, 1991.
- Patton, H. and G. Zandt, Seismic moment tensors of western U.S. earthquakes and implications for the tectonic stress field, *J. Geophys. Res.*, 96, 18,245-18,259, 1991.
- Patton, H. J. and W. R. Walter, Regional moment:magnitude relations for earthquakes and explosions, submitted to *Geophys. Res. Letters*, 1992.
- Stevens, J. L., Estimation of secular moments from explosion-generated surface waves, *Bull. Seism. Soc. Am.*, 76, 123-151, 1986.
- Stevens, J. L., and S. M. Day, The physical basis of $m_b:M_s$ and variable frequency magnitude methods for earthquake/explosion discrimination, *J. Geophys. Res.*, 90, 3009-3030, 1985.
- Stump, B. W., R. E. Reinke, K. H. Olsen, and L. R. Johnson, Isotropic and deviatoric characterization of the Coalora nuclear explosion in Yucca flats, submitted to *Geophys. J.*, 1992.
- Taylor, S. R., M. D. Denny, E. S. Vergino, and R. E. Glaser, Regional discrimination between NTS explosions and western U.S. earthquakes, *Bull. Seism. Soc. Am.*, 79, 1142-1176, 1989.
- Wyss, M., Stress estimates of South American shallow and deep earthquakes, *J. Geophys. Res.*, 75, 1529-1544, 1970.

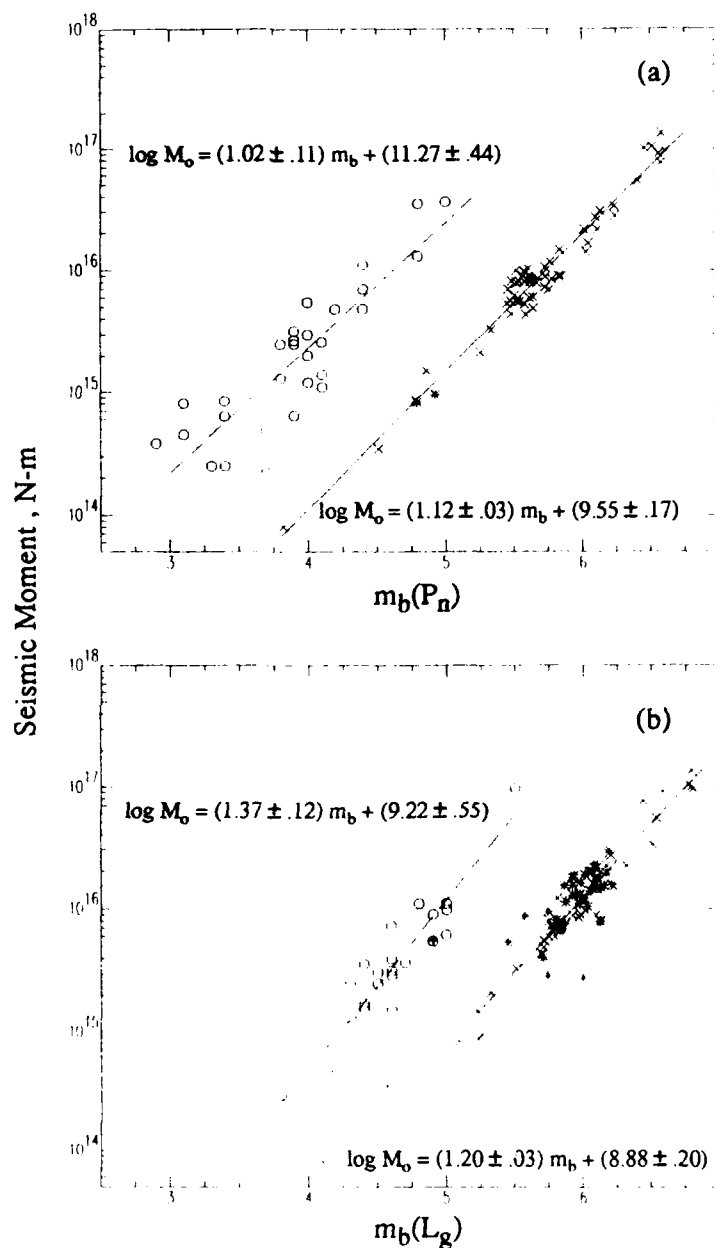


Figure 1. Regional $M_o:m_b$ relations for earthquakes and explosions. (a) Circles are $m_b(P_n)$ data for western U. S. earthquakes. The x's and stars are data for NTS explosions fired in tuff and alluvium, respectively. The solid dot is the Towanda explosion. (b) Circles are $m_b(L_g)$ data for eastern North America earthquakes. The x's and stars are data for NTS and KTS explosions, respectively. The circle with cross is the Massachusetts Mountain earthquake, and solid dot is the Piledriver explosion.

FROM RIFT TO RIFT: THE YAMAL PENINSULA-LAKE BAIKAL DEEP SEISMIC SOUNDING PROFILE

Keith F. Priestley, University of Cambridge, Cambridge, UK
John J. Cipar, Phillips Laboratory, Hanscom AFB, Ma 01731

CONTRACT NO.: F19628-90-K-0046

OBJECTIVE: Analysis of Asian upper mantle structure

RESEARCH ACCOMPLISHMENTS:

The 2400-km long "RIFT" profile recorded in 1982, extends across the Siberian platform from the Yamal Peninsula to Kyakhta (Fig. 1). Seismograms from three nuclear shot points were recorded. The northernmost shot point (SP 245) is in western Norilsk within the West Siberian rift on the northwest edge of the Siberian Platform. This failed rift developed in Triassic time (235-215 mya) during the initial breakup of Pangea. Following the extinction of extension, the rift was buried beneath approximately 15 km of sediment. The profile extends southeast across the Tunguss Basin, a region of Late Paleozoic extension and widespread intraplate flood basalts, to the presently active Baikal rift. The central shot point (SP 173) is in western Tura within the Tunguss Basin, approximately 700 km southeast of the first shot point. Data from this shot extends 560 km northwest reversing a section of the profile from the first shot point and 1700 km southeast across the Baikal rift. The southernmost shot point (SP 35) is located 250 km north of Lake Baikal. Data from this shot extends 325 km to the south across the Baikal rift and nearly 2200 km to the north reversing both the northern and central shots.

The nuclear shots were recorded at 200 sites each equipped with the "Taiga" seismic system (Chichinin et al., 1969). The sensors had a natural frequency of 1.5 Hz and the recording system as a whole had a usable bandwidth between 0.5-20 Hz. In addition to the nuclear shots a detailed system of crustal observations has also been made. Chemical explosions (3000-5000 Kg each) were detonated at approximately 70 km intervals along the profile and recorded on reversed profiles 250-300 km long. One of these, SP 36, is shown in Fig. 5.

The record sections for the three nuclear shots are shown in Figs. 2,3,4. There are clear differences in the seismograms from the three explosions that imply the velocity structure of the lithosphere is variable along the profile. Near each shot point, crustal arrivals are prominent, especially the P_g phase. The mantle refractions (P_n) start to be recorded as the first arrival at epicentral distances of 150-200 km and appear as a weak arrival in these figures, but can be clearly seen in the digital data. At longer ranges, the first arrivals have variable amplitudes and arrival times which reflect real variations in the lithosphere as they are correlated over several hundred kilometers. Likewise, amplitude variations are complex. For example, in the distance range 1300-1500 km for SP 245 (Fig. 2), high amplitudes that begin after the first arrival at 1300 km progressively move forward, becoming the first arrival at 1500 km. This pattern is characteristic of a reflected phase from a high velocity layer. Several repetitions of this structure indicate complex layering within the upper several hundred kilometers of the mantle. At least some, if not all, of these observations may be due to lateral variations in structure (Pavlenkova and Egorkin, 1983).

At longer ranges, arrivals from the mantle transition zone can be observed, particularly in the long profile from SP 245. The reflection/refraction from the 410-km discontinuity is a clear secondary arrival beginning about 1700 km, becoming the first arrival by 2200 km. At 2100-2300 km range, a bright reflection from the 660-km discontinuity can be observed at about 12 sec reduced time. There is no clear evidence of the 550-km discontinuity described by Shearer (1990), although the seismograms in this distance range are complex and a weak discontinuity may be lurking within the record section. Also notable is the considerable difference between the record section for SP 245 (Fig. 2) and SP 35 (Fig. 4) at comparable transition zone ranges. Whereas SP 245 indicates strong arrivals from transition zone discontinuities, the SP 35 data do not show such prominent arrivals. At this stage it is unclear whether this observation is the result of lateral variation in the mantle or some surface feature which may mask the arrivals.

First arrival times and prominent secondary arrival times for SP 245 are compared to two published models for the Eurasian upper mantle (Fig. 6): model K8 (Given and Helmberger, 1980) was derived using long-period seismograms of Soviet nuclear blasts recorded in Europe, while model KCA (King and Calcagnile, 1976) was derived from P-wave phase velocity measurements at NORSAR. As noted above, the first-arrival observations define a continuous travel time branch of variable amplitude with long-wavelength, 1- 1.5 sec travel time variations in the 750 to 1450 km range. Neither upper mantle model accounts for these travel time anomalies. The chief difference between the two models is the presence of a low-velocity zone (LVZ) between 140-220 km in K8 as well as a higher gradient in K8 between the LVZ and the 420-km discontinuity. The K8 LVZ produces a pronounced shadow zone in the travel time curve, which is not supported by the observations. KCA, on the other hand, with a smooth upper mantle, generally predicts the overall shape of the observed travel time curve. Neither model accounts for the late arrivals in the 250-750 km range. Both models generally predict the arrival times of waves from the transition zone discontinuities. In general, KCA accounts for the overall shape and amplitude behavior of the SP 245 travel time observations.

The observed phase arrival data from SP 245 constitute one of the most complete and detailed sets of regional travel times anywhere in the world, and in this section, we describe a new reference model for central Asia based on forward modeling of these data. The starting model was KCA modified with a crustal section that more closely agrees with the close-in observations. Crustal thickness ranges from 47 km in the West Siberian rift to 42 km beneath the Siberian craton. However our model implicitly assumes the same crust along the entire profile since no station corrections are applied. The travel time curve is shown in Fig. 7 compared to the observed arrival times; the velocity-depth function is shown in the inset. The main features of the model are a 44-km thick crust which overlies a complicated upper mantle. While the details are important for fitting the structure of the travel time curve, the basic structure of the upper mantle above the transition zone consists of material with P-wave velocities ranging between 8.25 km/sec at the Moho to 8.53 km/sec at 225 km. At 225 km depth, velocities increase abruptly to 8.63 km/sec and higher. This basic structure is readily apparent in the travel time curve. Superimposed on this overall structure are finer features such as the strong gradient between 117 and 123 km depth that produces the triplication at about 1000 km range. There is little evidence for a pronounced LVZ as is found in model K8 (Given and Helmberger, 1980), although small velocity reversals are required

to terminate several branches of the travel time curve. The worst fit is in the distance range 700-1000 km with up to 1.5 sec discrepancy. Extensive modeling of the high phase velocity segment A-A' (Fig. 7) indicates velocities near 8.58 km/sec at 75 km depth. Since this branch is not observed on other record sections, we believe it may be a high velocity body of limited lateral extent which cannot be modeled by the one dimensional calculations used in the present analysis.

The transition zone is similar to other upper mantle models. The upper discontinuity lies at 425 km depth and is modeled as a sharp discontinuity with a velocity increase of 5.6%. The strong reflection from the lower discontinuity is best modeled as a 4.9% velocity increase over the depth range 656.5-659 km. Velocities below the 425-km discontinuity are well-constrained by a set of strong arrivals. On the other hand, similar strong arrivals cannot be seen from the 660-km discontinuity indicating a weak gradient below 660 km.

CONCLUSIONS AND RECOMMENDATIONS:

We have presented record sections from three nuclear explosions detonated in central Siberia. The longest record section extends 2400 km and shows detailed arrivals from the crust through the mantle transition zone. An interpretation of the observed arrival times by forward modeling indicates no pronounced upper mantle low velocity zone, and an important change in the mantle at 225 km depth where the P-wave velocities change from 8.25-8.5 to 8.63 km/sec and higher. The transition zone is similar to other models of the upper mantle. The reversed and overlapping coverage afforded by this data set will allow a particularly precise view into the upper mantle of central Siberia. We plan to extend this analysis to examine the 2-dimensional structure of the upper mantle beneath the Siberian Platform using 2-dimensional ray tracing and inversion of the waveforms.

REFERENCES:

- Chichinin, I.S., G.V. Yegorov, A.V. Yemelianov, and A.J. Bochanov (1969), Portable Telemonitored Seismic Equipment "Taiga", in *Methods of Seismic Research*, 95-119, Nauka, Moscow.
- Given, J. W. and D. V. Helmberger (1980), Upper mantle structure of Northwestern Eurasia, *J. Geophys. Res.*, 85, 7183-7194.
- King, D.W. and G. Calcagnile (1976). P-wave velocities in the upper mantle beneath Fennoscandia and western Russia, *Geophys. J. R. astr. Soc.*, 46, 407-.
- Pavlenkova, N.I. and A.V. Yegorkin (1983), Upper mantle heterogeneity in the northern part of Eurasia, *Phys. Earth Planet. Int.*, 33, 180-193.
- Shearer, Peter M. (1990), Seismic Imaging of Upper-Mantle Structure with New Evidence for a 520-km Discontinuity, *Nature*, 344, 121-126.
- Zonenshain, Lev P., Michael I. Kuzmin, and Lev M. Natapov (1990), *Geology of the USSR: A Plate-Tectonic Synthesis*, Geodynamics Series, vol. 21, American Geophysical Union, Washington, DC.

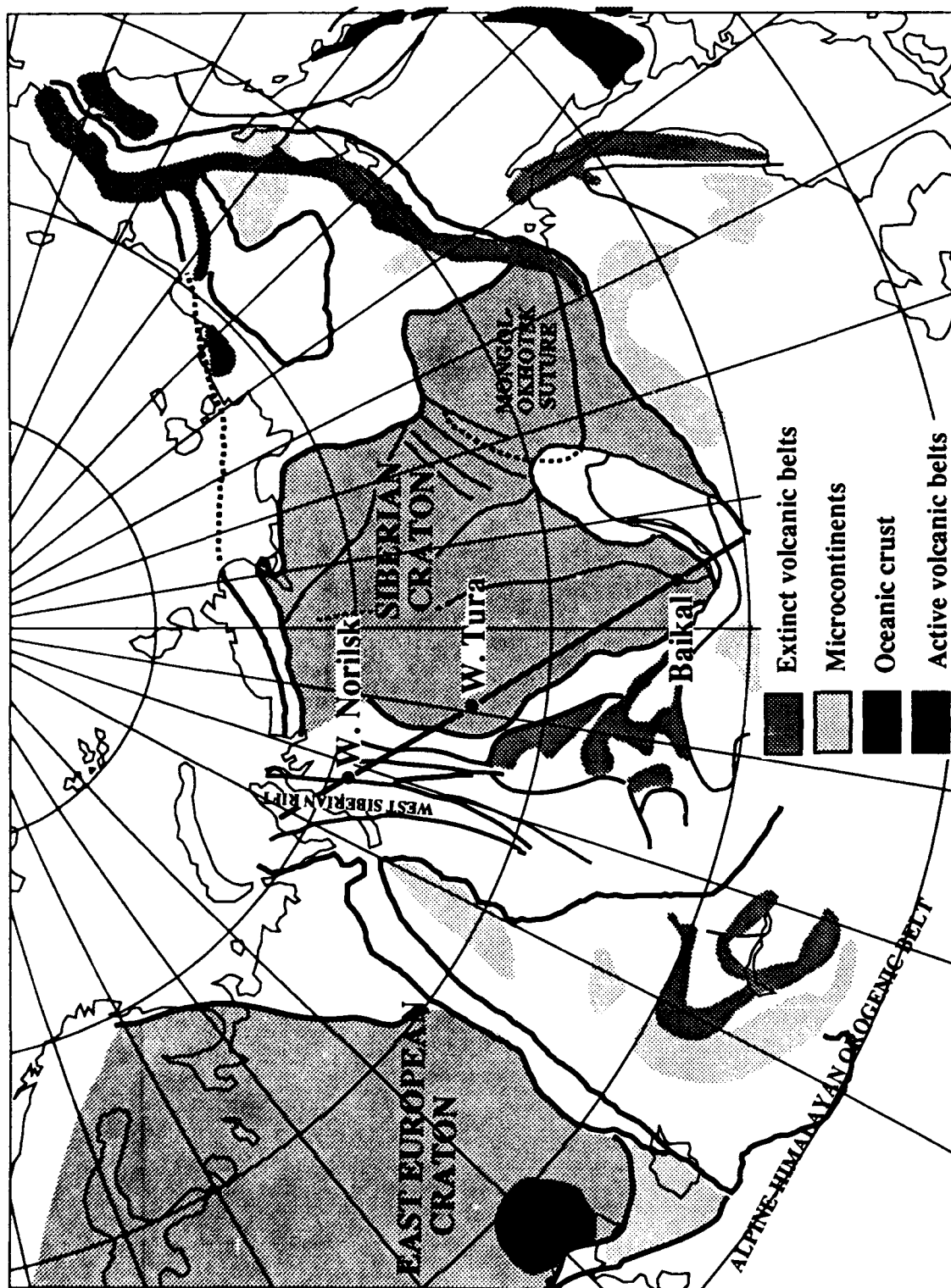


Figure 1. Location of the seismic profile with respect to the simplified geology of Asia. Solid circles denote the W. Norilsk, W. Tura, and Baikal shot points

Fig. 2

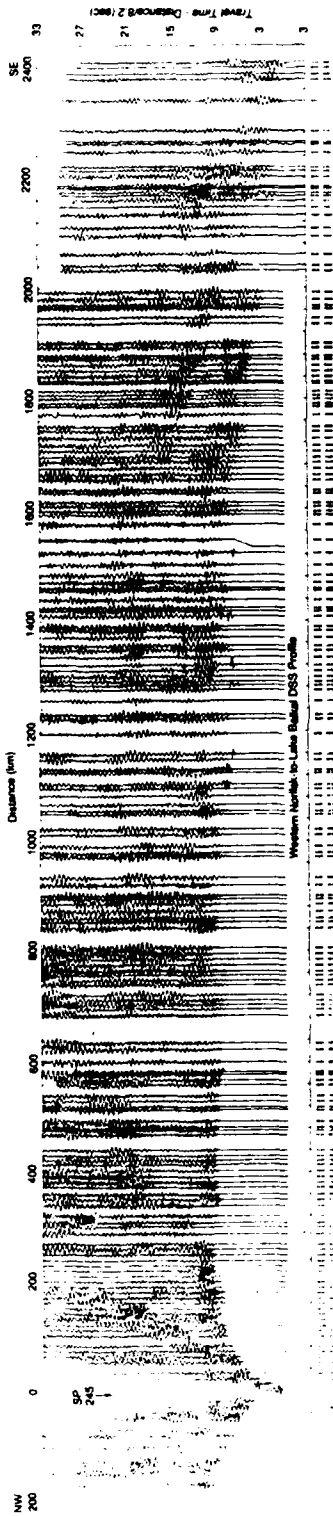


Fig. 3

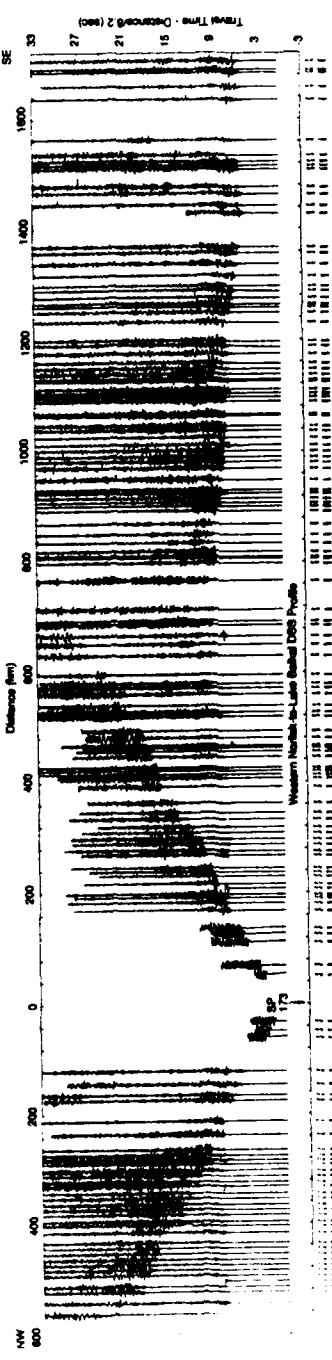
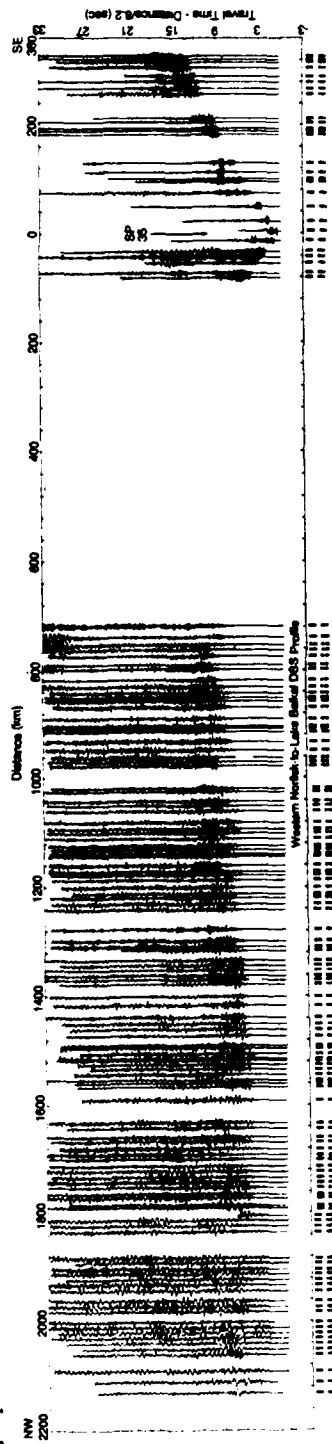


Fig. 4



Figures 2,3,4. Record sections for the three nuclear explosions. The seismograms have been reduced by a velocity of 8.2 km/sec.

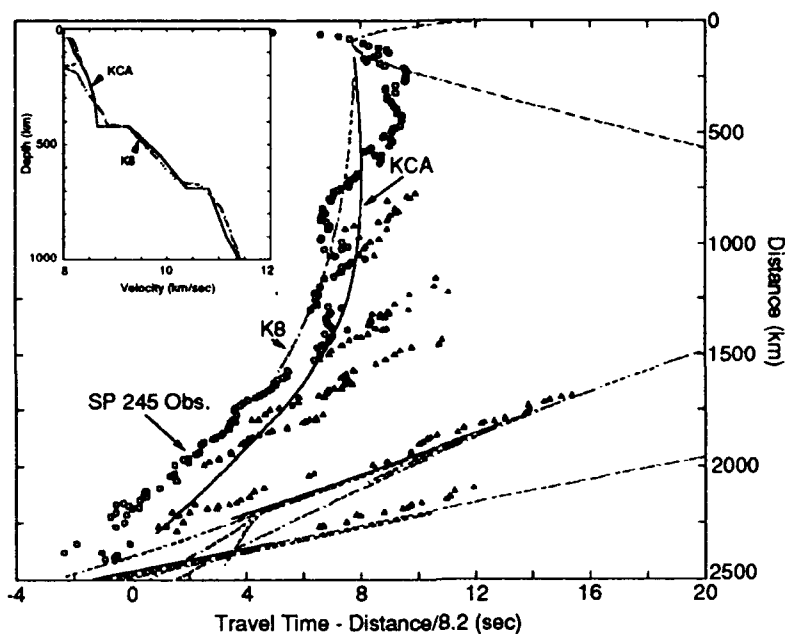


Figure 6. Comparison of the observed arrival times from shot point SP 245 (open circles and triangles) with travel times predicted from models KCA (solid line, King and Calcagnile, 1976) and K8 (dashed line, Given and Helmberger, 1980). The inset shows the velocity-depth functions for both models.

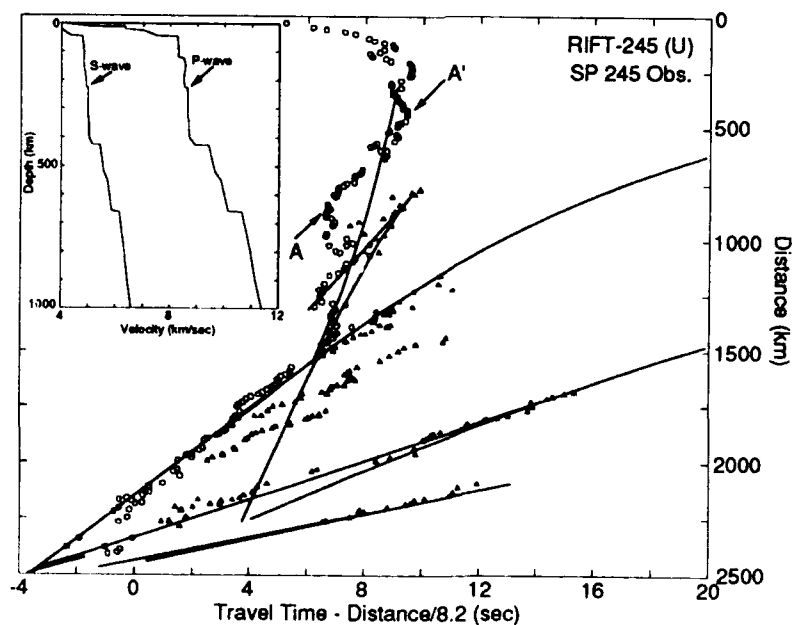


Figure 7. Comparison of the observed arrival times for shot point SP 245 (circles for first arrivals, triangles for later arrivals) and predictions for the RIFT-245 reference model. The inset shows the velocity-depth function.

NEURAL NETWORK PROCESSING OF SEISMIC SIGNAL PARAMETERS FOR SMALL EVENT IDENTIFICATION

Jay J. Pulli[†] and Paul S. Dysart[‡]

[†]Radix Systems, Inc., 201 Perry Parkway, Gaithersburg, MD 20877

[‡]SAIC, 1710 Goodridge Drive, McLean, VA 22102

Contract No. F29610-91-C-DB10

OBJECTIVE

The objective of this research is to test the applicability of artificial neural networks (ANN's) to the problem of small seismic event identification. Our plan calls for the training and testing of an ANN for each station (or array) of a monitoring system using a database of independently identified events. Each ANN produces a preliminary identification based on signal parameters extracted from the event's *Pn*, *Sn*, and *Lg* waves. Final event identification is performed by combining each station's preliminary identification. The system is to be installed as an online processing module of the Intelligent Monitoring System (IMS) for a period of testing and evaluation.

RESEARCH ACCOMPLISHED

Research to date has focused on the following tasks: compilation of the training database, signal parameter extraction and analysis, ANN design, and ANN training and testing.

Compilation of the Training Database. ANN's are not *programmed* but are *trained* using a database of *ground truth*. In our research, this means a database of signal parameters extracted from small regional seismic events which have been independently (and confidently) identified. To date, we have focused our attention on events recorded by the Scandinavian small aperture arrays. Approximately 300 events have been examined; currently, our training database consists of 98 identified events (see Figure 1). The compilation of the training database has been a time-consuming process, with independent and verifiable identifications difficult to obtain. However, we have just received the ANN training database compiled by Sereno and Patnaik (1992); this database is currently being analyzed for inclusion in our experiments.

Parameter Extraction. All of the waveform data are visually reviewed prior to parameter extraction. This insures that data irregularities, such as dropouts, spikes, aliasing, and dead channels will not contaminate the parameter estimation.

P_n , S_n , L_g and noise windows are selected with the aid of time-frequency plots. Currently, 12 parameters are extracted from the waveforms. These parameters are chosen to describe characteristics of the source such as multiplicity, duration, shear excitation, and extent. The 12 parameters are listed in Table 1. Additional information, such as distance, azimuth, magnitude, region, and SNR are stored with the parameters to allow ANN experimentation with database subsets (e.g. identification performance as a function of SNR).

Parameter Analysis. Before ANN design takes place, a number of statistical analyses are performed on the parameter dataset. These analyses are chosen to gain insight into the dataset, including the interrelationship of parameters, their relative importance, and their dimensionality. For each parameter, the difference in scaled means for the two source types (Figure 2) points to parameters which may be important for identification. Figure 2 shows that the largest difference in parameters for the two source types are for parameters 2, 3, and 6. The variance calculation (Figure 3) shows that there is a much larger variance in all of the parameters for the earthquakes than for the explosions. The Kolmogorov-Smirnov test checks for the normality of the parameter distributions. Correlation analysis reveals any obvious redundancies among the parameters (Figure 4). For example, we find that the S_n and L_g spectral ratios are highly correlated, while the TMF is negatively correlated with distance (which is expected from attenuation). Stepwise discriminant analysis (Enslein et al., 1977) ranks each parameter in terms of its relative contribution to the dataset, and is thus used to reduce the dataset to a reasonable number of significant parameters (Figure 5). The six most significant parameters are numbers 6, 3, 2, 4, 5, and 8.

ANN Design. We have primarily used the backpropagation ANN architecture during this research. A single hidden layer is used, since this is sufficient to model any continuous function (Cybenko, 1989). The number of nodes in the hidden layer is chosen with the aid of a Principal Components Analysis (PCA) of the data (Jackson, 1991). PCA is basically an eigenvalue analysis applied to the covariance matrix of the extracted signal parameters. The magnitude of the PC's (Figure 6) indicates a dominance of the first three roots. The cumulative percentage of the variance of the PC's (Figure 7) shows that the first three PC's account for over 85% of the data variance. Based on the statistical analysis and PCA, the current ANN architecture (Figure 8) consists of an input layer with 6 nodes, a single hidden layer with 3 nodes, and an output layer with 2 nodes (earthquake or explosion). The design is consistent with the Kolmogorov sufficiency theorem (Kolmogorov, 1957) which states that the maximum number of hidden nodes equals $2M+1$, where M is the number of inputs.

ANN Training and Testing. Conventional training strategies, such as input normalization, epoch size selection, and learning/recall scheduling are employed during our ANN experiments. Training times are generally less than one hour. The ANN's are evaluated by randomly selecting 50% of the events for training, and

testing with the remaining 50%. An alternative strategy is the *leave-one-out* procedure. A Confusion Matrix for the 98 sample training database is shown in Figure 9. Here, 49 events were used for training, and 49 for testing (equal explosion/earthquake sampling). The matrix shows that all 49 explosions were correctly identified, whereas 46 earthquakes were correctly identified.

CONCLUSIONS AND RECOMMENDATIONS

We have found that ANN's are an effective tool in the processing of seismic signal parameters for event identification. With careful analysis of the training set prior to design, many pitfalls and criticisms of ANN processing can be avoided. Although an ANN can literally fit a model to any dataset, the objective is to use the smallest possible ANN architecture which is consistent with the dimensionality of the data. Additionally, the importance of the training set cannot be overemphasized. Nearly all of the events studied represent uncontrolled cases from the point of view of the seismologist. Careful tracking of the evidence leading to the independent identification should be a top priority.

The next step in our research is to analyze the training set compiled by Sereno and Patnaik (1992). Then, we will test the performance of the ANN's with respect to region, magnitude, number of stations, number of phases, and SNR. We will also investigate the use of single central elements vs. total arrays for parameter estimation and its effect on the ANN's. Finally, the identification software will be installed and tested as an online processing module for the IMS.

REFERENCES

- Cybenko, G. (1989), Approximation by superpositions of a single function, *Mathematics of Control, Signals, and Systems*, 2, 303-314.
- Enslein, K.A., A. Ralston, and H. Wilf (1977), *Statistical Methods for Digital Computers*, Wiley Interscience, 454 pp.
- Jackson, J.E. (1991), *A User's Guide to Principal Components*, Wiley & Sons, Inc.
- Kolmogorov, A.N. (1957), On the representations of continuous functions of many variables by superpositions of continuous functions of one variable and addition, *Doklady Akademii Nauk USSR*, 114, 953-956.
- Sereno, T.J. and G.B. Patnaik (1992), Data to test and evaluate the performance of neural network architectures for seismic signal discrimination, Phillips Laboratory Scientific Report PL-TR-92-2110(I), 53 pp.

| Table 1. Extracted Signal Parameters | |
|--------------------------------------|------------------------------------------|
| 1 | Broadband Pn/Lg spectral ratio |
| 2 | Broadband Pn/Sn spectral ratio |
| 3 | Mean cepstral variance of Pn, Sn, and Lg |
| 4 | Pn/Lg spectral ratio, 2-5 Hz |
| 5 | Pn/Sn spectral ratio, 2-5 Hz |
| 6 | Pn/Lg spectral ratio, 5-10 Hz |
| 7 | Pn/Sn spectral ratio, 5-10 Hz |
| 8 | Pn/Lg spectral ratio, 10-20 Hz |
| 9 | Pn/Sn spectral ratio, 10-20 Hz |
| 10 | TMF of Pn |
| 11 | TMF of Sn |
| 12 | TMF of Lg |

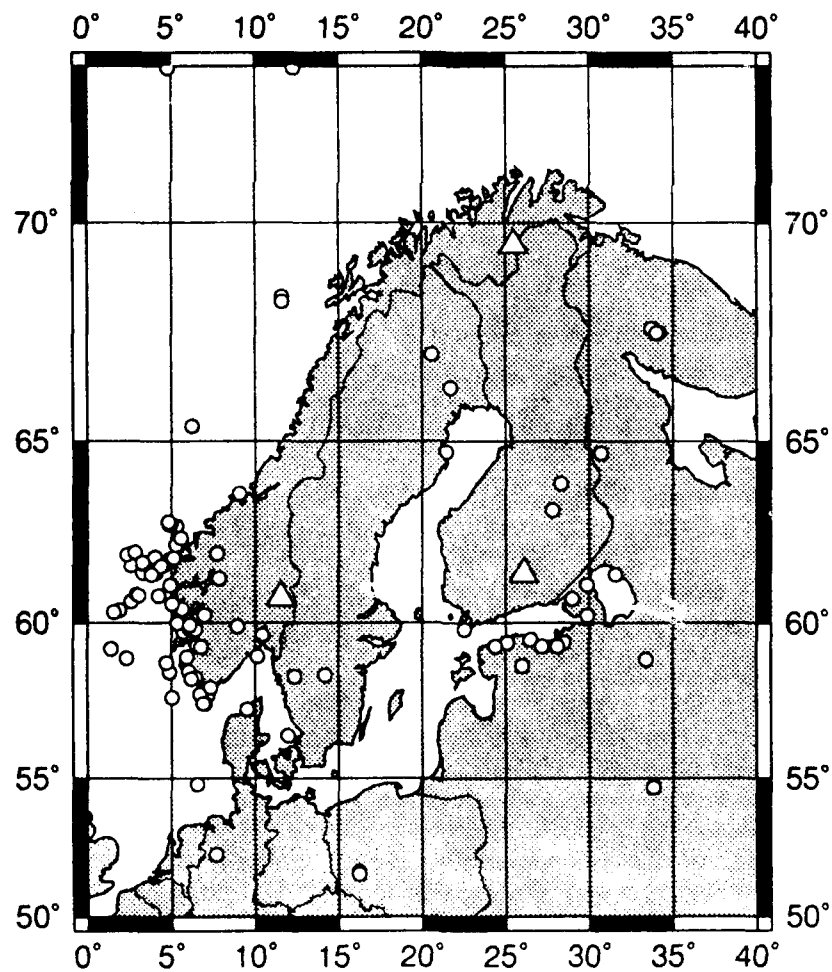


Figure 1. Map of origins in the current training database.

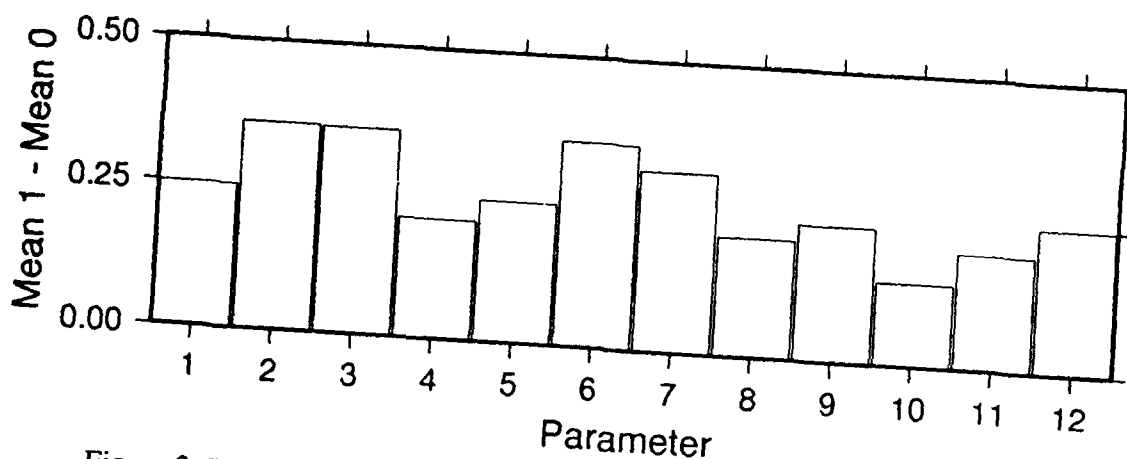


Figure 2. Difference in signal parameter means between earthquakes and explosions

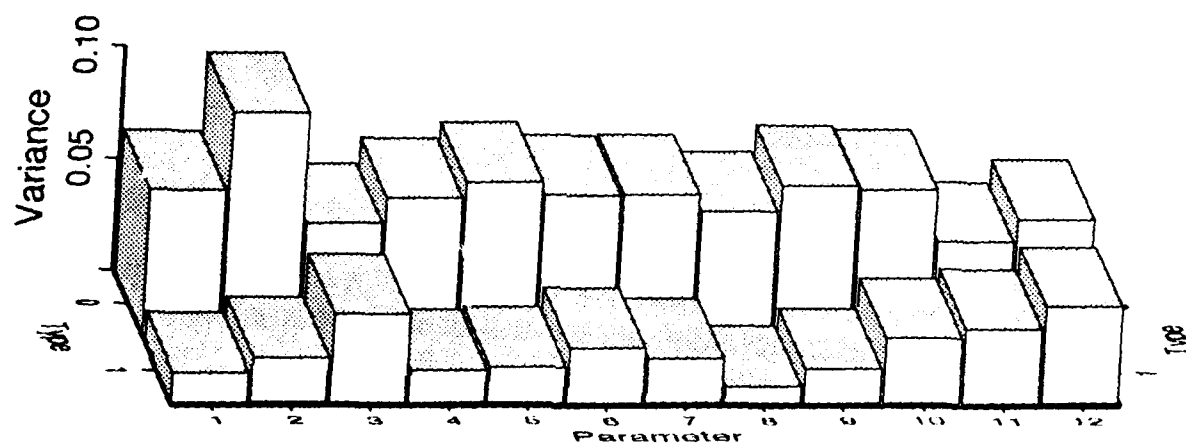


Figure 3. Variance of signal parameters for earthquakes (0) and explosions (1).

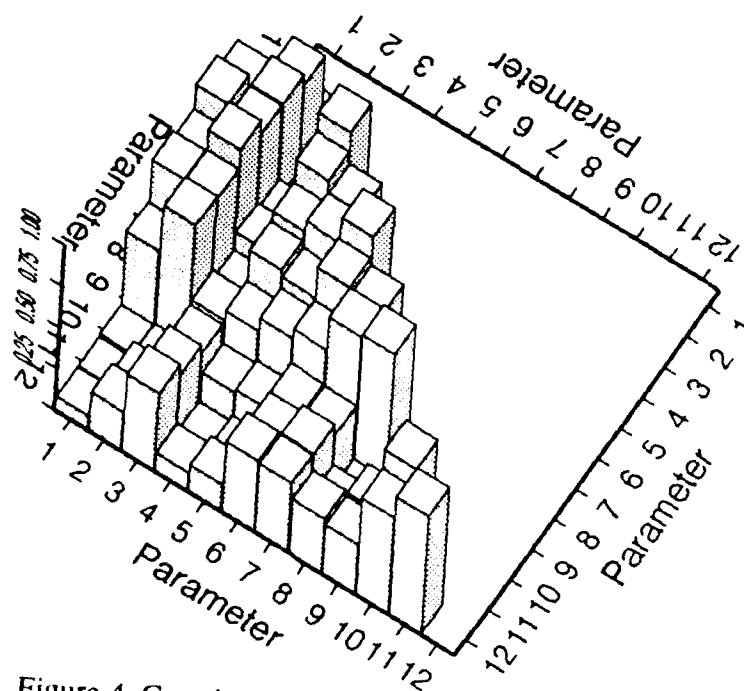


Figure 4. Correlation matrix of signal parameters.

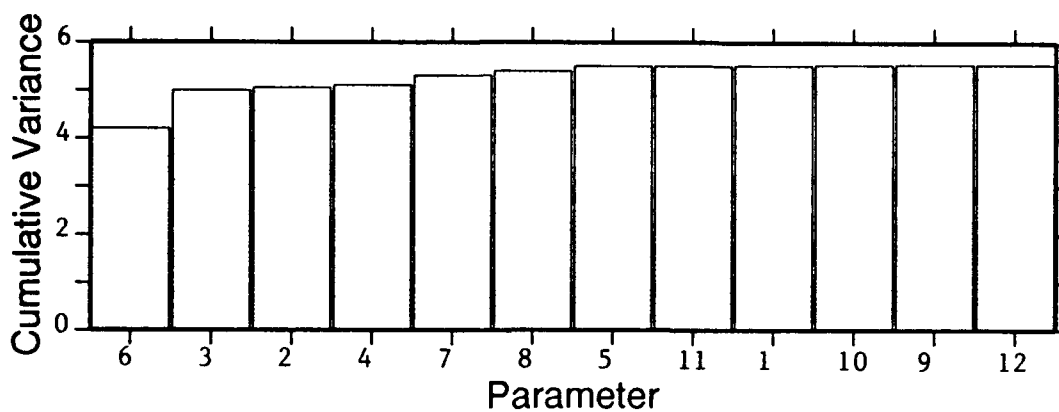


Figure 5. Stepwise discriminant analysis.

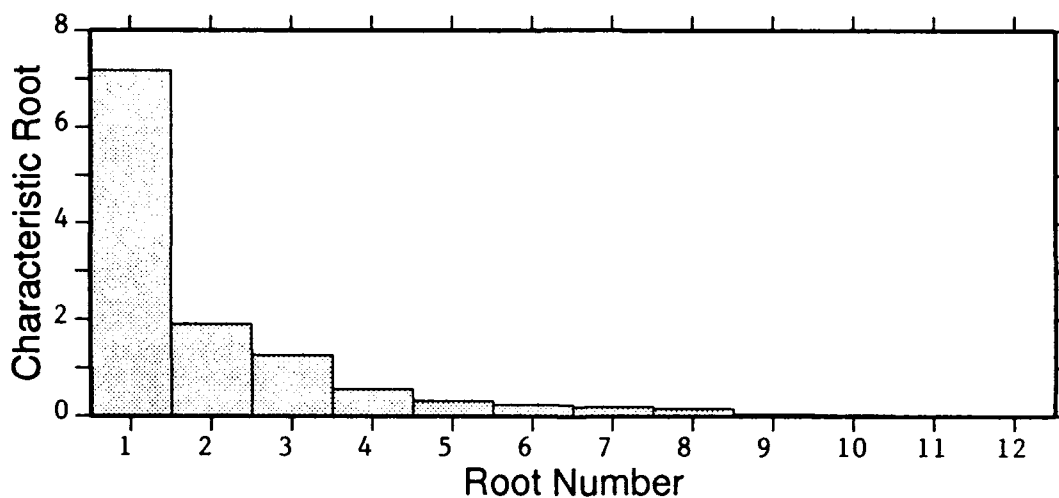


Figure 6. SCREE plot of the training set.

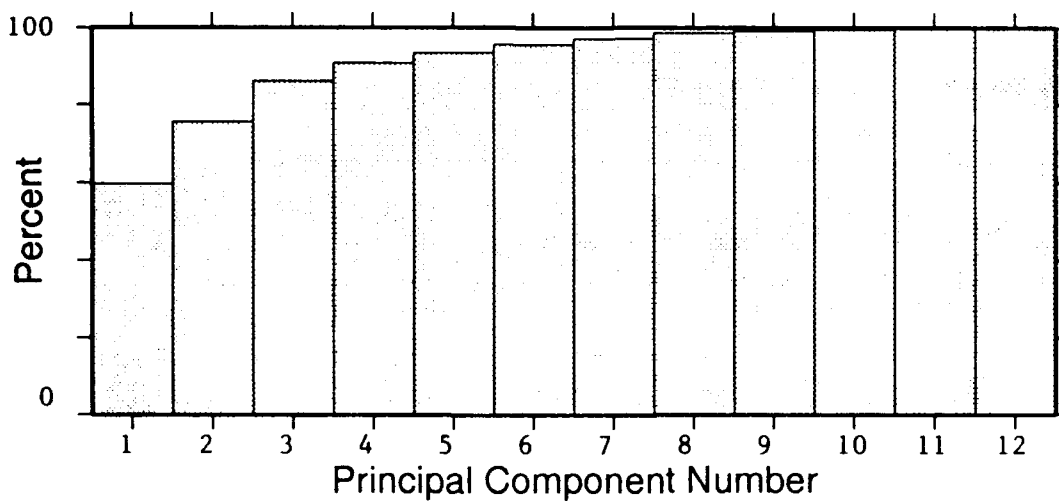


Figure 7. Cumulative percentage of variance of principal components.

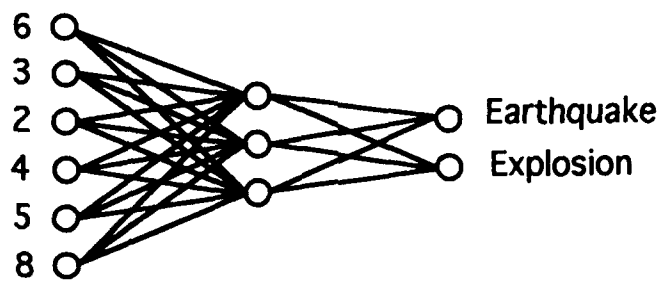


Figure 8. Neural network architecture for identification.

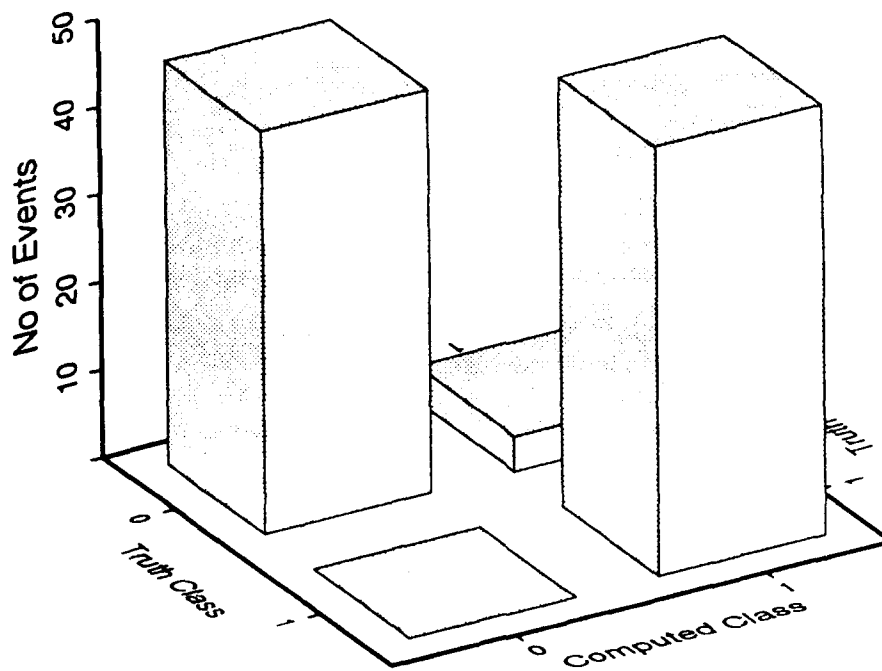


Figure 9. Confusion matrix for identification experiment.

INITIAL VISIT TO THE BOROVOYE GEOPHYSICAL OBSERVATORY, NORTH KAZAKHSTAN

Paul G. Richards, Won-Young Kim (Columbia University)
and Göran Ekström (Harvard University)

F29601-91-K-DB09

OBJECTIVE

In March 1990 at an IRIS workshop, Soviet seismologists told us of a seismic station in Northern Kazakhstan that has been operated to very high standards since 1966. The station maintains an archive for several hundred nuclear explosions (several digital seismograms per shot), and tens of thousands of earthquakes. Some data examples were received in March 1991. In the summer of 1991 two of us visited the station, which is at Borovoye (station code BRV), 53° 03' 29" North, 70° 16' 58" East. We were the first visitors from the United States, and our goal was to learn the history of the station; to obtain descriptions of the instrumentation; and to evaluate the data - especially, the digital archive.

RESEARCH ACCOMPLISHED

We found that the Borovoye Geophysical Observatory has a staff of about 80 people, and that the principal activity is the recording and analysis of about fifty channels of digital seismic data, derived from instruments all in the same vault. The site is on a pluton about 200 km across, with an ill-defined (but deep) Moho and monolithic granites. The site has excellent capabilities for recording NTS explosions, owing to low noise (see Figure 1), and a focussing effect that makes signals from NTS about 0.3 - 0.4 magnitude units larger at BRV than would be expected on the basis of their ISC magnitude. The Observatory has also been the testing site for almost all the major developments of seismic instrumentation in the USSR since the mid-1960's.

Notes on the Main Digital Seismic Systems Operated at BRV

Beginning in 1966, with continuous operation since 1967, the digital seismic system known as KOD (КОД in Russian) was operated until November, 1973. This system used three-component, short-period SKM (СКМ in Russian) seismometers (nominal seismometer period, 3.5s; nominal damping, 0.7). Polarity of all three components, in all digital data we have seen from the KOD system, is reversed. Usually the data are recorded at two different gain levels, listed by Adushkin and An (Table 2 of *Izvestiya: Fizika Zemli*, pp 47-59, December, 1990) as 3,000 counts/micron (normal), and 300 counts/micron (low-gain). A detailed description of the KOD system, and the data format of the associated 17-track wide tape, is given by Shishkevish ("Soviet Seismographic Stations and Seismic Instruments, Part II", R-1647-ARPA, RAND, Santa Monica, June 1975). This format can have a glitch at regular (30s) intervals due to data replacement by a time stamp. Though the KOD system was replaced by better systems (see below), it is important as one of the few digital systems in the late 1960's - early 1970's.

The second main digital system, known as STsR (СТР in Russian), has operated from February, 1973 to the present day. The system consists of two similar parts which operate separately (different seismometers and data loggers). The STsR-SS equipment (СТР-СС in Russian) records at lower gain levels. The STsR-TSG equipment (СТР-ТСГ in Russian) is said to be better for all purposes except strong ground motion recording, and is generally reckoned to be the best system ever operated at BRV.

The STsR-TSG system has many channels, based mostly on modified Kirnos seismometers, with sensitivities as high as 100,000 counts/micron. It is possible to control remotely the period and mass position of these instruments, which typically weigh about 70

kilograms each. The basic instruments are known as KS (short-period) and DS (long-period) (respectively КС and ДС in Russian). If the letter "M" is added, as KSM and DSM, the instrument has a stronger magnet, allowing twice the gain. If letter "V" (Russian В) is included, as KSVM (КСВМ), this signifies a sensitive channel, with special electronics. However, the most sensitive channel (short-period) is based on a KSM instrument, using a low noise amplifier (sensitivity 100,000 counts/micron).

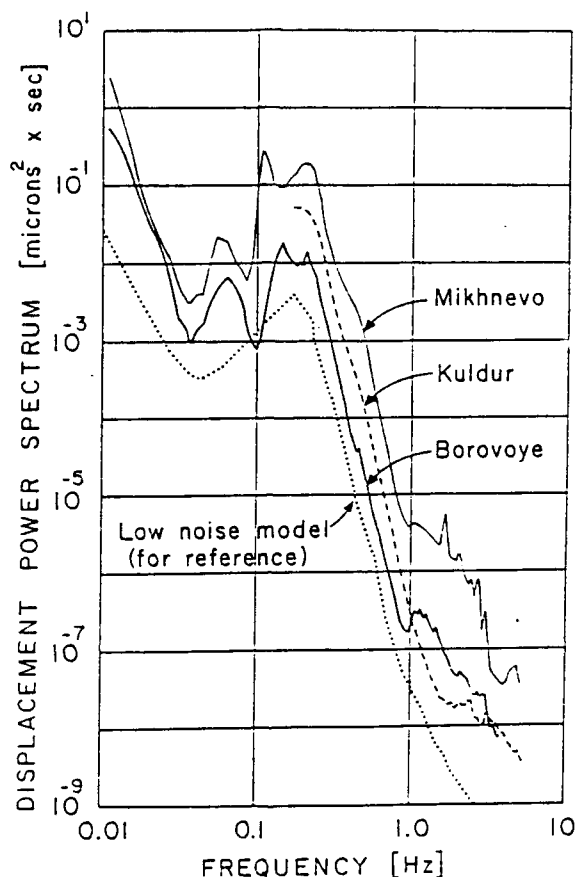


Figure 1. Power spectra of Earth noise at three seismic stations in the USSR, as measured by Nicholai Pleskach. A low-noise model (personal communication from Jon Peterson) is shown for reference.

The STsR-TSG system appears to have 20 channels of digital information: 3 components from KS and DS; 3 components from KSM and DSM, each at 2 gain levels; and a vertical component from KSVM at 2 gain levels.

Nominal gains/sensitivities of the STsR system are listed by Adushkin and An (Izvestiya: Fizika Zemli, Table 2 of pp 47-59, December 1990). But in practice the instrumental characteristics have frequently been changed. We were shown extensive tables listing gains at different frequencies for different time periods, for the many channels of digital data.

The third main system is known as ASSTs (АССЦ in Russian, these letters standing for "Automatic Digital Seismic Station"). It employs feedback seismometers, has operated from April, 1990 to the present day, and is described in the doctoral thesis of Igor Bashilov. The system utilizes a broadband seismometer and records long-period, short-period, and broadband channels. The seismometer, known as SSM-S (ССМ-С in Russian), is said to suffer from long-period

noise, and the electronics too are noisy. The good feature of the system is its high dynamic range, achieved through gain-ranging. Some channels use a logarithmic amplifier, with amplitude linearly related to magnitude.

All three of these main systems are approximately flat to ground displacement over a range of frequencies.

Timing for these three systems has been good to ± 10 ms for the 25 years of digital recording. For the last 10 years, timing has come from the "exact time service of the USSR."

Routine Data Analysis and Reporting Practice at BRV

There are three types of routine reporting: urgent, daily, and weekly. Urgent and daily reporting is via teletype to Obninsk. A weekly seismicity bulletin is published at Borovoye. Urgent reporting is done within the hour after a *P*-wave arrival from a large event. It was stated that a computer estimate of hypocentral coordinates is available two minutes after a *P*-wave arrival with good signal-to-noise ratio.

At approximately zero hours GMT, a daily message is sent to Obninsk, using a standard format for transferring level 1 data (arrival times, amplitudes, periods) recorded at BRV. An agreement has been concluded between Obninsk and the USGS/NEIC in Golden, Colorado concerning the rapid transfer between Golden and Obninsk of this type of data for large events.

We were told that BRV detects about 1000 seismic events every month, and that about 100 are routinely processed (including an estimate of source location) using only the data from this station. This information is summarized in a weekly bulletin, published in Borovoye. On July 30, 1991, we were given a copy of the bulletin for July 18 - July 24. It contains level 1 information on about 400 arrivals, and location estimates plus magnitudes for 17 events. Many of the reported arrivals are multiple reports of the same phase (e.g. the main *P*-wave) on different instruments. The weekly bulletin contains a wealth of information on global seismicity. Table 1 lists the hypocenter estimate, origin time estimate, and magnitude, as reported in the BRV weekly bulletin for July 18 - July 24. Table 2 gives the corresponding information from USGS/NEIC Quick Determination of Epicenter (QED) listings, which of course are based on data from many stations around the world. We have included in Table 2 only those QED events with magnitude greater than 5.5, or which were reported by BRV. Data in italics in Table 2 are based on BRV data taken from Table 1, to enable comparisons between BRV and QED for those eleven events in common. The last two columns of Table 2 give the azimuth and distance from BRV to the estimated epicenter.

We were told that BRV has a detection capability down to magnitude 4.2 for all parts of the globe. At some distances (e.g. in the core shadow) the detection is based on a phase other than *P*. It will be interesting to see the basis for this claim. We saw several charts used at BRV to provide azimuth and distance corrections to the initial azimuth/distance estimates, in order to provide the location estimates circulated by the Borovoye Observatory. From a comparison of italicized (BRV) and non-italicized numbers (QED) in the last two columns of Table 1, and by direct comparison of epicenter estimates, it is apparent that the single station location capability of BRV has RMS errors around 2° in distance (zero mean) and 5° in azimuth (around a mean about 5° lower in value).

We were told that whereas OBN operates LP instruments at gains of only 250 to 500, BRV is able to operate LP instruments at gains of 10,000 to 20,000. However, if events are detected only via surface wave signals, such events are not included in the Borovoye bulletin.

The work of routine analysis appears to be done mainly by women living a few km away in the town of Borovoye. With years of experience, several have become highly proficient in seismogram reading. Work is done around the clock in three shifts. More and more of the work is

| UTC TIME | LAT° | LONG° | MPV | MLH | MPV | REGION | AZ° | AZ° | DELTA° |
|-------------|--------|---------|----------|-----|--------|---------------------|--------|----------|----------|
| HRMNSec | (COMP) | (COMP) | (MANUAL) | | (COMP) | | (COMP) | (MANUAL) | (MANUAL) |
| 1991 JUL 18 | | | | | | | | | |
| 045446.0 | 2.32S | 130.91E | 6.0 | - | - | NEW GUINEA | | 130.0 | 74.8 |
| 091521.0 | 3.53S | 129.39 | 5.1 | - | - | SERAM, INDONESIA | | 132.0 | 75.0 |
| 115615.0 | 44.57N | 19.06E | 5.8 | 5.5 | 6.04 | YUGOSLAVIA | 276.7 | | 34.1 |
| 203349.0 | 5.78S | 10.79W | 5.0 | - | 5.02 | MID-ATLANTIC RIDGE | 259.4 | | 89.3 |
| 1991 JUL 19 | | | | | | | | | |
| 012758.0 | 46.31N | 24.23E | 4.9 | - | 5.06 | ROMANIA | 270.6 | | 30.0 |
| 1991 JUL 20 | | | | | | | | | |
| 114844.0 | 52.25N | 165.63W | 6.2 | 5.7 | - | ALEUTIAN ISLANDS | | 30.0 | 64.8 |
| 1991 JUL 21 | | | | | | | | | |
| 143302.0 | 29.81N | 91.65E | 4.9 | - | 5.30 | CHINA | 147.0 | | 28.0 |
| 225913.0 | 1.38N | 124.40E | 6.2 | 5.2 | - | SULAWESI, INDONESIA | | 130.0 | 68.2 |
| 1991 JUL 22 | | | | | | | | | |
| 141328.0 | 41.86N | 52.60E | 5.4 | 3.8 | - | CASPIAN SEA COAST | 239.0 | | 16.3 |
| 171252.0 | 21.29N | 139.95E | 5.3 | - | 5.37 | MARIANA ISLANDS | 91.6 | | 61.0 |
| 1991 JUL 23 | | | | | | | | | |
| 112208.0 | 8.27N | 126.25E | 6.0 | - | 6.12 | MINANAO, PHIL. IS. | 123.7 | | 63.4 |
| 132543.0 | 3.04N | 93.64E | 6.3 | 5.1 | - | SUMATERA ISLAND | | 150.0 | 53.6 |
| 174545.0 | 38.67N | 21.41E | 4.6 | - | 4.65 | GREECE | 261.3 | | 36.1 |
| 211637.8 | 3.82S | 131.53E | 5.5 | - | 5.49 | NEW GUINEA (h=100) | 130.3 | | 76.4 |
| 1991 JUL 24 | | | | | | | | | |
| 094345.5 | 41.64N | 37.64E | 5.6 | 5.0 | | BLACK SEA | | 253.0 | 24.6 |
| 135416.7 | 20.22S | 22.76E | 5.4 | - | 5.39 | SOUTH AFRICA | 224.1 | | 84.0 |
| 152446.0 | 45.29N | 82.04E | 4.7 | - | - | USSR-CHINA BORDER | | 135.0 | 10.9 |

Table 1. The last page of the BRV weekly bulletin for 1991 July 18-24, giving epicenter estimates and magnitudes for seventeen earthquakes. Some columns are worked up automatically on the ASSTs system (COMP); some are done by hand (MANUAL).

NEIC QUICK EPICENTER DETERMINATIONS, compared with
BRV SINGLE STATION EPICENTER DETERMINATION

| UTC TIME HRMNSEC | LAT | LONG | DEP | GS | MAGS | SD | STA | REGION--COMMENTS | AZ (BRV) | DELTA (BRV) |
|---------------------|---------|----------|------|-----|------|-----|------|---------------------------|----------|-------------|
| | | | MB | | Msz | | USED | | | |
| 1991 JUL 18 | | | | | | | | | | |
| 115633.9 | 44.880N | 22.280E | 33N | 5.8 | 5.6 | 1.1 | 121 | ROMANIA | 274.9 | 32.0 |
| 115615.0 | 44.57N | 19.06E | | 5.8 | | | 1 | YUGOSLAVIA | 276.7 | 34.1 |
| 1991 JUL 19 | | | | | | | | | | |
| 012732.8 | 45.373N | 21.255E | 33N | 5.6 | | 1.0 | 82 | ROMANIA | 276.4 | 32.4 |
| 012758.0 | 46.31N | 24.23E | | 4.9 | | | 1 | ROMANIA | 275.9 | 30.1 |
| 1991 JUL 20 | | | | | | | | | | |
| 114847.5 | 54.553N | 161.637W | 36D | 5.8 | 5.5 | 1.3 | 133 | ALASKA PEN. | 30.6 | 64.5 |
| 114847.5 | 52.25N | 165.63W | | 6.2 | | | 1 | ALEUTIAN ISLANDS | 34.1 | 65.1 |
| 1991 JUL 21 | | | | | | | | | | |
| 225909.1 | 3.007N | 128.477E | 33N | 5.8 | 5.2 | 1.0 | 67 | NORTH OF HALMAHERA | 114.6 | 68.9 |
| 225913.0 | 1.38N | 124.40E | | 6.2 | | | 1 | SULAWESI, INDONESIA | 119.2 | 68.1 |
| 1991 JUL 22 | | | | | | | | | | |
| 171245.5s | 23.669N | 143.961E | 33N | 5.0 | 4.1 | 1.8 | 18 | VOLCANO ISL REGION | 87.7 | 61.7 |
| 171252.0 | 21.29N | 139.95E | | 5.3 | | | 1 | MARIANA ISLANDS | 92.7 | 61.1 |
| 1991 JUL 23 | | | | | | | | | | |
| 112209.9 | 5.813N | 125.957E | 146s | 5.6 | | 1.3 | 63 | MINDANAO, PHIL. ISLS | 115.2 | 65.2 |
| 112208.0 | 8.27N | 126.25E | | 6.0 | | | 1 | MINDANAO, PHIL. ISLS | 113.4 | 63.4 |
| 132545.8 | 3.790N | 95.986E | 33N | 5.8 | 5.1 | 0.9 | 105 | OFF W COAST OF N SUMATERA | 147.4 | 53.5 |
| 132543.0 | 3.04N | 93.64E | | 6.3 | | | 1 | SUMATERA | 150.5 | 53.5 |
| 174545.2s | 34.631N | 25.631E | 33N | 4.3 | 3.9 | 1.4 | 20 | CRETE | 257.7 | 36.4 |
| 174545.0 | 38.67N | 21.41E | | 4.6 | | | 1 | GREECE | 266.6 | 36.2 |
| 211624.3s | 6.155S | 130.373E | 33N | 5.8 | 4.6 | 1.3 | 32 | BANDA SEA | 118.1 | 77.6 |
| 211637.8 | 3.82S | 131.53E | 100 | 5.5 | | | 1 | NEW GUINEA | 115.8 | 76.3 |
| 1991 JUL 24 | | | | | | | | | | |
| 094542.7 | 36.483N | 44.072E | 33N | 5.5 | 5.6 | 1.0 | 105 | IRAN-IRAQ BDR REG. | 238.4 | 24.7 |
| 094545.5 | 41.64N | 37.64E | | 5.6 | | | 1 | BLACK SEA | 255.6 | 24.7 |
| 135447.9 | 18.382S | 34.721E | 10G | 5.1 | 5.1 | 1.1 | 37 | MOZAMBIQUE | 214.4 | 77.5 |
| 135416.7 | 20.22S | 22.76E | | 5.4 | | | 1 | SOUTH AFRICA | 224.2 | 83.8 |

Table 2. A comparison between the Quick Epicenter Determination (QED) listings of the US Geological Survey, and the epicenter determinations of the BRV bulletin, for the eleven events on both lists for the week of 1991 July 18-24. Lines in the table giving BRV measurements/estimates are italicized. For this week, all eight QED events with magnitude (NEIC) greater than or equal to 5.5 are in the BRV bulletin. Three smaller QED events are also listed by BRV. Each list has just one deep earthquake, but for QED it is the Philippines event of July 23 and for BRV it is the "New Guinea" event (Banda Sea, according to QED) of July 23. Finally, note that the complete BRV listing (Table 1) contains six events not listed by QED.

being transferred to computer-based analysis, using the ASSTs system. A paper by Kedrov and Ovtchinnikov, describing the automatic processing at "an experimental station in Eastern Kazakhstan....near Kokchetav" (it is obviously Borovoye, though this is not stated) appears in the Bulletin of the Seismological Society of America, special issue of December, 1990.

Extent of Data Archive

On a typical day at BRV, the last three days of continuously recorded digital data for all channels are available on disk. An archive tape is then made for one day. The whole process of building the archive has been limited principally by the cost of acquiring magnetic tape. Thus in the routine processing of the data, phases are identified and data windows with phases are collected (about 100 files per day) in the data archive. Anything that looks like signal is saved, even if the source of the signal cannot be identified. There is no archive of continuous data. The archive consists of approximately 5000-10000 17-track tapes. Each tape contains around 10 megabytes of data. We were told that the archive contains 70 gigabytes of data going back to 1966. The station has archived 2 gigabytes of data per year in recent years.

Subsequent to our visit we made many further inquiries concerning the contents of the archive, details of tape formats, and the condition of all the old tapes. We understand that there is a separate archive of about 1,100 tapes for nuclear explosions: virtually all explosions since the mid 1960's are included, for explosions conducted by France, China, USSR, UK and USA. Also, the Borovoye archive includes digital recordings made at Garm (Tadjikistan), and Talgar (Kazakhstan) and a few other Soviet-operated stations, for some nuclear explosions (including some from Lop Nor). Figure 2 shows two BRV recordings of two double explosions at the Kazakhstan test sites (distance about 700 km). The upper example is from 1972, the lower from 1978. In each case, an explosion at Degelen Mountain (DM) is followed about 10 s later by a larger explosion from the Shagan River (SM) test site. Since this is digital data, we can look at the two Degelen signals on an expanded scale and compare them as in Figure 3. The excellent agreement of the two waveforms, recorded about six years apart, shows that these events were located very close to each other.

CONCLUSIONS AND RECOMMENDATIONS

The Borovoye digital seismogram archive is unique from many perspectives. Most important, for modern research, is the high quality data recorded at regional distance for some hundreds of nuclear explosions conducted at the Semipalatinsk test sites, in Western Kazakhstan, and at Lop Nor. But the earthquake archive also is important, particularly for assessment of the capability to monitor seismic activity in Southern and Central Asia.

We have placed some examples of BRV seismograms, in AH format, with the Center for Seismic Studies. Some of our preliminary analyses of BRV signals are described in a related paper ("Studies of RMS Lg Data") at this meeting.

Our "initial visit" was a small project, and our trip report (September 1991) noted that the archive was physically deteriorating. We pointed out that an effort to salvage the archive and make it useful would entail a two-step process. First, to copy all the wide tapes (approx. 7500, holding about 70 gigabytes) to a modern recording medium. (The wide tapes are 17 track, and can hold up to 24 channels of digital information.) Second, working with BRV personnel, to incorporate all necessary information on instrument responses, and to generate a new archive in a modern format easily used by the international community. Now, twelve months later, we have made significant progress in implementing both these recommendations.

Finally, we note that the "discovery" of Borovoye by scientists from the West has opened up many new avenues for joint research with scientists in Russia and Kazakhstan. About 20 scientists and technicians from the U.S. associated with the Joint Seismic Program are working at Borovoye in summer and fall, 1992.

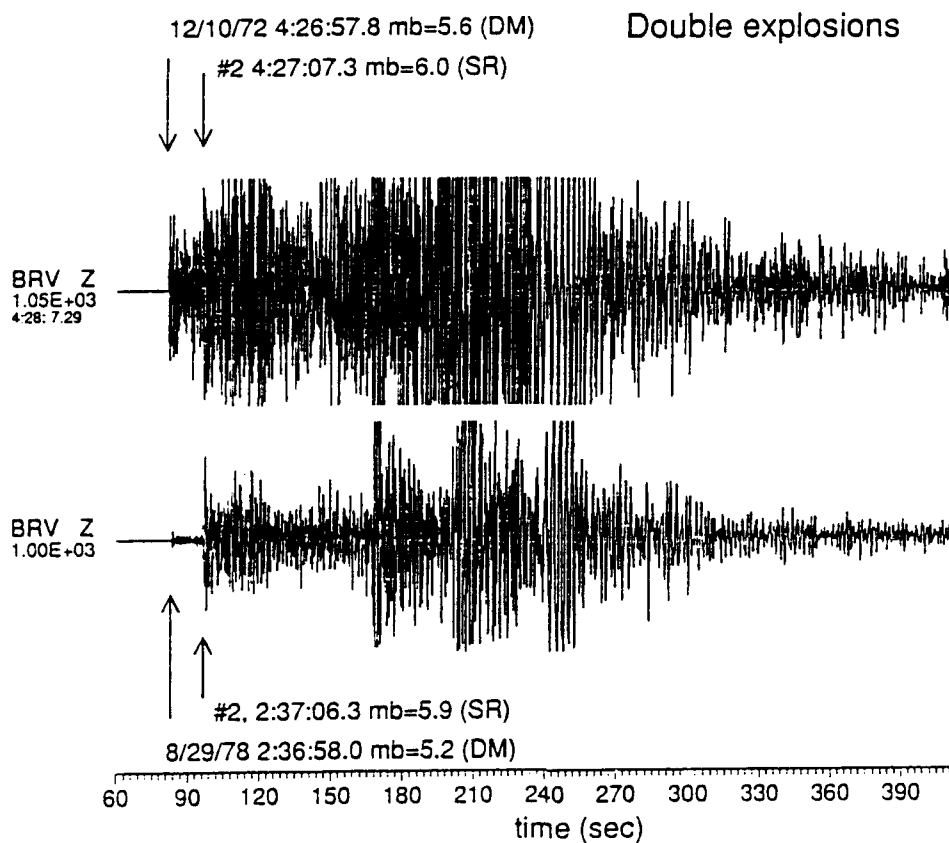


Figure 2: The short-period BRV records of two double explosions.

Events on 8/29/78 2:36:58.0 & 12/10/72 4:26:57.8 @Degelen mb=5.2 & 5.6

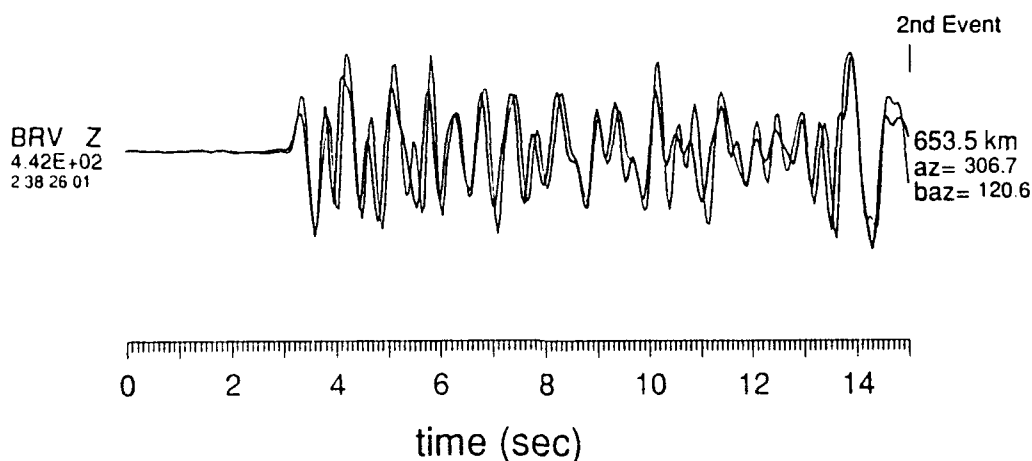


Figure 3: Comparison of two Dege'len explosions, recorded at BRV.

Regional Wave Propagation and High-Frequency/Low-Frequency Energy Level Discriminant

by C. K. Saikia¹, D. V. Helmberger² and L. J. Burdick¹

¹Woodward Clyde Consultants, 566 El Dorado Street, Pasadena, CA 91101

²Seismological Laboratory, CIT, Pasadena, CA 91125

Contract F29601-91-C-DB01

OBJECTIVES: Our primary objective is to estimate the source characteristics of explosions and earthquakes for small magnitude events within the Soviet Union and China using regional waveform modeling techniques. The regional waveforms are complex but can be modeled to a relatively high frequency using a vertically stratified crustal waveguide. Therefore, this study requires calibration of the regional wave propagation characteristics. We have completed the calibration of crustal structure around WMQ (Urumqi) using the digital earthquake data from China and waveguides around BAY (Bayanul), KKL (Karklinsk) and BRV (Borovoye) using explosion generated digital data in the Soviet Union. These calibrated crustal models are used to synthesize both explosion and earthquake seismograms at regional distances and evaluate the strength of the $M_L:M_o$ discriminant originally proposed by Helmberger *et al.* (1991).

RESULTS: The new digital seismic stations in the IRIS/IDA and Chinese networks are providing additional information regarding regional wave propagation within the Eurasian continent. In this study, we have used the digitally recorded regional seismograms at GAR (Garm), KIV (Kislovask), KMI (Kunming), BRV, KKL, BAY and WMQ (Figure 1). To understand the regional waveguide around WMQ, KIV, GAR and KMI, we have selected regional waveforms from earthquakes having large magnitudes so that they are recorded teleseismically. The teleseismic data is used to fix event mechanism, depth and time function. The events modeled to date have exhibited relatively clear depth phases at teleseismic ranges, particularly the direct S and sS pairs. The crustal models for the stations located in the Soviet Union are calibrated by modeling the digital data of the Soviet JVE of September 14, 1988. The crustal model proposed by Langston (1990) was found adequate for modeling the entire long-period waveform recorded at BAY and KKL. These stations are 255 km away from the JVE location at east Kazakh (Shagan river). The waveguide from the Shagan river to BRV is complex and is developed by modeling the JVE digital data recently released to CSS by Richards *et al.* (1992).

This report will begin with the modeling of regional waveforms at WMQ showing the influence of a layered crustal structure. Similar modeling results will be presented on the waveforms recorded from the JVE within the Soviet Union. Additionally, we shall discuss the source characteristics of the Soviet JVE in terms of the reduced potential (Ψ_∞), B and K (Helmberger and Hadley, 1981). The results from a numerical experiment will be presented to further suggest that the energy ratio in the (WASP) and (3090) bands, as previously discussed by Helmberger *et al.* (1991), will possibly discriminate an explosion from an earthquake.

Calibration of Crustal Structure at WMQ

Many earthquakes of different magnitudes have been recorded at WMQ from regional distances. We have chosen an earthquake from the Kazakh-Xinjiang border region that occurred on June 14, 1990 (12:47:28.8s, 47.869N 85.076E, PDE). This is a large magnitude earthquake, m_b of 6.1, and was recorded digitally at many teleseismic stations. We collected the digital seismograms at all these stations from the U.S. Geological Survey, Seismological Laboratory at Albuquerque. Of these, we used the P and SH waves only from the broadband stations i.e., COL, KEV and HRV to examine the source process. Using the direct and the depth phases, we successfully modeled both the P and SH waves and found that this earthquake is a complex event and consists of two sources separated by about 5s. The time function of each source is a triangle with equal rise and fall off time of 0.3s. The focal mechanism published in the PDE monthly listing was a moderately well controlled solution and was used in this study. The depth of the event is shallower at 35 km than the source depth of 58 km reported in the PDE listing. The agreement between the synthetic and observed teleseismic waveforms is shown in Figure 2. The major features are in good agreement.

Having established the source complexity and event depth, we have attempted to model the regional P_n and S_n waveforms recorded at WMQ, located 495 km away from the epicenter. We used two crustal models, one consisting several layers (taken from Barker, 1991) and the other an approximate model consisting of one layer lying above a half space to model the regional waveforms. To investigate the relative effects of the two structure models, we have computed frequency-wavenumber synthetic seismograms using the computer code FILON_AS (Saikia, 1992). The comparison between the data and the synthetic seismograms for both vertical and radial components is shown in Figure 2. Clearly, the synthetic seismograms computed for the layered crust exhibit a better agreement to the data although a correlation of the various phases can be observed in the synthetics from the two crustal models. The relative amplitude of the high-frequency P_n waveforms, especially of the initial P_g window relative to the P_n window, is generally influenced by the velocity structure within the upper stratified crust (Saikia and Burdick, 1991). This feature is also observed in the recorded waveforms at WMQ. The evolution of the P_n is as strong as the starting of the S_n waves in the recorded data and is reflected in the synthetic seismograms of the layered model much more closely than in the half-space model.

Calibration of the Regional Structure in Soviet Union

The objective of this study was to examine the influence of crustal structure on the digital waveforms that were recorded from the 1988 Soviet JVE explosion at three stations: BAY, KKL and BRV. Of these, the path from the JVE explosion site to BRV is highly interesting because the extent of new data that have already been released and are expected to be released from the Borovoye Geophysical Observatory (Richards *et al.*, 1992). The first digital seismic system at the Borovoye observatory operated continuously from 1967 to 1973 and the second system has operated continuously from 1973 to 1992. Thus, we expect a large amount of seismic data to be available to the scientific community from the Soviet nuclear test site for both earthquake and explosion sources. Station BRV is located at about 690 km from the east Kazakh test site. This is a regional distance and the short-period waveforms are expected to be affected by the waveguide. To calibrate this crustal structure, it is desirable to use waveforms from events that have been studied in great detail. The most suitable event for this purpose is the Soviet JVE explosion because it has been recorded at several near-regional distances.

The following strategy was adopted to calibrate the crustal structure along the path from the east Kazakh test site to Borovoye. First, we determine the source information of the Soviet JVE explosion. This is accomplished by modeling both the body and the Rayleigh waves recorded at BAY and KKL (Figure 3). The parameters defining the source function have the following values: $\Psi_\infty = 2.0$, $B = 1$ and $K = 16$ obtained by comparing the synthetic seismograms with the recorded data. The explosion seismograms were computed at 255 km for these two stations using the crustal model suggested by Langston (1990). We neglected the influence of tectonic release because this effect has previously been shown as minimal in the study of Walter and Patton (1990). An anelastic medium was used with a Q_β distribution of 150 and 500 in the upper 12 and 24 km of the crust respectively. For the remaining crust, a Q_β of 1500 was used. The relation $Q_\alpha = 2Q_\beta$ was used for the entire crust. Ψ_∞ was determined by taking the ratio of peak amplitudes of Rayleigh waves obtained by convolving both the data and the synthetic with a (3090) instrument response. The other two parameters B and K were determined by modeling the body-wave data. The initial body-wave part of the data is shown separately for a 9s time window. Figure 3 shows a comparison between data and synthetic seismogram at these two stations at different frequency bands. The seismograms shown on the left correspond to the displacement waveforms as recorded (top two seismograms for KKL and bottom two for BAY) and as predicted (middle two seismograms). The seismograms on the right correspond to those obtained after convolving with the (3090) instrument.

To model the crustal structure to BRV, we have used the seismogram recorded on the DS seismic system which has a frequency band-width approximately from 0.015 Hz to 1.3 Hz (see Figure 2 of Richards *et al.* 1992). This is a relatively long-period recording system but with enough high-frequency response to trap the short-period features on a seismogram. To ensure that the JVE waveforms recorded at BRV are stable, we compared these waveforms with those recorded on the same system from two other explosions, corresponding to the explosions of November 11, 1988 (03:30:06.26s, $M_b = 5.2$) and April 3, 1988 (01:33:08.12s, $M_b = 5.99$) respectively. The waveforms are remarkably similar.

To develop the final crustal model, we started with the generalized ray theory seismograms consisting mainly of the P_mP and pS_mS rays. The first ray was used to define the thickness and the average P velocities in a layer over a half-space model. The half-space P velocity was fixed by correctly predicting the travel time of the first recorded P onset. The second ray was used to define an average S velocity within the layer relative to the P velocity so that the onset of the S_m waveforms can be predicted. The recorded seismograms showed three distinct phases within the initial 45s. The initial phase is a P_n wave. To model the arrival times of the remaining two phases, a Conrad discontinuity was needed. The phase which follows the P_n is a Moho reflected phase with the remaining phase coming from the Conrad discontinuity. This initial model was then further discretized in a manner so that the Rayleigh waves and the other high-frequency body waves can be modeled. The final model is shown in Figure 4. The layering structure near the surface was needed to model the Rayleigh waves and the gradient structure across the crust-mantle transition zone was needed to produce appropriate shape and strength of the P_n and S_m waves.

The above model was used to synthesize the final seismograms. The Green's function computed for the explosion using the F-K algorithm was convolved with the source function and with a minimum-phase instrument response. Figure 5 shows a comparison between the data and synthetic for both vertical and radial components and for both the DS recording system and the 3090 instrument. While the synthetic waveforms are in good agreement with the data, the mismatch in the peak amplitudes is significant. We believe that this is possibly caused by the instrument rather than by any other source. The tectonic-release component could not be an explanation because both KKL and BRV are oriented along a similar azimuth and such an amplitude discrepancy does not exist at KKL. Therefore, we propose to use the amplitude mismatch factor obtained by comparing the 3090 instrument response at BRV as a correction factor for the DS system until a better understanding is available.

Possible Energy Level Discriminant

A relatively large number of Streckeisen seismograms of earthquakes and explosions are presently available for events occurring in the western United States. The upper panel of Figure 6 displays the JVE explosion (Kearsarge $M_b = 5.7$) and Yucca Mountain earthquake of June 29, 1992 ($M_b = 5.7$) as recorded at PAS. The middle traces display the broadband displacements in cm while the upper traces display the simulated long-period 3090 (gain 2250) response and the lower traces the simulated short-period Wood-Anderson (gain 2800) response. Note that the P waves are stronger for the explosion and the S waves are stronger for the earthquake as expected. Moreover, the long-period excitation of the earthquake is substantially higher than the explosion. This feature suggests that $M_L:M_o$ i.e., the short-period/long-period level ratio can be a discriminant, as it appears to be the case in the southern US as reported by Woods *et al.* (1992) in this volume. In the next few figures we will briefly explore this phenomenon theoretically, starting the bottom half of Figure 6. Since we have a good crustal model and adequate source representation of an explosion and an earthquake, we can predict theoretically what we should expect at various distances and depths. We assume that earthquakes are double couples represented by a time function defined by ($\delta_1 = 0.25$, $\delta_2 = 0.5$, $\delta_3 = 0.25$) and $M_o = 1 \times 10^{23}$ dyne-cm (Cohn *et al.*, 1982). These parameters are appropriate for a stress drop of about 20 bars, commonly observed in tectonic regions. Results from three fundamental faults are displayed as Wood-Anderson synthetics and conventional long-period 3090's (Figure 6). In this case, we assume the explosion and earthquake excitations are independent of depth. Results at a depth of 0.64 km are given in Figure 7. The lower half of this figure displays accumulated energy plots where explosions (two top traces marked as ZEX and REX) show their enhanced P waves very clearly. One possible discriminant appear to be the P-wave/S-wave energy ratio but this discriminant could be influenced by the radiation pattern. The high-frequency/low-frequency energy levels of the complete waveforms could also be used which may be influenced by depth-dependent Rayleigh waves. Since the Rayleigh waves decay slower than the body waves, it probably has a range dependence as well. The most stable measure found by examining these synthetic seismograms appears to be the ratio of short-period/long-period energy level excluding the surface waves. These ratios are given in the table shown in Figure 8. These results are based on three depths and three ranges as indicated. The numbers show some scatter but appear to separate the population. Unfortunately, earthquakes are associated with a tremendous variation in stress drops and these results may easily change for a high stress-drop event. Nonetheless, the $M_L:M_o$ discriminant appears viable as is demonstrated in the lower half of Figure 8. Therefore, we think our approach has merit.

RECOMMENDATIONS

It appears that some useful discriminants can be constructed from regional phases. However, at this stage it is important to understand more about various crustal waveguides that are controlling the frequency behavior so that discriminant can be placed on a theoretical basis. This is particularly important in southern Asia where the crustal structure is rapidly varying. The problem is compounded by the complex continental collision tectonics and associated "odd" earthquakes. Given these problems, assessment of the observational variation in various possible discriminants is extremely important if it is possible, especially when we are attempting the "first blast" identification capability. Thus, we suggest extensive analysis of those stations recording both explosions and earthquakes so that a knowledge-based catalogue can be established. Understanding the observations at digital stations such as Borovoye is of obvious importance which is why we have embarked on this detailed modeling study.

References

- Cohn S. N., T. L. Hong and D. V. Helmberger (1982). The Oroville earthquakes: A study of source characterization and site effect, *J. Geophys. Res.*, 87, 4585-4594.
- Helmberger, D. V., D. Dreger, L. Zhao (1991). Source retrieval from regional seismograms, 13th Annual PL/DARPA Seismic Research Symposium, 249-260. **PL-TR-91-2208, ADA241325**
- Helmberger, D. V. and D. M. Hadley (1981). Seismic source functions and attenuation from local and teleseismic observations of the NTS events, Jorum and Handley, *Bull. Seis. Soc. Am.*, 71, 51-67.
- Langston, C. A. (1990). High frequency tectonic release from the Soviet JVE explosion of September 14, 1988, 12th Annual DARPA/GL Seismic Research Symposium, 302-308. **GL-TR-90-0212, ADA226635**
- Richards, P. G., W-Y Kim, and G. Ekstrom (1992). Borovoye Geophysical Observatory, Kazakhstan, *EOS, Transactions, AGU*, Vol 73, No 18, May 5, 201p.
- Saikia, C. K. and L. J. Burdick (1991). Fine structure of P_n waves from explosions, *J. Geophys. Res.*, 96, 14,383-14,401.
- Saikia, C. K. (1992). Modified frequency-wavenumber algorithm for regional seismograms using Filon's quadrature - Modeling of L_g waves in eastern North America, *Bull. Seis. Soc. Am.* (Manuscript in preparation).
- Walter, W. R. and H. Patton (1990). Tectonic release from the Soviet Joint Verification Experiment, *Geophys. Res. Lett.* Vol 17, No 10, 1517-1520.
- Woods, B. B., S. Kedar and D. V. Helmberger (1992). $M_L:M_o$ as regional seismic discriminants, 14th Annual PL/DARPA Seismic Research Symposium, 16-17 September. **PL-TR-92-2210**



Figure 1. Map showing geographical locations of the stations used in this study. Stations are marked by triangles. This cross symbol correspond to the location Soviet JVE explosion of September 14, 1988.

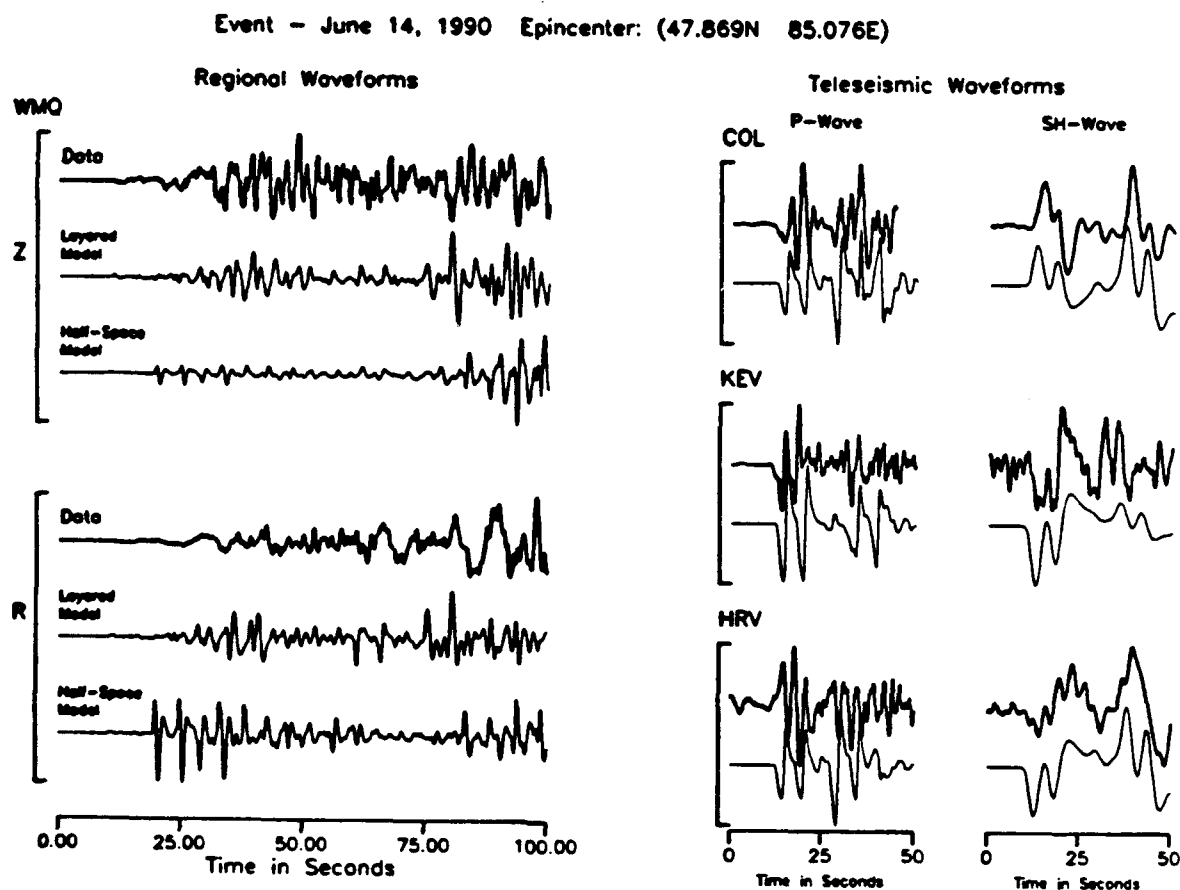


Figure 2. Displays the comparison between the observed and the synthetic seismograms both at regional and teleseismic distances. Left: Figure shows the relative effect of crustal structure on the P_n and S_n waves from June 14, 1990 event ($M_b = 6.1, PDE$) at a Chinese digital station WMQ ($R=495\text{km}$). Right: P and SH wave modeling for the same event at three teleseismic stations. Source information was derived from this study.

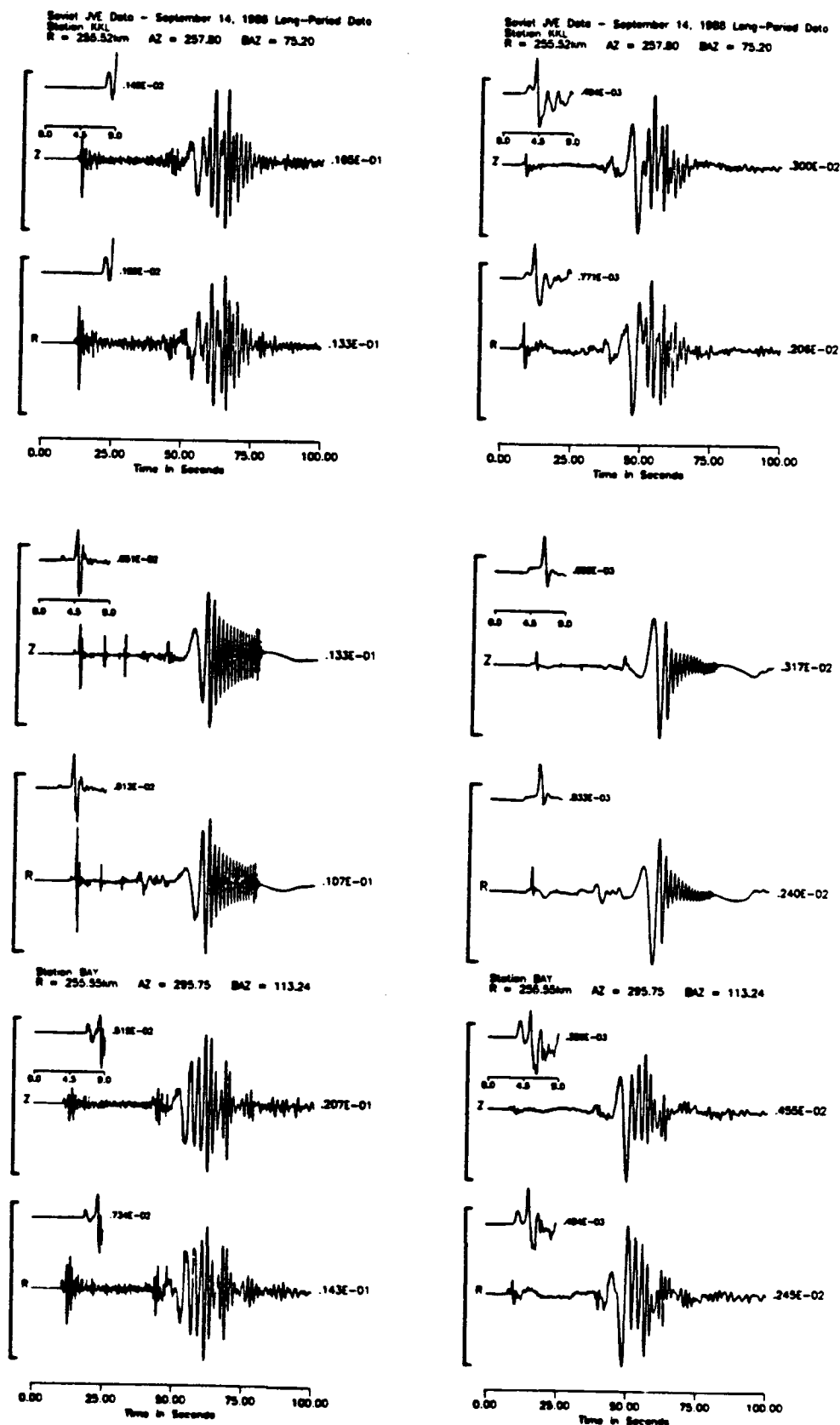


Figure 3. Modeling of Soviet JVE explosion data at BAY and KKL stations. Original data supplied by William R. Walter have been corrected for the instrument response. The synthetic seismograms computed using frequency-wavenumber method are shown in the middle two traces. Left: the long-period seismograms as recorded and simulated (body-waves are used to estimate B and K ; right: the same seismograms as displayed in the left but with an additional filter of long-period 3090 response (fundamental-mode Rayleigh waves are used to estimate Ψ_{ω}).

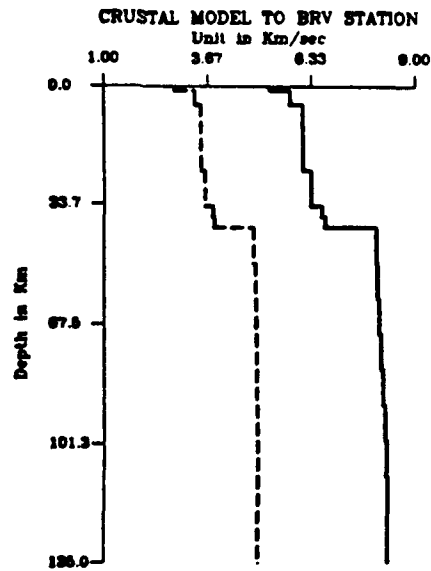


Figure 4. Calibrated crustal model for the path from the Soviet JVE explosion location

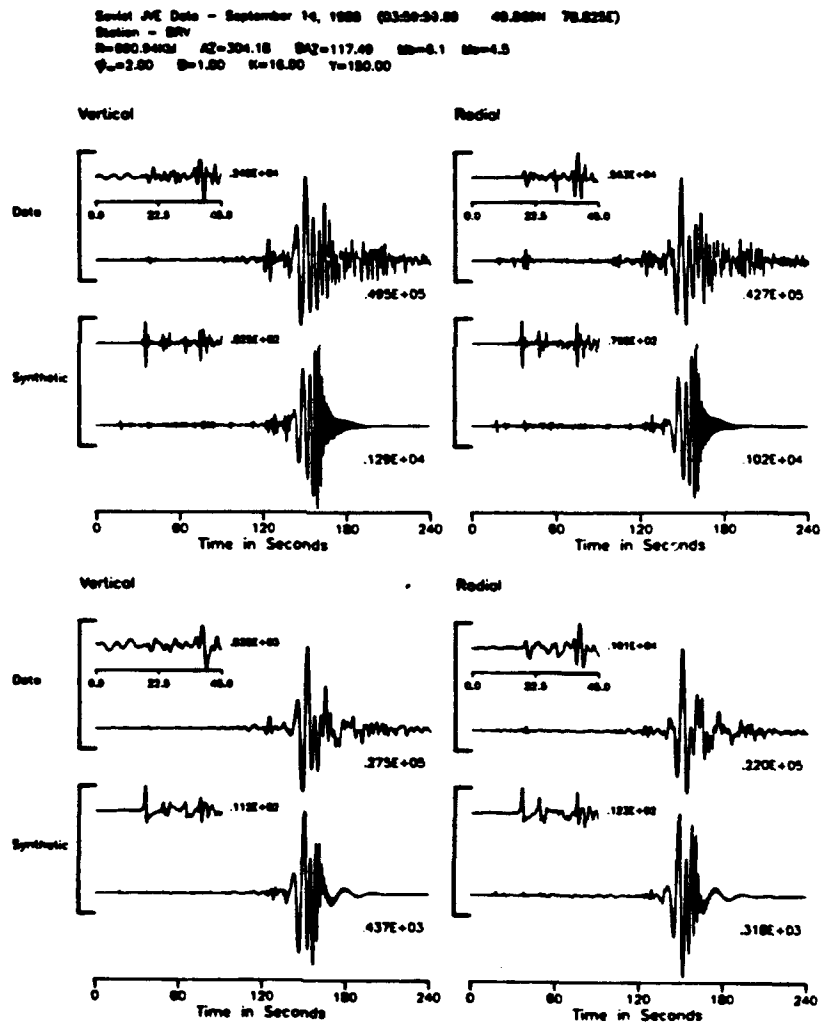
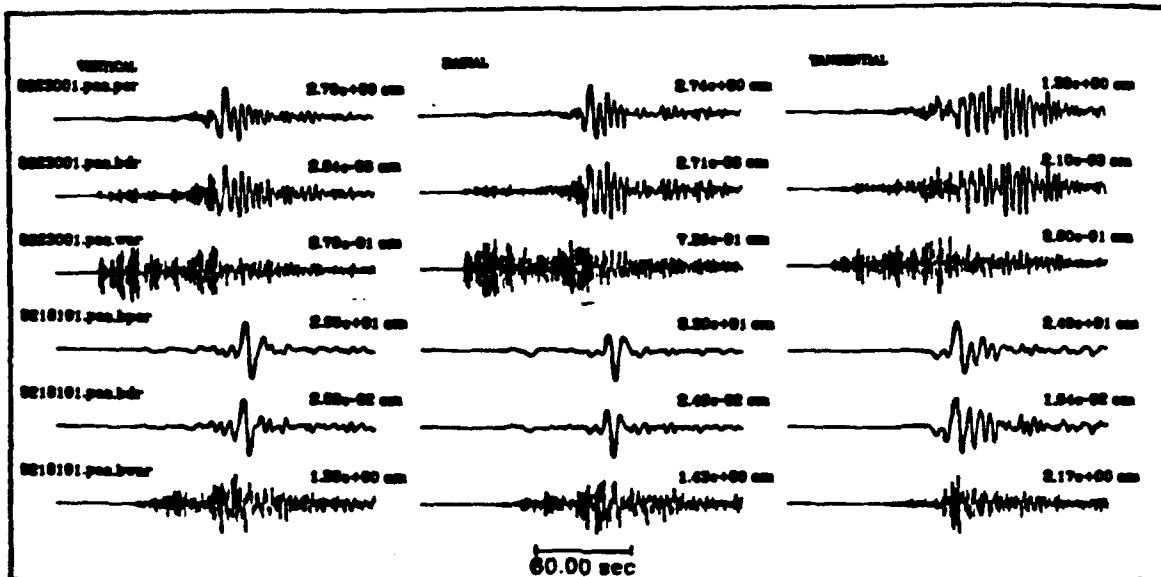


Figure 5. Modeling of the vertical and radial component seismograms from Soviet JVE explosion recorded on the DS digital system at BRV. The comparison shown in the upper two seismograms is for the data as recorded and that shown in the bottom two seismograms is after convolving the seismograms with a long-period 3090 instrument. (Source model obtained in Figure 3 is used; note the peak amplitude discrepancy).



Explosion Vs Earthquake Seismograms

R=690.0km h=8.00km

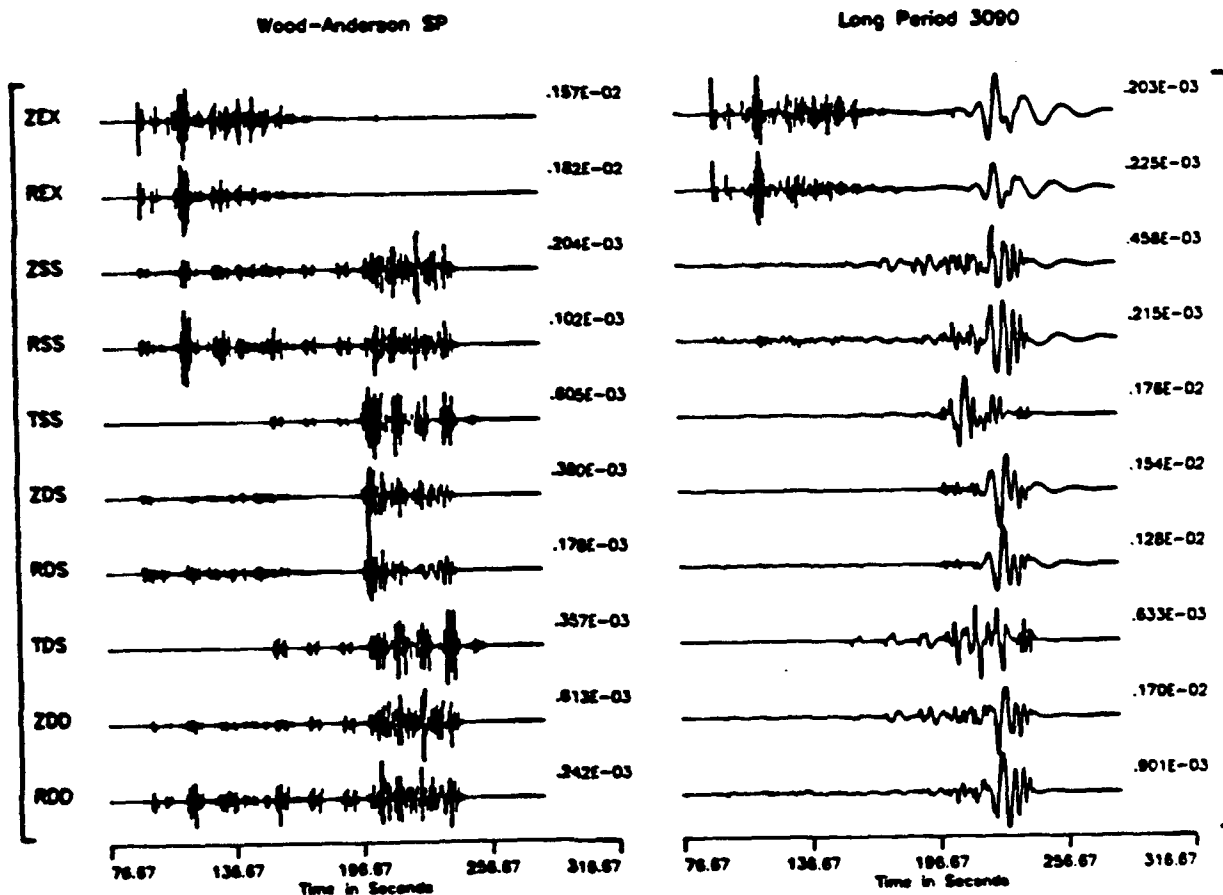


Figure 6. Top panel: Displays the United States JVE explosion (Kearsarge, $M_b = 5.7$) and a Yucca mountain earthquake of June 29, 1992 ($M_b = 5.7$ recorded at PAS (Pasadena). Also shown are the simulated Wood-Anderson short period and 3090 long-period responses. Note that the P waves are stronger for the explosion and S waves for the earthquake. Bottom panel: Simulated short-period Wood-Anderson and long-period 3090 seismograms for both earthquake and explosion sources at 690 km for a source depth of 8.0 km. Borovoye crustal structure was used. The enhanced P waves for explosion seismograms (ZEX and REX) appear suitable for discrimination.

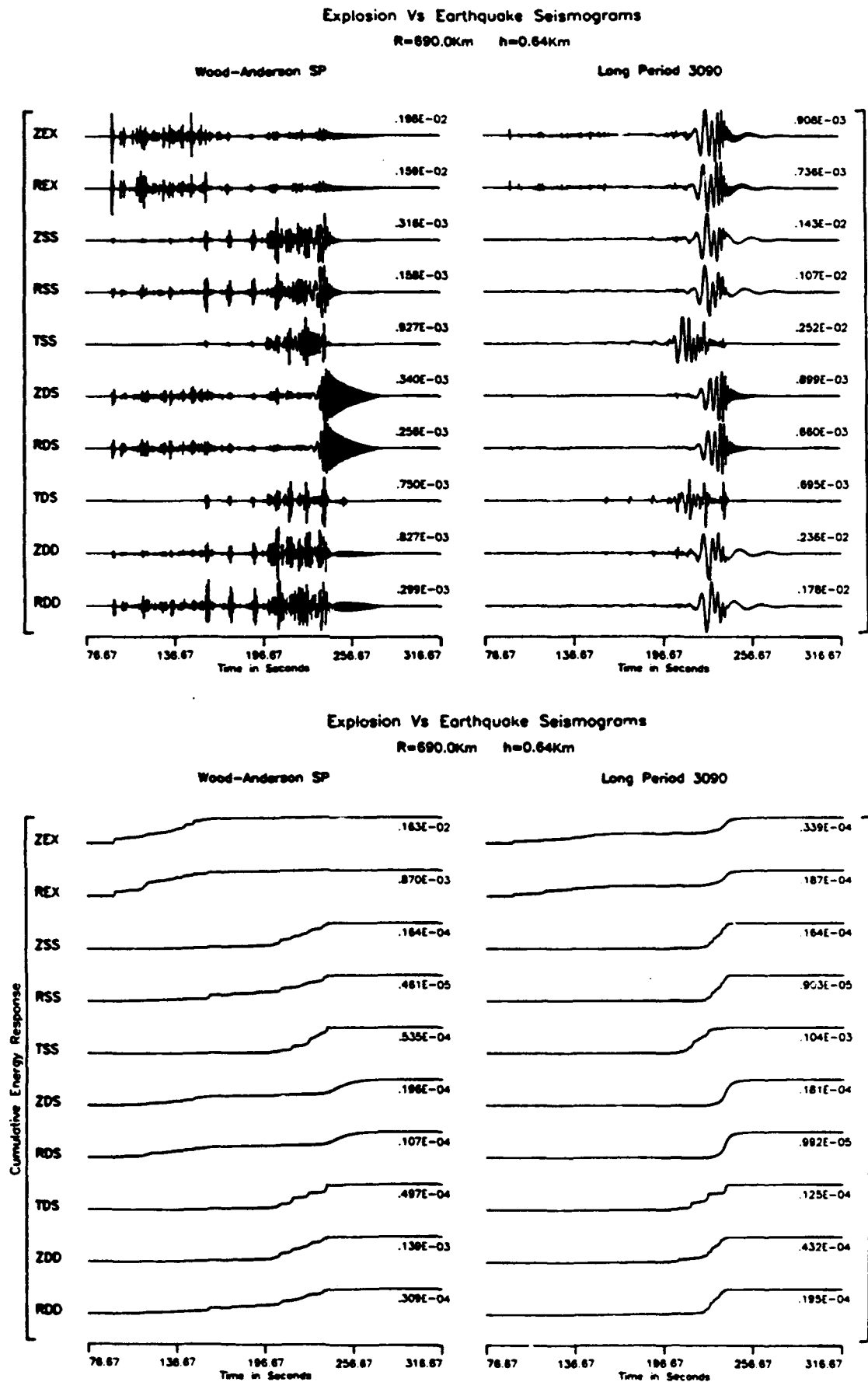


Figure 7. Top panel: same explanation as given for the bottom panel in Figure 6. The source is buried at a depth of 0.64 km. Bottom panel: Displays the corresponding cumulative energy curves. The ratios of short-period/long-period energy ratio seem to separate the population (see Figure 8).

| Δ | depth | EX | SS | DS | DD |
|----------|---------|-----|----|----|----|
| 173 km | .64 km | 83 | 7 | 5 | 12 |
| | 4.00 km | 111 | 12 | 2 | 8 |
| | 8.00 km | 128 | 13 | 14 | 11 |
| 255 km | .64 km | 110 | 22 | 19 | 23 |
| | 4.00 km | 92 | 8 | 13 | 9 |
| | 8.00 km | 95 | 14 | 7 | 6 |
| 690 km | .64 km | 113 | 9 | 26 | 8 |
| | 4.00 km | 108 | 3 | 9 | 2 |
| | 8.00 km | 109 | 4 | 4 | 4 |

M_L vs. Log Moment

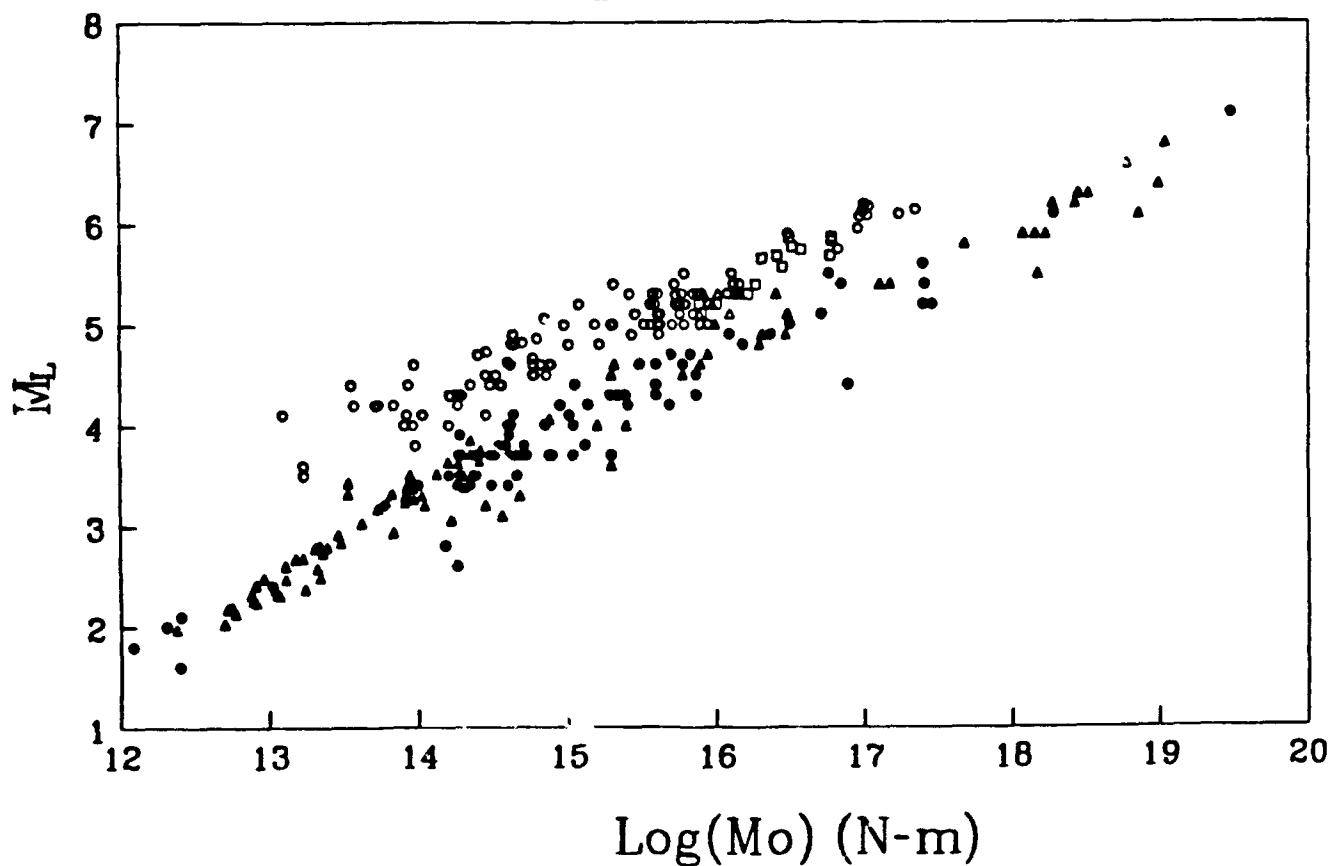


Figure 8. Top: Table of energy ratios excluding the surface waves for both earthquake (SS=strike-slip, DS=dip-slip and DD=45° dip slip) and explosion (EX) as a function of distance and depth. The explosion numbers do separate well from the corresponding earthquake numbers and also are independent of depth and range. Bottom: Figure showing the $M_L:M_0$ discriminant which appears viable as a possible discriminant (taken from Woods *et al.*, 1992).

CHARACTERIZATION OF REGIONAL PHASE PROPAGATION IN EURASIA USING DATA FROM HISTORIC NUCLEAR EXPLOSIONS IN THE U.S.S.R.

Susan Y. Schwartz and Ron Mandel
University of California, Santa Cruz

Contract No. F29601-91-K-DB18

Objective

The use of regional phases to determine the yield of nuclear explosions and to discriminate them from earthquake sources presently requires either the calibration of particular source receiver paths or improvement in our understanding of regional phase generation and propagation. To enhance both our knowledge of path specific propagation and the nature of regional phases we have analyzed a new data set of hand digitized Soviet explosions and earthquakes. The objectives of this study are to quantify the various factors effecting regional phase generation and propagation such as explosion yield, shot burial depth, source velocity, and crustal structure and to test the usefulness of previously proposed earthquake/explosion discriminants in Eurasia.

Research Accomplished

A remarkable correlation between amplitude and explosion yield has made the Lg phase extremely useful for seismically determining the yield of nuclear explosions. An important caveat, however, has been the necessity of obtaining calibrated explosions for each site/station network. The calibration accounts for unknown differences in the efficiency of coupling explosion yield into Lg for different test sites and for variations in Lg propagation along different paths. An improved understanding of the Lg phase, both its origin and propagation, could eliminate the need for calibration explosions in yield determination. Spectral properties of the Lg phase have also proved very useful for source discrimination; however, particular discriminants that perform well in one geologic setting often perform less satisfactorily in others. An improved understanding of the Lg phase will help to reveal the mechanisms underlying Lg discriminants and make their application more successful. Due to the importance, yet lack of understanding of the Lg phase, our first year of work has focussed on an empirical study of the spectral properties of Lg and other regional phases using a new data set of hand digitized waveforms of nuclear explosions at Semipalatinsk and Matorchkin Shar recorded at several Soviet stations. We compare our results with similar analyses performed by others using different data.

The data set of hand digitized Soviet nuclear explosions consists primarily of explosions at the Semipalatinsk test site (81 of 102 shots) recorded at ten different Soviet stations. We concentrate on regional phases from Arti (ARU) since this station recorded a large number of the explosions at Semipalatinsk, located about 13.5° away. Most of the other stations recorded too few explosions or are located too far from Semipalatinsk (greater than 15°) to be useful in our analysis. Figure 1 shows examples of hand digitized waveforms recorded at ARU from explosions at 3 different subregions of the Semipalatinsk test site (Degelen, top 2 traces; northeast Balapan, middle 2 traces; and southwest Balapan, bottom 2 traces). All six explosions have ISC body wave magnitudes between 5.8 and 5.9. The signal to noise ratios and data quality are very high for explosions of this magnitude as well as for the smallest explosions with magnitudes of only 4.8. The explosion on 10/12/80 (third trace in Figure 1) contains a region of the seismogram, between the P and Lg arrival, where no data were digitized. Small regions of data dropout are fairly common with the hand digitized seismograms; however, they occur outside of the phases of interest and should not effect our analysis. At 13° , the regional P wave is quite complicated consisting of diving P wave energy, Pn and possibly Pg, depending on the

structure of the crust and lid along the propagation path. Both regional P and Lg are clearly visible on all traces and are labeled in Figure 1.

An apparent deficiency of high frequency Lg relative to regional P in explosion spectra has been observed and exploited by several researchers to discriminate between earthquakes and nuclear explosions at both NTS (Murphy and Bennett, 1982) and East Kazakh (Bennett et al., 1990; Chan et al., 1990). Several mechanisms underlying this observation have been proposed such as non-geometrical excitation of shear energy by interaction of a P spherical waveform with the free surface (S^*) and scattering of explosion generated Rg into S. Figure 2 shows amplitude contours in the frequency/time domain (vespagrams) for 2 magnitude 5.9 explosions at southwest Balapan (left plot) and Degelen (right plot). The enrichment of high frequencies in the regional P wave relative to Lg is clear at both test sites but is more pronounced at southwest Balapan. To further investigate differences in the spectral character of regional phases generated at the different test sites, we computed RMS amplitudes for regional P and Lg phases for all explosions at Semipalatinsk recorded at ARU. This included 12 explosions at Degelen and Murzhik, 13 explosions at northeast Balapan, and 18 explosions at southwest Balapan. We measured RMS amplitudes in frequency bands between 0.5-1.0, 1.0-2.0, 2.0-4.0, and 4.0-6.0 Hz. Since the instrument response at ARU varied slightly over the 22 years of collected data, all recordings were normalized to a common instrument prior to measurement. Lg amplitudes were calculated following the procedure defined by Israelsson (1991) where measurements are made in the group velocity window 3.1 to 3.7 km/s. All amplitudes were corrected for background noise and maximum instrument magnification.

Figure 3 summarizes our findings where mean values and standard deviations of P/Lg ratios for three different test sites are plotted versus center frequency. Explosions from all test sites indicate an increase in this ratio with frequency which reflects the deficit of high frequency energy in the Lg phase apparent in the vespagrams of Figure 2. Above 1 Hz, explosions at southwest Balapan have consistently higher P/Lg ratios than explosions at the other two test sites. This is consistent with the bias between body wave and Lg magnitudes for the two regions of Balapan reported by Ringdal and Marshall (1989) from NORSAR data and Israelsson (1992) from analysis of the entire hand digitized Soviet data set. The larger P/Lg ratios for southwest Balapan explosions relative to Degelen are also consistent with the spectral ratios determined from Shagan River explosions recorded at the Chinese Digital Network station WMQ (Gupta et al., 1990). Based on the spectral behavior of Lg from Shagan River explosions recorded at WMQ, Gupta et al. (1991) proposed that low-frequency Lg probably results from the scattering of explosion generated Rg into S. They showed that for a narrow frequency band, the slope of the best fit line on a plot of $\log(Pn/Lg)$ versus shot depth had a value very near that theoretically predicted by simple scattering of Rg to S. For five explosions at Degelen and Murzhik and three explosions at Balapan that have published depths (Bocharov et al., 1989), we plotted $\log(P/Lg)$ versus shot depth in four narrow frequency bands and found no relationship between the slope of the best fit line and the center frequency as predicted by Rg to S scattering. Our results suggest that simple Rg to S scattering alone is not a sufficient mechanism to generate Lg, and that this phase may result from several different mechanisms operating simultaneously.

The P/Lg ratio recorded at station WMQ has proved to be an effective discriminant between explosions at the Semipalatinsk test site and nearby earthquakes (Chan et al., 1990; Bennett et al., 1990). Unfortunately, this discriminant has not performed so successfully in the western United States, where Lynnes et al. (1990) found that source/receiver path are more important than source type in determining P/Lg ratios. To test this discriminant in a different region of Eurasia, we compared P/Lg ratios from hand digitized explosions at the Azghir test site with ratios from digital waveforms of an earthquake on 5/14/89, near Azghir recorded on IRIS/IDA stations. Figure 4 shows the location of the earthquake and explosion sources and the recording stations along with a plot of P/Lg ratios versus center frequency. For the common station OBN, the explosion and earthquake source are well separated in the frequency range between 0.5 and 3 Hz. Three explosions at Azghir have been recorded at ARU which is located at a similar distance to Azghir as OBN. The P/Lg ratios for these three explosions are also plotted in Figure 4. These ratios are higher than the explosion recorded at CBN, and enhance the

separation between earthquake and explosion populations. Unfortunately our data, like that of Lynnes *et al.* (1990), also shows evidence for the influence of propagation path on P/Lg ratios. The P/Lg ratios determined at KIV for the 1989 earthquake (distance about 9°) lie within or very near to the explosion ratios (Figure 4). Our results emphasize the importance of propagation path on P/Lg ratios and caution against using this ratio for discrimination without path calibration.

Conclusions and Recommendations

As seismic discrimination efforts shift emphasis from detection of nuclear explosions in Eurasia to other parts of the world having no previous history of nuclear testing, comparison of phase ratios between earthquake and explosion populations will no longer be possible. To make advances in seismic monitoring of non-proliferation treaties, it will be very important to establish the variability of proposed discriminants, such as phase ratios, in earthquake populations. If earthquake sources alone show little variation in regional phase ratios, than ratios from unknown sources that differ dramatically from the earthquake population can be reliably identified as explosions. If, on the other hand, earthquakes of comparable magnitude and depth, located at similar distances, reveal a large scatter in phase ratios, than that ratio will be useless for non-proliferation monitoring. Our second year of work will concentrate on evaluating the variability of various regional discriminants among earthquakes in Eurasia. We have obtained analog recordings of many earthquakes in Eurasia from the same network of stations contained in the hand digitized explosion data set. Regional phases from several of these events have already been digitized and a preliminary profile is shown in Figure 5. We expect to enhance our earthquake coverage and to systematically evaluate the potential performance of a variety of discriminants for non-proliferation treaty monitoring.

References

- Bennett, T.J. , J.F. Scheimer, A.K. Campanella, and J.R. Murphy (1990). Regional discrimination research and methodology implementation: Analysis of CDSN and Soviet IRIS data, GL-TR-90-0194, Airforce Geophysics Laboratory, Hanscom Air Force Base, MA. ADA230251
- Bocharov, V.S., S.A. Zelentsov, and V.N. Mikhailov (1989). Characteristics of 96 underground nuclear explosions at the Semipalatinsk test site, Atomic Energy 67 (3).
- Chan, W.W., R. Baumstark, and R.K. Cessaro (1990). Spectral discrimination between explosions and earthquakes in central Eurasia, GL-TR-90-0217, Airforce Geophysics Laboratory, Hanscom Air Force Base, MA. ADA230048
- Gupta, I.N., W.W. Chan, and R.A. Wagner, A comparative study of regional phases from underground nuclear explosions at East Kazakh and Nevada test sites, GL-TR-90-0170, Airforce Geophysics Laboratory, Hanscom Air Force Base, MA. ADA230567
- Gupta, I.N., C.S. Lynnes, and R.A. Wagner, Studies of near-source and near-receiver scattering and low-frequency Lg from East Kazakh and NTS explosions, Final Report 16 April 1989-15 July 1991, PL-TR-91-2287, Phillips Laboratory, Hanscom Air Force Base, MA. ADA248046
- Israelsson, H., (1992). RMS Lg as a yield estimator in Eurasia, Final Technical Report, Airforce Phillips Laboratory, Hanscom Air Force Base, MA. PL-TR-92-2117
- Lynnes, C.S., R. Baumstark, R.K. Cessaro, and W.W. Chan (1990). Pg/Lg discrimination in the western United States, GL-TR-90-0167, Airforce Geophysics Laboratory, Hanscom Air Force Base, MA. ADA226819
- Murphy, J.R. and T.J. Bennett (1982). A discrimination analysis of short-period regional seismic data recorded at Tonto Forest Observatory, Bull. Seismol. Soc. Am., 72, 1351-1366.
- Ringdahl, F., and P.D. Marshall (1989). Yield determination of Soviet underground nuclear explosions at the Shagan River test site, in: NORSAR Semiannual Tech. Summary, 1 Oct 1988--31 March 1989, NORSAR Sci Rep. 2- 88/89, Kjeller, Norway.

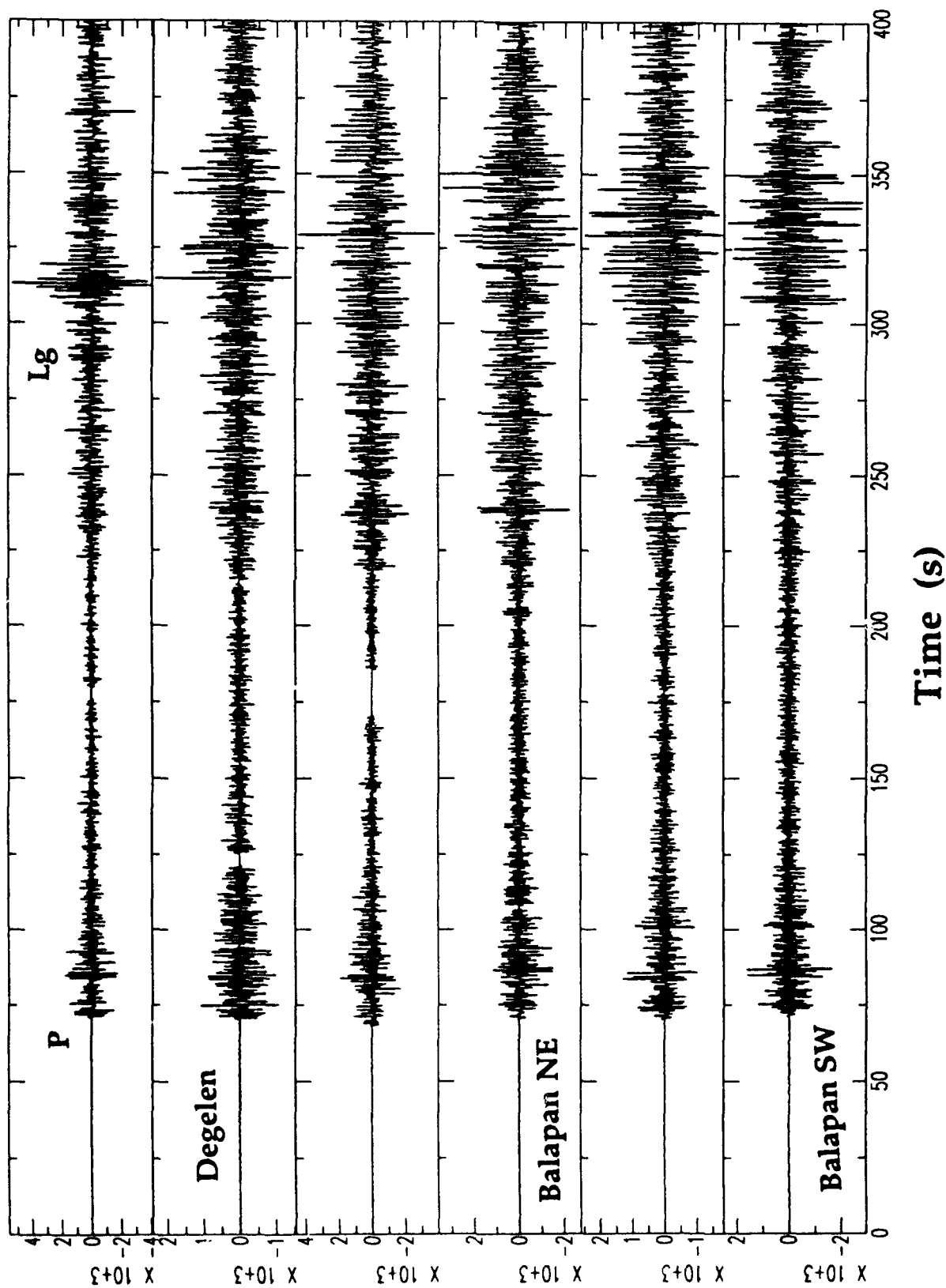


Figure 1 Hand digitized vertical component seismograms for 6 different explosions at 3 test sites recorded at Arti (AKU) located approximately 13° away.

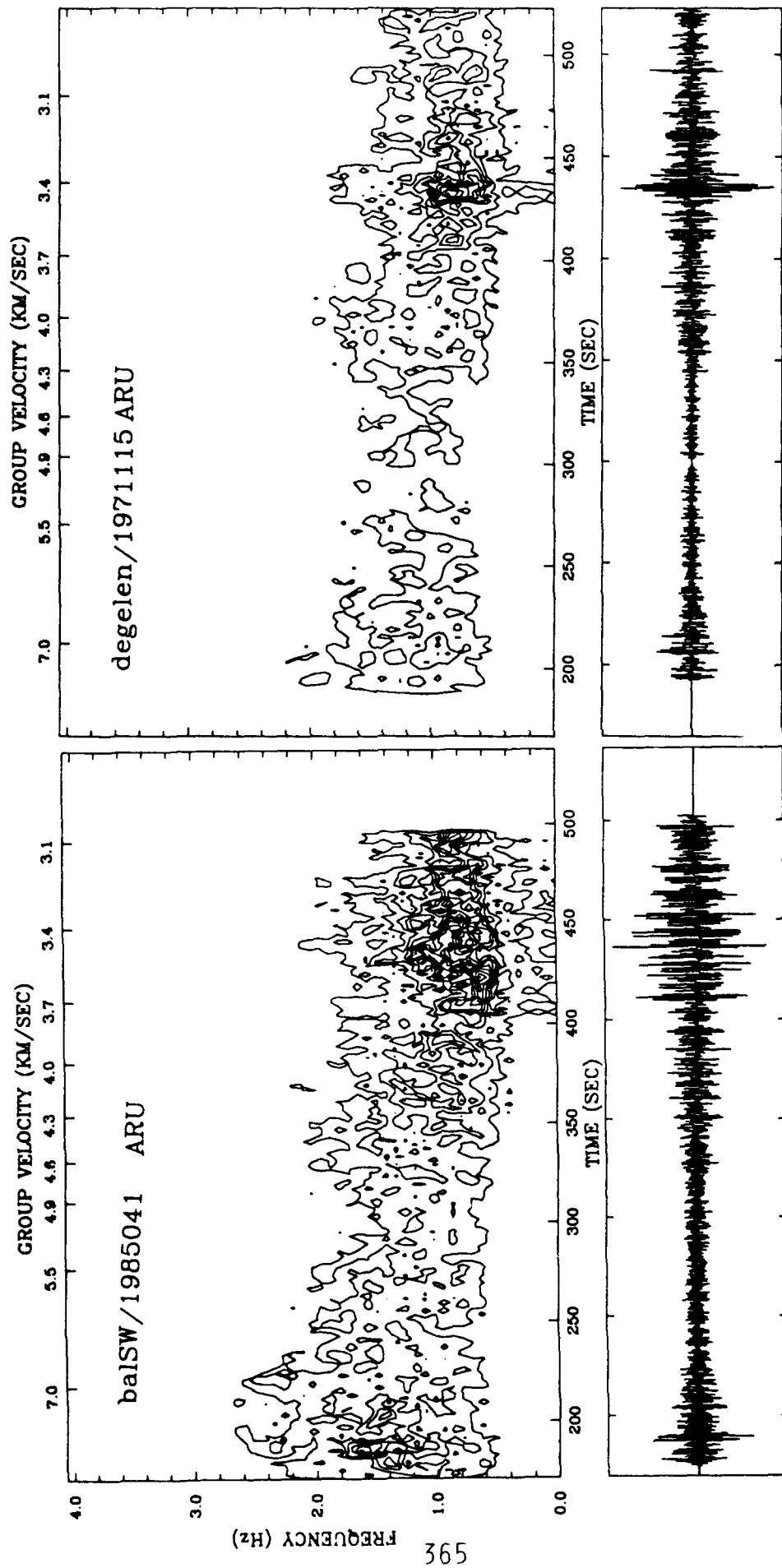


Figure 2 Amplitude contours in the frequency/time domain for magnitude 5.9 explosions at southwest Balapan (left) and Degelen (right) recorded at ARU.

Explosions Recorded at Station ARU

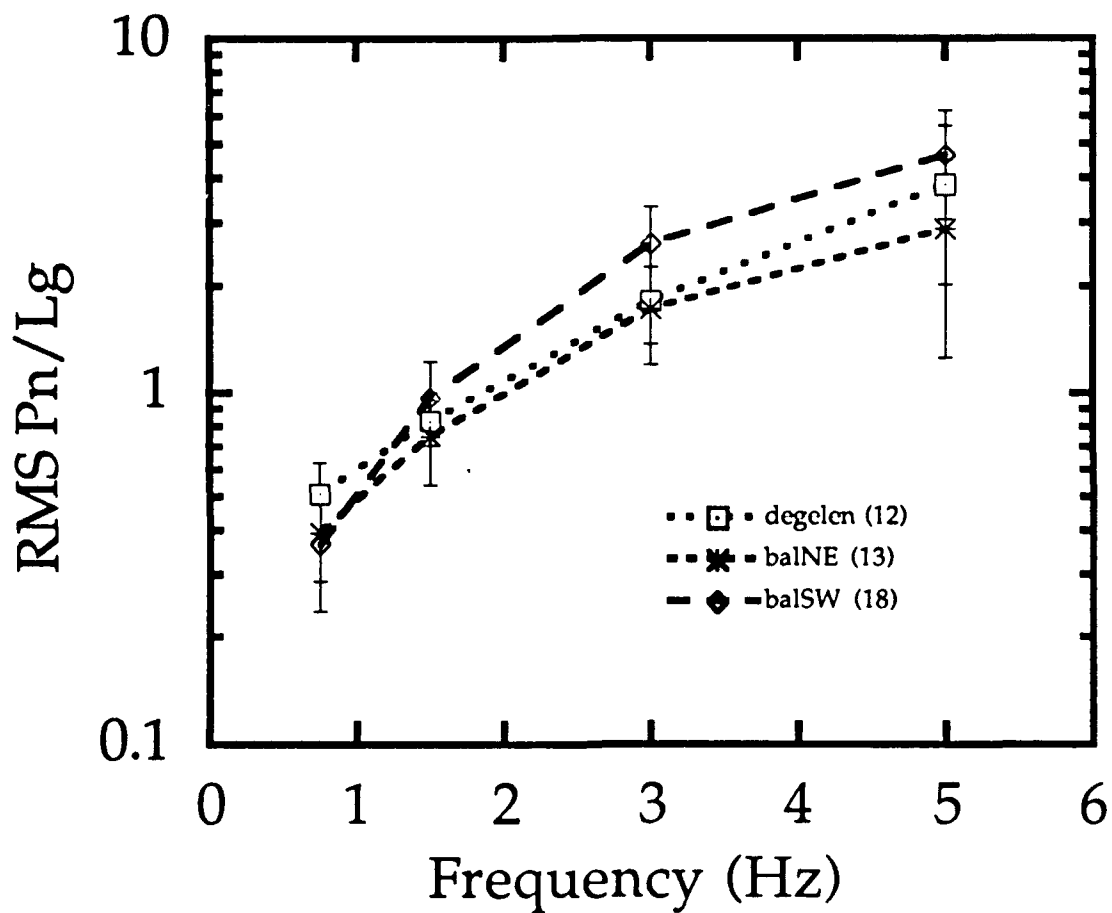


Figure 3. Plot of average P/L_g ratio versus center frequency for explosions at 3 different test sites recorded at ARU. The small numbers in parenthesis represent the number of explosions averaged for each test site.

Earthquakes and Explosions at Azghir

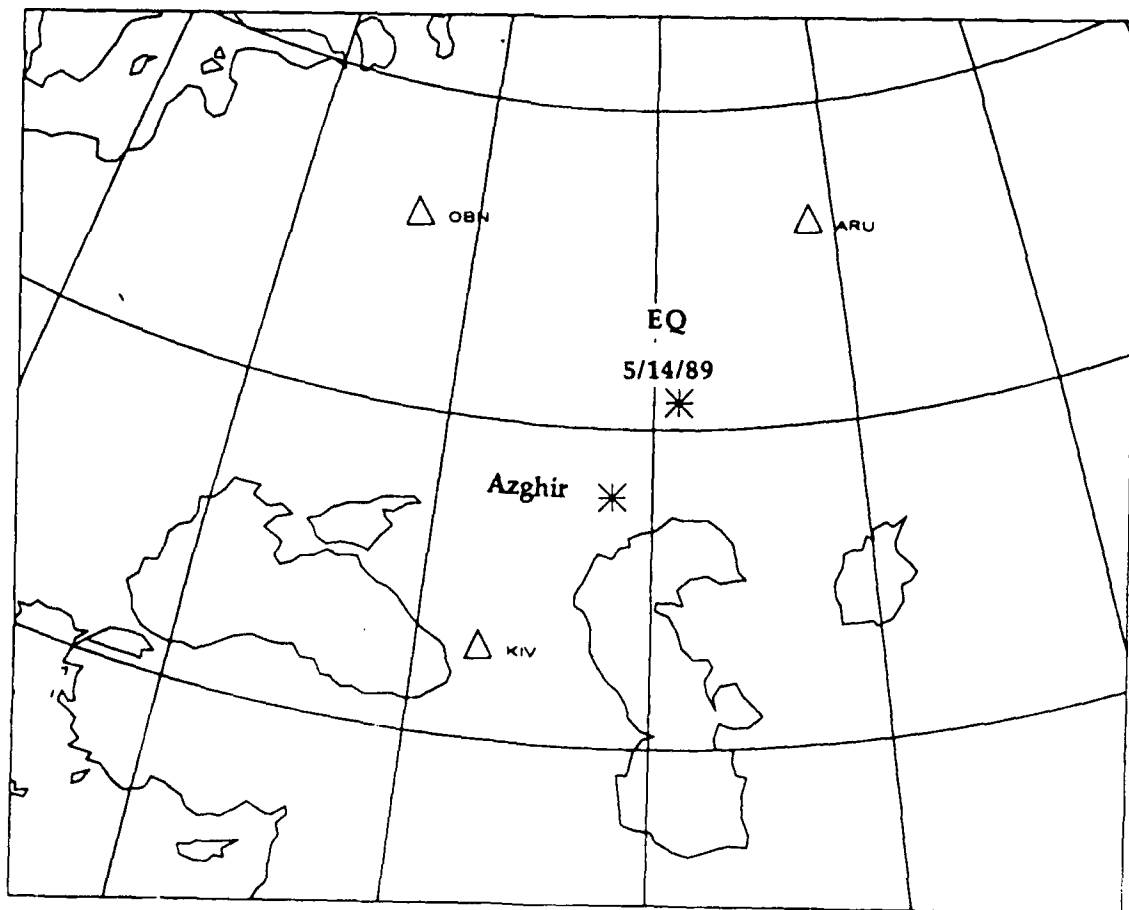
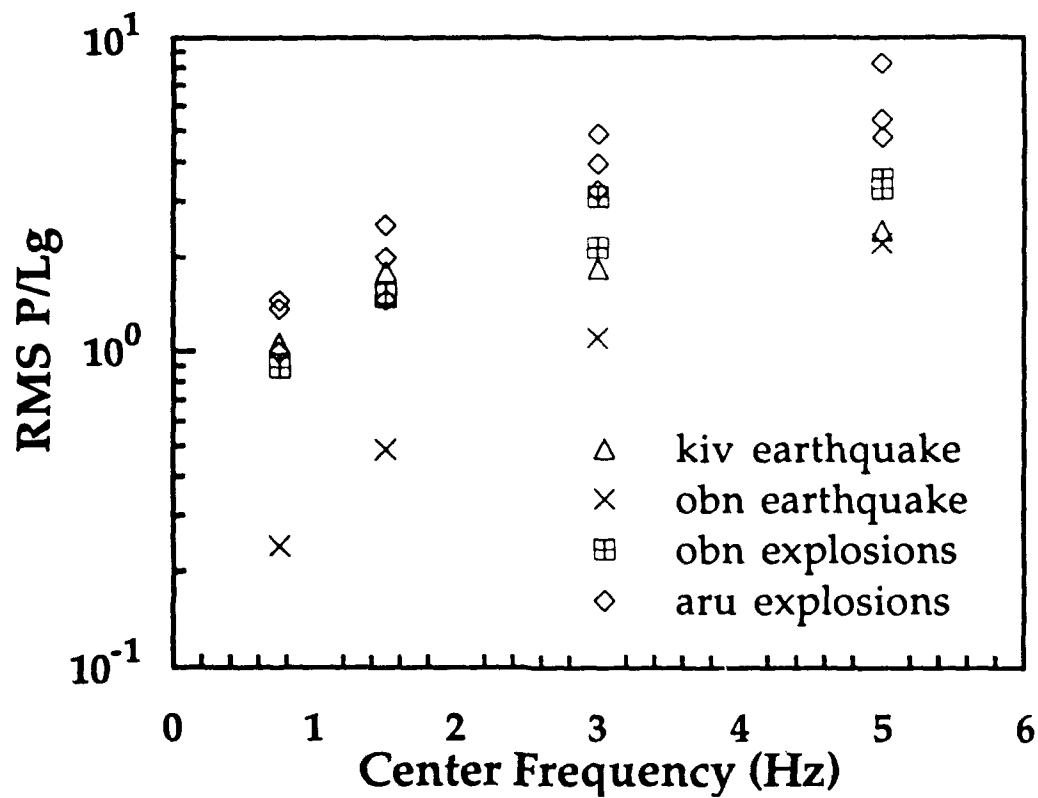


Figure 4. Plot of P/Lg ratio versus center frequency for 3 explosions at Azghir and a nearby earthquake recorded at various stations (top). The map indicates the source/receiver geometries involved.

Soviet Earthquake Data

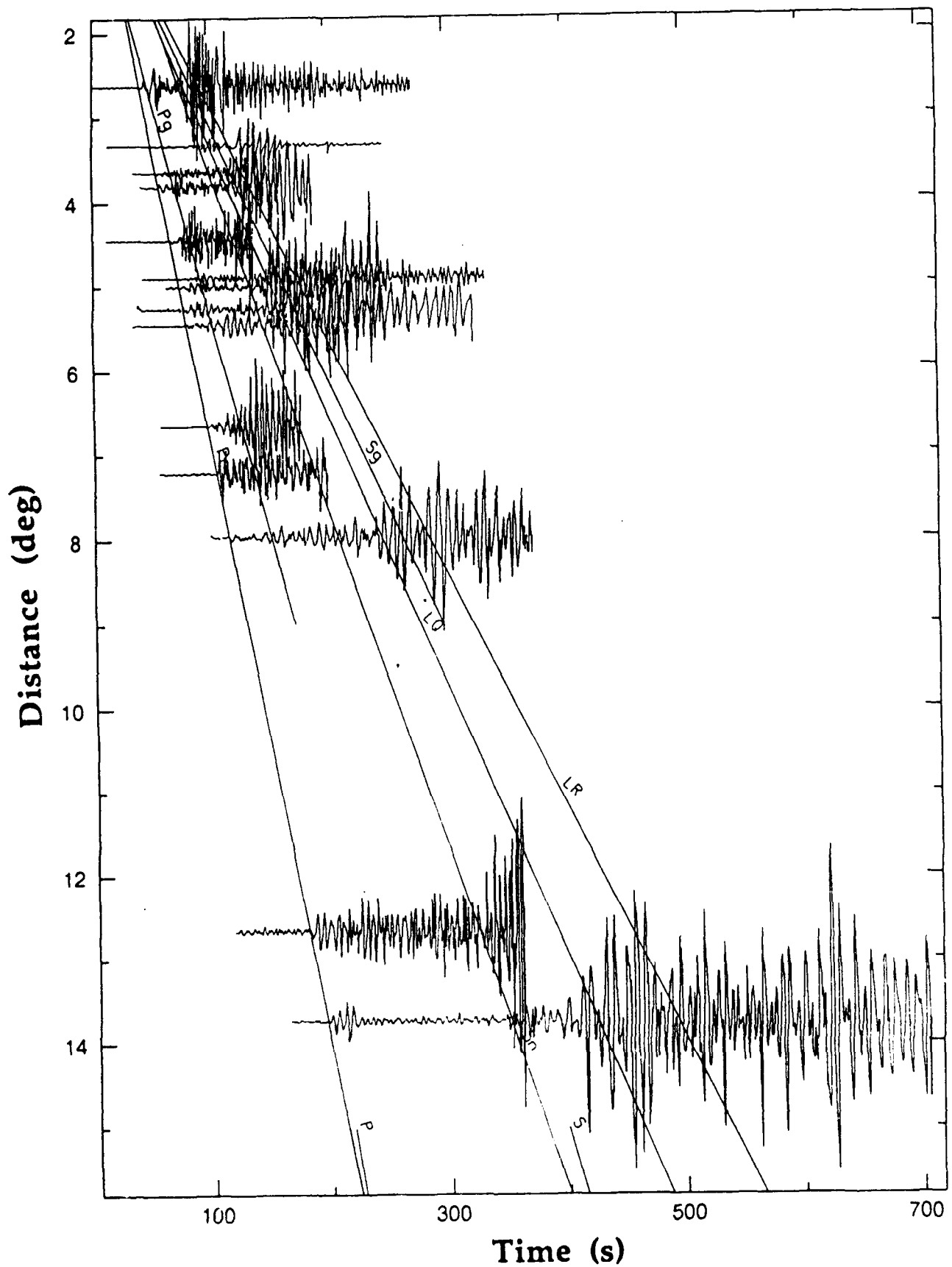


Figure 5 Hand digitized earthquake data from Soviet stations in the explosion data set. Regional phase arrival times are plotted.

ANALYSIS OF THE EFFECTS OF EURASIAN CRUSTAL AND UPPER MANTLE STRUCTURE ON REGIONAL PHASES USING BROADBAND SEISMIC DATA

Susan Y. Schwartz, Thorne Lay and Joseph Beckers
University of California, Santa Cruz

Contract No. F19628-90-K-0041

Objective:

This research effort is directed at determination of regionalized upper mantle and crustal structure for paths in Eurasia by modeling the P and PP waveforms at regional and upper mantle distances. We have established that complete modeling of the entire P to PP interval can provide good constraints on the gross structure of the crust and upper mantle lid, which exerts a profound influence on regional phases. Our objective is to relate observed variations in crustal and lid structure to the behavior of regional phases; to assess propagation effects on the Pn and Lg phases that are used in discrimination and yield estimation procedures.

Research Accomplished:

Our first year of effort was dedicated to developing a quantitative understanding of complicated upper mantle distance PP phases. Through a modeling study for paths under Europe and North America, we established the PP waveform characteristics that are useful for determining the crustal thickness and upper mantle lid velocity gradient. A significant portion of the energy associated with the PP phase preferentially samples the depth range of interest, yielding constraints on the velocity gradients, with gross time variations between P and PP placing integral constraints on the structure. Crustal reverberations profoundly affect the PP waveform, and can be used to determine near bounce-point crustal thickness. If the paths are sufficiently homogeneous (a condition plausibly satisfied in large stretches of the Eurasian lithosphere), coherent whispering gallery phases may be observed as precursors to the PP phase. Identification and modeling of this energy, particularly for broadband signals, places tight constraints on the velocity gradient in the lid, which in turn plays a major role in the frequency dependent geometric spreading of the Pn phase.

The ongoing stage of this analysis includes a data-intensive modeling of P and PP waveforms recorded within central Eurasia. Numerous broadband seismograms have been collected for earthquakes recorded by the Chinese Digital Seismic Network stations as well as IDA-IRIS stations in the C.I.S.. The strong lateral variations in crustal and upper mantle structure in this region make modeling efforts a daunting undertaking, but this is typical of the situation to be encountered in non-proliferation or low threshold treaty monitoring situations. Given the absence of a history of nuclear testing by which to calibrate various paths and discriminants, we must determine the structure in the crust and lid as well as possible so that we can quantitatively account for regional phase propagation characteristics.

For this presentation we will focus our attention on data traversing China. A subset of the paths for which we have high quality broadband waveforms is shown in Figure 1. Data for the IRIS stations for the corresponding events have just become available and will extend the coverage into the Siberian platform. Corresponding waveforms, identified by the path number are shown in the two profiles in Figure 2. These are both the broadband signals as well as the waveforms filtered with a long-period WWSSN instrument response. The latter filtering helps in the refinement of source mechanism and source time function characteristics, along with simplifying the identification of upper mantle triplication phases. The traces are aligned with the Pn/P travel time curve for the IASP91 model to eliminate travel time fluctuations for this preliminary inspection. Note the complete coverage that can be obtained at upper mantle distances under

China, spanning the triplications for both P and PP. Strong secondary arrivals are seen from 22° to 24°, which are too late to correspond to the back branch of the 400-km triplication, but are not expected to involve PP energy. The PP waveforms are particularly pronounced beyond 30°, corresponding to the onset of the triplication of the PP wavefield. While different corridors must actually be treated separately, the signals in the composite profile are surprisingly coherent.

Using data such as these, we are in the process of modeling the structure on different paths, attempting to match the complete waveform information from P through PP. This requires careful calculation with a reflectivity method, since our previous work has shown that WKBJ or ray theory modeling of the waveforms is inadequate at these ranges. In addition to matching the mantle triplication features, which is important for understanding the overall interference effects, our focus is on the secondary reverberations following P and preceding PP. This includes wave energy which is turning above the transition zone. Several initial velocity structures have been considered, three of which are shown in Figure 3. These include the platform/shield K8 of Given and Helmberger (1980) and the shield model S25 of LeFevre and Helmberger (1989), along with a model for China derived from ScS_n reverberations (Revenaugh, personal communication). These models vary in the absolute velocity of the lid as well as in the lid gradient with depth.

Reflectivity synthetics for these three models are shown in Figure 4. Profiles along a fixed azimuth are shown, with the source being the same for all three profiles. The differences in the waveforms are quite pronounced, both in the subtle triplication interference and the more pronounced variations in the energy before and after PP. The MEU2 model produces high frequency PP arrivals at distances as close as 28°, which are not observed in the data, and the PP-P differential times are several seconds too large. Model S25 provides a relatively good fit to the triplication features and the differential timing, and matches the secondary arrivals from 22°-24° fairly well, suggesting that crustal reverberations are important for these arrivals. However, the energy between P and PP is much stronger than observed. Part of this energy is the back branch of the 400-km triplication, and part of it is the whispering gallery phase established in the lid for model S25. The lack of a positive gradient in the lid of Model MEU2 reduces the latter energy substantially, with model K8 giving intermediate results.

Modeling of all of the data is underway, and regionalized upper mantle structures will be presented for diverse corridors. In parallel with this model development, we are constructing profiles of high frequency regional phases for the associated structures to assess the implications for yield estimation and discrimination applications. This is being pursued using a suite of one-dimensional synthetic seismogram algorithms appropriate for regional and upper mantle distances.

Conclusions and Recommendations:

Seismic monitoring of non-proliferation treaties requires both discrimination and yield estimation capabilities along paths for which there is no previous history of nuclear testing. Procedures for determining the detailed crustal and uppermost mantle structure along such paths using earthquake signals are important, so that the behavior of regional phases that are used in discrimination and yield estimation procedures can be characterized on a path by path basis. We are working to develop and apply such procedures using complete waveform modeling of P and PP signals from regional to teleseismic distances. This approach provides gross characterization of crustal waveguide properties and upper mantle lid structure. This program complements ongoing efforts to characterize details of the crustal waveguide by complete waveform modeling of broadband regional phases. Continued development and application of broadband P and PP waveform modeling for regional and upper mantle distances will improve existing tools for characterizing the structure along which signals from possible clandestine tests will propagate.

Given, J. W., and D. V. Helmberger, 1980. Upper mantle structure of northwestern Eurasia, *J. Geophys. Res.*, **85**, 7183-7194.

LeFevre, L. V., and D. V. Helmberger, 1989. Upper mantle P velocity structure of the Canadian Shield, *J. Geophys. Res.*, **94**, 17,749-17,765.

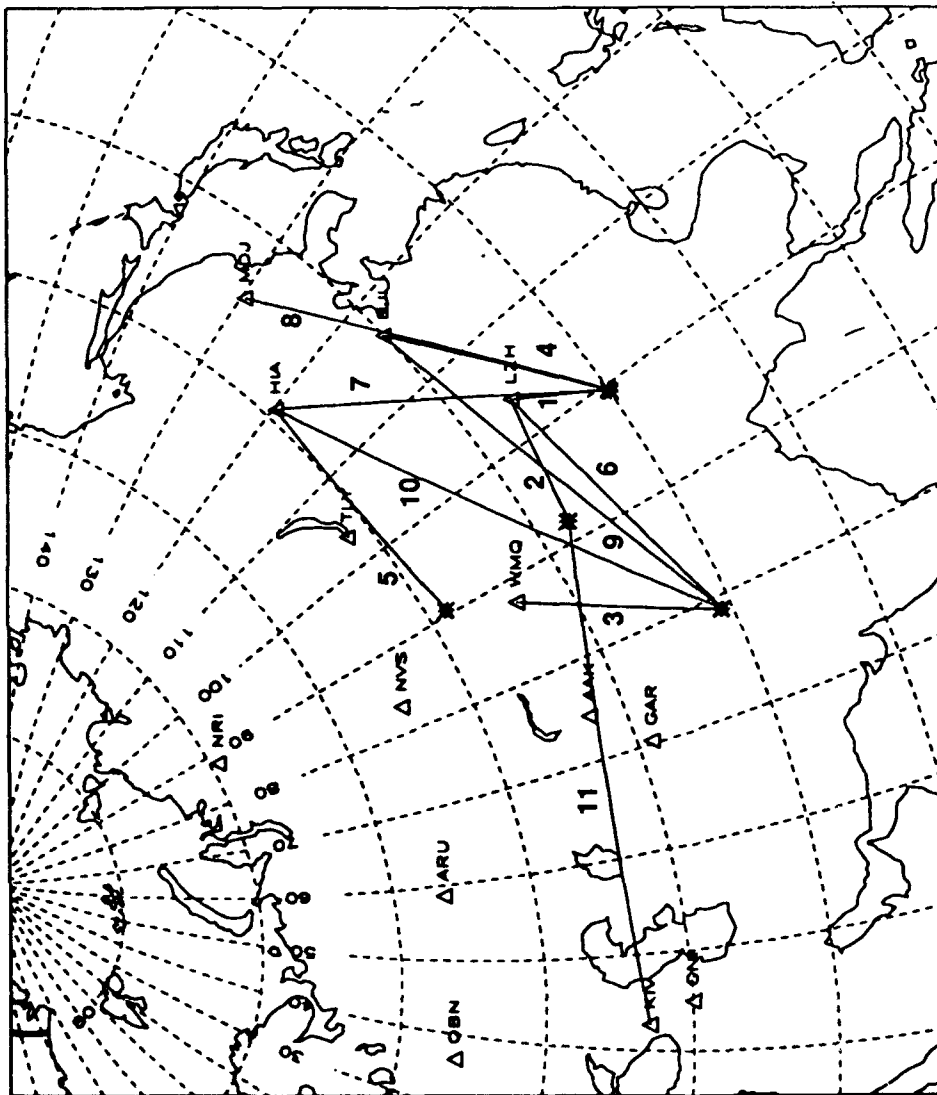
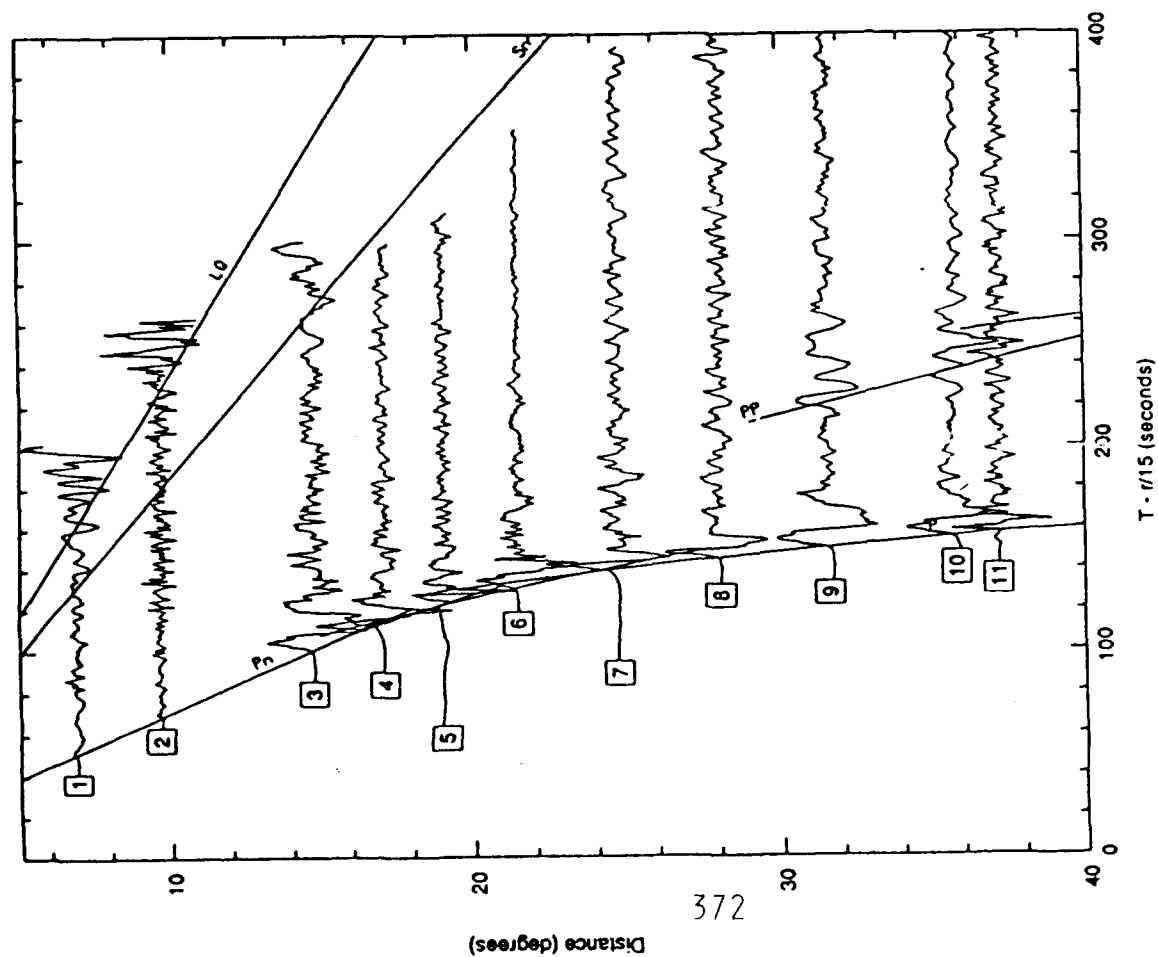


Figure 1 Map showing the location of earthquakes (stars) and stations (triangles) for which regional and upper mantle waveforms are shown in Figure 2.

Observed broadband data



Observed data convolved with long-period response

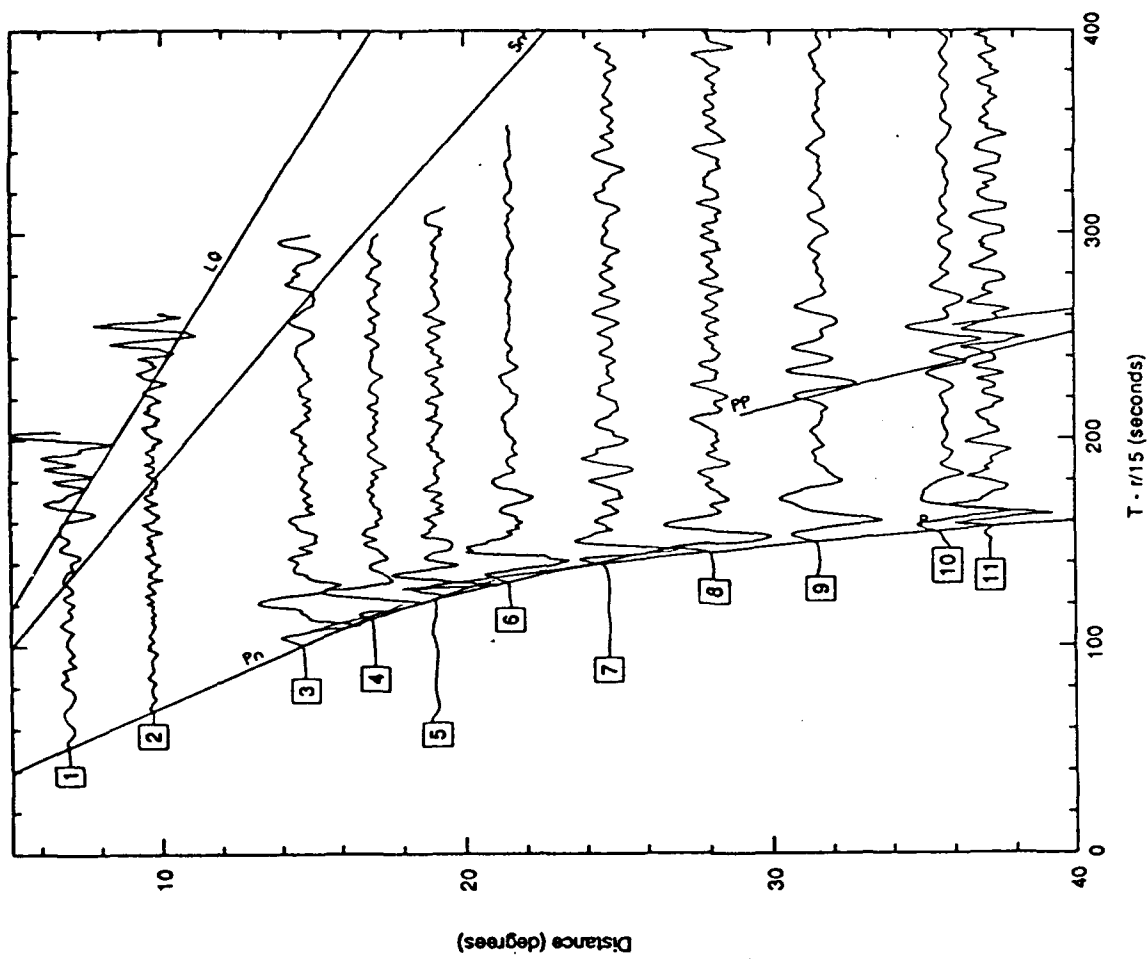


Figure 2. Vertical component broadband (left) and simulated long-period waveforms (right) for the earthquake/station pairs shown in Figure 1.

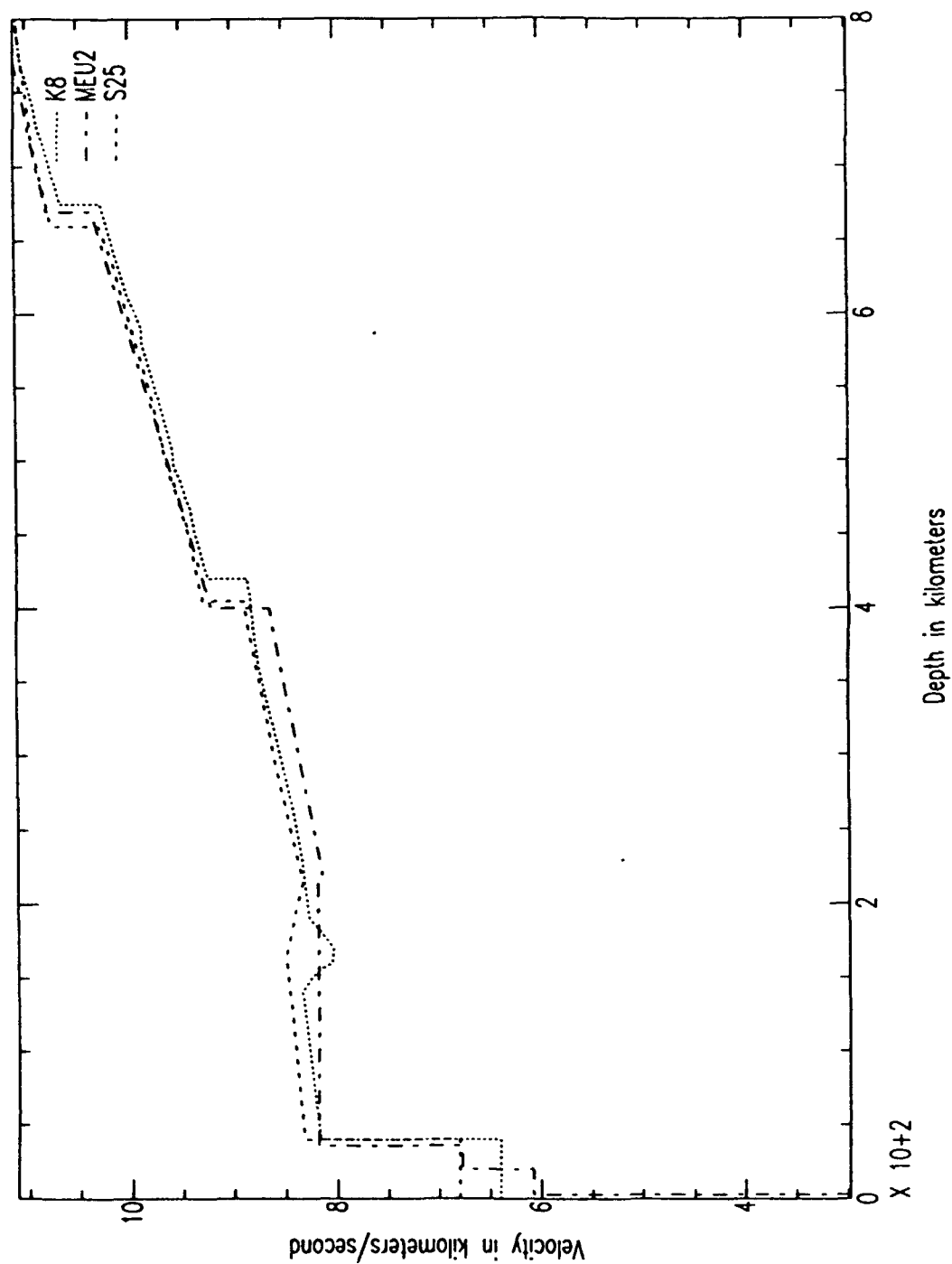


Figure 3. Three upper mantle P wave models used to construct the reflectivity synthetics shown in Figure 4. S25 from LeFevre and Helmberger (1989); K8 from Given and Helmberger (1980); and MEU2 from Revenaugh (personal comm., 1992).

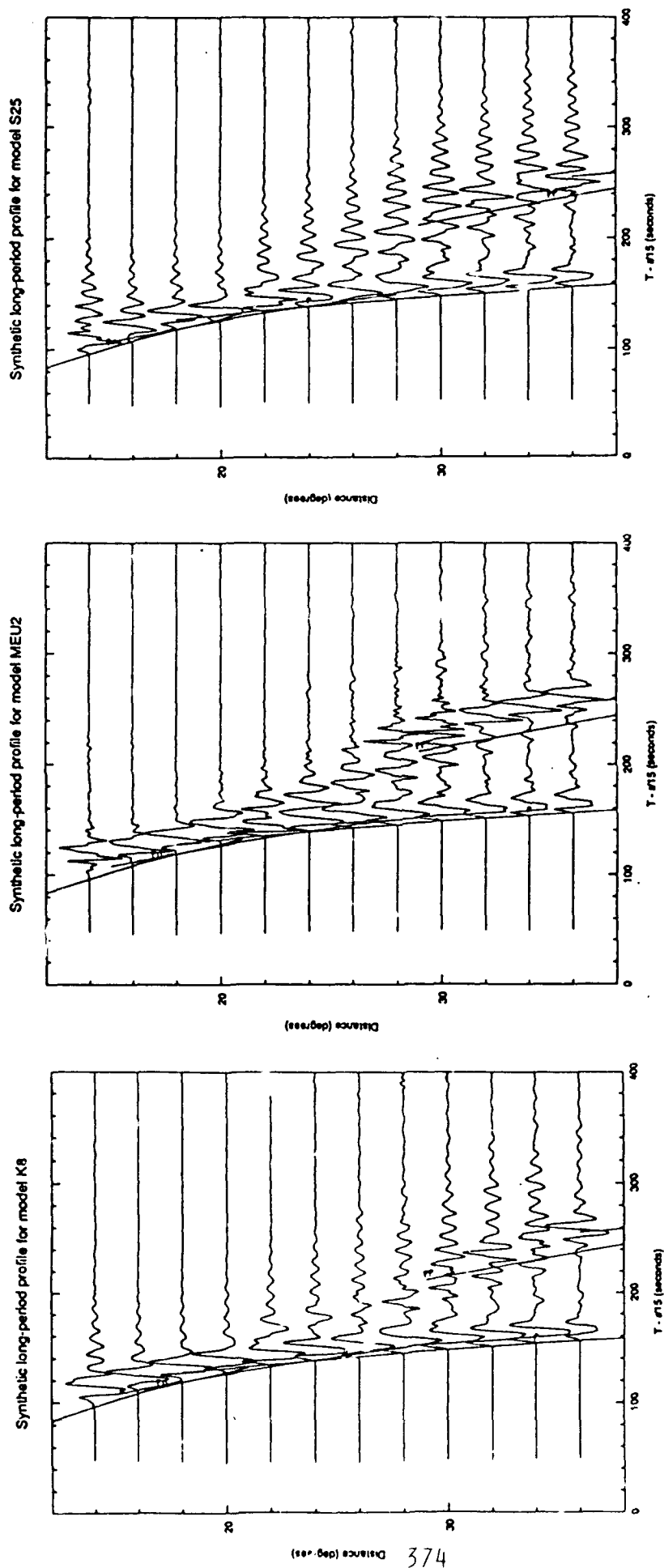


Figure 4. Long-period reflectivity profiles constructed for the upper mantle velocity models shown in Figure 3.

Limits on aspherical structure in the outer core

Peter Shearer, Guy Masters and John Orcutt

Institute of Geophysics and Planetary Physics (A-025) Scripps Institution of Oceanography,
University of California at San Diego, La Jolla CA 92093

Contract No. F19628-90-K-0053

OBJECTIVE

Our research goal has been to extend our work on the radially symmetric P and S velocity structure of the mantle to the additional phases that are contained in the ISC's catalogue (e.g. PcP, ScS, PP, SS PKP, SKS, PKIKP, etc.). During the course of our proposed study we intend to develop a self-consistent set of mantle and core velocity models and station corrections, utilizing all the available phase data in the ISC catalogue. This set of models will not only be of great use in any study of the Earth's interior, but will also improve greatly the locatability of earthquakes utilizing a global network of seismic stations. Our shorter term goal in this paper is to use *PKP* travel time data from the International Seismological Centre (ISC) to constrain possible aspherical structure in Earth's outer core and compare these results with current analyses of anomalous splitting of normal modes which suggest such structure.

RESEARCH ACCOMPLISHED

We have examined travel times for core phases collected by the International Seismological Centre (ISC) from 1964 to 1987 in an attempt to either resolve or place upper bounds on hypothetical outer-core velocity structures. We extract 50,297 *PKP(BC)* travel times (145° to 156° range), 15,286 *PKP(DF)* times (110° to 135°) and 16,963 *PKP(AB)* times (150° to 165°). We exclude *PKP(DF)* at longer ranges to avoid contamination by possible inner-core structure. All picks are examined (i.e. the ISC phase identifications are discarded), corrected for ellipticity, and the Toy station corrections applied. The ISC earthquake locations and origin times are used; the events are not relocated. Zero depth events are excluded as well as picks which follow a likely P-wave pick on the same seismogram (this should eliminate most depth phases).

We bin the data into summary rays using 15° cells in turning point position and ray azimuth. A fairly coarse increment was used since the data are sparse and we are mostly interested in any low-order structure. Estimates for the residual within each bin are obtained by finding the peak in a heavily smoothed histogram of the residuals. Standard errors for these estimates are estimated with a bootstrap technique which randomly resamples the data. This method introduces less bias than simply computing the mean within some fixed window (which will tend to reduce the size of the anomaly).

Results of this procedure are shown in Figures 1-3. Positive residuals are shown in black (slow

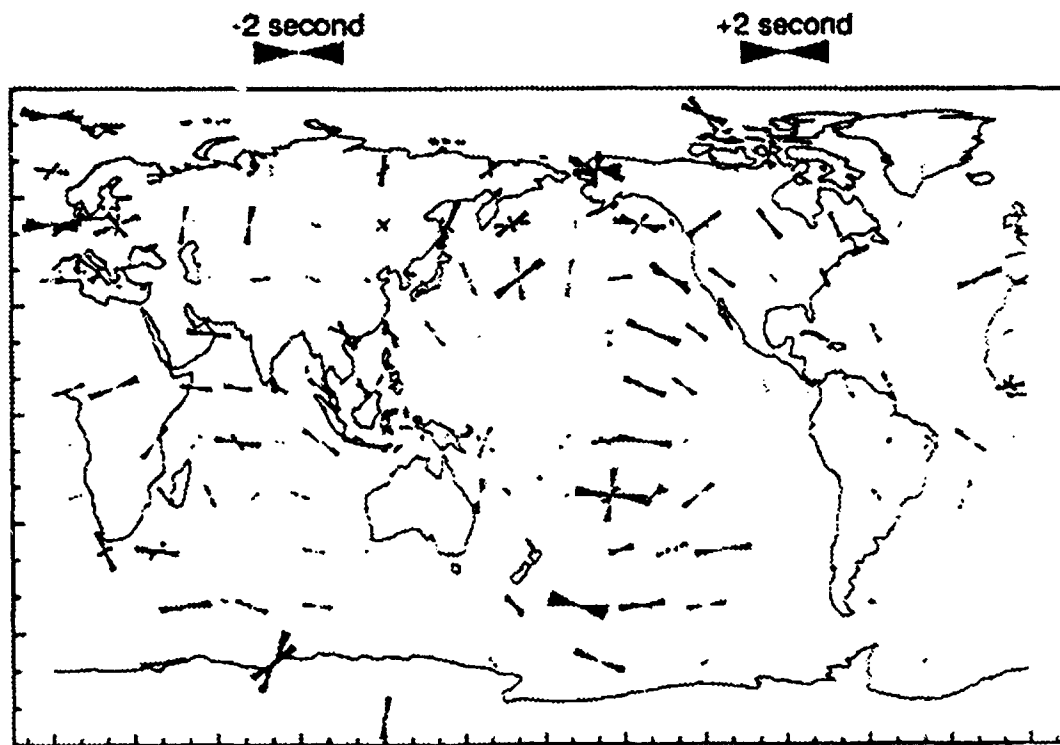


Figure 1. PKP(BC) residuals binned and plotted at turning point location. Positive (slow) anomalies are shown as black, negative (fast) anomalies as gray. The azimuth of the ray at the turning point is indicated by the angle of the plot. Only residuals with estimated standard errors less than 0.5 s are plotted.

anomalies) and negative residuals are shown in gray (fast anomalies). The position of the turning point bin is indicated on the map, with the angle of the wedges showing the local ray azimuth at the turning points and the length of the wedge showing the size of the residual. Bins are only shown if the estimated standard error is less than 0.5 s. These plots reveal how sparse the ray coverage is (most of the turning point bins contain data from only one azimuth). However, there is coherence between adjacent summary rays suggesting that these times are indicative of structure in the mantle or core.

Recent analyses of anomalous splitting of normal mode spectral peaks (e.g., Ritzwoller *et al.*, 1986; Widmer *et al.*, 1992) have suggested the possibility of aspherical structure in the Earth's outer core. The models suggested contain axi-symmetric velocity perturbations of spherical harmonic degree 2 in which velocities are about 0.5% faster near the poles than at the equator (i.e. a C_{20} anomaly). These models predict travel time anomalies of several seconds in PKP phases which travel through the outer core. However, the PKP times plotted in Figures 1-3 do not exhibit obvious C_{20} anomalies. Plots of predicted vs. actual PKP travel times show large scatter with no clear correlation. Figure 4 shows the change in misfit variance when the data are corrected for an outer core velocity model which can explain the anomalous splitting data. The solid line is for PKP(DF), the long-dashed line for PKP(BC) and the short dashed line for PKP(AB). The outer core model increases the data variance by 50 to 80%.

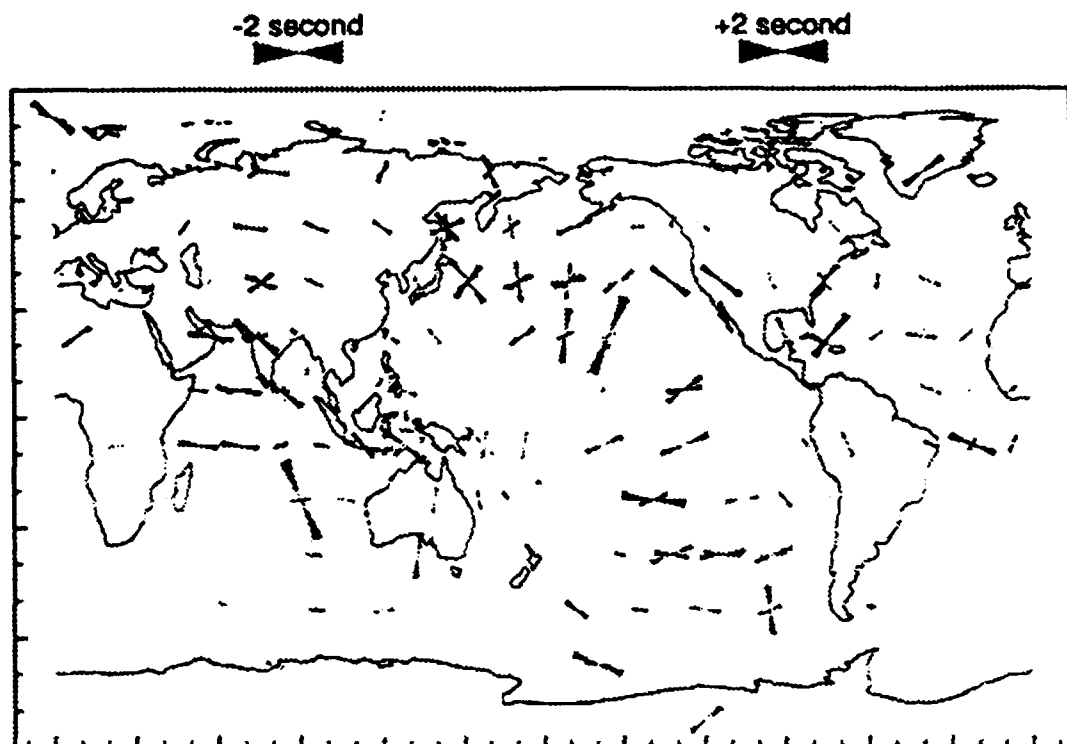


Figure 2. PKP(DF) residuals binned and plotted at turning point location. Positive (slow) anomalies are shown as black, negative (fast) anomalies as gray. The azimuth of the ray at the turning point is indicated by the angle of the plot. Only residuals with estimated standard errors less than 0.5 s are plotted.

These results did not use any correction for mantle heterogeneity. We experimented with scaled versions of shear-wave models but found that these did not predict ISC *P*-wave residuals very well. Instead, we have elected to use LO2.56, the Harvard lower mantle *P*-wave model. Figure 5 shows the variance change which results when this model is applied to *P* and *PKP* data. The *P* analysis uses 35,300 picks from 85 to 100°, binned and averaged exactly the same way as the *PKP* data. LO2.56 reduces the variance of these data by about 20%. The best variance reduction for *P* is achieved with a scaling of unity, indicating that the model amplitude is about right. The results for *P* are reassuring since LO2.56 is based on ISC *P*-wave data; however, it is somewhat disturbing that a greater variance reduction is not achieved. Figure 5 also shows the results of applying this model to *PKP* data – the variance of these data are increased by 40 to 50%. A tiny variance reduction can be achieved if LO2.56 is reduced in size by about a factor of 5.

As an experiment, we applied a correction to the *PKP* times based on the full LO2.56 model. However, in light of the large variance increase that results, it is questionable whether this should be done. Figure 6 is analogous to Figure 4 and shows the variance change as a function of C_{20} anomaly size for the LO2.56 corrected data. The mantle corrections do not have a large effect on the results.

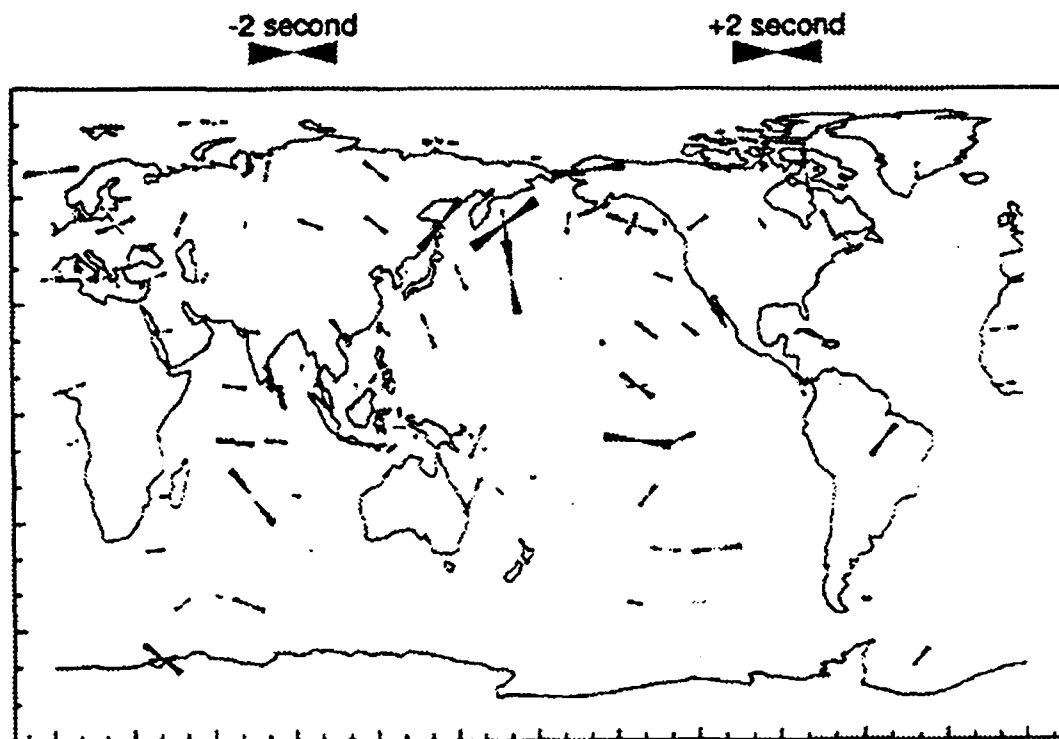


Figure 3. *PKP(AB)* residuals binned and plotted at turning point location. Positive (slow) anomalies are shown as black, negative (fast) anomalies as gray. The azimuth of the ray at the turning point is indicated by the angle of the plot. Only residuals with estimated standard errors less than 0.5 s are plotted.

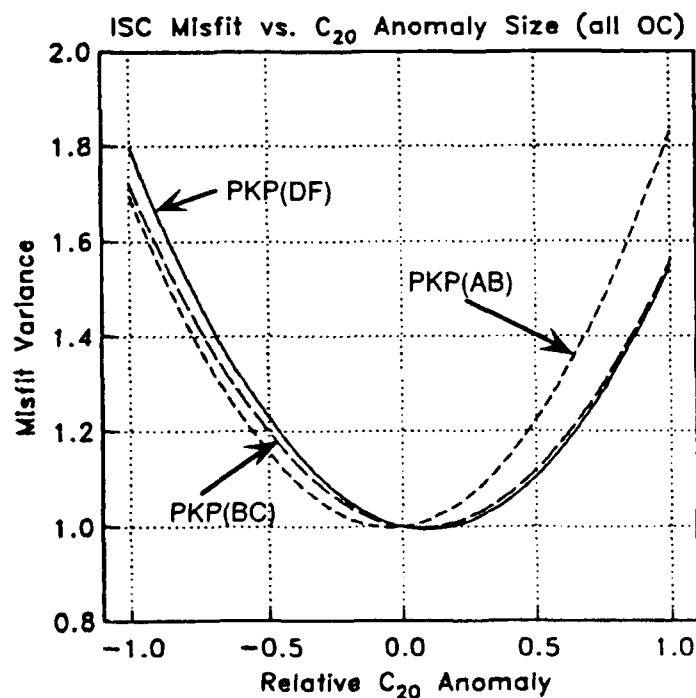


Figure 4. Variance of misfit to ISC residual bins as a function of relative size of outer core C_{20} velocity heterogeneity. *PKP(DF)* is shown as a solid line *PKP(BC)* as a dashed line, and *PKP(AB)* as a dotted line. A C_{20} anomaly which can explain the mode splitting data (scaled to a relative size of unity) increases the variance of the ISC data by 50 to 80%

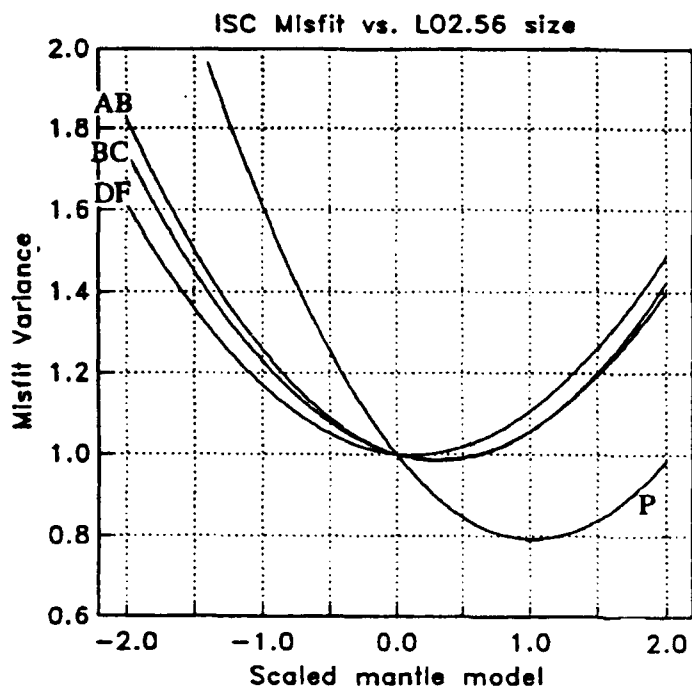


Figure 5. Variance of misfit to ISC residual bins as a function of the relative size of the mantle heterogeneity model LO2.56. This model improves the fit to the *P*-wave data but increases the scatter in *PKP* travel times.

CONCLUSIONS AND RECOMMENDATIONS

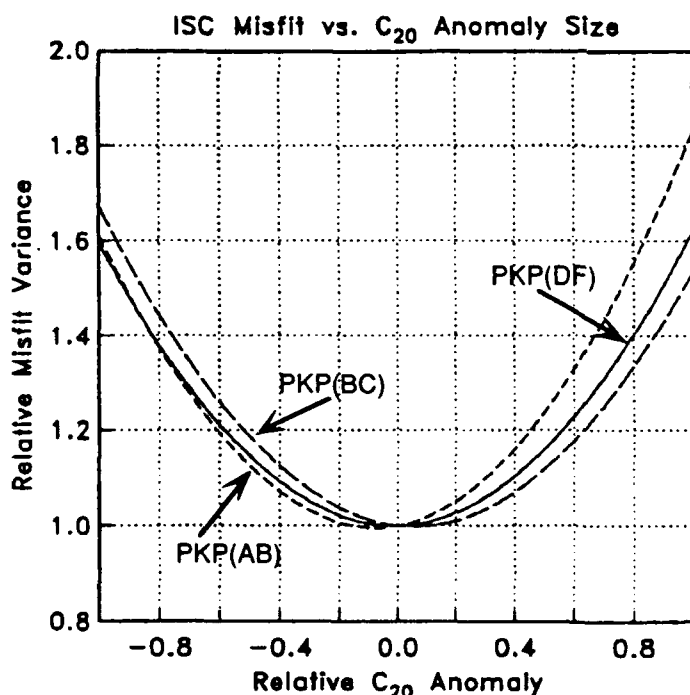


Figure 6 Variance of misfit to LO2.56 corrected ISC residual bins as a function of relative size of outer core C_{20} velocity heterogeneity. *PKP(DF)* is shown as a solid line, *PKP(BC)* as a dashed line, and *PKP(AB)* as a dotted line. The mantle corrections do not greatly change the results (compare Figures 4 and 6).

We have examined *PKP* travel times from the ISC and find that they appear inconsistent with outer core velocity anomalies of the size required to explain anomalous mode splitting data. We are currently exploring the effect of confining the anomaly to particular depth ranges within the outer core. Preliminary results indicate that the ISC data are less inconsistent with models in which the anomaly is confined to near the surface of the outer core, but that this improvement is nevertheless too small to reconcile the travel time and mode data. We are also experimenting with outer core anisotropy models and higher order heterogeneity models. However, so far the source of the bulk of the anomalous mode splitting

remains unknown.

The need to correct core phase data for the effects of mantle heterogeneity is a problem in these analyses. Most of the coherent signal in *PKP* data is probably due to mantle heterogeneity; however, current mantle models do not account for the signal. This is most likely due to limitations in the mantle models rather than an indication of core structure. A promising approach for future analyses will be to include both *P* and *PKP* data in inversions for mantle velocity structure to see if a model can be found which is consistent with both data sets.

REFERENCES

Ritzwoller, M., G. Masters, and F. Gilbert, 1986, Observations of anomalous splitting and their interpretation in terms of aspherical structure, *J. Geophys. Res.*, 91, 10,203—10,228.

Widmer, R. G. Masters, and F. Gilbert, 1992, Observably split multiplets — data analysis and interpretation in terms of large-scale aspherical structure, *Geophys. J. Int.*, in press.

MULTIVARIATE CALIBRATION AND YIELD ESTIMATION

Robert H. Shumway
Division of Statistics
University of California, Davis

PL Contract No. F19628-91-K-0033

OBJECTIVE

There are two important problems in monitoring nuclear tests using seismic and other means, either in a proliferation or treaty monitoring environment. The first is calibrating an assumed relation between the yield of a nuclear test and a vector of observed magnitudes. For example, we may measure body wave magnitudes, m_b and L_g , for a number of nuclear tests and seek to calibrate some function to the observed data which will allow prediction of yield from the magnitude vector. The prediction of yield and its associated uncertainty from observations on a future magnitude vector is the second important problem of interest in this report.

To illustrate the nature of the first problem, consider a set of 16 explosions from the Russian site at Semipalatinsk for which yields have been published in Bocharov et al (1989) and Vergino (1989). The data (listed in Section 5) are plotted in Figure 1 where it is fairly clear that a linear model relating both magnitudes to the logarithm of the announced yield would not be unreasonable. The only apparent deviation from linearity is the second event where the m_b value seems out of line. Fitting linear regressions of the two magnitudes on log-yield seems to be a natural way of estimating a calibration relation.

Note that all of these events are from the same region and it is unlikely that monitoring in a proliferation environment could yield such a large calibration set. Furthermore, the slopes and intercepts may vary considerably depending on the location of the event and the location of the network monitoring the event (see Heasler et al, 1990). One would more likely have available a much smaller group of say 5 or 6 vector magnitudes with announced yields as well as some prior information about the nature of the slopes and intercepts. The prior values could be based on geologic factors and (or) expert opinion. Given this more limited situation, one could still calculate a classical linear regression of the magnitude vector on yield that would make no use of prior knowledge. One could also ignore the calibration data completely and just use some prior probability distribution for the slope and intercept values based on an uncertainty derived from expert opinion. Alternatively, there is a third Bayesian calibration approach that makes optimal use of both the data and prior information. We will investigate all three approaches in this report.

In the past, there have been close-in hydrodynamic measurements called CORRTEx made on yield; these measurements are generally thought to be more accurate than seismic magnitudes. One can either regard these measurements as highly accurate magnitude surrogates with unit slope and zero intercept or as errors in variables measurements on yield. We discuss a multivariate errors in variables approach on site-replicated magnitudes, using CORRTEx as an additional measurement on yield.

Yield estimation on the basis of the calibration relation is the second important problem we consider in this paper. We assume that new yields corresponding to vector magnitudes are fixed and unknown. Then, the predictive distribution (see Atchison and Dunsmore, 1975) of the magnitudes in both the classical and Bayesian frameworks will be functions of the univariate yield. Inverting the predictive magnitude distribution then gives a confidence interval on the unknown future yield. An approach using the classical (non-Bayesian) method of Fieller (1954) in the univariate case was used in Rivers et al (1986) and in Picard and Bryson (1992). The extension of the classical method to the multivariate case is due to Brown (1982). For the Bayesian case, we choose to regard the yields as being fixed and unknown rather than as random with uniform prior distributions as in Brown (1982) and Picard and Bryson (1992). The use of the predictive distribution, without integrating over yields, gives a classical confidence interval rather than the Bayesian interval which would be characterized by the conditional distribution of yield given the magnitude vector in the usual Bayesian approach.

RESEARCH ACCOMPLISHED

To summarize the approach taken here, we have integrated material from Shumway and Der (1990) and Shumway (1990) with the emphasis changed from monitoring a possible Threshold Test Ban Treaty (TTBT) to monitoring the possible worldwide proliferation of nuclear weapons. A new section is included that revises the yields using maximum likelihood and a Bayesian set of priors for the intercept slope vector. This allows yield estimation using only prior information and no data or using prior information and one or more CORRTEx measurements.

To accomplish the above, we first introduce the simple linear model relating elements of the magnitude vector to log yield. Included in this specification are the slope and intercept uncertainty, formulated in one case using a bivariate normal prior, and the magnitude uncertainty, formulated using the multivariate inverted Wishart (chi-square) distribution. We then show how the slope and intercept can be calibrated using classical (data only), Bayesian (prior only or combined prior data) and errors in variables models. A second Bayesian approach is introduced that allows more generality in formulating the prior information on slopes and intercepts but assumes that the covariance matrix is fixed. For yield estimation, there is a predictive approach using both the classical and Bayesian assumptions and a Bayesian approach using the empirical Bayes estimators for the slopes and intercepts.

In order to give a simple example illustrating the the various techniques developed in this research, we consider a set of 16 Semipalatinsk events for which yields were published in Bocharov et al (1989) and Vergino (1989). For this set of 16 events, we obtained the network averaged body wave magnitudes m_b , corrected for receiver terms as well as the near-source focusing and defocusing effects from Jih and Shumway (1991). The second component that may be useful is root mean squared error computed from L_g magnitudes at a network of Soviet stations at regional distances (1000-4000 km) as given by Israelsson (1991). The magnitudes are plotted against the log-yields, w in Figure 1 and we note the excellent agreement with the linear model (2.1). The exception is the m_b value for the second event which seems low compared to the L_g and the other points. The sample computations here will assume that the magnitude vector and yield values are available for the first six events (above the line in the table) and these six events form the calibration set. The symbols for the six events are shaded in Figure 1 and we see that they cover a reasonable range of yields.

We assume also that prior information in the form of expert opinion puts the intercepts of the two lines at 4.4 and the slopes at .9. The uncertainties are defined by assigning standard deviations of .2 to the intercept vectors, .1 to the slope vectors and a correlation of -.5 between the intercept and slope. We always assume that the m_b and L_g yield adjusted magnitudes have standard deviations .05 and .03 respectively with correlation .3. Figure 1 shows the regression line at the expected values and it is clear that it lies above the line that might be implied by the data. Inferring yields from this line will lead to severe underestimates. Figure 2 shows the uncertainty region for the intercept and slope; the intercept is between 3.9 and 4.9 approximately 95% of the time with the comparable assumptions on slope involving the interval .65 to 1.15. The assumed correlation (slope increases as the intercept gets smaller) of -.5 restricts this variation somewhat.

In the case where we wish to incorporate CORRTEx values, it seems reasonable to regard the observation on CORRTEx yield as another element in the magnitude vector with intercept 0 and slope 1. Then, the prior distribution has three components and we may assigned the prior standard deviations of intercept and slope for the CORRTEx magnitude to be a small number (.03 in the present example) with no correlation between the intercept and slope.

Table 1 below shows the estimated intercepts and slopes for various methods. The first two lines are the result of simple multivariate regressions not involving the use of prior information. We see that the calibration regression on the first six events differs somewhat from the regression on all 16 events. In particular, the low m_b value pulls the intercept down to 3.92 and increases the slope to .98. The regression on the full set of 16 events gives a more representative line. This shows how far wrong one can go when there is a presumed outlier and we depend on the small calibration sample.

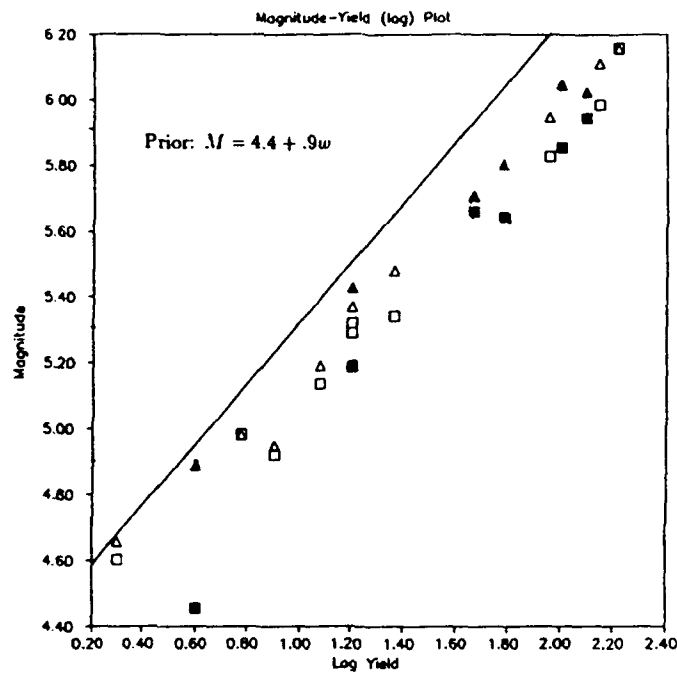


Figure 1: Magnitude-Yield Relations for m_b (squares) and L_g (triangles) from 16 Semipalatinsk Explosions. Calibration events are shaded. Prior regression line has intercept 4.4 and slope .9.

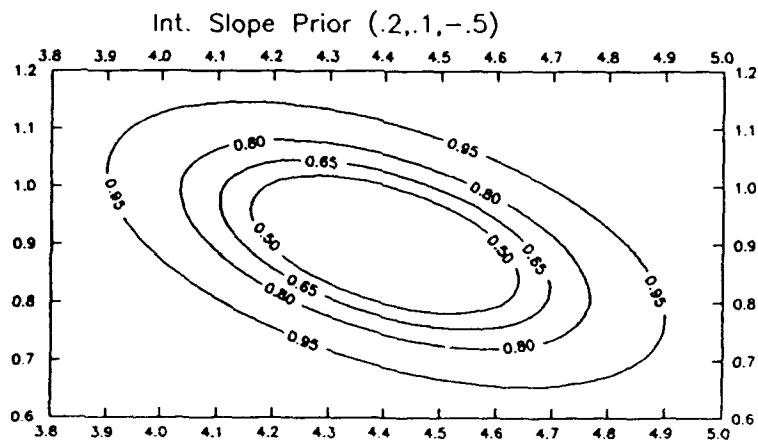


Figure 2: Prior Distribution of Intercept and Slope with means 4.4 and .9 respectively and standard deviations .2 and .1 with correlation -.5. Contours are cumulative probability that the intercept-slope pair is contained within the region.

Table 1: Estimated Slopes and Intercepts for Semipallatinsk

| | Intercepts | | Slopes | |
|--------------------------|------------|-------|--------|-------|
| | M_b | L_g | M_b | L_g |
| Data (16 events) | 4.22 | 4.34 | .83 | .83 |
| Data (6 events) | 3.92 | 4.45 | .98 | .77 |
| Bayes Prior | 4.40 | 4.40 | .90 | .90 |
| Bayes-Data (6 events) | 3.97 | 4.43 | .96 | .78 |
| Bayes-CORRTEX (6 events) | 3.97 | 4.45 | .96 | .78 |

The pure Bayes approach calibrates with the assumed prior distribution and these prior assumptions are reproduced in row 3 of Table 1. Combining the prior assumptions with the first 6 calibration events again pulls the m_b intercept down and the slope up but the L_g slope and intercept are quite close to what obtains for the entire 16 points. All three methods give nearly the same answer when applied to the calibration set.

For the CORRTEX based estimator, we use the empirical Bayes estimators, with yields evaluated by a maximum likelihood procedure. The posterior uncertainties are evaluated and lead to the estimated standard deviations .06, .04, .009, .04, .02, .009 for the three intercepts and three slopes.

The result of applying the methodologies summarized above to get yield estimators for Events 7-16 are shown in Table 2. One can compare the estimated yields with the announced yields to estimate how well each method works. The pure Bayes estimator involves only prior information. Combining data and the prior information gives the Bayes-data estimator.

Table 2: Yield Estimation Results for Semipallatinsk
(6 calibration events)

| Event | Yield | Data Driven | Pure Bayes | Bayes-Data | CORRTEX |
|-------|-------|-------------|------------|------------|-----------|
| 7 | 90 | 90*(2.01) | 53(2.39) | 87(1.61) | 86(1.36) |
| 8 | 16 | 18(1.85) | 12(2.28) | 17(1.60) | 17(1.30) |
| 9 | 12 | 11(1.86) | 7(2.28) | 10(1.63) | 11(1.28) |
| 10 | 23 | 23(1.94) | 15(2.24) | 23(1.59) | 23(1.31) |
| 11 | 16 | 18(1.89) | 12(2.27) | 17(1.60) | 17(1.30) |
| 12 | 6 | 6(1.75) | 4(2.33) | 6(1.68) | 6(1.26) |
| 13 | 8 | 5(1.82) | 4(2.33) | 5(1.69) | 6(1.26) |
| 14 | 2 | 2(1.73) | 1(2.48) | 2(1.83) | 2(1.22) |
| 15 | 165 | 185(2.12) | 98(2.56) | 170(1.66) | 165(1.39) |
| 16 | 140 | 145(2.07) | 81(2.47) | 140(1.65) | 135(1.38) |

* Uncertainty factors shown in ()

The results make it clear that the pure Bayes approach goes wrong because of the choice of a slightly erroneous prior; all yields are underestimated although the uncertainty number is large enough to put all of the announced yields in the predicted uncertainty region. The data-driven regression estimator does reasonably well except for overestimating the two highest yields; again the uncertainty intervals include the true values. Both the Bayes-data and CORRTEX methods do quite well. The Bayes-CORRTEX estimator should do well since there is an extra observation in the vector. For the particular example given here, the Bayes-CORRTEX method assigned weighting coefficients .21, .60, .33 to m_b , L_g and the CORRTEX yield respectively.

CONCLUSIONS AND RECOMMENDATIONS

There are many plausible approaches to calibration and estimation in the multivariate case. One must not only be prepared to work with calibration data when it is available but must be willing to develop a yield estimator when no calibration data is provided. It is the second of these two situations that may pertain more often in the current testing environment where monitoring worldwide proliferation is of primary interest. In such an environment, the use of prior information provided by expert panels and by seismic studies of different regions of the earth becomes paramount. The emphasis shifts from an approach that is heavily weighted towards calibration from samples, possibly involving CORRTEx yields, to one that is oriented towards formulating more accurate prior distributions. Because of the emphasis up to this point on the monitoring of a threshold test ban treat (TTBT), the research summarized in this report concentrates on the sampled data approach.

However, it should be pointed out that the predictive Bayes method is just such a approach because it uses only prior information and needs no calibration sample. The specification of the prior information involves expressing the joint uncertainty in the slope-intercept vectors in terms of a multivariate normal distribution. The mean value of this multivariate normal contains the expected slopes and intercepts whereas the uncertainty is specified through a covariance matrix. Geometrically this involves being able to intuitively choose elliptical uncertainty contours of the form given in Figure 2 that express our prior information about the slope and intercept.

The slope-intercept prior is proportional to the yield- adjusted magnitude covariance matrix which may also be subject to some uncertainty. Although the densities are restricted in some sense, they tend to emulate what one might regard as reasonable prior specifications for uncertainty about the covariance matrix. If the above prior densities are not flexible enough, the approach involving a second more general set of priors can be applied. This does impose the restriction that we must be willing to fix the yield adjusted magnitude covariance matrix at some known value. This set of priors seems to be the only realistic way that one can incorporate the errors in variable observation on CORRTEx into the magnitude vector. The posterior variances of the slope-intercept vector will be weighted properly by the CORRTEx variance in this particular configuration.

Unfortunately, any Bayes approach involves the risk of using an incorrect prior so that the estimated posterior yield might be quite far off. However the uncertainty factors will increase in proportion to the variance covariance structures of the slope-intercept vectors and the yield-adjusted magnitude vector. Therefore, the overall statements including the uncertainty factor will include the true yield 95% of the time if the uncertainty of the prior intercepts and slopes is assigned in a realistic fashion. This was seen in the example shown in Table 2.

REFERENCES

- Aitchison, J. and I.R. Dunsmore (1975). *Statistical Prediction Analysis*, Cambridge: Cambridge University Press.
- Bocharov, V.S., S.A. Zelentsov and V.I. Mikhailov (1989). Characteristics of 96 underground nuclear explosions at the Semipalatinsk test facility. *Atomic Energy*, **67**(3), 210- 214 (in Russian).
- Brown, P.J. (1982). Multivariate calibration. *J.R. Statist. Soc.*, **B 44**, 287-221.
- Dempster, A.P., N.M. Laird and D.B. Rubin (1977). Maximum likelihood from incomplete data via the EM algorithm. *J. Royal Statist. Soc., Ser. B*, **39**, 1-38.
- Fieller, E.C. (1954). Some problems in interval estimation. *J.R. Statist. Soc.*, **B 16**, 175-185.
- Heasler, P.G., R.C. Hanlen, D.A. Thurman and W.L. Nicholson (1990). Application of general linear models to event yield estimation. Pacific Northwest Lab Report No. PNL-CC-1801 171.
- Israelsson, H. (1991). RMS magnitudes, explosion yields and shots of events at the Semipalatinsk test range. Forthcoming Technical Report, Science Applications International Corp., Center for Seismic Studies, 1300 N. 17th St., Suite 1450, Arlington, VA 22209.
- Jih, R.S. and Shumway, R.H. (1991). Magnitude-yield regression with uncertain data: A Monte-Carlo approach with applications to Semipalatinsk underground nuclear explosions, TGAL-92-11, Semi-Annual Technical Report No. 2, Teledyne Geotech, Alexandria, VA.
- Picard, R. and M. Bryson (1992) Calibrated seismic verification of the Threshold Test Ban Treaty. *J. Amer. Statist. Assoc.*, **87**, 293-299.
- Rivers, D.W., R.H. Shumway and R. Wagner (1986). Statistical analysis of explosion magnitudes and yields. *The Vela Program*. A. Kerr, Ed., 771-779, Arlington: Executive Graphic Services.
- Shumway, R.H. and Z.A. Der (1990). Multivariate calibration and yield estimation for nuclear tests. Preprint November 21, 1990.
- Shumway, R.H. (1991). Multivariate calibration and yield estimation with errors in variables. Preprint, November 6, 1991.
- Vergino, E.S. (1989). Soviet test yields, *EOS, Trans. Amer. Geophys. Union* 1511+, Nov. 28, Corrections and Additions, 1569, Dec. 26.

CORRTEX Analysis System

*R. Stagat, W. Wortman, D. Terry, S. Moore, M. Frolli, Mission Research Corporation
K. McLaughlin, S. Peyton, S-CUBED
T. Ahrens, California Institute of Technology*

F29601-90-C-0064

Objective

The CORRTEX Analysis System (CAS) is a set of workstation-based analysis tools for estimating yields and their uncertainty using hydrodynamic data provided under TTBT protocols. The CORRTEX (COntinuous Reflectometry Radius versus Time EXperiment) method, which is used by the United States for on-site underground test monitoring, is illustrated in Figure 1. CAS combines advanced methods of physical modeling, experimentally measured equations of state, coupled statistical analyses, and computer graphical environments in an open-ended framework that makes the methodology and assumptions used readily apparent. CAS's novel contributions to CORRTEX analysis methods are its advanced treatment of the error budget that accounts for all known sources of uncertainty and the way it couples this treatment with the yield estimate. An associated visualization module is being developed to provide both analysts and non-experts with useful insights into the physics and analysis methods used in CORRTEX yield estimation.

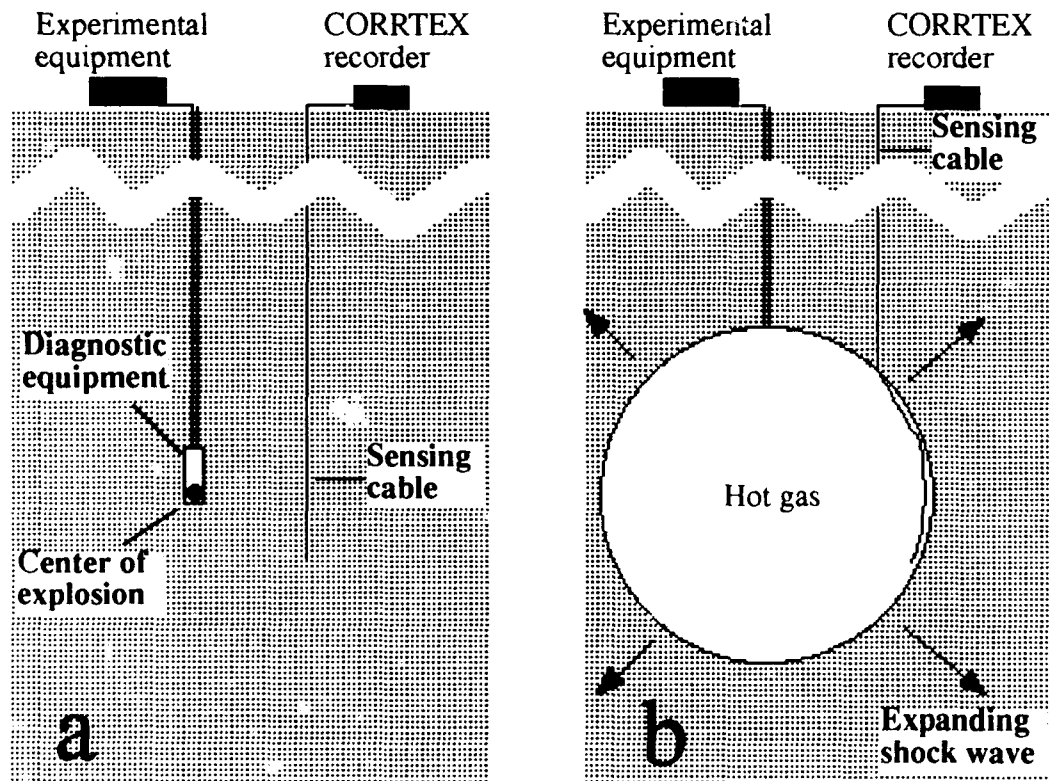


Figure 1. CORRTEX geometry illustrating (a) emplaced device with satellite-hole sensing cable, and (b) progressive crushing of cable by expanding shock wave.

Research Accomplished

CAS resides on a SUN workstation operating with Oracle DBMS, X-Windows, a Motif-based graphical user interface, and analysis codes written in C and Fortran. For each event it stores CORRTEX cable crush data, borehole survey data, well log information, and equation-of-state (EOS) data obtained from analyzing core samples. An analyst can graphically display each of these elements to verify the consistency of the data.

Every step of an analysis, or case, is saved in the database so an analyst can retrace his route and, if desired, branch to different options for alternate analysis procedures. Thus, for each case, a printable audit trail is available with the complete history of the analysts choices and the final results to which they led.

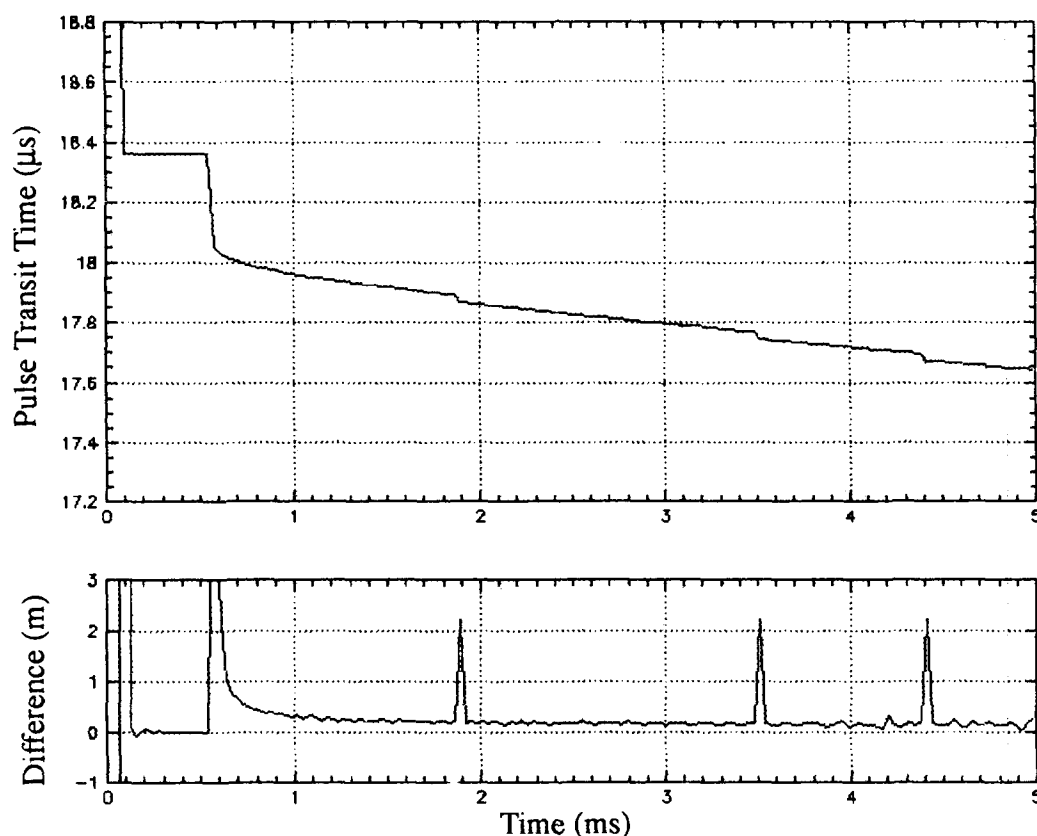


Figure 2. Raw CORRTEX Time-of-Flight data.

CAS's analysis tools include some that are widely used in this field and others that were developed specifically for CAS. Data reduction tools preprocess raw CORRTEX data, as in Figure 2, and convert them into radius versus time histories for all cables. This includes an automated technique to remove fiducial loops and use satellite hole survey data to compute uncrushed cable length vs. time. Knowing the cable position relative to the source, either from an emplacement hole survey or from a fit to the data, then provides shock radius vs. time, $R(t)$, along the direction to the cable, as shown in Figure 3. This $R(t)$ is compared to a yield standard to establish the yield estimate.

Yield standards may be generated using resident 1-D and 2-D finite difference hydrody-

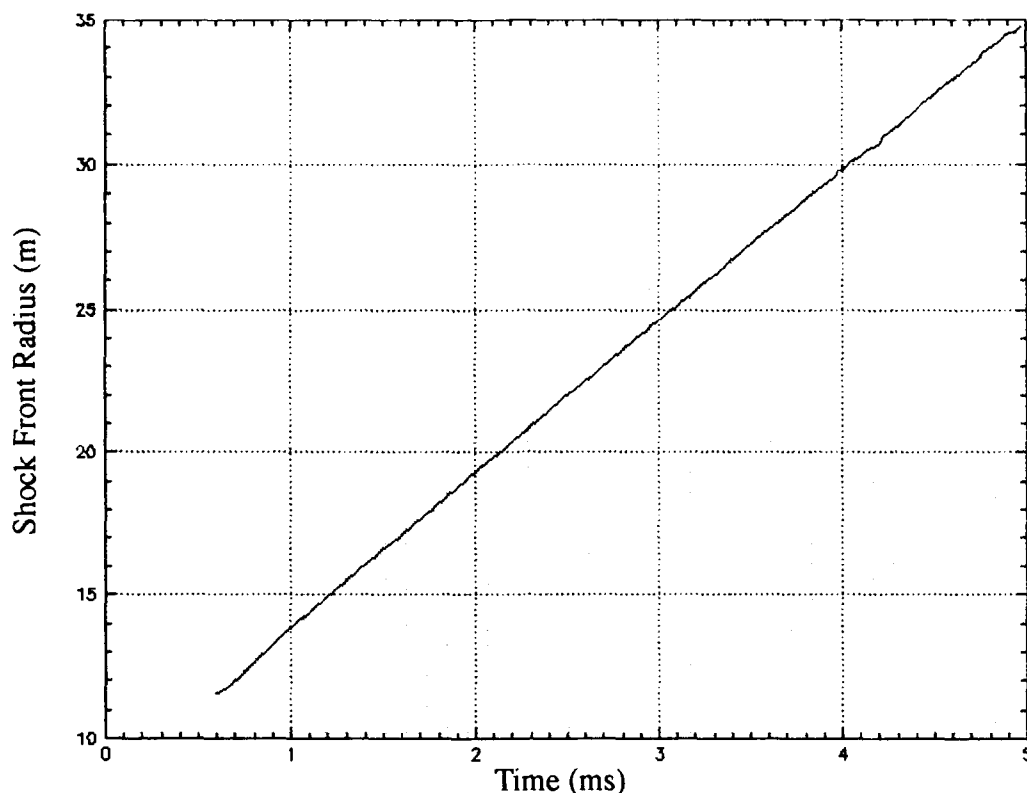


Figure 3. Processed Radius vs. Time CORRTEx data.

dynamic algorithms or from historical event data in the same medium. Computed standards use an experimentally measured Hugoniot, as shown in Figure 4, and other EOS data to compute a radius vs. time curve. CAS can then, for example, use simulated event scaling to compare the calculated standard with observed results to estimate the yield using conventional cube root scaling. The database has a collection of experimental $R(t)$ curves from historical events which can also be used to provide a yield standard for similar event scaling. Both of these methods provide apparent yield vs. time, and the analyst can choose a time window over which CAS will compute a mean yield in the conventional manner. However, CAS's utility is most evident in its use of a powerful statistical procedure to choose an optimally weighted window that implicitly accounts for all known uncertainties that affect the yield estimate and the correlations in those uncertainties. The result is an explicitly computed weight function which optimizes the window and which also provides a measure of the uncertainty of the estimated yield.

Coupled yield and uncertainty estimates are based on contributions from several error sources, including source characteristics, survey uncertainty, EOS uncertainty, and other factors. For each basic parameter that is uncertain, CAS treats the parameter as a stochastic variable and estimates its probability distribution. Using an approximate analytic hydrodynamic model due to Lamb and Moss, it generates many $R(t)$ realizations, using suitably distributed realizations of all stochastic variables, and compares each $R(t)$ prediction with the standard case to obtain an apparent yield vs. time series. Statistical variations of the stochastic parameters produce statistical variation of these yield vs. time series. For example, uncertainty in the Hugoniot is represented by a range of correlated parameters, and this can be used to produce a set of Hugoniot realizations as shown in Figure 5. Monte Carlo variations due to the EOS, source conditions, survey errors, and CORRTEx variability are then used to compute thousands of $R(t)$ realizations, as in Figure 6.

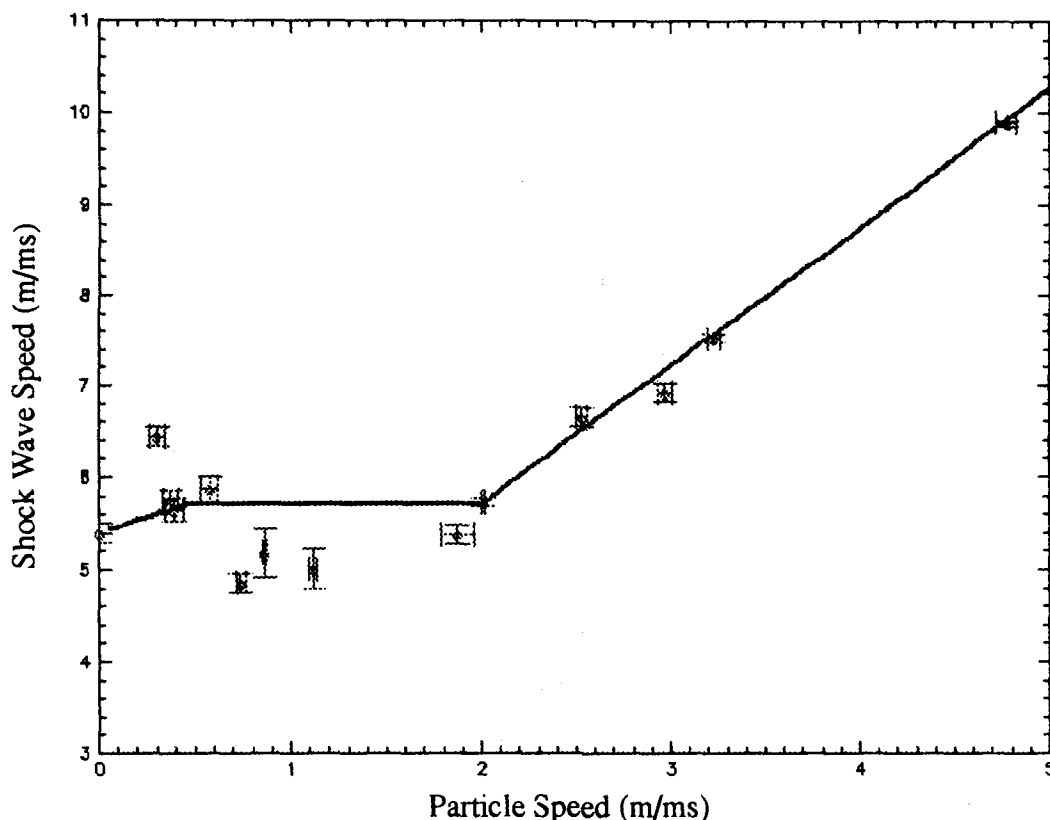


Figure 4. Hugoniot Measurements obtained from CalTech.

Using cube root scaling on a point-by-point basis, the $R(t)$ realizations are converted to $Yield(t)$ estimates as shown in Figure 7. Using second order statistics obtained from such a suite of realizations, CAS computes weights that are optimal (in the sense of minimizing the final uncertainty) for combining the elements of a typical yield vs. time series to obtain a single best estimate of the yield.

Correlations in the yield vs. time series that result from correlations in the behavior of underlying parameters are vital in determining the weights. If the data were uncorrelated from point to point, this weighting would be just $1/\sigma^2$ but, due to correlations, this is far from the actual case. Optimal weights concentrate in the conventional time window automatically, so there is no need to make ad hoc assumptions about the best time interval. A typical weight function so determined is shown in Figure 8. Generally, early times are deweighted due to source region uncertainties, while late times are deweighted due to strong correlations caused by a constant acoustic propagation speed. In addition to their use for yield estimates, weight functions also provide a related measure of the goodness-of-fit to the data. The multitude of realizations generated in the uncertainty analysis determine a joint probability distribution of the difference between the estimated and true yields and the goodness-of-fit. Consequently, the experimentally determined goodness-of-fit parameter can be translated into a conditional probability density of yields, as illustrated in Figure 9, thus providing an internally consistent uncertainty at any desired degree of confidence.

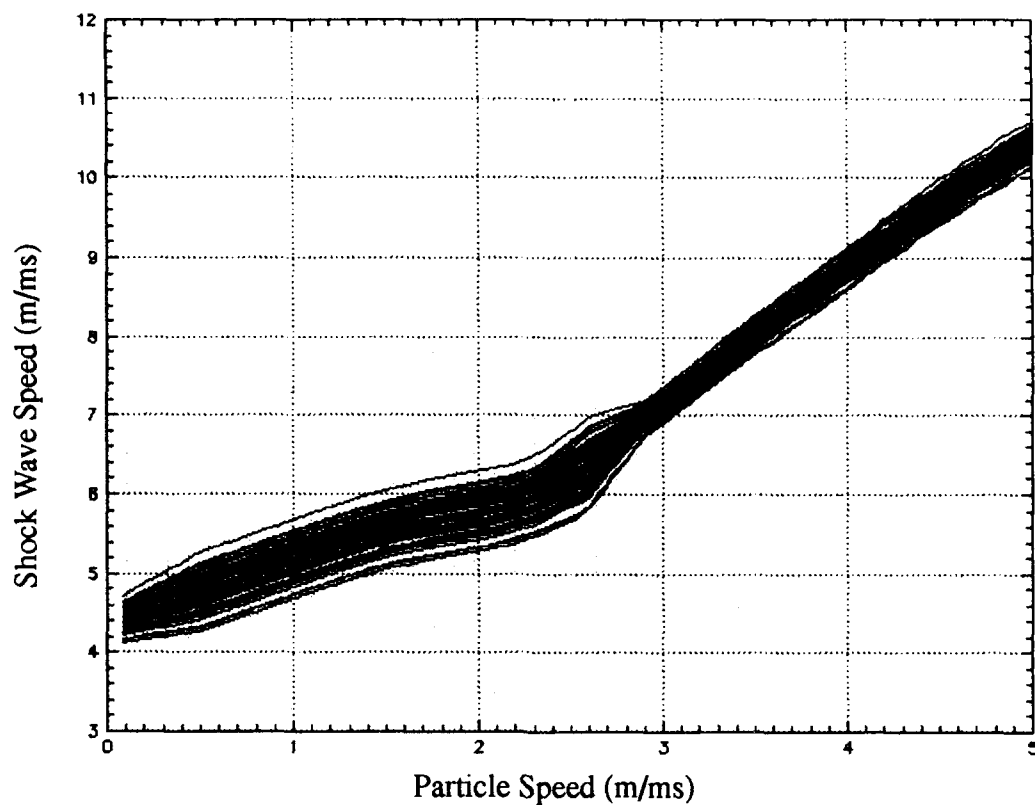


Figure 5. Monte Carlo Hugoniot Realizations.

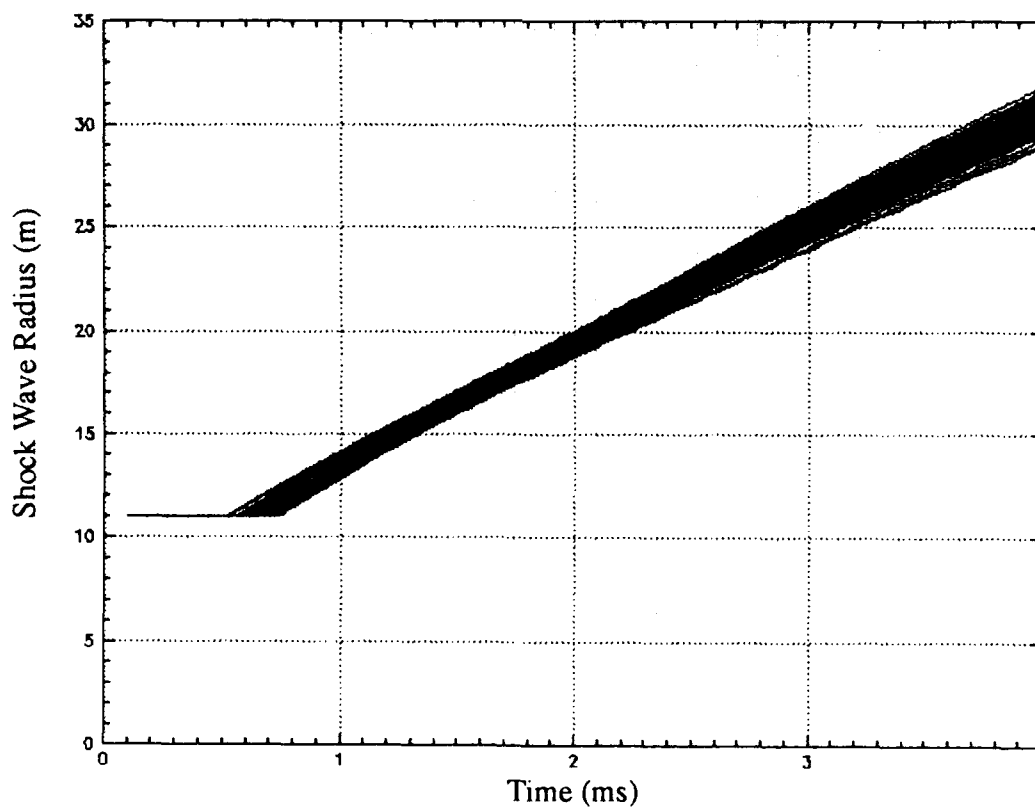


Figure 6. Monte Carlo Shock Wave Radius Realizations.

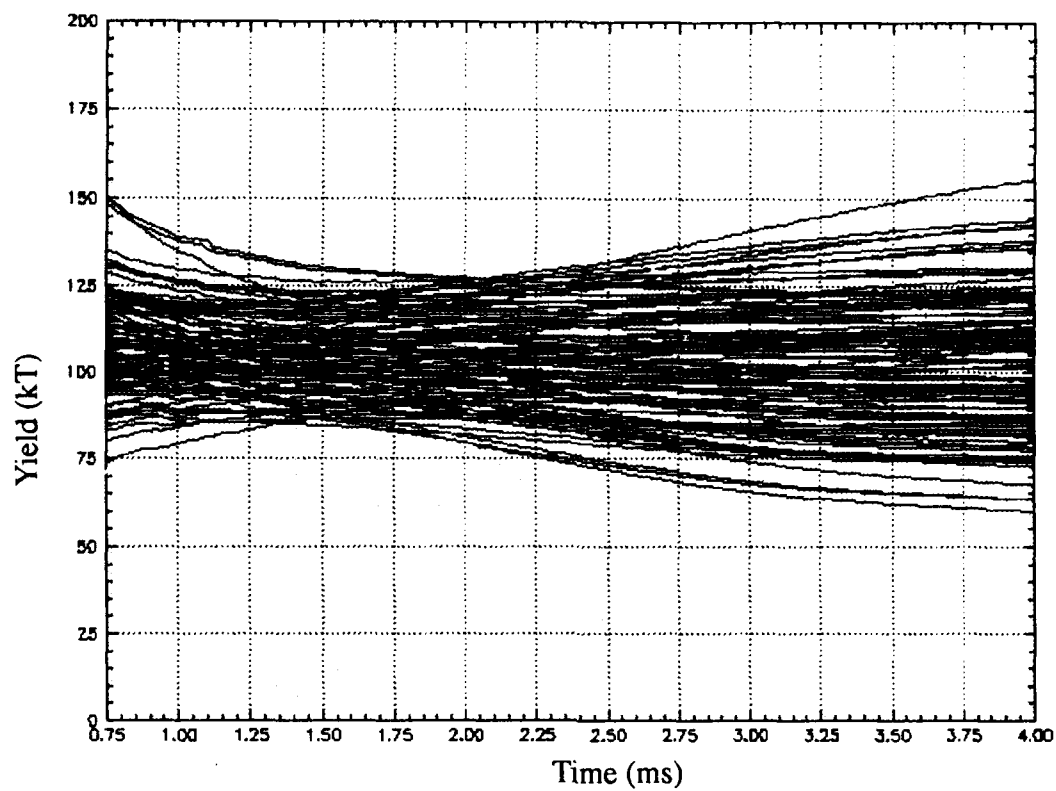


Figure 7. Computed Yield vs. Time Realizations.

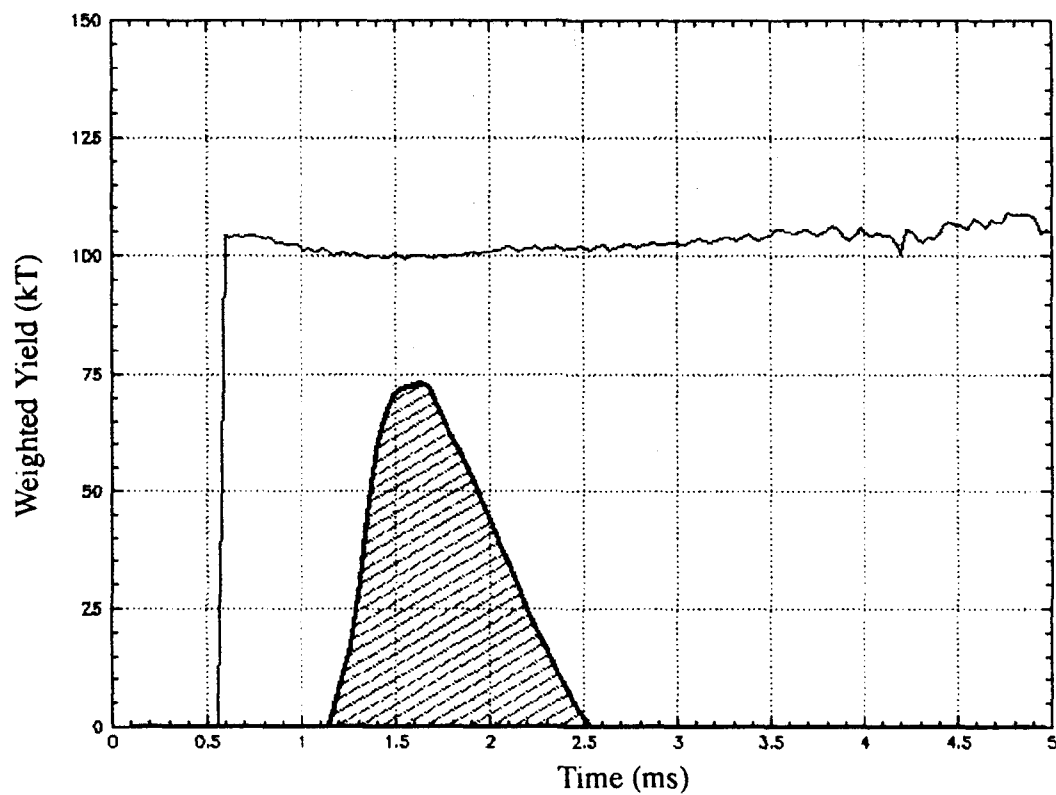


Figure 8. Optimally Weighted Yield Estimate.

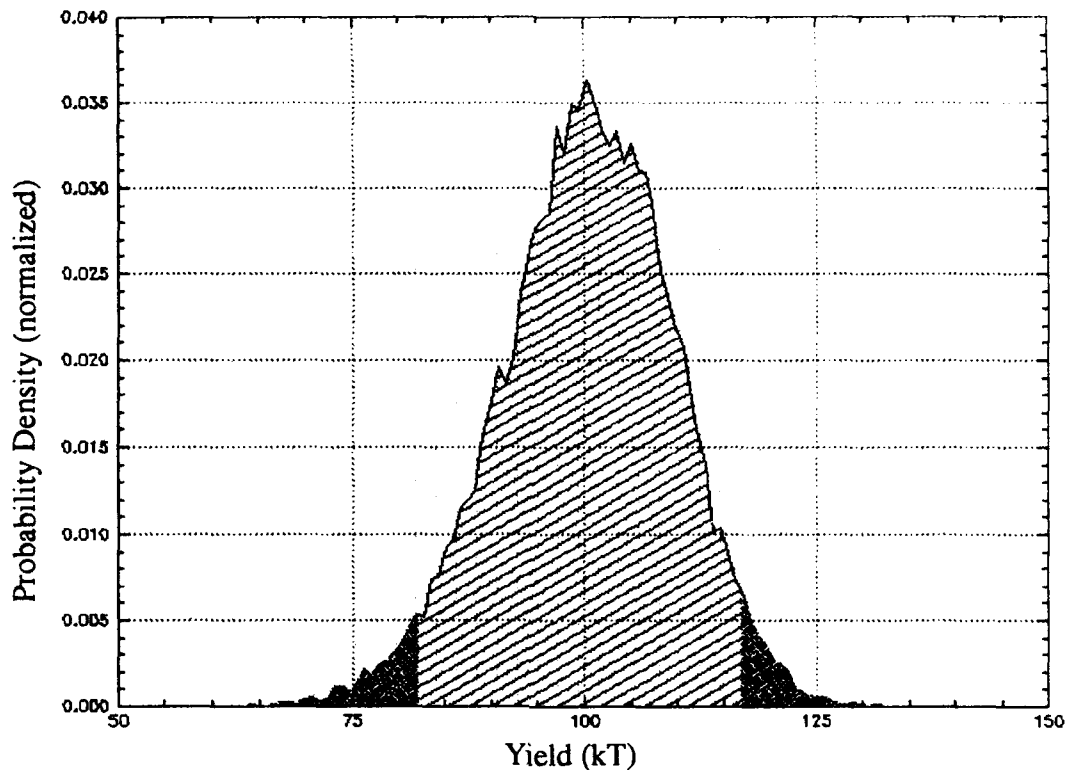


Figure 9. Statistically Computed Yield Probability Density Function.

Conclusions and Recommendations

The CAS methodology is designed to provide a fully documented estimate of the yield from a CORRTEx-monitored event performed under the TTBT protocols. It includes standard analysis methods developed by the national labs, adds a user-friendly graphical environment, and supplies an optimal statistical method to provide coupled yield and uncertainty estimates. CAS provides a report for each case processed that documents both assumptions used and intermediate results. It has been configured so improved analysis methodologies can be added in a straightforward manner to incorporate techniques that might be appropriate for different materials or yield regimes. CAS is installed on a SUN workstation at the Center for Seismic Studies and at AFTAC.

Acknowledgements

We would like to thank Fred Lamb and Jeremiah Sullivan, University of Illinois Urbana-Champaign Physics Department, for helpful discussions involving hydrodynamic yield estimation, and Gary McCartor and Buddy Gray, Southern Methodist University, for their help in the statistical uncertainty analysis.

References

- Lamb, F. K., An approximate solution for ground shock propagation, *University of Illinois Program in Arms Control, Disarmament, and International Security*, Rep. WP-2-87-2, Feb. 1987.
- Moss, W. C., A method to estimate the yield of an underground nuclear explosion, *J. Appl. Phys.*, 63, 4771-4773, 1988.

EQUIVALENT SEISMIC SOURCE FUNCTIONS FOR CHEMICAL AND NUCLEAR EXPLOSIONS

Brian W. Stump and Xiaoning Yang
Department of Geological Sciences
Southern Methodist University
Dallas, Texas 75275-0395

Contract: F29601-91-K-DB20

OBJECTIVE:

This report focuses on work conducted in the last year to quantify the energy coupling of ripple-fired chemical explosions. The motivation for this research is a desire to understand the physical processes that are unique to these types of events. These attributes can in turn be used as a basis for discriminating quarry explosions from nuclear explosions in the case of nonproliferation monitoring. Specific emphasis in these studies is placed on documenting the spatial and temporal characteristics of these sources. Near-source ground motions in conjunction with source information such as individual charge location in space and time and yield are used to document source effects on the observed waveforms. Individual charges in these arrays of explosions are typically of cylindrical geometry rather than the spherical symmetry often assumed for contained explosions. A second motivation of this work is the investigation of the effect of this cylindrical geometry on the radiated wavefield.

RESEARCH ACCOMPLISHED:

A set of cooperative experiments were designed and implemented in the last year in conjunction with a large coal mining operation in the mid-west. Arrays of explosive charges are used in this particular mining operation to move 35-65 ft of overburden to expose the coal seam. Single shots in this operation can exceed 100,000 lbs of explosives with single charges in the arrays less than 2,000 lbs.

The goals of these experiments were three-fold. The first was the quantification of the single, cylindrical sources that are used in the full scale production shots. The second objective of the experimental plan was the quantification of the effects of timing, location and charge size in an array of explosions. Previous work indicated that timing variations lead to significant spectral variations. This earlier work was done primarily with close-in data ($< 500\text{m}$) and so in this case we wanted to extend our observational ranges to several kilometers. The final part of our experimental plan was designed to determine the variability in waveforms observed in a typical explosive mining operation since a number of authors have suggested that a pattern recognition procedure might be useful in identifying quarry blasts.

EXPERIMENTAL PLAN: With the experimental goals in mind an array of accelerometers and velocity instruments were emplaced both in the mine as close as 100 m from the explosions and out to distances of 6 km for the purposes of documenting the ground motions. On the bench directly behind the explosions three-component accelerometers were installed for monitoring strong ground motion. Figure 1 displays the close-in instruments deployed. All sites that begin with the designation B were the accelerometers on the bench behind the shots. This array was designed to provide good azimuthal coverage of the radiated wavefield so that the effect of the rock face in front of the explosive could be assessed. At the greater distances, 2 Hz velocity instruments (designated with an L) were deployed. Two additional three-component velocity transducers were deployed at 6 km and are not shown in the figure. These last two instruments provided us with the opportunity to assess the importance of more complex propagation path effects.

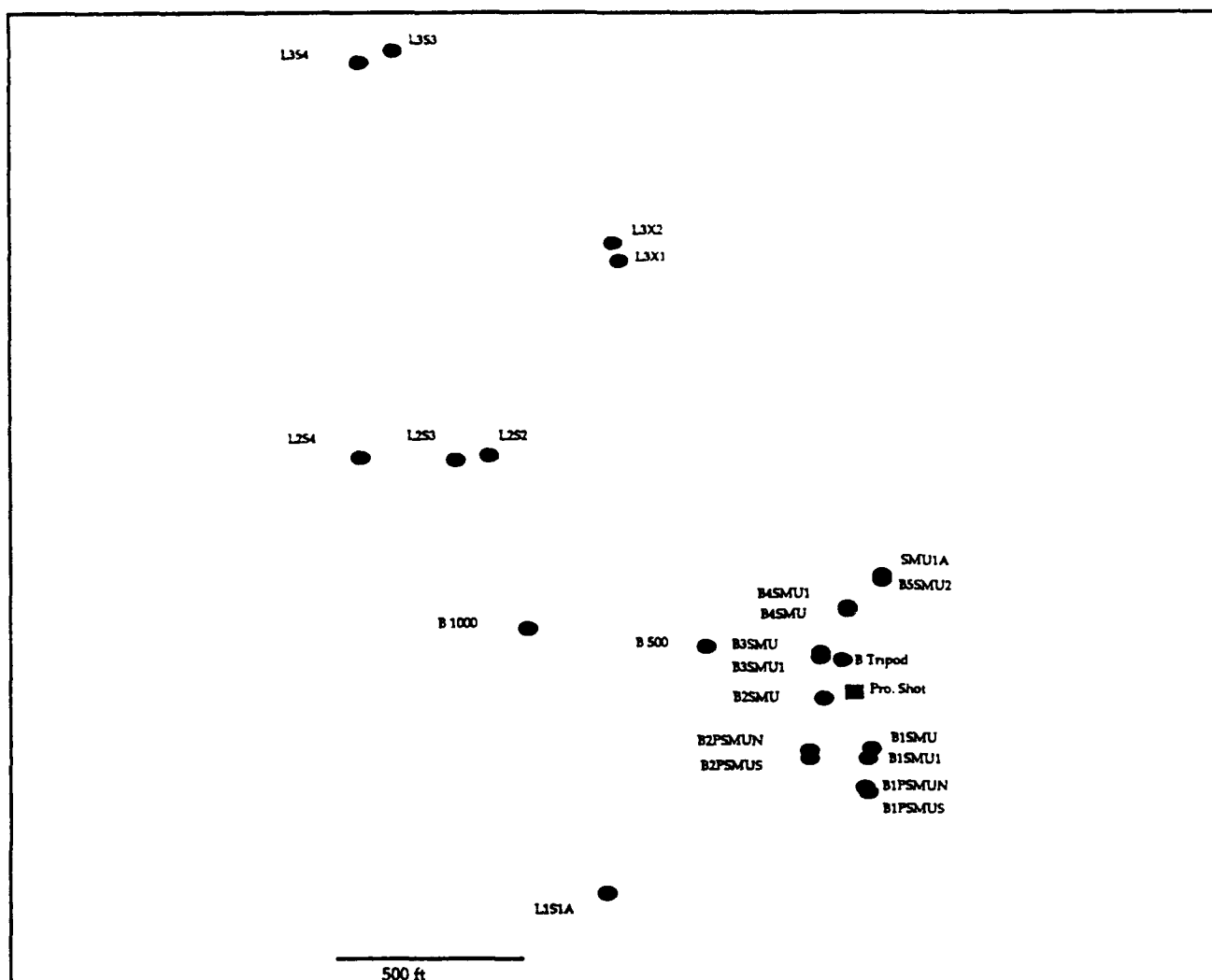


Figure 1: Instrumentation plan for the seismic monitoring experiment. All acceleration and velocity instruments are designated by an ellipse. The test production shot is represented by the square.

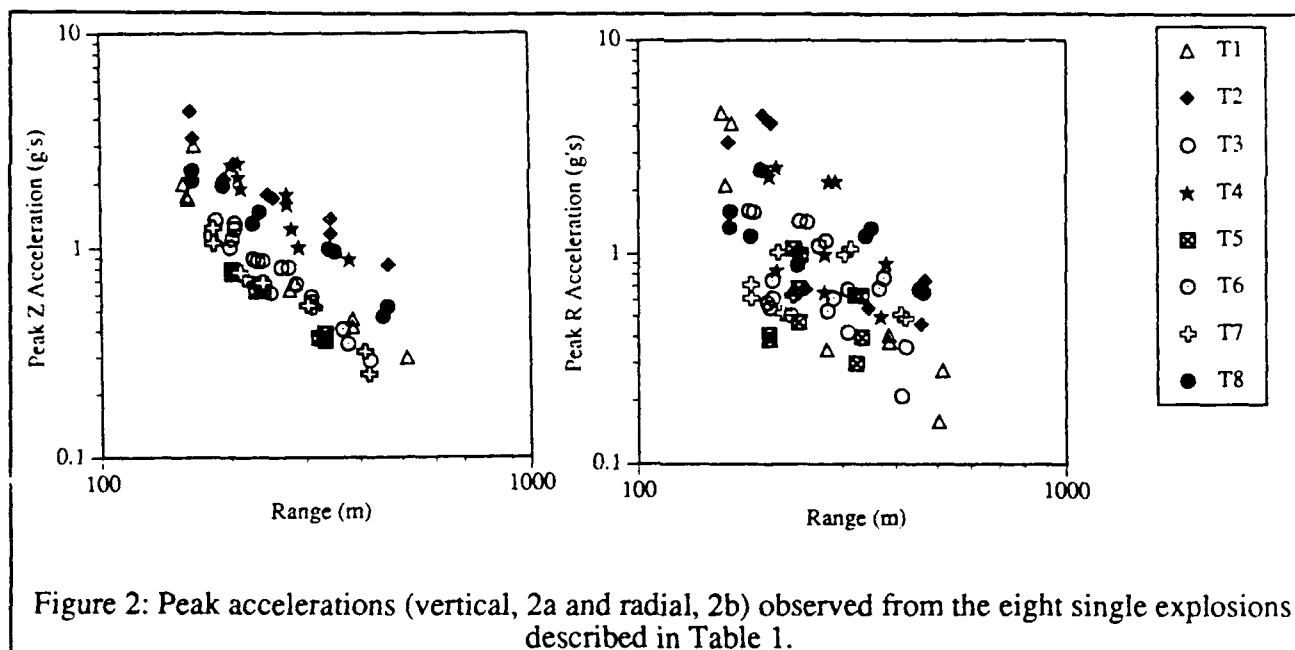
SITE CHARACTERIZATION: The mine where the tests were conducted consisted of two benches each of which rises 30-40 feet above the mine floor where the coal is being extracted. Shallow refraction data were taken on each bench to constrain the velocity model for the near-source observations. The first bench which overlies the coal consists of a shale sequence with a thin weathered layer. The weathered layer thickness is 3 m with a P velocity of 500 m/s and a S velocity of 250 m/s. The rest of the shale produced a P velocity of 2400 m/s and S velocity of 1000 m/s. Reversed data indicates a planar structure. The second bench consisted of an alluvium section. Again a near-surface weathered layer was identified with a thickness of approximately 4 m and a P velocity of 570 m/s. Marginal shear wave data were recovered. The rest of the alluvium with a thickness of 14 to 16 m produced a P velocity of 1600 m/s. The second bench refraction data also yielded P velocities for the underlying shales that were consistent with the first bench results.

SINGLE EXPLOSION DATA: Eight, single cylindrical sources were detonated and ground motion data recovered to investigate the importance of charge type and configuration on the radiated seismic energy. Different yields of both ANFO and Emulsion explosives were used. Two tests were detonated with an air column or deck directly above the explosive while the remaining six, single shots were backfilled with stemming and drill cuttings. The air decks were designed to investigate proposed enhanced motions from such configurations. All charge holes were 12.25

inches in diameter. Table 1 summarizes the eight sources.

| Shot Designation | Explosive Column (ft) | Explosive Type | Overburden (ft) | Air Deck (ft) |
|------------------|-----------------------|----------------|-----------------|---------------|
| T1 | 4 | ANFO | 13 | 0 |
| T2 | 10 | Emulsion | 17 | 0 |
| T3 | 3 | Emulsion | 17 | 0 |
| T4 | 10 | ANFO | 18 | 0 |
| T5 | 3 | ANFO | 15 | 3 |
| T6 | 3 | Emulsion | 17 | 3 |
| T7 | 3 | ANFO | 17 | 0 |
| T8 | 10 | Emulsion | 18 | 0 |

Initial analysis of the accelerometer data from the eight single charges indicates the importance of the charge size on the radiated wavefield. As a simple measure of these effects peak vertical and radial acceleration were measured from all the recovered data. These peak accelerations are plotted against source-receiver range in Figure 2. The vertical acceleration (2a) data show a good separation between the three largest shots (T2, T4 and T8: all solid symbols) from the other data. The smaller size explosions are grouped together approximately a factor of 2.5 below. Scatter within any one explosion is slightly less than a factor of two which makes the interpretation of coupling differences among individual explosions problematic. It is difficult to separate the effects of either the explosive type or the air decks in this initial representation of the single explosion data.



The radial acceleration data in Figure 2b does not show as clear a separation of events according to charge size. As noted in the experimental design, the accelerometer sites spanned a significant number of azimuths. The increased scatter in the peak radial acceleration data may represent azimuthal radiation effects around the source. Similar scatter is observed in the transverse motions. The free face directly in front of the cylindrical charge will result in azimuthal effects in the radiation and mixed radial and transverse motions.

Further work is warranted in order to quantify both coupling differences between explosions and the effects of the free face on the observations. Azimuthal radiation patterns will be explored. Coupling in different frequency bands will also be quantified. With the well constrained site

geology we intend to conduct numerical modeling to investigate possible geometrical contributions to the data.

TEST PRODUCTION SHOT: In order to quantify the effects of individual detonation time and location in an array of explosions typical of a mining operation, a small scale production shot was accomplished on the same bench as the single shots. The individual charges in the array were emplaced in the same manner as the single charges. Standard production detonators were used in the array. These detonators are known to have significant variations between design and actual shot times. In order to document these effects two procedures were used to determine individual detonation time within the array. The first technique consisted of high speed photography which recorded the flash of detonator cord at the surface which was connected to the subsurface detonator. Velocity of detonation measurements (VODR) were also made in each hole which provided initiation time and burn velocities within the explosive. The two measurements of detonation time agreed with one another to within 2 msec. Figure 3 displays the design and observed detonation times for the sixteen explosions in the array.

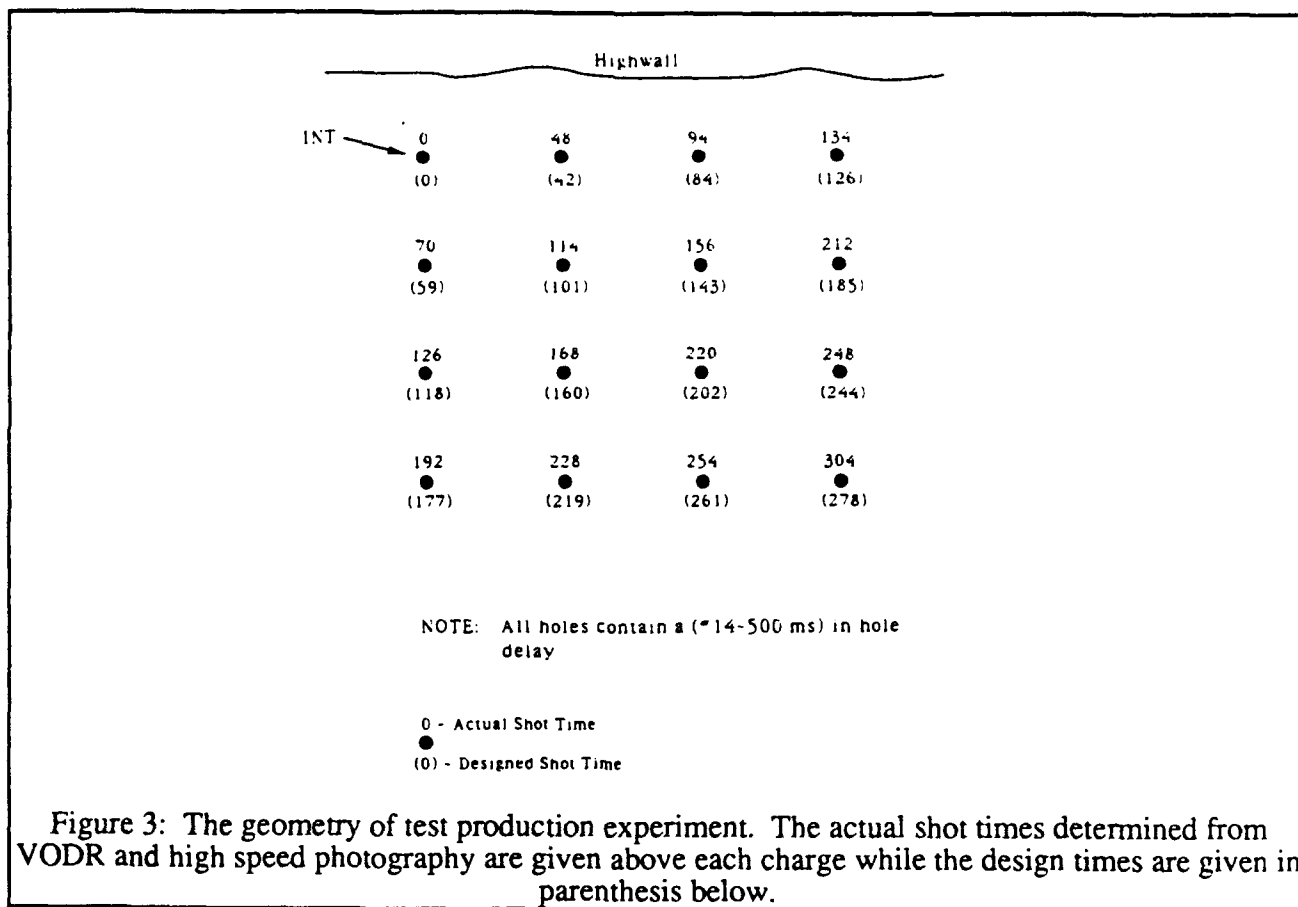
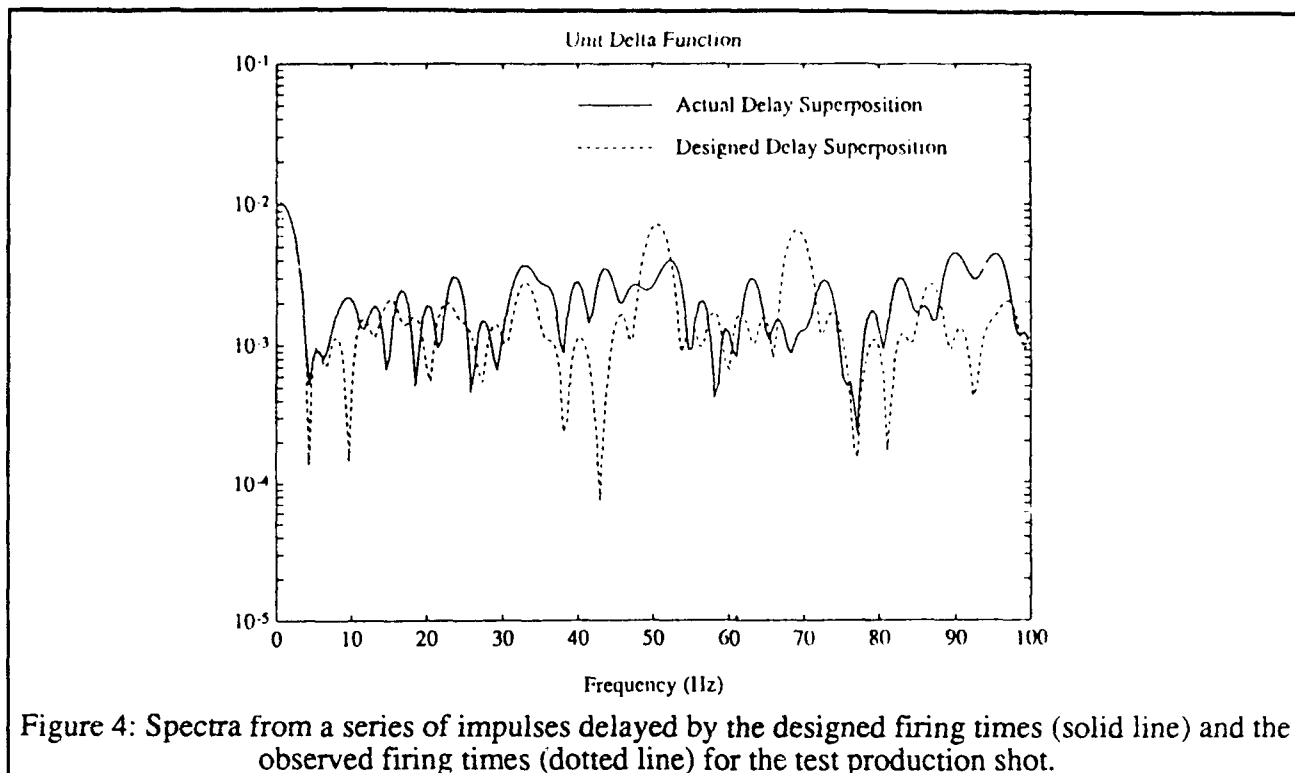
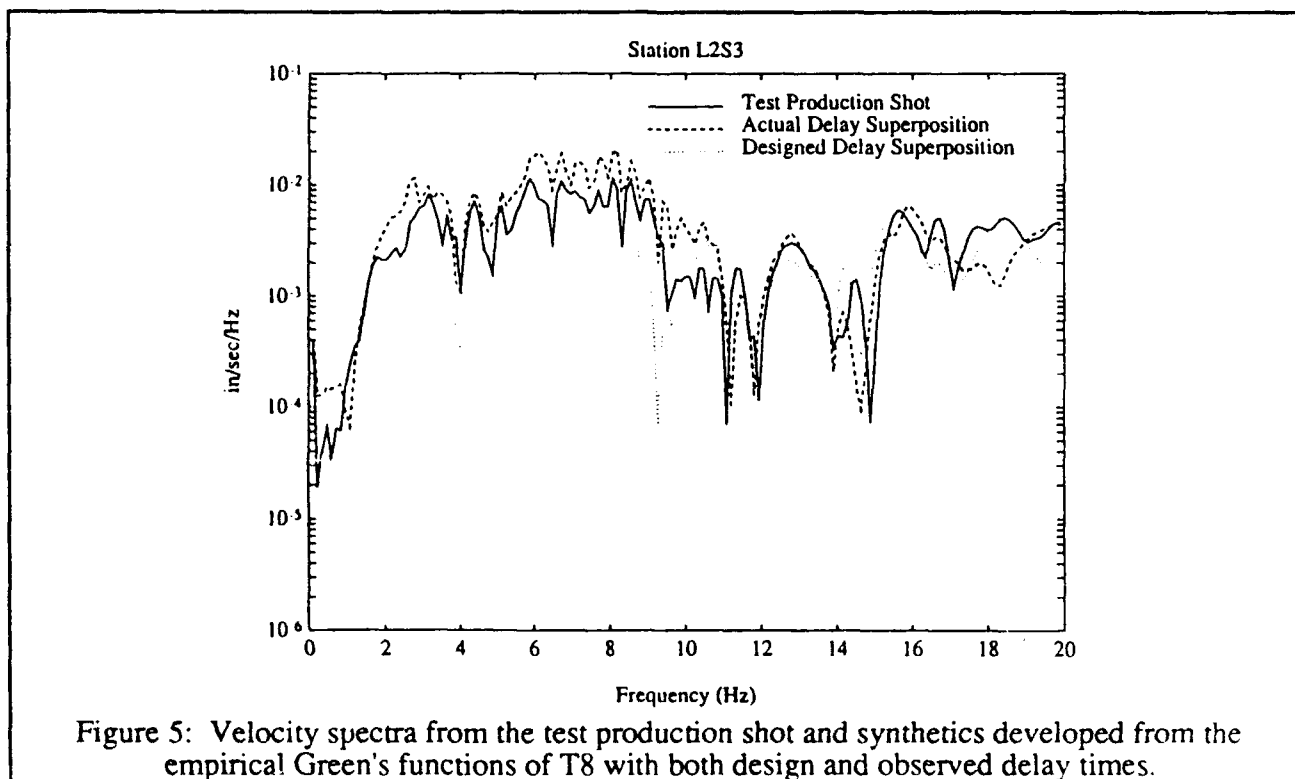


Figure 3: The geometry of test production experiment. The actual shot times determined from VODR and high speed photography are given above each charge while the design times are given in parenthesis below.

Variations between design and observed detonation times as large as 26 msec were documented. The effect of these shot time variations on the radiated spectra were investigated by calculating the spectra for a series of impulses at the design delay times (designed delay superposition) and the observed delay times (actual delay superposition). Comparison of the two spectra in Figure 4 shows little difference below 4 Hz but as much as an order of magnitude difference between the design and actual spectra at higher frequencies. In this example it is quit difficult to identify regular spectral peaks and holes in the actual delay superposition although the design superposition produces some rather large spectral variations.

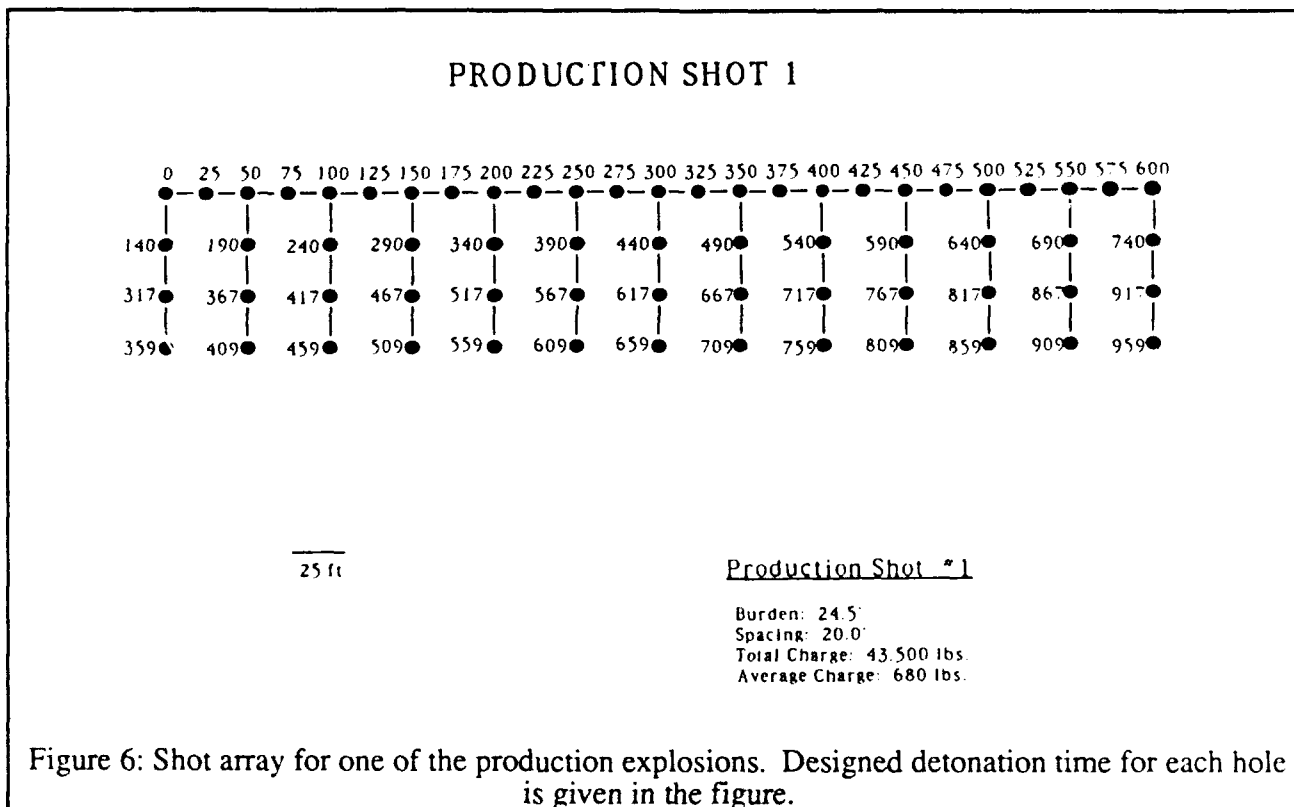


The waveforms from the single cylindrical tests can be used as empirical Green's functions to test for linear superposition in the test production shot. The data at station L2S3 (Figure 1) from T8 was used in this investigation. The vertical velocities from the test production shot are compared to synthetics generated with the observed delay times and the design delay times in Figure 5.



As found in the spectra from the impulse responses, the large spectral holes in the synthetics with the design delay times are not found in the data. The synthetics based upon the actual delay times match the observational data better and do not include the large spectral holes. It is interesting to note that in the frequency band from 2-10 Hz that the synthetics slightly over estimate the spectral levels actually observed. Individual charges in the test production shot were not all the same yield. This fact was taken into account in the synthetics by scaling the absolute amplitude of the empirical Green's functions by the yield. This scaling may not be completely appropriate.

PRODUCTION SHOTS: The final portion of our study was the monitoring of several of the mines normal production shots for overburden removal. These shots were larger in yield than our experimental ones and consisted of total explosive weights between 40,000-90,000 lbs. The purpose of this final part of the experimental work was to document source repeatability. During the extended monitoring, a series of three shots were detonated all with the same timing and spacing characteristics. The production shots were within 250 feet of one another. The design delay times and explosion spacing is given in Figure 6. The three shots were all detonated on the same day and recorded by our seismic array. The first two shots had nearly identical total charge weight as illustrated in Figure 6, 43,500 lbs. The third shot in the series had deeper explosive emplacement holes and thus a total charge weight of 87,077 nearly twice that of the first two.



Observed velocity spectra from the three production explosions are compared in Figure 7 to investigate the importance of source timing and spacing on these observations. If there was little variation between the design and actual shot times and if the depth of the individual charges has little effect other than total level one might expect the three spectra to closely follow one another. As the figure indicates, there are significant differences in both spectral level and shape between the three production explosions. Between 1 and 2 Hz the spectral levels between the three shots vary by as much as an order of magnitude. The third production shot as expected is the largest of the three in most of this band. Spectral scalloping is identified in the data but no consistent pattern is observed from shot to shot. Comparison of this data with spectra from the single shot experiments

indicates that a great deal of the variability in the spectral shape is due to propagation path effects. One can conjecture that just as in the test production shot, variations in actual detonation times destroyed strong spectral peaks and troughs.

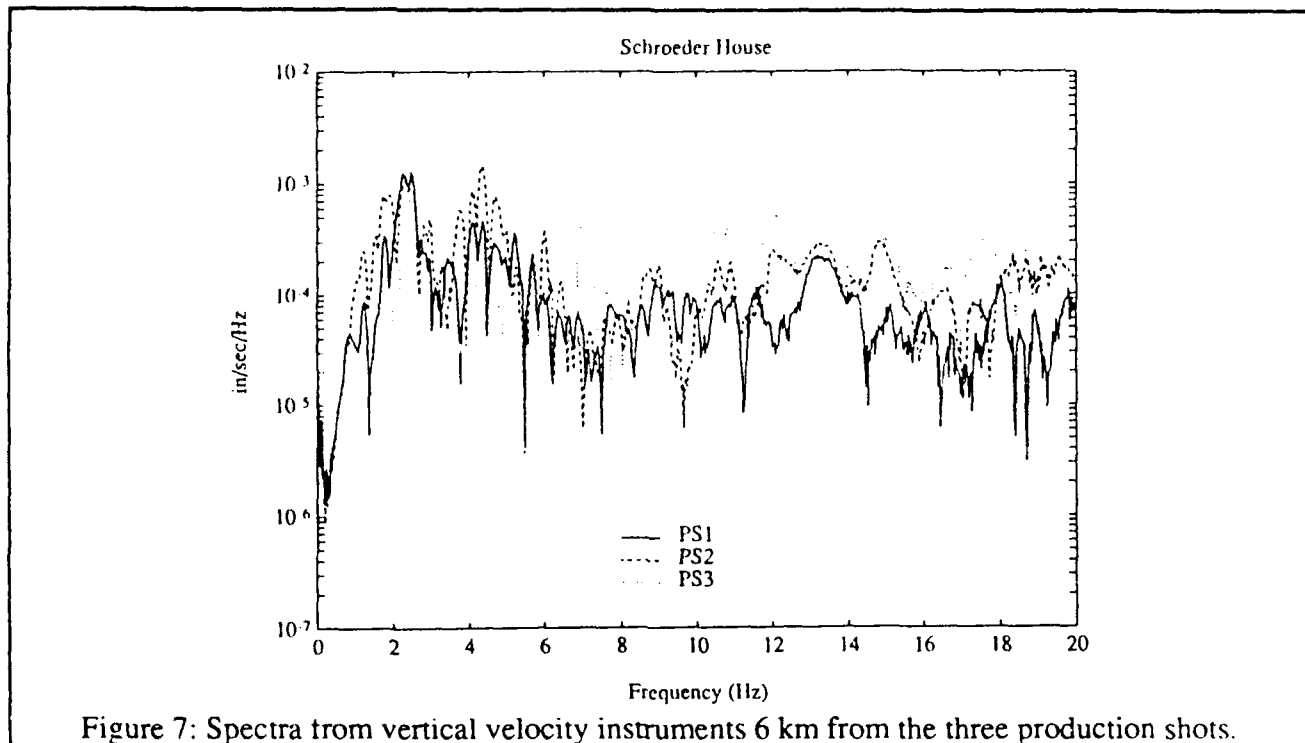


Figure 7: Spectra from vertical velocity instruments 6 km from the three production shots.

CONCLUSIONS AND RECOMMENDATIONS: The experimental program has documented variations within individual cylindrical charges, a portion of which is attributable to the size of the single charge. Additional amplitude variations particularly apparent on radial and transverse observations may be indicative of azimuthal variations introduced by the proximity of the free face to the cylindrical charge. We intend to extend our analysis of the single charge data in order to resolve these effects. Azimuthal radiation patterns will be determined and moment tensor inversions will be completed. Frequency domain effects will also be documented. These effects may be responsible for the generation of strong shear waves from mining explosions.

Variations between design and actual detonation times have been documented with both high speed photography and velocity of detonation measurements. These observations coupled with single source empirical Green's functions have allowed us to assess the importance of these variations on observational data. At high frequencies (>4 Hz) the sharp peaks and troughs predicted by the design delay times are destroyed by shot time variations resulting in observed spectra which reflect a strong contribution from propagation path effects.

Significant differences in waveforms from different production shots within a single mining operation are observed. These differences extend to frequencies as low as 1 to 2 Hz. Three production shots with identical explosion spacing and design detonation times fired within 250 feet and 40 minutes of one another produce quite different waveforms and spectra. Some of the difference may be attributed to differences between actual and design shot times. Unfortunately, there was no documentation of actual shot times in these production shots. The other major difference between the shots is that the third explosion had shot holes that were nearly twice as deep as the first two and thus the total explosive weight was larger by a factor of two.

Analysis of IMS Locations of Mine Blasts and RMS L_g Magnitudes in Scandinavia

A. Suteau-Henson, V. Z. Ryaboy, F. Rivière-Barbier, H. Israelsson, and J. A. Carter
Center For Seismic Studies, 1300 North 17th Street, Arlington, VA 22209
Contract No. F29601-92-C-0005

OBJECTIVE

The Intelligent Monitoring System (IMS, Bache *et al.*, 1990) routinely estimates locations and magnitudes of regional events using recordings from arrays and three-component (3-C) stations. The objective of this study is to show how region-specific knowledge derived from "ground truth" (e.g. mine locations and DSS observations) can be applied to improve automated locations. Also, a new method of magnitude estimation, based on RMS L_g amplitudes, is proposed, and its results compared with the M_L estimates in the IMS.

RESEARCH ACCOMPLISHED

For the part of this study aimed at improving automated locations, we selected near-regional events recorded at ARCESS after November 1990, most of which were located using a single-array. The seismicity around ARCESS is characterized by clusters of events. Many of these clusters are located near known mines, and their centers are often offset from the mine locations. Events in the clusters usually have temporal patterns of seismicity indicative of mining activity (e.g. nearly all events occur between certain hours of the day). Assuming that these events actually are mine blasts, and therefore can be given (nearly) exact locations, we identify the causes of the observed location errors, and propose methods to correct location bias and reduce the scatter. We illustrate our approach using explosions from the Kiruna mine in Northern Sweden (290 km southwest of ARCESS, Figure 1). This mine blasts regularly at around 11:30 (local time) each night and is the major source of mining activity in the area (personal communication from Kiruna mine management). DSS profiles, primarily from POLAR, are available to the southeast of the Kiruna - ARCESS travel-path. Comparison of "ground truth" and IMS locations shows a distance bias of over 20 km (from Kiruna towards ARCESS), and an azimuth bias of approximately 5° (Figure 1). Azimuth estimation, phase identification (as it pertains to distance estimation), and time picking are investigated.

Azimuth Bias and Scatter

For single-array locations by the IMS, azimuths from $f-k$ analysis for all defining phases are weighted and averaged to obtain the azimuth used in the location (Bratt and Bache, 1988). *A-priori* estimates of the standard deviation (s.d.) based on the "quality" and azimuth resolution of each $f-k$ spectrum are used as weights. In this section we show that the scatter in the IMS azimuth estimate for explosions from a particular mining area can be reduced by applying, for each phase

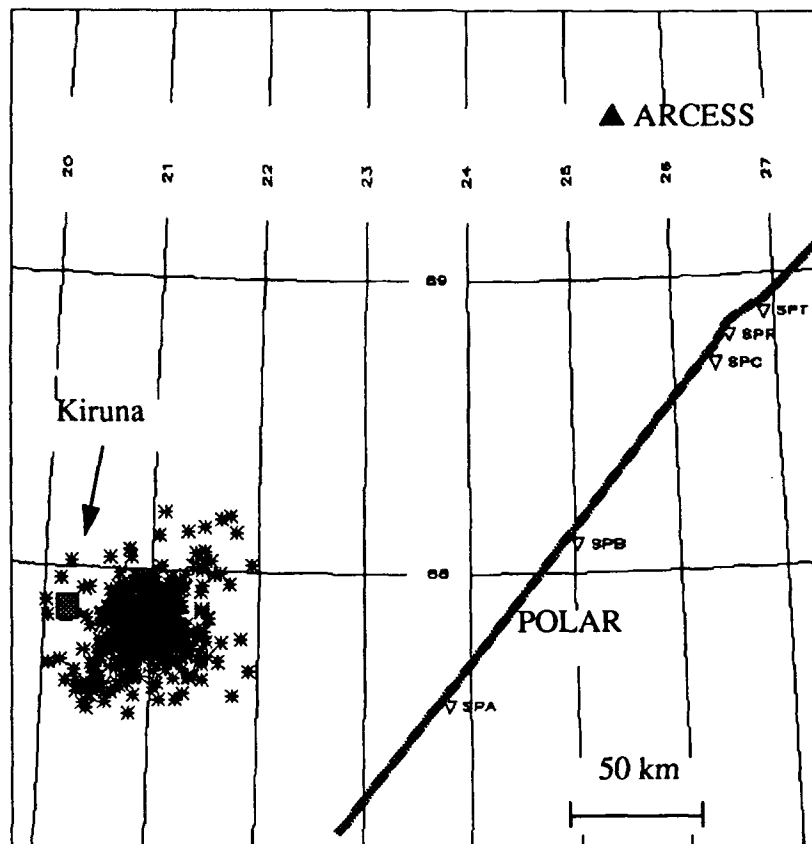


Figure 1: Map showing the locations of ARCESS and events from the Kiruna mine (asterisks). The mine location is indicated by a square. Also shown is the POLAR DSS profile (grey line).

type, a correction and a signal-to-noise dependent weight. Furthermore, mine locations, when available, can be used to correct for bias.

This method is illustrated using explosions from the Kiruna mine and, for comparison, from the Apatity mining area (400 km southeast of ARCESS). The IMS bases its locations on arrival times and azimuths that are derived from “defining” phases. At Kiruna and Apatity, the majority of the defining phases are those labeled “ P_n ” and “ L_g ” by the IMS. The f - k azimuths of these phases for the Kiruna and Apatity events are displayed as a function of signal-to-noise ratio (SNR) in Figure 2. The scatter is larger for L_g than for P_n , particularly at Apatity, and the s.d. is a function of SNR. An exponential can be fit to the s.d. of the data, in agreement with theoretical results by Harris (1990). The means of the P_n and L_g azimuths differ by 3° at Apatity; while at Kiruna, they are similar, but are biased by 5° from the true mine azimuth.

Using phase-dependent weights that are based on the observed s.d. and that vary with SNR, we have recalculated the azimuths for these events. Applying appropriate corrections and weights results in a s.d. decrease for the azimuth estimates from 1.90° to 1.67° at Kiruna, and from 2.89°

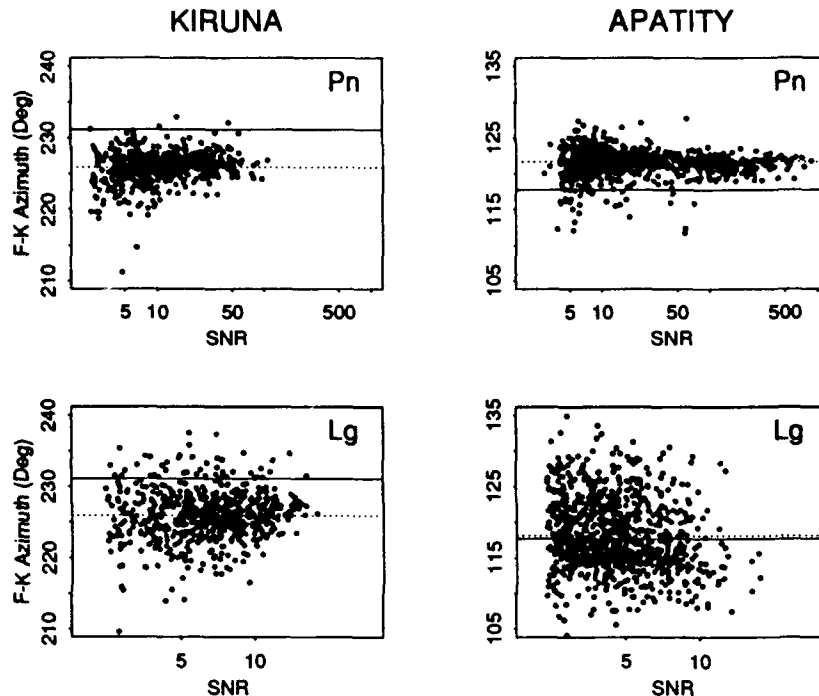


Figure 2: *F-k azimuths of Pn and Lg are displayed as a function of SNR for Kiruna (left) and Apatity (right) events. The dotted lines represent the means of the observations, and the solid lines correspond to the Kiruna or Apatity azimuths.*

to 1.95° at Apatity. A similar analysis was performed for other event clusters around ARCESS. An improvement is usually obtained when there are enough events for proper model fitting, and when the *P*-phase has less scatter in its azimuths than “*Lg*”. The observed scatter in the “*Lg*” slowness vectors may be caused by inconsistent phase picks, as shown below.

Distance Bias

The waveforms of nine high-SNR events from the Kiruna mine were analyzed to determine the cause of the observed 20 km distance bias. Comparing IMS travel-time tables to DSS data from the northern Baltic Shield has shown that pronounced *Pn*-wave travel-time anomalies are not observed in this area (Ryaboy, 1992; Ryaboy *et al.*, 1992). Therefore, we can assume that the distance bias is due to either phase mis-identification or consistently early picks, rather than inaccurate travel-time tables. Phase identifications in the IMS are determined using an automated procedure, and then reviewed by an analyst (Bache *et al.*, 1990). For these events, the first arrivals are identified as *Pn* and the first intensive phases in the *S*-wave group are identified as *Lg*. We compared the IMS phase identifications to DSS data from the POLAR DSS profile (Luosto *et al.*, 1989; see Figure 1). As a typical example, Figure 3 shows a comparison of the IMS and DSS phase identifications on a coherent beam formed for one of these events. The arrival times of the

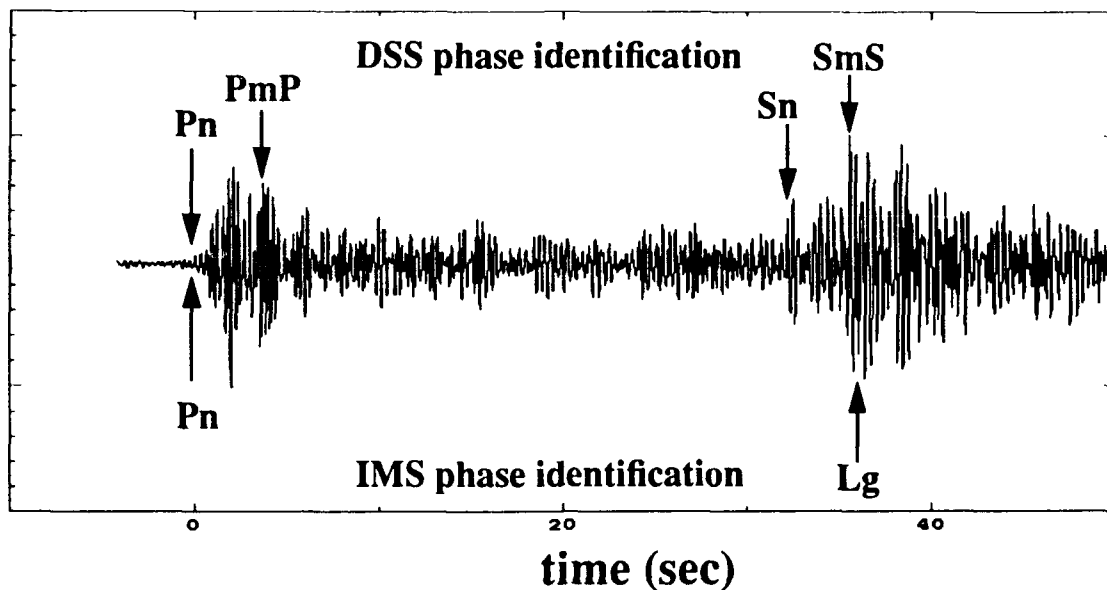


Figure 3: Comparison of the IMS and DSS phase identifications on a coherent beam (bandpass-filtered from 2 to 8 Hz) of a Kiruna mine blast recorded at ARCESS on 04/01/91.

phases identified along the POLAR DSS profile were measured at a distance of 290 km, the true distance between Kiruna and ARCESS. One can see that the wave labeled "Lg" by the IMS corresponds to *SmS* (reflected shear wave from Moho), reliably identified from the DSS data. By renaming the "Lg" as *SmS*, and using *Pn* and *SmS* arrival times and travel-time curves inferred from the POLAR DSS observations, this bias would be eliminated.

Distance Scatter

The large number of events in this dataset were used to study the consistency of phase picks in an attempt to reduce the scatter of the distance estimates for the IMS. We compared three different methods of picking an arrival; the automatic picking procedure in the IMS that is based on STA/LTA; the re-timed picks of the IMS analyst; and a method based on the RMS trace. There was very little scatter in the picks of the *Pn* phase, so we have concentrated on the main *S*-type phase. The RMS trace for fifteen events from three different mines are plotted in Figure 4. For the top ten events (ARCESS recordings of two different Kiruna area mines) the maxima of the RMS traces for the *S*-type phase are within a second of each other. For the bottom five events (GERESS recordings of a German mine at the same epicentral distance), the maxima occur four seconds later. The maximum of the RMS trace is consistent for a given area, but is region-specific. Table 1 synthesizes the results from a larger study of the consistency of the phase picks using these three methods. The waveforms used for this study were first carefully aligned by eye (it was assumed that they all had the same origin), then standard deviations of the *S*-phase arrival-time picks were calculated for all three methods. The table shows that the s.d. is smallest for the RMS method.

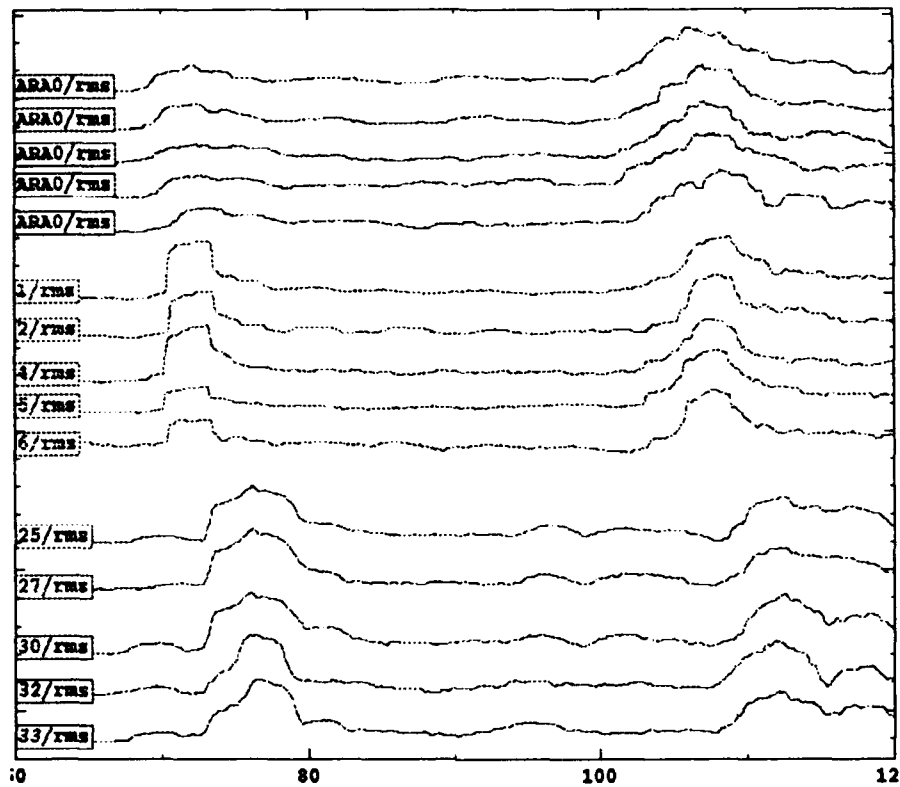


Figure 4: RMS traces computed for 3 different groups of events located at nearly the same distance from the recording array. The top five events (at ARCESS) are from the Kiruna mine, the middle five (at ARCESS) are from the vicinity of Kiruna, and the bottom five (at GERESS) are from a mine in Germany.

Table 1: Standard Deviation of S-phase Arrival Times

| | Expert System | Analyst | RMS |
|-------------------|---------------|---------|--------|
| Kiruna main mine | 1.10 s | 1.48 s | 0.30 s |
| Kiruna close mine | 0.88 s | 2.28 s | 0.20 s |
| German mine | 1.29 s | 1.25 s | 0.77 s |

$M_L(Lg)$

Magnitudes $M_L(Lg)$ were calculated for the IMS arrays with an automatic procedure based on RMS amplitudes in the group velocity window 3.10-3.65 km/s of array-element waveforms band-pass filtered between 1.5-4 Hz. The amplitude attenuation could be described as the product of geometrical spreading and a non-elastic attenuation term decaying with a rate of 0.0018 per km. Estimates of site amplification for individual array elements appear mostly independent of azimuth. Ranging over about 0.2 magnitude unit (m.u.) or more for a given array, they correlate with prevailing noise levels (Figure 5a) and local geology (Figure 5b). The scatter of magnitudes based

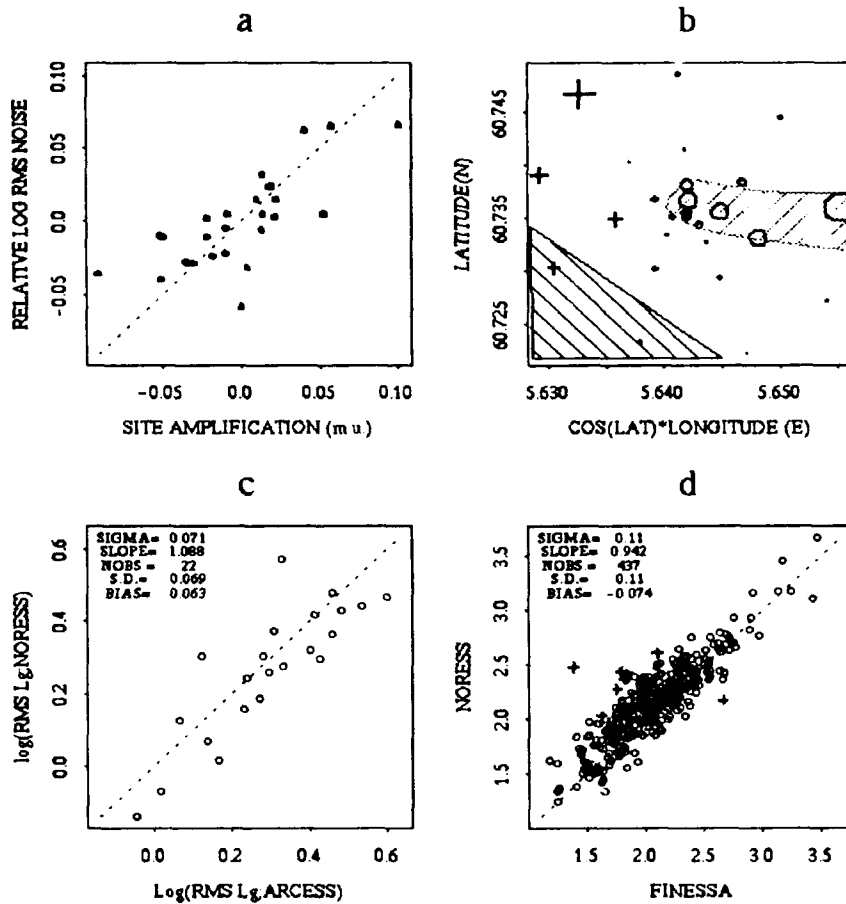


Figure 5: (a) Comparison of site amplifications and relative noise amplitudes of the elements at NORESS. (b) Site amplifications (+ = positive and circle = negative) for NORESS as a function of location. The triangular-shaped rhyolite and narrow zone of gabbro (with low amplifications) are interspersed in granite. (c) Comparison of RMS $M_L(Lg)$ at ARCESS and NORESS for a suite of closely-spaced mining events in the Baltic Shield. (d) Comparison of RMS $M_L(Lg)$ at FINESA and NORESS for 427 events broadly distributed in Fennoscandia and Western Russia.

on RMS L_g amplitudes is about half that of L_g magnitudes based on the STA/LTA currently used in the IMS. Array magnitudes (assumed independent) were formed as averages over element magnitudes corrected for site amplifications, and compared. Standard deviations of network magnitudes (averages over array magnitudes) are around 0.04 and 0.07 m.u. for relative magnitudes of closely spaced events and for absolute magnitudes of broadly distributed events, respectively (Figure 5c-d).

CONCLUSIONS AND RECOMMENDATIONS

Region-specific knowledge of bias and SNR-dependent scatter for the f - k azimuths of regional phases can be used to improve azimuth estimation in the IMS. DSS observations help identify regional phases, which eliminates distance bias caused by phase mis-identifications. Furthermore, the location scatter can be reduced by using RMS amplitudes to more consistently pick S -type phases. Finally, the scatter in M_L magnitudes is decreased when RMS amplitude measurements are used for the L_g phase.

REFERENCES

- Bache, T. C., S. R. Bratt, J. Wang, R. M. Fung, C. Kobryn, and J. W. Given (1990). "The Intelligent Monitoring System", *Bull. Seism. Soc. Am.* **80**, 1833-1851.
- Bratt, S. R., and T. C. Bache (1988). "Locating events with a sparse network of regional arrays", *Bull. Seism. Soc. Am.* **78**, 780-798.
- Harris, D. B. (1990). "Comparison of the direction estimation performance of high-frequency seismic arrays and three-component stations", *Bull. Seism. Soc. Am.* **80**, 1951-1968.
- Luosto, U., E.R. Flueh, C.-F. Lund and working group (1989). "The crustal structure along the POLAR profile from seismic refraction investigations", *Tectonophysics* **162**, 51-85.
- Rivière-Barbier, F. and L.T. Grant (1992). "Cluster Analysis of Closely Spaced Mining Blasts as a Method of Event Location", submitted to *Bull. Seism. Soc. Am.*
- Ryaboy, V.Z. (1992). "A new P_n reference travel-time curve for Scandinavia and north-western Russia inferred from DSS data: its residuals and implications for seismic array data processing" (abstract), *Seismological Research Letters* **63**, No. 1, 44.
- Ryaboy, V.Z., R. J. Stead, and L. T. Grant (1992). "Relocation of regional seismic events recorded by the IMS within the Baltic shield using path-dependent travel-time curves calibrated by DSS data" (abstract), *Seismological Research Letters* **63**, No. 1, 44.

Eurasian Bulletin Produced by the Intelligent Monitoring System from Four Arrays and Six IRIS/IDA Stations

Swanger, H. J., Sereno, T. J., Williams, D. J.

SAIC, 10260 Campus Point Drive, San Diego, CA 92121

Ryall F.

SAIC, Center for Seismic Studies, 1300 N 17th Street, Suite 1450,
Arlington, VA 22209

Contract Numbers: MDA972-92-C-0026 and MDA903-91-C-0151

Objective:

The primary objective of this project is to expand DARPA's Intelligent Monitoring System (IMS) to include data from six IRIS/IDA stations in the CIS. IMS is a knowledge-based system with software architecture and operating procedures to facilitate acquisition of new knowledge to improve performance. With these stations we extend IMS to handle this new class of data.

As a by-product of the project, we produce a bulletin of Eurasian events that can be used for research. The 61 days that have been processed so far provide a bulletin of 1405 events with at least three defining phases at two or more stations.

Research Accomplished:

Operational procedures for bulletin construction

The IMS (described in Bache *et al.*, 1991), has been processing all data from four NORESS-type arrays in Europe since March 1991. The processing begins with near real-time automatic signal detection and feature extraction. A knowledge-based automatic association program, ESAL, interprets these features to group detections that belong to common events, identifies the phases and locates events. The results are then reviewed by an analyst who may accept, edit or reject the events from the ESAL bulletin. This processing is done at NORSAR. The results after analyst review (about 60-70 well-located events per day) are archived in the database management system at the Center for Seismic Studies.

A second instantiation of IMS is operated intermittently to incorporate data from the IRIS/IDA stations located in the CIS. Waveforms for these stations are archived at the UCSD/IGPP Data Collection Center in San Diego. These data are generally available within 1-2 months of real time.

The IRIS/IDA data are processed at IGPP for signal detection and feature extraction. The results are merged at CSS with the signal detections in the final (i.e. after analyst review) IMS bulletin produced at NORSAR. This merged detection list and the NORSAR-produced bulletin origins are input to ESAL. In ESAL terminology, these earlier analyst-reviewed origins are "previous" events used as starting solutions. ESAL is configured to: (1) preserve the previous solutions unchanged, or (2) add IRIS/IDA detections to the previous origins thereby changing them, and/or (3) form new origins with IRIS/IDA and array detections not associated with previous origins. Continuous waveforms from the IRIS/IDA archive and event segments from the earlier IMS interpretation of the array data were used for subsequent analyst review of the ESAL interpretation of the data from the full network.

Three-component data processing and interpretation

For automated interpretation the principle difference between array and single-station data is that F-K can be computed for arrays. The azimuth and slowness from F-K are used in every stage of the automated interpretation of array data. Slowness is used to differentiate P waves from S waves. Azimuth is used for grouping phases from common events. Azimuth and slowness inconsistency indicates inappropriate associations. Azimuth and slowness are used for location. ESAL's success with array data is largely because the F-K estimates are robust.

For three-component data azimuth and slowness must be inferred from the waveform polarization. In the IMS we use the principle component analysis method of Jurkevics (1988). The P-wave azimuths and slownesses obtained with this method are not nearly as robust as those from F-K with array data. S-wave azimuths can be estimated under certain assumptions, but we have found such estimates too inconsistent to be useful. Thus, automated interpretation of three-component data is much more difficult than the interpretation of array data. Some examples illustrate this point.

For array data ESAL uses the slowness to classify arrivals P or S with nearly 99% identification accuracy. For three-component data ESAL uses rectilinearity and horizontal-to-vertical amplitude ratios to achieve about 90% identification accuracy. About 75% of all events seen by the IMS network are single-station regional events, most with only one P phase and one S phase. If either is misidentified, the event can not be formed. Therefore, very high accuracy in determining initial wave type is crucial for a good final bulletin. Patnaik *et. al.* (1992) have shown that neural networks can effectively combine the polarization information with phase context to substantially improve initial phase identification accuracy, and these procedures are being added to the IMS processing of three-component data.

ESAL forms regional events at arrays by grouping phases with similar azimuths. This doesn't work for three-component data since we don't have S-wave azimuths. Instead, we assume that any S phase following a P phase within a certain time window and with compatible amplitude is in the same event group. This allows all true regional events to be found, assuming the P and S are properly identified, but at a cost of generating many false events. So far, we find that the ratio of false events to analyst-accepted events increases a factor of 17 when we add the IRIS/IDA data.

Array estimates of azimuth and slowness may be effectively used to identify inappropriate associations (e.g., they provide consistency checks). In regional networks with hundreds of detections per day, false events will often be found by rules seeking arrival-time consistency. Accurate estimates of azimuth and slowness can be used to reject most of them. For three-component data azimuth and slowness estimates can be made for P waves, but they can be very unreliable, and the quality varies greatly with station. For example, Figure 1 shows the distribution of azimuth errors from four stations (relative to corresponding PDE locations) for the phases Pn, Pg and P for all events in the our bulletin. For comparison, note that the standard deviations of azimuth errors for the Fennoscandian arrays are 7 degrees for regional phases and 12 degrees for teleseisms. Arti (ARU) appears to perform nearly as well as the arrays, but the remaining stations have varying degrees of reliability. The distribution at Kislovodsk (KIV) is so skewed that it suggests that the polarity of the horizontal components are incorrect. Actually, this appears not to be the case. Riviere-Barbier *et al.* (1992) note a sudden change in the polarization about one second after the onset time, and the automated polarization estimates are biased to the west by this errant signal. Since the dominant seismicity is to the east, the azimuth errors cluster near 180 degrees. At all the IRIS/IDA stations inaccurate P-wave azimuths and the lack of any S-wave azimuths results in numerous false events, missed associations and poor single-station locations, and these problems must be repaired by the analyst.

Bulletin characteristics

As of August 1992, 61 days (21 May- 30 June 1991 and 6-25 July 1991) has been processed and analyzed for the combined IMS-IRIS/IDA network. The bulletin (Figure 2) contains 1405 events that have at least three defining phase from at least two stations. These acceptable event criteria guarantee accurate locations for regional events seen by the arrays. However, the location may be poor for events which have locations influenced by azimuth estimates from three-component stations and for teleseisms seen by only a few stations. There are 510 events located with five or more phases.

About 70% of the events are within regional distance (< 20 degrees) of at least one station. Most are located near the arrays in Fennoscandia or in the Hindu Kush region in close proximity to the IRIS/IDA stations at Garm and Ala-Archa. About one third of the latter events are also observed by one or more of the IMS arrays. In all, about 30% of the events are observed by at least one array and one IRIS/IDA station. Many of the events in common among the two sets of stations are regional to the IRIS/IDA stations and teleseismic to the arrays. The IMS arrays alone typically locate about 7 teleseisms/day. The IRIS/IDA stations add few new teleseisms, about 1/day, but they help considerably in improving the location accuracy of the 8 teleseism/day in the complete bulletin.

Only about 25% of the events can be found in the PDE. This is not too surprising given that more than half of the events in our bulletin are regional events seen by only the four arrays. The detection threshold for the arrays in Fennoscandia is well below the threshold for the PDE. A large proportion of the Hindu Kush events in the IMS bulletin are not recorded in the PDE. This will be discussed in more detail later.

For a 20 day period an effort was made to identify all single-station regional events produced by the network. We found about 19/day at from the IRIS/IDA stations, with 46% from Garm and 22% from Ala-Archa. Such events are routinely retained in the IMS bulletin generated from the arrays, but for the IRIS/IDA stations such events are generally not located very accurately. That is, the azimuths from the three-component data are often not reliable, and single-station events require at least one azimuth for location. Thus, single-station events from IRIS/IDA stations are not particularly useful for research studies that require accurate locations, but they can be useful for developing techniques for improved feature extraction and phase identification.

Data from the Hindu Kush area

The IRIS/IDA stations at Garm and Ala-Archa are located within 1000 km of the Hindu Kush region, and they detect nearly five events per day from that region. About 14% of these events are also seen by at least one of the four arrays. The 61-day bulletin includes 320 events from this region with at least three defining phases from at least two stations. Depths range from the surface to below 200 km and magnitudes appear to be as small as m_l 3.0.

Only 33 of the 320 events were found in the PDE. There were a few events in the PDE that were not in the combined bulletin, but these events occurred during periods when the station Garm was not recording. The distribution of the PDE magnitudes suggests an m_b threshold of about 4.5 for this region. The number of events seen by the combined IMS-IRIS/IDA network suggests a detection threshold that is 1 magnitude unit less. We do not have any local magnitude relations for this area, so the actual magnitudes of the events are difficult to verify. As an approximation, we used the P wave amplitudes recorded at Garm, corrected for inverse distance spreading assuming a compressional Q of 1000. The corrected amplitudes were calibrated with the actual m_b values given in the PDE bulletin. The resulting "local" magnitudes have a peak at magnitude 3.5 and go as low as 2.8.

The waveform character observed at Garm or Ala-Archa is a often very good indicator of source depth. The absence of Lg and the short S-wave coda seen at regional distances at Ala-Archa is generally a good indicator of a sub-crustal depth. The S-P times at these stations, along with the teleseismic P at the other stations, constrain the depth quite well. There are examples from this bulletin where depth could be constrained well with these data while the PDE location could not constrain the depth.

Conclusions and Recommendations:

We have successfully extended the IMS automated and interactive data interpretation system to integrate data from six IRIS/IDA stations in the CIS with data from four arrays in Europe. For automated interpretation the most important difference between the array and three-component data is the lack of a robust alternative to F-K analysis for three-component processing. The azimuth and slowness information from F-K is central to automatic interpretation of array data. Without accurate azimuth and slowness estimates, automatic interpretation of detected events can only be done by accepting a much higher rate of false events. The IMS interactive analysis tools allow the analyst to move quickly through the data to reject these false alarms and make other

appropriate corrections. Thus, a high rate of false events is tolerable, if not desirable. The processing and interpretation are being improved to reduce the false events problem and improve (especially by adding more knowledge to ESAL) the interpretation of all events detected by the network.

As a side benefit of this phase of IMS development, we are producing a Eurasian bulletin which includes more than 1400 events. This bulletin is available in the Center for Seismic Studies database management system and should provide a resource for many kinds of research efforts.

References:

Bache, T. C., S. R. Bratt, J. W. Given, T. D. Schroeder, H. J. Swanger, and J. Wang (1991). The intelligent monitoring system version 2. *Quarterly Technical Report #7*, SAIC-91/1137, San Diego CA.

Jurkevics, A. (1988). Polarization analysis of three-component array data. *BSSA* 78, 1725-1743.

Patnaik, G. B., T. J. Sereno, M. J. Mortell, and R. D. Jenkins (1992). A Regional Seismic Data Set, and Results on Automated Interpretation of Seismic Data Using Neural Networks. this meeting.

Riviere-Barbier, F., A. Suteau-Henson, V. Z. Ryaboy, and J. A. Carter (1992). Analysis of Three-Component Data from IRIS/IDA Stations in the USSR. *BSSA* 82, 192-220.

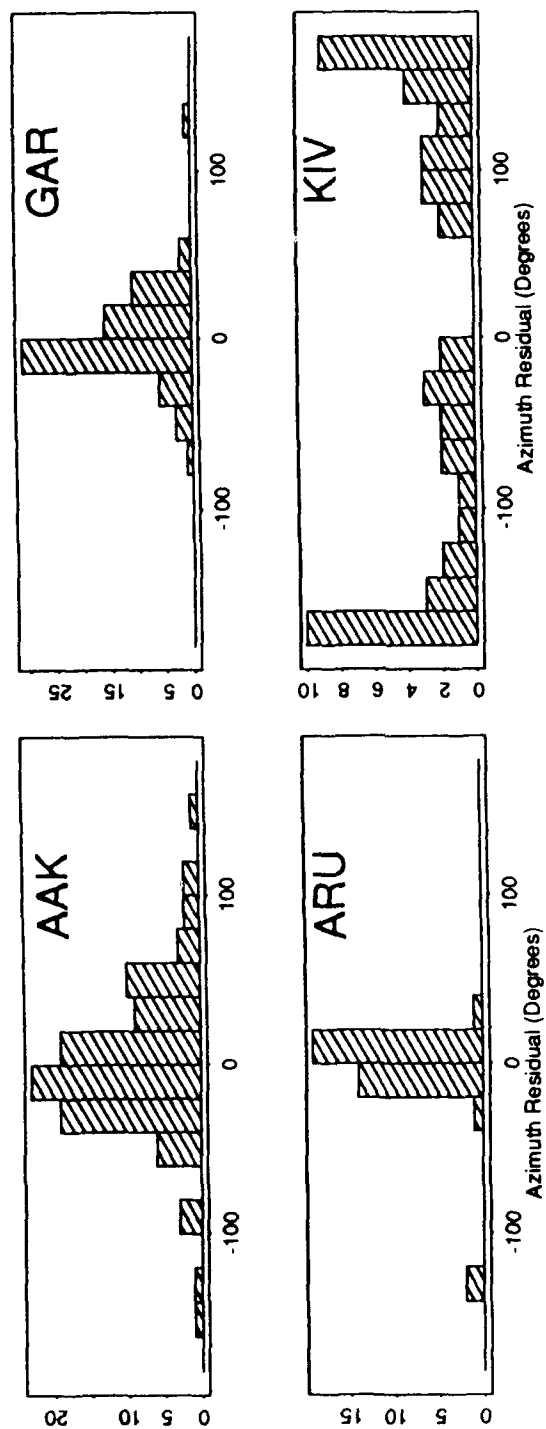


Figure 1. Distribution of P wave station-to-event azimuth errors using PDE locations for IRIS/IDA stations Ala-Archa (AAK), Arti (ARU), Garm (GAR) and Kislovodsk (KIV).

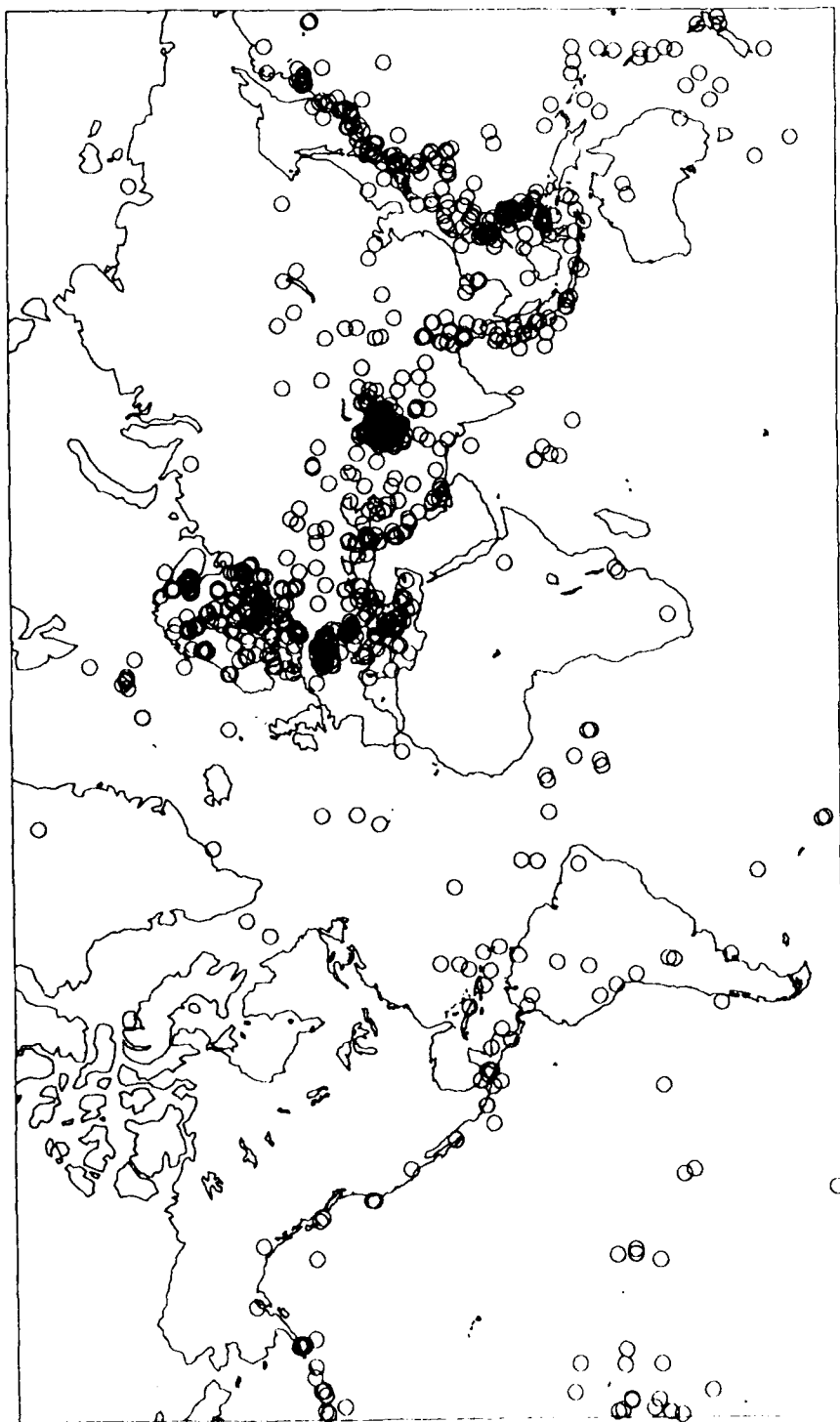


Figure 2. Plot of the locations of 1405 events produced during a 61-day period using four European high-frequency arrays and six IRIS/IDA stations in the CIS. Only those events with at least three defining phases from at least two stations are shown.

ANALYSIS OF SMALL SEISMIC EVENTS NEAR AZGIR, KAZAKHSTAN: IMPLICATIONS FOR IDENTIFYING CHEMICAL AND DECOUPLED NUCLEAR EXPLOSIONS IN A MAJOR SALT DOME PROVINCE

Lynn R. Sykes and Paul Lyubomirskiy

Lamont-Doherty Geological Observatory, Columbia University, Palisades NY 10964

CONTRACT NO. F19628-90-K-0059

OBJECTIVES

The detonation of nuclear explosions by Russia or any of the other countries of the former Soviet Union in large underground cavities under either a Low-Yield (LYTTBT) or a comprehensive test ban treaty would constitute the greatest challenge to U.S. verification efforts. That evasion scenario sets the limit on how low a yield can be verified effectively. The OTA Report *Seismic Verification of Nuclear Testing Treaties* found that between 1 to 2 and 10 kilotons (kt) the most critical method of evasion is that of nuclear testing in large cavities in salt domes. It concluded that no method of evading a monitoring network is credible above 10 kt and that several evasion scenarios, including testing in cavities in bedded salt and in hard rocks, are possible below 1 to 2 kt.

Our work address a number of aspects of the problem of clandestine nuclear testing in large cavities in salt domes, bedded salt and hard rock--what types of evasions scenarios are plausible based on geological and engineering constraints, which ones are likely to escape detection by the U.S. and which ones are likely to be identified. Particular attention is given to the critical yield regime from 1 to 10 kt, where scientific research over the next few years seems most likely to have a major impact on the verifiability of a LYTTBT and on the crucial question of how low in yield can we go in effective verification under various evasion scenarios. Recently, Russian scientists have stated that several decoupled nuclear explosions were conducted in salt near Azgir in cavities of previous large explosions. Our work this year focused on past nuclear testing at Azgir and attempts to identify nuclear explosions with magnitudes, m_b , that range from 3.1 to 6.1 and to identify how many chemical explosions of various m_b 's have occurred per year in the area near Azgir. We believe this information is crucial in ascertaining the number of chemical explosions per year that must be discriminated from small decoupled nuclear explosions in and near a major salt dome province under LYTTBT's with yield limits of 1 to 10 kt. We also are synthesizing data from engineering, rock mechanics and geological sources on the properties of salt in situ, the feasibility of constructing and then removing water from cavities in salt formed by solution mining, and the stability of large underground cavities in salt and hard rock.

RESEARCH ACCOMPLISHED

Magnitude-Yield Relations for Nuclear Explosions in Salt and Feasibility of using Cavities Created by Past Explosions for Decoupled Testing. During the first year of this con-

tract Sykes (1991*a, b*) focused on deriving revised m_b values for Soviet underground nuclear explosions at Shagan River and those conducted in salt in various areas of the Commonwealth of Independent States (C.I.S.). I derived improved magnitude-yield relationships, especially for explosions of small yield and for nuclear explosions of all sizes in salt. I redetermined yields of all known underground nuclear explosions at Shagan River through May 1988 as well as yields of all events of $m_b \geq 4.5$ in salt in various areas of the C.I.S. Data on Azgir explosions of yields 1.1 to 100 kt were used to derive the relationship

$$m_b = 4.456 + 0.787 \log Y \quad (1)$$

for tamped nuclear explosions in salt in regions like Azgir that are typified by low attenuation (high Q) for P waves. Most thick salt deposits of the C.I.S. are located in high Q areas. In contrast, seismic data on past U.S. nuclear explosions in salt are poor since those events were small and were conducted 25 to 30 years ago when teleseismic P wave data were few and generally of low signal-to-noise ratio. I found that a fully-coupled (tamped) nuclear explosion of 1 kt in salt at Azgir has an m_b of 4.46; decoupled events of 1 and 10 kt have m_b 's of 2.61 and 3.40 respectively (assuming a decoupling factor of 70). Those m_b 's are higher than has generally been thought previously.

An inventory was completed of Soviet nuclear explosions in and near thick salt deposits. The maximum yields of decoupled nuclear explosions that could be detonated in the cavities produced by those events were calculated assuming STERLING/SALMON conditions, i.e. a decoupling factor (DF) of 70. Those cavities (assuming they remain standing) are concentrated in the area of extensive salt deposits to the north of the Caspian Sea, mainly at Azgir. An important consideration in identifying cavities in salt created by past nuclear explosions is that the yields of decoupled explosions in them for a DF of 70 cannot be larger than about 7% of that of the explosion that created the cavity. Thus, since the U.S. knows of all tamped Soviet explosions in salt down to a few kilotons or smaller, we also know about all existing cavities created by past nuclear explosions that could be used for decoupled events of DF 70 down to a fraction of a kiloton. The largest nuclear tests, up to a maximum of 7 to 8 kt, that could be conducted at DF's of 70 in cavities created by past nuclear explosions in the C.I.S. are largely confined to the Azgir site itself. Possibilities for decoupled testing are more restricted in the area of bedded salt to the northwest of Lake Baikal.

A 23 Year Catalog of Small Seismic Events from Azgir Region Complete down to m_b 3.1. A catalog was compiled using data from the PDE, ISC and the Lasa and Norsar arrays of all known seismic events in the North Caspian region bounded by 45°-50°N and 45°-50°E (Fig. 1) from 1969 through 1991. Dr. F. Ringahl kindly provided listings of Norsar detections and magnitudes. From 1966 to 1984 the region was the site of 26 nuclear explosions of $m_b > 4.5$ near either Azgir, Astrakhan or Lake Aralsor, all of which are well located by either standard reporting services, JHD or master-event techniques. Their yields range from 1 to 100 kt (Adushkin et al., 1992). Events of $m_b \geq 4.5$ (equivalent via eqn. 1 to a tamped nuclear explosion of 1 kt) from that region have been regularly reported by ISC since 1966. The Norsar (NAO) and/or Lasa (LAO) arrays (and occasionally ISC) have lo-

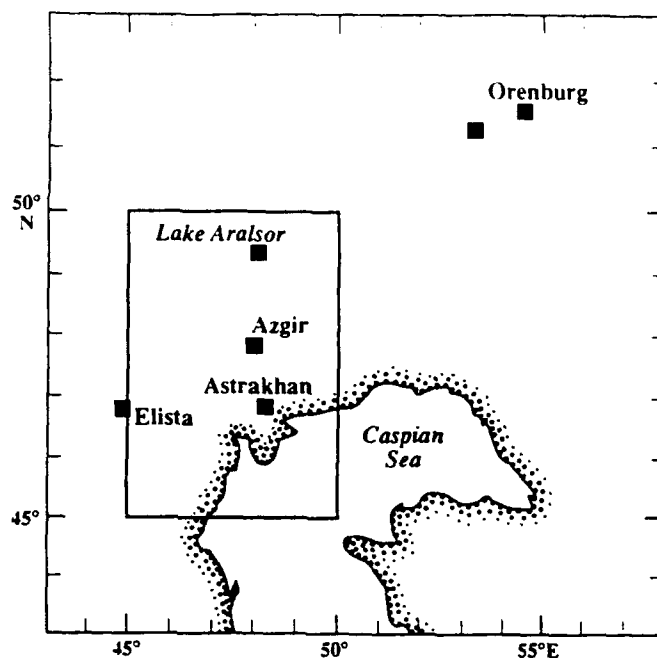


Fig. 1. North Caspian Region showing sites of nuclear explosions in and near thick salt deposits (squares) and area of special study of small seismic events (inner box).

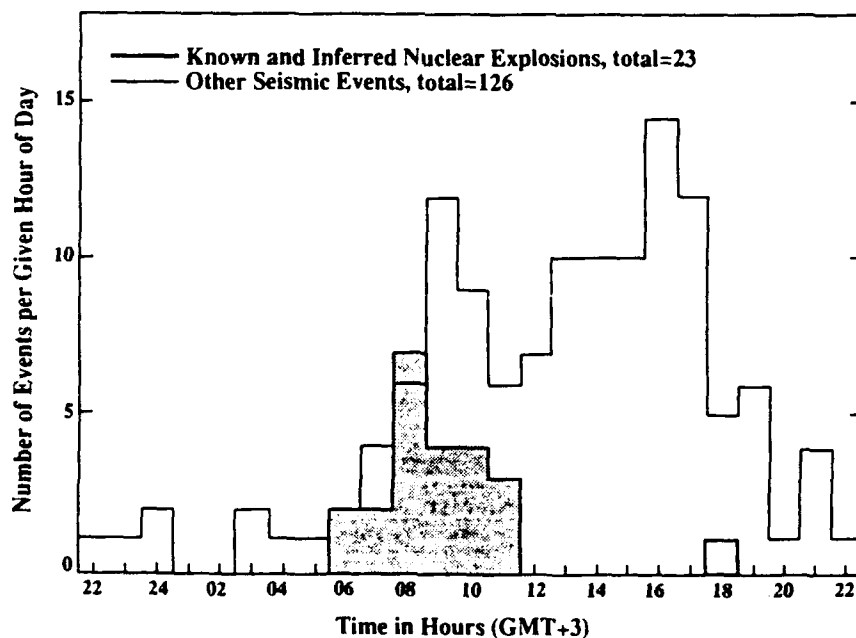


Fig. 2. Histograms of times to nearest hour of day of known and inferred nuclear explosions (hatched region) and other seismic events in special study area outlined in Fig. 1.

cated 133 small ($m_b < 4.5$) events in the region but with location accuracies that are generally poorer than for the above large explosions.

Station corrections for m_b were derived using several large underground explosions at Azgir and applied to other seismic events from the above study area. Those for NAO, -0.48; Hagfors, -0.50; LAO, -0.52 were applied in deriving revised m_b 's for the small events. The revised magnitudes of those events are all about 0.5 m_b units less than the original determinations, indicating that they are, in fact, systematically smaller than their uncorrected magnitudes would suggest. As described later the catalog of small events is complete for the 23-year period down to a very low magnitude, 3.1. It should be recognized that that value is a true teleseismic m_b and not a value based on near or regional seismic waves such as Lg.

The large explosions and nearly all of the small events exhibit strong clustering during daylight hours (Fig. 2), indicating that few, if any, are earthquakes. Testing practice since 1971 for the above large explosions and for nearly all Soviet PNEs has been to detonate them to within a few seconds of a given hour. The small events, most of which are interpreted to be chemical explosions, however, are distributed randomly in time during the hour. That chemical explosions were usually not detonated exactly on an exact hour is somewhat surprising. It is probably indicative that the conduct of a nuclear explosion, unlike most chemical explosions in the sub-kiloton range, requires great coordination among large groups of people, some of whom are widely scattered. These factors necessitate planning for the exact time of the nuclear event well ahead of time. It can be seen in Fig. 2 that the detonation of nuclear events has usually been confined to morning hours, i.e. to a narrower time frame than chemical explosions.

All of the origin times and, with one exception, all of the locations computed using data from the Norsar array alone for large explosions at Azgir are within ± 12 sec and 150 km of those computed by the ISC. Seven of the 133 small events fall within 12 s of an exact hour during daylight; some or all of the 7 may be either very small tamped or small decoupled nuclear explosions. Their revised m_b 's range from 3.02 to 4.45 (Table 1). The largest of the 7 occurred on 25 Apr. 1975, was reported by ISC and was relocated by Marshall et al. (1991) near the 1968 PNE explosion at Azgir with an announced yield of approximately 25 kt. While we cannot expect clandestine testing under future treaties to be conducted exactly at a given hour, study of the above 7 events should prove fruitful in work on the discrimination of chemical explosions and small nuclear explosions.

Numbers of Chemical Explosions per Year Requiring Discrimination from Decoupled Nuclear Explosions. Cumulative numbers of the remaining small events from 1969 to 1991 in both the entire study area and within 150 km of Azgir are shown in Fig. 3. The slope, b , of the frequency- m_b relation is about 2.7 for $3.6 \leq m_b \leq 4.0$ and 1.1 from m_b 3.1 to 3.6. The recomputed m_b 's were converted into equivalent nuclear yields in tons at the top of Fig. 3. In a study of blasting activity in the U.S. Richards et al. (1992) report $b \sim 3$ for chemical yields from 100 to 1000 tons and $b \sim 1$ from 1 to 100 tons, nearly identical to the slopes found in Fig. 3 for similar yield ranges. That the data in Fig. 3 fall below the

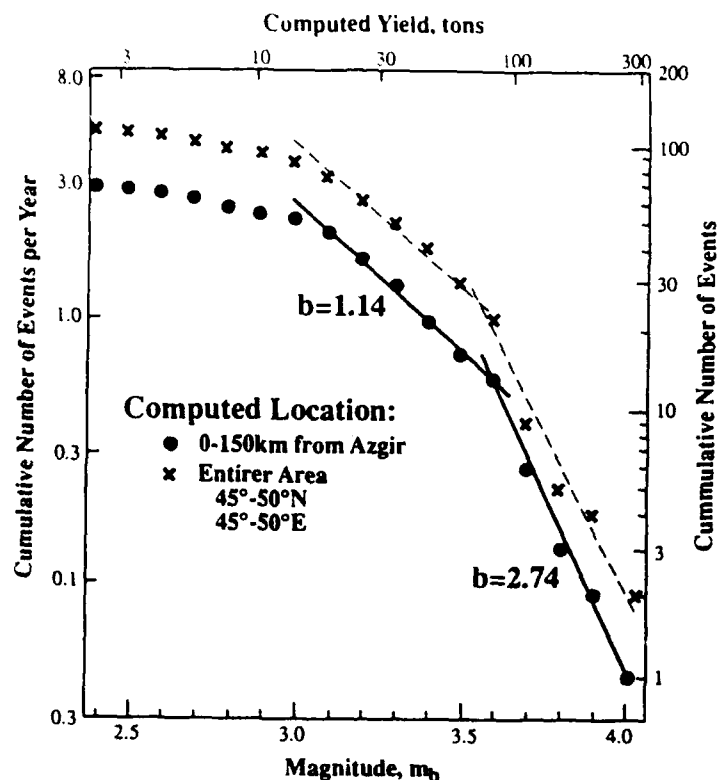


Fig. 3. Cumulative number (N) of events $\geq m_b$ that are not known or inferred to be nuclear explosions in study area (x's) and within 150 km of Azgir (solid circles). Most, and perhaps all, events are chemical explosions. Values of b fit by eye for relationships $\log N = a - bm_b$.

Table 1. Small Seismic Events in Azgir Region, 1969-1991 that Fulfill Origin-Time Criterion for being either Small Tamped or Decoupled Nuclear Explosions

| Date | Origin Time Hr. Mn. Sec. | Lat (°N) | Long (°E) | $m_b \pm \text{SEM}$ | $n(m_b)$ | Location made by |
|----------------|-----------------------------|-------------|--------------|----------------------|----------|---------------------------|
| July 14, 1972 | 14 59 49.0 | 50.0 | 46.4 | $3.14 \pm .07$ | 2 | ISC |
| Apr. 25, 1975 | 05 00 02.4 | 47.81 | 47.80 | $4.45 \pm .13$ | 7 | Marshall et al. (1991) |
| Mar. 29, 1976 | 06 59 50.0 | 46.4 | 47.9 | 4.02 | 1 | NORSAR |
| Oct. 14, 1977 | 07 00 02.0 | 48.0 | 48.0 | 3.42 | 1 | NORSAR |
| Sept. 12, 1978 | 05 00 01.0 | 48.0 | 48.0 | 3.02 | 1 | NORSAR |
| Jan. 10, 1979 | 07 59 53.0 | 46.9 | 48.3 | $4.36 \pm .14$ | 2 | NORSAR |
| Aug. 29, 1980 | 04 00 09.0 | 48.9 | 47.0 | 3.22 | 1 | NORSAR |

All locations except that for 1975 event may be uncertain by 150 km.

line $b = 1.14$ for $m_b < 3.1$ is reasonably attributed to incompleteness of the catalog at smaller magnitudes. The similarities of the data in Fig. 3 to U.S. blasting practices indicates that the catalogue is complete for $m_b \geq 3.1$.

Of the 73 remaining small events located within 150 km of Azgir, the largest in 23 years was a single event of m_b 4.0. Chemical explosions of $m_b \geq 3.5$ and those of $m_b \geq 3.0$ have occurred about 0.7 and 2.6 times per year. m_b 's of 3.0 and 3.5 correspond to yields of about 3 and 13 kt for nuclear explosions with decoupling factors of 70 times and 1 and 4.5 kt for those decoupled by a factor of 30 as in the example reported by Adushkin et al. (1992).

SPOT Satellite Images. We have processed digital tapes of recent SPOT images of the Azgir area. Shot points and roads leading up to 8 to 10 of them can be recognized in Fig. 4 even though the events occurred 13 to 26 years ago. We are in the process of developing a 3-D (stereoscopic) image of the testing area using SPOT images taken from different zenith angles to better examine each shot point. We are using the large 1971 Azgir explosion as a master seismic event to relocate the larger Azgir explosions with respect to the shot points identified with the SPOT data.

CONCLUSIONS AND RECOMMENDATIONS

A catalog is assembled of small seismic events for a 5° by 5° area near Azgir of the North Caspian salt dome province (about 45% of the province's area) that is shown to be complete down to m_b 3.1 since 1969. That m_b corresponds to a tamped nuclear explosion of 0.02 kt and to yields of about 1.4 and 4 kt for decoupling factors of 30 and 70. Seven small events of m_b 3.02 to 4.45 fulfill an origin-time criterion for being either very small tamped or small decoupled nuclear explosions. Of the 126 other small events in the area, most or all of which are taken to be chemical explosions, the largest 2 in 23 years were of m_b 4.0. Chemical explosions of $m_b \geq 3.5$ and those of $m_b \geq 3.0$ occurred about 1.3 and 4.5 times per year in the entire study area. Thus, the number of chemical explosions per year in that area that must be discriminated as such from small decoupled nuclear events is small even at m_b 3.0. There is a pressing need to bring together seismic data from arrays in Europe and from stations in Eastern Europe and the C.I.S. to provide more accurate locations of chemical explosions in this and other areas of thick salt deposits of the western C.I.S.

References

- Adushkin, V.V., I. O. Kitov, O. P. Kuznetsov and D. D. Sultanov, Seismic efficiency of decoupled nuclear explosions, *Geophys. Res. Lett.*, submitted, 1992.
- Marshall, P. D., R. C. Lilwal, R. C. Stewart and I. Marsden. Seismometer array recordings of P waves from explosions in the North Caspian USSR area, *Atomic Weapons Research Establishment Report 0 4/91*, 1-192, 1991.
- Richards, P. G., D. A. Anderson and D. W. Simpson, A survey of blasting activity in the United States, *Bull. Seismol. Soc. Amer.*, **82**, 1416-1433, 1992.
- Sykes, L.R., Yields of Underground Nuclear Explosions at Azgir and Shagan River, USSR and Implications for Identifying Decoupled Nuclear Testing in Salt, Sci. Rpt. 1, PL-TR-92-2002, Phillips Laboratory, 1991. ADA250971

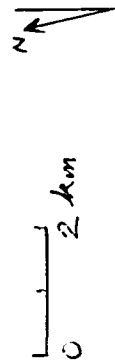


Fig. 4. Image of Azgir nuclear testing area made by processing digital tape of SPOT satellite photo taken in 1988. Town of Azgir at convergence of many roads and tracks at lower left. Main testing area from 1971 to 1979 is at upper right of center.

Generalized Beamforming for Automatic Association

D. W. A. Taylor and S. K. Leonard, ENSCO, Inc., 445 Pineda Ct. Melbourne, FL 32940

Contract No. F19628-91-C-0172

OBJECTIVE

Automatic association of seismic signals is a computationally intensive and error prone task. Current techniques for automatic association and location typically suffer in both computational performance and accuracy, particularly when the number of input detections increases. These effects are due primarily to the established combinatorial searching algorithms used to form initial events. In this research effort, generalized beamforming, originally applied by Ringdal and Kvaerna (1989) to the regional association problem, is extended to provide the foundation for a global seismic association system. This technique forms initial events by a non-combinatorial method, allows the exploitation of all the observed detection data (not just arrival time) and provides a framework for applying knowledge gained from experts to automatically identify false or erroneous events. Generalized beamforming, necessarily associates all possible events without relying on the success of a seed location algorithm. Furthermore, the computer runtime increases only linearly with increasing data volume.

Existing association algorithms use the arrival time of seismic signals (and occasionally estimates of observed slowness) to find a pattern that is consistent with a potential source region. These algorithms typically employ a seed location scheme which finds a preliminary set of associated detections. The seed location technique uses one of several approaches that computes an initial trial epicenter. These techniques essentially search multiple combinations of candidate detections that could contribute to the "seed" event. An event is declared to be found if a location can be computed from the input detections. Following the determination of the initial seed location, a search is conducted for other associated detections.

This general approach to automatic association has three primary deficiencies that may be alleviated with generalized beamforming. First, because of the combinatorial nature of the searching process, the computational cost increases exponentially with an increase in the number of input detections. While this may be acceptable at the current monitoring threshold, the computational cost will increase dramatically when monitoring thresholds are decreased and additional stations contribute data. Generalized beamforming does not employ such combinatorics to form initial events, therefore the time complexity of the algorithm increases only linearly and remains manageable as the data volume increases.

Second, because current association and seed location algorithms rely primarily on time of arrival, the processes can form many false events from random, erroneous combinations of detections. In practice, automatic processes can form as many false events as real events. Application of consistency parameters are shown to enhance performance, and in some cases are required to form initial events. Generalized beamforming uses all available signal information (time, azimuth, velocity, amplitude, period, etc.) but does not require any parameter except time. Faulty associations can be identified automatically by applying these consistency tests based on the observed data.

Finally, the existing techniques for automatic association are known to fail for certain circumstances of input data. In these cases the automatic system will not associate accurate detection data, missing events altogether. The method used with generalized beamforming is complete. All possible combinations of detections are necessarily associated, forming a "preliminary event" to be evaluated for its realness.

In this research effort, the generalized beamforming technique is extended to develop an automatic process for associating global seismic signals. Our objectives are to optimize the efficiency and accuracy of initial event formation using the generalized beam, to exploit all available detection information, to define a framework for using knowledge obtained from expert seismic data analysts to process the preliminary events, and most importantly to test and evaluate the technical ability of the procedure.

RESEARCH ACCOMPLISHED

Our approach to the global automatic association problem is to apply the generalized beamforming technique to form initial events; in effect, we discretize the earth into a finite set of potential epicenters and procedurally "beamform" a network to each of these epicentral regions employing detection parameters such as azimuth and slowness in addition to arrival time. Initial events are examined for consistency among the detection set (*e.g.* variability of predominant period and magnitude), and individual detections within an event are evaluated for consistency with the epicentral region (*e.g.* "expectedness" of detection data from a station.) Inconsistent detections are eliminated from the initial events; most false events are subsequently disbanded due to sparseness of data. Remaining events are evaluated using *a priori* knowledge of seismic characteristics of the potential epicentral region and are disbanded or rated in terms of quality or "realness".

During the initial phases of the research, we subdivided the globe into equally spaced grid points. Each such grid point corresponds to a potential epicenter. A circular epicentral region encompassing each potential epicenter is defined with a radius slightly greater than half of the distance between the points. With this geometry, each epicentral region overlaps with every adjacent region to ensure complete coverage of the earth. Using generalized beamforming we "beamform" a network to each of these pre-defined epicentral regions and process the beams independently.

A key factor for the computational efficiency of this processing scheme is that grid point locations are predetermined. We can compute much of the station/grid point information required (such as, distance, azimuth, travel time, velocity, etc.) before processing and store these data in a database to be accessed directly and quickly. Additionally, information that cannot be computed (*e.g.* stations that are "expected" to detect an event from a given grid point) can be acquired from expert analysts and stored in a "knowledge base" for individual grid points.

Grid point spacing is an important consideration with generalized beamforming in the global sense. Ringdal and Kvaerna addressed the regional problem by using grid points separated by slightly more than 1 degree. Such a tightly packed grid is unacceptable for the global problem primarily because the uncertainty associated with the teleseismic data will not accommodate this resolution. Depth certainly cannot be resolved with small epicentral regions. Furthermore, the number of grid points to be processed is formidable; 19,754 grid points are required to cover the globe if each epicentral region has a radius of 1 degree. Only 49 are required when the grid points represent a circular region having a radius of 20 degrees. However, there is a trade-off with the larger radius. A greater number of detections are involved when a network is beamformed to a larger area, producing a potentially unmanageable number of initial events. A practical solution is to discretize the earth into grid points representing a 20 degree radius and again into points representing a radius of 5 degrees. The volume of data can be reduced by beamforming to the grid point regions with 20 degree radii to form initial events. New beams and preliminary events are formed utilizing only the data defining the initial events for the points (representing a radius of 5

degrees) contained within the larger region. Figures 1a and 1b show the projection of grid points with epicentral regions having a radius of 20 degrees and 5 degrees, respectively. The overlap of the epicentral regions (defined by the circles) allows complete coverage of the globe.

A generalized beam is formed independently for each grid point. In terms of association, travel time remains the key discriminant between which detections can possibly be associated to the same event. Accordingly, a super-set of all detections that can form all possible events can be constructed based on arrival time. Figure 2 schematically shows how this time correlation, or generalized beamforming, is conducted for one grid point.

The large circle in Figure 2a defines the epicentral region whose center is the grid point shown by the asterisk. The triangle represents a station where a detection has occurred at time DetTime. If an event occurred at the near edge of the circle, the travel time to the station would be TT_1 (which in our case is computed using the IASPEI-91a travel times.) Similarly, if the event occurred at the far edge of the circular epicentral region, the travel time to the station would be TT_2 . We can conclude, then, that if the observed detection at the station was caused by an event within this epicentral region, then the origin time of the event would be bounded by

$$OTime_1 = DetTime - TT_1 + e_1, \text{ and}$$

$$OTime_2 = DetTime - TT_2 - e_2,$$

where e_1 and e_2 represent the variability in arrival time due to random errors, source effects and path effects. These two origin times define a window of time in which the event could have occurred. Since a similar time window applies to any other detection, we can search for an origin time that is consistent at enough stations to define an event.

In practice, azimuth and velocity can also be used as an effective association discriminant with generalized beamforming. The near and far edges of the epicentral region described by the circle in Figure 2a (with variability) define an expected velocity range for each station. Similarly, the two points of intersection of the circular region with a line perpendicular to the azimuth defines a range in azimuth for each station. The observed velocity and azimuth (if available) for a detection caused by an event from the region must correlate with the respective ranges defined by the epicentral regions.

Figure 2b shows a set of these origin time windows computed from six detections. Along the bottom is a time series that shows the number of detections that are consistent with the origin time for that grid point. This is the generalized beam, where we have formed a network beam in origin time to this epicenter. The dashed line represents the "event detection" threshold. When the number of detections meets this threshold an initial or preliminary event (PE) is declared. Because a PE may have an long time duration, we subdivide each PE into equal time intervals of less than five seconds. All combinations of detections within that time interval is formed to create a sub-preliminary event (SPE) that will receive further analysis.

Generalized beamforming will form all events for which accurate detection data exist. This assurance holds because, if the detections are truly associated to the same event, the origin times, azimuths and velocities will be consistent. Because of the size of the earth and the corresponding length of travel times of primary phases, there are frequent random alignments of arrival times for a global network that erroneously indicate association to a nonexistent event. These false events can contain detections from other "real" events. Furthermore, automatic detectors frequently record multiple detections for an actual arrival. The result may be many instances of an

event with slightly different combinations of detections. Resolving the conflicts for detections between events within a grid point to identify real events and eliminate false events requires careful consideration.

Many of the conflicts among events within a grid point are resolved using the HYPO location algorithm. Initially, each SPE is evaluated independently, assuring the consistency of the detections with respect to observed slowness, observed amplitude and the predominant period. They are submitted to the HYPO process if enough data remains. Detections with inconsistent travel time residuals are eliminated. The remaining detection set is reprocessed or the event is disbanded due to sparseness of data. If the event remains intact, the location is tested to determine whether the hypocenter is adequately close to the grid point. If not, the event is disbanded.

Testing is being conducted with a data set of 22 hours of automatically generated detection data from a 17 station global network. When testing is complete, a second data set is available for a "blind" test. The results from the generalized beamforming association technique are being compared with a bulletin produced by expert seismic analysts. In all cases the real events are represented by an SPE. At this stage, however, there is typically a set of SPEs that correspond to the real event with detection sets that are generally similar, with the exception of a few detections. Some random SPEs may also remain representing false or erroneous events. An additional processing step is made to resolve the conflicts between detection data that are contributing to multiple SPEs, to identify the real event within the set of similar SPEs and to detect the false events. To accomplish this, a quality rating is assigned to each remaining SPE based on the following factors:

1. number of detections defining the event,
2. timing of detections from the same station,
3. root mean square (rms) residual of the detection set,
4. "competing" residuals from stations grouped by proximity,
5. "expectedness" of stations.

Evaluation of these factors serves two purposes: resolving conflicts at a grid point, and then resolving conflicts between grid points. The SPEs defining real events must be identified from a group of SPEs with similar detection sets. Commonly, the correct SPE has the largest detection set. Automatic signal detectors often record multiple detections at a station in the coda of an actual signal. The initial detection is most often the real detection. The SPE with the earliest detection times will receive a higher quality rating for this criteria. Rms residuals only provide a crude guide to the quality of a given SPE. Travel time residuals from stations located within the same region are generally similar for seismic events. An SPE will be down-rated in terms of quality if travel time residuals from stations within the same general location compete, meaning some have a high negative value, and the others a high positive value. The SPE corresponding to the real event will be consistent in terms of "expectedness", in other words, those stations which are most expected to detect an event from the epicentral region. The real SPE will be consistent with what we know about seismic events and receive a high quality rating. The detections in the highest quality SPE are removed from the other SPEs. These other SPEs are usually disbanded due to sparseness of data, or identified as having a very low quality rating.

Once the redundant SPEs have been eliminated, the remaining events must be evaluated to determine whether they represent real seismic events or whether they are just random correlations of data. The same evaluation factors and criteria are applied between events and grid points as

within a grid point. The quality of fit of the data to the grid point information is the primary decision making tool.

The preceding steps yield a final event bulletin. The final system output will include an appraisal of the results. The framework provided by generalized beamforming is a vehicle for storing and applying site-specific information. This final appraisal process can include such advice to the analyst as which additional stations are expected given the grid point location and magnitude, which detections are only marginally consistent with the event, whether events have historically occurred at the location, or any other phenomena based on historical observations. In addition, an overall determination of the quality, or confidence, in the event can be reported.

CONCLUSIONS AND RECOMMENDATIONS

Approximately one year remains of the current two-year research effort. Results of tests to date indicate the processing framework of generalized beamforming can be effectively utilized as a means of performing global teleseismic automatic association. The approach successfully forms all possible initial events and provides an excellent vehicle for exploiting observed detection information and applying expert knowledge.

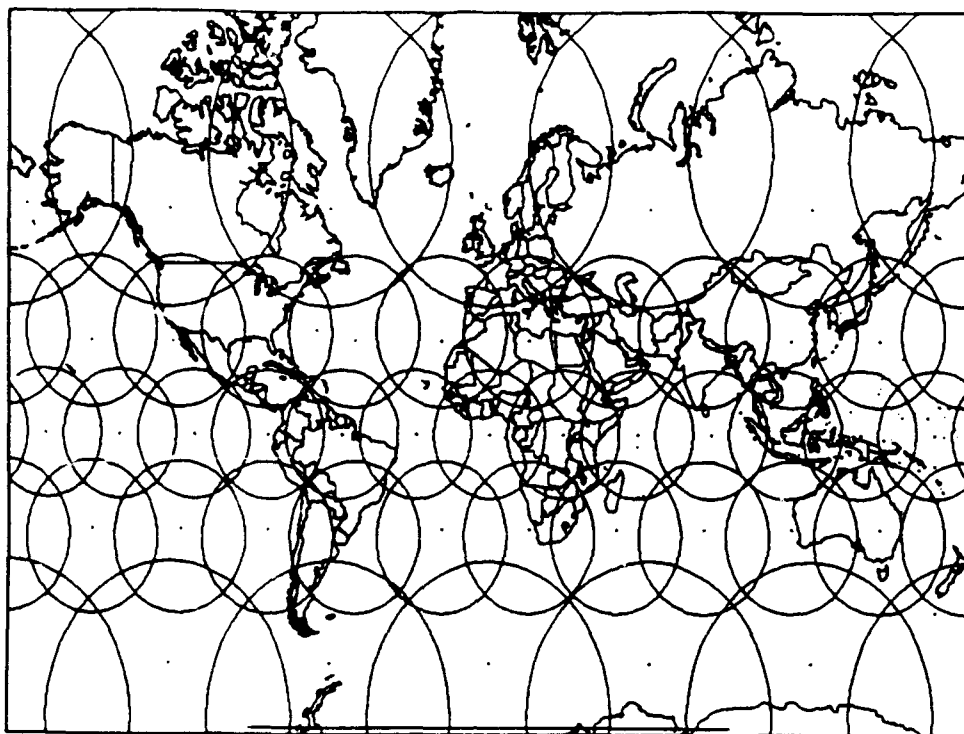
Because of the non-combinatorial nature of generalized beamforming, the computation time increases only linearly with the number of detections. Other factors that affect runtime (quality of the detection data, seismicity in the region of the epicenter, epicenter spacing, other available "knowledge", etc.) are under evaluation. Since this process is suitable for parallel processing, multiple computers or faster computers could further decrease the computational costs.

Future work will continue to expand upon the established basis for conflict resolution within a grid point and between grid points. The grid point spacing and exact locations will be optimized to provide a foundation for expert analysts to establish a knowledge base for each point. Finally, a procedure to properly associate later phases to events that have other defining phases should be integrated into the system.

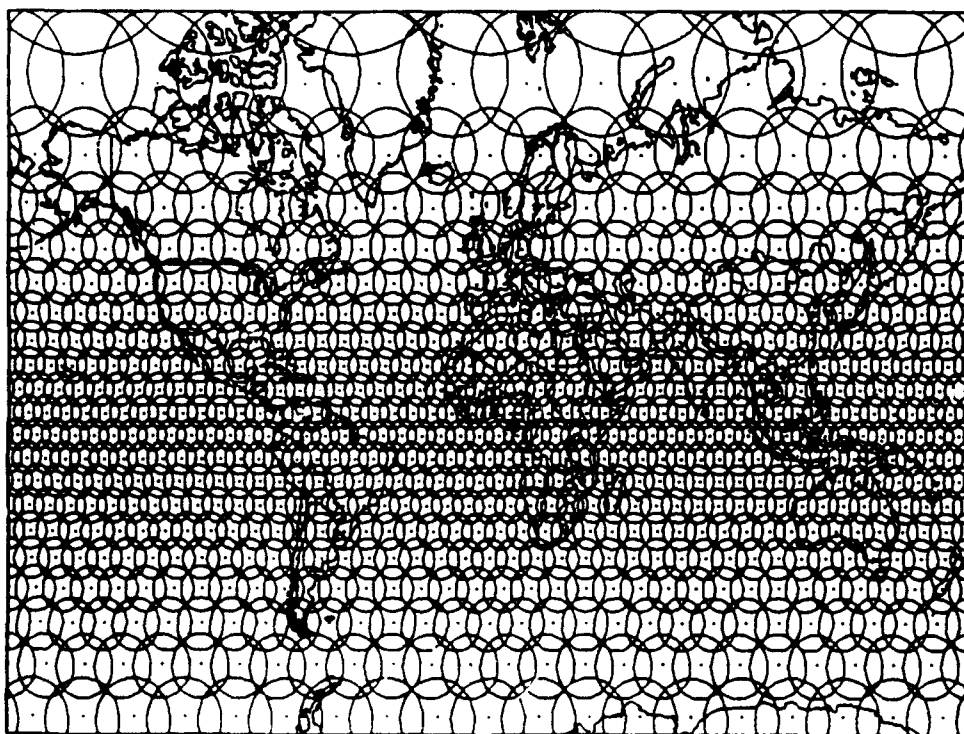
REFERENCES

Kennett, B.L.N., editor (1991). *IASPEI 1991 Seismological Tables*, Research School of Earth Sciences, Australian National University.

Ringdal, F. and T. Kvaerna (1989). A multi-channel processing approach to real time network detection, phase association, and threshold monitoring, *Bull. Seism. Soc. Am.*, 79. 780-798.

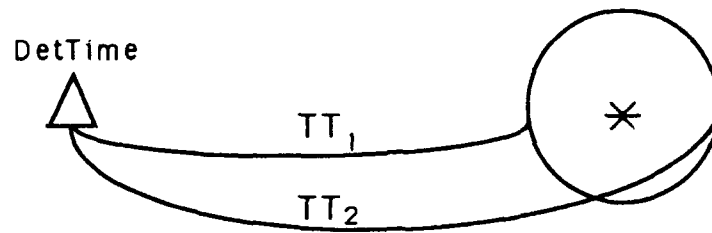


(a)

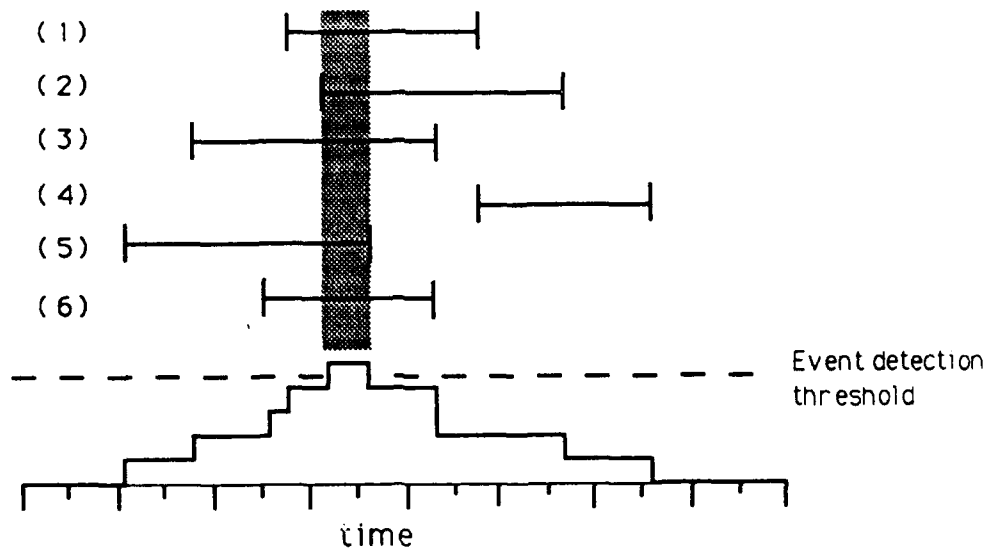


(b)

Figure 1: Projection of grid points and associated epicentral regions with (a) 20 degree radius and (b) 5 degree radius.



(a)



Preliminary Event formed from:
(1), (2), (3), (5), (6).

(b)

Figure 2: Schematic diagram demonstrating the formation of a generalized beam.

LOCATION AND WAVEFORM MODELING OF SHAGAN RIVER NUCLEAR EXPLOSIONS FROM SATELLITE IMAGES AND REGIONAL SEISMOGRAMS

Clifford H. Thurber and Howard R. Quin
University of Wisconsin-Madison

Contract #F19628-90-K-0047

OBJECTIVES:

Data from the IRIS GSN stations in the CIS and the former NRDC-SAS regional seismic network in Kazakhstan, along with other data released by the CIS, present unique opportunities to investigate event location, crustal structure, and wave propagation in the CIS, especially in the area of the Kazakhstan nuclear test site (KTS). We are carrying out a program of detailed analysis of body-wave data from regional events recorded by these stations, in conjunction with other regional and teleseismic network data, with the primary goal of improving event location capability at regional and teleseismic distances. Data from events within the CIS are presently being used in the investigation of the following problems related to regional and teleseismic event location:

- 1) determination of absolute locations for Soviet nuclear explosions at Shagan River;
- 2) determination of improved source region and receiver region velocity structures and their utility for event location. Data from recent Soviet nuclear tests and information released recently on numerous historical Soviet nuclear tests are of critical value in addressing these tasks. Satellite images of the KTS area are used to provide direct information on the absolute locations of events.

RESEARCH ACCOMPLISHED:

Teleseismic locations of the most recent 20 explosions at Shagan River and their estimated uncertainties are shown in Figure 1. The locations were computed using algorithm JED (Douglas, 1967) with the epicenter of the 1988 JVE fixed at its location determined from a rectified satellite image. The site of the 1988 JVE is easily recognized in high resolution satellite images, as it has been documented in several publications (including Leith and Simpson (1990), and Murphy et al. (1991)). Thus it serves as an appropriate master event for estimating the relative locations of other recent events. Event depths were fixed at a depth scaled to yield following Jih and Wagner (1991). These locations provide the starting point for our analysis of a set of time sequence satellite images.

A set of SPOT satellite images of the Shagan River area were acquired for analysis. All the images were Level 1B corrected, so that basic geometric distortions were corrected in the images. The starting point in the analysis process is image rectification, that is, establishment of a geographic coordinate system and transformation of the image pixels to it. For the transformation, 9 events from the Bocharov et al. (1989) list were employed as ground control points, 7 from Shagan River and two nearby throwout craters known as T-1 and T-2 (Leith and Simpson, 1990). We adopted a linear rectification of a October 15, 1989 panchromatic image as our reference image, as it made use of what is presumed to be the most exact information with the least amount of image warping, and produced an excellent fit to the ground control points (RMS misfit of less than 5 pixels). Other images were registered to it for purposes of comparison.

The process of identifying the sites of the other 19 post-1986 explosions involved the comparison of the time-sequence SPOT images with the estimated event locations indicated in Figure 1. The association process for a number of events was quite simple in cases where good temporal coverage was available and/or the sites were well separated from other relatively recent activity. Association was most difficult for some of the smaller explosions and for those events in

close spatial and temporal proximity to others. The lack of complete SPOT image coverage of the area between June 1986 and August 1988 also hampered our efforts, as the August 1987 image did not cover the west-northwestern portion of Shagan River.

Figure 2 shows an example of "before and after" SPOT images of areas containing identified explosion sites (shown as negatives for improved contrast) in images acquired on June 17, 1986 and October 15, 1989, respectively. The image is 800 pixels wide by 600 pixels high, or about 8 by 6 km. The geographic locations and event associations for these and other sites are indicated in Table 1. We have very high confidence in the identification of the explosion emplacement points for 14 of the 20 explosions with $m_b > 5$ post-dating 1986. For two events (84 and 89), the presence of preexisting features lends some doubt to our identification. For two other events (87 and 99), our identifications conflict with teleseismic locations. Finally, for two events (85 and 92), the complexity of the surrounding features makes identification quite difficult. Improved temporal image coverage and/or availability of additional multispectral images from other sources might help resolve these uncertainties. Unfortunately, existing LANDSAT imagery either predates (LSS) or postdates (TM) the relevant time period.

In Figure 3, the locations derived from satellite image analysis are compared to the locations from JED (Figure 1). The mislocation vectors mostly trend east-west, while the major axes of the error ellipses trend north-south. The mean mislocation is 1.2 km for the 19 unconstrained events, compared to an average dimension of the error ellipse axes of 0.7 km. The image location falls within the JED 95% confidence ellipse for only 5 events. Doubling the size of the error ellipses increases this to 10 events. Clearly, JED seriously underestimates event mislocation. In particular, event mislocation in longitude greatly exceeds the JED estimate. We suggest that nonuniform observation (Pavlis, 1992) is the primary cause of this discrepancy.

In the synthetic seismogram work, a velocity model for the KTS region has been developed using near-regional (< 500 km) P waveform data from the NRDC/SAS network and the reflectivity method (Mallick and Frazer, 1987) for computing synthetic seismograms. The model is very successful at reproducing characteristics of observed seismograms at distances less than 300 km (Quin and Thurber, 1992). Our crustal model for the Kazakhstan region has a 4.5 to 6.5 km/sec upper crust (to 15 km depth), a middle and lower crust that increases in velocity from 6.5 to 7.05 km/sec, and a crust-mantle boundary at about 50 km depth. Compared to the model of Leith (1987) derived from DSS studies, our upper crust has a slightly lower velocity and our lower crust has a slightly higher velocity, similar to the results of Priestley et al. (1988). A relatively sharp crust-mantle boundary (about 5 km thick) was needed to match the observed difference in the Pn and PmP arrival times. This is in contrast to the receiver function results of Priestley et al. (1988) for the structure beneath station KKL, which suggested a 10 to 15 km thick transitional Moho. This model is being used as a source-region model for mid-regional (500 to 1000 km) modeling of KTS explosion waveforms using data from CIS stations. We are utilizing the generalized ray method (Langston, pers. comm.) for computing synthetic seismograms modified to incorporate different source and receiver structures. An examination of the Cagniard integration method indicates that the amplitude and phase of the arriving waves can be broken down into separate functions of the source and receiver models, with the downgoing wave propagating through the source region and the upgoing wave propagating through the receiver region. This provides a first-order approximation to a laterally heterogeneous structure. We are in the process of developing receiver velocity models for stations NVS, BRV, and FRU. Different source-region and receiver-region models are essential for successful waveform matching at these stations. An example for station BRV is shown in Figure 4.

CONCLUSIONS AND RECOMMENDATIONS:

The absolute event locations for recent Shagan River nuclear explosions have potential value for a variety of studies. Methods for improving location estimates and uncertainties (Crosson and VanDecar, 1990; Pavlis, 1992) could be tested with these events. They could be used as controlled sources for waveform modeling studies (Goldstein et al., 1992) and tomographic studies (McLaughlin et al., 1992). The characteristics of the emplacement points might provide some information on explosion yield and depth of burial. All of these types of analyses could prove useful for the monitoring of nuclear explosions at other historic and possibly future test sites. We are continuing our analysis using LANDSAT MSS images to infer absolute locations for pre-1986 Shagan River nuclear explosions.

Our waveform modeling results have been successful for near-regional data around KTS using reflectivity synthetics and for mid-regional data using modified generalized rays. We have begun to examine the utility of the improved velocity models for purposes of event relocation. For the near-regional case, improved modeling of the phase PmP yields a significant reduction in focal depth uncertainty. For the mid-regional case, our efforts are hindered by the scarcity of multiple observations of individual events. We are continuing our efforts in modeling data at far-regional distances (1000 to 2000 km), including IRIS stations in the CIS.

REFERENCES:

- Bocharov, V. S., S. A. Zelentsov, and V. N. Mikhailov, Characteristics of 96 underground nuclear explosions at the Semipalatinsk test site, Atomnaya Energiya, **67**, 1989.
- Crosson and VanDecar, Determination of teleseismic relative phase arrival times using multi-channel cross correlation and least squares, Bull. Seism. Soc. Am., **80**, 150-169, 1990.
- Douglas, A., Joint epicentre determination, Nature, **215**, 47-48, 1967.
- Goldstein, P., W. R. Walter, and G. Zandt, Upper mantle structure beneath the Soviet platform using a source array of nuclear explosions, J. Geophys. Res., in press, 1992.
- Jih, R.-S., and R. A. Wagner, Recent methodological developments in magnitude determination and yield estimation with applications to Semipalatinsk explosions, PL-TR-91-2212(I), 1991. **ADA244503**
- Leith, W., Geology of NRDC seismic station sites in eastern Kazakhstan, USSR, U.S. Geol. Surv. Open File Rep., **87-597**, 13 pp., 1987.
- Leith, W., and D. W. Simpson, Monitoring underground nuclear tests, in Commercial Observation Satellites and International Security, St. Martin's Press, NY, 1990.
- Mallick, S., and L. N. Frazer, Practical aspects of reflectivity modeling, Geophysics, **52**, 1355-64, 1987.
- McLaughlin, K. L., J. R. Murphy, and B. W. Barker, A lithospheric velocity anomaly beneath the Shagan River test site. Part 2. Imaging and inversion with amplitude transmission tomography, Bull. Seism. Soc. Am., **82**, 999-1017, 1992.
- Murphy, J. R., J. L. Stevens, D. C. O'Neill, B. W. Barker, K. L. McLaughlin, and M. E. Marshall, Development of a comprehensive seismic yield estimation system for underground nuclear explosions, PL-TR-91-2161, 36 pp., 1991. **ADA240814**
- Pavlis, G. L., Appraising relative earthquake location errors, Bull. Seism. Soc. Am., **82**, 836-859, 1992.
- Priestley, K. F., G. Zandt, and G. E. Randall Crustal structure in eastern Kazakh, USSR, from teleseismic receiver functions, Geophys. Res. Lett., **15**, 613-616, 1988.
- Quin, H. R., and C. H. Thurber, Seismic velocity structure and event relocation in Kazakhstan from secondary P phases, submitted to Bull. Seismol. Soc. Am., March 1992.

Table 1. Locations of Shagan River explosions from SPOT images

| N | YrMoDa | Latitude (°N) | Longitude (°E) |
|-----|--------|---------------|----------------|
| 82 | 870312 | 49.9400 | 78.8178 |
| 83 | 870403 | 49.9308 | 78.7878 |
| 84 | 870417 | 49.8831 | 78.6708 |
| 85 | 870620 | 49.9325 | 78.7603 |
| 86 | 870802 | 49.8806 | 78.8750 |
| 87 | 871115 | 49.8675 | 78.7792 |
| 88 | 871213 | 49.9514 | 78.7925 |
| 89 | 871227 | 49.8805 | 78.6939 |
| 90 | 880213 | 49.9322 | 78.8681 |
| 91 | 880403 | 49.9214 | 78.9092 |
| 92 | 880504 | 49.9453 | 78.7539 |
| 93 | 880614 | 50.0364 | 78.9675 |
| 94 | 880914 | 49.8781 | 78.8239 |
| 95 | 881112 | 50.0467 | 78.9689 |
| 96 | 881217 | 49.8797 | 78.9236 |
| 97 | 890122 | 49.9411 | 78.7869 |
| 98 | 890212 | 49.9167 | 78.7142 |
| 99 | 890708 | 49.8797 | 78.7597 |
| 100 | 890902 | 50.0094 | 78.9856 |
| 101 | 891019 | 49.9300 | 78.9456 |

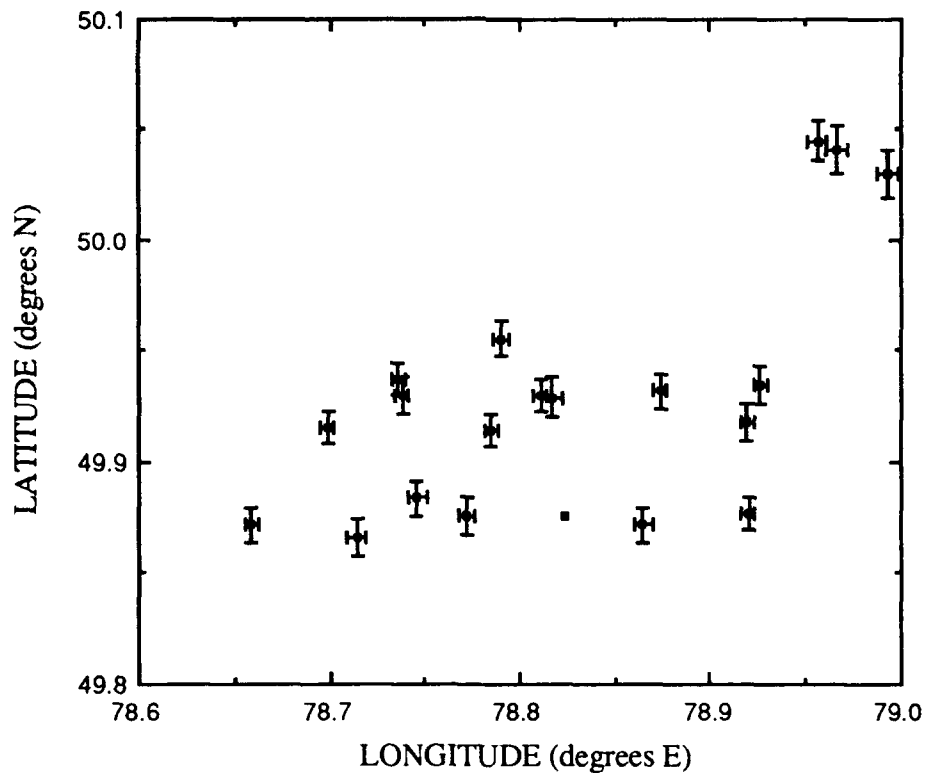


Figure 1. JED locations of the most recent 20 Shagan River nuclear explosions (post 1986) with the 1988 JVE used as the master event.

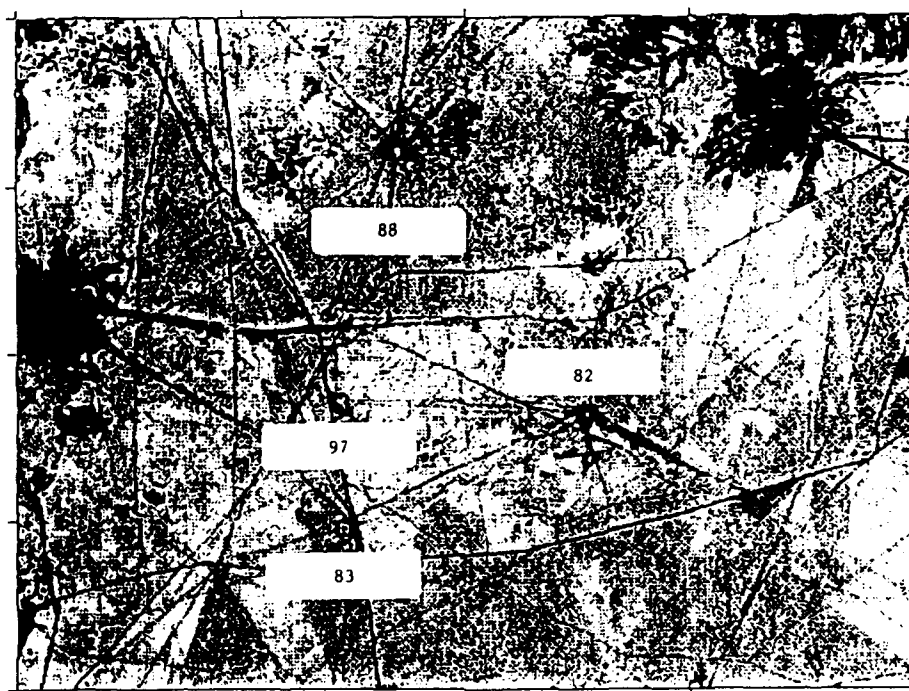
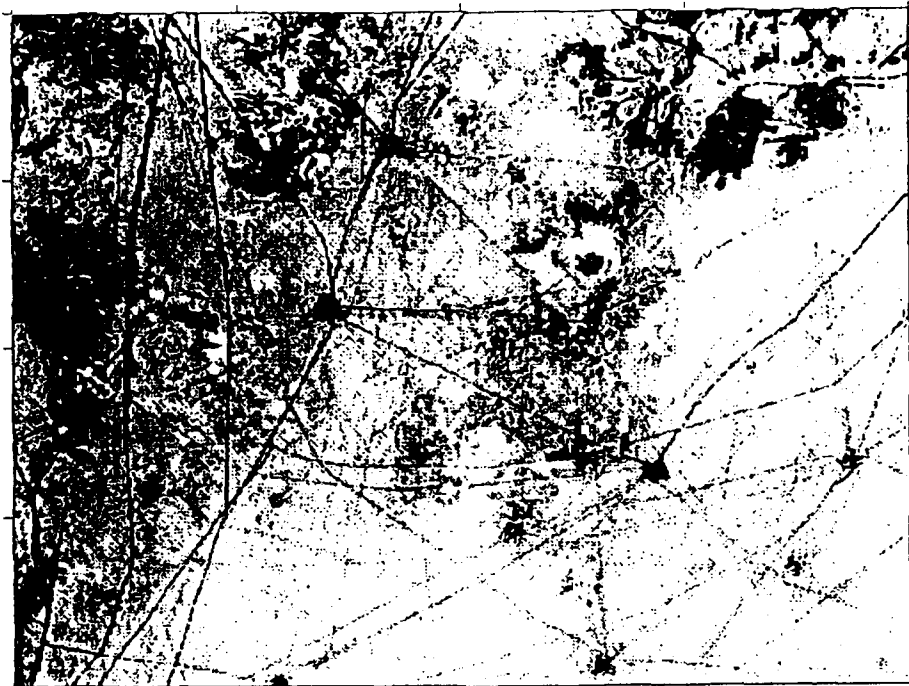


Figure 2. Before and after SPOT image for a set of identified explosion sites. The images are from June 17, 1986 (top), and October 19, 1989 (bottom) and show the explosion (listed by event number) adjacent to the identified site. The image covers the area just to the north of the JVE, showing events 82 (below center), 83 (above center), 88 (below center), and 97 (above center).

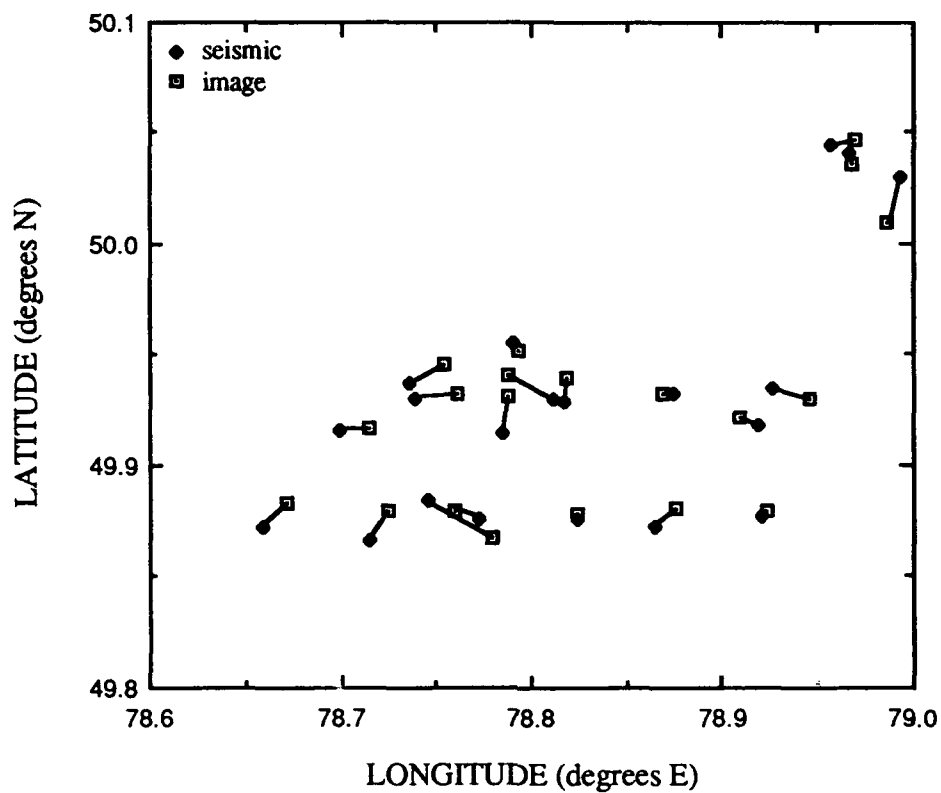


Figure 3. Comparison of SPOT image (squares) and JED teleseismic (diamonds) locations for the most recent 20 nuclear explosions at Shagan River. Mislocations greatly exceed the bounds of the error ellipses indicated in Figure 1.

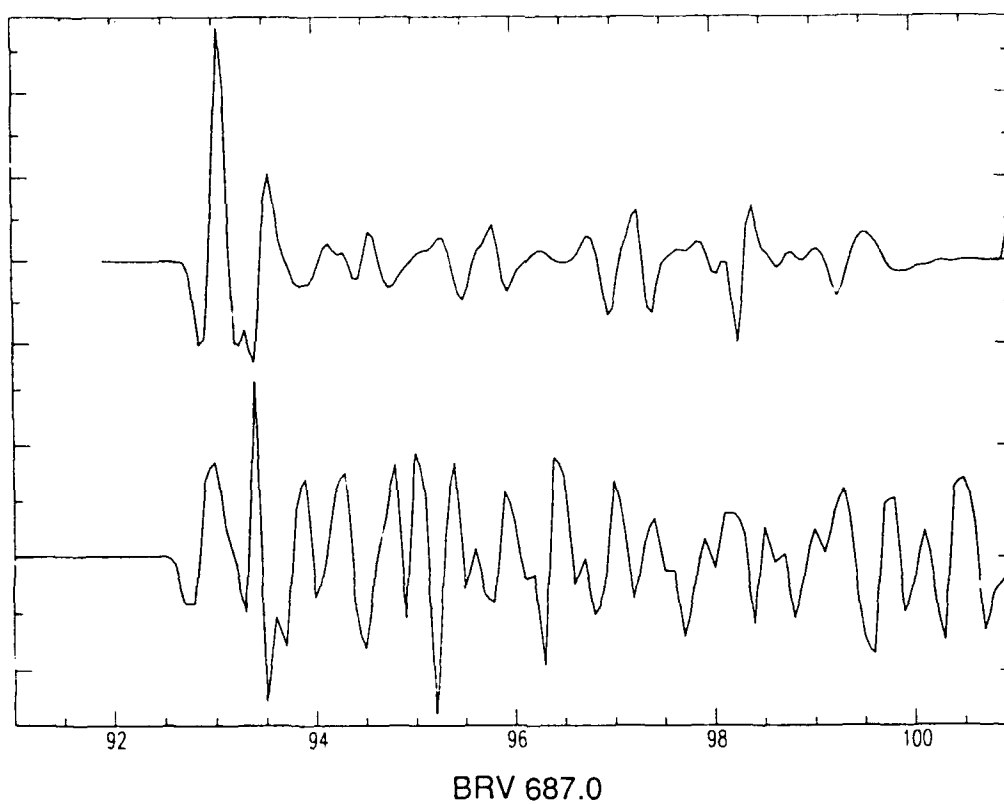


Figure 4. Comparison of synthetic (top) and stacked observed (bottom) vertical component seismograms for KTS explosions observed at station Borovoye, using a split source and receiver structure modification to the generalized ray method.

RESEARCH ON MONITORING AT REGIONAL DISTANCES: SCATTERING FROM SMALL-SCALE HETEROGENEITIES

M. N. Toksöz, R. T. Coates, E. E. Charrette and W. L. Rodi

Earth Resources Laboratory
Department of Earth, Atmospheric, and Planetary Sciences
Massachusetts Institute of Technology
Cambridge MA 02139

Contract No. F29601-91-K-DB15

OBJECTIVE

The objective of this research is to quantify the effects of scattering on regional seismograms used in the monitoring of underground nuclear explosions. In particular, scattering by small-scale heterogeneity near a receiver or array of receivers is known to cause variability in seismogram features such as traveltimes, amplitudes and coda. Such variability is significant over distance scales ranging down to several meters. Our approach to understanding small-scale scattering effects is to characterize the ground motion variability observed at dense arrays of seismometers, and to develop numerical modeling techniques for scattering in complex media to explain the observations.

RESEARCH ACCOMPLISHED

We will summarize the results of two studies of the effects of scattering due to near-receiver, small-scale heterogeneity: one on ground motion variability observed across dense seismic arrays, and the other on the comparison of scattering models and the limitations of Born approximations.

Analysis of Ground Motion Variability

We investigated the variability in ground motion at closely spaced bedrock sites in the absence of strong topography, analyzing data from the NORESS, ARCESS and FINESA seismic arrays and from a dense array of seismometers deployed at Pinyon Flat Observatory, California, as part of an IRIS-PASSCAL experiment (see Owens *et al.*, 1991).

We measured ground motion variability primarily in terms of coherency, which can be directly calculated from seismograms and expresses variability as a function of both spatial separation and frequency. A limitation of this measure, however, is that it is not sensitive to amplitude variations (Toksöz *et al.*, 1991b) and these must be considered separately. The lagged coherency between two seismograms $s_1(t)$ and $s_2(t)$ is defined as (Jenkins and Watts, 1969; Harichandran and Vanmarcke, 1984)

$$C_{12}(\omega) = \frac{S_{12}(\omega)}{[S_{11}(\omega)S_{22}(\omega)]^{1/2}}$$

where S_{11} and S_{22} are the auto-spectra of s_1 and s_2 , respectively, and S_{12} is the cross-spectrum between s_1 and s_2 , lagged in time to remove time shifts due to traveling wave propagation. Although C_{12} is a complex quantity, here we shall use only its magnitude, which can vary between 0 and 1. A detailed discussion of our methods of computing coherency is given in Toksöz *et al.* (1991b).

Data from the NORESS, ARCESS and FINESA arrays were analyzed by Dainty & Toksöz (1990) and Toksöz *et al.* (1991a,b). These arrays have diameters of 2–3 km and minimum seismometer spacings of 150–200 m. The seismometers are 1 Hz vertical velocity instruments placed on crystalline basement, with the overburden excavated if necessary. The events analyzed were quarry blasts at ranges of 200–350 km, the useful frequency range being 2–10 Hz for these events. Coherencies were computed for the Lg phase, the largest amplitude phase on the seismograms. A detailed discussion of the data and two interpretations are given in Toksöz *et al.* (1991b).

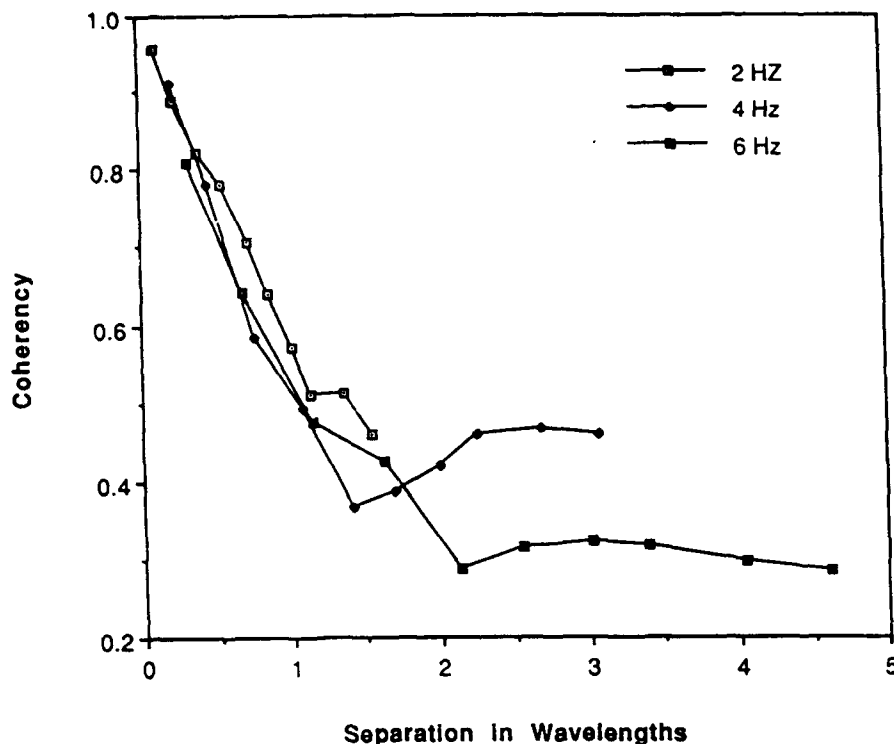


Figure 1: Coherency vs. receiver separation at NORESS for 2, 4 and 6 Hz, based on a 25 s window around the Lg phase recorded from a quarry blast at a range of 324 km. Each point is an average over several receiver pairs having a common distance separation. Distance has been normalized to the wavelength appropriate for each frequency.

Figure 1 shows the Lg coherency vs. receiver separation at three frequencies (2, 4, 6 Hz) as measured at NORESS from one of the events. These measurements are typical results. The frequency smoothing employed is such that coherencies of about 0.3 and higher can be determined, which probably explains the "floor" evident at this level. It is seen that at these frequencies coherency declines with increasing separation from a high value at close separations. The decline is faster at higher frequencies in such a way that the data appear to follow a single master curve when distance is normalized to the wavelength. Coherency declines to 0.5 within about one wavelength.

The Pinyon Flat Observatory is located in southern California at approximately 33.6°N, 116.4°W, on what was assumed to be a relatively homogeneous batholith. The array contains 58 three-component stations spaced approximately 7 m in the dense part of the array and 21 m on the extended arms (see Owens *et al.*, 1991, for a complete description). Here, we present data from an earthquake occurring on 24 May 1990 almost due south of the array at an epicentral distance of 11.6 km and a focal depth of 7.9 km. We chose a subset of the locations for analysis, consisting of a south arm and an east arm. Further results of our analysis are given in Toksöz *et al.* (1992).

The frequency content of the data is mainly in the range 5–30 Hz. We found that above about 15 Hz the seismograms are very incoherent even at a spacings less than a wavelength, which is probably due to horizontally propagating scattered waves in the very near surface. Because of this, and to be able to compare to band-limited finite-difference synthetics, we computed coherencies from band-pass filtered seismograms in the frequency range 1–12 Hz. The top portion of Figure 2 shows a filtered seismogram observed from the 24 May 1990 event. Figure 3 (top) shows the observed coherency vs. separation at 10 Hz for the shear wave (see time window in Figure 2), as determined from the filtered vertical component seismograms at several sites. On average, it is seen that coherency is high at this frequency, although between individual pairs of seismograms it can be quite low. The coherency declines with increasing separation as expected. For the N-S (nearly radial) component, coherency was similar but higher at separations above 200 m. The wavelength of S waves at 10 Hz is around 200 m, so we conclude that the

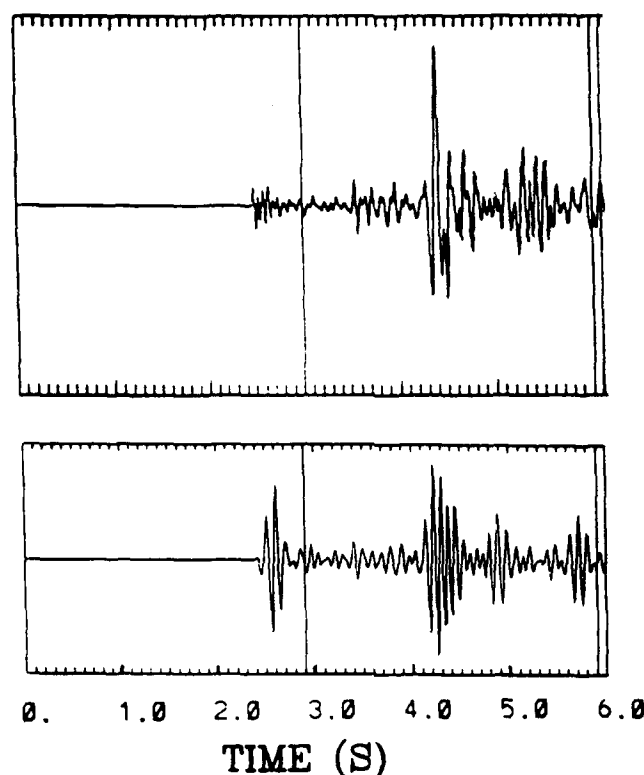
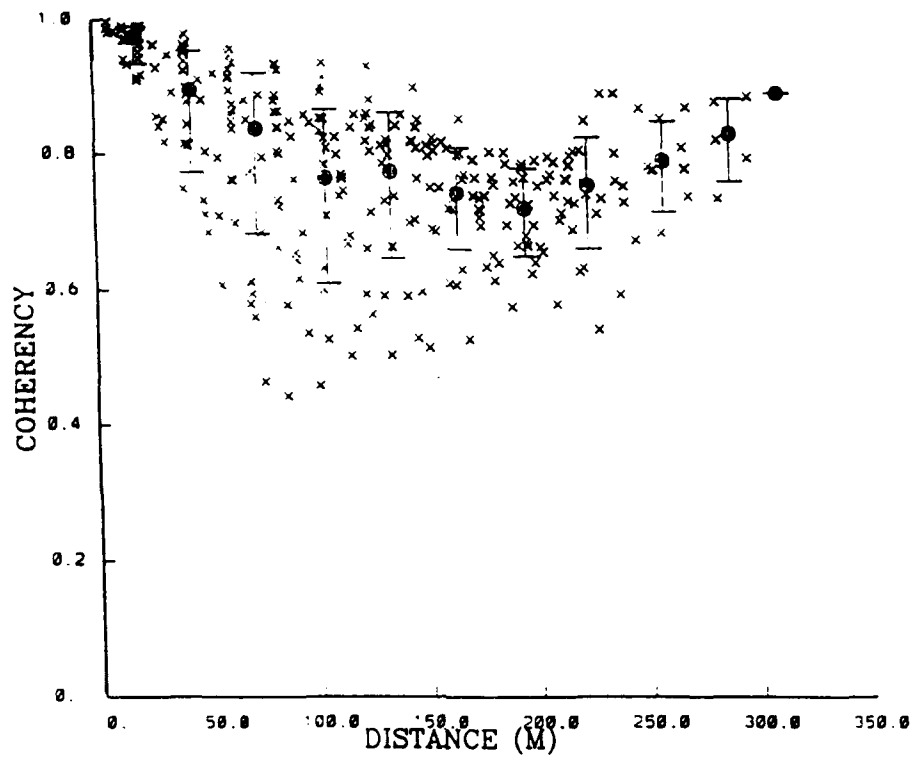


Figure 2: (Top) Observed vertical component seismogram from the center seismometer of the Pinyon Flat array, from the 24 May event. The window for coherency analysis is indicated. (Bottom) Finite-difference synthetic seismogram from a "random media" model.

Pinyon Flat seismograms are somewhat more coherent than those of the NORESS data shown earlier (Figure 1).

To gain insight into the type of geological structure which might generate the ground motion variability observed at Pinyon Flat, a 2-D elastic finite difference modeling program (Charrette, 1991) was used to generate synthetic data for two earth models. The first consists of a 0.4 km thick homogeneous layer above a homogeneous half-space, representing a weathered layer over-lying granitic bedrock. The P and S wave velocities in the weathered layer were 4.0 km/s and 2.3 km/s respectively, and the density 2000 kg/m³. In the underlying half-space the P and S wave velocities increased to 6.0 km/s and 3.45 km/s and the density to 3000 kg/m³. The second model is obtained by superposing random velocity heterogeneities on the first model. The random heterogeneities in both the upper and lower parts of the model are characterized by a zeroth order von Karman (or self-similar) autocorrelation function (e.g. Frankel and Clayton, 1986; Toksöz *et al.*, 1991b). This function was chosen because it contains fluctuations at a wide range of length scales. In the lower part of the model the vertical and horizontal correlation lengths of the von Karman function are both 1.5 km and the RMS deviation is 5% of the mean value. In the upper part of the model the horizontal correlation length is 0.4 km and the vertical correlation length is 0.1 km. The RMS deviation is 15% of the mean value. The P to S velocity ratio is held fixed in both layers.

The bottom portions of Figures 2 and 3 show some results of the finite-difference calculations generated with the second (random media) model. The comparison between the array data and the corresponding computations is promising. The synthetics agree well with the essential features of the observed seismograms (Figure 2) except for P wave amplitudes, which probably is due to event source mechanism not being taken into account. The vertical component coherencies of the synthetics are less coherent than the observed data (Figure 3) but the opposite is true for the horizontal component coherencies (not



SYNTHETIC Z

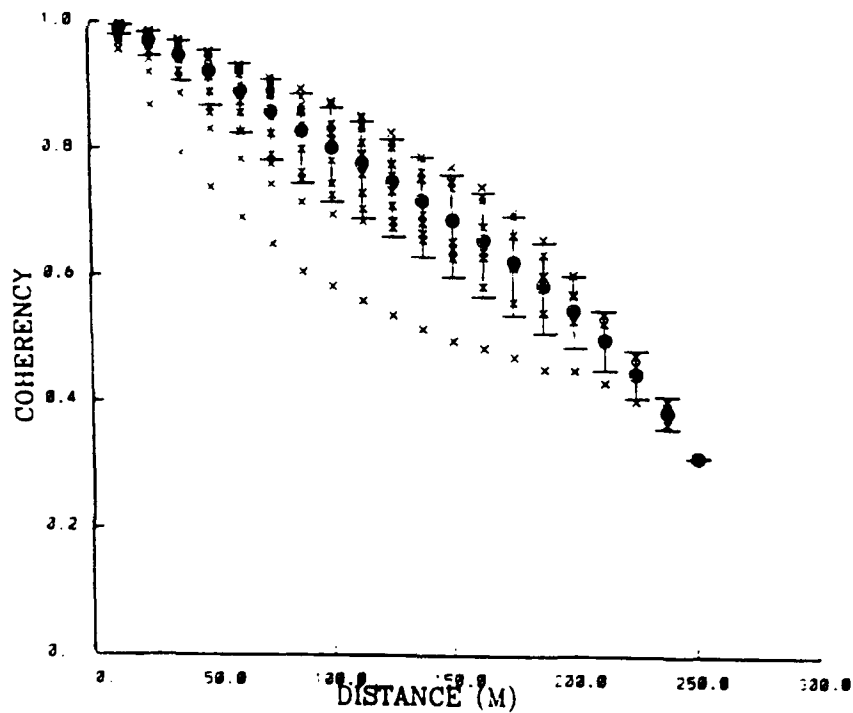


Figure 3: (Top) Coherency vs. receiver separation at 10 Hz, observed at Pinyon Flat from the 24 May 1990 earthquake. (Bottom) Coherency vs. separation from the random media model synthetics.

shown).

Comparison of Scattering Methods

We investigated the accuracy of two single scattering methods for modeling 2-D elastic wave propagation in random media: the first (distorted) Born approximation (e.g. Chernov, 1960; Hudson & Heritage, 1981; Wu & Aki, 1985), and a recently introduced method known as the "Generalized Born approximation" (Coates, 1990; Chapman & Coates, 1991; Coates & Chapman, 1991). We will refer to the first of these methods henceforth as the Conventional Born approximation to distinguish it from the second.

We tested these methods by comparing their solutions with numerical (finite difference) solutions obtained with an algorithm due to Charrette (1991). Although the finite difference solutions are subject to numerical errors, extensive efforts were made through design and testing to minimize the problems of numerical dispersion and anisotropy which can distort finite difference results. We therefore regard the finite difference results as exact solutions of the wave equation for our purposes.

Our numerical experiments used a plane P wave source field incident on various 2-D isotropic elastic models. The parameters of each model were generated as stationary, Gaussian, zero-mean random fields superposed on a homogeneous background model. The background model had a P velocity of 1.732 km/s, S velocity of 1.0 km/s and density of 10^6 kg/km³. The upper 0.05 km of each model contained no random fluctuations so as to facilitate the introduction of the incident wave in the finite difference algorithm. The heterogeneous region of each model comprised the region between 0.05 and 1.05 km in depth.

Two categories of random media were considered. In one, the "impedance models," the impedances (or densities) vary while the P and S velocities are held constant. In the other, the "velocity models," the velocities vary while the impedances are held constant. For each of these categories we examined synthetics from two realizations of a random medium: one based on an autocorrelation function with a Gaussian spatial dependence and one with an exponential dependence, the latter leading to models with more high wavenumber content. Thus the numerical experiments were performed with a total of four models. In all cases the correlation length of the autocorrelation function was 0.03 km and the RMS deviation of parameters from the background was 10%. The correlation length was chosen to match the dominant P wavelength of the incident signal, which is the point at which velocity variations scatter energy most efficiently (Charrette, 1991).

As an example of the results, calculated seismograms for the Gaussian velocity model are shown in Figure 4. The figure shows the vertical component seismograms at a line of receivers located at increasing depth and thus increasing distance from the source.

Our full set of calculations show that velocity variations scatter more strongly and with greater high frequency components than do impedance variations with the same correlation function. Similarly, coda generated by a rougher correlation function (the exponential) has more high frequency content than coda produced by a smoother one (Gaussian).

The Conventional Born approximation and Generalized Born approximation methods were quite successful in modeling the effects of the impedance variations, which generated weak, predominately backscattered signals (results not shown). The two single scattering methods generate very similar results in the impedance models, with the Conventional Born approximation being most successful in the exponential impedance model with its predominance of very short scale length scatterers.

In the models characterized by velocity variations the single scattering methods did badly, as can be seen from Figure 4. The Conventional Born approximation failed both to conserve energy and to realistically model the radiation patterns of the scattered signals. The Generalized Born approximation also failed due to the failure to conserve energy. However, in contrast to the Conventional Born approximation the predicted radiation patterns appeared to be more realistic, for example later coda was more accurately modeled and the erroneous forward scattering predicted by the Conventional Born approximation was significantly reduced.

CONCLUSIONS AND RECOMMENDATIONS

Our work indicates that in the frequency range 1-10 Hz, volume heterogeneity in the crust is a viable explanation of the ground motion variability observed at seismic arrays on bedrock, in the absence of

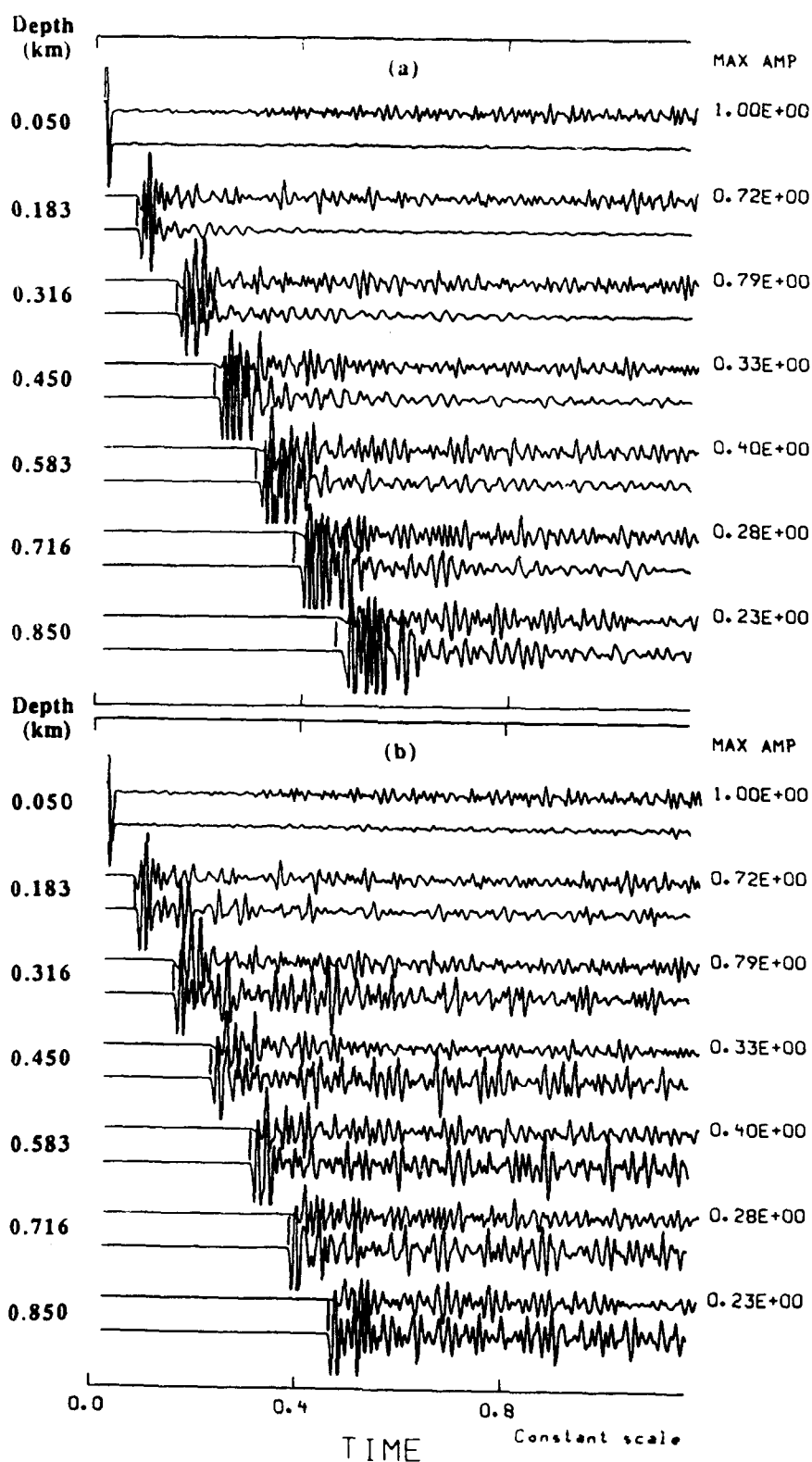


Figure 4: Vertical displacement synthetic seismograms at several depths for the Gaussian velocity model using (a) the finite difference scheme (upper trace) and the Conventional Born approximation (lower trace) and (b) the finite difference scheme (upper trace) and the Generalized Born approximation (lower trace). All traces are clipped at 20% of the peak source amplitude. The maximum amplitudes of the finite difference synthetics are shown on the right.

strong topography. At Pinyon Flat Observatory, our results suggest that heterogeneity may be similar to the von Karman type, i.e. it contains fluctuations at all length scales, with an RMS velocity fluctuation of a few percent in the crust, increasing near the surface. Frequencies above 20 Hz do not fit so easily into this model. The observed data are very incoherent even at closely spaced stations, as noted in other investigations at Pinyon Flat (Vernon *et al.*, 1991). This suggests very near receiver, i.e. very near surface, scattering is dominating.

We have shown the usefulness of finite difference modeling in random media as a tool for studying scattering from small-scale heterogeneity. Given the computational limitations of this approach, however, faster methods based on approximations are desirable, and are essential for modeling high frequencies at regional distances. For certain types of media, at least, where scattering is due to impedance and not velocity variations, methods based on the Born approximation are a feasible alternative. When velocity scattering is important though, such single scattering methods are adequate only when velocity perturbations are quite small in scale or magnitude.

REFERENCES

- Chapman, C. H. and Coates, R. T., 1991. Seismic waveform modeling of high-frequency body waves, In: *Directions in electromagnetic wave modeling*, eds. H.L. Bertoni and L.B. Felsen, Plenum, New York.
- Charrette, E. E., 1991. Elastic wave scattering in random media, *Ph.D. Thesis*, Massachusetts Institute of Technology.
- Chernov, L. A., 1960. *Wave propagation in a random medium*, McGraw-Hill, New York.
- Coates, R. T., 1990. On the scattering of seismic waves, *Ph.D. Thesis*, Cambridge University, U.K.
- Coates, R. T. and Chapman, C. H., 1991. Generalized Born scattering of seismic waves in a 3-D elastic medium, *Geophys. J. Int.*, **107**, 231-263.
- Dainty, A. M., and M. N. Toksöz, 1990. Array analysis of seismic scattering, *Bull. Seis. Soc. Am.*, **80**, 2242-2260.
- Frankel, A. and Clayton, R. W., 1986. Finite difference simulations of seismic scattering: implications for the propagation of short-period seismic waves in the crust and models of crustal heterogeneity, *J. Geophys. Res.*, **91**, 6465-6489.
- Harichandran, R. S. and Vanmarcke, E. H., 1984. Space-time variation of earthquake ground motion, Res. Rept. R84-12, Dept. of Civil Engineering, Massachusetts Institute of Technology.
- Hudson, J. A. and Heritage, J. R., 1981. The use of the Born approximation in seismic scattering problems, *Geophys. J. R. astr. Soc.*, **66**, 221-240.
- Jenkins, G. M. and Watts, D. G., 1969. *Spectral Analysis and its Applications*, Holden-Day, San Francisco, pp. 321-341.
- Owens, T. J., Anderson, P. N. and McNamara, D. E., 1991. Data report for the 1990 Pinyon Flat high frequency array experiment, PASSCAL Data Report #91-002, IRIS Data Management Center, 1408 N.E. 45th Street, Second Floor, Seattle.
- Toksöz, M. N., Dainty, A. M. and Charrette, E. E., 1991a. Spatial variation of ground motion due to lateral heterogeneity, *Structural Safety*, **10**, 53-77.
- Toksöz, M. N., Dainty, A. M. and Charrette, E. E., 1991b. Coherency of ground motion at regional distances and scattering, *Phys. Earth Planet. Int.*, **67**, 162-179.
- Toksöz, M. N., A. M. Dainty and R. Coates, 1992. Effects of lateral heterogeneities on seismic motion, *Proc. ESG1992 Int. Symp. on Effects of Geology on Seismic Motion*, Odawara, Japan.
- Vernon, F. L., Fletcher, J., Carroll, L., Chave, A. and Sembera, E., 1991. Coherence of seismic body waves from local events as measured by a small-aperture array, *J. Geophys. Res.*, **96**, 11981-11996.
- Wu, R. S. and Aki, K., 1985. Scattering characteristics of elastic waves by an elastic heterogeneity, *Geophysics*, **50**, 582-595.

RESEARCH IN REGIONAL SEISMOLOGY: THE EFFECTS OF ANISOTROPY AND HETEROGENEITY

M. Nafi Toksöz and Batakrihna Mandal

Earth Resources Laboratory
Department of Earth, Atmospheric, and Planetary Sciences
Massachusetts Institute of Technology, Cambridge, MA 02139

Contract No. F19628-90-K-0057

OBJECTIVE

The objective of this study is to examine the effects of anisotropy and heterogeneity at or near the source on radiation patterns of seismic waves from explosions, including shear wave generation. We study the source radiation patterns of P and S waves for explosions in an anisotropic medium and in a heterogeneous medium in order to determine the mechanism(s) of the generation of shear waves from explosions.

RESEARCH ACCOMPLISHED

Introduction

An important problem in seismic monitoring of nuclear explosions is the understanding of the seismic radiation patterns from explosive sources in a complex medium. To retrieve the source parameters from the observed seismograms at regional distances requires the extensive study of wave propagation effects along the path, as well as the source region. The source radiation pattern strongly depends on the properties of the source region. One interesting observation is shear (SH) wave generations from explosions. Various mechanisms have been proposed to account for this, such as tectonic release, path heterogeneities, scattering near the source, and seismic anisotropy (Gupta and Blandford, 1983; Burger *et al.*, 1986; Johnson, 1988; McLaughlin and Jih, 1988; Ben-Menahem and Sena, 1990; Mandal and Toksöz, 1990, 1991; Taylor *et al.*, 1991). In previous studies (Mandal and Toksöz, 1990, 1991), we showed that an explosion in an anisotropic medium generates azimuth-dependent P and SV waves and significant amounts of SH waves. However, these studies were limited to layered media, with laterally homogeneous properties.

In the present study we generalize the theoretical/numerical approaches to laterally heterogeneous, isotropic, and anisotropic media. We show the relative effects of the source region (1 km radius) properties and those of the propagation path. We compare the radiation patterns from explosions in a heterogeneous medium with those in an anisotropic medium. Furthermore, we calculate radiation patterns in media where anisotropy is introduced by micro-scale phenomena (regional stress, grain orientations, micro-fractures) with those due to macro-scale joints and faults.

The ultimate objective of this work is to identify the diagnostic features of regional seismograms which can isolate the source medium effects, including heterogeneity and anisotropy.

Finite Difference Algorithm for Anisotropic and Heterogeneous Media

We developed a finite difference algorithm to study the source radiation patterns in anisotropic and heterogeneous media. When considering a point source radiation pattern we prefer to use a cylindrical coordinate system. The cylindrical coordinate finite difference algorithm limits the anisotropic medium to an azimuthal symmetric medium. This algorithm is the discretized form of the first-order velocity-stress formulation of the wave equation on a staggered grid (Virieux, 1986). We consider the r and z axes as the symmetry axes. Simple sponge absorption layers are used at the bottom and the left boundary of the grid to avoid the unwanted reflections at the boundary. The proper discretization in space and time have also been considered to minimize the well known dispersion problem for finite-difference

computation. Finally, we successfully implemented the algorithm on the Earth Resources Laboratory's MIMD parallel computer (nCUBE-2). The algorithm in the parallel computer decomposes the whole grid into subgrids. Each processor computes the finite-difference computations in the subgrid and receives information at the edges of the subgrid from adjacent processors. With this approach we are able to compute the large models for wave propagation at regional distances.

Radiation Patterns

In two previous papers (Mandal and Toksöz, 1990, 1991) we showed that the radiation from explosion sources is affected strongly by the presence of anisotropy, including the generation of shear waves and radiation patterns that mimic double couple sources in isotropic media. Such effects are usually attributed to tectonic release from either triggered faults or relaxation of prestress at the shot point. Here, we go one step further and study explosive sources in laterally heterogeneous isotropic and anisotropic media. We have used various combinations of source and propagation medium properties. In these numerical experiments, we assumed a typical isotropic medium ($V_P = 6$ km/sec, $V_S = 3.46$ km/sec and $\rho = 2.6$ gm/cc) as the reference. The two anisotropic media are produced by introducing the micro-fractures in one case and macro-fractures (or joints) in this reference medium (Mandal and Toksöz, 1992). The heterogeneous medium is derived by introducing random velocity variations with exponential correlation function. The horizontal and vertical correlation lengths used are equal.

We compared the radiation pattern from an explosion source in a homogeneous (reference) medium to those from explosions in "complex" media. We considered the source region to be 1 km in radius and the rest of the medium to be the path. The "complex" media are produced by making the source region and propagation path isotropic, anisotropic (micro-scale or macro-scale joints) and/or randomly heterogeneous.

We computed the seismograms, using 5 Hz center frequency, at two circular arrays in a vertical plane with radii of 2 and 4 km. We displayed the waveforms as radial (the particle motion along the θ direction) and tangential (perpendicular to θ) direction. For comparisons of different media, we display all the figures using the same scale. Figure 1a shows the waveforms due to an explosion source in our reference homogeneous-isotropic medium. The radial component shows the circular radiation pattern of P waves and no shear waves. Figure 1b shows the same for the explosion source in the randomly heterogeneous medium, with a correlation length of 0.5 km and 5% rms velocity variation. The results show the variation of P-wave amplitudes, some scattered shear waves, but no distinct shear wave radiation pattern.

Figure 2 shows the waveforms for two different types of anisotropic media. In Figure 2a the anisotropy is due to uniform aligned micro-cracks and in Figure 2b to the aligned joints. These two media have similar P-wave velocities, but different quasi-SV velocities. Explosive sources in both media produce strong shear waves. The jointed medium produces a radiation pattern similar to a double-couple shear wave source. The micro-fractured medium (Figure 2a) produces a complicated shear wave radiation pattern.

Figure 3 shows seismograms for the complex model where the source region is anisotropic and the propagation medium is isotropic. Figure 3a can be compared to Figure 2a. The shear wave radiation pattern is noticeable but is altered somewhat due to propagation in an isotropic medium. Figure 3b can also be compared to Figure 2b.

Figure 4a shows the seismograms for the isotropic source medium and anisotropic (joints) propagation medium. In this case, the transverse component is not as strong, as shown in Figure 3. Figure 4b refers to the anisotropic source medium and heterogeneous propagation medium. Again, strong shear waves are generated at the source but are modified by propagation and scattering in a heterogeneous, isotropic medium.

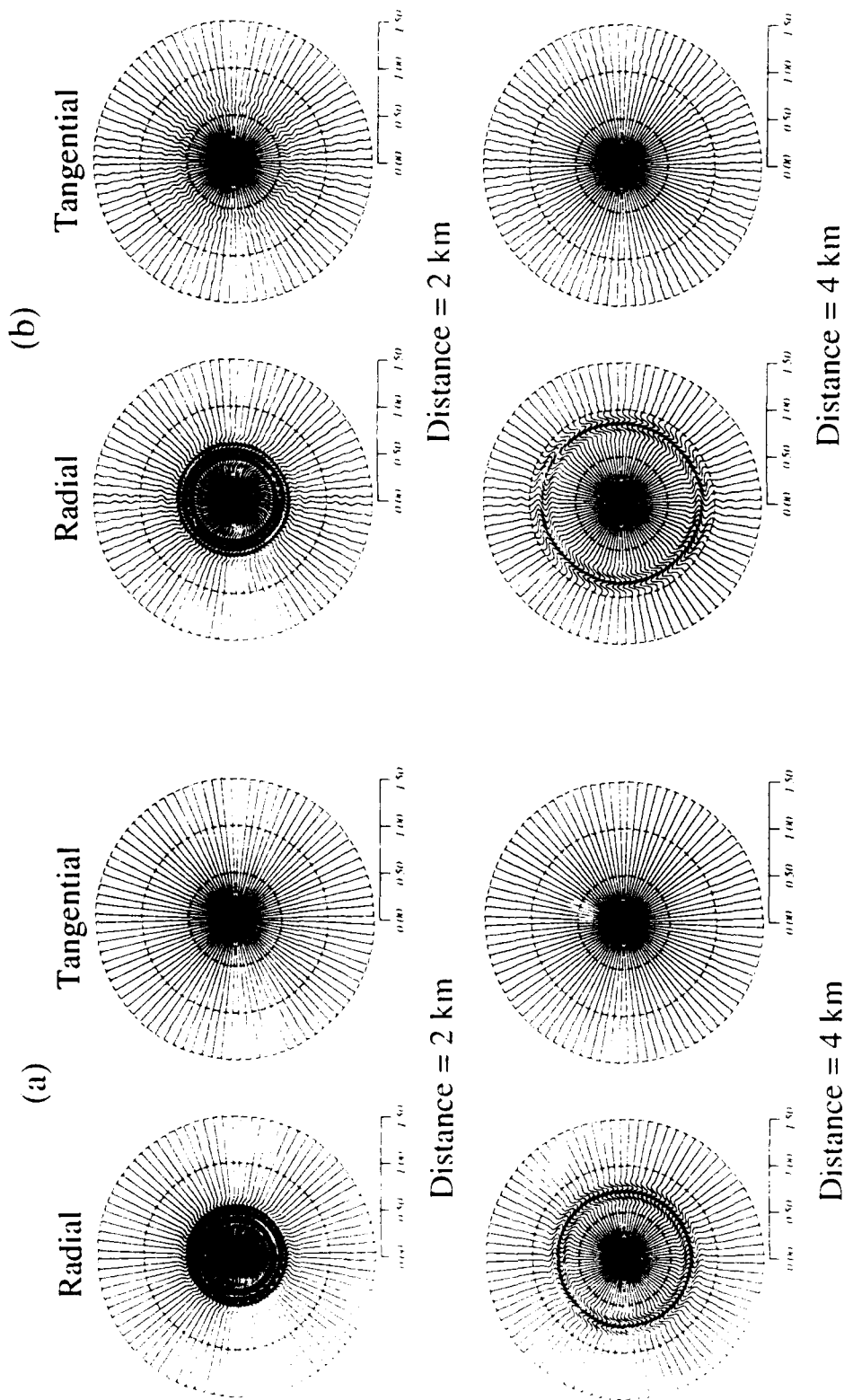
CONCLUSIONS AND RECOMMENDATIONS

Theoretical studies of seismic wave generation by explosive sources in homogeneous, randomly heterogeneous, isotropic media and anisotropic laterally heterogeneous media were conducted, and radiation patterns studied. Because of the directional dependence of the compliance of the material, an explosion detonated in an anisotropic medium will have a nonisotropic radiation pattern and can generate a significant amount of shear waves, including transverse (SH) components. We also found different radiation patterns for two different anisotropic media (micro- and macro-fractures) with similar P-wave velocity variations. The heterogeneous medium could not produce as strong a shear wave as an anisotropic medium. The results from laterally heterogeneous ("complex") media suggest that the source in an anisotropic medium can generate stronger shear waves than the source in other media. For future study we recommend the following:

1. Continue the theoretical investigation of explosive sources in complex media, including anisotropy and heterogeneities.
2. Determine the P and S energy ratio with the degree of anisotropy and heterogeneity.
3. Compare the theoretical results with seismograms from explosions.

REFERENCES

- Ben-Menahem, A. and A.G. Sena, 1990, Seismic source theory in stratified anisotropic media, *J. Geophys. Res.*, **95**, 15,395-15,427.
- Burger, R., T. Lay, T. Wallace, and L. Burdick, 1986, Evidence of tectonic release in long-period S-waves from underground explosions at Novaya Zemlya Test Sites, *Bull., Seism. Soc. Am.*, **76**, 733-755.
- Gupta, I.N. and R.R. Blandford, 1983, A mechanism for generation of short-period transverse motion from explosions, *Bull. Seism. Soc. Am.*, **73**, 571-591.
- Johnson, L.R., 1988, Source characteristics of two underground nuclear explosions, *Geophys. J.*, **95**, 15-30.
- Mandal, B. and M.N. Toksöz, 1990, Computation of complete waveforms in general anisotropic media—results from an explosion source in an anisotropic medium. *Geophys. J. Int.*, **103**, 33-45.
- Mandal, B. and M.N. Toksöz, 1991, Effects of an explosive source in an anisotropic medium, *AGU Monograph "Explosion Source Phenomenology"*, **65**, 261-268.
- Mandal, B. and M.N. Toksöz, 1992, Scale of anisotropy: A theoretical study of velocity anisotropy from micro- and macro-fractures, submitted to *Rev. of Geophysics*.
- McLaughlin, K.L. and R.S. Jih, 1988, Scattering from near-source topography teleseismic observation and numerical simulations, *Bull. Seism. Soc. Am.*, **78**, 1319-1414.
- Taylor, S.R., H.J. Patton, and P.G. Richards (eds.), 1991, *Explosion Source Phenomenology*, Geophysical Monograph 65, American Geophysical Union, Washington, DC, 268 pp.
- Virieux, J., 1986, P-SV wave propagation in heterogeneous media: Velocity-stress finite-difference method, *Geophysics*, **51**, 889-901.



Isotropic Medium, $V_p=6$ Km/S, $V_s=3.46$ Km/S, $f_c=5$ Hz, Explosion

Heterogeneous Medium (Exponential, $Corl=.5$ km, $rms=5\%$), $f_c=5$ Hz

Figure 1: Waveforms at two different vertical circular arrays with radius 2 km (top) and 4 km (bottom). The radial component is the particle velocity along the direction of the radial line and the tangential component is perpendicular to the radial line. (a) The source is in the isotropic medium. (b) The source is in the heterogeneous medium. The heterogeneous model is designed using an exponential function with the same vertical and horizontal correlation length of 0.5 km with 5% rms velocity deviation.

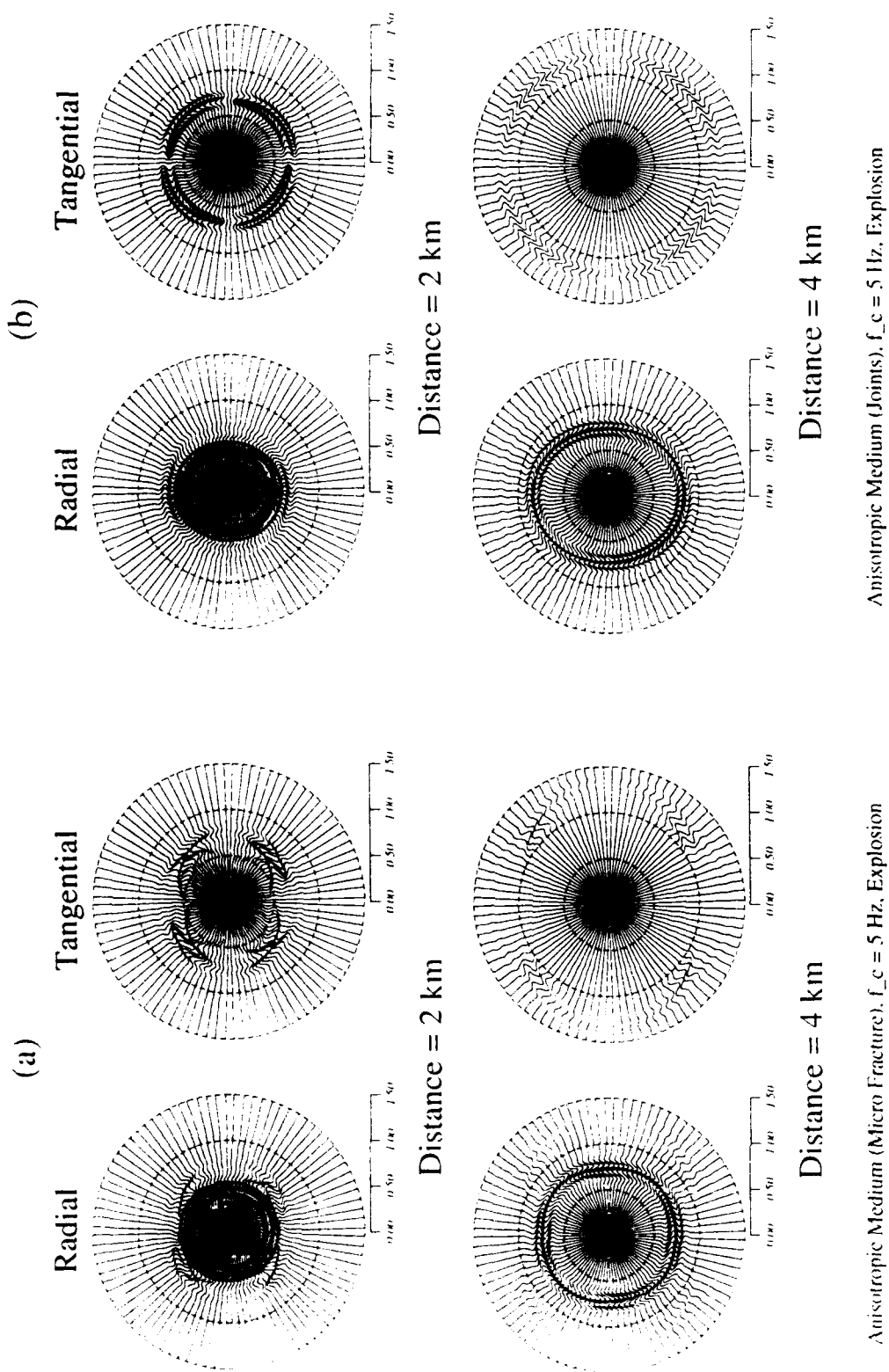


Figure 2: The source in anisotropic media: (a) In a micro-fracture medium with 10% fracture density and 0.001 aspect ratio. (b) In a macro-fracture medium consisting of 100 joints/meter with specific stiffness 15×10^{12} Pa/m. The shear waves have different radiation patterns.

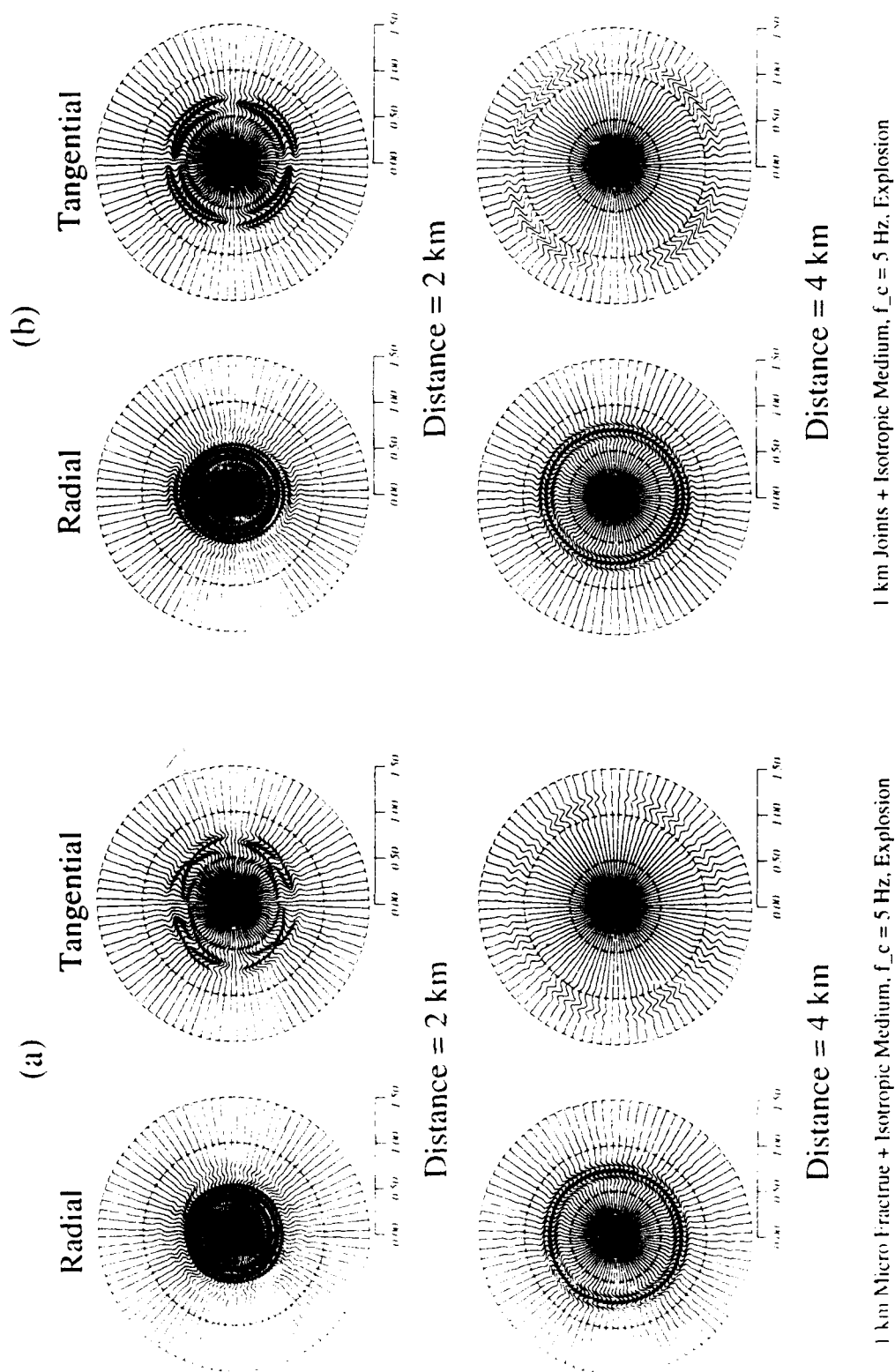


Figure 3: Complex media. The source medium with 1 km radius is anisotropic and the propagation medium is isotropic. The source is (a) in a micro-fracture medium, and (b) in a macro-fracture medium. The anisotropic models are the same as in Figure 2.

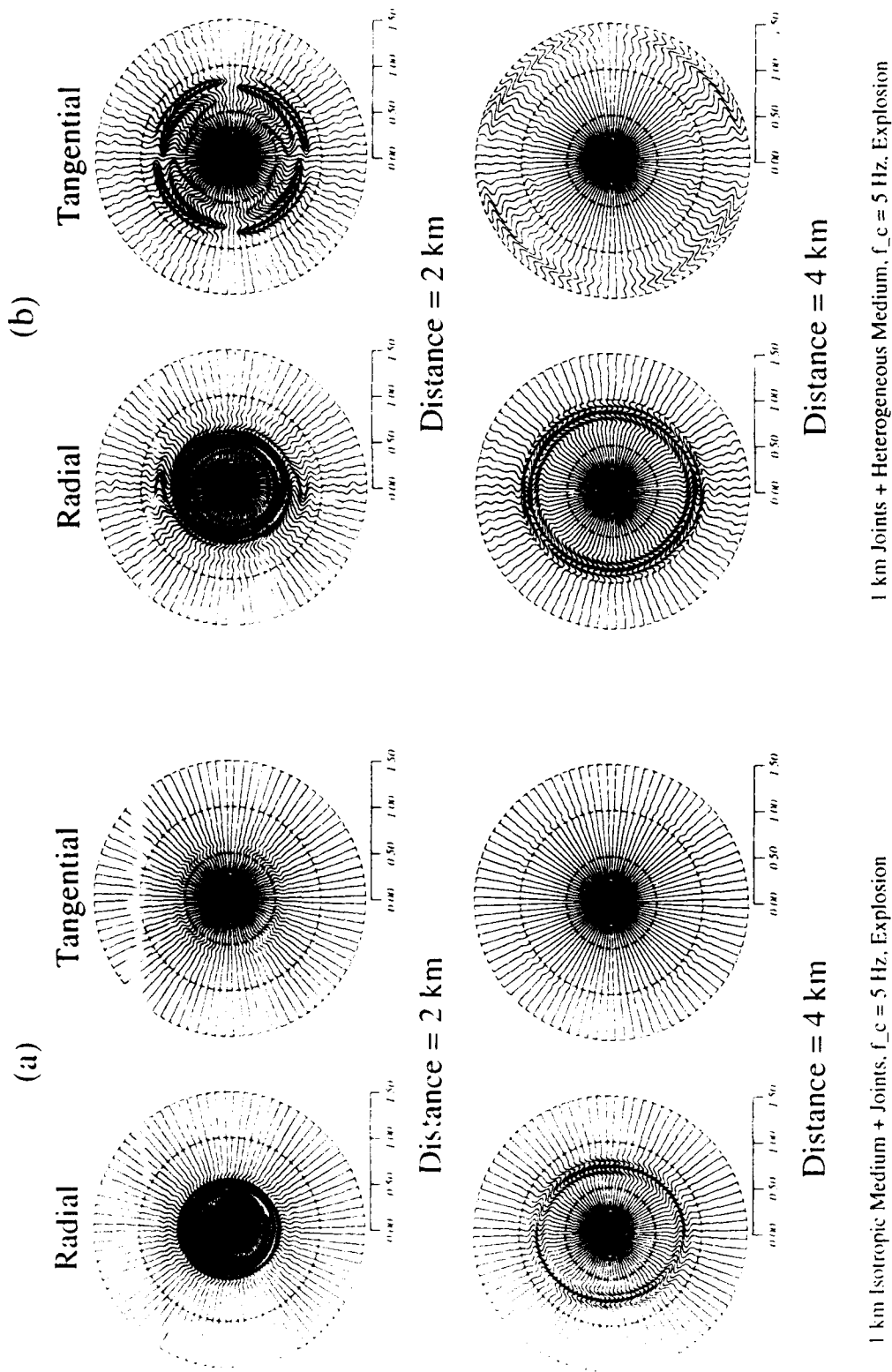


Figure 4: Complex media. The source is (a) in an isotropic medium, and (b) in a macro-fracture medium. The propagation medium is (a) macro-fractured (same as described in Figure 2b), and (b) randomly heterogeneous (same as in Figure 1b).

Short-Period Regional Phases from Fennoscandian arrays

Kristín S. Vogfjörð and C. A. Langston
Department of Geosciences
Pennsylvania State University
University Park, PA 16802

Contract No. F19628 90-K-0044

Objective:

Proper phase identification is necessary for accuracy in event location and for source-depth discrimination with regional arrays. Characteristics of the local and regional wave propagation, therefore need to be known. Our objective is to determine the characteristics of short-period, local and regional wave propagation near the Fennoscandian arrays, ARCESS, NORESS, and FINESA. Also to extract information about crustal and upper mantle velocity structure in these regions from travel times, amplitudes, phase velocities and backazimuths of individual phases and to assess the effects of lateral variations in the structure on the wave propagation.

Research Accomplished:

The IMS database has been searched for high quality events at local at regional distances from the ARCESS array, to obtain reliable phase-velocity and backazimuth estimates for crustal and upper mantle phases. Despite a wealth of data only one event of significant amplitude has been found within 150 km distance of the array, thus limiting the constraints that can be put on crustal velocity structure. Thirty events in the distance range 60 to 570 km from ARCESS have already been analyzed. Magnitudes are between 1.8 and 3.2 and the backazimuth range is between 30° and 250°. Except for the few events in the Caledonian region north of the array, all are located within the Archaean or Precambrian region of the shield, with propagation paths within those regions. Event locations and structural units are shown in Figure 1, where IMS locations are indicated by triangles and relocated positions, which in most cases coincide with known mines, are indicated by solid circles. Mislocations in distance are due to missed onset of Lg, while backazimuth mislocations are caused by variations in backazimuth for the different phases of an event. Backazimuth mislocations are most prominent for mine explosions at Nikel and for quarry explosions on the Varanger Peninsula northeast of the array. A few of the events studied are probable earthquakes, but only in one event have depth phases been clearly identified.

Phase velocities and backazimuths of main arrivals are obtained from f-k analysis of the events. A composite of array beams is then used to represent each event on record sections, constructed for the different azimuthal ranges, in order to study the behavior of crustal and upper mantle phases with distance and azimuth. Phase-velocity dispersion curves of Rg waves, obtained from 12 events located east of ARCESS are also being used to deduce the near-surface velocity structure under the array. This is also being done for previously studied events from the NORESS array in southern Norway (Vogfjörð and Langston, 1991), from which 6 Rg waves have been obtained.

A record section of composite seismograms from explosions east of ARCESS, is shown in Figure 2. Travel-time curves for major crustal and upper mantle phases are superimposed. The model used for the calculation is a plane layered approximation to the velocity structure along the POLAR refraction profile (Luosto et al., 1989), which crosses the region east of ARCESS.

The model assumes constant crustal thickness of 42 km, which approximates the average crustal thickness under the northern part of the POLAR Profile. The main characteristics of wave propagation in the region east of ARCESS are clearly seen on the record section: Large-amplitude Rg waves, which are seen out to 400 km distance, large-amplitude upper-mantle waves (Pn), single Moho reflections (PmP and SmS) dominating between 150 and 250 km distance and double Moho reflections (2×PmP and 2×SmS) dominating between 350 and 400 km distance, while the single reflection has diminished in amplitude.

The Moho reflections from the event on Varanger Peninsula, at 150 km distance are not matched by the travel-time curves, but can be accurately matched with a 45-km-thick crust. The backazimuth of the Moho reflections is also 5° greater than that of the crustal phases, Pg and Sg, which properly locate the event. This indicates a westward dip in the Moho, from the thinner crust to the east. No Rg waves are observed from this location, although it coincides with a quarry. The Rg wave is probably attenuated when crossing the Tanaffjord. Pg is the first arrival in the event from the Sydvaranger mine, at 180 km distance, suggesting a Moho deeper than 42 km, but the event is composed of a series of impulsive explosions making it difficult to determine the PmP-Pg time, required to obtain the crustal thickness. We have not been able to find a simple explosion from this mine. Due to the large-amplitude P waves from the explosion at 350 km distance, a 2×PmP-PmS phase is observed 21 s after Pn. Synthetic waveform calculations predict this phase, however it is generally not observed.

The record section of events from southwest of ARCESS (Figure 3) includes an earthquake at 180 km distance and a probable earthquake at approximately 60 km distance. Although none of the events have observable Rg waves the two most distant ones are probably explosions, since they approximately coincide with the Kiruna and Malmberget mines. The two farthest events have been high-pass filtered at 2 Hz to make phases clearer. The crustal thickness on the FENNOLORA profile in this area is around 45 km (Guggisberg et al., 1991), so travel-time curves for a 45-km-thick crust are superimposed on the record section. From this record section it appears that the first Moho reflection dominates to at least 350 km, Pn is of large amplitude and the amount of high-frequency scattered energy is greater than on the previous record section.

No clear depth phases are observed from the event at 60 km distance, and its source depth is probably within 1 km of the surface. The event at 180 km however has clear discernible depth phases, sPg and sPmP, at approximately 16 s on the plot. These can be matched with the source at 32 km depth and a crustal thickness of 45 km. The phase velocity of the first arrival in the event also identifies it as Pn, requiring a substantial source depth.

Phase velocity has been obtained as a function of frequency for the observed Rg waves at ARCESS and NORESS. The dispersion curves obtained are plotted in Figure 4, as well as the mean, weighted by the maximum amplitude of the Rg wave, and the standard error of the mean. The maximum power in the Rg wave is around 1 Hz. Higher frequencies are increasingly attenuated and the 3-km array-aperture, limits the resolution to frequencies above 1 Hz. The dispersion curve is plotted for the frequency range where power is $\geq 1\%$ of the maximum. The events recorded at NORESS are at 45 and 83 km distance, with the events from 45 km distance containing significant energy up to 2 Hz. Thus allowing resolution of velocity variations between 1 and 3 km below the surface. More observations, however, are needed from this distance for a reliable estimate. The Rg waves from 83 km distance are more attenuated, especially at higher frequencies. The mean phase velocity at frequencies between 1 and 1.2 Hz is $2.98 \pm .038$ km/s and $2.88 \pm .032$ km/s at 1.4 Hz, indicating that velocity decreases as the surface is approached. The events near ARCESS, producing Rg waves are located at distances of 175, 210 and 350 km. The phase velocity can therefore only be obtained for frequencies up to 1.4 Hz, allowing resolution of velocities between 2 and 3 km below the surface. From the weighted mean it can be seen that phase velocity around 1 Hz is $3.15 \pm .014$ km/s and at 1.3 Hz it has increased to $3.30 \pm .023$ km/s, indicating higher velocities near the surface.

Conclusions and Recommendations:

Evidence of lateral velocity variations in the region due east from ARCESS are seen in explosions from the Nikel mine. High-frequency phases from this location appear to have greater backazimuths than phases dominated by lower frequencies. Propagation through the Pechenga suture zone may be causing this. The velocity profile obtained from the Kola superdeep bore hole, which penetrates the Pechenga Belt near Nikel, shows higher velocities in the top 6.7 km of the well, than in the section below (Kozlovsky, 1987). A northward dipping high-velocity layer, obtained at shallow depth under the POLAR profile and coinciding with the Lapland Granulite Belt (Gaál, G. et al., 1989) may also cause propagation-path variations. The Lg wave train from some events at easterly azimuths may be affected by this structure. In these events, Lg is dominated by low frequencies (~ 2 Hz) of unusually low phase velocities (~ 3.3 km/s) mixed in with the normal 4.6 km/s phase velocity. The higher near-surface velocities under the ARCESS array, as inferred from the Rg-wave dispersion study can also contribute to produce low observed phase velocities.

A westward dipping Moho can be inferred at 75 km distance northeast of ARCESS, from the 5° difference in backazimuths between the crustal phases and the Moho reflections from the quarry on Varanger Peninsula.

Depth phases have been detected in one event at 32-km depth in the ARCESS region. These phases however are small and for shallow source depths, may not be discernible from the coda following the direct arrivals. We will attempt to extract the focal mechanism of this event.

The mean dispersion curves obtained for NORESS and ARCESS will be used to infer shallow velocity structure under each array. The Rg-wave dispersion study will not be carried out on data from FINESA; with an aperture of only 1.4 km FINESA does not resolve phase velocities of Rg well, but a study of the propagation characteristics around the array will be performed.

References

- Gaál, G., A. Berthelsen, R. Gorbatshev, R. Kesola, M. I. Lehtonen, M. Marker and P. Raase (1989). Structure and Composition of the Precambrian crust along the Polar profile in the northern Baltic Shield, *Tectonophysics*, 4162, 1-25.
- Guggisberg, B., W. Kaminski and C. Prodehl, (1991). Crustal structure of the Fennoscandian Shield: A travelttime interpretation of the long-range FENNOLORA seismic refraction profile, *Tectonophysics*, 195, 105-137.
- Kozlovsky, Ye. A. (Editor) (1987). *The Superdeep Well of the Kola Peninsula*, Springer-Verlag, Berlin, Germany, 558 pp.
- Luosto, U., E. R. Flueh, C.-E. Lund and working group, (1989). The crustal structure along the POLAR Profile from seismic investigations, *Tectonophysics*, 162, 51-85.
- Vogfjörd, K. S. and C. A. Langston (1991). Analysis of regional events recorded at NORESS, *Bull. Seism. Soc. Am.*, 80, 2016-2031.

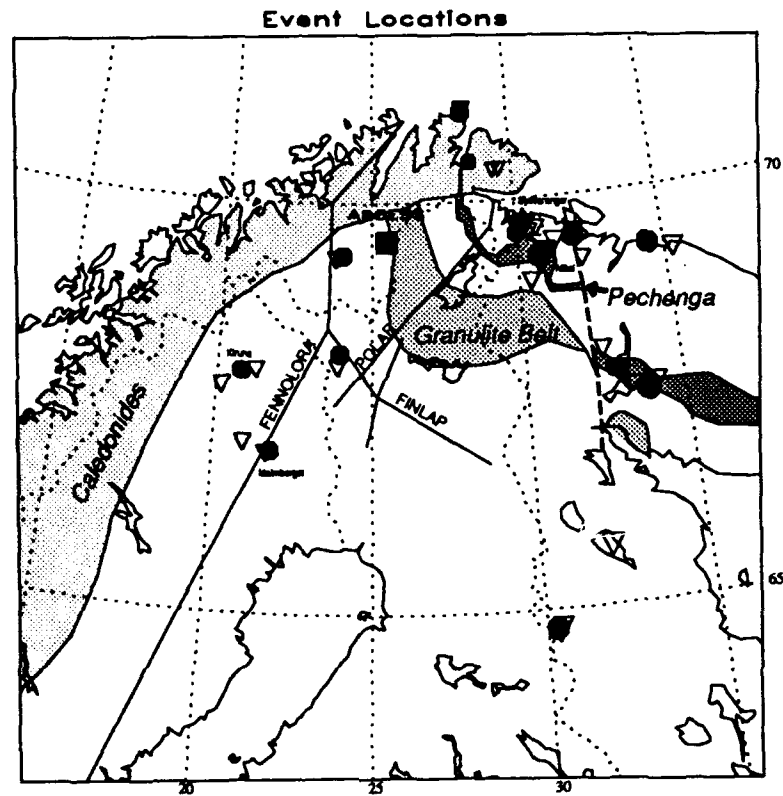


Figure 1. Map showing locations of events (triangles) and relocations (solid circles). The Caledonian region, the Lapland Granulite Belt and the Pechenga suture zone are all shaded. Some refraction profiles are also identified.

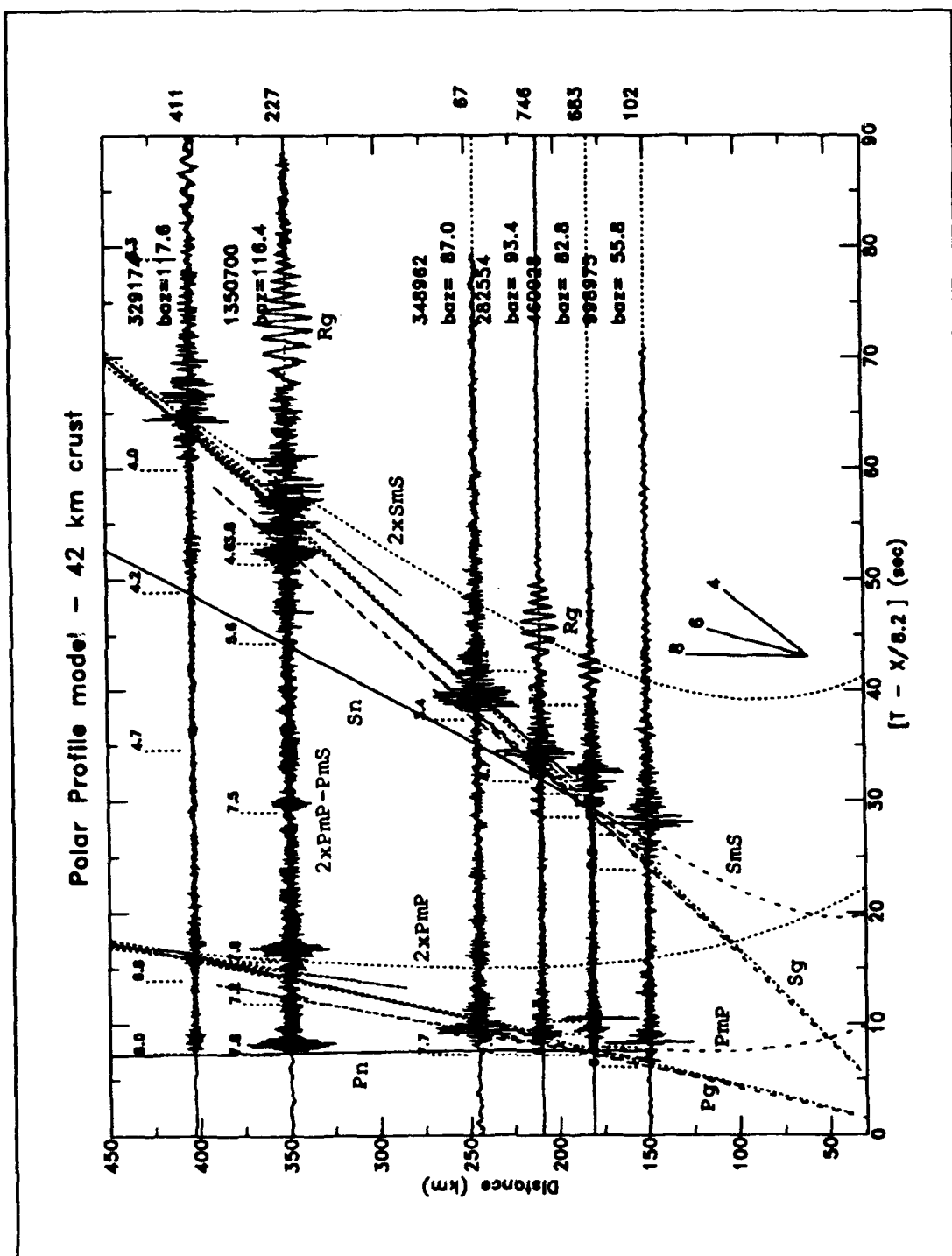


Figure 2. Composite-seismogram record-section of explosions located east of ARCESS. Traces are normalized to maximum amplitude, which is shown at the right of each trace. Travel-time curves for a 42-km-thick crust are superimposed on the plot. Phase velocities of the major phases are indicated above traces.

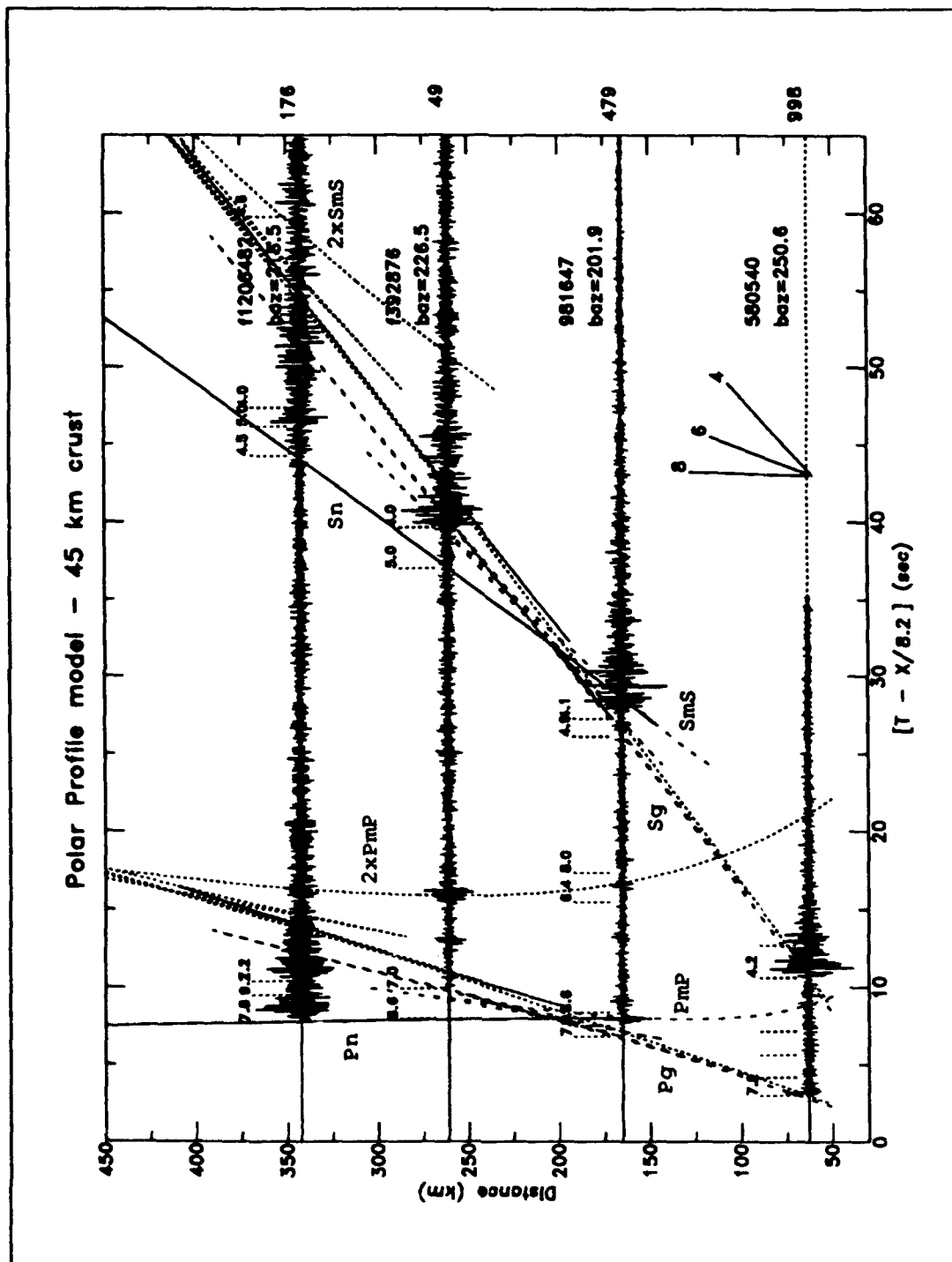


Figure 3. Composite-seismogram record-section of events southwest of ARCESS, with travel-time curves superimposed. No Rg waves are observed. The event at 160 km distance is an earthquake at 32 km depth. The depth phases, sPg and sPmP, with the appropriate phase velocities can be seen at 16 s on the plot.

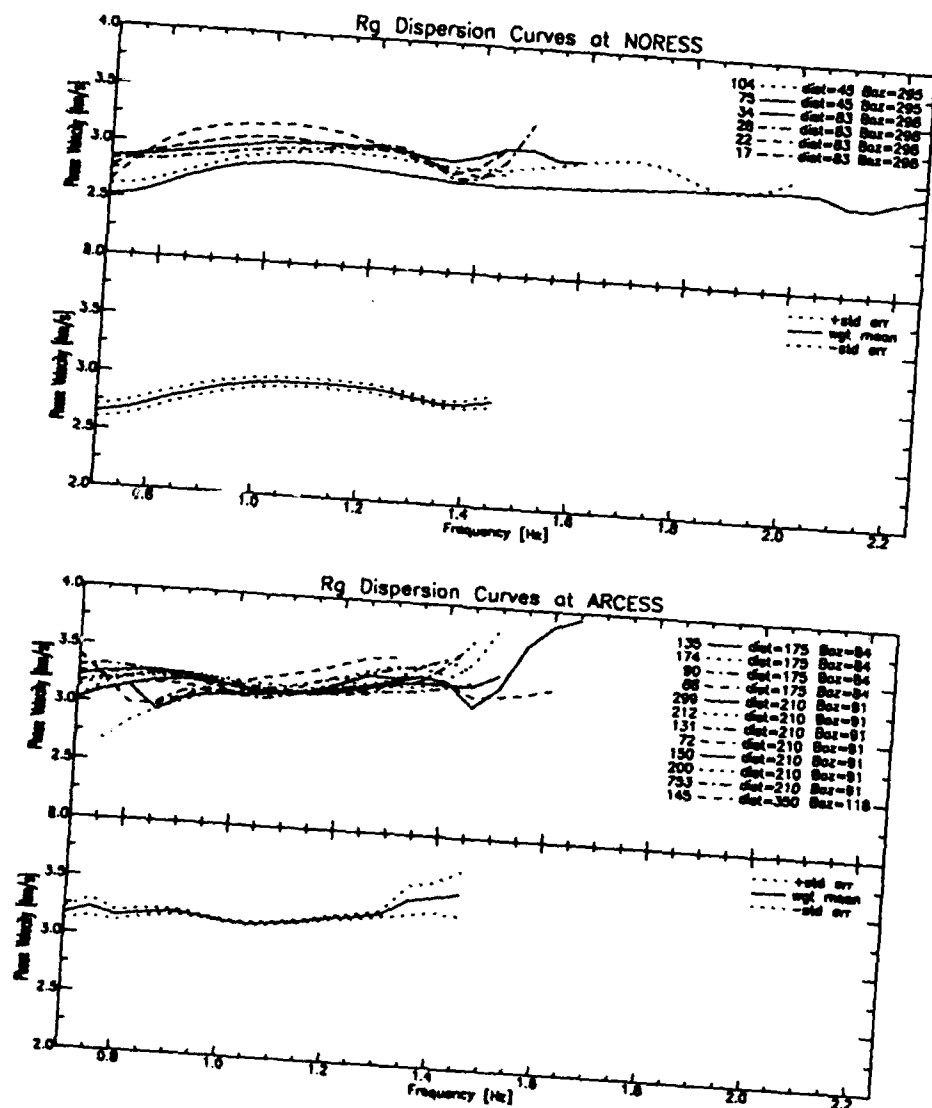


Figure 4. Rg phase-velocity dispersion: curves for NORESS and ARCESS. Weighted mean curves are also shown together with standard error curves. Curves are weighted by maximum amplitude, shown in front of each trace.

REGIONAL DISTANCE RECORDINGS OF LARGE MINING EXPLOSIONS: DISTANCE DEPENDENT DISCRIMINATION

Terry C. Wallace

Department of Geosciences
University of Arizona
Tucson, Arizona 85721

Contract: F19628-90-K-0038

Objective:

Regional distance seismology will play an important role in monitoring a non-proliferation treaty or a restricted, low yield test agreement. The two technical facets of such monitoring are the discrimination between explosions and earthquakes, and discrimination between chemical and nuclear explosions. The focus of this research has been on the chemical/nuclear explosion identification. Most large mining explosions have a unique signature in the frequency domain due to the "ripple fire" detonation of explosions *separated by small distances and times*. Ripple fire produces a unique spectral signature which is strongly scalloped, and this signature can be used to discriminate between chemical and nuclear explosions (Smith, 1988; Baumgardt and Ziegler, 1988; Hedlin et al., 1988; Suteau-Henson and Bache, 1988). This nuclear/chemical explosion discriminant is best at very high frequencies (> 20 Hz), but many of the GSN and Soviet-IRIS stations are limited by a sampling rate of 20 sps. We are attempting to better quantify the signature of ripple fire explosions as a function of travel path, propagation distance and shot configuration by studying chemical explosions in the southwestern U.S., Missouri and Germany recorded on broadband instruments.

Research Accomplished:

Much of the recent work in seismic yield determination and discrimination has emphasized the use of regional distance data. There are several advantages to using regional distance data. First, regional distance seismic stations can significantly reduce the detection threshold over that achieved by teleseismic monitoring. The L_g amplitude recorded at regional distances provides a very stable yield estimate. Finally, spectral discriminate based on the fact that earthquakes produce more high frequency seismic energy than explosions can be used with a high degree of confidence to small magnitudes ($m_b \sim 3.5$). Although much work remains to be done on quantifying the effects of travel

path on discrimination and yield determination, the outstanding problem in regional distance verification is the identification and characterization of large chemical explosions. Is it possible to always discriminate between nuclear and chemical explosions? Is it feasible to develop an evasion scenario in which a nuclear explosion is fired in conjunction with a series of chemical explosions? The only way to answer these questions is to develop a data base of observations which can be analysed in terms of travel path, explosion configuration and recording instrumentation. We have begun to develop data base which now contains 712 recordings with travel paths ranging from 12 km to 1456 km. The travel paths represent many different geologic environments, many different blasting procedures and two orders of magnitude in explosion size.

Most chemical explosion discriminates have been investigated for very high frequencies (40 Hz) because the spectra stripping is most obvious when broad band width is used. Unfortunately, the high frequencies attenuate rapidly for many regions; the effectiveness of a scalloping discriminate is strongly dependent on travel path, which is probably a reflection of variation in attenuation. We have used a lower pass band (20 cps) to detail the effectiveness of various parameterization of spectra stripping as function of distance. We have developed a significance test for scalloping based on the strength of the holes, and their periodicity. A spectra which has strongly developed, periodic scalloping will have a significance of 1; a non periodic scalloping will have a much lower significance. For the various regions studied we have developed relationships between significance versus distance.

The Southwestern U.S. Chemical Explosion: We used the recordings at two IRIS stations (ANMO and TUC) which are equipped with STS -1 seismometers to develop a catalogue of explosions. 16 mines or quarries produced a least one usable seismogram at ANMO, which resulted in 136 recordings. The size of the explosions ranges from 17,000 to 171,000 pounds. The travel paths cross several different geologic provinces (the Rio Grande Rift, the Colorado Plateau, the Datil Plains), and attenuation ($Q\beta$) probably varies by a factor of 3. The mines in northern New Mexico and Arizona are primarily coal; the mines in southern New Mexico and Arizona are open pit copper mines. In general, the coal mines have larger explosions but the signal amplitude corrected for distance is smaller than those explosions from copper mines. The frequency content is higher, suggesting that attenuation is not responsible for the reduction in amplitude, but rather, it is the result of the explosion medium.

Figure 1 shows 9 mines which produced recording at TUC. Table 1 gives the coordinates of the mines and the size of the largest explosion recorded from a given mine.

Several of the mines have multiple explosions daily, and blasting practices varies considerably between mines. We have developed a catalogue of 393 explosions recorded at TUC. Figure 2 shows a comparison between the waveforms from an earthquake (July 28, 1992, $M_L = 2.8$) and copper mining explosion approximately the same distance from TUC. A causal inspection of the whole waveform spectra does not offer obvious discrimination between the earthquake and explosion. However, if a sonogram is constructed the spectral hole at 3 Hz persists for the explosion ; the significance algorithm assigned this waveform a value of 0.82.

Explosions in stable continental regions: the Midwest US and Europe. We have collected chemical explosion waveforms recorded on the IRIS station CCM (Cathedral Caves, Missouri) and the Graftenberg Array (GRF) in Germany. At present we have cataloged about 80 events recorded on CCM, although all are much smaller than the Southwestern U.S. explosions. We have collected approximately 100 records from 19 different sources from GRF; the largest event was a magnitude 2.8 explosion.

Conclusions and Recommendations:

Preliminary analysis of waveforms from mine explosions in the southwest United states indicates that characteristic spectral scalloping disappears beyond distances of 890 km. The significance indicator is typically less than .40 at this distance, and the explosions are indistinguishable from shallow earthquakes. This is the result of the attenuation of the high frequencies; we also document this effect in the spectral ratio of Pn and Pg phases. Using the Taylor et al. (1988) algorithm which compares a high frequency and a low-frequency pass band (6 to 8 Hz and 1 to 2 Hz, respectively), the Pn and Pg phases both behave similar to earthquakes with like travel paths.

The waveforms collected thus far for stable continental paths indicate that the significance indicator does not drop to a value of 0.40 until 1,050 - 1,100 km. We have not yet collected any earthquakes in these regions for direct comparison.

We have correlated the 'significance' with a number of parameters such as Pn velocity, roughness of topography, and Sn velocity as a function of distance. Sn velocity appears to be the best indicator of the range over which a scalloping discriminate is effective. For Sn velocities of less than 4.3 km/s the discriminate fails 25% of the time beyond 800 km. For Sn velocities greater than 4.4 km/s, the discriminate fails 25 % of the time beyond 1100 km.

References:

- Baumgardt, D.R. and K. A. Ziegler (1988). Spectral evidence for source multiplicity in explosions: application to regional discrimination of earthquakes and explosions, Bull. Seism. Soc. Am., 78, 1773-1795.
- Hedlin, M., J. Orcutt, B. Minster and H. Gurrola (1989). The time-frequency characteristics of quarry blasts, earthquakes and calibration explosions recorded in Scandinavia and Kazakhstan, USSR, in 11th DARPA/AFGL SESIMIC RESEARCH SYMPOSIUM, P 40-48. GL-TR-90-0301, ADA229228
- Smith, A.T. (1988). High-frequency seismic observations and models of chemical explosions: implications for the discrimination of ripple-fired mining blasts, Bull. Seism. Soc. Am.
- Suteau-Henson, A. and T.C. Bache (1988). Spectral characteristics of regional phases recorded at NORESS, Bull. Seism. Soc. Am., 78, 708-725.

Figure Captions:

Figure 1: Location of sources recorded at TUC

Figure 2: A comparison between a small earthquake (left) and an earthquake (right) recorded at TUC. The traces are raw broadband ground velocity.

Explosion Sources in the Southwestern U.S.

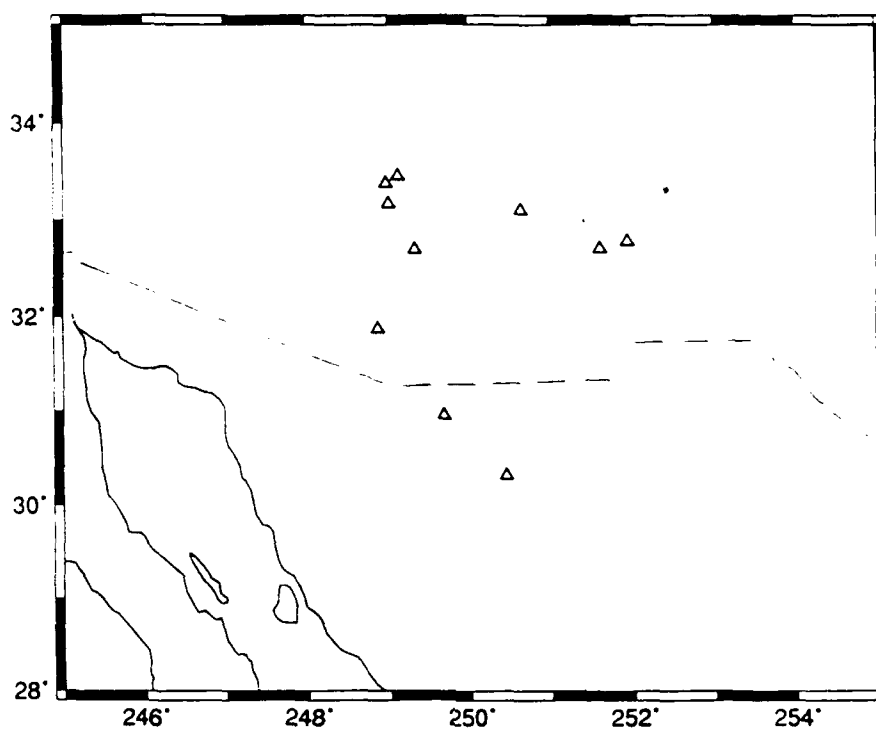
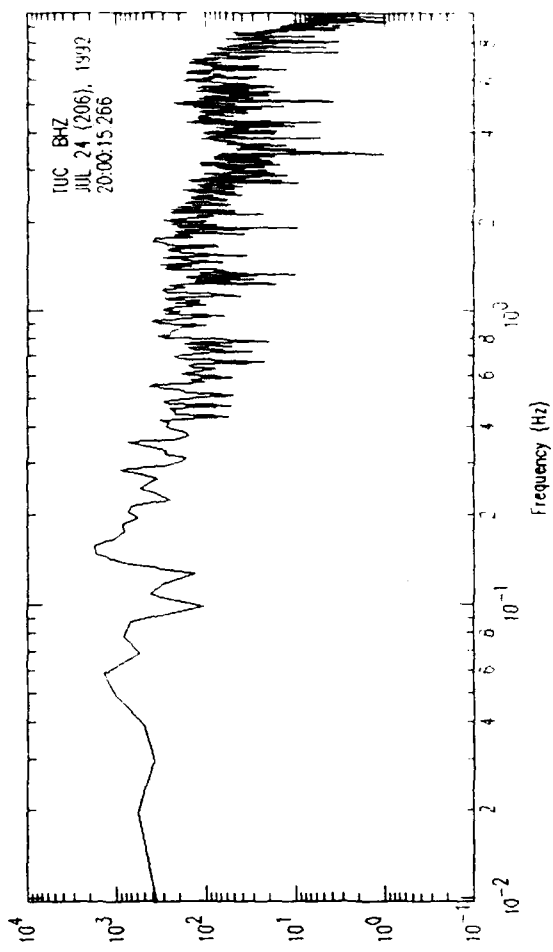
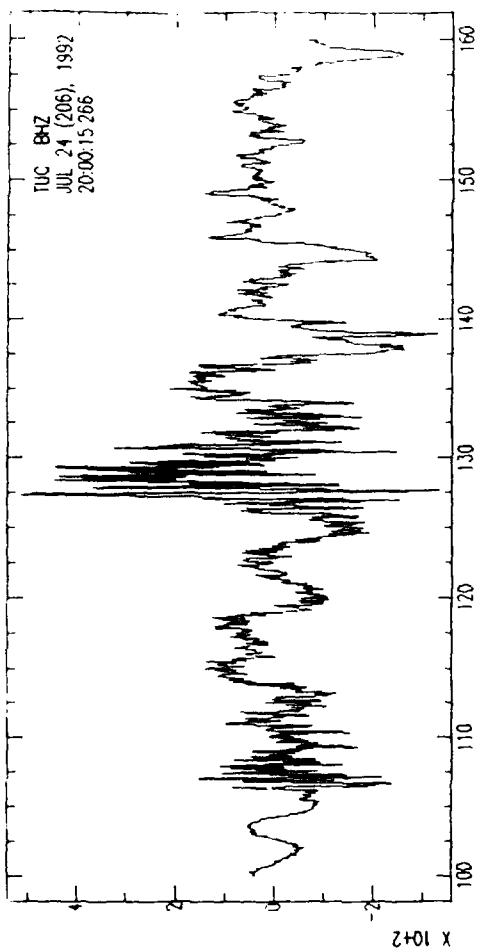
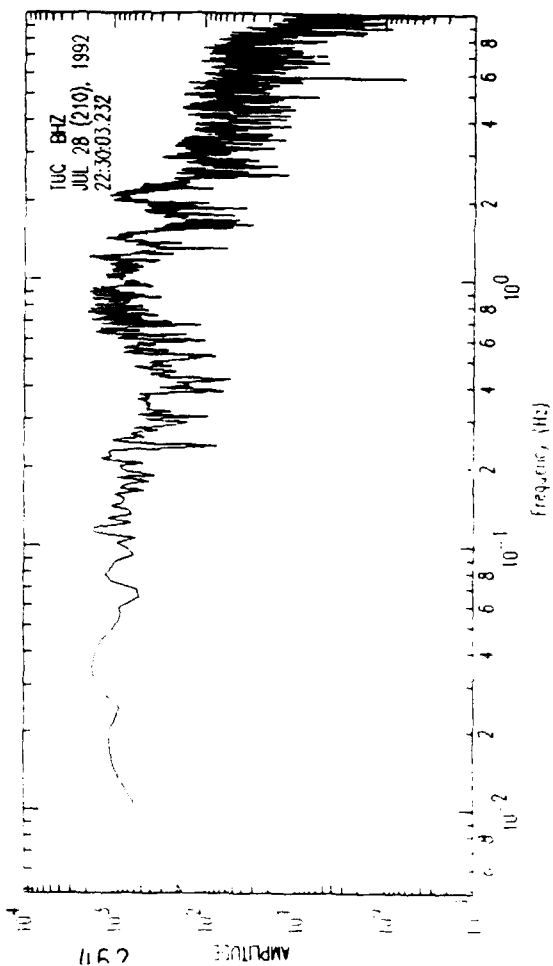
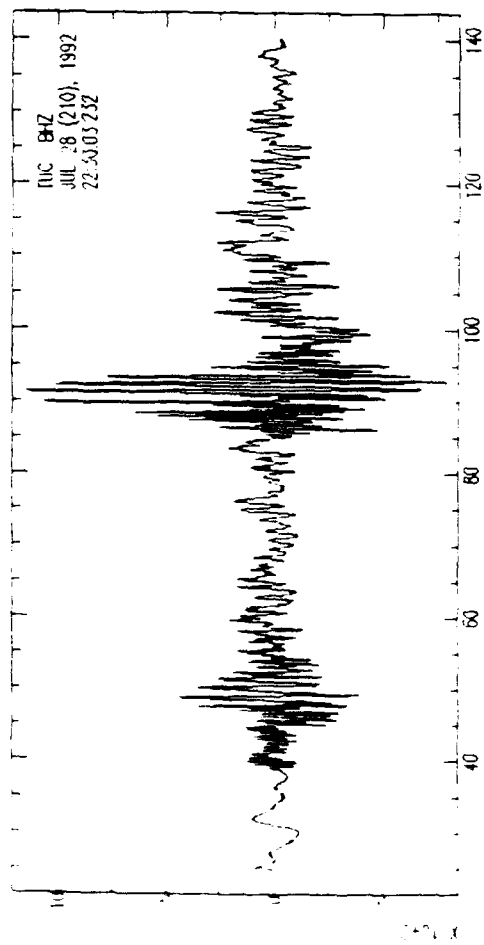


Table 1: Source Locations in the Southwestern U.S.

| Source Name | Lat | Long | Elevation | M _L |
|--------------|-----------|------------|-----------|----------------|
| Cananea | 30 57.606 | 110 19.560 | 1700 | 2.4 |
| Chino Pit | 32 47.432 | 108 4.149 | 2000 | 2.6 |
| Morenci | 33 6.396 | 109 21.420 | 1311 | 2.4 |
| Nacozari | 30 19.600 | 109 33.000 | 1000 | 2.1 |
| Pinto Valley | 33 27.360 | 110 53.250 | 1341 | 2.3 |
| Live Oak | 33 23.160 | 111 2.292 | 1280 | 2.2 |
| Ray | 33 10.440 | 111 0.000 | 610 | 2.2 |
| San Manuel | 32 41.831 | 110 41.131 | 914 | 2.7 |
| Sierrita | 31 52.196 | 111 8.431 | 1219 | 2.1 |
| Tyrone | 32 42.576 | 108 24.127 | 1829 | 2.6 |



$M_L:M_0$ as a Regional Seismic Discriminant

BRADLEY B. WOODS, SHARON KEDAR AND DONALD V. HELMBERGER

CALIFORNIA INSTITUTE OF TECHNOLOGY

CONTRACT No. F19628-90-K-0049

INTRODUCTION

Objective: Our primary objective is to develop techniques for source discrimination and source strength estimation for small events. To retrieve this information requires working with regional phases.

Results: Two significant advances in observational seismology have occurred since investigations of explosions using surface waves during the seventies. One is the large-scale upgrade and augmentation of seismic networks with broadband, high dynamic range instruments. The other is the increased sophistication in source parameterization of earthquakes and explosions, in particular moment tensor solutions, which more precisely quantify seismic sources. Moment is a measure of the long-period excitation of the source. With several three component, broadband stations it is feasible to invert for the source function using regional body waves (Dreger & Helmberger, 1991) or surface waves (Yelin and Patton, 1990), (Kanmori and Given, 1980), (Thio and Kanamori, 1992). M_0 should better reflect the long-period source characteristics of a source than does M_s , so that its use should improve the long-period vs. short-period discriminant.

We re-examine the utility of long-period vs. short-period energy measures in the context of regional seismic records. The study area is shown in fig. 1. It includes central and southern California, western Nevada and the northern Baja, Mexico. Events shown in this paper are marked with stars. This region is unique in that there is a large amount of natural seismicity, as well that from the Nevada Testing Site (NTS). A large number of seismic networks monitor and record seismicity throughout the region, creating a large amount of data useful for this study.

With M_0 serving as a long-period energy measure, we employ local magnitude, M_L , (Richter, 1935 & 1958) as a measure of short-period energy. The classical M_L is computed from the peak horizontal displacements on a Wood-Anderson torsion instrument, which is a high pass filter peaked around 1.0 second. Teleseismic P-wave phases measured to determine body-wave magnitudes are typically of the same period, so that the peak 1 second energy should be a good measure of the short-period source spectrum. There are several advantages of using M_L . One is that it is a simple measurement to make and is easy to obtain to to very small magnitudes. Secondly, it is a routine source quantification used by many seismic networks. We will make use of M_L magnitudes from several network catalogs.

From visual inspection of broadband recordings of regional earthquakes and explosions it is apparent that these two type of source show distinctly different spectral content. Fig. 2 compares records of Kearsarge, a Pahute event of 150 Kt ($m_b = 5.5$), to two earthquakes: Lee Vining (10/24/90, $m_b = 5.0$) and Yucca Mountain (6/29/92, $m_b = 5.7$). The three events, all recorded, at PAS are roughly the same distance away (see fig. 1). For each event the record is played out with a Press-Ewing 30-90 (PE-3090) long-period instrument (top trace), as broadband displacement (middle trace), and with a Wood-Anderson short-period (WA-SP) instrument (bottom trace). Peak amplitudes are given to the right of each trace.

For Kearsarge the ratio of peak long-period to short-period amplitude is 3.08, 3.78 and 1.60 for the vertical, radial and tangential component, respectively. On the long-period tangential component no fundamental Love wave is apparent; only later arriving, higher frequency, higher mode phases believed to be multi-pathing are evident. This, too is evidence of an isotropic source. For Lee Vining the ratio of peak long-period to short-period amplitude is 6.59, 4.48 and 4.76 for the vertical, radial and tangential components. The tangential component also has a large fundamental mode Love wave. For Yucca Mountain the ratio of peak long-period to short-period amplitude is 22.18, 23.08 and 11.47 for the vertical, radial and tangential components. Again a large Love wave is observed.

Fig. 3 shows an analogous plot of seismograms recorded at Goldstone (GSC) for the explosion Bexar ($m_b = 5.6$), located very close to the Kearsarge shot point, and the two previous earthquakes. Again for the explosion no long-period Love wave is observable on the tangential component; only high frequency multi-path surface waves are visible. The ratio of peak long-period to short-period amplitude for Bexar is 2.64, 1.26 and 1.26 for vertical, radial and tangential component, respectively. For Lee Vining the ratio of peak long-period to short-period amplitude is 4.52, 5.28 and 14.40 for the vertical, radial and tangential components. For Yucca Mountain the respective ratios are 10.11, 2.54 and 2.20.

These sets of records corroborate the observation that explosions are richer in short-period energy relative to long-period energy, compared to earthquakes. We shall show that this spectral difference is even more evident when path effects, such as attenuation, are accounted for, and can be used as an effective regional discriminant.

We compiled seismic moments (M_0) and local magnitudes (M_L) for explosions at NTS, earthquakes throughout central and southern California, western Nevada and northern Baja California, Mexico. A number of sources were used for both magnitude types. M_L values are taken from the CIT catalog, the Lawrence Livermore Array (Peppin and McEvilly, 1974), the Northwestern Mexico Seismic Network (Vidal and Munguia, 1991). For recent events (1991-1992) in Nevada and the California-Nevada Border region, M_L 's were determined from the array of eight broadband stations shown in Fig. 1. To calculate these M_L 's, an attenuation curve developed by Kanamori *et al* (1992) was used.

Whereas the M_L 's used are all determined in essentially the same fashion, the seismic moments used were determined through a variety of means. Moments determined from time domain body-wave inversions were taken from Dreger and Helmberger (1990 and 1991) and Ma and Kanamori (1991). Time domain moments determined by forward modelling and comparative amplitude ratios are obtained from Bent and Helmberger, (1991). The moments from Baja California events were determined from body-wave low-frequency spectral levels by Vidal and Munguia, (1991) after Brune (1970, 1971).

Surface wave moments were obtained from a variety of sources. Time domain moments determined from the peak to peak amplitude (PPA) of the dominant Airy Phase of the Rayleigh wave are taken from Woods and Harkrider, (1992). The moment is determined from the ratio of the observed record's PPA to that of a synthetic seismogram with a given input moment. Fig. 4 plots comparisons of vertical waveform fits for the 55 station network used in the study; the top, darker trace is the data. It can be seen that the surface wave waveforms are well fit.

Surface wave spectral moments were also used. Thio and Kanamori (1992), obtained source parameters from the broadband TERRAScope network for earthquakes throughout southern California for a wide range of magnitudes. Their inversion uses both Rayleigh wave and Love wave spectra and employs the technique of Kanamori and Given, (1981). Stevens (1986) determined spectral moments from Rayleigh waves for large NTS explosions. Many of the path structures determined in his study were used to generate the synthetics shown in Fig. 4. Given and Mellman (1986) performed spectral moment tensor inversions of large NTS blasts, too. In their study they included Love wave spectra and inverted the data for the isotropic source as well as a double couple source associated with tectonic release. The data sets for these last two studies overlap substantially. The moment values were found to be similar, so that for events for which two moments were available, the Stevens' (1986) moment was used.

Fig. 5 displays M_L vs. log Moment (N-M) plotted for 173 earthquakes and 128 explosions. Earthquake points are plotted as shaded-in symbols. Circles represent data taken from broadband studies using TERRAScope data and include the studies by Thio and Kanamori (1992), Dreger and Helmberger (1990 and 1991), and Ma and Kanamori (1991). All other earthquakes are marked by a solid triangle. Explosions are denoted by open symbols which correspond to the three studies of NTS explosions cited previously. Two striking features stand-out on this plot. One is how well this discriminant appears to work. There is a significant separation of earthquakes and explosions with this discriminant, with no real overlap of the two populations, although several earthquakes do near the region where explosions plot.

This discriminant also works at all scale sizes. Whereas some researchers have reported that at low magnitudes the two populations converge with respect to their $m_b:M_0$ ratio, it appears that explosions and

earthquakes follow their respective scaling laws over wide range of magnitudes and moments; for earthquakes this is true over seven and a half orders of magnitude. It should be noted that the earthquakes with a log moment below 13.0 were determined from local stations ($D < 75$ km) and would not be detectable at regional distances. They are included here only to show the continuity of the linear scaling relationship between M_L and log Moment for earthquakes. It is important to note when looking at this plot that the data are taken from a number of sources. M_L 's were determined from different networks and the moments were calculated in a variety of ways. Yet we obtain this distinct separation of the two populations.

CONCLUSION

The $M_L:M_0$ criterion is a robust method to discriminant regional seismic events. M_0 can be determined in many different ways, some of which require only sparse broadband networks. One disadvantage to determining moments is that most methods require accurate Green's functions in order to obtain accurate moments. Recent studies modeling regional phases show that this needn't be a tedious problem. M_L is one of the simplest quantifications of an earthquake or explosion to obtain. Because both these source parameters can be obtained from a sparse broadband network, this discriminant can be applied throughout the world as more broadband stations similar to those of the IRIS network come on line. This discriminant is limited by the detection threshold capability of long-period data. This level turns out to be at the $M_L > 3.6$ for explosions and $M_L > 3.1$ for earthquakes.

Fig. 6 shows the Yucca Flat blast Floyd data recorded at four TERRAscope stations and played-out with PE-90 and WA-SP instruments. Note the amplitudes; for the actual analog instruments these signal would not be detectable. M_L for this event is 4.0 and its log moment is 14.20. Assuming it is a shallow explosion above the water table, the yield can be inferred to be less than 10 Kt from the moment-yield scaling relationships determined for NTS by Woods and Harkrider (1992). Were it detonated in hard rock below the water table, it would correspond to a two kiloton explosion. We estimate that were this event 2.5 times lower in yield it would still be possible to obtain its moment.

Above the yield thresholds described in the last paragraph, this discriminant would work well as a companion test, or check, for other, high-frequency, discrimination methods, particularly for events in the $4.0 < m_b < 5.0$ for which teleseismic methods no longer work.

REFERENCES

- Bent, A. L. and D. V. Helmberger, 1991. A Re-examination of Historic Earthquakes in the San Jacinto Fault Zone, California. *Bull. Seism. Soc. Am.*, 81, 2289-2309.
- Brune, J. N., 1970. Tectonic Stress and the Spectra of seismic Shear Waves from Earthquakes, *J. Geophys. Res.*, 75, 4997-5009.
- Dreger, D. S. & D. V. Helmberger, 1990. Broadband Modeling of Local Earthquakes, *Bull. Seism. Soc. Am.*, 80, 1162-1179.
- Dreger, D. S. & D. V. Helmberger, 1991. Source Parameters of the Sierra Madre Earthquake from Regional and Local Body Waves, *Geophys. Res. Lett.*, 18, 2015-2018.
- Evernden, J. F., W. J. Best, P. W. Pomeroy, T. V. McEvilly, J. M. Savino and L. R. Sykes, 1971. Discrimination between Small-Magnitude Earthquakes and Explosions, *J. Geophys. Res.*, 76, 8042-8055.
- Given, J.W. and G.R. Mellman, 1986. Estimating Explosion and Tectonic Release Source Parameters

of Underground Nuclear Explosions from Rayleigh and Love Wave Observations, *DARPA Report AFGL-TR-86-0171*, **ADB110040**

Kanamori, H. & J. W. Given, 1981. Source Parameters Determined from Long Period Surface Waves, *Phys. Earth Planet. Int.*, **11**, 312-332.

Lambert, D. G. & S. S. Alexander, 1971. Relationship of Body and Surface Wave Magnitudes for Small Earthquakes and Explosions, *Final AFTAC Report VELA T/2706*, *Teledyne Geotech.*

Liebermann, C. R. & Pomeroy, P. W., 1969. Relative Excitation of Surface Waves by Earthquakes and Underground Explosions, *J. Geophys. Res.*, **74**, 1575-1590.

Ma, K. F. and H. Kanamori, 1991. Aftershock sequence of the 3 December 1988 Pasadena Earthquake, *Bull. Seism. Soc. Am.*, **81**, 2310-2319.

Peppin, W.A. and T.V. McEvilly, 1974. Discrimination among Small Magnitude Events on Nevada Test Site, *Geophys. J. R. astr. Soc.*, **37**, 227-243.

Schlittenhardt, J., 1988. Seismic Yield Estimation Using Teleseismic P- and PKP-waves Recorded at the GRF-(Gräfenberg) array, *Geophys. J. Int.*, **95**, 163-179.

Stevens, J. L., 1986. Estimation of Scalar Moments from Explosion-Generated Surface Waves, *Bull. Seism. Soc. Am.*, **76**, 123-151.

Thio, H. K. & H. Kanamori, 1992. Source Parameters for a Slew of Events Using TERRAScope DATA, *to be published*.

Vidal, A. and L. Munguia, 1991. Local Magnitude and Source Parameters for Earthquakes in the Peninsular Ranges of Baja California, Mexico, *Bull. Seism. Soc. Am.*, **81**, 2254-2267.

Woods, B. B. and Harkrider, D. G., 1992. Determining Surface Wave Magnitudes from Regional NTS Data, *submitted to Geophys. J. Int.*.

Yelin, T.S. and H.J. Patton, 1991. Seismotectonics of the Portland, Oregon Region, *Bull. Seism. Soc. Am.*, **81**, 109-130.

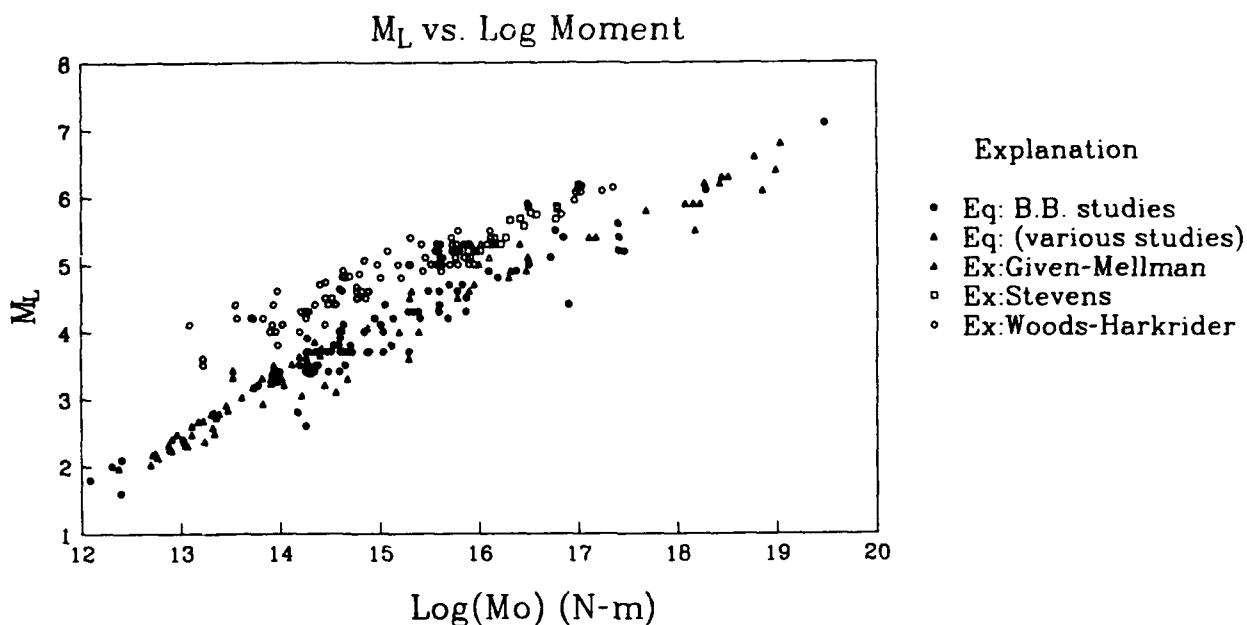


Figure 5. M_L vs. $\log M_0$ for 173 earthquakes and 128 explosions.

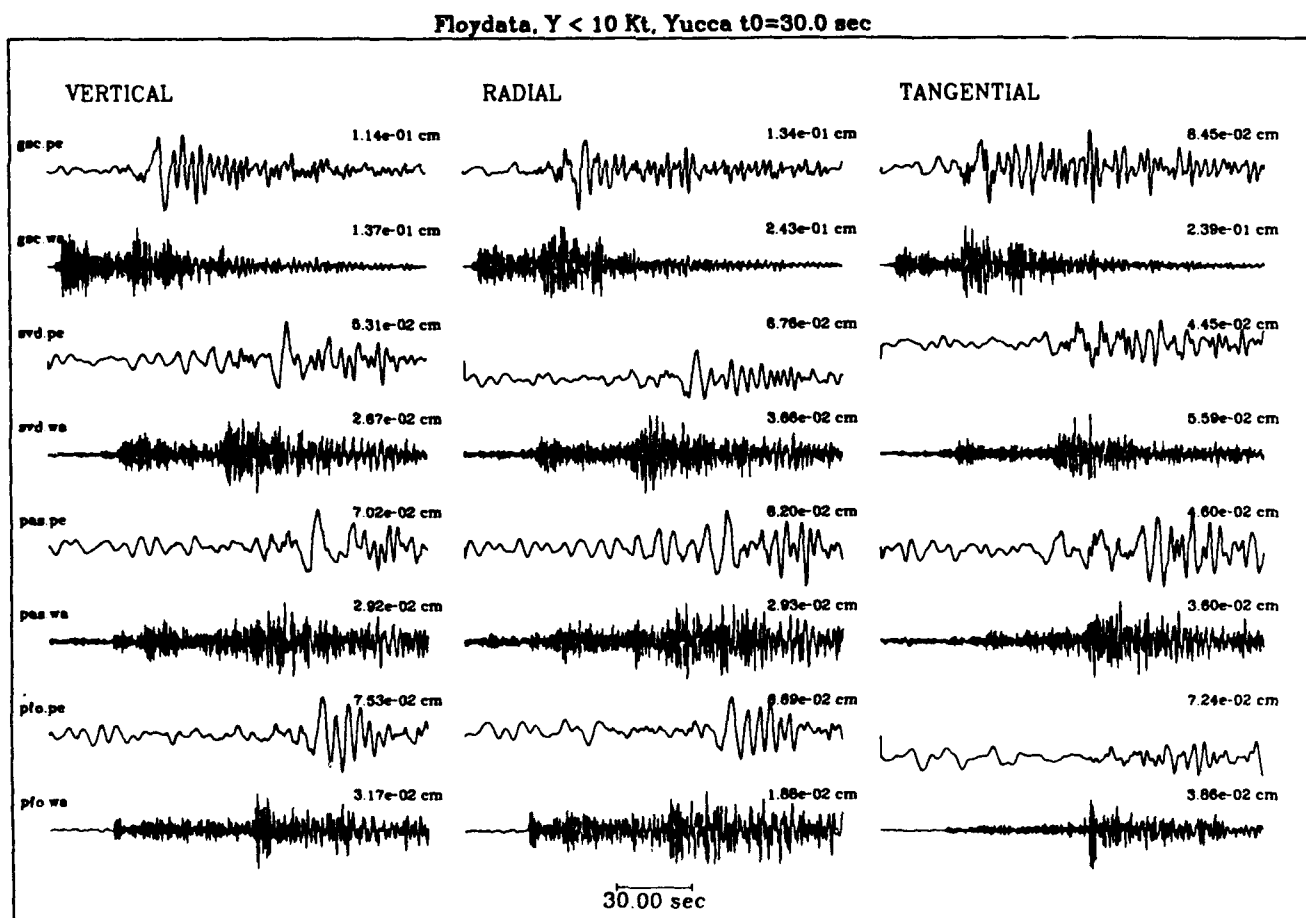


Figure 6. A small Yucca Flat explosion Floyd data recorded at TERRAscope stations and played out on Press-Ewing and Wood-Anderson instruments.

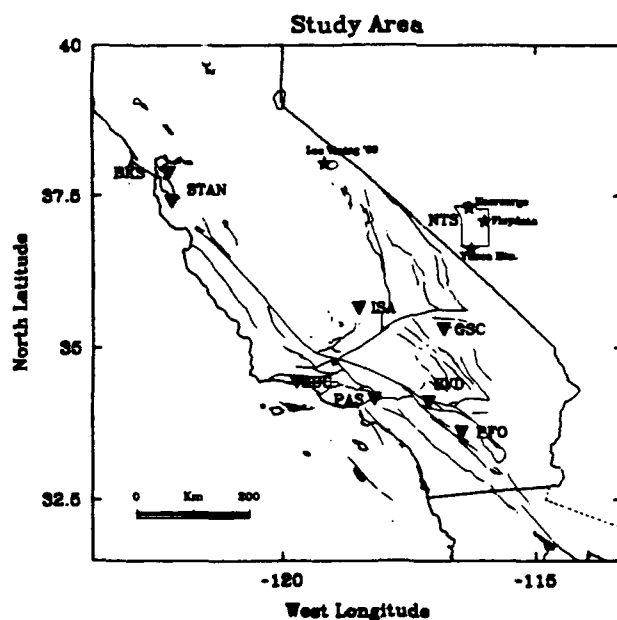


Figure 1. Map showing the study area. Broadband stations are shown with triangles, events shown in this report are denoted by stars.

Kearsarge, Lee Vining and Yucca Mtn at PAS

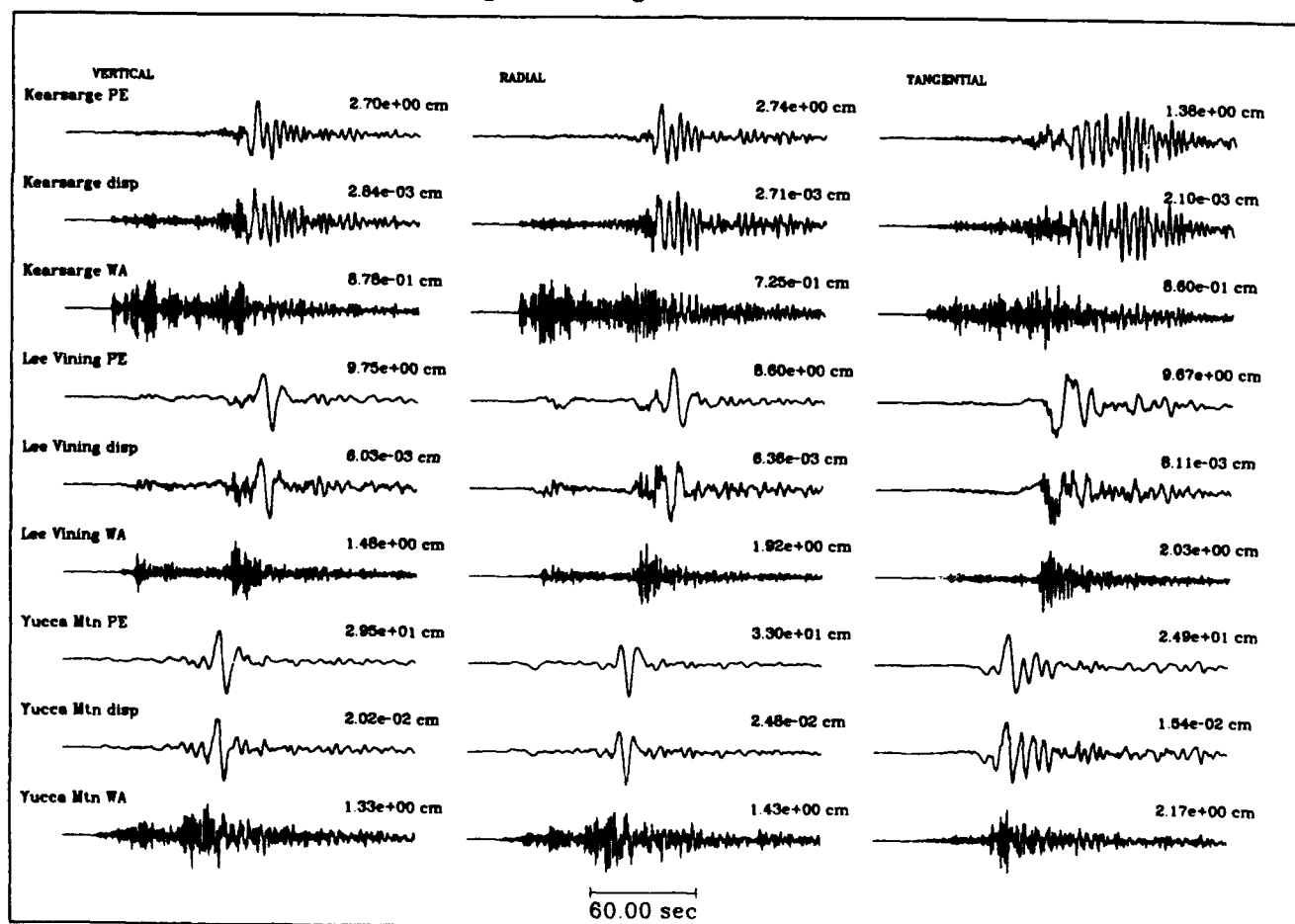


Figure 2. Broadband records of Kearsarge and two earthquakes, recorded at PAS and played out with long-period and short-period instruments.

Bexar, Lee Vining and Yucca Mtn at GSC

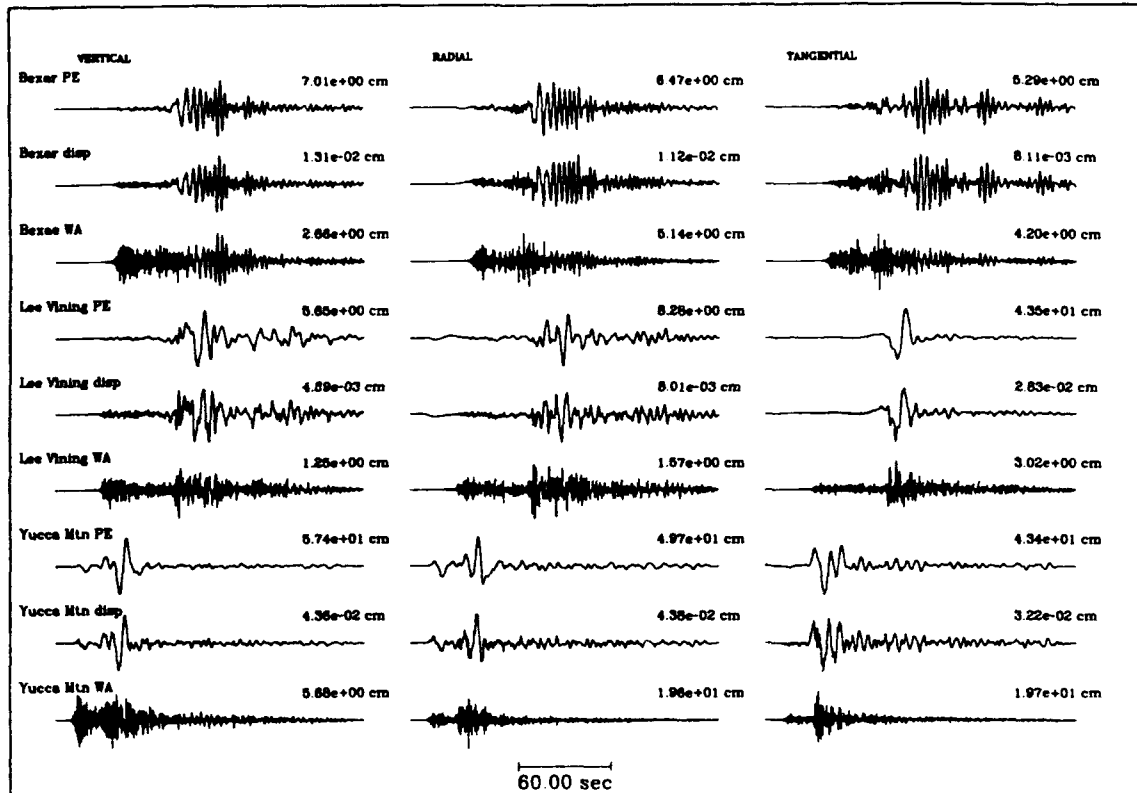


Figure 3. Broadband records of Bexar and two earthquakes, recorded at GSC and played out with long-period and short-period instruments.

Data vs. Synthetic (vertical component)

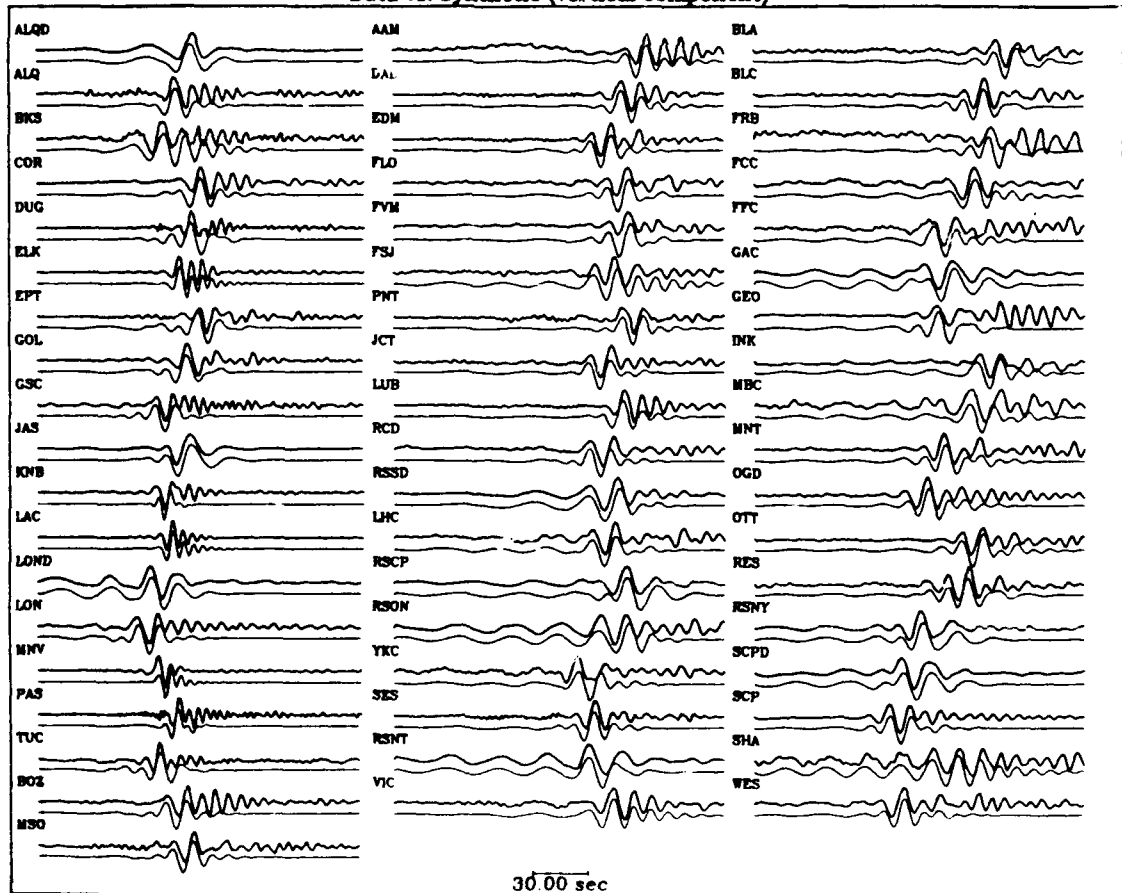


Figure 4. Comparison of synthetic and real fundamental Rayleigh waves for a regional network from which seismic moments are determined. The data are the upper, darker traces.

Tomography of China using surface waves from CDSN

Francis T. Wu

Anatoli Levshin

Department of Geological Sciences
State University of New York
Binghamton, New York 13902-6000

Intern. Inst. of Earthquake Prediction Theory
and Mathematical Geophysics
Russian Academy of Sciences
Moscow, Russia

Contract NO: F1962890K0042

OBJECTIVE

The project aims at deciphering the crustal structures in China and eastern Asia using data from the Chinese Digital Seismic Network (CDSN) stations. We have completed a regionalized surface wave group velocity analyses for China (Wu, 1989; Wu and Barker, 1992). In those studies, China was divided into many regions based on tectonic characteristics, surface geology, the Bouguer anomaly map (Fig. 1) and known crustal structures. As is commonly acknowledged, the result of regionalization studies may be biased because of these a priori assumptions. As a complement to the regionalized study, we have subjected the same data to a tomographic inversion. In contrast to the regionalization, tomographic inversion does not require assumptions concerning the lateral variations of seismic velocities. The objectives of the current study are to provide an image of a vast continental area in terms of apparent seismic velocity distribution, and to provide a check on the soundness of the choice of regionalization schemes.

RESEARCH ACCOMPLISHMENT

Overview

The dispersion curves from earlier studies (Wu 1989; Wu and Barker, 1992) were augmented with data from Taiwan events that were not included in earlier dataset. With this additional data, southeastern China is covered by enough paths to resolve the velocities there. The tomography is performed using a program written by Ditmar and Yanovskaya (1987).

Data

Figure 1 shows the location of the 69 events and the CDSN stations. Because of the wide dynamic range of the CDSN seismic system, although the records stay on scale for magnitude 7 earthquakes, surface waves from $M_s \sim 4.3$ can be used to determine group velocities in the 20-70 second range. The use of small earthquakes actually is beneficial in that group velocities from large events at regional distances may be affected by rupture propagation (Press et al., 1961; Wu, 1992). The 69 events used in this study are located within and around the study area (Fig. 1), yielding altogether more than 200 Love and Rayleigh dispersion curves. The group velocity dispersion curves are determined with an interactive multiple filter group velocity program on workstations, allowing rapid group velocity determination and visual quality control.

Surface wave tomographic methodology

The method used in this study is described in detail in Keilis-Borok (1989). It is based on the formalism of Backus and Gilbert (Ditmar and Yanovskaya, 1987).

The first step involves the transformation of spherical coordinates θ, ϕ to that of x, y . The resulting integral equation:

$$t_j = \int_{(x_j, y_j)}^{(x_{0j}, y_{0j})} V^{-1}(x, y) ds$$

is solved using the group travel times between source and the station pairs (x_{0j}, y_{0j}) and (x_j, y_j) .

Resolution

The resolution of the tomographic inversion is shown in Figure 2. It depends on the path coverage and is a rather conservative estimate of the spatial resolution of the method Keilis-Borok (1989). In areas where the path coverage is poor, the spatial resolution falls off sharply.

Main features in the tomographic images at different periods and their tectonic significance

The tomographic analysis was performed for both Love and Rayleigh waves at the periods of 20 to 70 at 10 second interval. During the Seismic Research Symposium, all results will be shown. In this paper, we shall only present figures showing images of group velocities at 20 and 60 seconds for Rayleigh and Love waves, but we shall describe the main features seen in all the images obtained. It is to be expected that most of the details clearly displayed in color images are not visible in gray-scale images.

The dominant feature in China, in term of lateral group velocity variation, is that for 40 seconds or longer period Love waves and 30 seconds or longer Rayleigh wave, the values are higher in eastern China than in western China. The readily recognizable features are described below.

(1) The most impressive feature in the images for periods longer than 40 seconds in the case of Love waves (Fig. 4) and longer than 30 seconds in the case of Rayleigh waves (Fig. 6) is the group velocity low in the Tibetan region (centered around 35°N and 90°E). The low coincides with the large low in Bouguer gravity anomalies as shown in Fig. 1. The group velocity gradient on the eastern and northern sides of the plateau is quite high, reflecting the sudden change in crustal thickness. This low is seen clearly at 70 seconds. Since the crustal thickness under the plateau is known to be about 70 km, our results are not surprising, but the fact that the plateau is delineated so clearly reflects the power of surface wave tomography. At 20 seconds, the group velocities are relatively high in the plateau area; the velocities at shallow depth are not particularly low in comparison to other areas.

(2) At periods shorter than 30 seconds, a clear low for both Rayleigh and Love wave group velocities exists in eastern China with its center at 30°N and 120°E, southeast of station BJI, extending out to the area behind the Okinawa Trench (Fig. 3 and Fig. 5). At longer periods, the contrast in group velocities with the surrounding areas diminishes and the center moves toward the east (Figs. 4 and 6). This low is most probably associated with deep sedimentary basins in that area.

(3) The Tianshan area west of the Lop Nor Test Site (LNTS) is generally a low velocity area (Figs. 3, 4, 5, and 6), but LNTS itself sits on a high velocity feature. North of LNTS, the Bogda Mountains, is topographically much lower than Tianshan and there are several basins within this mountain chain. The Turfan basin is the largest; it is an east-west elongated basin (with a length of about 700 km), and has an elevation of -154 m. The Bouguer gravity anomalies over the Bogda Mountains relatively high (-130 mgal) comparing to those of the Tianshan (-300 mgal).

(4) Southeastern China, opposite Taiwan, is an area of noticeably high group velocities. This area has extensive outcrops of granitic intrusives. The Bouguer anomalies is lower there than the surrounding regions. The high velocity is evidently associated with the presence of the intrusives.

Acknowledgement

We wish to thank Paul Wessel and W. H. F. Smith for providing excellent software for illustration purposes. Dr. Alan Jones of SUNY Binghamton assisted in various stages of this research.

References

- Ditmar, P.G. and T. B. Yanovskaya, A generalization of the Backus-Gilbert method for estimation of lateral variations of surface wave velocity, *Izv. AN SSSR, Fizika Zemli (Solid Earth)*, no. 6, 30-40, 1987.
- Keilis-Borok, V. I. (ed.), *Seismic Surface Waves in a Laterally Inhomogeneous Earth*, Kluwer Academic Publishers, Dordrecht/Boston/London, 1989.

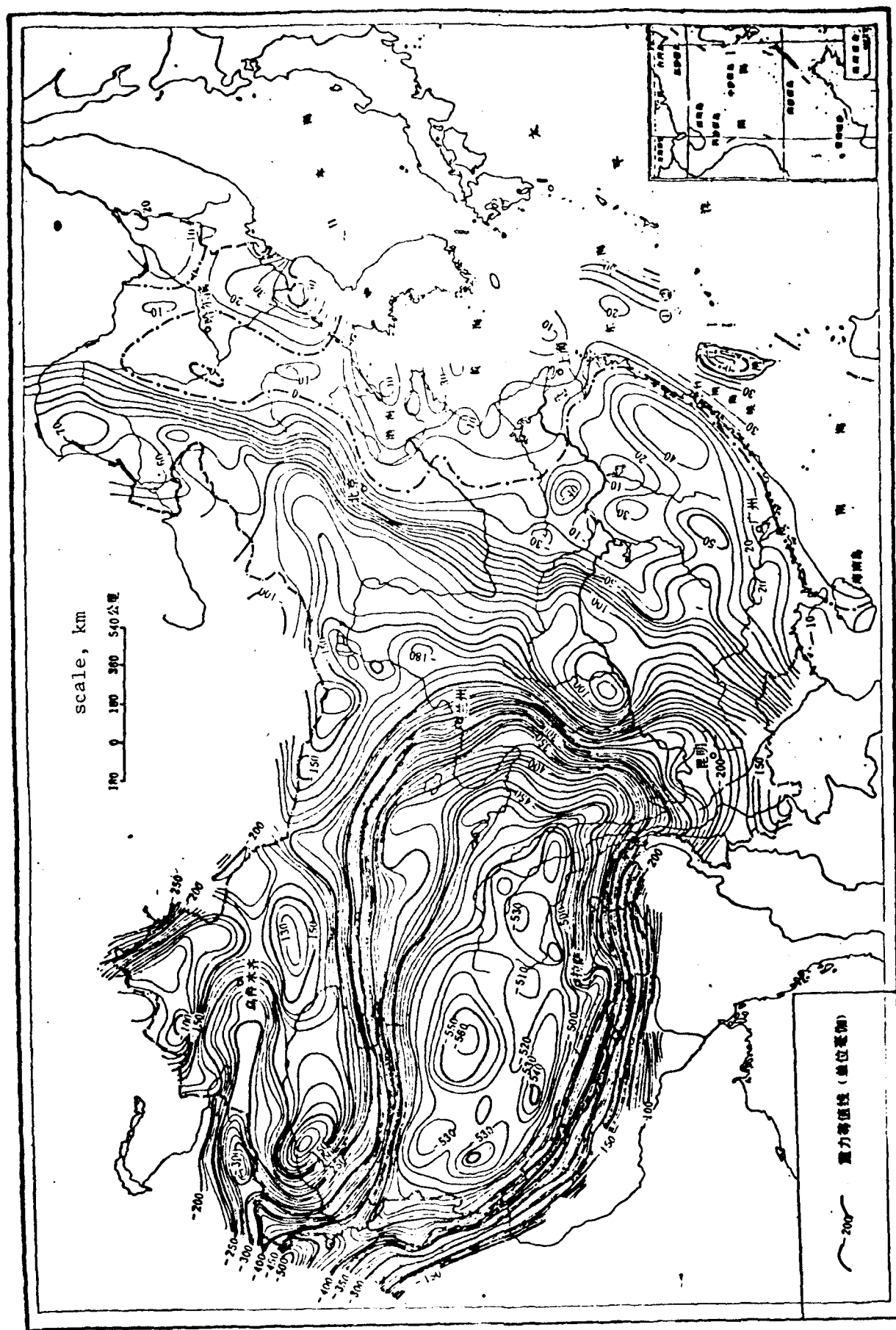


Figure 1. Bouguer gravity anomaly map for China.

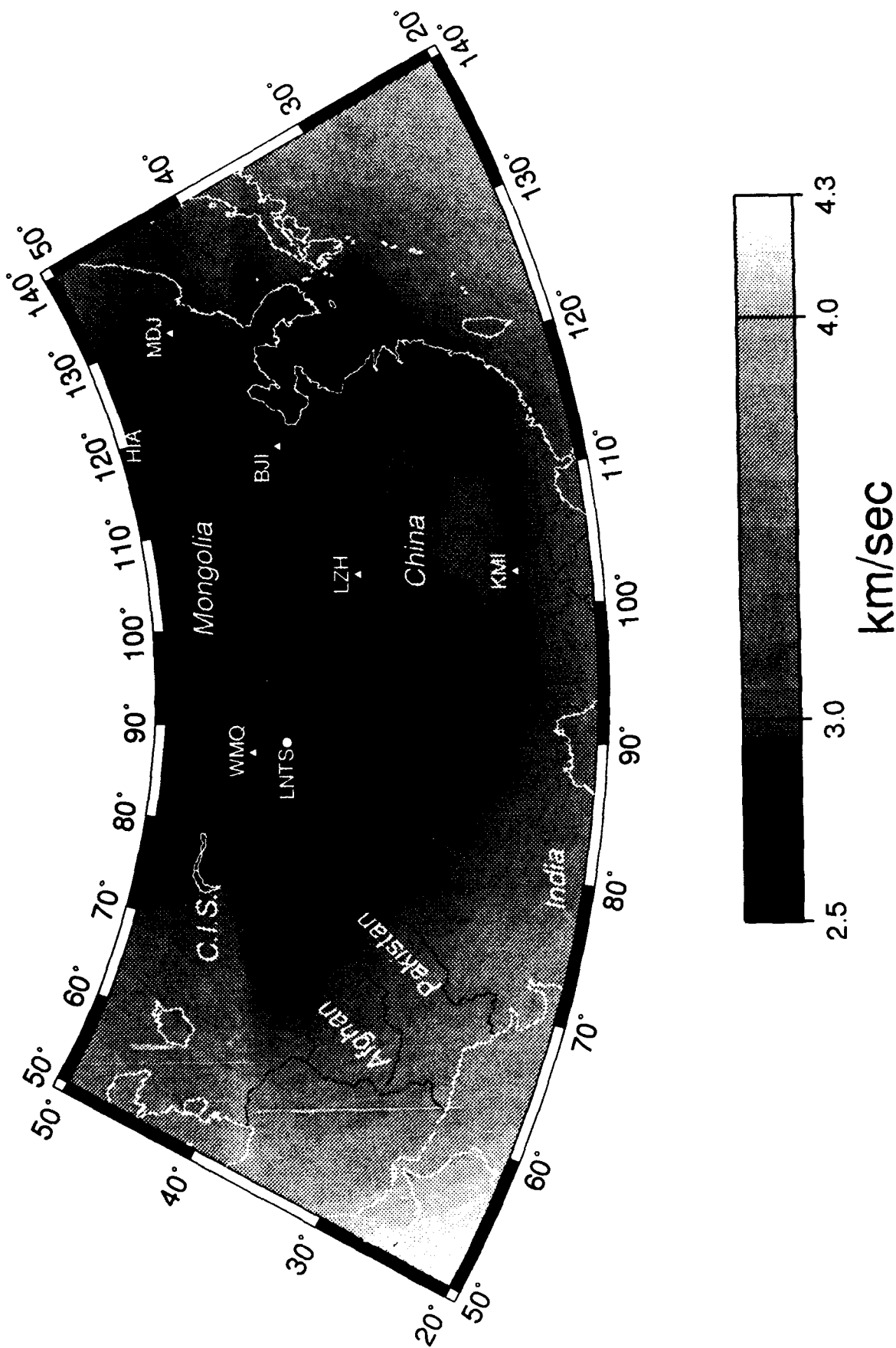


Figure 2. Resolution of the tomographic inversion. The measure is a rather stringent one and the actual spatial resolution is expected to be somewhat better. The resolution depends mostly on the distribution of the wave paths and is nearly the same for different period. The triangles show the locations of the CDSN stations (BJI, MDJ, LZH, KMI and WMQ). LNTS = Lop Nor Test Site. These notations are the same for later figures of tomographic results.

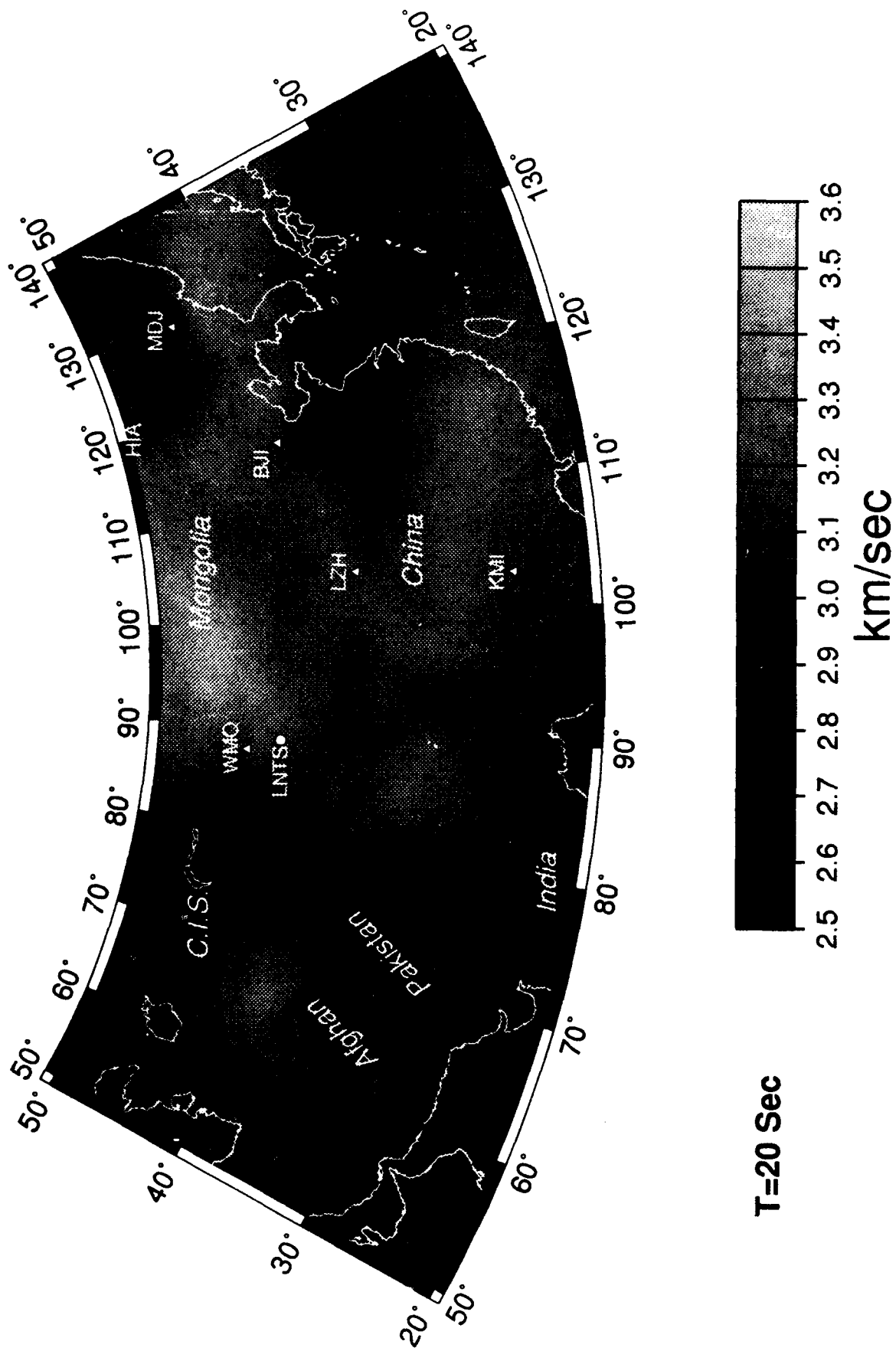


Figure 3. Love wave group velocity tomography for 20 seconds. See figure 2 for symbols.

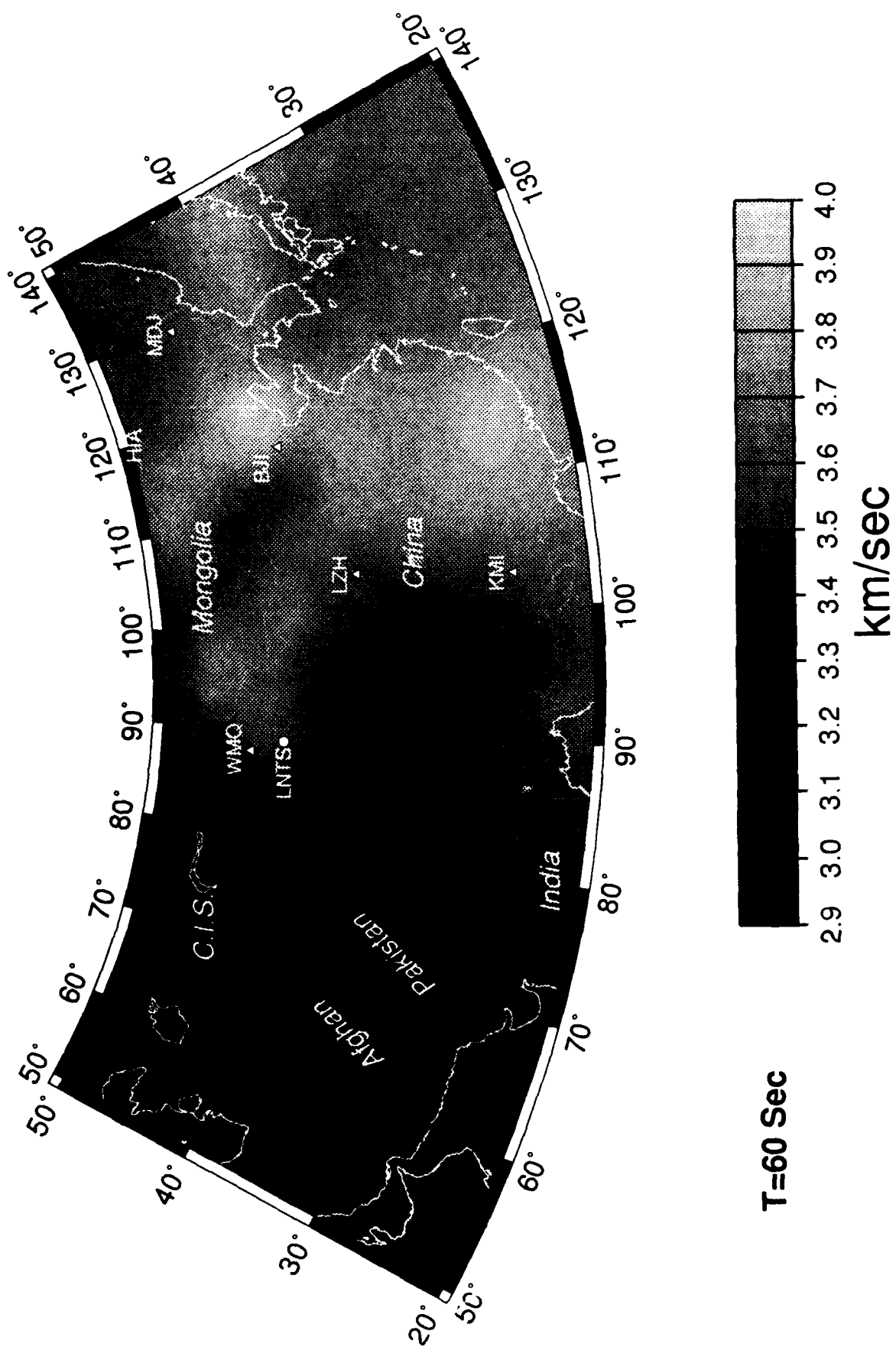


Figure 4. Love wave group velocity tomography for 60 seconds. See figure 2 for symbols.

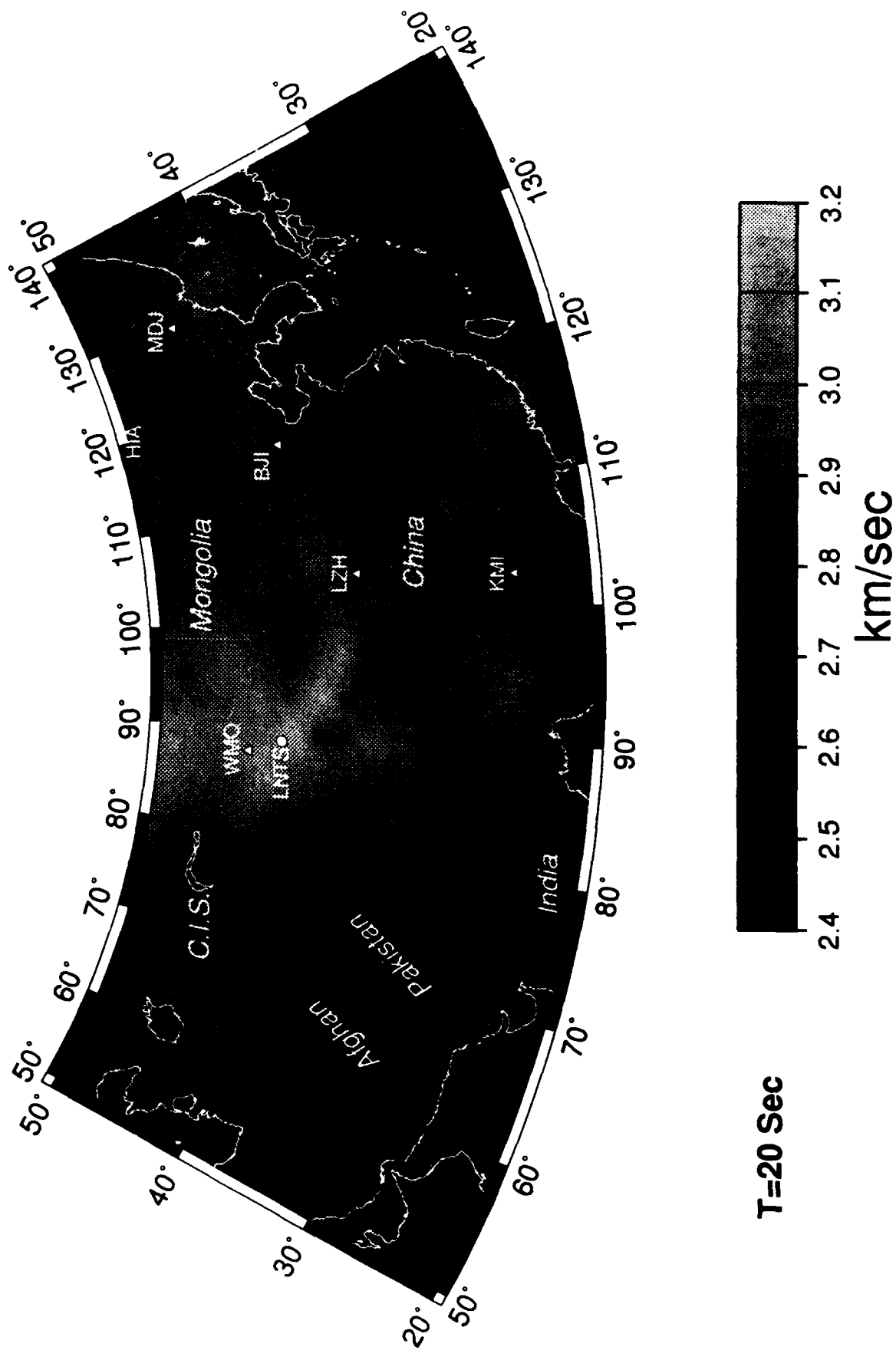


Figure 5. Rayleigh wave group velocity tomography for 20 seconds. See figure 2 for symbols.

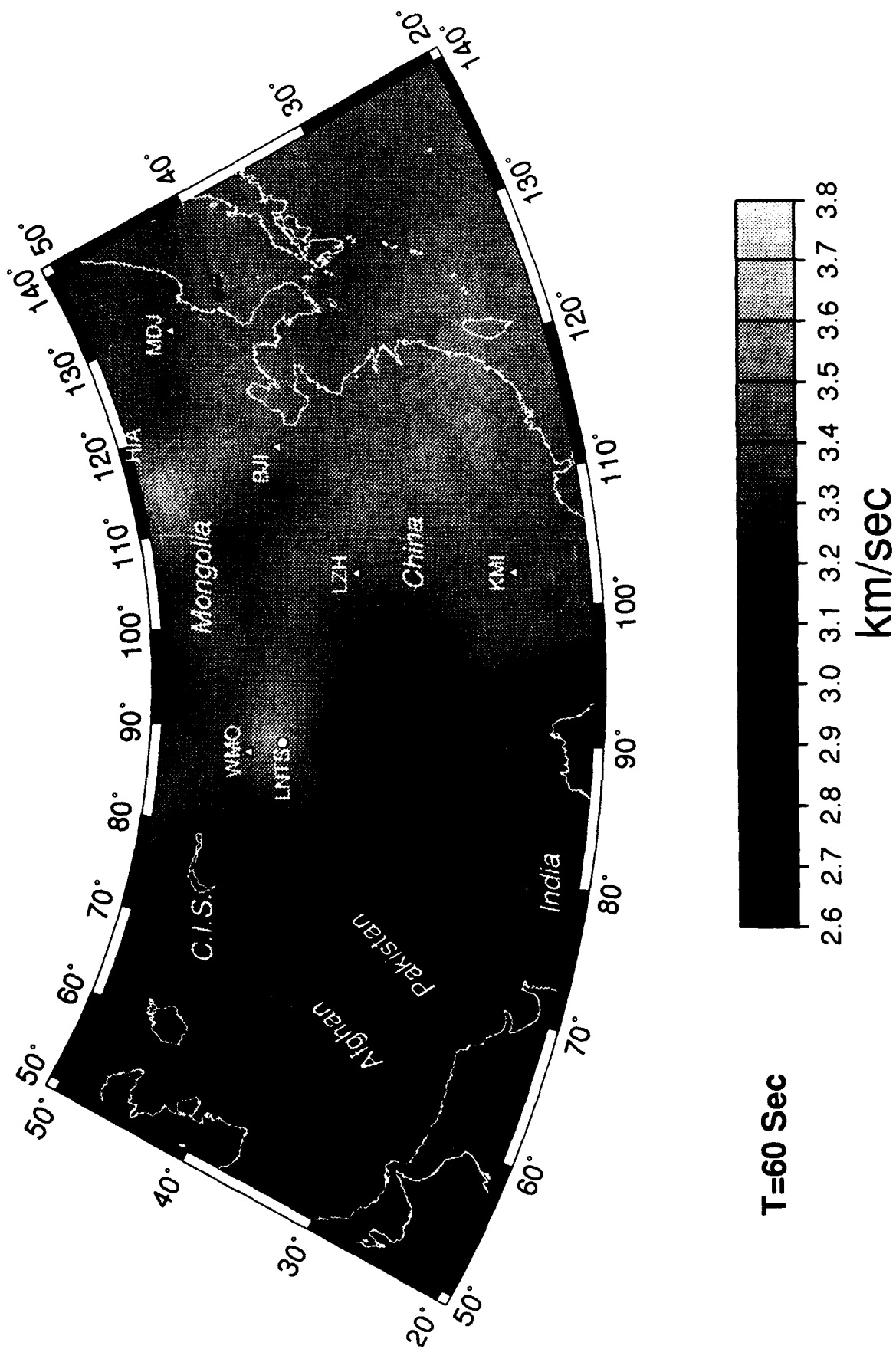


Figure 6. Rayleigh wave group velocity tomography for 60 seconds. See figure 2 for symbols.